

Correlator-based approaches in real and imaginary frequencies

Exact and numerical results for correlated electrons

Anxiang Ge



Munich 2025

Correlator-based approaches in real and imaginary frequencies

Exact and numerical results for correlated electrons

Anxiang Ge

A dissertation submitted
to the Faculty of Physics at the
Ludwig-Maximilians-Universität München
for the degree of
DOCTOR RERUM NATURALIUM



Munich, February 24, 2025

First referee: Prof. Dr. Jan von Delft
Second referee: Prof. Dr. Lode Pollet
Day of submission: February 24, 2025
Day of the oral examination: April 8, 2025

Zusammenfassung

(Summary in German)

Bei stark korrelierten Materialien bricht das Einteilchen-Bild für Elektronen zusammen und faszinierende emergente Phänomene treten zutage. Diese Effekte können durch Korrelationsfunktionen erfasst werden. Für Systeme im thermischen Gleichgewicht gibt es zwei gut etablierte Formalismen. Der Matsubara-Formalismus (MF) baut die Gleichgewichtsbedingung durch eine Wick-Rotation in Korrelatoren ein. Diese verwandelt sie in Funktionen imaginärer Zeiten oder Frequenzen. Während MF-Korrelatoren direkten Zugang zu statischen Größen bieten, erfordern dynamische Observablen eine analytische Fortsetzung auf die reelle Achse, um sie mit experimentellen Ergebnissen vergleichen zu können. Leider ist die analytische Fortsetzung numerischer Daten ein äußerst schlecht konditioniertes Problem. Im Keldysh-Formalismus (KF) sind Korrelatoren Funktionen von reellen Zeiten und Frequenzen, was einen direkten Vergleich mit experimentellen Daten ermöglicht. Dieser Vorteil geht jedoch auf Kosten einer zusätzlichen Indexstruktur und kontinuierlicher Frequenzargumente. Das Hauptziel dieser Arbeit ist, eine Reihe von vielversprechenden Methoden der Quantenfeldtheorie (QFT) voranzutreiben, die im KF mit reellen Frequenzen formuliert sind.

Im ersten Teil stellen wir eine Real- und Imaginärfrequenz-Studie mit zwei verwandten QFT-Methoden vor: die Parquet-Gleichungen und die funktionale Renormierungsgruppe (fRG). Die Vorhersagekraft dieser beiden diagrammatischen Methoden wird typischerweise durch die verwendeten diagrammatischen Trunkierungen beeinträchtigt. In Kombination mit anderen Methoden sind sie jedoch vielversprechende Kandidaten für die Untersuchung von stark korrelierten Systemen. Hier liegt unser Schwerpunkt auf algorithmischen Entwicklungen, für die wir das Anderson-Störstellenmodell als Benchmark-System untersuchen. Die Arbeit im KF (anstelle des MF) führt zu einer Reihe von numerischen Herausforderungen. Daher wurden in früheren Arbeiten typischerweise weitere Approximationen für den Vierpunkt-Vertex oder für die Gleichungen verwendet. Um den Weg für weitere Entwicklungen zu ebnen, zeigen wir hier, dass es in der Tat möglich ist, auf weitere (als die in den Methoden inhärenten) Approximationen zu verzichten. In dem Bereich in welchem konvergierte Parquet-Ergebnisse vorliegen, finden wir eine gute Übereinstimmung mit Referenzdaten aus der numerischen Renormierungsgruppe. Die 1-Loop-Flussgleichungen der fRG liefern zwar Ergebnisse für einen größeren Parameterbereich, aber die Abweichungen sind dafür in der Regel größer als bei den Parquet-Ergebnissen.

Im zweiten Teil gehen wir der Frage nach, wie Matsubara-Korrelatoren analytisch zum KF fortgesetzt werden können. Unsere Arbeit baut auf der Spektraldarstellung auf, die von Kugler, Lee und von Delft hergeleitet wurde. Sie fanden heraus, dass Korrelatoren mit formalismusunabhängigen, systemabhängigen partiellen Spektralfunktionen (PSF) und formalismusabhängigen Kernen aufgebaut werden können. Unter Verwendung ihrer Ergebnisse entwickeln wir eine allgemeine Strategie für die analytische Fortsetzung von Mehrpunkt-Korrelatoren. Wir gewinnen zunächst alle PSFen aus analytischen Fortsetzungen des Matsubara-Korrelators. Wenn wir diese in die spektrale Darstellung von Keldysh-Korrelatoren einsetzen, erhalten wir MF-zu-KF-Fortsetzungsformeln. Ähnlich wie bei den bekannten Zweipunkt-Korrelatoren lassen sich alle Keldysh-Komponenten durch eine Linearkombination analytisch fortgesetzter MF-Korrelatoren mit statistischen Faktoren ausdrücken. Explizite Formeln werden für die wichtigsten Fälle vorgestellt, insbesondere allgemeine Dreipunkt-Korrelatoren und fermionische Vierpunkt-Korrelatoren.

Summary

(Summary in English)

For strongly correlated materials the single-particle picture breaks down for electrons, giving rise to fascinating emergent phenomena. These effects can be captured using correlation functions. For systems in thermal equilibrium, two well-established formalisms are available. The Matsubara formalism (MF) encodes the equilibrium condition into correlators via a Wick rotation, transforming them into functions of imaginary time or frequency. While MF correlators provide direct access to static quantities, dynamic observables require analytic continuation to the real axis to be comparable to experimental results. Unfortunately, despite recent advances, the analytic continuation of numerical data remains a highly ill-conditioned problem. In the Keldysh formalism (KF) correlators are expressed in real time or frequency, allowing direct comparison to experimental data. However, this advantage comes at the cost of an additional index structure and continuous frequency arguments. The main goal of this thesis is to advance a set of promising quantum field theory (QFT) methods which are formulated in the real-frequency KF.

In the first part we present a real- and imaginary-frequency study with two related QFT methods: the parquet equations and the functional renormalization group (fRG). The predictive power of these two methods is typically impaired by the employed diagrammatic truncations. But in combination with other techniques, they hold promise for the study of strongly correlated systems. Here, our focus is on algorithmic developments, using the Anderson impurity model as a benchmark. Working in the KF instead of the MF introduces significant numerical challenges. Hence, previous studies have typically relied on additional approximations to the four-point vertex or to the underlying equations. To pave the way for further extensions, we here show that it is indeed possible to avoid approximations beyond those that are inherent to the methods. In the regime in which converged parquet results are available we find good agreement with reference data from the numerical renormalization group. While the 1-loop flow equations of fRG cover a broader range of parameters, the results generally exhibit larger deviations compared to the parquet method.

In the second part of this thesis we address the problem of analytically continuing Matsubara correlators to the Keldysh formalism. Our approach builds on the spectral representation derived by Kugler, Lee, and von Delft, which expresses correlators in terms of formalism-independent but system-dependent partial spectral functions (PSFs) and formalism-dependent kernels. Using this foundation, we propose a general strategy for the analytic continuation of multi-point correlators. We first extract all PSFs via analytic continuation of the Matsubara correlators. Inserting these into the spectral representation of Keldysh correlators yields explicit MF-to-KF continuation formulas. As with two-point correlators, all Keldysh components can be expressed in terms of linear combinations of analytically continued MF correlators with statistical factors. We provide explicit formulas for the most relevant cases, including general three-point correlators and fermionic four-point correlators.

Publications

This dissertation contains the following journal articles, listed in order of appearance:

- P1** *Multiloop flow equations for single-boson exchange fRG*
 M. Gievers, E. Walter, **A. Ge**, J. von Delft, and F.B. Kugler
 Sec. 3.2 / arXiv:2201.04878 Eur. Phys. J. B, 95, 108 (2022)
- P2** *MatsubaraFunctions.jl: An equilibrium Green's function library in the Julia programming language*
 D. Kiese, **A. Ge**, N. Ritz, J. von Delft, and N. Wentzell
 Sec. 4.4 / arXiv:2309.12511 SciPost Phys. Codebases 24 (2024)
- P3** *Real-frequency quantum field theory applied to the single-impurity Anderson model*
A. Ge, N. Ritz, E. Walter, S. Aguirre, J. von Delft, and F.B. Kugler
 Sec. 4.2 / arXiv:2307.10791 Phys. Rev. B, 109, 115128 (2024)
- P4** *Analytic Continuation of Multipoint Correlation Functions*
A. Ge, J. Halbinger, S.B. Lee, J. von Delft, and F.B. Kugler
 Sec. 5.2 / arXiv:2311.11389 Ann. Phys. 536, 2300504 (2024)
- P5** *KeldyshQFT: A C++ codebase for real-frequency multiloop functional renormalization group and parquet computations of the single-impurity Anderson model*
 N. Ritz, **A. Ge**, E. Walter, S. Aguirre, J. von Delft, and F.B. Kugler
 Sec. 4.3 / arXiv:2405.20996 J. Chem. Phys. 161, 054118 (2024)

Two further publications, not included in this thesis, are currently in preparation:

- P6** *Numerical fulfillment of the $U(1)$ Ward identity and the parquet equations for real-frequency correlation functions from the multipoint numerical renormalization group*
 N. Ritz, **A. Ge**, M. Pelz, J. von Delft, and F.B. Kugler
- P7** *Computing local vertex functions from NRG using Tensor Cross Interpolation*
 M. Frankenbach, **A. Ge**, M. Ritter, N. Ritz, J. von Delft

Acknowledgments

I would like to thank the many people whose support not only helped me navigate the various challenges in the course of my PhD journey, but who turned the past four years into an invaluable and enriching experience.

First and foremost, I am deeply grateful to Jan von Delft for being an exceptional supervisor. None of my projects would have been thinkable without him. He somehow manages to find the golden mean, the perfect balance between giving me the freedom to explore ideas and actively driving progress – whether by asking me the right questions, by connecting me with the right people, or by making sure that I have all needed resources. His passion for teaching is equally admirable as his tireless quest for effective science communication. Beyond guiding our research, he also shows genuine care for everyone’s well-being.

I would also like to extend my sincere thanks to Lode Pollet for co-refereeing this thesis, for his thoughtful guidance as member of my IMPRS thesis advisory board and for introducing me to many-body physics during my Bachelor thesis.

I am deeply indebted to my collaborators whose expertise and teamwork significantly enriched my research. My projects benefited greatly from Fabian Kugler’s profound knowledge of quantum field theory, the foundational work laid by Elias Walter and Santiago Aguirre and the productive collaborations with Nepomuk Ritz, Marcel Gievers, Johannes Halbinger, Dominik Kiese and Seung-Sup Lee.

Overall, I very much enjoyed the pleasant and supportive environment at the chair. The highly motivating atmosphere was complemented by engaging discussions at the mensa – often about physics, but thankfully not always – occasional diversions in *the office* and enjoyable after-work gatherings. All of this is thanks to my incredible colleagues. In addition to those already mentioned, I want to thank Andreas Gleis, Benedikt Schneider, Björn Sbierski, Felipe Picoli, Gün Gunal, Héloïse Albot, Jheng-Wei Li, Jeongmin Shim, Marc Ritter, Markus Frankenbach, Markus Scheb, Mathias Pelz, Ming Huang, Oleksandra Kovalska, Simone Foderà and Toni Guthardt. A special thank you to our ever-cheerful secretary Kathrin Higgen, whose support greatly facilitated our work.

I am also grateful to the IMPRS-QST graduate school and its coordinator, Sonya Gzyl, for providing a structured program to foster our academic growth, as well as for organizing summer schools, workshops and various enriching activities.

My appreciation also goes to Nepomuk Ritz, Marcel Gievers, and Markus Frankenbach for their invaluable feedback on this thesis.

Finally, I am profoundly thankful to my dear friends from both my hometown and Munich for their encouragement, my parents for raising me up and supporting me in every possible way, my siblings for their playful mockery and my girlfriend, Melinda, for her boundless love and belief in me. Being surrounded by such wonderful people gave me the strength to overcome the most challenging times, but also made the bright moments in these past years even more enjoyable.

Contents

Zusammenfassung (Summary in German)	i
Summary (Summary in English)	iii
Publications	v
Acknowledgments	vii
1 Introduction	1
1.1 Motivation	1
1.2 Outline and scope	2
2 Methodological background	5
2.1 Correlators – definition and basic properties	5
2.1.1 Thermal expectation values	6
2.1.2 Matsubara formalism	7
2.1.3 Keldysh formalism	8
2.1.4 Note on conventions	10
2.1.5 Example: Two-point correlators	11
2.1.5.1 Matsubara two-point correlators	11
2.1.5.2 Keldysh two-point correlators	12
2.1.5.3 Notes on analytic continuation	14
2.1.6 Comparison of the formalisms	14
2.2 Diagrammatic language for fermionic theories	15
2.2.1 Green’s functions and observables	15
2.2.2 Green’s functions in the functional integral formulation	17
2.2.3 Diagrammatic representation of one- and two-particle Green’s functions	19
2.2.4 Exact diagrammatic equations	21
2.2.4.1 Parquet theory	21
2.2.4.2 Functional renormalization group	24
2.2.4.3 Approximations	27
2.2.5 The Anderson impurity model and its diagrammatic description . . .	29
2.2.5.1 Symmetries and vertex parametrizations	30
2.2.5.2 Frequency parametrization of the vertex	33
3 Multiloop flow equations for the single-boson exchange decomposition	37
3.1 Overview	37
3.2 Publication: <i>Multiloop flow equations for single-boson exchange fRG</i>	38
3.3 Notes on implementations	61
4 Quantum field-theoretic study of the Anderson impurity model	63
4.1 Overview	63
4.2 Publication: <i>Real-frequency quantum field theory applied to the single-impurity Anderson model</i>	65

4.3	Publication: <i>KeldyshQFT: A C++ codebase for real-frequency multiloop functional renormalization group and parquet computations of the single-impurity Anderson model</i>	90
4.4	Publication: <i>MatsubaraFunctions.jl: An equilibrium Green's function library in the Julia programming language</i>	113
5	Analytic Continuation – Relations between imaginary- and real-frequency functions	149
5.1	Overview	149
5.2	Publication: <i>Analytic Continuation of Multipoint Correlation Functions</i> . . .	150
6	Conclusion and outlook	197
A	Hubbard atom	199
A.1	Asymptotic decomposition	200
A.2	SBE decomposition	201
B	Multiloop convergence in Matsubara and Keldysh formalism	203
	Bibliography	211

1 Introduction

1.1 Motivation

Strongly correlated materials present both opportunities and challenges for the scientific community. On one hand, they exhibit remarkable physical phenomena some of which hold significant technological potential [Ang08]. On the other hand, their theoretical description is notoriously difficult since strong electron correlations render single-particle approximations ineffective. In these materials, the interaction and kinetic energy are comparable, such that electrons are neither fully localized nor fully itinerant. The most prominent discovery on this field is the phenomenon of high-temperature superconductivity which was found for the first time in a class of ceramic materials (cuprates) by Bednorz and Müller 1986 [BM86]. Despite all experimental and theoretical efforts the microscopic mechanisms responsible for the emergence of high-temperature superconductivity are still not fully understood.

The two-dimensional one-band Hubbard model is deemed the ‘minimal’ model for cuprates and has received much attention in the past decades. It is a tight-binding model with a single orbital per lattice site. Electrons can hop between sites and experience Coulomb repulsion only when they occupy the same site. Despite its apparent simplicity, a complete and quantitatively accurate prediction of the physical regimes and observables remains an open challenge.

In the presence of strong correlations exact solutions only exist in certain limits. For example, the Bethe ansatz works for one-dimensional systems [EFG⁺05] and dynamical mean-field theory (DMFT) is exact in the limit of infinite dimensions [GKKR96]. However, many systems of interest are two- or three-dimensional. Indeed, the majority of applicable methods is of numerical nature, each coming with approximations and algorithmic constraints. A multi-method study [SWicv⁺21] recently confirmed that all state-of-the-art methods are limited in their applicability. For example, purely diagrammatic methods are impaired by diagrammatic truncations. And while the DMFT is a powerful method to predict local correlations, spatial fluctuations are beyond reach due to the inherent approximations. However, these limitations may be overcome by combining multiple methods. A promising class of approaches are diagrammatic extensions of DMFT [RHT⁺18] which use input from DMFT and include non-local correlations with diagrammatic techniques.

The common theme of many numerical methods is their focus on correlation functions. These encode interesting, experimentally observable quantities such as the single-particle spectrum, the susceptibility to external perturbations and transport coefficients. Two well-established frameworks are available for studying systems in thermal equilibrium: the Matsubara formalism (MF) [Mat55, Abr65] and the Keldysh formalism (KF) [Sch61, Kel, Kam11]. The MF directly incorporates the equilibrium condition by a Wick rotation $t \rightarrow -i\tau$, such that correlators are functions of imaginary times or frequencies. The KF is more general and also works for systems out of equilibrium. KF correlators are functions of real times and frequencies but have an additional index structure with 2^ℓ Keldysh components for ℓ -point functions. Since the choice of methods is typically guided by the finite amount of numerical resources, correlators are commonly computed in the MF. Using the formal equivalence of MF and KF two-point correlators, dynamic observables are then obtained via analytic continuation to real times or frequencies. However, the analytic continuation of

numerical data is a difficult problem due to the highly ill-conditioned Matsubara kernel, see e.g. Ref. [SOOY17]. To circumvent this issue, our strategy focuses on the development of methods which directly work within the KF.

In fact, real-frequency observables can already be computed for quantum impurity models for which the numerical renormalization group (NRG) [BCP08] is a well-established method. Since impurity solvers play a central role in the DMFT scheme, DMFT can also be implemented in real frequencies. An important recent development was the extension of NRG to the computation of multipoint vertex functions [KLvD21, LKvD21, LHS⁺24] which are needed as input into DMFT extension schemes for including non-local correlations [RVT12].

Building on these advancements, this thesis focuses on the development of quantum field-theoretic (QFT) methods in both real and imaginary frequencies. Specifically, we cover the parquet equations and the functional renormalization group (fRG), which both are promising candidates for diagrammatic extensions of DMFT. While they provide a formally exact framework, approximations are inevitable and require a ‘reasonably’ chosen external input. The viability and consequences of various approximations are still subject of current research. Nevertheless, it is known that these methods can guarantee the fulfillment of the Pauli principle and an unbiased treatment of all interaction channels by construction [Bic04]. For a reliable prediction of the physical regimes in the presence of competing ordering instabilities such properties are highly desirable. However, these approximations may lead to violations of conservation laws (such as charge conservation) which would undermine the quantitative reliability of transport calculations. The degree to which conservation laws are fulfilled gives information on the quality of the obtained results [CGKH⁺22, P6]. Ensuring their fulfillment is, however, not our focus.

1.2 Outline and scope

Below we present the specific problems that are addressed in this thesis; detailed introductions and motivations will be given at the beginning of each section. The remainder of this thesis is structured as follows:

- In Chapter 2, we first give a general introduction to ℓ -point correlators in the MF and KF. We give further details in the chapters in which they are needed. As a specific type of correlator we then introduce Green’s functions and discuss how they encode one- and two-particle quantities. They can be represented in terms of the self-energy and the vertex, which are central objects in the QFT methods which we review thereafter: the parquet equations and the functional renormalization group (fRG). Since the vertex is a four-point function, an efficient parametrization is required to make it numerically tractable. Thus, concrete parametrizations of diagrammatic objects and equations are discussed in a section on the Anderson model.
- The single-boson exchange (SBE) decomposition offers a numerically appealing parametrization for the vertex and defines a promising approximation [HLK21]. While parquet-like equations for SBE components have already been derived [KV19], we complement them in Chapter 3 with a derivation of the fRG flow equations including the multiloop extension in different approximations. These have been published in [P1] where we also review previous results and relate the SBE to other decompositions.
- In Chapter 4, we solve both the one-loop fRG equations and the parquet approximation for the single-impurity Anderson model and compare their results to those obtained using the numerical renormalization group (NRG). First we present real-frequency results from computations in the Keldysh formalism in Ref. [P3]. The implementation

details are explained in the code publication [P5]. While the Keldysh results have the advantage that the obtained dynamical observables can be directly compared to experiment, calculations are more demanding than in the MF. In our real-frequency study we used Matsubara results to verify the results at zero frequency. For calculations in the MF Ref. [P2] introduces a `Julia` library which offers flexible data containers and standard routines for diagrammatic calculations.

- For real-frequency methods all equations need to be formulated in the KF. However, also in formal derivations the MF is often more convenient. Unfortunately, for many years the exact correspondence between multipoint functions in the MF and the KF was not known (even though partial solutions did exist). In Chapter 5 we therefore present a general strategy for the analytic continuation of MF ℓ -point correlators to the KF. While this formal development does not solve the problem of analytic continuation of numerical Matsubara data, it helps deepen our understanding of correlators in both formalisms.
- The Hubbard atom is a popular benchmark model, as it can be solved exactly and has a non-trivial self-energy and vertex. Their MF formulas are therefore presented in App. A in the asymptotic and single-boson exchange decomposition.
- Lastly, in App. B we investigate the convergence of the multiloop fRG scheme in the number of loops and self-energy iterations in the MF and KF. We further show exemplary plots of the multiloop contributions in the KF and discuss the numerical implications of the study.

2 Methodological background

In this chapter, we will review some basic concepts in quantum many-body physics which are relevant for the description of solid state systems and their observables. While these are also summarized in the publications [P1]-[P5], we find it beneficial to present a general overview in a streamlined notation for both formalisms.

First, we present the definition and general properties of correlators in the Matsubara and Keldysh formalisms in Sec. 2.1. This sets the stage for Ref. [P4] where we study how Matsubara and Keldysh multipoint correlators are related by analytic continuation. For our diagrammatic studies, we then focus on Green's functions, which are correlators of creation and annihilation operators. Their diagrammatic representation is discussed in Sec. 2.2. There, we also summarize the quantum field theoretic methods for their computation which are subject of the remaining publications [P1, P2, P3, P5].

2.1 Correlators – definition and basic properties

We are primarily interested in measurable quantities which can be expressed as time-ordered correlation functions or *correlators* for short. These objects encode expectation values and the (auto)correlation of quantum mechanical operators which represent, e.g., the creation and annihilation of fermionic or bosonic particles, their density or magnetization. In the following section we define correlators in the Matsubara and Keldysh formalisms. Most of the following material is well-known in the literature. The purpose of this section is to introduce the most relevant properties of correlators and to establish notational conventions, mostly following Ref. [KLvD21] for general correlators and Refs. [JS10, Wal21] for fermionic Green's functions and related diagrammatic methods.

In this thesis we consider solid state systems in thermal equilibrium which can be described by a time-independent Hamiltonian \hat{H} . Thus, time-translational invariance and frequency conservation are fulfilled. The microscopic time evolution of a general quantum state $|\psi\rangle$ is governed by the Schrödinger equation, i.e., given a state at initial time t_0 we obtain one at any time t by

$$|\psi(t)\rangle = \hat{U}(t, t_0) |\psi(t_0)\rangle, \quad (2.1)$$

with the unitary time evolution

$$\hat{U}(t, t_0) = \exp \left\{ -i \int_{t_0}^t d\tilde{t} \hat{H} \right\} = \exp \{-i\hat{H}(t - t_0)\}. \quad (2.2)$$

Depending on $t_0 \gtrless t$, the evolution is forward or backward in time and consecutive time evolutions can be combined, e.g., giving $\hat{U}(t, t_1)\hat{U}(t_1, t_0) = \hat{U}(t, t_0)$. For the most part, however, we focus on operators and work in the Heisenberg picture where the states are static and operators \hat{O} are evolved by

$$\hat{O}(t) = e^{i\hat{H}t} \hat{O} e^{-i\hat{H}t}. \quad (2.3)$$

To keep the discussion general, we do not specify the operators \hat{O} here. In this section we present a general formulation for correlators. Only later, in Sec. 2.2.3, we specialize in Green's functions, which are correlators of creation and annihilation operators and can be expressed in the functional integral formulation.

2.1.1 Thermal expectation values

For a comprehensive presentation of correlators in the subsequent sections we now introduce thermal expectation values, which are encoded in so-called *partial spectral functions* (PSF), and study their properties. PSFs fully encode the system-specific information and are formalism-independent. These are then combined with formalism-specific kernels to obtain Matsubara or Keldysh correlators [KLvD21].

Thermal expectation values $\langle \dots \rangle$ are weighted ensemble averages. Explicitly, for a canonical ensemble with inverse temperature $\beta = 1/T$, we have

$$\langle \hat{O}(t) \rangle = \text{Tr} \left[\hat{O}(t) \hat{\rho} \right] = \sum_{\underline{1}} \langle \underline{1} | \hat{O}(t) \hat{\rho} | \underline{1} \rangle, \quad (2.4)$$

where the density matrix is defined as $\hat{\rho} = e^{-\beta \hat{H}} / Z$ with partition function $Z = \text{Tr} [e^{-\beta \hat{H}}]$.¹ In the last expression the trace is expressed as a sum over a complete set of orthonormal states $|\underline{1}\rangle$.

We encode thermal expectation values for the product of ℓ operators $\hat{\mathbf{O}} = (\hat{O}^1, \dots, \hat{O}^\ell)$ at times $\mathbf{t} = (t_1, \dots, t_\ell)$ in the so-called ℓ -point *partial spectral functions* (PSF)

$$\mathcal{S}[\hat{\mathbf{O}}](\mathbf{t}) = \langle \hat{O}^1(t_1) \cdots \hat{O}^\ell(t_\ell) \rangle, \quad (2.5a)$$

which in the frequency domain read

$$\mathcal{S}[\hat{\mathbf{O}}](\boldsymbol{\varepsilon}) = \frac{1}{(2\pi i)^\ell} \left[\prod_{i=1}^{\ell} \int_{\mathbb{R}} dt_i \right] e^{i\boldsymbol{\varepsilon} \cdot \mathbf{t}} \mathcal{S}[\hat{\mathbf{O}}](\mathbf{t}). \quad (2.5b)$$

Using the energy eigenbasis, we can provide an explicit formula for the PSFs. We denote energy eigenstates by $|\underline{i}\rangle$ with corresponding eigenenergies $E_{\underline{i}}$, i.e., $\hat{H} |\underline{i}\rangle = E_{\underline{i}} |\underline{i}\rangle$ and $\sum_{\underline{i}}$ is a sum over the complete set of orthonormal energy eigenstates. Integers $i = 1, \dots, \ell$ are used to distinguish different sets. By repeated insertion of the identity $\mathbb{1} = \sum_{\underline{i}} |\underline{i}\rangle \langle \underline{i}|$ into Eq. (2.4) we obtain the Lehmann representation

$$\mathcal{S}[\hat{\mathbf{O}}](\mathbf{t}) = \frac{1}{Z} \sum_{\underline{1}, \dots, \underline{\ell}} e^{-\beta E_{\underline{1}}} \prod_{i=1}^{\ell} \left[O_{\underline{i}\underline{i+1}}^i e^{it_i(E_{\underline{i}} - E_{\underline{i+1}})} \right], \quad (2.6a)$$

$$\mathcal{S}[\hat{\mathbf{O}}](\boldsymbol{\varepsilon}) = \frac{1}{Z} \sum_{\underline{1}, \dots, \underline{\ell}} e^{-\beta E_{\underline{1}}} \prod_{i=1}^{\ell} [O_{\underline{i}\underline{i+1}}^i \delta(\varepsilon_i + E_{\underline{i}} - E_{\underline{i+1}})], \quad (2.6b)$$

where we abbreviated the matrix elements $O_{\underline{i}\underline{i+1}} = \langle \underline{i} | \hat{O} | \underline{i+1} \rangle$ and identified $\ell + 1$ with 1.

Now, we are in the position to deduce properties of PSFs which derive from the particular form of the equilibrium density matrix. Firstly, following Ref. [BM61], we briefly summarize the analytic properties of the PSF. For this purpose we consider complex-valued times $t \in \mathbb{C}$.

¹ For a grand-canonical ensemble the density-matrix yields $\hat{\rho} = e^{-\beta(\hat{H} - \mu \hat{N})} / Z$, $Z = \text{Tr} [e^{-\beta(\hat{H} - \mu \hat{N})}]$. The additional term, $-\mu \hat{N}$, is typically absorbed in the Hamiltonian. In this thesis we will not explicitly consider it. The necessary modifications for a grand-canonical ensemble can be found in Ref. [JPS10], for instance.

Focusing on the imaginary parts, $t \rightarrow -i\tau$ with $\tau \in \mathbb{R}$, Eq. (2.6a) gives

$$\mathcal{S}[\hat{\mathcal{O}}](-i\boldsymbol{\tau}) = \frac{1}{Z} \sum_{\underline{1}, \dots, \underline{\ell}} O_{1\underline{2}}^1 e^{(\tau_1 - \beta - \tau_\ell)E_{\underline{1}}} \prod_{i=2}^{\ell} \left[O_{i\underline{i+1}}^i e^{(\tau_i - \tau_{i-1})E_{\underline{i}}} \right]. \quad (2.7)$$

Provided that the ensemble average in Eq. (2.6a) converges absolutely, we can conclude that the PSF is well-defined and analytic for complex times (see, e.g., [FB06, BM61]) on a region of \mathbb{C} where the imaginary parts, $\tau = -\text{Im}(t)$, fulfill

$$\tau_\ell + \beta \geq \tau_1 \geq \tau_2 \geq \dots \geq \tau_\ell. \quad (2.8)$$

Furthermore, by cyclicity of the trace, $\text{Tr}[\hat{A}\hat{B}\hat{C}] = \text{Tr}[\hat{B}\hat{C}\hat{A}]$, and using the formulas in Eqs. (2.6a) and (2.6b) we find the Kubo–Martin–Schwinger (KMS) relations [Kub57, MS59] for complex times \boldsymbol{t} or real frequencies $\boldsymbol{\varepsilon}$:

$$\begin{aligned} \mathcal{S}[\hat{\mathcal{O}}^1, \dots, \hat{\mathcal{O}}^\ell](t_1, \dots, t_\ell) &= \mathcal{S}[\hat{\mathcal{O}}^2, \dots, \hat{\mathcal{O}}^\ell, \hat{\mathcal{O}}^1](t_2, \dots, t_\ell, t_1 + i\beta) \\ &= \mathcal{S}[\hat{\mathcal{O}}^\ell, \hat{\mathcal{O}}^1, \dots, \hat{\mathcal{O}}^{\ell-1}](t_\ell - i\beta, t_1, \dots, t_{\ell-1}), \end{aligned} \quad (2.9a)$$

$$\begin{aligned} \mathcal{S}[\hat{\mathcal{O}}^1, \hat{\mathcal{O}}^2, \dots, \hat{\mathcal{O}}^\ell](\varepsilon_1, \varepsilon_2, \dots, \varepsilon_\ell) &= e^{\beta\varepsilon_1} \mathcal{S}[\hat{\mathcal{O}}^2, \dots, \hat{\mathcal{O}}^\ell, \hat{\mathcal{O}}^1](\varepsilon_2, \dots, \varepsilon_\ell, \varepsilon_1) \\ &= e^{-\beta\varepsilon_\ell} \mathcal{S}[\hat{\mathcal{O}}^\ell, \hat{\mathcal{O}}^1, \dots, \hat{\mathcal{O}}^{\ell-1}](\varepsilon_\ell, \varepsilon_1, \dots, \varepsilon_{\ell-1}). \end{aligned} \quad (2.9b)$$

These relations imply that PSFs of cyclically permuted operators are not independent. They are either related by shifts along the imaginary time axis [cf. Eq. (2.9a)] or by an exponential factor [cf. Eq. (2.9b)].

Having defined PSFs and studied their basic properties we are now ready to combine them into Matsubara and Keldysh correlators in the following sections.

2.1.2 Matsubara formalism

The Matsubara formalism treats thermal correlation functions and has become widely popular both in analytical and in numerical works. It relies on the fact that the density matrix amounts to a time evolution along imaginary times by the inverse temperature β . The special properties of equilibrium PSFs, Eq. (2.8) and (2.9), are directly incorporated via a Wick rotation $t \rightarrow -i\tau$ such that ℓ -point Matsubara correlators are defined as

$$\mathcal{G}[\hat{\mathcal{O}}](\boldsymbol{\tau}) = (-1)^{\ell-1} \langle \mathcal{T}[\hat{\mathcal{O}}^1(-i\tau_1) \cdots \hat{\mathcal{O}}^\ell(-i\tau_\ell)] \rangle. \quad (2.10)$$

The conventional sign factor $(-1)^{\ell-1}$ is introduced for consistency with later sections and the imaginary-time ordering, \mathcal{T} , rearranges the operators $\hat{\mathcal{O}}^i$ by their time arguments τ_i . Explicitly writing out the time ordering, we obtain

$$\mathcal{G}[\hat{\mathcal{O}}](\boldsymbol{\tau}) = \sum_p \zeta^p \mathcal{K}(\boldsymbol{\tau}_p) \mathcal{S}[\hat{\mathcal{O}}^p](-i\boldsymbol{\tau}_p), \quad (2.11a)$$

with the Matsubara kernel

$$\mathcal{K}(\boldsymbol{\tau}_p) = \prod_{i=1}^{\ell-1} [-\theta(\tau_{\bar{i}} - \tau_{\bar{i+1}})]. \quad (2.11b)$$

Here, the sum \sum_p runs over all permutations of the indices $(1, \dots, \ell) \xrightarrow{p} (\bar{1}, \dots, \bar{\ell})$ where we abbreviate $\bar{i} = p(i)$. Correspondingly, the tuples $\hat{\mathcal{O}}^p = (\hat{\mathcal{O}}^{\bar{1}}, \dots, \hat{\mathcal{O}}^{\bar{\ell}})$ and $\boldsymbol{\tau}_p = (\tau_{\bar{1}}, \dots, \tau_{\bar{\ell}})$

contain the permuted operators and times. The sign factor ζ^p encodes the crossing symmetry: For an even or odd number of exchanges of fermionic operators it gives $\zeta^p = +1$ or $\zeta^p = -1$, respectively. Using the step function

$$\theta(\tau) = \begin{cases} 1 & \text{for } \tau \geq 0, \\ 0 & \text{else,} \end{cases} \quad (2.12)$$

the Matsubara kernel \mathcal{K} encodes the time ordering, i.e., it ensures that the non-vanishing permutations p fulfill

$$\tau_{\bar{1}} \geq \dots \geq \tau_{\bar{\ell}}. \quad (2.13)$$

Further, from the KMS condition (2.9a) we conclude that the Matsubara correlator is periodic (anti-periodic) in its imaginary time argument τ_i if the corresponding operator \hat{O}^i is bosonic (fermionic). Thus, Matsubara correlators \mathcal{G} can be represented by a Fourier series. Note that, due to Eq. (2.8), MF correlators are only guaranteed to be well-defined for time arguments τ_i within an interval of length β . However, we may (anti-)periodically extend the domain with the Fourier series representation.

The frequency representation of Matsubara correlators reads

$$\mathcal{G}[\hat{O}](i\omega) = \prod_{i=1}^{\ell} \left[\int_0^{\beta} d\tau_i e^{i\omega_i \tau_i} \right] \mathcal{G}[\hat{O}](\tau). \quad (2.14)$$

Due to the (anti-)periodicity in the times τ_j , the Matsubara frequencies $i\omega_j$ are given by

$$i\omega_j = \begin{cases} i2m_j\pi T & \text{for bosonic } \hat{O}^j, \\ i(2m_j + 1)\pi T & \text{for fermionic } \hat{O}^j, \end{cases} \quad m_j \in \mathbb{N}. \quad (2.15)$$

A Lehmann representation for MF correlators on the frequency domain has been derived in Refs. [KLvD21, HSS23]. The product structure in Eq. (2.11a) becomes a convolution in the frequency representation,

$$\mathcal{G}[\hat{O}](i\omega) = \sum_p \zeta^p \left[\prod_{i=1}^{\ell} \int_{\mathbb{R}} d\varepsilon_i \right] \mathcal{K}(i\omega_p, \varepsilon_p) \mathcal{S}[\hat{O}^p](\varepsilon_p), \quad (2.16)$$

where $\mathcal{S}[\hat{O}^p](\varepsilon_p)$ is the real-frequency PSF (2.5b). More explicit formulas for the MF kernel will be provided later in Sec. 5 and the particularly relevant case of two-point correlators will be discussed in Sec. 2.1.5.

2.1.3 Keldysh formalism

The Keldysh formalism is a versatile quantum field-theoretic framework that can treat systems both in and out of equilibrium. Unlike the MF, it works directly with real times or frequencies, which comes at the cost of a doubled time contour. While the doubled time contour only fully unfolds its potential in the path integral formulation (see Sec. 2.2.2), we here illustrate its origin. Let us revisit the expectation value of operator $\hat{O}(t)$ at time t :

$$\langle \hat{O}(t) \rangle = \text{Tr} [U(t_0, t) \hat{O} U(t, t_0) \rho_0] = \text{Tr} [U(t_0, \infty) U(\infty, t) \hat{O} U(t, t_0) \rho_0], \quad (2.17)$$

which can be interpreted as follows (reading from right to left): An initial state, ρ_0 , is prepared at initial time t_0 , evolved *forward* to time t where the measurement of \hat{O} is done, and then

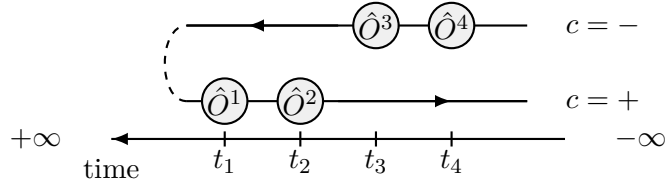


Figure 2.1 Illustration of contour ordering in the KF: Operators are time-ordered \mathcal{T} on the forward branch ($c = -$) and anti-time-ordered $\overline{\mathcal{T}}$ on the backward branch ($c = +$). The arrow on the Keldysh contour indicates the order of operators from right to left. For the above times, t_1, \dots, t_4 , the contour-ordered expression in Eq. (2.18) reads $\zeta \hat{\mathcal{O}}^2(t_2^+) \hat{\mathcal{O}}^1(t_1^+) \hat{\mathcal{O}}^3(t_3^-) \hat{\mathcal{O}}^4(t_4^-)$ where ζ is -1 if fermionic operators have been exchanged an odd number of times and $\zeta = +1$ otherwise.

is evolved *backward* to t_0 . The initial time t_0 is typically set to the infinite past, $t_0 = -\infty$. For the last equality we inserted $\mathbb{1} = U(t, \infty)U(\infty, t)$. Both forward and backward contour thus span the entire real axis. Unlike the Matsubara formalism, the Keldysh formalism does not (directly) employ that the density matrix ρ corresponds to the time evolution by the imaginary time $i\beta$. Rather, it remains in the real-time representation and has to account for both forward and backward time evolution by defining a contour ordering: Operators are ordered along the time contour as indicated in Fig. 2.1. The contour argument t^c consists of time t and contour index c which labels the two time evolution branches, $c = -$ for the forward and $c = +$ for the backward branch. For the example in Fig. 2.1, we obtain

$$\begin{aligned} \mathcal{T}_c[\hat{\mathcal{O}}^1(t_1^+) \hat{\mathcal{O}}^2(t_2^+) \hat{\mathcal{O}}^3(t_3^-) \hat{\mathcal{O}}^4(t_4^-)] &= \overline{\mathcal{T}}[\hat{\mathcal{O}}^1(t_1^+) \hat{\mathcal{O}}^2(t_2^+)] \mathcal{T}[\hat{\mathcal{O}}^3(t_3^-) \hat{\mathcal{O}}^4(t_4^-)] \\ &= \zeta \hat{\mathcal{O}}^2(t_2^+) \hat{\mathcal{O}}^1(t_1^+) \hat{\mathcal{O}}^3(t_3^-) \hat{\mathcal{O}}^4(t_4^-), \end{aligned} \quad (2.18)$$

i.e., contour ordering moves operators with contour indices $c = +$ to the left and $c = -$ to the right. The time ordering \mathcal{T} and anti-time ordering operator $\overline{\mathcal{T}}$ then sort the operators by their time arguments in decreasing and increasing order, respectively. The sign ζ accounts for the exchanges of fermionic operators, $\zeta = +1$ for an even and $\zeta = -1$ for an odd number of exchanges.

Thus, the ℓ -point Keldysh correlator is defined in the time domain as

$$\mathcal{G}^c[\hat{\mathcal{O}}](\mathbf{t}) = (-i)^{\ell-1} \langle \mathcal{T}_c[\hat{\mathcal{O}}^1(t_1^{c_1}) \dots \hat{\mathcal{O}}^\ell(t_\ell^{c_\ell})] \rangle, \quad (2.19a)$$

and in the frequency domain as

$$\mathcal{G}^c[\hat{\mathcal{O}}](\boldsymbol{\omega}) = \left[\prod_{i=1}^{\ell} \int_{\mathbb{R}} dt_i \right] e^{i\boldsymbol{\omega} \cdot \mathbf{t}} \mathcal{G}^c[\hat{\mathcal{O}}](\mathbf{t}). \quad (2.19b)$$

Compared to the MF, every KF correlator obtains an additional contour index structure with 2^ℓ components. There is a slight redundancy due to causality. This can be most easily seen after a Keldysh rotation. The transformation from contour indices $c = -, +$ to Keldysh indices $k = 1, 2$ is defined by the Keldysh rotation matrix $D^{k,c} = (-c)^k / \sqrt{2}$, giving

$$\mathcal{G}^k[\hat{\mathcal{O}}] = \sum_c \prod_{i=1}^n D^{k_i c_i} \mathcal{G}^c[\hat{\mathcal{O}}]. \quad (2.20)$$

In the Keldysh basis we can convince ourselves that the $\mathcal{G}^{1\dots 1}$ component vanishes. For fixed time arguments we can focus on the operator $\hat{\mathcal{O}}(t^c)$ whose time argument t is strictly larger than the others'. In the example shown in Fig. 2.1 $\hat{\mathcal{O}}^1$ carries the largest time argument t_1 . By nature of the contour ordering both choices for the contour index $c = \pm$ give the

same ordering. Keldysh rotation to the Keldysh index $k = 1$ subtracts these to give zero. Therefore, the correlator $\mathcal{G}^{1\dots 1}$ vanishes for almost all times \mathbf{t} .²

On the frequency domain, the spectral representation of KF functions reads

$$\mathcal{G}^k[\hat{\mathcal{O}}](\boldsymbol{\omega}) = \sum_p \zeta^p \left[\prod_{i=1}^{\ell} \int_{\mathbb{R}} d\varepsilon_i \right] \mathcal{K}^k(\boldsymbol{\omega}_p, \boldsymbol{\varepsilon}_p) \mathcal{S}[\hat{\mathcal{O}}^p](\boldsymbol{\varepsilon}_p), \quad (2.21a)$$

with Keldysh kernels

$$\mathcal{K}^k(\boldsymbol{\omega}_p, \boldsymbol{\varepsilon}_p) = \prod_{i=1}^{\ell} \left[\int_{\mathbb{R}} dt_i e^{it_i(\omega_i - \varepsilon_i)} \right] \mathcal{K}^k(\mathbf{t}_p). \quad (2.21b)$$

Note that the spectral representation of MF and KF correlators only differ by the kernel [see Eq. (2.16)]. For explicit expressions for ℓ -point kernels, we again refer to Sec. 5 or to Refs. [KLvD21, HSS23]. The two-point correlators for both formalisms will be discussed in Sec. 2.1.5.

2.1.4 Note on conventions

Due to the time-independent Hamiltonian, ℓ -point correlators and PSFs are invariant under time translation. This property implies that the Fourier transforms come with a frequency conserving factor, $\sum_{i=1}^{\ell} \omega_i = 0$, if one keeps an explicit dependence on all ℓ arguments. Alternatively, time-translational invariance is typically used to set the last time argument, $\tau_{\ell} = 0$, to zero. The Fourier transform is then defined as a function of $\ell - 1$ frequencies, namely

$$S[\hat{\mathcal{O}}](\varepsilon_1, \dots, \varepsilon_{\ell-1}) = \frac{1}{(2\pi)^{\ell-1}} \left[\prod_{i=1}^{\ell-1} \int_{\mathbb{R}} dt_i e^{i\omega_i t_i} \right] \mathcal{S}[\hat{\mathcal{O}}^1, \dots, \hat{\mathcal{O}}^n](t_1, \dots, t_{\ell-1}, 0), \quad (2.22a)$$

$$G[\hat{\mathcal{O}}](i\omega_1, \dots, i\omega_{\ell-1}) = \left[\prod_{i=1}^{\ell-1} \int_0^{\beta} d\tau_i e^{i\omega_i \tau_i} \right] \mathcal{G}[\hat{\mathcal{O}}^1, \dots, \hat{\mathcal{O}}^n](\tau_1, \dots, \tau_{\ell-1}, 0), \quad (2.22b)$$

$$G^k[\hat{\mathcal{O}}](\omega_1, \dots, \omega_{\ell-1}) = \left[\prod_{i=1}^{\ell-1} \int_{\mathbb{R}} dt_i e^{i\omega_i t_i} \right] \mathcal{G}^k[\hat{\mathcal{O}}^1, \dots, \hat{\mathcal{O}}^n](t_1, \dots, t_{\ell-1}, 0). \quad (2.22c)$$

Such a choice is useful for explicit parametrizations since an ℓ -point function effectively depends on $\ell - 1$ times or frequencies. However, the introduced notational asymmetry complicates many expressions. For the sake of compact formulas, it proves to be beneficial to retain the dependence on all ℓ frequencies $\boldsymbol{\omega} = (\omega_1, \dots, \omega_{\ell})$.

To distinguish functions with explicit dependence on $\ell - 1$ and ℓ frequencies, we use roman (G) and calligraphic (\mathcal{G}) symbols. Obviously, they contain the same information and are related by

$$\begin{aligned} S[\hat{\mathcal{O}}](\boldsymbol{\varepsilon}) &= \delta(\varepsilon_1 + \dots + \varepsilon_{\ell}) S[\hat{\mathcal{O}}](\varepsilon_1, \dots, \varepsilon_{\ell-1}), \\ \mathcal{G}[\hat{\mathcal{O}}](i\boldsymbol{\omega}) &= \beta \delta_{0, \omega_1 + \dots + \omega_{\ell}} G[\hat{\mathcal{O}}](i\omega_1, \dots, i\omega_{\ell-1}), \\ G^k[\hat{\mathcal{O}}](\boldsymbol{\omega}) &= 2\pi \delta(\omega_1 + \dots + \omega_{\ell}) G^k[\hat{\mathcal{O}}](\omega_1, \dots, \omega_{\ell-1}), \end{aligned}$$

² The exception for exactly equal time arguments is thoroughly analyzed in Refs. [Kam11, Klö19]. We can mostly avoid this subtlety by considering non-vanishing (potentially infinitesimal) time shifts. Also, the exceptions form a set with zero measure and thus have no influence on the correlator in the frequency representation. A notable example where equal-time correlators are needed is the computation of the Hartree value, which is discussed in App. E of Ref. [P3].

where the Kronecker and Dirac delta on the right explicitly encode frequency conservation. For calligraphic symbols frequency conservation is explicit whereas it is implicit for roman symbols. The spectral representations can be equally written in terms of the roman symbols (see Ref. [KLvD21])

$$G[\hat{\mathcal{O}}](i\omega_1, \dots, i\omega_{\ell-1}) = \sum_p \left[\prod_{i=1}^{\ell-1} \int_0^\beta d\varepsilon_i \right] K(i\omega_{\bar{1}}, \dots, i\omega_{\bar{\ell-1}}, \varepsilon_{\bar{1}}, \dots, \varepsilon_{\bar{\ell-1}}) S[\hat{\mathcal{O}}^p](\varepsilon_{\bar{1}}, \dots, \varepsilon_{\bar{\ell-1}}), \quad (2.23a)$$

$$G^k[\hat{\mathcal{O}}](\omega_1, \dots, \omega_{\ell-1}) = \sum_p \left[\prod_{i=1}^{\ell-1} \int_{\mathbb{R}} d\varepsilon_i \right] K^k(\omega_{\bar{1}}, \dots, \omega_{\bar{\ell-1}}, \varepsilon_{\bar{1}}, \dots, \varepsilon_{\bar{\ell-1}}) S[\hat{\mathcal{O}}^p](\varepsilon_{\bar{1}}, \dots, \varepsilon_{\bar{\ell-1}}), \quad (2.23b)$$

in which case one has to consistently use the roman symbols and the ℓ -th frequency is defined consistently with frequency conservation, i.e., $\varepsilon_\ell = -\sum_{i=1}^{\ell-1} \varepsilon_i$. Thereby one may, for example, write $S[\hat{\mathcal{O}}^2, \hat{\mathcal{O}}^1](-\varepsilon_1)$ instead of $S[\hat{\mathcal{O}}^2, \hat{\mathcal{O}}^1](\varepsilon_2)$. In summary, the distinction between roman and calligraphic symbols is usually not necessary, and they can be used interchangeably if frequency conservation is given.

The notation with $\ell - 1$ frequencies is very common for two-point correlators which effectively depend on one frequency only. These correlators will be presented in the next section.

2.1.5 Example: Two-point correlators

Two-point correlators, $G[\hat{\mathcal{O}}^1, \hat{\mathcal{O}}^2]$, are of particular relevance in physics. They describe a wide range of observables such as the spectrum of single-particle excitations, the linear response to an external force or the fluctuation (auto-correlation) of local particle density or magnetization. They have a rather clear structure and have been extensively studied in the literature. While we postpone the discussion of physical observables to Sec. 2.2.1, we here present the general structure of two-point correlators.

First, we present the spectral representation of two-point correlators in the MF and the KF. We then show how these correlators are connected through analytic continuation and the fluctuation-dissipation theorem (FDT). For notational convenience we drop the operators in $G[\hat{\mathcal{O}}^1, \hat{\mathcal{O}}^2]$ unless they are ambiguous.

2.1.5.1 Matsubara two-point correlators

For two-point functions the Matsubara kernel reads [KLvD21, HSS23]

$$\mathcal{K}(i\omega_1, i\omega_2; \varepsilon_1, \varepsilon_2) = \beta \delta_{0, \omega_1 + \omega_2} \left[\frac{1}{i\omega_1 - \varepsilon_1} - \frac{\beta}{2} \delta_{0, \omega_1} \delta_{0, \varepsilon_1} \right], \quad (2.24)$$

where δ_{0, ω_1} only contributes if the Matsubara frequency ω_1 vanishes. This is only possible for bosonic Matsubara frequencies. The $\delta_{0, \varepsilon_1}$ contribution is only present if the PSF has finite weight at $\varepsilon_1 = 0$, i.e., if the PSF has a Dirac-delta contribution at $\varepsilon_1 = 0$. To separate these contributions, we decompose the PSF into a regular $\tilde{\mathcal{S}}$ and an anomalous $\hat{\mathcal{S}}$ part, $\mathcal{S} = \tilde{\mathcal{S}} + \hat{\mathcal{S}}$. The anomalous contribution $\hat{\mathcal{S}}(t_1, t_2) = C$ is constant in time, and in the frequency representation it reads $\hat{\mathcal{S}}(\varepsilon_1, \varepsilon_2) = C \delta(\varepsilon_1) \delta(\varepsilon_2)$. On the other hand, the regular $\tilde{\mathcal{S}}$ is free of such contributions. Note that the KMS condition (2.9a) sets the two anomalous

PSFs to be equal, i.e.,

$$\hat{S}[\hat{O}^1, \hat{O}^2](t_1, t_2) = C = \hat{S}[\hat{O}^2, \hat{O}^1](t_2, t_1). \quad (2.25)$$

Inserting the kernel (2.24) into the spectral representation (2.16), we obtain the well-known result

$$G(i\omega_1) = \tilde{G}(i\omega_1) + \hat{G}(i\omega_1), \quad (2.26a)$$

with the regular and anomalous contributions, \tilde{G} and \hat{G} , given, respectively, by

$$\tilde{G}(i\omega_1) = \int_{\mathbb{R}} d\varepsilon_1 \frac{S^{\text{std}}(\varepsilon_1)}{i\omega_1 - \varepsilon_1} \quad (2.26b)$$

$$\hat{G}(i\omega_1) = -\beta\delta_{0,\omega_1}C. \quad (2.26c)$$

Above we identified the *standard* spectral function S^{std} which is typically used for the spectral representation of two-point functions [BM61, AS10]. In terms of PSFs it reads

$$S^{\text{std}}[\hat{O}^1, \hat{O}^2](\varepsilon_1) = S[\hat{O}^1, \hat{O}^2](\varepsilon_1) - \zeta S[\hat{O}^2, \hat{O}^1](-\varepsilon_1), \quad (2.26d)$$

While anomalous contributions \hat{G} are neglected in many texts, Ref. [WFHT22] pointed out that they encode correlations which persist to arbitrarily large times and, hence, lead to long-term memory effects. Furthermore, under certain conditions, they indicate degeneracies in the many-body energy spectrum. In Sec. 2.1.5.3 we show how anomalous contributions are treated during analytic continuation to Keldysh correlators. While this has been known for two-point functions, the fate of anomalous contributions during analytic continuation to higher-point functions had not been fully clarified until recently [P4].

2.1.5.2 Keldysh two-point correlators

For the KF we choose the Keldysh basis in which the two-point correlator reads

$$G^{k_1 k_2} = D^{k_1 c_1} G^{c_1 c_2} (D^T)^{c_2 k_2} = \begin{pmatrix} G^{11} & G^{12} \\ G^{21} & G^{22} \end{pmatrix} = \begin{pmatrix} 0 & G^A \\ G^R & G^K \end{pmatrix}. \quad (2.27)$$

The non-zero Keldysh components are conventionally called *retarded* G^R , *advanced* G^A and *Keldysh* G^K components. Explicitly, these components give (for $t_1 \neq 0$)

$$G^{12}[\hat{O}_1, \hat{O}_2](t_1, 0) = +i \langle [\hat{O}_1(t_1), \hat{O}_2(0)]_{\zeta} \rangle \theta(-t_1), \quad (2.28a)$$

$$G^{21}[\hat{O}_1, \hat{O}_2](t_1, 0) = -i \langle [\hat{O}_1(t_1), \hat{O}_2(0)]_{\zeta} \rangle \theta(t_1), \quad (2.28b)$$

$$G^{22}[\hat{O}_1, \hat{O}_2](t_1, 0) = -i \langle [\hat{O}_1(t_1), \hat{O}_2(0)]_{-\zeta} \rangle, \quad (2.28c)$$

where $[\hat{A}, \hat{B}]_{\zeta} = \hat{A}\hat{B} - \zeta\hat{B}\hat{A}$ is an (anti)commutator.

To obtain the spectral representation of KF correlators in frequency space we can use that the Fourier representation of the step function reads

$$\mp i\theta(\pm t) = \int_{\mathbb{R}} \frac{d\omega}{2\pi} \frac{e^{-i\omega t}}{\omega \pm i0^+} = \lim_{\gamma \searrow 0} \int_{\mathbb{R}} \frac{d\omega}{2\pi} \frac{e^{-i\omega t}}{\omega \pm i\gamma}, \quad (2.29)$$

where we shifted the real frequency ω by an infinitesimal imaginary part $i0^+$. As indicated, this infinitesimal is understood as a limit. (Note that the order of the limit and the frequency integral is crucial.) On the other hand, a constant contribution in the time domain amounts to a Dirac delta in the frequency domain. The latter can be equally written as

$$\mp\pi\delta(\omega) = \text{Im} \frac{1}{\omega \pm i0^+}, \quad (2.30)$$

where the right-hand side shows an infinitesimally sharp Lorentzian peak. The latter formula is a direct consequence of the real-line version of the Sokhotski-Plemelj theorem [BB15]

$$\frac{1}{\omega \pm i0^+} = \mp i\pi\delta(\omega) + \text{P} \frac{1}{\omega}, \quad (2.31)$$

where the P denotes a principle-value integral which excludes the singularity on the interval $[-0^+, 0^+]$.

In frequency space we thus have

$$G^{k_1 k_2}(\omega_1) = \begin{pmatrix} G^{11}(\omega_1) & G^{12}(\omega_1) \\ G^{21}(\omega_1) & G^{22}(\omega_1) \end{pmatrix} = \begin{pmatrix} 0 & G^A(\omega_1) \\ G^R(\omega_1) & G^K(\omega_1) \end{pmatrix}, \quad (2.32a)$$

where the product in the time domain, Eq. (2.28), becomes a convolution, i.e.,

$$G^A(\omega_1) = \int_{\mathbb{R}} d\varepsilon_1 \frac{S^{\text{std}}(\varepsilon_1)}{\omega_1 - \varepsilon_1 - i0^+}, \quad (2.32b)$$

$$G^R(\omega_1) = \int_{\mathbb{R}} d\varepsilon_1 \frac{S^{\text{std}}(\varepsilon_1)}{\omega_1 - \varepsilon_1 + i0^+}, \quad (2.32c)$$

$$G^K(\omega_1) = -i2\pi[S[\hat{O}^1, \hat{O}^2](\omega_1) + \zeta S[\hat{O}^2, \hat{O}^1](-\omega_1)]. \quad (2.32d)$$

Here, we again identified the standard spectral function (2.26d).

Let us consider the typical case of real standard spectral functions, $S^{\text{std}}(\varepsilon) \in \mathbb{R}$. For example, this is the case if the operators are adjoint, $\hat{O}^2 = (\hat{O}^1)^\dagger$. Then, we can verify the well-known relations

$$G^A(\omega_1) = [G^R(\omega_1)]^*, \quad (2.33a)$$

$$S^{\text{std}}(\omega_1) = \frac{-1}{\pi} \text{Im} G^R(\omega_1), \quad (2.33b)$$

$$\begin{aligned} G^K(\omega_1) &= -i2\pi\{S[\hat{O}^1, \hat{O}^2](\omega_1) + \zeta S[\hat{O}^2, \hat{O}^1](-\omega_1)\} \\ &\stackrel{\text{KMS}}{=} -i2\pi(1 + \zeta e^{-\beta\omega_1})S[\hat{O}^1, \hat{O}^2](\omega_1) \\ &\stackrel{\text{KMS}}{=} -i2\pi \frac{1 + \zeta e^{-\beta\omega_1}}{1 - \zeta e^{-\beta\omega_1}} S^{\text{std}}[\hat{O}^1, \hat{O}^2](\omega_1) - i4\pi\hat{S}[\hat{O}^1, \hat{O}^2](\omega_1) \\ &\stackrel{(2.33b)}{=} \left[\coth \frac{\beta\omega_1}{2} \right]^\zeta 2i \text{Im} G^R(\omega_1) - i4\pi\delta(\omega_1)C, \end{aligned} \quad (2.33c)$$

where we used Eq. (2.30) for Eq. (2.33b). Equation (2.33c) relates the retarded and Keldysh component and is known as the *fluctuation-dissipation theorem* (FDT). For its derivation we used the KMS condition (2.9b) for the regular PSFs $\tilde{\mathcal{S}}$. In contrast, the anomalous $\hat{\mathcal{S}}$ needs to be treated separately since the coth-factor would diverge for $\zeta = +1$ and $\omega_1 = 0$. Note that Eqs. (2.33a) and (2.33b) imply that the spectral function can be obtained from the retarded and advanced component. These components are therefore of particular interest.

2.1.5.3 Notes on analytic continuation

The spectral representation (2.26b) reveals that the regular MF correlator defines a function $\tilde{G}(z)$ of complex variable z which is analytic away from the real axis, i.e., $z \notin \mathbb{R}$. Hence, the function $\tilde{G}(z)$ has two regions of analyticity which are separated by the real axis.

By comparison of Eq. (2.26b), (2.32b) and (2.32c), we further find that the retarded and advanced correlator can be obtained from the regular Matsubara correlator by analytic continuation, i.e.,

$$\tilde{G}(i\omega_1) \xrightarrow{i\omega_1 \rightarrow \omega_1 \pm i0^+} G^{R/A}(\omega_1). \quad (2.34)$$

To obtain the Keldysh component, G^K , we can use the FDT (2.33c), i.e., we insert Eq. (2.34) for the retarded component G^R and read off the coefficient C from the anomalous Matsubara correlator \hat{G} , see Eq. (2.26c). Thus, the anomalous Matsubara correlator, \hat{G} , can only enter the Keldysh component, G^K . In summary, by the relations (2.33c) and (2.34) we see that all components of the two-point Keldysh correlator can be obtained by analytic continuation of the Matsubara correlator.

The analytic continuation formula (2.34) is deduced from the spectral representation. It shows that the retarded and advanced correlator have their domain on the boundaries of the regions of analyticity of $\tilde{G}(z)$. One may wonder whether the reasoning can be inverted: Do functions with similar analytic properties always have a spectral representation? For general complex functions, $\chi(z)$, which are analytic on the upper half plane, $\text{Im}(z) > 0$, and vanish for large $|z|$, the Kramers–Kronig relations [AWH13] can be applied. These relate the real and imaginary part of χ by

$$\text{Re } \chi(\omega) = -\frac{1}{\pi} \text{P} \int_{\mathbb{R}} \frac{\text{Im } \chi(\omega')}{\omega - \omega'} d\omega', \quad (2.35a)$$

$$\text{Im } \chi(\omega) = \frac{1}{\pi} \text{P} \int_{\mathbb{R}} \frac{\text{Re } \chi(\omega')}{\omega - \omega'} d\omega', \quad (2.35b)$$

or by the Sokhotski-Plemelj formula (2.31)

$$\chi(\omega) = -\frac{1}{\pi} \int_{\mathbb{R}} \frac{\text{Im } \chi(\omega')}{\omega - \omega' + i0^+} d\omega', \quad (2.36)$$

such that the imaginary part $\frac{-1}{\pi} \text{Im } \chi$ can be interpreted as a spectral function for χ . This relation was deduced in Ref. [Lut61] for self-energies which, unlike correlators, have no native Lehmann representation.

2.1.6 Comparison of the formalisms

A direct comparison between the Keldysh and Matsubara formalism explains the wide popularity of the latter. As explicitly shown for two-point functions, both are formally equivalent. However, ℓ -point correlators have an additional index structure with 2^ℓ components in the KF. Further, Keldysh correlators are functions of continuous times and frequencies. At finite temperature ($\beta < \infty$) MF correlators $\mathcal{G}(i\omega)$ are only evaluated on a discrete set of Matsubara frequencies (2.15). The imaginary time arguments in $\mathcal{G}(\tau)$ are also continuous, but are only needed on an interval of length β . These properties make the Matsubara formalism much more convenient for numerical implementations.

However, numerically, Matsubara correlators face the problem that their arguments are imaginary. They have to be analytically continued to obtain physical observables at finite real times or frequencies. Even though there have been numerous advances in the field of

analytic continuation [FYG21, ZG24], quantitative results are still strongly impaired by the ill-conditioned Matsubara kernel. For example, in Ref. [SOOY17] it has been shown that the singular values of two-point Matsubara kernels decay super-exponentially. This means that slight errors in the imaginary-frequency data might correspond to large variations in real frequencies (cf. Ref. [COS18] for a study of the singular values and orthogonal basis functions for spectra and correlators). The Keldysh formalism circumvents this problem since it directly works in real times and frequencies. Furthermore, it also allows the treatment of non-equilibrium systems [Kad18, JS10, Klö19] which are, however, not covered in this thesis.

2.2 Diagrammatic language for fermionic theories

Above we introduced correlators for general operators which can be fermionic, bosonic or mixed. In this thesis we are mostly interested in a QFT treatment of interacting fermions. For such systems we aim to introduce the most relevant diagrammatic objects and relations which are needed in the subsequent sections. To avoid notational redundancies, we will introduce a multi-index notation. While the details of multi-index contractions depend on the system and formalism it allows us to write compact and formalism-independent diagrammatic equations.

2.2.1 Green's functions and observables

Fermionic many-body systems can be described by a second-quantized Hamiltonian, $\hat{H}[\hat{\mathbf{a}}^\dagger, \hat{\mathbf{a}}]$, which is expressed in terms of the annihilation and creation operators $\hat{a}_x^{(\dagger)}$. These are labelled by the one-particle quantum numbers x describing the particle's physical degrees of freedom which may include spin, lattice site or orbital indices, for instance. Bold symbols $\hat{\mathbf{a}}^{(\dagger)}$ denote tuples containing all combinations of quantum numbers x . The Hamiltonian takes the general form

$$\hat{H} = \hat{H}_0 + \hat{H}_{\text{int}}, \quad (2.37a)$$

$$\hat{H}_0[\hat{\mathbf{a}}^\dagger, \hat{\mathbf{a}}] = \sum_{x_1, x_1'} \hat{a}_{x_1'}^\dagger (H_0)_{x_1' | x_1} \hat{a}_{x_1}, \quad (2.37b)$$

$$\hat{H}_{\text{int}}[\hat{\mathbf{a}}^\dagger, \hat{\mathbf{a}}] = -\frac{1}{4} \sum_{x_1', x_2', x_1, x_2} \hat{a}_{x_1'}^\dagger \hat{a}_{x_2'}^\dagger (\Gamma_0)_{x_1' x_2' | x_1 x_2} \hat{a}_{x_2} \hat{a}_{x_1}, \quad (2.37c)$$

where all creation operators are ordered to the left of annihilation operators (normal ordering). The term $(H_0)_{x' | x}$ typically describes a hopping or an external potential and the term $(\Gamma_0)_{x' y' | x y}$ describes an instantaneous interaction between two particles and is anti-symmetric under exchange of two primed or unprimed indices.

The diagrammatic methods described in the subsequent sections are used to compute *Green's functions* which are correlators of the creation and annihilation operators. In particular, we are interested in one-particle Green's functions (*propagators*)

$$G_{x_1 | x_1'} = \mathcal{G}[\hat{a}_{x_1}, \hat{a}_{x_1'}^\dagger], \quad (2.38a)$$

and two-particle Green's functions

$$G_{x_1 x_2 | x_1' x_2'}^{(4)} = \mathcal{G}[\hat{a}_{x_1}, \hat{a}_{x_2}, \hat{a}_{x_2'}^\dagger, \hat{a}_{x_1'}^\dagger], \quad (2.38b)$$

where the index convention is chosen consistently with [JPS10, Wal21], i.e., primed/unprimed indices are used for incoming/outgoing particles. The superscript on $G^{(4)}$ is added here to distinguish it from the one-particle Green's function but can be left out if unambiguous.

One-particle Green's functions reveal the single-particle spectrum S^{std} of a system which can be read off from the retarded propagator [see Eq. (2.33b)]. In experiments S^{std} can be determined with spectroscopic measurements [Hüf07].

To understand the usefulness of two-particle Green's functions, note that one can form composite operators from creation/annihilation operators by setting them to equal times or contour arguments. Let us consider a single-site electron model for which the spin $\sigma = \uparrow, \downarrow$ is the only physical index. This is exactly the case for the Anderson impurity model, which we present in detail in Sec. 2.2.5, and the Hubbard atom, App. A. The number operators $\hat{n}_\sigma = \hat{a}_\sigma^\dagger \hat{a}_\sigma$ count the number of spin- σ electrons. Correlators of number operators can be obtained from the two-particle Green's function by taking the limit (here exemplified in the MF)

$$\mathcal{G}[\hat{n}_\uparrow, \hat{n}_\downarrow](\tau_1, \tau_2) = \lim_{\tau_2' \searrow \tau_1} \lim_{\tau_1' \searrow \tau_2} \mathcal{G}[\hat{a}_\uparrow, \hat{a}_\downarrow, \hat{a}_\downarrow^\dagger, \hat{a}_\uparrow^\dagger](\tau_1, \tau_2, \tau_2', \tau_1'), \quad (2.39)$$

where we take the limits from above to ensure the correct ordering of the composite $\hat{n}_\sigma = \hat{a}_\sigma^\dagger \hat{a}_\sigma$. In a suitable frequency parametrization, such as for example

$$\mathcal{G}(\tau_1, \tau_2, \tau_1', \tau_2') = \frac{1}{\beta^3} \sum_{\omega, \nu, \nu'} G(i\omega, i\nu, i\nu') e^{i\nu(\tau_1 - \tau_2') + i\nu'(\tau_1' - \tau_2) + i\omega(\tau_2 - \tau_2')}, \quad (2.40)$$

the limit in Eq. (2.39) amounts to Matsubara frequency sums over the two-particle Green's function

$$G[\hat{n}_\uparrow, \hat{n}_\downarrow](i\omega) = \frac{1}{\beta^2} \sum_{\nu, \nu'} G[\hat{a}_\uparrow, \hat{a}_\downarrow, \hat{a}_\downarrow^\dagger, \hat{a}_\uparrow^\dagger](i\omega, i\nu, i\nu'), \quad (2.41)$$

where we used frequency conservation to parametrize ℓ -point correlators with $\ell - 1$ independent frequencies.

In the Keldysh formalism we obtain fully analogous results. Since the ordering is determined by contour parameters, t^c , we also need to set contour indices c_i equal to form composite operators, i.e.,

$$\mathcal{G}^{c_1 c_2}[\hat{n}_\uparrow, \hat{n}_\downarrow](t_1, t_2) = - \lim_{t_1' \rightarrow t_1} \lim_{t_2' \rightarrow t_2} \mathcal{G}^{c_1 c_2 c_2 c_1}[\hat{a}_\uparrow, \hat{a}_\downarrow, \hat{a}_\downarrow^\dagger, \hat{a}_\uparrow^\dagger](t_1, t_2, t_2', t_1'). \quad (2.42)$$

Later we will work with Keldysh indices k_i , for which the index structure becomes slightly more complicated (see [P3] for details).

In Sec. 4 we further combine number operators to the density $\hat{d} = \hat{n}_\uparrow + \hat{n}_\downarrow$ and the magnetization operator $\hat{m} = \hat{n}_\uparrow - \hat{n}_\downarrow$ which gives us density $d = \langle \hat{d} \rangle$ and magnetization $m = \langle \hat{m} \rangle$ as observables on the one-particle level. To gauge the system's response to external perturbations we also compute the susceptibilities. For example, the susceptibility in the density channel reads (here in the MF)

$$2\chi_d(\tau) = G[\hat{d} - d, \hat{d} - d](\tau) = - \langle \mathcal{T} \hat{d}(\tau) \hat{d} \rangle + \langle \hat{d} \rangle^2, \quad (2.43)$$

where we included the factor 2 on the left to match the convention in Sec. 4. The Kubo formula from linear response theory reveals that retarded susceptibilities encode the system's reaction to weak perturbations (see e.g. Ref. [Col15]). Examples for these perturbations are the application of an electric or magnetic field. For more examples and the related experimental techniques we refer to, e.g., Ref. [AS10]. In Sec. 2.1.5 we have already mentioned that Matsubara correlators need to be analytically continued to obtain the retarded correlator, e.g., $\chi_d^R(\omega) = \chi_d(i\omega \rightarrow \omega + i0^+)$. While the retarded component χ_d^R describes the linear response,

the Keldysh component χ_d^K contains the symmetrized autocorrelation of fluctuations (2.28c). In thermal equilibrium both quantities are related by the fluctuation-dissipation theorem (2.33c).

2.2.2 Green's functions in the functional integral formulation

Next, we present how Green's functions can be written in the functional integral formulation. It is the basis for the quantum field theory methods presented in Sec. 2.2.3 and facilitates derivations of diagrammatic relations. For conciseness, we will merely reference such derivations and will not go into detail here. A comprehensive introduction to the functional integral formulation and its versatile tools can be found in Ref. [KBS10]. In the following we introduce fundamental diagrammatic notions and the compact multi-index notation.

Before presenting detailed formulas for the functional integral formulations in MF and KF, we anticipate that the time- or contour-ordered expectation value can be written as coherent state path integral

$$\langle \mathcal{T}[\dots] \rangle = \frac{1}{Z} \int \mathcal{D}[\bar{\phi}, \phi] \dots e^{S^M[\bar{\phi}, \phi]}, \quad (2.44a)$$

$$\langle \mathcal{T}_c[\dots] \rangle = \frac{1}{Z} \int \mathcal{D}[\bar{\phi}, \phi] \dots e^{iS^K[\bar{\phi}, \phi]}, \quad (2.44b)$$

where all creation and annihilation operators $\hat{a}_x^{(\dagger)}$ are replaced by Grassmann fields $\bar{\phi}_x$ and ϕ_x . Hence, e.g., the MF propagator reads $G_{x_1|x_1'}(\tau_1|\tau_1') = -\langle \mathcal{T}[\phi_{x_1}(\tau_1)\bar{\phi}_{x_1'}(\tau_1')] \rangle$. Notably, the action in both formalisms can be written in an abstract multi-index notation

$$S[\bar{\phi}, \phi] = \bar{\phi}_{1'}(G_0^{-1})_{1'|1}\phi_1 + \frac{1}{4}\bar{\phi}_{1'}\bar{\phi}_{2'}(\Gamma_0)_{1'2'|12}\phi_2\phi_1, \quad (2.44c)$$

where G_0^{-1} encodes the quadratic and Γ_0 the quartic part of the action. The multi-indices $1 = (c_1, t_1, \sigma_1, \dots)$ parametrize the ϕ - and $\bar{\phi}$ -fields. Their exact content depends on the Hamiltonian and the formalism. Using the Einstein notation we sum or integrate over doubly occurring indices. The details for the multi-index contractions will be presented below.

To derive the path integral in the Matsubara formalism we use that the density matrix can be expressed as an imaginary time evolution, i.e., $\hat{\rho} = \hat{U}(-i\beta, 0) = \exp\{-\int_0^\beta \hat{H}(\tau)d\tau\}$. At each point along the time evolution we insert a set of coherent states (see e.g., [Neg18]). This allows us to rewrite the time-ordered thermal expectation value $\langle \dots \rangle$ as a path integral over field configurations where the fields, $\phi_x(\tau)$ and $\bar{\phi}_x(\tau)$, are functions of imaginary times. The trace, $\text{Tr}[\dots]$, imposes the boundary condition that the fields $\bar{\phi}(\tau)$ and $\phi(\tau)$ are antiperiodic on the interval $[0, \beta]$, i.e., we have $\phi(\beta) = \zeta\phi(0)$. The Matsubara action then reads [Neg18]

$$S^M[\bar{\phi}, \phi] = \int_0^\beta d\tau \left\{ -\sum_x \bar{\phi}_x(\tau)\partial_\tau\phi_x(\tau) - H[\bar{\phi}(\tau), \phi(\tau)] \right\}. \quad (2.45)$$

By insertion of the general Hamiltonian (2.37) and comparison with Eq. (2.44c) we read off

$$(G_0^{-1})_{x_1'|x_1}(\tau_1'|\tau_1) = \delta(\tau_1' - \tau_1)[- \partial_{\tau_1} \mathbb{1}_{x_1'|x_1} - (H_0)_{x_1'|x_1}], \quad (2.46a)$$

$$(\Gamma_0)_{x_1', x_2'|x_1 x_2}(\tau_1', \tau_2'|\tau_1, \tau_2) = \delta(\tau_1' = \tau_2' = \tau_1 = \tau_2)(\Gamma_0)_{x_1', x_2'|x_1 x_2}, \quad (2.46b)$$

and the contraction of multi-index i in Eq. (2.44c) amounts to

$$“\sum_i” = \int_0^\beta d\tau_i \sum_{x_i}. \quad (2.47)$$

Apart from its compactness, another strength of the multi-index notation is that we can systematically change the basis for the fields. We demonstrate this by a change to Fourier space. Since the fields are antiperiodic on the interval $[0, \beta]$ we can express them as Fourier series

$$\phi(\tau) = \frac{1}{\beta} \sum_{\omega} e^{-i\omega\tau} \phi(\omega), \quad \bar{\phi}(\tau) = \frac{1}{\beta} \sum_{\omega} e^{i\omega\tau} \bar{\phi}(\omega), \quad (2.48)$$

with ω evaluated on the fermionic Matsubara frequencies. Inserting this into Eq. (2.45) we obtain a path integral over fields in frequency space and read off

$$(G_0^{-1})_{x_1'|x_1}(i\omega_1'|i\omega_1) = \beta \delta_{\omega_1' - \omega_1} [i\omega_1 \mathbb{1}_{x_1', x_1} - (H_0)_{x_1'|x_1}], \quad (2.49a)$$

$$(\Gamma_0)_{x_1' x_2'|x_1 x_2}(i\omega_1', i\omega_2'|i\omega_1, i\omega_2) = (\Gamma_0)_{x_1' x_2'|x_1 x_2} \beta \delta_{\omega_1' + \omega_2', \omega_1 + \omega_2}. \quad (2.49b)$$

Hence, we can use the multi-index notation equally in the frequency domain if we define the contraction over a multi-index in Eq. (2.44c) as

$$“\sum_i” = \frac{1}{\beta} \sum_{\omega_i} \sum_{x_i}, \quad (2.50)$$

where the sum over Matsubara frequencies comes with the usual factor of $\frac{1}{\beta}$.

By an analogous path integral construction the Keldysh action reads [Kam11]

$$S^K[\bar{\phi}, \phi] = \int_{\mathcal{C}} dt^c \left\{ \sum_x \bar{\phi}_x(t^c) i\partial_{t^c} \phi_x(t^c) - H[\bar{\phi}(t^c), \phi(t^c)] \right\} \quad (2.51a)$$

$$= \int_{-\infty}^{\infty} dt \sum_c (-c) \left\{ \sum_x \bar{\phi}_x^c(t) i\partial_t \phi_x^c(t) - H[\bar{\phi}^c(t), \phi^c(t)] \right\}, \quad (2.51b)$$

where we integrate the contour variable t^c along the Keldysh contour in the first line. In the second line we separated the contour argument t^c into time t and contour index c to obtain the conventional representation of Keldysh functions where the fields read $\phi_x^c(t)$, allowing for Fourier transformation and Keldysh rotation. The density matrix $\hat{\rho}$ merely enters as a weight and boundary condition for the fields and is typically absorbed into the measure of the path integral. By comparison with Eq. (2.44c), we find that the Keldysh action is determined by

$$(G_0^{-1})_{x_1'|x_1}^{c_1'|c_1}(t_1'|t_1) = -c_1 \delta_{c_1', c_1} \delta(t_1' - t_1) [i\partial_{t_1} \mathbb{1}_{x_1', x_1} - (H_0)_{x_1'|x_1}], \quad (2.52a)$$

$$(\Gamma_0)_{x_1' x_2'|x_1 x_2}^{c_1' c_2'|c_1 c_2}(t_1', t_2'|t_1, t_2) = -c_1 \delta_{c_1' = c_2' = c_1 = c_2} \delta(t_1' = t_2' = t_1 = t_2) (\Gamma_0)_{x_1' x_2'|x_1 x_2}, \quad (2.52b)$$

with multi-index contractions (2.44c) now defined as

$$“\sum_i” = \sum_{c_i} \int_{\mathbb{R}} dt_i \sum_{x_i}. \quad (2.53)$$

While the Keldysh action (2.51) most obviously reveals its origin from contour ordering, we typically work in the frequency representation and in the Keldysh basis, which requires us to

change the basis. Again, we can insert the Fourier representation of the fields

$$\phi(t) = \int_{\mathbb{R}} \frac{d\omega}{2\pi} e^{-i\omega t} \phi(\omega), \quad \bar{\phi}(t) = \int_{\mathbb{R}} \frac{d\omega}{2\pi} e^{i\omega t} \bar{\phi}(\omega), \quad (2.54)$$

and the Keldysh rotation according to Eq. (2.20) which gives us the multi-index contraction

$$\text{“} \sum_i \text{”} = \sum_{k_i} \int_{\mathbb{R}} \frac{d\omega_i}{2\pi} \sum_{x_i}, \quad (2.55)$$

while the bare interaction becomes

$$\begin{aligned} (\Gamma_0)_{x_1'x_2'|x_1x_2}^{k_1'k_2'|k_1k_2}(\omega_1', \omega_2' | \omega_1, \omega_2) &= 2\pi \delta(\omega_1' + \omega_2' - \omega_1 - \omega_2) (\Gamma_0)_{x_1'x_2'|x_1x_2} \\ &\times \begin{cases} \frac{1}{2} & \text{for } \sum_{i=1',2',1,2} k_i \text{ odd,} \\ 0 & \text{else.} \end{cases} \end{aligned} \quad (2.56)$$

For explicit parametrizations one typically uses symmetry relations such as frequency conservation to reduce the number of arguments (see Sec. 2.2.5.1 for an example). This is highly convenient for numerical computations. However, the introduced asymmetry typically leads to rather cumbersome formulas. In the following sections, we will mostly use the compact multi-index notation. This way, diagrammatic equations can be written concisely for any formalism. The chosen formalism and parametrization can then be inserted afterwards.

Note on conventions: In the previous section the convention for Fourier transforms in Sec. 2.1 had to be applicable to arbitrary operators. In contrast, the convention in this section [see Eqs. (2.48) and (2.54)] facilitates the bookkeeping of frequencies in diagrammatics. As the fields $\bar{\phi}_x$ and ϕ_x are interpreted as incoming or outgoing particles, their Fourier transforms are defined with opposite signs. Frequency conservation thus means that the sum of incoming frequencies equals the sum of outgoing ones. For propagators $G_{x_1|x_1'}(i\omega_1)$, this means that they can be unambiguously labeled with a single frequency argument which stands both for the incoming and outgoing frequency.

Note on equal-time Green's functions: While the ordering of operators at equal contour arguments was left ambiguous in Sec. 2.1, this ambiguity is resolved for Green's functions [Kam11, Klö19]. To see this, note that the operators in the Hamiltonian (2.37) appear at equal times (or contour arguments in the Keldysh action). The normal-ordering of the Hamiltonian is essential for the replacement of operators $\hat{a}^{(\dagger)}$ by fields, $\phi/\bar{\phi}$, in the path integral construction. For consistency with the path integral formulation we thus choose normal ordering for operators with the same contour argument.

2.2.3 Diagrammatic representation of one- and two-particle Green's functions

In this section we show how the one- and two-particle Green's functions can be expressed diagrammatically. We further define self-energy and vertex which are central objects in the diagrammatic methods presented in Sec. 2.2.4.

First, we review some notions of perturbation theory. While plain perturbation theory is not our main tool, it helps understand the QFT methods discussed below. Diagrammatic representations are typically used in perturbative expansions for weak interactions. For a non-interacting theory ($\Gamma_0 = 0$), the Gaussian integrals in Eqs. (2.44a) and (2.44b) can be solved exactly. This *bare propagator* (G_0)_{1|1'} can indeed be identified with the inverse of

the (G_0^{-1}) in the quadratic part of the action. Starting from the non-interacting system, we may treat a small interaction Γ_0 by Taylor expansion of the interacting part of the action in orders of Γ_0 . By Wick's theorem, we obtain expressions involving the bare propagator, G_0 , and bare interaction Γ_0 . To facilitate the bookkeeping one can represent the resulting expressions with diagrams. Using the multi-index notation we write (bare) propagators as

$$G_{11'} = \overleftarrow{1 \quad 1'} , \quad G_{0;11'} = \overleftarrow{1 \quad 1'} , \quad (2.57)$$

where the arrow points in the direction of unprimed indices. The bare interaction is represented as

$$\Gamma_{0;1'2'|12} = \begin{array}{c} 2 \quad 2' \\ \swarrow \quad \searrow \\ \bullet \\ \nearrow \quad \nwarrow \\ 1' \quad 1 \end{array} . \quad (2.58)$$

Here, the short arrows indicate how a propagator line can be attached. The diagrams resulting from a perturbative expansion are graphs, containing the vertices Γ_0 as nodes and bare propagators G_0 as lines. When a vertex and a propagator touch, the corresponding multi-index is contracted. Such *internal* indices are mere summation/integration variables. The *external* indices are externally determined function arguments. Hence, there are ℓ external indices for a diagram representing an ℓ -point function. Examples for four-point diagrams are shown in Fig. 2.2.

While Wick's theorem puts equal emphasis on all types of diagrams, the full set of diagrams can be deduced from a smaller subset. An important subset are *connected* diagrams. A diagram is called connected if all vertices and propagators are linked, i.e., viewing the diagram as an undirected graph one can start at any vertex/propagator and reach any vertex/propagator by travelling along the links of the graph. Otherwise, a diagram is *disconnected*.

Even more restrictive is the set of *one-particle irreducible* (1PI) diagrams. A connected diagram is called 1PI if cutting a single propagator line does not result in a disconnected diagram. Otherwise, it is called one-particle reducible (1PR). The 1PI ℓ -point vertex diagrams $\Gamma^{(\ell)}$ are the 1PI subset of ℓ -point diagrams. Quite remarkably, the 1PI vertex diagrams are sufficient to deduce the full set of diagrams for Green's functions [Neg18]. By the Dyson equation the propagator G can be expressed as

$$G_{1|1'} = G_{0;1|1'} + G_{0;1|2'} \Sigma_{2'|2} G_{2|1'} , \quad (2.59)$$

$$\overleftarrow{1 \quad 1'} \underset{G}{=} \overleftarrow{1 \quad 1'} \underset{G_0}{=} + \overleftarrow{1 \quad 2'} \underset{G_0}{=} \textcircled{\Sigma} \overleftarrow{2 \quad 1'} \underset{G}{=} ,$$

which is a recursive relation involving the bare propagator G_0 and the self-energy Σ . The latter is equivalent to the 1PI two-point vertex. The Dyson equation can be solved for G giving

$$G_{1|1'} = [G_0^{-1} - \Sigma]_{1|1'}^{-1} . \quad (2.60)$$

This equation first seems to be a mere reparametrization of the correlator. But it also implies that a perturbative approximation of the self-energy Σ is more systematic and economic than a perturbative expansion of the propagator G . Concretely, for every approximation of the self-energy the Dyson equation constructs propagator diagrams up to infinite order by resummation.

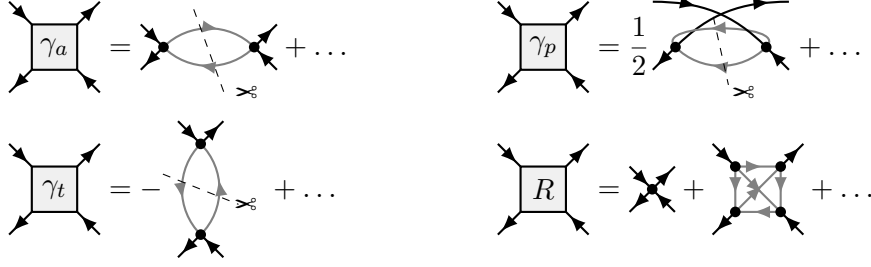


Figure 2.2 Illustration of the parquet decomposition. We show the diagrams of the lowest order in perturbation theory for the 2PR vertices γ_r . The dashed lines indicate cuts which disconnect the diagram. In the parquet approximation the 2PI vertex R is approximated by $R = \Gamma_0$, thereby truncating diagrams of fourth order in the bare interaction.

Similarly, the two-particle Green's function can be expressed as [Roh13, JS10]

$$G_{12|1'2'}^{(4)} = G_{12|1'2'}^{(4)\text{dis}} + G_{12|1'2'}^{(4)\text{con}}, \quad (2.61a)$$

$$G_{12|1'2'}^{(4)\text{dis}} = c_F [G_{1|1'} G_{2|2'} + \zeta G_{1|2'} G_{2|1'}], \quad (2.61b)$$

$$G_{12|1'2'}^{(4)\text{con}} = -G_{1|3'} G_{2|4'} \Gamma_{3'4'|34} G_{3|1'} G_{4|2'}, \quad (2.61c)$$

$$\begin{array}{c} \begin{array}{c} 2' \\ \longrightarrow \\ \hline G^{(4)} \\ \hline \\ \longleftarrow \\ 1 \end{array} \begin{array}{c} 2 \\ \longrightarrow \\ \hline \\ \hline \\ \longleftarrow \\ 1' \end{array} = \begin{array}{c} 2' \\ \longrightarrow \\ \hline \\ \hline \\ \longleftarrow \\ 1 \end{array} \begin{array}{c} 2 \\ \longrightarrow \\ \hline \\ \hline \\ \longleftarrow \\ 1' \end{array} + \zeta \begin{array}{c} 2' \\ \downarrow \\ \hline \\ \hline \\ \uparrow \\ 1 \end{array} \begin{array}{c} 2 \\ \downarrow \\ \hline \\ \hline \\ \uparrow \\ 1' \end{array} - \begin{array}{c} 2' \\ \longrightarrow \\ \hline \\ \hline \\ \longleftarrow \\ 1 \end{array} \begin{array}{c} 4 \\ \longrightarrow \\ \hline \\ \hline \\ \longleftarrow \\ 3' \end{array} \begin{array}{c} 4' \\ \longrightarrow \\ \hline \\ \hline \\ \longleftarrow \\ 3 \end{array} \begin{array}{c} 2 \\ \longrightarrow \\ \hline \\ \hline \\ \longleftarrow \\ 1' \end{array}, \end{array}$$

where $G^{(4)\text{dis}}$ is the disconnected part describing propagation without any scattering and $G^{(4)\text{con}}$ is the connected part. The constant c_F is introduced for consistency with our definition of correlators and depends on the formalism and gives $c_F = -1$ for the MF and $c_F = -i$ for the KF. The 1PI four-point vertex $\Gamma^{(4)}$ encodes the renormalized interaction between two particles and is typically just called vertex $\Gamma \equiv \Gamma^{(4)}$ in this thesis. By virtue of the tree expansion (2.61c) the vertex is obtained from the connected four-point Green's function by amputating the four external propagator legs [KBS10].

2.2.4 Exact diagrammatic equations

Above we introduced diagrams in the context of bare perturbation theory. There are, however, also exact equations relating the fully renormalized propagator, self-energy and two-particle interaction vertex. We present two sets of equations: the parquet equations and the flow equations of the functional renormalization group. However, while they are exact, approximations are inevitable for finding a solution to them. We discuss the so-called parquet approximation and the 1-loop truncation which are used for our numerical studies in Sec. 4.

2.2.4.1 Parquet theory

Here we present an overview of the parquet equations without delivering a derivation. A modern review with derivations from generating functionals can be found in [Bic04, Kug19, EKKH23].

As explained above, vertex diagrams in Γ are 1PI 4-point diagrams. These can be further classified by their two-particle (ir)reducibility. A diagram is called *two-particle irreducible*

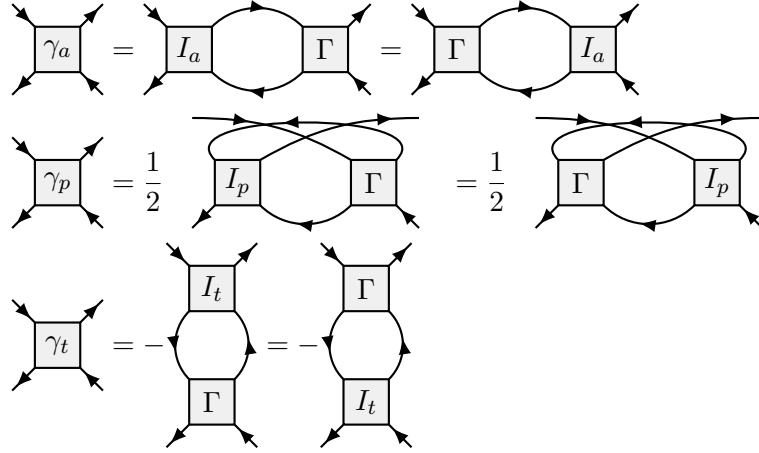


Figure 2.3 Diagrammatic depiction of the Bethe–Salpeter equations (2.66) for the three channels $r = a, p, t$.

(2PI) if cutting two propagator lines does not result in a disconnected diagram. Otherwise, the diagram is called *two-particle reducible* (2PR). Figure 2.2 shows examples for 2PR diagrams, where the dashed lines indicate how a cut can disconnect a diagram. For a fermionic theory, there are three ways of cutting two lines to disconnect the four external indices. They correspond to different channels which we here denote by a , p and t . Every 2PR vertex diagram can be unambiguously classified by one of these channels. This gives us the parquet decomposition

$$\Gamma = R + \gamma_a + \gamma_p + \gamma_t, \quad (2.62)$$

where R is fully 2PI and the γ_r 's are 2PR in channel $r = a, p, t$. Figure 2.2 illustrates the parquet decomposition with the diagrams of the lowest orders in perturbation theory.

We can also distinguish two-particle (ir)reducibility with respect to a certain channel. This gives us the decompositions

$$\Gamma = I_a + \gamma_a = I_p + \gamma_p = I_t + \gamma_t, \quad (2.63)$$

where γ_r is reducible and the I_r irreducible in channel r . The latter contains

$$I_r = R + \gamma_{\bar{r}}, \quad (2.64a)$$

where $\gamma_{\bar{r}}$ denotes the vertices which are 2PR in the *other* channels, explicitly

$$\gamma_{\bar{a}} = \gamma_p + \gamma_t, \quad \gamma_{\bar{p}} = \gamma_a + \gamma_t, \quad \gamma_{\bar{t}} = \gamma_a + \gamma_p. \quad (2.64b)$$

With the above definitions we can write down the three Bethe–Salpeter equations. Fig. 2.3 shows them in the form of diagrams. Explicitly, they can be written in matrix notation

$$\gamma_r = \Gamma \circ \Pi_r \circ I_r = I_r \circ \Pi_r \circ \Gamma, \quad (2.66)$$

$$\Sigma = - \text{tadpole} - \frac{1}{2} \text{loop} \quad (2.65)$$

Figure 2.4 Diagrammatic depiction of the Schwinger–Dyson equation (2.71). The first term on the right-hand side is the Hartree contribution, which is constant in the frequency domain.

by introducing the pair propagators

$$\Pi_{a;34|3'4'} = c_F G_{3|3'} G_{4|4'}, \quad (2.67a)$$

$$\Pi_{p;34|3'4'} = \frac{1}{2} c_F G_{3|3'} G_{4|4'}, \quad (2.67b)$$

$$\Pi_{t;43|3'4'} = -c_F G_{3|3'} G_{4|4'}, \quad (2.67c)$$

which contain the channel-dependent prefactors indicated in the diagrams in Fig. 2.3. The constant c_F is a formalism-dependent factor which gives a trivial $c_F = 1$ in the Matsubara formalism and $c_F = -i$ in the Keldysh formalism.³ The \circ -operation contracts the indices depending on the channel r of the involved pair propagator Π_r , explicitly

$$a : [A \circ B]_{12|34} = A_{16|54} B_{52|36}, \quad (2.68a)$$

$$p : [A \circ B]_{12|34} = A_{12|56} B_{56|34}, \quad (2.68b)$$

$$t : [A \circ B]_{12|34} = A_{62|54} B_{15|36}, \quad (2.68c)$$

which amounts to an ordinary matrix multiplication in each channel if the indices are suitably reordered and grouped, i.e.,

$$\Gamma_{1',2'|1,2} = \text{square with } \Gamma \text{ and legs } 2, 2', 1', 1 \mapsto \begin{cases} \Gamma_{(1',2),(1,2')} & \text{for } a \text{ channel,} \\ \Gamma_{(1',2'),(1,2)} & \text{for } p \text{ channel,} \\ \Gamma_{(2',2),(1',1)} & \text{for } t \text{ channel.} \end{cases} \quad (2.69)$$

The Bethe–Salpeter equations are complemented by the Dyson equation (2.59) and the Schwinger–Dyson equation (SDE) to form the parquet equations. The SDE is shown diagrammatically in Fig. 2.4 and can be derived from Heisenberg’s equation of motion [RVT12] or with a functional approach [KBS10]. By defining the loop

$$L(\Gamma, G)_{1'1} = -c_F \Gamma_{1'2'|12} G_{2|2'}, \quad (2.70)$$

we can write the SDE as

$$\Sigma = L(\Gamma_0, G) + \frac{1}{2} L(\Gamma_0 \circ \Pi_a \circ \Gamma, G) = L(\Gamma_0, G) + \frac{1}{2} L(\Gamma_0 \circ \Pi_p \circ \Gamma, G), \quad (2.71)$$

which computes the self-energy from the propagator, the full and the bare vertex.

Note that the parquet equations provide no recipe to determine the 2PI vertex R . However, for a given R the parquet equations are a closed set of self-consistent equations for the self-energy and vertex. In our study in Sec. 4 we choose the parquet approximation which sets $R = \Gamma_0$ and will be discussed in Sec. 2.2.4.3.

³ Note that this prefactor depends on the conventions chosen in the definition of Green’s functions and vertices and therefore deviates by a minus sign from [HMPS04, JS10].

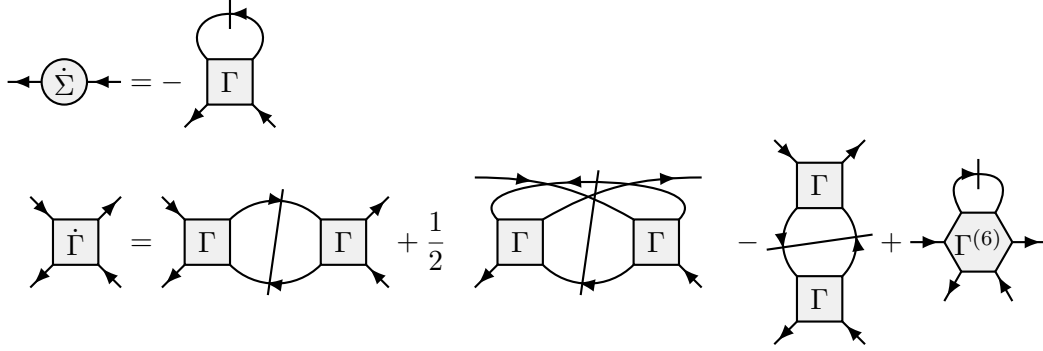


Figure 2.5 1-loop flow equations for self-energy and vertex derived from the Wetterich equation. Propagators and pair propagators crossed by the single line denote a derivative $\left. \frac{d}{d\Lambda} \right|_{\Sigma^\Lambda = \text{const.}}$ which ignores the Λ -dependence of the self-energy.

2.2.4.2 Functional renormalization group

The functional renormalization group (fRG) follows a very different strategy [KBS10]: By introducing a regulator into the bare propagator G_0^Λ the action gains a dependence on the continuous flow parameter $\Lambda \in [\Lambda_i, \Lambda_f]$. Consequently, also the propagator G^Λ , self-energy Σ^Λ , and vertex Γ^Λ become Λ -dependent. The regulator is chosen to render the action trivial for initial Λ_i and to recover the original action for final Λ_f . One possibility to obtain a trivial action is by ensuring $G_0^{\Lambda_i} = 0$ for which the only non-vanishing diagrams are the bare interaction Γ_0 and the Hartree contribution of the self-energy [JS10]. The theory at Λ_i and Λ_f are connected by a flow, i.e., by flow equations for self-energy $\dot{\Sigma} = d\Sigma/d\Lambda$ and vertex $\dot{\Gamma} = d\Gamma/d\Lambda$. To obtain the desired quantities one needs to integrate the flow equations with the given initial condition at Λ_i . For the self-energy this explicitly reads $\Sigma^{\Lambda_f} = \int_{\Lambda_i}^{\Lambda_f} d\Lambda \frac{d\Sigma^\Lambda}{d\Lambda}$. One traditional derivation of flow equations introduces the Λ -dependent regulator into the generating functionals for Green's functions and vertices to derive the Wetterich equation which is a flow equation for these functionals [Wet93, KBS10]. The Wetterich equation results in an infinite hierarchy of flow equations for 1PI vertex diagrams as indicated in Fig. 2.5, where we see that the flow of the four-point vertex $\dot{\Gamma}^\Lambda$ depends on the six-point vertex $\Gamma^{(6)}$. The latter is a function of 5 independent frequencies. While the Wetterich equation provides an equation for $\dot{\Gamma}^{(6)}$ its evaluation is numerically intractable. The flow equations are therefore typically approximated by neglecting the contribution from the six-point vertex. We call the truncated version of Fig. 2.5 the *1-loop flow equations*. Explicitly these read

$$\dot{\Sigma} = L(\Gamma, S), \quad (2.72a)$$

$$\dot{\Gamma} = \sum_r \Gamma \circ \dot{\Pi}_{r;S} \circ \Gamma, \quad (2.72b)$$

where the *single-scale propagator*, S^Λ , is defined as the derivative of the propagator G^Λ while ignoring the Λ -dependence of the self-energy Σ^Λ . Diagrammatically, we depict it by a propagator which is crossed by a single line

$$S_{1|1'}^\Lambda = \left. \frac{dG_{1|1'}^\Lambda}{d\Lambda} \right|_{\Sigma^\Lambda = \text{const.}} = 1 \text{---} \left| \leftarrow 1' \right., \quad (2.73)$$

and analogously the differentiated pair propagator in Eq. (2.72b) is defined as

$$\dot{\Pi}_{r;S}^\Lambda = \left. \frac{d\Pi_r^\Lambda}{d\Lambda} \right|_{\Sigma^\Lambda = \text{const.}}. \quad (2.74)$$

In Fig. 2.5 $\dot{\Pi}_{r;S}$ is depicted by a pair of propagators crossed by a single straight line. The truncation of the equation in Fig. 2.5 introduces a number of problems. When the six-point vertex is neglected, the flow equation does not contain a full derivative of the vertex. Therefore, different choices for the regulator lead to different results. This regulator dependence is sometimes counted as a strength of fRG since it allows the practitioner to make a physically reasonable choice. In the absence of a clear heuristic it is, however, not possible to tell which regulator leads to the best approximation.

In recent years, the problem of regulator dependence has been addressed by the multiloop extension of the flow equations [KvD18b, KvD18c, KvD18a]. Unlike the traditional derivation, it chooses the parquet equations as starting point. And like in the parquet approach, the 2PI vertex R has to be supplied as an external input. Therefore, R is assumed to be Λ -independent. By applying a total Λ derivative to both sides of the parquet equations one then obtains the multiloop flow equations. Due to the appearance of $\dot{I}_r = \dot{\gamma}_{\bar{r}}$ on the right-hand side, the flow equations for the 2PR vertices need to be inserted iteratively, leading to a loop expansion of the 2PR vertices

$$\dot{\gamma}_r = \sum_{\ell=1}^{\infty} \dot{\gamma}_r^{(\ell)} \quad (2.75)$$

where the contributions for each ℓ are given in Fig. 2.6.

The pair propagators crossed by two lines represent a *full* Λ derivative (as opposed to the equation in Fig. 2.5)

$$\dot{\Pi}_r^\Lambda = \frac{d}{d\Lambda} \Pi_r^\Lambda, \quad (2.76)$$

with which the flow equations for the vertices read

$$\dot{\Gamma} = \sum_{r=a,p,t} \sum_{\ell=1}^{\infty} \dot{\gamma}_r^{(\ell)}, \quad (2.77a)$$

$$\dot{\gamma}_r^{(1)} = \Gamma \circ \dot{\Pi}_r \circ \Gamma, \quad (2.77b)$$

$$\dot{\gamma}_r^{(2)} = \dot{\gamma}_{r;L}^{(2)} + \dot{\gamma}_{r;R}^{(2)}, \quad (2.77c)$$

$$\dot{\gamma}_r^{(\ell>2)} = \dot{\gamma}_{r,L}^{(\ell)} + \dot{\gamma}_{r,C}^{(\ell)} + \dot{\gamma}_{r,R}^{(\ell)}, \quad (2.77d)$$

with

$$\dot{\gamma}_{r,L}^{(\ell)} = \dot{\gamma}_{\bar{r}}^{(\ell-1)} \circ \Pi_r \circ \Gamma, \quad (2.77e)$$

$$\dot{\gamma}_{r,R}^{(\ell)} = \Gamma \circ \Pi_r \circ \dot{\gamma}_{\bar{r}}^{(\ell-1)}, \quad (2.77f)$$

$$\dot{\gamma}_{r,C}^{(\ell)} = \dot{\gamma}_{\bar{r};R}^{(\ell-1)} \circ \Pi_r \circ \Gamma = \Gamma \circ \Pi_r \circ \dot{\gamma}_{\bar{r};L}^{(\ell-1)}. \quad (2.77g)$$

The flow of the self-energy becomes

$$\dot{\Sigma} = \dot{\Sigma}_{\text{std}} + \dot{\Sigma}_{\bar{t}} + \dot{\Sigma}_t, \quad (2.77h)$$

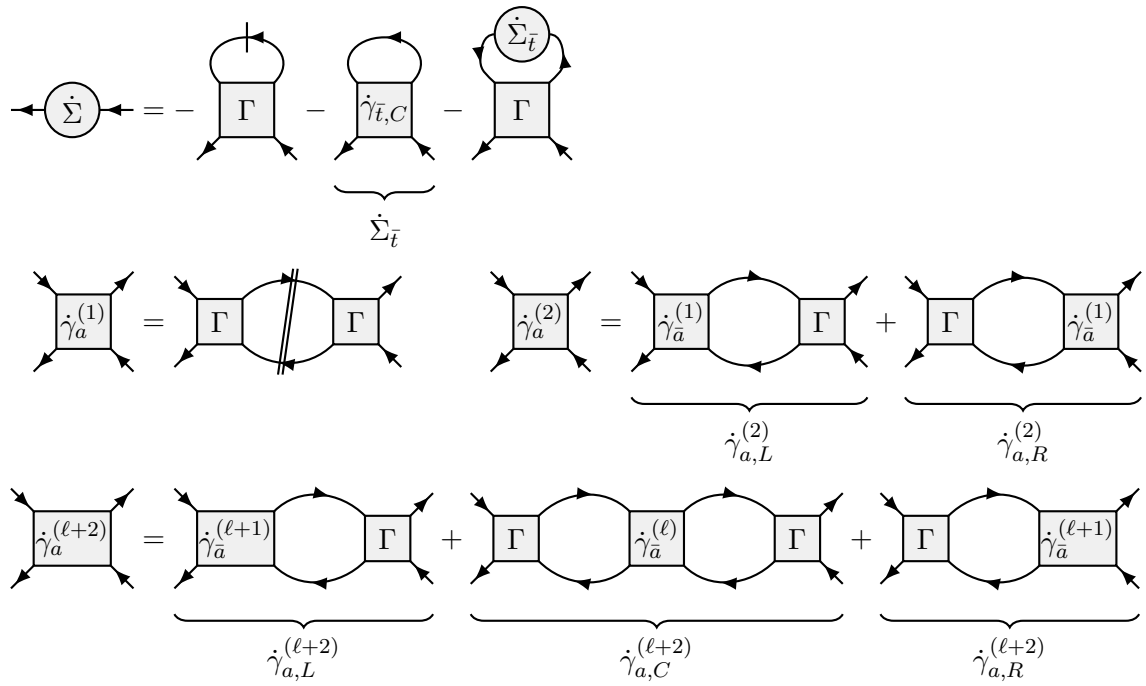


Figure 2.6 Diagrammatic depiction of the mRG flow equations: The vertex flow is exemplified for the 2PR vertex γ_a . The doubly crossed pair propagator denotes that a full Λ derivative is applied to Π_a . Note that the vertex flow at loop order $\ell + 1$ can be computed by insertion of contributions from loop order ℓ . The ‘center’ contributions $\dot{\gamma}_{r,C}$ of the vertex flow feeds back into the self-energy flow, creating a self-consistency condition for $\ell \geq 3$.

where the contributions on the right are

$$\dot{\Sigma}_{\text{std}} = L(\Gamma, S), \quad (2.77i)$$

$$\dot{\Sigma}_{\bar{t}} = L\left(\sum_{\ell} \hat{\gamma}_{\bar{t}, C}^{(\ell)}, G\right), \quad (2.77j)$$

$$\dot{\Sigma}_t = L(\Gamma, G\dot{\Sigma}_{\bar{t}}G). \quad (2.77k)$$

A comparison with the conventional flow equations (2.72) reveals striking similarities: The self-energy flow (2.72a) is identical to $\dot{\Sigma}_{\text{std}}$ (2.77i) and the 1-loop contribution of the mfRG vertex flow (2.77b) is identical to the vertex flow in (2.72b) after a Katanin substitution [Kat04], $\ddot{\Pi}_{r;S} \rightarrow \ddot{\Pi}_r$, which was introduced to improve the fulfillment of Ward identities. Hence, the truncated equations (2.72) generate the subset of $\ell = 1$ diagrams from mfRG equations and are therefore referred to as 1-loop equations.

Comparison of parquet and (m)frg equations: Since the mfRG equations are derived from the parquet equations, a fully converged mfRG result should fulfill parquet self-consistency [KvD18a]. Hence, the parquet and mfRG equations are formally equivalent if both apply the same approximation to the 2PI vertex R . For practical purposes, the difference between the two methods lies in the efficiency of the involved algorithmic procedures.

The convergence of mfRG results to a parquet solution has been thoroughly investigated for the Anderson impurity model at weak to intermediate coupling in the MF [CGKH⁺22]. In App. B a similar investigation is presented in the MF and KF. There we further discuss the algorithmic differences between the parquet and the mfRG scheme. Most importantly, in both methods one needs to find a high-dimensional fixed point of coupled non-linear equations. (For the mfRG scheme the $\ell \leq 3$ -loop contributions introduce a self-consistency condition.) Hence, they both suffer from the difficulty to find a unique converged fixed point in certain regimes.

In contrast, to solve the 1- or 2-loop flow equations (2.72) one does not need to solve self-consistent equations. Instead, the flow of self-energy $\dot{\Sigma}$ and vertex $\dot{\Gamma}$ is fully determined by the non-differentiated functions Σ and Γ . Therefore, a wider range of parameters can be reached. But the solutions suffer from the truncation as discussed in the next section.

2.2.4.3 Approximations

In the following we summarize the different approximations which are made in the parquet approach and in the frg. They are inevitable to render the equations closed and solvable. However, they lead to a number of problems and limit the applicability of the methods.

Firstly, the 1-loop flow equations (2.72) are obtained by neglecting the six-point contribution in Fig. 2.5. As mentioned above, the truncation of the flow equation introduces a dependence on the regulator. While calculations in the MF are possible for a variety of regulators (see e.g. Ref. [CGKH⁺22]), for the KF, Ref. [JS10] found that many regulators lead to violations of physical relations such as causality and fluctuation-dissipation relations. Thus, the physical implications and applicability of the approximation in the 1-loop flow equations depends on the chosen regulator. Furthermore, it is argued in Ref. [KvD18b] that the 1-loop flow equations are biased towards so-called ladder diagrams which are, however, particularly prone to divergences. The truncation also leads to ambiguities in the computation of the susceptibilities [THK⁺19, KvD18a]. However, if one is not interested in quantitative reliability, it has been shown that the 1-loop flow equations already capture the leading logarithmic contributions for the x-ray edge singularity, the interacting resonant level model and Luttinger liquids [DJ21, KPBM10, MAE⁺08].

The parquet and mfRG equations can be discussed together since these methods are formally equivalent [KvD18a].⁴ They both require the 2PI vertex R as external input and therefore involve the same approximations. It is clear that a ‘reasonable’ approximation of R is crucial. For lattice models one may approximate it with a local vertex $R = R_{\text{DMFT}}$ which is computed from dynamic mean-field theory (DMFT) [GKKR96]. Diagrammatic methods that rely on DMFT input are summarized under the term *diagrammatic extensions of DMFT* [RVT12]. While DMFT only captures local correlations, spatial correlations are included with diagrammatic methods. Inserting the DMFT vertex into the parquet equations or the fRG flow equations are the basic ideas of the dynamical vertex approximation (D Γ A) [TKH07] and the DMF²RG [TAB⁺14]. Indeed, DMFT solvers are available both for imaginary- and real-frequency vertices. Imaginary frequency vertices can be computed with, e.g., Quantum Monte-Carlo methods [GML⁺11] and real-frequency vertices have become available due to a recently developed multipoint extension of the numerical renormalization group (NRG) [LKvD21, LHS⁺24]. Reference [P6] investigates whether NRG vertices fulfill physical and diagrammatic identities for Anderson impurity model (see Sec. 2.2.5). However, while diagrammatic extensions of DMFT have shown promising results (see e.g., [EHHK20, KWK⁺24]) they are beyond the scope of this thesis. Our goal is to pave the way for these methods by first developing purely diagrammatic methods which can be extended in the future.

The R chosen in our purely diagrammatic study in Sec. 4 is given by the parquet approximation (PA) which sets the 2PI vertex $R = \Gamma_0$ to the bare vertex. This approximation neglects diagrams starting at the fourth order in the bare interaction $\mathcal{O}(\Gamma_0^4)$ (as indicated in Fig. 2.2). Nevertheless, the parquet approximation possesses a number of convenient properties as summarized in Refs. [Bic04, Kug19]. One of them is the fulfillment of crossing symmetry which is a consequence of the Pauli principle. This also resolves the Fierz ambiguity for Hubbard-like interactions [KWK⁺24]. It has been shown that two-particle self-consistency guarantees the fulfillment of the Mermin–Wagner theorem which is important for two-dimensional systems [MW66, VT97]. Another property is the unbiased and two-particle self-consistent treatment of channels in the Bethe–Salpeter equations where all two-particle channels are coupled by inter-channel feedback. As physical susceptibilities are encoded in different channels this is particularly important in the presence of competing ordering instabilities. Furthermore, lower-dimensional quantities such as physical susceptibilities and three-point vertices are encoded in the high-frequency asymptotics of the vertex [WLT⁺20]. Using a suitable frequency parametrization of the vertex, these quantities can be directly read off without further postprocessing. Parquet self-consistency also resolves the ambiguity in the computation of the susceptibilities [THK⁺19, KvD18a, WLT⁺20]. There is numerical evidence [CGKH⁺22] that sum rules for susceptibilities and certain Ward identities are fulfilled while others are violated in the non-perturbative regime. Since Ward identities are consequences of conservation laws [KBC⁺10], the violation indicates that the solution found by the parquet approximation is non-conserving. In fact, it has been shown that the fulfillment of both conservation laws and parquet self-consistency can only be achieved by the exact solution [Smi92]. Which of these properties is preferred over the other depends on the concrete physical problem in question. In our studies in Chapter 4, we prioritize parquet self-consistency and use Ward identities only to gauge the quality of a result.

⁴ Note however, to go beyond the parquet approximation the self-energy flow might have to be adapted since its derivation in Ref. [KvD18a] explicitly assumes the parquet approximation.

2.2.5 The Anderson impurity model and its diagrammatic description

In this section, we present the Anderson impurity model (AIM) and give an overview of its diagrammatic ingredients in the MF and KF. The second-quantized Hamiltonian of the AM reads

$$\hat{H} = \hat{H}_0 + \hat{H}_{\text{hyb}} + \hat{H}_{\text{int}}, \quad (2.78a)$$

$$\hat{H}_0 = \epsilon_d \sum_{\sigma=\uparrow,\downarrow} \hat{d}_\sigma^\dagger \hat{d}_\sigma + \sum_{\mathbf{k}} \sum_{\sigma=\uparrow,\downarrow} \epsilon_{\mathbf{k}} \hat{c}_{\sigma\mathbf{k}}^\dagger \hat{c}_{\sigma\mathbf{k}}, \quad (2.78b)$$

$$\hat{H}_{\text{hyb}} = \sum_{\mathbf{k}} \sum_{\sigma=\uparrow,\downarrow} V \hat{c}_{\sigma\mathbf{k}}^\dagger \hat{d}_\sigma + \text{h.c.}, \quad (2.78c)$$

$$\hat{H}_{\text{int}} = U \hat{d}_\uparrow^\dagger \hat{d}_\uparrow \hat{d}_\downarrow^\dagger \hat{d}_\downarrow. \quad (2.78d)$$

This model describes an impurity site ($d_\sigma^{(\dagger)}$) that is coupled to a non-interacting bath ($c_{\sigma\mathbf{k}}^{(\dagger)}$). The system is occupied by electrons with spin $\sigma = \uparrow, \downarrow$. On the impurity site electrons experience an instantaneous on-site repulsion U . The chemical potential ϵ_d on the impurity will be set to $\epsilon_d = -U/2$ if we want to achieve half filling [Roh13]. The hopping between impurity and bath is quantified by V .

The (bare) propagator does not depend on the spin index since above Hamiltonian respects $SU(2)$ spin symmetry [Roh13]. As the c fields appear at most quadratically we can integrate them out in the functional integral in Eqs. (2.44). The resulting action takes the form of Eq. (2.44c), but now it is a functional of the d -fields only. The Matsubara and retarded bare propagator for the d fields read

$$G_0(i\nu) = \frac{1}{i\nu - \epsilon_d + \Delta(i\nu)}, \quad (2.79a)$$

$$G_0^R(\nu) = \frac{1}{\nu - \epsilon_d + \Delta^R(\nu) + i0^+}, \quad (2.79b)$$

where the hybridization Δ encodes the corrections for hopping from the impurity to the bath, propagation through the bath and hopping back to the impurity (see e.g., Eq. (2.62) in Ref. [JS10]). Explicitly, the hybridization reads

$$\Delta(i\nu) = -Vg(i\nu)V^*, \quad (2.80a)$$

$$\Delta^R(\nu) = -Vg^R(\nu)V^*, \quad (2.80b)$$

where $g(\nu)$ is the local propagator of the c fields. Since we are typically not interested in the specific band structure of the bath we assume a box-shaped spectrum for $g(\nu)$, i.e., $\text{Im}(g^R(\nu)) = -\pi\theta(D - |\nu|)$ where D is the half bandwidth, such that we obtain

$$g(i\nu) = -2i \arctan(D/\nu), \quad (2.81a)$$

$$g^R(\nu) = \ln \left| \frac{\nu + D}{\nu - D} \right| - i\pi\theta(D - |\nu|). \quad (2.81b)$$

To derive $g(i\nu)$, we inserted the spectrum in Eq. (2.26b) and for g^R we used Eq. (2.33b) and the Kramers–Kronig relations (2.35). In Sec. 4 we take the wide-band limit $D \rightarrow \infty$ such that the hybridization simplifies to

$$\Delta(i\nu) = i\Delta \text{sgn}\nu, \quad (2.82a)$$

$$\Delta^R(\nu) = i\Delta, \quad (2.82b)$$

where we defined the constant $\Delta = \pi|V|^2$ for convenience.

For the bare interaction Γ_0 we can first focus on the spin indices and obtain in the MF

$$\Gamma_{0;\sigma_1\sigma_2|\sigma_1'\sigma_2'} = U[\delta_{\sigma_1\sigma_2}\delta_{\sigma_2\sigma_1'} - \delta_{\sigma_1\sigma_1'}\delta_{\sigma_2\sigma_2'}]. \quad (2.83)$$

In the Keldysh formalism, the contour index structure can be read off from the action (2.51) where we see that only equal times and equal contour indices contribute

$$\Gamma_{0;\sigma_1\sigma_2|\sigma_1'\sigma_2'}^{c_1c_2|c_1'c_2'} = -c_1\delta_{c_1=c_2=c_1'=c_2'}\Gamma_{0;\sigma_1\sigma_2|\sigma_1'\sigma_2'}. \quad (2.84)$$

After a Keldysh rotation this becomes

$$\begin{aligned} \Gamma_{0;\sigma_1\sigma_2|\sigma_1'\sigma_2'}^{k_1k_2|k_1'k_2'} &= \Gamma_{0;\sigma_1\sigma_2|\sigma_1'\sigma_2'} \sum_{c=\pm} (-c) \prod_{i=1,2,1',2'} D^{k_i|c} \\ &= \begin{cases} \frac{1}{2}\Gamma_{0;\sigma_1\sigma_2|\sigma_1'\sigma_2'} & \text{for } \sum_{i=1,2,1',2'} k_i \text{ odd,} \\ 0 & \text{else.} \end{cases} \end{aligned} \quad (2.85)$$

This concludes the summary of the Anderson impurity model and the quantities defining its reduced action, i.e., G_0 and Γ_0 .

2.2.5.1 Symmetries and vertex parametrizations

After defining the model and its bare propagator and vertex, we are in a position to solve the parquet or flow equations within the parquet approximation. However, for our study in Sec. 4 an efficient evaluation of the Bethe–Salpeter and flow equations is key. Above, we have written vertices in the compact notation $\Gamma_{1'2'|12}$ where each multi-index i runs over all contour arguments (τ_i or $t_i^{c_i}$) and all one-particle quantum numbers σ_i . In the presence of symmetries, the number of non-redundant components can be strongly reduced, which is particularly important for the parametrization of the vertex Γ . Symmetries reduce both the number of vertex components that need to be stored and the number of components that need to be computed. Since each contribution to the vertex flow, Eqs. (2.77b) and (2.77e)–(2.77g), has the same matrix-product structure as the Bethe–Salpeter equations (2.66) it suffices here to focus on the latter.

In Ref. [Roh13] the symmetries of the AIM are derived in the Matsubara formalism. While most results can be carried over to the Keldysh formalism, there are some notable differences in the formalisms [JPS10]. In this section we will summarize the key findings for both formalisms. For the sake of conciseness we exclusively present results for the two-particle correlators in the time domain. Symmetry relations in the frequency domain can be obtained by inserting the Fourier transformation in the desired frequency convention.

First we discuss properties that can be derived from the definition of correlators, Eqs. (2.10) and (2.19a): By crossing symmetry the exchange of two operators leads to

$$G_{12|1'2'} = -G_{21|1'2'} = -G_{12|2'1'} = G_{21|2'1'}. \quad (2.86)$$

Under complex conjugation of a correlator, the operators are modified due to the relation

$$\text{Tr} [\hat{A}\hat{B} \dots \hat{D}]^* = \text{Tr} [\hat{D}^\dagger \dots \hat{B}^\dagger \hat{A}^\dagger]. \quad (2.87)$$

Applying this to annihilation and creation operators $\hat{a}^{(\dagger)}(-i\tau)$ or $\hat{a}^{(\dagger)}(t)$ and by suitable exchange of operators one then finds

$$[G_{\sigma_1\sigma_2|\sigma_1'\sigma_2'}(\tau_1, \tau_2|\tau_1', \tau_2')]^* = G_{\sigma_1'\sigma_2'|\sigma_1\sigma_2}(-\tau_1', -\tau_2' | -\tau_1, -\tau_2), \quad (2.88a)$$

$$[G_{\sigma_1\sigma_2|\sigma_1'\sigma_2'}^{k_1k_2|k_1'k_2'}(t_1, t_2|t_1', t_2')]^* = (-1)^{1+\sum_i k_i} G_{\sigma_1'\sigma_2'|\sigma_1\sigma_2}^{k_1'k_2'|k_1k_2}(t_1', t_2'|t_1, t_2). \quad (2.88b)$$

Another property which is quickly confirmed for the AIM is a special behavior under time-reversal is [RVT12, JPS10], by checking that the second-quantized Hamiltonian exclusively contains real coefficients in front of the creation and annihilation operators. Inserting a particle-number basis one finds that all operator matrix elements in the PSFs are real. For Matsubara correlators we thereby deduce

$$G_{\sigma_1\sigma_2|\sigma_1'\sigma_2'}(\tau_1, \tau_2|\tau_1', \tau_2') \in \mathbb{R}, \quad (2.89)$$

whereas the KF merely uses this property (together with the equilibrium condition) to obtain generalized fluctuation-dissipation relations (gFDR) which reduce the number of independent Keldysh components. For a derivation of gFDRs and explicit formulas we refer to Refs. [WH02, JPS10, P4].

The SU(2)-spin symmetry is a bit more intricate. By explicit calculation, Ref. [RVT12] confirms that the spin operators \hat{S}_i ($i = x, y, z$) commute with the Hamiltonian of the AIM. It follows that the total spin is conserved and the non-vanishing 2-particle Green's functions are reduced to the six components

$$G_{\sigma\sigma|\sigma\sigma}, \quad G_{\sigma\bar{\sigma}|\sigma\bar{\sigma}}, \quad G_{\sigma\bar{\sigma}|\bar{\sigma}\sigma}, \quad (2.90)$$

where a barred spin is flipped, i.e., $\bar{\uparrow} = \downarrow, \bar{\downarrow} = \uparrow$. Invariance under a global spin flip further reduces the components to three. Since the last two components in Eq. (2.90) are related by crossing symmetry, $G_{\uparrow\downarrow\downarrow\uparrow}(\tau_1, \tau_2|\tau_1'\tau_2') = -G_{\uparrow\downarrow\uparrow\downarrow}(\tau_1, \tau_2|\tau_2'\tau_1')$, and the first one can be obtained from the others [Roh13], i.e.,

$$G_{\uparrow\uparrow\uparrow\uparrow} = G_{\uparrow\downarrow\uparrow\downarrow} + G_{\uparrow\downarrow\downarrow\uparrow}, \quad (2.91)$$

one could reduce the representation of the vertex to one spin component, for example $\Gamma_{\uparrow\downarrow\uparrow\downarrow}$.

The representation of spin components in terms of single-particle spins $\sigma = \uparrow, \downarrow$ directly follows from the general multi-index formulas. However, under SU(2)-spin symmetry a different parametrization is more convenient for the evaluation of Bethe–Salpeter equations. Indeed, the BSEs become spin-diagonal for SU(2)-symmetric systems if the following spin combinations are used [Bic04, RVT12]:

$$G_{D/M} = G_{\uparrow\uparrow\uparrow\uparrow} \pm G_{\uparrow\downarrow\uparrow\downarrow}, \quad (2.92)$$

$$G_{T/S} = G_{\uparrow\downarrow\uparrow\downarrow} \pm G_{\uparrow\downarrow\downarrow\uparrow}, \quad (2.93)$$

which are called the *density*, *magnetic*, *triplet* and *singlet* spin channel. The BSE in the t channel is diagonal in the density, magnetic and $G_{\uparrow\downarrow\uparrow\downarrow}$ channel. Since the BSE in the t and a channel are related by crossing symmetry, the spin diagonal combinations of the latter are typically not considered. Lastly, the BSE in the p channel is diagonal in the singlet, triplet and $G_{\uparrow\downarrow\uparrow\downarrow}$ channel where the triplet channel is identical to the $G_{\uparrow\uparrow\uparrow\uparrow}$ channel by Eq. (2.91).

Above we already mentioned that setting the on-site potential to $\epsilon_d = -U/2$ yields a particle-hole symmetric Hamiltonian which effectively means that correlators are invariant

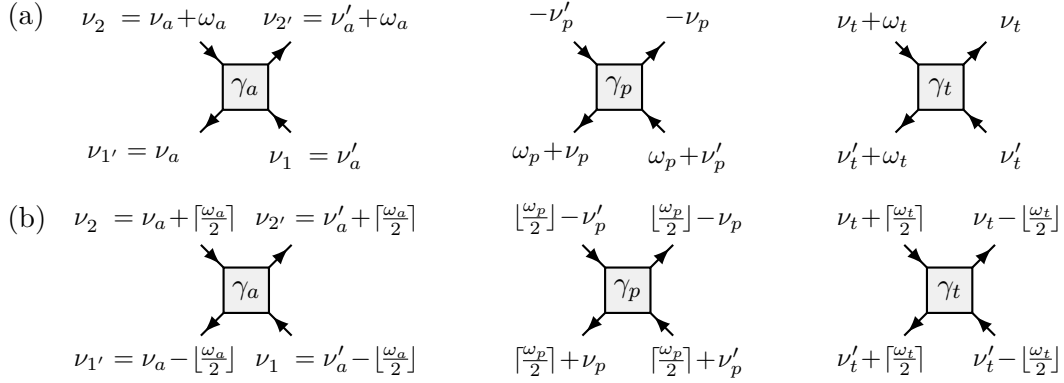


Figure 2.7 Frequency conventions (a) without and (b) with $\lceil \frac{\omega}{2} \rceil$ -shift. The shown frequency convention in (b) corresponds to the one chosen in [P3] and is obtained from (a) by subtracting $\lceil \frac{\omega_r}{2} \rceil$ from all legs. The Gauss brackets, $\lceil \cdot \rceil$ or $\lfloor \cdot \rfloor$, are needed in the Matsubara formalism and here indicate rounding down or up to the next bosonic frequency. They ensure that all legs carry fermionic Matsubara frequencies. For the continuous frequencies in the Keldysh formalism no rounding is needed.

under a global replacement of creation by annihilation operators (and vice versa) [Roh13].

$$G_{\sigma_1\sigma_2|\sigma_1'\sigma_2'} = \mathcal{G}[\hat{d}_{\sigma_1}\hat{d}_{\sigma_2}, \hat{d}_{\sigma_1'}^\dagger, \hat{d}_{\sigma_2'}^\dagger] = \mathcal{G}[\hat{d}_{\sigma_1}^\dagger, \hat{d}_{\sigma_2}^\dagger, \hat{d}_{\sigma_1'}, \hat{d}_{\sigma_2'}]. \quad (2.94)$$

To express the last expression as a Green's function one can either exchange operators or apply complex conjugation and use Eq. (2.87). For the latter one obtains

$$G_{\sigma_1\sigma_2|\sigma_1'\sigma_2'}(\tau_1, \tau_2|\tau_1', \tau_2') = [G_{\sigma_1\sigma_2|\sigma_1'\sigma_2'}(-\tau_1, -\tau_2|-\tau_1', -\tau_2')]^*, \quad (2.95a)$$

$$G_{\sigma_1\sigma_2|\sigma_1'\sigma_2'}^{k_1k_2|k_1'k_2'}(t_1, t_2|t_1', t_2') = (-1)^{1+\sum_i k_i} [G_{\sigma_1\sigma_2|\sigma_1'\sigma_2'}^{k_1k_2|k_1'k_2'}(t_1, t_2|t_1', t_2')]^*. \quad (2.95b)$$

Lastly, it has been shown that SU(2)-spin symmetry and particle-hole symmetry collude to provide the additional relation [see Eq. (2.135) in Ref. [Roh13]]

$$G_{\uparrow\downarrow|\uparrow\downarrow}(z_1, z_2|z_1', z_2') = G_{\uparrow\uparrow|\uparrow\uparrow}(z_1', z_1|z_2', z_2) + G_{\uparrow\downarrow|\uparrow\downarrow}(z_2', z_1|z_1', z_2), \quad (2.96)$$

where z_i denotes the imaginary time τ_i for Matsubara and contour argument t_i^c for Keldysh Green's functions. Inserting Eq. (2.96) into the singlet or triplet channel we obtain

$$G_{S/T}(z_1, z_2|z_1', z_2') = G_{D/M}(z_1', z_1|z_2', z_2) \pm G_{D/M}(z_2', z_1|z_1', z_2). \quad (2.97)$$

Above we summarized symmetry relations for the two-particle Green's function. The relations can be directly applied to the full vertex Γ due to their close relation to the two-particle correlator (2.61). Additional subtleties arise when one focuses on individual 2PR vertices γ_r which appear on the left-hand side of the BSE, for example. Since the 2PR channels $r = a, p, t$ correspond to the index pairings according to Eq. (2.69), we can read off diagrammatic channels by comparing the indices. For instance, crossing symmetry (2.86) relates the a and t channel, e.g., $\gamma_{t;1'2'|12} = -\gamma_{a;1'2'|21}$. Further, Eq. (2.97) relates the p and t channel on the left- and right-hand side, respectively. These symmetries can thus be used to reduce the number of channels for which the BSE has to be evaluated.

2.2.5.2 Frequency parametrization of the vertex

In the following we discuss the frequency parametrization and frequency structure of the full four-point vertex Γ . For conciseness, we leave out all other arguments and indices and focus on the frequency arguments. In both the Matsubara and Keldysh formalisms, we now denote the frequencies by real function arguments, e.g., $\gamma_a(\omega_a, \nu_a, \nu'_a)$. We point out the differences between continuous real frequencies ω and discrete imaginary frequencies $i\omega$ only when they arise.

Firstly, due to frequency conservation the four fermionic frequencies of the vertex legs are related,

$$\nu_{1'} + \nu_{2'} = \nu_1 + \nu_2, \quad (2.98)$$

and the vertex effectively depends on three frequencies. There is a large variety of frequency conventions in the literature. The frequency convention in Sec. 2.1.4 parametrizes the vertex with three fermionic frequencies, e.g., $\nu_{1'}$, $\nu_{2'}$ and ν_1 . Another possibility is a parametrization with three bosonic frequencies as shown in Refs. [KHP⁺08, P3]. In Fig. 2.7, we show the conventions where each 2PR vertex γ_r is parametrized with a bosonic transfer frequency ω_r and two fermionic frequencies ν_r, ν'_r . These conventions are well suited for the evaluation of the BSEs (2.66) and flow equations (2.77) which all have the matrix structure according to Eq. (2.68). Using the above conventions the BSE in the $r = a, p, t$ channel, for example, reads (here exemplified for the MF)

$$\gamma_r(i\omega_r, i\nu_r, i\nu'_r) = \frac{1}{\beta} \sum_{\tilde{\nu}} \Gamma(i\omega_r, i\nu_r, i\tilde{\nu}) \Pi_r(i\omega_r, i\tilde{\nu}) I_r(i\omega_r, i\tilde{\nu}, i\nu'_r), \quad (2.99)$$

where we suppressed physical quantum numbers. We see that the bosonic transfer frequency ω_r is identical in all functions, which is a consequence of frequency conservation and the index pairings in Eq. (2.69), i.e.,

$$\omega_a = \nu_2 - \nu_{1'} = \nu_{2'} - \nu_1, \quad \omega_p = \nu_{1'} + \nu_{2'} = \nu_1 + \nu_2, \quad \omega_t = \nu_2 - \nu_{2'} = \nu_{1'} - \nu_1. \quad (2.100)$$

For fixed ω_r , the fermionic frequencies $\nu_r^{(i)}$ in Eq. (2.99) have a matrix product structure.

Having chosen a frequency convention, we can represent the vertex $\gamma_r(\omega_r, \nu_r, \nu'_r)$ with its values on sampling frequencies. Each frequency direction has a frequency grid, and together they form a three-dimensional rectilinear grid. In the MF our frequency grids contain the smallest discrete Matsubara frequencies which are chosen symmetrically around the origin. If the behaviour outside the frequency box is known, one may extrapolate the data. Since the frequencies are continuous in the KF, we can distribute the sampling points more densely around the origin, where vertex typically shows sharp features. Values in between sampling points have to be determined by interpolation.

In Ref. [P3], we adopt the convention with $\frac{\omega}{2}$ -shifts as depicted in Fig. 2.7(b). In this convention vertex structures are centered around the origin. By inserting the frequency conventions into the symmetry relations in Sec. 2.2.5.1, it can be seen that this convention leads to particularly symmetric formulas which is convenient for the symmetry reduction of the vertex components. Note that, in the Matsubara formalism the $\frac{\omega}{2}$ -shifts have to be rounded to ensure that all legs carry fermionic Matsubara frequencies. The Gauss brackets lead to rather cumbersome expressions for the frequency conversions between the channels. The opposite is the case for the convention in Fig. 2.7(a). It leads to impractical symmetry relations between frequencies on and outside a rectilinear grid of sampling points. The

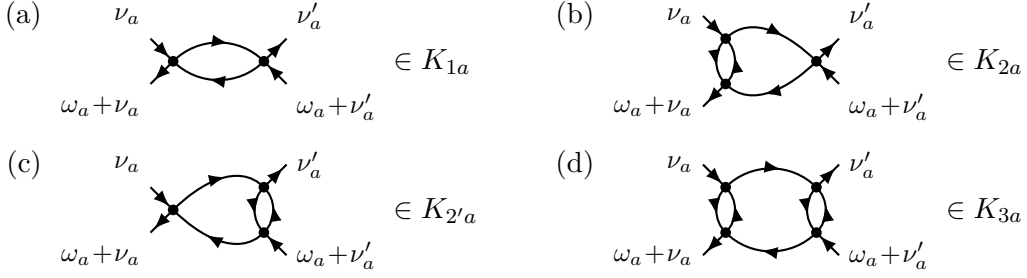


Figure 2.8 Illustration of asymptotic functions of γ_a : We show the lowest-order diagrams which contribute to the asymptotic functions (2.101) of the 2PR vertex γ_a . The frequency arguments follow the a -channel convention in Fig. 2.7(a). Note how the dependence on the fermionic frequency $\nu_a^{(l)}$ is lost if the two corresponding external legs connect to the same bare vertex Γ_0 . Since Γ_0 is frequency independent apart from a frequency conserving term, only the bosonic transfer frequency ω_r enters the arguments of the internal propagator lines. Otherwise, if two left/right external legs connect to two different bare vertices, the fermionic frequency $\nu_a^{(l)}$ does enter the arguments of internal propagator lines. This leads to a suppression of the diagrammatic contribution for large $|\nu_a^{(l)}| \rightarrow \infty$.

formulas for cross-channel mapping, however, do not require Gauss brackets for Matsubara frequencies.

A crucial difference between correlators and vertices lies in their behavior at high frequencies. While correlators decay to zero in all frequency directions the situation is a bit more complicated for vertices. For example, the bare vertex Γ_0 is constant in any frequency direction. The high-frequency asymptotics and their relations to physical observables have been thoroughly studied in Ref. [WLT⁺20]. In the following we summarize the classification of vertex contributions, but refer to the original paper for further details.

Taking the limit of large fermionic frequencies for the 2PR vertices, $\gamma_r(\omega_r, \nu_r, \nu'_r)$, gives the asymptotic function

$$K_{1r}(\omega_r) = \lim_{|\nu'_r| \rightarrow \infty} \lim_{|\nu_r| \rightarrow \infty} \gamma_r(\omega_r, \nu_r, \nu'_r), \quad (2.101a)$$

which exclusively depends on the bosonic transfer frequency ω_r . Similarly, the remaining asymptotic functions are given by

$$K_{2r}(\omega_r, \nu_r) = \lim_{|\nu'_r| \rightarrow \infty} \gamma_r(\omega_r, \nu_r, \nu'_r) - K_{1r}(\omega_r), \quad (2.101b)$$

$$K_{2'r}(\omega_r, \nu'_r) = \lim_{|\nu_r| \rightarrow \infty} \gamma_r(\omega_r, \nu_r, \nu'_r) - K_{1r}(\omega_r), \quad (2.101c)$$

where K_{1r} is subtracted to obtain a function that truly depends on two frequencies and decays to zero when taking the high-frequency limit in the remaining frequencies. The remaining part of the 2PR vertex is called K_{3r} and decays in any frequency direction. Hence, the decomposition into high-frequency asymptotics results in the following representation of the 2PR vertex:

$$\gamma_r(\omega_r, \nu_r, \nu'_r) = K_{1r}(\omega_r) + K_{2r}(\omega_r, \nu_r) + K_{2'r}(\omega_r, \nu'_r) + K_{3r}(\omega_r, \nu_r, \nu'_r). \quad (2.101d)$$

This representation shows that, e.g., K_{1r} gives contributions for arbitrarily large $\nu_r^{(l)}$.

The high-frequency behavior of vertex contributions can also be understood by considering diagrams in perturbation theory. Figure 2.8 shows examples for vertex diagrams with different

asymptotic contributions to γ_a . As an example, let us consider the ‘eye diagram’ in Fig. 2.8(b). The two external lines on the right connect to the same bare vertex Γ_0 where the frequency $\omega_a + \nu'_a$ flows in and ν'_a flows out. The frequency ν'_a never enters as an argument of the internal propagators since Γ_0 is constant apart from a frequency conserving factor. Like all diagrams belonging $K_{2'r}$ it does not depend on ν'_r . On the left, the two external lines connect to two different bare vertices, thereby introducing an explicit dependence on ν_a and $\nu_a + \omega_a$. Furthermore, for large $|\nu_a|$ or $|\omega_a|$ the diagram has to vanish. If we use the frequency parametrization of another channel, the diagram vanishes for any high-frequency limit. For example, using the t -channel parametrization in Fig. 2.7(a) we have $\omega_a = \nu_t - \nu'_t$ and taking the limit $|\nu_t| \rightarrow \infty$ implies $|\omega_a| \rightarrow \infty$, for which all diagrams in γ_a vanish. Note, that the two limits in (2.101a) have to be taken one after the other to avoid pathologies such as limits with constant frequency combinations of the type $\nu_t - \nu'_t = \omega_a$.

For a more rigorous analysis we refer to the derivation of improved estimators for the vertex Γ in Ref. [LHS⁺24]. There it has been shown that the asymptotic functions K_{ir} with $i = 1, 2, 2'$ and the so-called *vertex core* can be written as a sum of two-, three- or four-point correlators (multiplied with self-energies). The vertex core (or *asymptotic rest-function*) is defined as

$$\varphi^{\text{asy}} = R - \Gamma_0 + K_{3a} + K_{3p} + K_{3t}, \quad (2.102)$$

and is the ‘truly’ three-dimensional part of Γ which vanishes for any high frequency limit.

In the asymptotic decomposition (2.101d) diagrammatic equations (such as parquet equations and symmetry relations) for all contributions can be conveniently derived by taking high-frequency limits on both sides. For example, by taking the limits $|\nu_r^{(i)}| \rightarrow \infty$ in the r -channel BSE we obtain

$$\lim_{|\nu_r| \rightarrow \infty} [\Gamma \circ \Pi_r \circ I_r](\omega_r, \nu_r, \nu'_r) = [(\Gamma_0 + K_{1r} + K_{2r'}) \circ \Pi_r \circ I_r](\omega_r, \nu'_r), \quad (2.103a)$$

$$\lim_{|\nu'_r| \rightarrow \infty} [\Gamma \circ \Pi_r \circ I_r](\omega_r, \nu_r, \nu'_r) = [\Gamma \circ \Pi_r \circ \Gamma_0](\omega_r, \nu_r). \quad (2.103b)$$

For a full set of explicit formulas in the asymptotic decomposition (for the parquet equations and mFRG flow equations), we refer to Refs. [P1, Wal21].

Lastly, we point out a technical hurdle due to the inter-channel feedback in the parquet and the flow equations. We discuss it for the example of the BSE in Eq. (2.99): The BSE for γ_r requires input from the other channels $\gamma_{\bar{r}}$. While the r -channel BSE is conveniently parametrized in the r -channel frequency convention, each 2PR vertex is stored in its own convention. Mapping a grid point to different channels might result in frequencies outside the frequency grid which requires inter- or extrapolation. This is particularly the case for non-equidistant grids. While we can optimize the parametrization to capture the relevant features (e.g., asymptotic functions) for each γ_r , these features get shifted and rotated by the cross-channel mapping. Hence, the cross-channel mapping complicates the representation of vertices and the evaluation of frequency integrals in the BSE. In our study in Sec. 4 we therefore use an adaptive quadrature algorithm which is agnostic of the sampling grids in its integrand.

3 Multiloop flow equations for the single-boson exchange decomposition

3.1 Overview

In Secs. 2.2.4.1 and 2.2.5.2 we described the parquet decomposition and asymptotic decomposition. In this section, we work with the single-boson exchange (SBE) decomposition, which was introduced in Ref. [KVC19]. It can be used as an alternative vertex parametrization, but also defines the so-called SBE approximation.

Unlike the parquet theory, the SBE decomposition distinguishes vertex diagrams by their U reducibility. Here, U is used as a synonym for the bare interaction Γ_0 since the decomposition is typically applied to systems with Hubbard interaction U , which is instantaneous and local. A vertex diagram is called U -reducible if ‘cutting’ a bare vertex results in a disconnected diagram. For the bare vertex, a ‘cut’ splits the attached indices into pairs. Since cutting U -reducible diagrams disconnects the external indices identically to the parquet decomposition, (almost) all U -reducible diagrams are 2PR (see Fig. 5 in [P1] for details). The bare vertex is the only exception, being U -reducible in all channels despite being 2PI. The SBE decomposition of the full vertex reads

$$\Gamma = \varphi^{U\text{irr}} + \nabla_a + \nabla_p + \nabla_t - 2U, \quad (3.1)$$

where $\varphi^{U\text{irr}}$ is the fully U -irreducible contribution, and the ∇_r are U -reducible in channel $r = a, p, t$. Since each ∇_r contains the bare vertex U we subtract U twice in the end.

The SBE decomposition shares many traits with the asymptotic decomposition. Firstly, it provides a convenient parametrization. The U -reducible terms ∇_r can be expressed in terms of two- and three-point functions. Only the fully U -irreducible contribution $\varphi^{U\text{irr}}$ has a ‘truly’ three-dimensional frequency dependence and vanishes for large frequencies. Secondly, these functions have physical interpretations, namely as screened interactions and renormalized Yukawa couplings between fermions and fermion bilinears such as $\bar{c}_\sigma c_{\sigma'}$ [KVC19]. In fact, the SBE and the asymptotic functions are related, as described in Ref. [P1].

Most importantly, the SBE decomposition defines the SBE approximation, which sets $\varphi^{U\text{irr}} = 0$. There is numerical evidence [HLK21] that the SBE approximation gives qualitatively reasonable results even for strong coupling, unlike the parquet approximation ($R = U$) and the asymptotic approximation. The latter sets the asymptotic rest function (2.102) to zero, i.e., $\varphi^{\text{asy}} = 0$. In the context of diagrammatic extensions of DMFT (cf. Sec. 4.1), one correspondingly has the choice which vertex component is approximated as local. While the dynamical vertex approximation [TKH07] originally approximated $R = R_{\text{DMFT}}$, Ref. [KV19] derived a set of self-consistent parquet-like equations which are closed by approximating the fully U -irreducible $\varphi^{U\text{irr}} = \varphi_{\text{DMFT}}^{U\text{irr}}$.

In [P1] we complement the parquet-like equations [KV19] with the derivation of multiloop flow equations for SBE objects in different approximations. These may be used for approaches in the spirit of DMF²RG [BTH⁺22], which start the flow with a local vertex computed with DMFT and solve the fRG equations to arrive at a lattice system. Such an approach would offer the benefits of mRG, such as regulator independence.

Multiloop flow equations for single-boson exchange fRG

by

M. Gievers,^{1,2} E. Walter,¹ A. Ge,¹ J. von Delft,¹ and F. B. Kugler³

¹ Arnold Sommerfeld Center for Theoretical Physics, Center for NanoScience, and

Munich Center for Quantum Science and Technology,

Ludwig-Maximilians-Universität München, 80333 Munich, Germany

² Max Planck Institute of Quantum Optics, Hans-Kopfermann-Straße 1, 85748 Garching,

Germany

³ Department of Physics and Astronomy, Rutgers University, Piscataway, NJ 08854, USA

reprinted on pages 39–60

Reproduced under terms of the CC-BY license.

***Eur. Phys. J. B* 95, 108 (2022),**

DOI: 10.1140/epjb/s10051-022-00353-6.

© 2024, The Authors, The European Physical Journal (EPJ).



Multiloop flow equations for single-boson exchange fRG

Marcel Gievers^{1,2}, Elias Walter¹, Anxiang Ge¹, Jan von Delft¹, and Fabian B. Kugler^{3,a}

¹ Arnold Sommerfeld Center for Theoretical Physics, Center for NanoScience, and Munich Center for Quantum Science and Technology, Ludwig-Maximilians-Universität München, 80333 Munich, Germany

² Max Planck Institute of Quantum Optics, Hans-Kopfermann-Straße 1, 85748 Garching, Germany

³ Department of Physics and Astronomy, Rutgers University, Piscataway, NJ 08854, USA

Received 13 January 2022 / Accepted 12 May 2022 / Published online 6 July 2022
© The Author(s) 2022

Abstract. The recently introduced single-boson exchange (SBE) decomposition of the four-point vertex of interacting fermionic many-body systems is a conceptually and computationally appealing parametrization of the vertex. It relies on the notion of reducibility of vertex diagrams with respect to the bare interaction U , instead of a classification based on two-particle reducibility within the widely used parquet decomposition. Here, we re-derive the SBE decomposition in a generalized framework (suitable for extensions to, e.g., inhomogeneous systems or real-frequency treatments) following from the parquet equations. We then derive multiloop functional renormalization group (mfRG) flow equations for the ingredients of this SBE decomposition, both in the parquet approximation, where the fully two-particle irreducible vertex is treated as an input, and in the more restrictive SBE approximation, where this role is taken by the fully U -irreducible vertex. Moreover, we give mfRG flow equations for the popular parametrization of the vertex in terms of asymptotic classes of the two-particle reducible vertices. Since the parquet and SBE decompositions are closely related, their mfRG flow equations are very similar in structure.

1 Introduction

The understanding of strongly correlated many-body systems like the two-dimensional Hubbard model remains an important challenge of contemporary condensed-matter physics [1]. For this, it is desirable to gain profound understanding of two-body interactions which are described by the full four-point vertex Γ .

A powerful technique for calculating the four-point vertex Γ is the functional renormalization group (fRG) [2, 3]. There, a scale parameter Λ is introduced into the bare Green's function $G_0 \rightarrow G_0^\Lambda$ in such a way that for an initial value $\Lambda \rightarrow \Lambda_i$ the theory (specifically, the calculation of the self-energy Σ^Λ and the four-point vertex Γ^Λ) becomes solvable, and after successively integrating out higher energy modes $\Lambda \rightarrow \Lambda_f$, the fully renormalized objects Σ and Γ are obtained.

Traditionally, fRG is formulated as an infinite hierarchy of exact flow equations for n -point vertex functions. However, since already the six-point vertex is numerically intractable, truncations are needed. A frequently-used strategy employs a one-loop (1ℓ) truncation of the exact hierarchy of flow equations by completely neglecting six-point and higher vertices. This can be justified,

e.g., from a perturbative [2] or leading-log [4] perspective. Another truncation scheme is given by the multiloop fRG approach, mfRG, which includes all contributions of the six-point vertex to the flow of the four-point vertex and self-energy that can be computed with numerical costs proportional to the 1ℓ flow [5–7]. In doing so, it sums up all parquet diagrams, formally reconstructing the parquet approximation (PA) [8, 9] if loop convergence is achieved. Converged multiloop results thus inherit all the properties of the PA. These include self-consistency at the one- and two-particle level (in that the PA is a solution of the self-consistent parquet equations [9]); the validity of one-particle conservation laws (but not of two-particle ones); and the independence of the final results on the choice of regulator (since the parquet equations and PA do not involve specifying any regulator). The mfRG approach was recently applied to the Hubbard model [10, 11], Heisenberg models [12, 13], and the Anderson impurity model [14].

A full treatment of the frequency and momentum dependence of the four-point vertex generally requires tremendous numerical resources. Hence, it is important to parametrize these dependencies in an efficient way, to reduce computational effort without losing information on important physical properties. One such scheme expresses the vertex as a sum of diagrammatic classes distinguished by their asymptotic frequency behavior [15, 16]: Asymptotic classes which remain nonzero when one or two frequency arguments are sent to infinity do

Marcel Gievers, Elias Walter and Anxiang Ge contributed equally to this work.

^a e-mail: kugler@physics.rutgers.edu (corresponding author)

not depend on these arguments, while the class depending on all three frequency arguments decays in each direction.

A related strategy is to express parts of the vertex through fermion bilinears that interact via exchange bosons [17, 18]. Partial bosonization schemes, which approximate the vertex through one [19–21] or several boson-exchange channels [22–24], have been employed within the dual boson formalism, used in diagrammatic extensions of dynamical mean field theory (DMFT) aiming to include nonlocal correlations.

A decomposition of the full vertex into single-boson exchange (SBE) parts, involving functions of at most two frequencies, and residual parts depending on three frequencies was developed in Refs. [25–30]. The guiding principle of the SBE decomposition is reducibility in the bare interaction U [25]. This criterion distinguishes SBE contributions, that are U -reducible, from multi-boson exchange and other contributions, that are not. The SBE approximation retains only the U -reducible part while neglecting all U -irreducible terms [26]. The SBE terms are expressible through bosonic fluctuations and their (Yukawa) couplings to fermions—the Hedin vertices—and thus have a transparent physical interpretation. Numerically, two- and three-point objects can be computed and stored more easily than a genuine four-point vertex.

Studies of the two-dimensional Hubbard model have shown that the SBE decomposition is a promising technique for computing the frequency and momentum dependences of the vertex [28–30]. In a 1ℓ fRG calculation, it was found that some of its essential features are already captured by its U -reducible parts, which are much easier to compute numerically than the U -irreducible ones [31]. Reference [31] also obtained results at strong interaction using DMF²RG, a method that makes use of a DMFT vertex as the starting point for the fRG flow [32–34]. Here, a very interesting aspect of the SBE decomposition is that the SBE approximation (neglecting U -irreducible contributions) remains a meaningful approximation also in the strong-coupling regime [35], which is not the case for a similar approximation scheme based on the parametrization through asymptotic classes while using functions of at most two frequency arguments.

Given these encouraging developments, it is of interest to have a strategy for computing the ingredients of the SBE approach—the bosonic propagators, the Hedin vertices, and the remaining U -irreducible terms—not only in 1ℓ fRG [31] but also in mfRG. In this paper, we therefore derive multiloop flow equations for the SBE ingredients. To this end, we start from the parquet equations to derive a general form of the SBE decomposition where the structure of non-frequency arguments is not specified. We then derive multiloop flow equations for the SBE ingredients, and finally illustrate the relation of these objects to the parametrization of the vertex in terms of two-particle reducible asymptotic classes [16, 31]. The numerical implementation of the resulting

SBE multiloop flow equations goes beyond the scope of this purely analytical paper and is left for the future.

The paper is organized as follows: In Sect. 2, we recapitulate the parquet equations, the corresponding mfRG flow equations, and the frequency parametrization of the four-point vertex adapted to each two-particle channel. In Sect. 3, we deduce the SBE decomposition from the parquet equations and derive multiloop flow equations for the SBE ingredients in two different ways. We also discuss the SBE approximation and its associated mfRG flow. In Sect. 4, we recall the definition of the asymptotic vertex classes and derive multiloop equations for these. We outline the relation between SBE ingredients and asymptotic classes and their respective mfRG equations. We conclude with a short outlook in Sect. 5. Appendices A and B illustrate the SBE ingredients and asymptotic vertex classes diagrammatically, while Appendix C describes the relation between our generalized notation of the SBE decomposition to that of the original papers. Finally, Appendices D and E give details on different definitions of correlators and susceptibilities and show their close relation to the SBE ingredients.

2 Recap of parquet and mfRG equations

The parquet equations and the associated multiloop fRG equations form the basis for the main outcomes of this paper. For ease of reference and use in future sections, we recapitulate the notational conventions and compactly summarize the main ingredients and results of the mfRG approach [5–7]. To make the presentation self-contained, we also recall from the literature the motivation for some of the definitions and conventions presented below.

2.1 Parquet equations

The action of a typical fermionic model reads

$$S = -\bar{c}_1' [G_0^{-1}]_{1'1} c_1 - \frac{1}{4} U_{1'2'|12} \bar{c}_1' \bar{c}_2' c_2 c_1, \quad (1)$$

with the bare propagator G_0 . The Grassmann fields c_i are labeled by a composite index i describing frequency and other quantum numbers, such as position or momentum, spin, etc. Throughout this paper, repeated i -indices are understood to be integrated over or summed over. Furthermore, U is the crossing symmetric bare interaction vertex, $U_{1'2'|12} = -U_{2'1'|12}$ (called Γ_0 in Refs. [6, 7]). We assume it to be energy-conserving without further frequency dependence, as in any action derived directly from a time-independent Hamiltonian. Our expression for the action (1) and later definitions of correlation functions are given in the Matsubara formalism [36] and for fermionic fields. However, our analysis can easily be transcribed to the Keldysh formalism [37], and/or to bosonic fields, by suitably adapting the content of the index i on c_i and adjust-

ing some prefactors. Such changes do not modify the structure of the vertex decomposition and flow equations that are the focus of this paper.

The time-ordered one- and two-particle correlators, $G_{1|1'} = -\langle c_1 \bar{c}_{1'} \rangle$ and $G_{12|1'2'}^{(4)} = \langle c_1 c_2 \bar{c}_{2'} \bar{c}_{1'} \rangle$, can be expressed in standard fashion [3] through the self-energy and the four-point vertex,

$$\Sigma_{1'|1} = \text{diagram with circle and arrows}, \quad \Gamma_{1'2'|12} = \text{diagram with square and arrows} \quad (2)$$

These contain all one-particle irreducible one- and two-particle vertex diagrams, respectively. Hence, these are (amputated connected) diagrams that cannot be split into two pieces by cutting a single bare propagator line.

The one-particle self-energy is related to the two-particle vertex via the Schwinger–Dyson equation (SDE) [9]. We do not discuss this equation much further because its treatment is similar for both vertex decompositions discussed below. On the two-particle level, the starting point of parquet approaches [9] is the parquet decomposition,

$$\Gamma = R + \gamma_a + \gamma_p + \gamma_t. \quad (3)$$

It states that the set of all vertex diagrams can be divided into four disjoint classes: the diagrams in γ_r , $r = a, p, t$, are two-particle reducible in channel r , i.e., they can be split into two parts by cutting two antiparallel (a), parallel (p), or transverse antiparallel (t) propagator lines, respectively. The diagrams in R do not fall apart by cutting two propagator lines and are thus fully two-particle irreducible. This classification is exact and unambiguous [16,38]. In the literature, the diagrammatic channels are also known as crossed particle–hole (ph $\leftrightarrow a$), particle–particle (pp $\leftrightarrow p$), and particle–hole (ph $\leftrightarrow t$) channel.

Since the four classes in the parquet decomposition are disjoint, one can decompose Γ w.r.t. its two-particle reducibility in one of the channels r , $\Gamma = I_r + \gamma_r$. Here, I_r comprises the sum of all diagrams irreducible in channel r and fulfills $I_r = R + \gamma_{\bar{r}}$ with $\gamma_{\bar{r}} = \sum_{r' \neq r} \gamma_{r'}$. The Bethe–Salpeter equations (BSEs) relate the reducible diagrams to the irreducible ones and can be summarized by

$$\gamma_r = I_r \circ \Pi_r \circ \Gamma = \Gamma \circ \Pi_r \circ I_r. \quad (4)$$

The Π_r bubble, defined as

$$\Pi_{a;34|3'4'} = G_{3|3'} G_{4|4'}, \quad (5a)$$

$$\Pi_{p;34|3'4'} = \frac{1}{2} G_{3|3'} G_{4|4'}, \quad (5b)$$

$$\Pi_{t;43|3'4'} = -G_{3|3'} G_{4|4'}, \quad (5c)$$

represents the corresponding propagator pair in channel r , see Fig. 1. (Note that $\Pi_{a;34|3'4'} = -\Pi_{t;43|3'4'}$

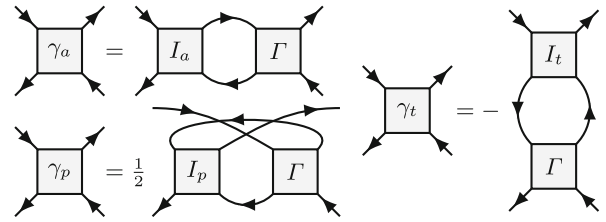


Fig. 1 Bethe–Salpeter equations in the antiparallel (a), parallel (p) and transverse (t) channels

is consistent with crossing symmetry.) The connector symbol \circ denotes summation over internal frequencies and quantum numbers (5, 6 in Eqs. (6) below) and its definition depends on the channel $r \in \{a, p, t\}$: When connecting Π_r (or other four-leg objects labeled by r) to some vertex, it gives

$$a : [A \circ B]_{12|34} = A_{16|54} B_{52|36}, \quad (6a)$$

$$p : [A \circ B]_{12|34} = A_{12|56} B_{56|34}, \quad (6b)$$

$$t : [A \circ B]_{12|34} = A_{62|54} B_{15|36}. \quad (6c)$$

By combining $\Gamma = I_r + \gamma_r$ with the BSEs (4), one can eliminate γ_r to get the “extended BSEs” [7] needed later:

$$\mathbb{1}_r + \Pi_r \circ \Gamma = (\mathbb{1}_r - \Pi_r \circ I_r)^{-1}, \quad (7a)$$

$$\mathbb{1}_r + \Gamma \circ \Pi_r = (\mathbb{1}_r - I_r \circ \Pi_r)^{-1}. \quad (7b)$$

Here, the channel-specific unit vertices $\mathbb{1}_r$, defined by the requirement $\Gamma = \mathbb{1}_r \circ \Gamma = \Gamma \circ \mathbb{1}_r$, are given by

$$\mathbb{1}_{a;12|34} = \delta_{13} \delta_{24}, \quad (8a)$$

$$\mathbb{1}_{p;12|34} = \frac{1}{2} (\delta_{13} \delta_{24} - \delta_{14} \delta_{23}), \quad (8b)$$

$$\mathbb{1}_{t;12|34} = \delta_{14} \delta_{23}. \quad (8c)$$

(For the p channel, the internal sum in $\mathbb{1}_p \circ \Gamma = \Gamma \circ \mathbb{1}_p$ runs over both outgoing (or ingoing) legs of Γ . Therefore, the crossing symmetry of the vertex, i.e., $\Gamma_{12|34} = -\Gamma_{21|34} = -\Gamma_{12|43}$, is transferred to $\mathbb{1}_p$, resulting in an expression more involved than for the other two channels.)

The combination of the Dyson equation $G = G_0(1 + \Sigma G)$, the SDE, the parquet decomposition (3), the three BSEs (4), and the definitions $I_r = \Gamma - \gamma_r$ constitutes the self-consistent *parquet equations*. The only truly independent object is the fully irreducible vertex R . If R is specified, everything else can be computed self-consistently via the parquet equations. However, R is the most complicated object: its diagrams contain several nested integrals/sums over internal arguments, whereas the integrals in reducible diagrams partially factorize. A common simplification, the *parquet approximation* (PA), replaces R by U , closing the set of parquet equations.

2.2 Parquet mFRG

The conventional mFRG flow equations can be derived from the parquet equations by introducing a regulator Λ into the bare propagator G_0 , thus making all objects in the parquet equations Λ -dependent [7]. The fully irreducible vertex R is treated as an input and is thus assumed to be Λ -independent, $R^\Lambda \approx R$. For instance, this assumption arises both in the PA where $R \approx U$ or in the dynamical vertex approximation DGA [39, 40] where $R \approx R^{\text{DMFT}}$ is taken from DMFT—here, we will not distinguish these cases explicitly. Taking the derivative of the SDE and the BSEs w.r.t. Λ then yields flow equations for Σ and Γ . Within the context of this paper, we will call this mFRG approach *parquet mFRG*, to distinguish it from an *SBE mFRG* approach to be discussed in Sect. 3.2.

When computing $\dot{\gamma}_r = \partial_\Lambda \gamma_r$ via the BSEs, one obtains terms including $\dot{I}_r = \sum_{r' \neq r} \dot{\gamma}_{r'}$. Thus, one has to iteratively insert the flow equation for γ_r into the equations of the other channels $r' \neq r$, yielding an infinite set of contributions of increasing *loop order*:

$$\dot{I} = \dot{\gamma}_a + \dot{\gamma}_p + \dot{\gamma}_t, \quad \dot{\gamma}_r = \sum_{\ell=1}^{\infty} \dot{\gamma}_r^{(\ell)}. \quad (9)$$

The individual ℓ -loop contributions read [5, 7]

$$\dot{\gamma}_r^{(1)} = \Gamma \circ \dot{H}_r \circ \Gamma, \quad (10a)$$

$$\dot{\gamma}_r^{(2)} = \dot{\gamma}_r^{(1)} \circ \Pi_r \circ \Gamma + \Gamma \circ \Pi_r \circ \dot{\gamma}_r^{(1)} \quad (10b)$$

$$\begin{aligned} \dot{\gamma}_r^{(\ell+2)} = & \dot{\gamma}_r^{(\ell+1)} \circ \Pi_r \circ \Gamma + \Gamma \circ \Pi_r \circ \dot{\gamma}_r^{(\ell)} \circ \Pi_r \circ \Gamma \\ & + \Gamma \circ \Pi_r \circ \dot{\gamma}_r^{(\ell+1)}. \end{aligned} \quad (10c)$$

where $\dot{\gamma}_r^{(\ell)} = \sum_{r' \neq r} \dot{\gamma}_{r'}^{(\ell)}$ and Eq. (10c) applies for $\ell+2 \geq 3$. In general, all terms at loop order ℓ contain $\ell - 1$ factors of Π and one \dot{H} (i.e., ℓ loops, one of which is differentiated), connecting ℓ renormalized vertices Γ . We have $\dot{H}_r \sim G\dot{G} + \dot{G}G$, where

$$\dot{G} = S + G\dot{\Sigma}G, \quad (11)$$

with the single-scale propagator $S = \dot{G}|_{\Sigma=\text{const}}$. Figure 2 illustrates Eqs. (10) diagrammatically in the a channel.

The flow equation for the self-energy, derived in Ref. [7] by requiring Σ to satisfy the SDE throughout the flow, reads

$$\dot{\Sigma} = - \left[\Gamma \right] - \left[\dot{\gamma}_{i,C} \right] - \left[\Gamma \right] \quad (12)$$

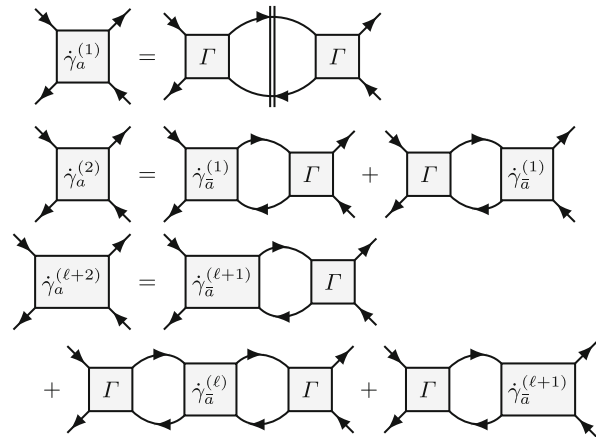


Fig. 2 Diagrammatic depiction of the mFRG flow equations (10) in the a channel. The double-dashed bubble \dot{H}_a represents a sum of two terms, $G\dot{G} + \dot{G}G$, where double-dashed propagators \dot{G} are fully differentiated ones (cf. Eq. (11))

It has Γ and $\dot{\gamma}_{i,C} = \sum_{\ell} \Gamma \circ \Pi_r \circ \dot{\gamma}_i^{(\ell)} \circ \Pi_r \circ \Gamma$ as input and holds irrespective of the choice of vertex parametrization. For this reason, we do not discuss the self-energy flow further in this paper, but it should of course be implemented for numerical work.

The 1ℓ contribution (10a) of the vertex flow, with the fully differentiated \dot{G} replaced by the single-scale propagator S in \dot{H}_r is equivalent to the usual 1ℓ flow equation. Using \dot{G} instead of S , as done in Eq. (10a), corresponds to the so-called Katanin substitution [41]: it contains the feedback of the differentiated self-energy into the vertex flow and already goes beyond the standard 1ℓ approximation. By adding higher-loop contributions until convergence is reached, one effectively solves the self-consistent parquet equations through an fRG flow. On the one hand, this ensures two-particle self-consistency and related properties mentioned in the introduction. On the other hand, it also provides a way of reaching a solution of the parquet equations by integrating differential equations. This may be numerically favorable compared to an iteration of the self-consistent equations. Particularly, when computing diagrammatic extensions of DMFT via DMF²RG, one then needs only the *full* DMFT vertex as an input, and not the r -(ir)reducible ones entering the parquet equations. This is helpful in the Matsubara formalism, where the r -(ir)reducible vertices sometimes exhibit divergences [42–46], and even more so when aiming for real-frequency approaches [47, 48].

2.3 Frequency parametrization

The four-point vertex Γ is a highly complicated object and must be parametrized efficiently. In this section, we summarize the frequency parametrization of the vertex adapted to the three diagrammatic channels.

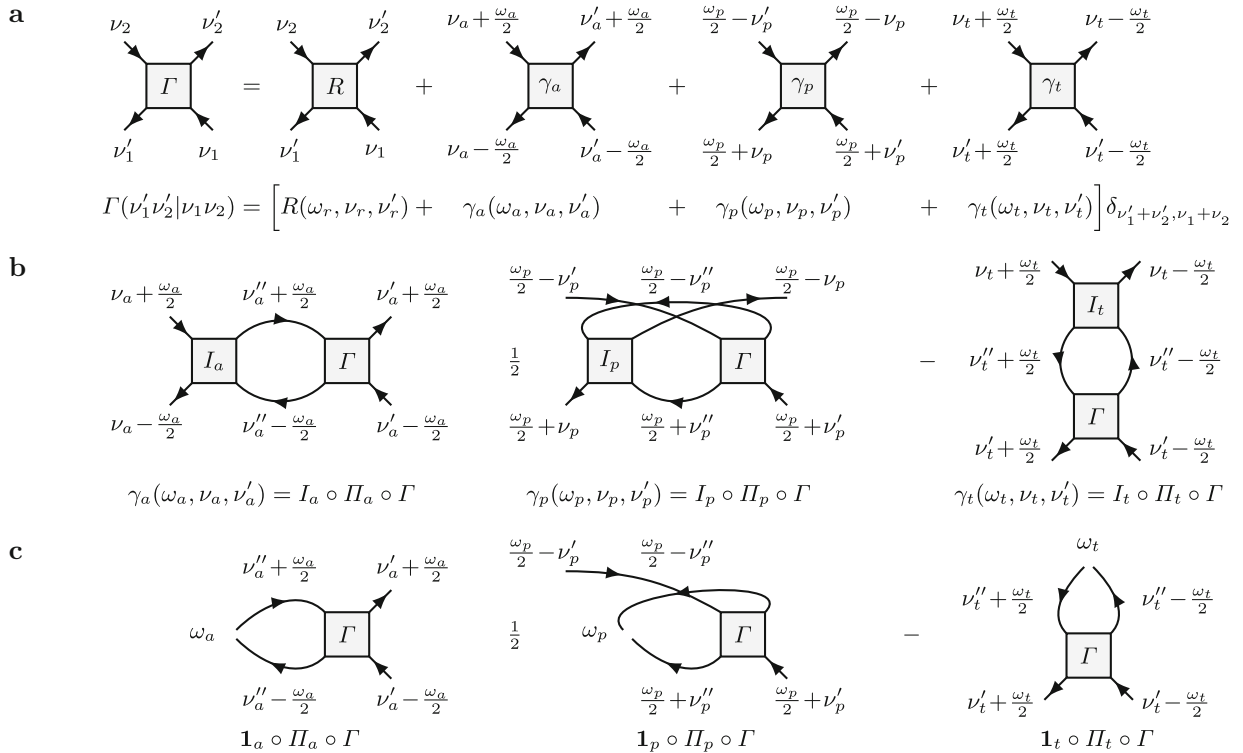


Fig. 3 Definition of the three channel-specific frequency parametrizations of the four-point vertex. **a** The vertex is nonzero only if the four fermionic frequencies satisfy $\nu_1' + \nu_2' = \nu_1 + \nu_2$. In that case, they can be expressed in three different ways through one bosonic transfer frequency, ω_r , and two fermionic frequencies, ν_r, ν_r' . Of course, each term can also be expressed through the frequencies $(\omega_r, \nu_r, \nu_r')$ of any of the three channels, as indicated here for R . **b** The choice of frequency arguments in each channel γ_a, γ_p , and γ_t is motivated by the structure of their BSEs (4). **c** Diagrammatic depiction of $\mathbf{1}_r \circ \Pi_r \circ \Gamma = \sum_{\nu_r'} \Pi_r \bullet \Gamma$ (Eqs. (22), third line), a four-leg object obtained by inserting $\mathbf{1}_r$ between U and Π_r (Eq. (21c)). The multiplication of $\mathbf{1}_r \circ$ onto $\Pi_r \circ \Gamma$ carries two instructions: draw Π_r such that the endpoints of the lines connected to $\mathbf{1}_r$ lie close together (awaiting being connected to U), and perform the sum over the fermionic frequency ν_r' of Π_r .

This parametrization is the building block for the SBE decomposition discussed in Sect. 3.

Focusing on the frequency dependence, we switch from the compact notation $\Gamma_{1'2'|12}$ to the more elaborate $\Gamma_{1'2'|12}(\nu_1'\nu_2'|\nu_1\nu_2)$, with frequency arguments written in brackets, and the subscripts now referring to non-frequency quantum numbers (position or momentum, spin, etc.). As mentioned earlier, we assume the bare vertex U to have the form

$$U_{1'2'|12}(\nu_1'\nu_2'|\nu_1\nu_2) = \delta_{\nu_1'+\nu_2', \nu_1+\nu_2} U_{1'2'|12}, \quad (13)$$

with $U_{1'2'|12}$ independent of frequency. If U is momentum-conserving without further momentum dependence, our treatment of frequency sums below may be extended to include momentum sums. To keep the discussion general, we refrain from elaborating this in detail. Note that, e.g., in the repulsive Hubbard model, our sign convention in Eq. (1) is such that $U_{\sigma\bar{\sigma}|\sigma\bar{\sigma}} = -U_{\bar{\sigma}\sigma|\sigma\bar{\sigma}} < 0$ (where, as usual, $\sigma \in \{\uparrow, \downarrow\}$, $\bar{\uparrow} = \downarrow, \bar{\downarrow} = \uparrow$).

Due to frequency conservation, one-particle correlators depend on only one frequency,

$$G_{1'1}(\nu_1', \nu_1) = \delta_{\nu_1', \nu_1} G_{1'1}(\nu_1). \quad (14)$$

Likewise, three frequencies are sufficient to parametrize the vertex. For each channel γ_r , we express the four fermionic frequencies $\nu_1', \nu_2', \nu_1, \nu_2$ at the vertex legs through a choice of three frequencies, a bosonic transfer frequency, ω_r , and two fermionic frequencies, ν_r and ν_r' . These are chosen differently for each channel (see Fig. 3a) and reflect its asymptotic behavior [16] as discussed in Sect. 4.1. We have

$$\gamma_{r;1'2'|12}(\nu_1'\nu_2'|\nu_1\nu_2) = \delta_{\nu_1'+\nu_2', \nu_1+\nu_2} \gamma_{r;1'2'|12}(\omega_r, \nu_r, \nu_r'), \quad (15)$$

with ω_r, ν_r, ν_r' related to ν_1', ν_1, ν_2 through

$$\begin{aligned} \nu_1' &= \nu_a - \frac{\omega_a}{2} = \nu_p + \frac{\omega_p}{2} = \nu_t' + \frac{\omega_t}{2}, \\ \nu_1 &= \nu_a' - \frac{\omega_a}{2} = \nu_p' + \frac{\omega_p}{2} = \nu_t - \frac{\omega_t}{2}, \\ \nu_2 &= \nu_a + \frac{\omega_a}{2} = -\nu_p' + \frac{\omega_p}{2} = \nu_t + \frac{\omega_t}{2}. \end{aligned} \quad (16)$$

This parametrization symmetrically assigns $\pm \frac{\omega_r}{2}$ shifts to all external legs. (In the Matsubara formalism, the bosonic Matsubara frequency closest to $\pm \frac{\omega_r}{2}$ is chosen for the shift.) With these shifts, crossing symmetries ensure that prominent vertex peaks are centered around $\omega_r = 0$, which is convenient for numerical work. However, other conventions are of course possible, too.

Though the frequencies ω_r, ν_r, ν'_r are tailored to a specific channel γ_r , one may also use them to define the r parametrization of the full vertex, writing

$$\Gamma_{1'2'|12}(\nu'_1 \nu'_2 | \nu_1 \nu_2) = \delta_{\nu'_1 + \nu'_2, \nu_1 + \nu_2} \Gamma_{1'2'|12}(\omega_r, \nu_r, \nu'_r). \tag{17}$$

Likewise, $R, \gamma_a, \gamma_p, \gamma_t$ can each be expressed as a δ symbol times a function of any of the variable sets $(\omega_r, \nu_r, \nu'_r)$. The r parametrization of $\Gamma \circ \Pi_r$ or $\Pi_r \circ \Gamma$ is obtained by inserting Eqs. (14) and (17) into Eqs. (6). The summations $\sum_{\nu_5 \nu_6}$ over internal frequencies can be collapsed using frequency-conserving δ symbols, leading to

$$[\Gamma \circ \Pi_r](\omega_r, \nu_r, \nu''_r) = \Gamma(\omega_r, \nu_r, \nu''_r) \bullet \Pi(\omega_r, \nu''_r), \tag{18a}$$

$$[\Pi_r \circ \Gamma](\omega_r, \nu''_r, \nu'_r) = \Pi(\omega_r, \nu''_r) \bullet \Gamma(\omega_r, \nu''_r, \nu'_r), \tag{18b}$$

where the bubble factors $\Pi_r(\omega_r, \nu''_r)$ are given by

$$\Pi_{a;34|3'4'}(\omega_a, \nu''_a) = G_{3|3'}(\nu''_a - \frac{\omega_a}{2}) G_{4|4'}(\nu''_a + \frac{\omega_a}{2}), \tag{19a}$$

$$\Pi_{p;34|3'4'}(\omega_p, \nu''_p) = \frac{1}{2} G_{3|3'}(\frac{\omega_p}{2} + \nu''_p) G_{4|4'}(\frac{\omega_p}{2} - \nu''_p), \tag{19b}$$

$$\Pi_{t;43|3'4'}(\omega_t, \nu''_t) = -G_{3|3'}(\nu''_t - \frac{\omega_t}{2}) G_{4|4'}(\nu''_t + \frac{\omega_t}{2}). \tag{19c}$$

In Eqs. (18), the connector \bullet by definition denotes an internal summation analogous to \circ , except that only non-frequency quantum numbers (position, spin, etc.) are summed over. Correspondingly, the bubble $\tilde{\Gamma} \circ \Pi_r \circ \Gamma$, involving two \circ connectors, has the r parametrization

$$\begin{aligned} & [\tilde{\Gamma} \circ \Pi_r \circ \Gamma](\omega_r, \nu_r, \nu'_r) \\ &= \sum_{\nu''_r} \tilde{\Gamma}(\omega_r, \nu_r, \nu''_r) \bullet \Pi_r(\omega_r, \nu''_r) \bullet \Gamma(\omega_r, \nu''_r, \nu'_r), \end{aligned} \tag{20}$$

see Fig. 3b. Here, one frequency sum survives, running over the fermionic frequency ν''_r associated with Π_r .

For future reference, we define unit vertices for non-frequency quantum numbers, $\mathbf{1}_r$, by $\Gamma = \mathbf{1}_r \bullet \Gamma = \Gamma \bullet \mathbf{1}_r$. (For a bare vertex with momentum conservation and no further momentum dependence, one could include a momentum sum, $\sum_{k''_r}$, in Eq. (20) and exclude momentum indices from the \bullet summation and $\mathbf{1}_r$.) The distinction between $\circ, \mathbf{1}$ and $\bullet, \mathbf{1}$, indicating if connectors and unit vertices include summations and δ symbols for frequency variables or not, will be needed for the SBE decomposition of Sect. 3. There, we will encounter bubbles involving one or two bare vertices, $U \circ \Pi_r \circ U$, $\tilde{\Gamma} \circ \Pi_r \circ U$, or $U \circ \Pi_r \circ \Gamma$. Expressing these in the form (20), the bare vertex U , since it is frequency independent, can be pulled out of the sum over ν''_r . To make

this explicit, we insert unit operators $\mathbf{1}_r$ next to U :

$$U \circ \Pi_r \circ U = U \bullet \mathbf{1}_r \circ \Pi_r \circ \mathbf{1}_r \bullet U, \tag{21a}$$

$$\tilde{\Gamma} \circ \Pi_r \circ U = \tilde{\Gamma} \circ \Pi_r \circ \mathbf{1}_r \bullet U, \tag{21b}$$

$$U \circ \Pi_r \circ \Gamma = U \bullet \mathbf{1}_r \circ \Pi_r \circ \Gamma. \tag{21c}$$

We suppressed frequency arguments for brevity, it being understood that equations linking Π_r and $\mathbf{1}_r$ use the r parametrization. Making the frequency sum involved in $\circ \Pi_r \circ$ explicit, we obtain four-leg objects,

$$\begin{aligned} [\mathbf{1}_r \circ \Pi_r \circ \mathbf{1}_r](\omega_r) &= \sum_{\nu''_r} \Pi_r(\omega_r, \nu''_r), \\ [\tilde{\Gamma} \circ \Pi_r \circ \mathbf{1}_r](\omega_r, \nu_r) &= \sum_{\nu''_r} \tilde{\Gamma}(\omega_r, \nu_r, \nu''_r) \bullet \Pi_r(\omega_r, \nu''_r), \\ [\mathbf{1}_r \circ \Pi_r \circ \Gamma](\omega_r, \nu'_r) &= \sum_{\nu''_r} \Pi_r(\omega_r, \nu''_r) \bullet \Gamma(\omega_r, \nu''_r, \nu'_r) \end{aligned} \tag{22}$$

that depend on only one or two frequency arguments (cf. Figure 3c) and are thus numerically cheaper than Γ . Note that, in general, $\mathbf{1}_r$ is not the unit operator w.r.t. the \circ connector, i.e., $\mathbf{1}_r \circ \Gamma \neq \Gamma \neq \Gamma \circ \mathbf{1}_r$ since \circ involves a frequency summation which does not affect $\mathbf{1}_r$.

3 SBE decomposition

We now turn to the SBE decomposition. It also yields an exact, unambiguous classification of vertex diagrams, now according to their U -reducibility in each channel. This notion of reducibility, introduced in Ref. [26], is very analogous to Π -reducibility, i.e., two-particle reducibility. A diagram is called U -reducible if it can be split into two parts by splitting apart a bare vertex U (in ways specified below) in either of the three channels. Otherwise, it is fully U -irreducible.

The SBE decomposition was originally formulated in terms of physical (charge, spin, and singlet pairing) channels which involve linear combinations of spin components. For our purposes, it is more convenient not to use such linear combinations (the relation between both formulations is given in Appendix C). Moreover, the original SBE papers considered models with translational invariance, with vertices labeled by three momentum variables. We here present a generalization of the SBE decomposition applicable to models without translational invariance, requiring four position or momentum labels. Starting from the BSEs, we use arguments inspired by Ref. [26] to arrive at a set of self-consistent equations for SBE ingredients which will also enable us to derive multiloop flow equations directly within this framework. In terms of notation, we follow Ref. [26] for the objects $\nabla_r, w_r, \bar{\lambda}_r, \lambda_r$ —with φ^{fir} there denoted φ^{Uirr} here—while we follow Ref. [30] for M_r and T_r (the latter instead of φ_r from Ref. [26]).

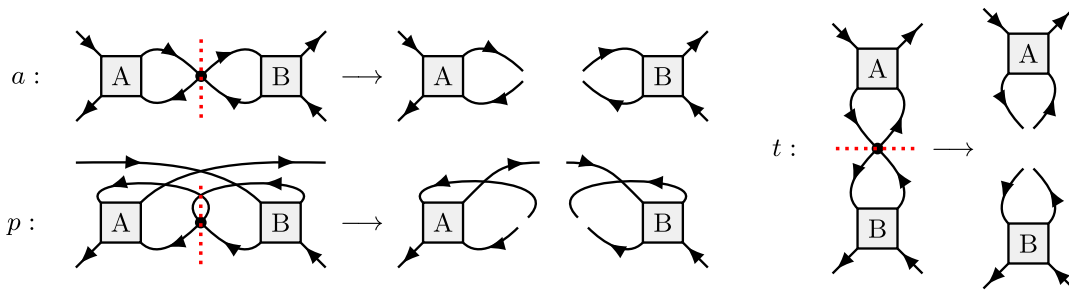


Fig. 4 Illustration of U - r -reducibility, analogous to Fig. 4 of [26]. A and B can be any vertex diagram or simply $\mathbf{1}_r$

3.1 Derivation of SBE decomposition from BSEs

As mentioned earlier, a vertex diagram is called two-particle reducible in a specified channel $r \in \{a, p, t\}$, or Π - r -reducible for short, if it can be split into two parts by cutting the two lines of a Π_r bubble (to be called *linking bubble*); if such a split is not possible, the diagram is Π - r -irreducible. The two-particle reducible vertex γ_r is the sum of all Π - r -reducible diagrams. Following Ref. [26], we now introduce a further channel-specific classification criterion. A Π - r -reducible diagram is called U - r -reducible if a linking bubble Π_r has two of its legs attached to the same bare vertex in the combination $U \circ \Pi_r$ or $\Pi_r \circ U$. Then, that bare vertex U , too, constitutes a link that, when “cut out”, splits the diagram into two parts. (To visualize the meaning of “cutting out U ” diagrammatically, one may replace U by $\mathbf{1}_r \bullet U \bullet \mathbf{1}_r$, and then remove U . This results in two pairs of legs ending close together, ready to be connected through reinsertion of U , see Figs. 3c and 4.) The lowest order U - r -reducible contribution to γ_r is $U \circ \Pi_r \circ U$. The lowest-order term of Γ , the bare vertex U (which is Π - r -irreducible), is viewed as U - r -reducible in all three channels, corresponding to the three possible ways of splitting its four legs into two pairs of two. All U - r -reducible diagrams describe “single-boson exchange” processes, in the sense that each link U connecting two otherwise separate parts of the diagram mediates a single bosonic transfer frequency, ω_r (as defined in Fig. 3), across that link, as will become explicit below.

All vertex diagrams that are not U - r -reducible are called U - r -irreducible. These comprise all multi-boson exchange (i.e., *not* single-boson exchange) diagrams from γ_r , and all Π - r -irreducible diagrams except the bare vertex (which is trivially U - r -reducible), i.e., all diagrams from $I_r - U = R - U + \sum_{r' \neq r} \gamma_{r'}$.

Next, we rewrite the parquet equations in terms of U - r -reducible and U - r -irreducible parts. We define ∇_r as the sum of all U - r -reducible diagrams, including (importantly) the bare vertex U , and M_r as the sum of all diagrams that are Π - r -reducible but U - r -irreducible, thus describing multi-boson exchange processes. Then, the Π - r -reducible vertex γ_r , which does not include U , fulfills

$$\gamma_r = \nabla_r - U + M_r. \tag{23}$$

Inserting Eq. (23) for γ_r into the parquet decomposition (3) yields

$$\Gamma = \varphi^{U\text{irr}} + \sum_r \nabla_r - 2U, \tag{24a}$$

$$\varphi^{U\text{irr}} = R - U + \sum_r M_r, \tag{24b}$$

where $\varphi^{U\text{irr}}$ is the fully U -irreducible part of Γ . The U subtractions ensure that the bare vertex U , which is contained once in each ∇_r but not in $\varphi^{U\text{irr}}$, is not over-counted. Some low-order diagrams of ∇_r , M_r , and R are shown in Fig. 5.

Just as γ_r , its parts ∇_r and M_r satisfy Bethe–Salpeter-type equations, which we derive next. Inserting Eq. (23) into the full vertex $\Gamma = I_r + \gamma_r$, we split it into a U - r -reducible part, ∇_r , and a U - r -irreducible remainder, T_r :

$$\Gamma = \nabla_r + T_r, \tag{25a}$$

$$T_r = I_r - U + M_r. \tag{25b}$$

The relation between the different decompositions of the full vertex implied by Eqs. (23)–(25) is illustrated in Fig. 6. Inserting Eqs. (23) and (25a) into either of the two forms of the BSEs (4) for γ_r , we obtain

$$\begin{aligned} \nabla_r - U + M_r &= I_r \circ \Pi_r \circ \nabla_r + I_r \circ \Pi_r \circ T_r \\ &= \nabla_r \circ \Pi_r \circ I_r + T_r \circ \Pi_r \circ I_r. \end{aligned} \tag{26}$$

This single set of equations can be split into two separate ones, one for $\nabla_r - U$, the other for M_r , containing only U - r -reducible or only U - r -irreducible terms, respectively. The first terms on the right are clearly U - r -reducible, since they contain ∇_r . For the second terms on the right, we write I_r as the sum of U and $I_r - U$, yielding U - r -reducible and U - r -irreducible contributions, respectively. We thus obtain two separate sets of equations,

$$\begin{aligned} \nabla_r - U &= I_r \circ \Pi_r \circ \nabla_r + U \circ \Pi_r \circ T_r \\ &= \nabla_r \circ \Pi_r \circ I_r + T_r \circ \Pi_r \circ U, \end{aligned} \tag{27}$$

$$\begin{aligned} M_r &= (I_r - U) \circ \Pi_r \circ T_r \\ &= T_r \circ \Pi_r \circ (I_r - U), \end{aligned} \tag{28}$$

the latter of which corresponds to Eq. (17) in Ref. [30]. In Eqs. (27), we now bring all ∇_r contributions to the

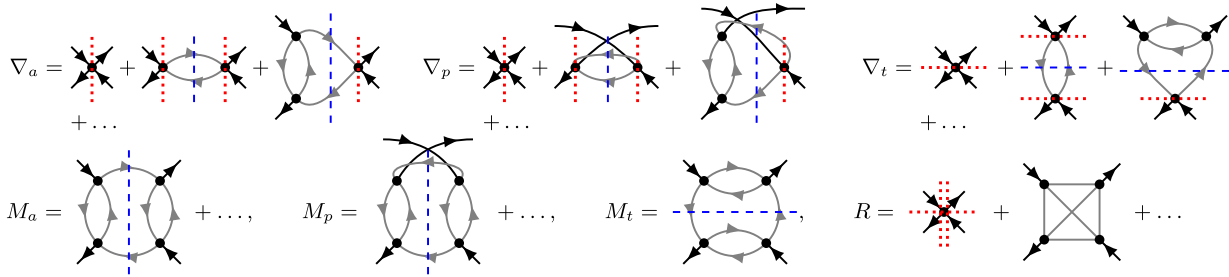


Fig. 5 Low-order diagrams for ∇_r , M_r , and R , illustrating Π - r -reducibility (blue dashed lines) and U - r -reducibility (red dotted lines; their meaning is made explicit in Fig. 4). ∇_r contains all U - r -reducible diagrams; except for the bare vertex, they all are Π - r -reducible, too. M_a contains all diagrams that are Π - a - but not U - a -reducible. All diagrams in R are neither Π - r - nor U - r -reducible, except for the bare vertex, which is U - a -, U - p - and U - t -reducible (as indicated by three red dotted lines)

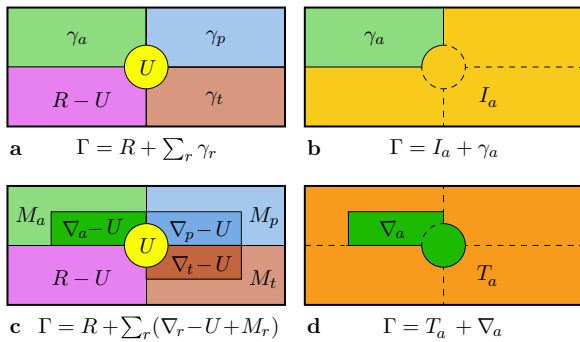


Fig. 6 Venn diagrams illustrating various ways of splitting the full vertex into distinct contributions. Panel **a** depicts the parquet decomposition (3), **b** the Π - a -reducible part γ_a and its complement I_a , **c** the SBE decomposition (24) (mimicking Fig. 6 of [26]), and **d** the U - a -reducible part ∇_a and its complement T_a . For $r = p, t$, the Π - r - and U - r -reducible parts and their complements can be depicted analogously

left,

$$\begin{aligned} (\mathbf{1}_r - I_r \circ \Pi_r) \circ \nabla_r &= U \circ (\mathbf{1}_r + \Pi_r \circ T_r), \\ \nabla_r \circ (\mathbf{1}_r - \Pi_r \circ I_r) &= (\mathbf{1}_r + T_r \circ \Pi_r) \circ U, \end{aligned} \quad (29)$$

and solve for ∇_r by evoking the extended BSEs (7):

$$\begin{aligned} \nabla_r &= (\mathbf{1}_r + \Gamma \circ \Pi_r) \circ U \circ (\mathbf{1}_r + \Pi_r \circ T_r) \\ &= (\mathbf{1}_r + T_r \circ \Pi_r) \circ U \circ (\mathbf{1}_r + \Pi_r \circ \Gamma). \end{aligned} \quad (30)$$

This directly exhibits the U - r -reducibility of ∇_r .

We now adopt the r parametrization and note a key structural feature of Eq. (30) for ∇_r : it contains a central bare vertex U , connected via $\circ \Pi_r \circ$ to either Γ or T_r or both. We may thus pull the frequency-independent U out of the frequency summations, so that $\circ \Pi_r \circ$ leads to $\bullet \mathbf{1}_r \circ \Pi_r \circ$ or $\circ \Pi_r \circ \mathbf{1}_r \bullet$, where the multiplication with $\mathbf{1}_r$ includes a sum over an internal fermionic frequency (recall Eqs. (21), (22) and Fig. 3).

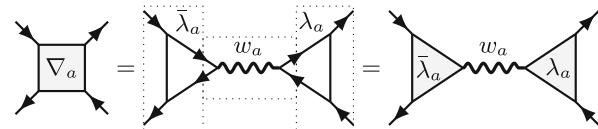


Fig. 7 Diagrammatic depiction of Eq. (33) (exemplified for the a channel), expressing the U - r -reducible vertex $\nabla_r = \bar{\lambda}_r \bullet w_r \bullet \lambda_r$ through two Hedin vertices, $\bar{\lambda}_r$, λ_r , and a screened interaction, w_r . The dashed boxes emphasize that $\bar{\lambda}_r$, w_r , λ_r all have four fermionic legs; those of w_r and the outer legs of $\bar{\lambda}_r$ and λ_r are amputated. Still, w_r depends on just a single, bosonic frequency and can hence be interpreted as an effective bosonic interaction. Its four legs lie pairwise close together since each pair stems from a bare vertex (see Eq. (43) and Fig. 3c). The two inward-facing legs of both $\bar{\lambda}_r$ and λ_r , connecting to w_r , are therefore also drawn close together, whereas the outward-facing legs are not. To depict this asymmetry in a compact manner, triangles are used on the right. For explicit index summations for all three channels, see Fig. 12 in Appendix A

Thus, Eq. (30) leads to

$$\begin{aligned} \nabla_r &= (\mathbf{1}_r + \Gamma \circ \Pi_r \circ \mathbf{1}_r) \bullet U \bullet (\mathbf{1}_r + \mathbf{1}_r \circ \Pi_r \circ T_r) \\ &= (\mathbf{1}_r + T_r \circ \Pi_r \circ \mathbf{1}_r) \bullet U \bullet (\mathbf{1}_r + \mathbf{1}_r \circ \Pi_r \circ \Gamma). \end{aligned} \quad (31)$$

In the first or second line, the expressions on the right or left of $\bullet U \bullet$, respectively, are U - r -irreducible. These factors are the so-called Hedin vertices [49] (cf. Ref. [30], Eq. (5)),

$$\bar{\lambda}_r(\omega_r, \nu_r) \equiv \mathbf{1}_r + [T_r \circ \Pi_r \circ \mathbf{1}_r](\omega_r, \nu_r), \quad (32a)$$

$$\lambda_r(\omega_r, \nu'_r) \equiv \mathbf{1}_r + [\mathbf{1}_r \circ \Pi_r \circ T_r](\omega_r, \nu'_r). \quad (32b)$$

In our notation, the Hedin vertices have four fermionic legs, but (importantly) depend on only two frequencies. Indeed, regarding their frequency dependence, they can be viewed as the U -irreducible, amputated parts of three-point response functions (see Appendix D and Ref. [26]). Then, Eqs. (32) have the structure of SDEs for a three-point vertex with a bare three-point vertex $\mathbf{1}_r$ (cf. Refs. [3, 7]). Via the Hedin vertices, ∇_r factorizes

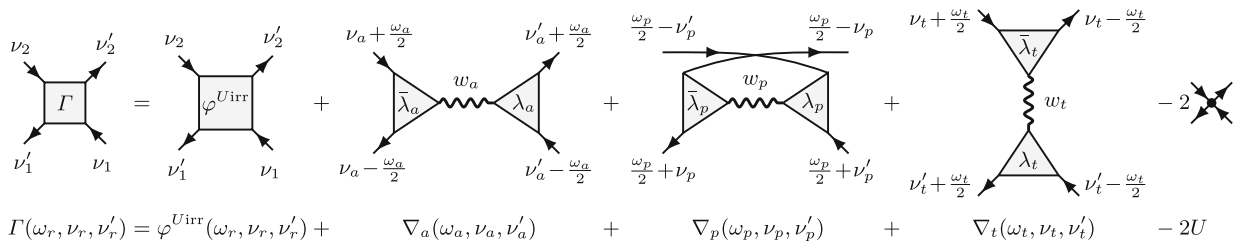


Fig. 8 SBE decomposition of the vertex Γ into U - r -irreducible and U - r -reducible contributions, with $r = a, p, t$. When connecting Hedin vertices to other objects, the two fermionic legs require a \circ connector, the bosonic leg a \bullet connector

into functions of at most two frequency arguments and is thus computationally cheaper than, e.g., γ_r . Following Refs. [26,30], we write

$$\nabla_r = \bar{\lambda}_r \bullet w_r \bullet \lambda_r, \tag{33}$$

where two U - r -irreducible Hedin vertices sandwich a U - r -reducible object, $w_r(\omega_r)$ (see Fig. 7). The object w_r depends only on the bosonic frequency ω_r and can be interpreted as a screened interaction. To find w_r explicitly, we first express Eq. (31) through Hedin vertices,

$$\begin{aligned} \nabla_r &= (\mathbf{1}_r + \Gamma \circ \Pi_r \circ \mathbf{1}_r) \bullet U \bullet \lambda_r \\ &= \bar{\lambda}_r \bullet U \bullet (\mathbf{1}_r + \mathbf{1}_r \circ \Pi_r \circ \Gamma). \end{aligned} \tag{34}$$

Then, $\Gamma = T_r + \nabla_r$ leads to implicit relations for ∇_r :

$$\begin{aligned} \nabla_r &= (\bar{\lambda}_r + \nabla_r \circ \Pi_r \circ \mathbf{1}_r) \bullet U \bullet \lambda_r \\ &= \bar{\lambda}_r \bullet U \bullet (\lambda_r + \mathbf{1}_r \circ \Pi_r \circ \nabla_r). \end{aligned} \tag{35}$$

Next, we insert Eq. (33) for ∇_r on both sides to obtain

$$\begin{aligned} \bar{\lambda}_r \bullet w_r \bullet \lambda_r &= \bar{\lambda}_r \bullet (U + w_r \bullet \lambda_r \circ \Pi_r \circ U) \bullet \lambda_r \\ &= \bar{\lambda}_r \bullet (U + U \circ \Pi_r \circ \bar{\lambda}_r \bullet w_r) \bullet \lambda_r. \end{aligned} \tag{36}$$

This implies that w_r satisfies a pair of Dyson equations,

$$\begin{aligned} w_r &= U + w_r \bullet \lambda_r \circ \Pi_r \circ U \\ &= U + U \circ \Pi_r \circ \bar{\lambda}_r \bullet w_r, \end{aligned} \tag{37}$$

which can be formally solved as

$$\begin{aligned} w_r &= U \bullet (\mathbf{1}_r - \lambda_r \circ \Pi_r \circ U)^{-1} \\ &= (\mathbf{1}_r - U \circ \Pi_r \circ \bar{\lambda}_r)^{-1} \bullet U. \end{aligned} \tag{38}$$

As desired, the screened interaction w_r is manifestly U - r -reducible, and depends on only a single, bosonic frequency, ω_r . To emphasize this fact, Eq. (38) can be written as

$$\begin{aligned} w_r &= U \bullet (\mathbf{1}_r - P_r \bullet U)^{-1} \\ &= (\mathbf{1}_r - U \bullet P_r)^{-1} \bullet U, \end{aligned} \tag{39}$$

where $P_r(\omega_r)$ is the polarization [30],

$$P_r = \lambda_r \circ \Pi_r \circ \mathbf{1}_r = \mathbf{1}_r \circ \Pi_r \circ \bar{\lambda}_r. \tag{40}$$

Regarding frequency dependencies, w_r can be viewed as a bosonic propagator and P_r as a corresponding self-energy; Eq. (40) then has the structure of a SDE for P_r involving the bare three-point vertex $\mathbf{1}_r$ [3,7].

Inserting Eq. (33) for ∇_r into Eq. (24a) for Γ , we arrive at the SBE decomposition of the full vertex of Ref. [26] in our generalized notation,

$$\Gamma = \varphi^{Uirr} + \sum_r \bar{\lambda}_r \bullet w_r \bullet \lambda_r - 2U, \tag{41a}$$

depicted diagrammatically in Fig. 8. For ease of reference, we gather all necessary relations for its ingredients:

$$w_r = U + U \bullet P_r \bullet w_r = U + w_r \bullet P_r \bullet U, \tag{41b}$$

$$P_r = \lambda_r \circ \Pi_r \circ \mathbf{1}_r = \mathbf{1}_r \circ \Pi_r \circ \bar{\lambda}_r, \tag{41c}$$

$$\bar{\lambda}_r = \mathbf{1}_r + T_r \circ \Pi_r \circ \mathbf{1}_r, \tag{41d}$$

$$\lambda_r = \mathbf{1}_r + \mathbf{1}_r \circ \Pi_r \circ T_r, \tag{41e}$$

$$T_r = \Gamma - \bar{\lambda}_r \bullet w_r \bullet \lambda_r, \tag{41f}$$

$$\varphi^{Uirr} = R - U + \sum_r M_r, \tag{41g}$$

$$M_r = (T_r - M_r) \circ \Pi_r \circ T_r = T_r \circ \Pi_r \circ (T_r - M_r). \tag{41h}$$

We collectively call Eqs. (41) the *SBE equations*. Together with the SDE for the self-energy and an input for the two-particle irreducible vertex R , the SBE equations are a self-consistent set of equations and thus fully define the four-point vertex Γ . They can either be solved self-consistently (as by Krien et al. in Refs. [27–30], where an analogous set of equations was set up), or via multiloop flow equations, derived in Sect. 3.2.

To conclude this section, let us point out the physical meaning of $\bar{\lambda}_r, w_r, \lambda_r$ by showing their relation to three-point vertices and susceptibilities. For this, a symmetric expression for w_r is needed, which can be obtained by comparing Eqs. (33) and (34) to deduce

$$\bar{\lambda}_r \bullet w_r = U + \Gamma \circ \Pi_r \circ U, \tag{42a}$$

$$w_r \bullet \lambda_r = U + U \circ \Pi_r \circ \Gamma, \tag{42b}$$

and inserting these into the Dyson equations (37):

$$w_r = U + U \circ \Pi_r \circ U + U \circ \Pi_r \circ \Gamma \circ \Pi_r \circ U. \quad (43)$$

Equations (42) and (43) can be expressed as

$$[\bar{\lambda}_r \bullet w_r](\omega_r, \nu_r) = \bar{\Gamma}_r^{(3)}(\omega_r, \nu_r) \bullet U, \quad (44a)$$

$$[w_r \bullet \lambda_r](\omega_r, \nu'_r) = U \bullet \Gamma_r^{(3)}(\omega_r, \nu'_r), \quad (44b)$$

$$w_r(\omega_r) = U + U \bullet \chi_r(\omega_r) \bullet U, \quad (44c)$$

where $\bar{\Gamma}_r^{(3)}, \Gamma_r^{(3)}$ represent full three-point vertices and χ_r susceptibilities, defined by

$$\bar{\Gamma}_r^{(3)}(\omega_r, \nu_r) = \mathbf{1}_r + [\Gamma \circ \Pi_r \circ \mathbf{1}_r](\omega, \nu_r), \quad (45a)$$

$$\Gamma_r^{(3)}(\omega_r, \nu'_r) = \mathbf{1}_r + [\mathbf{1}_r \circ \Pi_r \circ \Gamma](\omega_r, \nu'_r), \quad (45b)$$

$$\begin{aligned} \chi_r(\omega_r) &= [\mathbf{1}_r \circ \Pi_r \circ \mathbf{1}_r](\omega_r) \\ &\quad + [\mathbf{1}_r \circ \Pi_r \circ \Gamma \circ \Pi_r \circ \mathbf{1}_r](\omega_r). \end{aligned} \quad (45c)$$

(The bare vertices were pulled out in front of the frequency sums, exploiting their frequency independence.) The relation of $\bar{\Gamma}_r^{(3)}$ and $\Gamma_r^{(3)}$ to three-point correlators and response functions is described in Appendix D; the relation of χ_r to physical susceptibilities for a local bare interaction U is discussed in Appendix E.

3.2 SBE mFRG from parquet mFRG

Having defined all the SBE ingredients, we are now ready to derive mFRG flow equations for them—the main goal of this work. Our strategy is to insert the SBE decomposition of Eqs. (23) and (24) into the parquet mFRG flow equations (10) for the Π - r -reducible vertices γ_r . An alternative derivation, starting directly from the SBE equations (41), is given in Sect. 3.3.

We begin by differentiating the decomposition of the Π - r -reducible vertex $\gamma_r = \bar{\lambda}_r \bullet w_r \bullet \lambda_r - U + M_r$ (Eq. (23)) w.r.t. the flow parameter. Since $\dot{U} = 0$ (the bare vertex does not depend on the regulator), we obtain

$$\dot{\gamma}_r = \dot{\bar{\lambda}}_r \bullet w_r \bullet \lambda_r + \bar{\lambda}_r \bullet \dot{w}_r \bullet \lambda_r + \bar{\lambda}_r \bullet w_r \bullet \dot{\lambda}_r + \dot{M}_r. \quad (46)$$

The loop expansion $\dot{\gamma}_r = \sum_{\ell} \dot{\gamma}_r^{(\ell)}$ implies similar expansions for $\dot{w}_r, \dot{\bar{\lambda}}_r, \dot{\lambda}_r,$ and \dot{M}_r . Each term at a given loop order ℓ can be found from the mFRG flow (10) for $\dot{\gamma}_r^{(\ell)}$, by inserting the decomposition of the full vertex, $\Gamma = \bar{\lambda}_r \bullet w_r \bullet \lambda_r + T_r$ (Eq. (25a)) on the right of Eqs. (10).

The 1ℓ flow equation (10a) for $\dot{\gamma}_r^{(1)}$ has four contributions (shown diagrammatically for $\gamma_a^{(1)}$ in Fig. 9):

$$\begin{aligned} \dot{\gamma}_r^{(1)} &= (\bar{\lambda}_r \bullet w_r \bullet \lambda_r + T_r) \circ \dot{\Pi}_r \circ (\bar{\lambda}_r \bullet w_r \bullet \lambda_r + T_r) \\ &= T_r \circ \dot{\Pi}_r \circ \bar{\lambda}_r \bullet w_r \bullet \lambda_r \\ &\quad + \bar{\lambda}_r \bullet w_r \bullet \lambda_r \circ \dot{\Pi}_r \circ \bar{\lambda}_r \bullet w_r \bullet \lambda_r \\ &\quad + \bar{\lambda}_r \bullet w_r \bullet \lambda_r \circ \dot{\Pi}_r \circ T_r + T_r \circ \dot{\Pi}_r \circ T_r. \end{aligned} \quad (47)$$

By matching terms in Eqs. (46) and (47) containing factors of $\bar{\lambda}_r$ and λ_r or not, we obtain the 1ℓ SBE flow:

$$\begin{aligned} \dot{w}_r^{(1)} &= w_r \bullet \lambda_r \circ \dot{\Pi}_r \circ \bar{\lambda}_r \bullet w_r, \\ \dot{\bar{\lambda}}_r^{(1)} &= T_r \circ \dot{\Pi}_r \circ \bar{\lambda}_r, \\ \dot{\lambda}_r^{(1)} &= \lambda_r \circ \dot{\Pi}_r \circ T_r, \\ \dot{M}_r^{(1)} &= T_r \circ \dot{\Pi}_r \circ T_r. \end{aligned} \quad (48a)$$

This reproduces the 1ℓ SBE flow derived in Ref. [31] (their Eq. (18)). The higher loop terms can be found similarly from $\dot{\gamma}_r^{(2)}$ and $\dot{\gamma}_r^{(\ell+2)}$ of Eqs. (10b) and (10c). For each loop order ℓ , the $\dot{\gamma}_r^{(\ell)}$ factors on the right side of these equations can be expressed through the already known flow of $\dot{w}_r^{(\ell)}, \dot{\bar{\lambda}}_r^{(\ell)}, \dot{\lambda}_r^{(\ell)}$ and $\dot{M}_r^{(\ell)}$. We obtain the flow equations ($\ell + 2 \geq 3$)

$$\begin{aligned} \dot{w}_r^{(2)} &= 0, \\ \dot{\bar{\lambda}}_r^{(2)} &= \dot{\gamma}_r^{(1)} \circ \Pi_r \circ \bar{\lambda}_r, \\ \dot{\lambda}_r^{(2)} &= \lambda_r \circ \Pi_r \circ \dot{\gamma}_r^{(1)}, \\ \dot{M}_r^{(2)} &= \dot{\gamma}_r^{(1)} \circ \Pi_r \circ T_r + T_r \circ \Pi_r \circ \dot{\gamma}_r^{(1)}, \\ \dot{w}_r^{(\ell+2)} &= w_r \bullet \lambda_r \circ \Pi_r \circ \dot{\gamma}_r^{(\ell)} \circ \Pi_r \circ \bar{\lambda}_r \bullet w_r, \\ \dot{\bar{\lambda}}_r^{(\ell+2)} &= \dot{\gamma}_r^{(\ell+1)} \circ \Pi_r \circ \bar{\lambda}_r + T_r \circ \Pi_r \circ \dot{\gamma}_r^{(\ell)} \circ \Pi_r \circ \bar{\lambda}_r, \\ \dot{\lambda}_r^{(\ell+2)} &= \lambda_r \circ \Pi_r \circ \dot{\gamma}_r^{(\ell)} \circ \Pi_r \circ T_r + \lambda_r \circ \Pi_r \circ \dot{\gamma}_r^{(\ell+1)}, \\ \dot{M}_r^{(\ell+2)} &= \dot{\gamma}_r^{(\ell+1)} \circ \Pi_r \circ T_r + T_r \circ \Pi_r \circ \dot{\gamma}_r^{(\ell)} \circ \Pi_r \circ T_r \\ &\quad + T_r \circ \Pi_r \circ \dot{\gamma}_r^{(\ell+1)}. \end{aligned} \quad (48b)$$

Here, $\dot{\gamma}_r^{(\ell)}$, required for the flow at loop orders $\ell + 1$ and $\ell + 2$, can directly be constructed from the SBE ingredients using Eq. (46). Similarly as in Eqs. (10), all terms at loop order ℓ contain $\ell - 1$ factors of Π and one $\dot{\Pi}$, now connecting the renormalized objects $w_r, \bar{\lambda}_r, \lambda_r, T_r$.

The SBE mFRG flow equations (48) are the most important result of this work. For the a channel, they are depicted diagrammatically in Fig. 10. Equations (48) can be condensed into more compact ones, giving the full flow (summed over all loop orders, $\dot{w}_r = \sum_{\ell \geq 1} \dot{w}_r^{(\ell)}$, etc.) of the SBE ingredients; see the next section. The multiloop flow equation for the self-energy [5, 7] is given in Eq. (12).

3.3 SBE mFRG from SBE equations

In the previous section, we derived the SBE mFRG flow equations by inserting the SBE decomposition into the known parquet mFRG flow equations of the two-particle reducible vertices γ_r . They can also be derived without prior knowledge on the flow of γ_r , using the techniques of Ref. [7].

In the parquet setting of Ref. [7], one can view the Π - r -irreducible vertex I_r as the key ingredient for all equations related to channel r . In step (i), one uses I_r

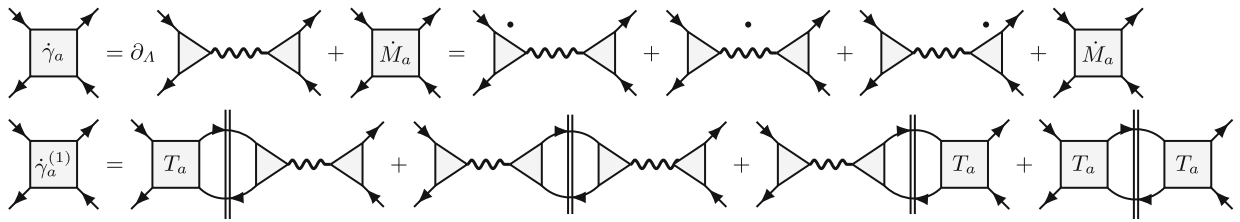


Fig. 9 SBE decomposition of the left and right sides of the $1l$ flow equation (10a) (Fig. 2) in the a channel. The first line depicts Eq. (46), the second Eq. (47). Equating terms with matching structure yields Eq. (48a), depicted in Fig. 10, first line

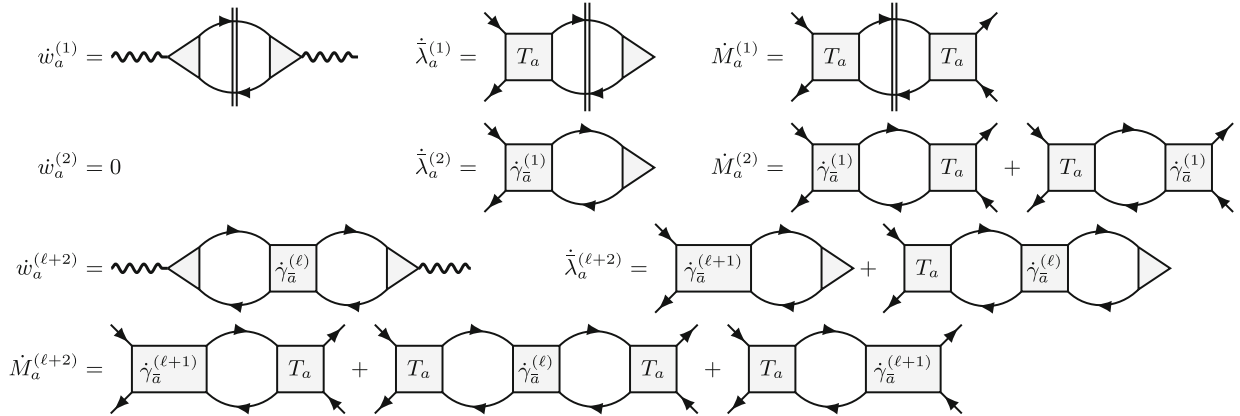


Fig. 10 Multiloop flow equations (48) for the ingredients of the SBE decomposition in the a channel

to generate γ_r and thus Γ through a BSE. Then, a post-processing of attaching and closing external legs yields (ii) (full) three-point vertices $\bar{\Gamma}_r^{(3)}$, $\Gamma_r^{(3)}$ and (iii) a susceptibility χ_r . The SBE setting can be understood in close analogy, with the only exception that one purposefully avoids generating U - r -reducible contributions, because these can (more efficiently) be constructed via $\nabla_r = \bar{\lambda}_r \bullet w_r \bullet \lambda_r$. To exclude U - r -reducible contributions, one uses in step (i) $I_r - U$ to generate M_r and thus T_r through a BSE. The same post-processing as before yields (ii) $\bar{\lambda}_r$, λ_r and then (iii) w_r or P_r .

Because of this structural analogy, the SBE mFRG flow equations can be derived in the exact same fashion as the parquet mFRG flow equation of Ref. [7]. One merely has to replace the variables according to the dictionary

$$\begin{aligned}
 I_r &\rightarrow I_r - U, & \gamma_r &\rightarrow M_r, & \Gamma &\rightarrow T_r, \\
 \bar{\Gamma}_r^{(3)} &\rightarrow \bar{\lambda}_r, & \Gamma_r^{(3)} &\rightarrow \lambda_r, & \chi_r &\rightarrow P_r.
 \end{aligned}
 \tag{49}$$

For clarity, we now spell out the structural analogies between the original parquet formalism and its SBE version, presenting similarly-structured expressions in pairs of equations, (a) and (b). For both approaches, the full vertex can be decomposed in several ways:

$$\Gamma = R + \sum_r \gamma_r = I_r + \gamma_r,
 \tag{50a}$$

$$\Gamma = R + \sum_r M_r + \sum_r (\nabla_r - U) = T_r + \nabla_r.
 \tag{50b}$$

Here, γ_r and M_r satisfy analogous BSEs,

$$\gamma_r = I_r \circ \Pi_r \circ \Gamma,
 \tag{51a}$$

$$M_r = (I_r - U) \circ \Pi_r \circ T_r,
 \tag{51b}$$

where the objects on the left reappear on the right through

$$\Gamma = I_r + \gamma_r,
 \tag{52a}$$

$$T_r = (I_r - U) + M_r.
 \tag{52b}$$

Relations (51) and (52) are used for step (i). Differentiation of Eq. (51a) yields the mFRG flow of $\dot{\gamma}_r$ as in Eq. (10) and Fig. 2a of Ref. [7]. Here, we replace the variables as above and start by differentiating Eq. (51b):

$$\begin{aligned}
 \dot{M}_r &= \dot{I}_r \circ \Pi_r \circ T_r + (I_r - U) \circ \dot{\Pi}_r \circ T_r \\
 &\quad + (I_r - U) \circ \Pi_r \circ \dot{I}_r + (I_r - U) \circ \Pi_r \circ \dot{M}_r \\
 \Rightarrow \dot{M}_r &= (\mathbf{1}_r - (I_r - U) \circ \Pi_r)^{-1} \circ \left[\dot{I}_r \circ \Pi_r \circ T_r \right. \\
 &\quad \left. + (I_r - U) \circ \dot{\Pi}_r \circ T_r + (I_r - U) \circ \Pi_r \circ \dot{I}_r \right].
 \end{aligned}
 \tag{53}$$

For the first argument of Eq. (53), we used $\partial_\Lambda(I_r - U) = \dot{I}_r$, as $\dot{U} = 0$. Next, we use the extended BSE $\mathbf{1}_r + T_r \circ \Pi_r = (\mathbf{1}_r - (I_r - U) \circ \Pi_r)^{-1}$ for M_r , cf. Eqs. (7) and

(51). Recollecting the terms, we obtain the flow of \dot{M}_r as

$$\begin{aligned} \dot{M}_r &= T_r \circ \dot{H}_r \circ T_r + \dot{I}_r \circ \Pi_r \circ T_r \\ &+ T_r \circ \Pi_r \circ \dot{I}_r \circ \Pi_r \circ T_r + T_r \circ \Pi_r \circ \dot{I}_r. \end{aligned} \quad (54)$$

A loop expansion with $\dot{I}_r = \dot{\gamma}_{\bar{r}} = \sum_{\ell} \dot{\gamma}_{\bar{r}}^{(\ell)}$ then yields our Eqs. (48) and Fig. 10.

For step (ii), we have the analogous relations

$$\bar{\Gamma}_r^{(3)} = \mathbf{1}_r + \Gamma \circ \Pi_r \circ \mathbf{1}_r, \quad \Gamma_r^{(3)} = \mathbf{1}_r + \mathbf{1}_r \circ \Pi_r \circ \Gamma, \quad (55a)$$

$$\bar{\lambda}_r = \mathbf{1}_r + T_r \circ \Pi_r \circ \mathbf{1}_r, \quad \lambda_r = \mathbf{1}_r + \mathbf{1}_r \circ \Pi_r \circ T_r. \quad (55b)$$

Differentiation of Eq. (55a) yields the mfRG flow of $\Gamma_r^{(3)}$ as in Eq. (42) and Fig. 7 of Ref. [7]. Here, we again replace the variables as above and differentiate Eq. (55b):

$$\begin{aligned} \dot{\lambda}_r &= \dot{T}_r \circ \Pi_r \circ \mathbf{1}_r + T_r \circ \dot{H}_r \circ \mathbf{1}_r, \\ \dot{\lambda}_r &= \mathbf{1}_r \circ \dot{H}_r \circ T_r + \mathbf{1}_r \circ \Pi_r \circ \dot{T}_r. \end{aligned} \quad (56)$$

As $\dot{T}_r = \dot{I}_r + \dot{M}_r$ (cf. Eq. (52b)), we insert the flow equation (54) for \dot{M}_r into Eq. (56) and use again Eq. (55b). This yields the flow equations

$$\begin{aligned} \dot{\lambda}_r &= T_r \circ \dot{H}_r \circ \bar{\lambda}_r + \dot{I}_r \circ \Pi_r \circ \bar{\lambda}_r + T_r \circ \Pi_r \circ \dot{I}_r \circ \Pi_r \circ \bar{\lambda}_r, \\ \dot{\lambda}_r &= \lambda_r \circ \dot{H}_r \circ T_r + \lambda_r \circ \Pi_r \circ \dot{I}_r + \lambda_r \circ \Pi_r \circ \dot{I}_r \circ \Pi_r \circ T_r. \end{aligned} \quad (57)$$

Their loop expansion reproduces Eqs. (48) and Fig. 10.

Finally, in step (iii), we have the relations

$$\chi_r = \Gamma_r^{(3)} \circ \Pi_r \circ \mathbf{1}_r = \mathbf{1}_r \circ \Pi_r \circ \bar{\Gamma}^{(3)}, \quad (58a)$$

$$P_r = \lambda_r \circ \Pi_r \circ \mathbf{1}_r = \mathbf{1}_r \circ \Pi_r \circ \bar{\lambda}_r. \quad (58b)$$

Differentiation of Eq. (58a) yields the mfRG flow of χ_r as in Eq. (44) and Fig. 8 of Ref. [7]. Replacing the variables as above one more time, we differentiate Eq. (58b):

$$\dot{P}_r = \mathbf{1}_r \circ \Pi_r \circ \dot{\lambda}_r + \mathbf{1}_r \circ \dot{H}_r \circ \bar{\lambda}_r. \quad (59)$$

After inserting Eqs. (55b) and (57), we eventually obtain

$$\dot{P}_r = \lambda_r \circ \left(\dot{H}_r + \Pi_r \circ \dot{I}_r \circ \Pi_r \right) \circ \bar{\lambda}_r. \quad (60)$$

The relation between \dot{P}_r and \dot{w}_r follows from the Dyson equation (41b) as

$$\dot{w}_r = U \cdot \dot{P}_r \cdot w_r + U \cdot P_r \cdot \dot{w}_r. \quad (61)$$

Solving this for \dot{w}_r yields

$$\dot{w}_r = (\mathbf{1}_r - U \cdot P_r)^{-1} \cdot U \cdot \dot{P}_r \cdot w_r = w_r \cdot \dot{P}_r \cdot w_r, \quad (62)$$

having inserted the inverted Dyson equations (39). A loop expansion of Eq. (60) yields:

$$\begin{aligned} \dot{P}_r^{(1)} &= \lambda_r \circ \dot{H}_r \circ \bar{\lambda}_r, \\ \dot{P}_r^{(2)} &= 0, \\ \dot{P}_r^{(\ell+2)} &= \lambda_r \circ \Pi_r \circ \dot{\gamma}_{\bar{r}}^{(\ell)} \circ \Pi_r \circ \bar{\lambda}_r. \end{aligned} \quad (63)$$

Inserting the loop expansion $\dot{P}_r^{(\ell)}$ into Eq. (62) for \dot{w}_r yields the same flow equation for w_r as in our Eqs. (48) and Fig. 10.

Depending on the specific model, it can be more efficient to calculate the flow of the polarization, \dot{P}_r , by Eqs. (63) instead of the flow of the screened interaction, \dot{w}_r , by Eqs. (48). The screened interaction on the contrary can be obtained by the inverted Dyson Eqs. (39).

Altogether, Eqs. (54), (57), (60) and (62) (with T_r given by $\Gamma - \nabla_{\bar{r}}$, Eq. (50b)) build a system of closed fRG equations, as full derivatives of the SBE equations (41). Hence, combined with an appropriate self-energy flow (cf. Eq. (12) and Ref. [7]), they yield regulator-independent results. To integrate the flow equations in practice, one employs the mfRG loop expansions (48) and (63).

3.4 mfRG flow of the SBE approximation

To reduce numerical costs, it may sometimes be desirable to approximate the flow of the vertex treating only objects with less than all three frequency arguments. The simplest choice is to restrict the flow to functions depending on a single frequency. In the present context, this corresponds to keeping all objects except w_r constant. With $\dot{\lambda}_r = 0 = \dot{\lambda}_r$, the flow of the polarization (59) is simply

$$\dot{P}_r = \lambda_r \circ \dot{H}_r \circ \mathbf{1}_r = \mathbf{1}_r \circ \dot{H}_r \circ \bar{\lambda}_r. \quad (64)$$

Hence, the flow equations of P_r and w_r completely decouple, and one effectively obtains a vertex consisting of three independent series of ladder diagrams. Nevertheless, such a flow may be helpful for code-developing purposes.

An approximation of the vertex with objects of at most two frequency arguments is given by the SBE approximation [26], which sets $\varphi^{U_{\text{irr}}} = 0$. More generally, one may also keep $\varphi^{U_{\text{irr}}} \neq 0$ constant during the flow, e.g., as obtained from DMFT (called SBE-DFA in Ref. [26]). This was used in a 1*l* implementation of DMF²RG in Ref. [31]. In the following, we will refer to the approximation of using a non-flowing U -irreducible part, $\dot{\varphi}^{U_{\text{irr}}} = 0$, as SBE approximation, regardless of whether $\varphi^{U_{\text{irr}}}$ is set to zero or not.

We now derive mFRG flow equations for the SBE approximation, so that $\dot{R} = 0$, as before, and furthermore $\dot{M}_r = 0$. For the most part, the SBE equations (41) remain unchanged. Only the BSE for M_r (41h) is not considered anymore, since now $\varphi^{U_{\text{irr}}} = R - U + \sum_r M_r$ is used as an input. The corresponding flow equations can be obtained as in Sect. 3.3. The flow of the polarization, the screened interaction and the Hedin vertices, prior to any transformation, is still given by Eqs. (59), (62) and (56) (collected here for convenience)

$$\begin{aligned} \dot{P}_r &= \mathbf{1}_r \circ \dot{H}_r \circ \bar{\lambda}_r + \mathbf{1}_r \circ \Pi_r \circ \dot{\lambda}_r \\ &= \dot{\lambda}_r \circ \Pi_r \circ \mathbf{1}_r + \lambda_r \circ \dot{H}_r \circ \mathbf{1}_r, \end{aligned} \tag{65a}$$

$$\dot{w}_r = w_r \bullet \dot{P}_r \bullet w_r, \tag{65b}$$

$$\dot{\bar{\lambda}}_r = T_r \circ \dot{H}_r \circ \mathbf{1}_r + \dot{T}_r \circ \Pi_r \circ \mathbf{1}_r, \tag{65c}$$

$$\dot{\lambda}_r = \mathbf{1}_r \circ \dot{H}_r \circ T_r + \mathbf{1}_r \circ \Pi_r \circ \dot{T}_r. \tag{65d}$$

However, the flow of $T_r = I_r - U + M_r$ now has no \dot{M}_r contribution. It is induced solely by $\dot{I}_r = \dot{\nabla}_{\bar{r}}$, the flow of the U -reducible contributions from complementary channels,

$$\dot{T}_r = \dot{\nabla}_{\bar{r}}, \tag{65e}$$

and thus is fully determined by $\dot{\bar{\lambda}}_r$, $\dot{\lambda}_r$ and \dot{w}_r .

Equations (65) can be rewritten by inserting the flow of the higher-point objects into the lower-point objects:

$$\dot{\bar{\lambda}}_r = T_r \circ \dot{H}_r \circ \mathbf{1}_r + \dot{\nabla}_{\bar{r}} \circ \Pi_r \circ \mathbf{1}_r, \tag{66a}$$

$$\dot{\lambda}_r = \mathbf{1}_r \circ \dot{H}_r \circ T_r + \mathbf{1}_r \circ \Pi_r \circ \dot{\nabla}_{\bar{r}}, \tag{66b}$$

$$\begin{aligned} \dot{P}_r &= \mathbf{1}_r \circ \dot{H}_r \circ \bar{\lambda}_r + \mathbf{1}_r \circ \Pi_r \circ T_r \circ \dot{H}_r \circ \mathbf{1}_r \\ &\quad + \mathbf{1}_r \circ \Pi_r \circ \dot{\nabla}_{\bar{r}} \circ \Pi_r \circ \mathbf{1}_r \\ &= \mathbf{1}_r \circ \dot{H}_r \circ \bar{\lambda}_r + \lambda_r \circ \dot{H}_r \circ \mathbf{1}_r \\ &\quad - \mathbf{1}_r \circ \dot{H}_r \circ \mathbf{1}_r + \mathbf{1}_r \circ \Pi_r \circ \dot{\nabla}_{\bar{r}} \circ \Pi_r \circ \mathbf{1}_r. \end{aligned} \tag{66c}$$

In the last line, we expressed $\mathbf{1}_r \circ \Pi_r \circ T_r$ in terms of the Hedin vertex $\lambda_r - \mathbf{1}_r$. Equations (66) are similar to the previous flow equations (57) and (60) of the more general case, but some occurrences of the Hedin vertices $\bar{\lambda}_r, \lambda_r$ on the right there are here replaced by their zeroth-order term $\mathbf{1}_r$. Evidently, the contributions needed to upgrade these $\mathbf{1}_r$ to $\bar{\lambda}_r, \lambda_r$ are omitted when setting $\dot{M}_r = 0$.

A loop expansion of the above equations then yields

$$\begin{aligned} \dot{P}_r^{(1)} &= \mathbf{1}_r \circ \dot{H}_r \circ \bar{\lambda}_r + \lambda_r \circ \dot{H}_r \circ \mathbf{1}_r - \mathbf{1}_r \circ \dot{H}_r \circ \mathbf{1}_r, \\ \dot{\bar{\lambda}}_r^{(1)} &= T_r \circ \dot{H}_r \circ \mathbf{1}_r, \\ \dot{\lambda}_r^{(1)} &= \mathbf{1}_r \circ \dot{H}_r \circ T_r, \end{aligned} \tag{67a}$$

$$\begin{aligned} \dot{P}_r^{(2)} &= 0, \\ \dot{\bar{\lambda}}_r^{(\ell+1)} &= \dot{\nabla}_{\bar{r}}^{(\ell)} \circ \Pi_r \circ \mathbf{1}_r, \\ \dot{\lambda}_r^{(\ell+1)} &= \mathbf{1}_r \circ \Pi_r \circ \dot{\nabla}_{\bar{r}}^{(\ell)}, \\ \dot{P}_r^{(\ell+2)} &= \mathbf{1}_r \circ \Pi_r \circ \dot{\nabla}_{\bar{r}}^{(\ell)} \circ \Pi_r \circ \mathbf{1}_r, \end{aligned} \tag{67b}$$

$$\dot{w}_r^{(\ell)} = w_r \bullet \dot{P}_r^{(\ell)} \bullet w_r. \tag{67c}$$

Apart from the fact that \dot{M}_r is not needed here, the other flow equations are also simpler than Eqs. (48) without \dot{M}_r , obtained from the full SBE equations. To be specific, Eqs. (48) contain $\bar{\lambda}_r$ or λ_r on the right of the flow equations for $\dot{\bar{\lambda}}_r^{(\ell)}$ or $\dot{\lambda}_r^{(\ell)}$, whereas the simplified Eqs. (67) contain $\mathbf{1}_r$ there, and, for $\ell \geq 2$, only one term where Eqs. (48) had two.

When using the above flow equations for the SBE approximation, the self-energy flow (12) should also be re-derived from either the SDE or the Hedin equation for Σ (e.g. Eq. (23) in Ref. [27]). Since the present paper focuses on vertex parametrizations, we leave a derivation of a suitably modified self-energy flow for future work. Here, it suffices to note that, when used together with such a modified self-energy flow, Eqs. (67) are again total derivatives of a closed set of equations. So, integrating the flow until loop convergence would yield the regulator-independent solution of the SBE approximation.

Transforming the self-consistent equations of the SBE approximation on the vertex level to an equivalent mFRG flow reveals its simplistic nature, with relations like $\dot{\lambda}_r^{(1)} = \mathbf{1}_r \bullet \dot{H}_r \bullet T_r$, and demonstrates how fRG offers an intuitive way to go beyond that, using, e.g., $\dot{\lambda}_r^{(1)} = \lambda_r \bullet \dot{H}_r \bullet T_r$ (still treating only functions of at most two frequencies). However, the latter flow would be regulator-dependent *per se*. It remains to be seen how severe the lack of regulator independence for this flow, as used, e.g., in Ref. [31], is.

The simplified schemes presented in this section [i.e., Eqs. (64) and (67)] are closed flow equations on the vertex level and thus offer an appealing way for approaching the full SBE mFRG equations (48). Thereby, SBE ingredients with more complicated frequency dependence can be taken into account successively during code development. To what extent they can succeed in actually capturing the essential physics of a given problem will have to be investigated on a case-by-case basis. Generally, we showed that mFRG offers a way to make the choice of a certain approximation regulator independent, either for the simplistic flow of the SBE approximation or for the full SBE mFRG flow reproducing the PA.

4 Asymptotic classes

In numerical implementations of parquet mFRG [10–14], it is useful to handle the numerical complexity of the vertex by decomposing it into asymptotic classes with well-defined high-frequency behaviors. It is convenient to compute the flow of these asymptotic classes using their own flow equations; here, we recapitulate their derivation. We also elucidate the close relation between vertex parametrizations using the parquet decomposition with asymptotic classes or the SBE decomposition, deriving explicit equations relating their ingredients.

These equations may facilitate the adaption of codes devised for parquet mfRG to SBE mfRG applications.

4.1 Definition of asymptotic classes

The parametrization of two-particle reducible vertices γ_r via asymptotic classes was introduced in Ref. [16] to conveniently express their high-frequency asymptotics through simpler objects with fewer frequency arguments. One makes the ansatz

$$\begin{aligned} \gamma_r(\omega_r, \nu_r, \nu'_r) &= \mathcal{K}_1^r(\omega_r) + \mathcal{K}_2^r(\omega_r, \nu_r) + \mathcal{K}_{2'}^r(\omega_r, \nu'_r) + \mathcal{K}_3^r(\omega_r, \nu_r, \nu'_r). \end{aligned} \tag{68}$$

Here, \mathcal{K}_1^r contains all diagrams having both ν_r legs connected to the same bare vertex and both ν'_r legs connected to another bare vertex. (For a diagrammatic depiction, see Appendix B, Fig. 14.) These diagrams are thus independent of ν_r, ν'_r and stay finite in the limit $|\nu_r| \rightarrow \infty, |\nu'_r| \rightarrow \infty$,

$$\lim_{|\nu_r| \rightarrow \infty} \lim_{|\nu'_r| \rightarrow \infty} \gamma_r(\omega_r, \nu_r, \nu'_r) = \mathcal{K}_1^r(\omega_r). \tag{69a}$$

\mathcal{K}_2^r (or $\mathcal{K}_{2'}^r$) analogously contains the part of the vertex having both ν'_r (or ν_r) legs connected to the same bare vertex while the two ν_r (or ν'_r) legs are connected to different bare vertices. Hence, it is finite for $|\nu'_r| \rightarrow \infty$ (or $|\nu_r| \rightarrow \infty$) but vanishes for $|\nu_r| \rightarrow \infty$ (or $|\nu'_r| \rightarrow \infty$):

$$\begin{aligned} \lim_{|\nu'_r| \rightarrow \infty} \gamma_r(\omega_r, \nu_r, \nu'_r) &= \mathcal{K}_1^r(\omega_r) + \mathcal{K}_2^r(\omega_r, \nu_r), \\ \lim_{|\nu_r| \rightarrow \infty} \gamma_r(\omega_r, \nu_r, \nu'_r) &= \mathcal{K}_1^r(\omega_r) + \mathcal{K}_{2'}^r(\omega_r, \nu'_r). \end{aligned} \tag{69b}$$

\mathcal{K}_3^r exclusively contains diagrams having both ν_r legs connected to different bare vertices, and likewise for both ν'_r legs. Such diagrams depend on all three frequencies and thus decay if any of them is sent to infinity. When taking the above limits for bubbles involving channels r' different from r , we obtain zero,

$$\lim_{|\nu_r| \rightarrow \infty} \gamma_{r' \neq r} = \lim_{|\nu'_r| \rightarrow \infty} \gamma_{r' \neq r} = 0, \tag{69c}$$

as each $\Pi_{r'}$ in $\gamma_{r'}$ has a denominator containing $\omega_{r' \neq r}$, which is a linear combination of ω_r, ν_r and ν'_r .

Since R explicitly depends on all frequencies, it decays to the bare vertex U at high frequencies, and the asymptotic classes can be obtained by taking limits of the full vertex. Explicitly, \mathcal{K}_1^r can be obtained from

$$\lim_{|\nu_r| \rightarrow \infty} \lim_{|\nu'_r| \rightarrow \infty} \Gamma(\omega_r, \nu_r, \nu'_r) = U + \mathcal{K}_1^r(\omega_r), \tag{70a}$$

taking the double limit in such a way that $\nu_r \pm \nu'_r$ is not constant, to ensure that all bosonic frequencies $|\omega_{r' \neq r}|$ go to ∞ [16]. Similarly, $\mathcal{K}_2^r, \mathcal{K}_{2'}^r$ can be obtained from

objects $\Gamma_2^r, \Gamma_{2'}^r$ defined via the limits

$$\Gamma_2^r(\omega_r, \nu_r) = \lim_{|\nu'_r| \rightarrow \infty} \Gamma(\omega_r, \nu_r, \nu'_r) = U + \mathcal{K}_1^r + \mathcal{K}_2^r, \tag{70b}$$

$$\Gamma_{2'}^r(\omega_r, \nu'_r) = \lim_{|\nu_r| \rightarrow \infty} \Gamma(\omega_r, \nu_r, \nu'_r) = U + \mathcal{K}_1^r + \mathcal{K}_{2'}^r. \tag{70c}$$

For each of the latter two limits, we denote the complementary part of the vertex (vanishing in said limit) by

$$\bar{\Gamma}_2^r(\omega_r, \nu_r, \nu'_r) = \Gamma - \Gamma_2^r = \mathcal{K}_{2'}^r + \mathcal{K}_3^r + \gamma_{\bar{r}} + R - U, \tag{70d}$$

$$\bar{\Gamma}_{2'}^r(\omega_r, \nu_r, \nu'_r) = \Gamma - \Gamma_{2'}^r = \mathcal{K}_2^r + \mathcal{K}_3^r + \gamma_{\bar{r}} + R - U. \tag{70e}$$

By taking suitable limits in the BSEs (4), the asymptotic classes can be expressed through the full vertex Γ and the bare interaction U [16]:

$$\mathcal{K}_1^r(\omega_r) = U \circ (\Pi_r + \Pi_r \circ \Gamma \circ \Pi_r) \circ U, \tag{71a}$$

$$\mathcal{K}_2^r(\omega_r, \nu_r) = \Gamma \circ \Pi_r \circ U - \mathcal{K}_1^r, \tag{71b}$$

$$\mathcal{K}_{2'}^r(\omega_r, \nu'_r) = U \circ \Pi_r \circ \Gamma - \mathcal{K}_1^r. \tag{71c}$$

Hence, they are directly related to the three-point vertices $\bar{\Gamma}_r^{(3)}, \Gamma_r^{(3)}$ and susceptibilities χ_r (cf. Eqs. (45) and Ref. [16]) as

$$\chi_r(\omega_r) = U^{-1} \bullet \mathcal{K}_1^r(\omega_r) \bullet U^{-1}, \tag{72a}$$

$$\bar{\Gamma}_r^{(3)}(\omega_r, \nu_r) = [U + \mathcal{K}_1^r + \mathcal{K}_2^r](\omega_r, \nu_r) \bullet U^{-1}, \tag{72b}$$

$$\Gamma_r^{(3)}(\omega_r, \nu'_r) = U^{-1} \bullet [U + \mathcal{K}_1^r + \mathcal{K}_{2'}^r](\omega_r, \nu'_r). \tag{72c}$$

\mathcal{K}_1^r diagrams are therefore mediated by the bosonic fluctuations described by the susceptibility χ_r , whereas \mathcal{K}_2^r and $\mathcal{K}_{2'}^r$ describe the coupling of fermions to these bosonic fluctuations via the three-point vertices $\bar{\Gamma}_r^{(3)}$ and $\Gamma_r^{(3)}$. This hints at the close relation between asymptotic classes and SBE components which is further discussed in Sec. 4.3.

4.2 mfRG equations for asymptotic classes

When the vertex is parametrized through its asymptotic classes, it is convenient to compute the latter directly during the flow, without numerically sending certain frequencies to infinity. This facilitates systematically adding or neglecting higher asymptotic classes. Therefore, we now derive explicit mfRG flow equations for the asymptotic classes, starting from the general multiloop flow equations (10), similar to the derivation of the mfRG flow equations for the SBE ingredients in Sect. 3.2. (For a diagrammatic derivation, see Refs. [50, 51].)

The parametrization (68) of γ_r in terms of asymptotic classes holds analogously at each loop order,

$$\dot{\gamma}_r^{(\ell)} = \dot{\mathcal{K}}_1^{r(\ell)} + \dot{\mathcal{K}}_2^{r(\ell)} + \dot{\mathcal{K}}_{2'}^{r(\ell)} + \dot{\mathcal{K}}_3^{r(\ell)}. \tag{73}$$

Then, each summand can be obtained from Eqs. (10) for $\dot{\gamma}_r^{(\ell)}$ by taking suitable limits of the fermionic frequencies ν_r, ν'_r , as specified in Eqs. (69). For example, consider a bubble of type $\Gamma \circ \dot{H}_r \circ \tilde{\Gamma}$, in the r representation of Eq. (20). In the limit $|\nu_r| \rightarrow \infty$, the first vertex reduces to $\Gamma_{2'}^r$ (Eq. (70c)), while for $|\nu'_r| \rightarrow \infty$, the second vertex reduces to $\tilde{\Gamma}_2^r$ (Eq. (70b)). Using Eq. (20), we thus obtain

$$\lim_{|\nu_r| \rightarrow \infty} \Gamma \circ \dot{H}_r \circ \tilde{\Gamma} = \Gamma_{2'}^r \circ \dot{H}_r \circ \tilde{\Gamma}, \tag{74a}$$

$$\lim_{|\nu'_r| \rightarrow \infty} \Gamma \circ \dot{H}_r \circ \tilde{\Gamma} = \Gamma \circ \dot{H}_r \circ \tilde{\Gamma}_2^r. \tag{74b}$$

By contrast, when taking these limits for bubbles involving channels r' different from r , we obtain zero,

$$\lim_{|\nu_r| \rightarrow \infty} \Gamma \circ \dot{H}_{r' \neq r} \circ \tilde{\Gamma} = 0, \quad \lim_{|\nu'_r| \rightarrow \infty} \Gamma \circ \dot{H}_{r' \neq r} \circ \tilde{\Gamma} = 0, \tag{74c}$$

by similar reasoning as that leading to Eq. (69c). In this manner, the 1ℓ flow equation (10a) for $\dot{\gamma}_r^{(1)}$ readily yields

$$\begin{aligned} \dot{\mathcal{K}}_1^r(1) &= \Gamma_{2'}^r \circ \dot{H}_r \circ \Gamma_2^r, \\ \dot{\mathcal{K}}_2^r(1) &= \tilde{\Gamma}_{2'}^r \circ \dot{H}_r \circ \Gamma_2^r, \\ \dot{\mathcal{K}}_{2'}^r(1) &= \Gamma_{2'}^r \circ \dot{H}_r \circ \tilde{\Gamma}_2^r, \\ \dot{\mathcal{K}}_3^r(1) &= \tilde{\Gamma}_{2'}^r \circ \dot{H}_r \circ \tilde{\Gamma}_2^r. \end{aligned} \tag{75a}$$

Similarly, the two-loop contribution $\dot{\gamma}_r^{(2)}$, Eq. (10b), yields

$$\begin{aligned} \dot{\mathcal{K}}_1^r(2) &= 0, \\ \dot{\mathcal{K}}_2^r(2) &= \dot{\gamma}_{\tilde{r}}^{(1)} \circ \Pi_r \circ \Gamma_2^r, \\ \dot{\mathcal{K}}_{2'}^r(2) &= \Gamma_{2'}^r \circ \Pi_r \circ \dot{\gamma}_{\tilde{r}}^{(1)}, \\ \dot{\mathcal{K}}_3^r(2) &= \dot{\gamma}_{\tilde{r}}^{(1)} \circ \Pi_r \circ \tilde{\Gamma}_2^r + \tilde{\Gamma}_{2'}^r \circ \Pi_r \circ \dot{\gamma}_{\tilde{r}}^{(1)}. \end{aligned} \tag{75b}$$

Due to Eq. (69c), $\dot{\mathcal{K}}_1^r(2)$ vanishes and $\dot{\mathcal{K}}_2^r(2)$ or $\dot{\mathcal{K}}_{2'}^r(2)$ contain no terms with $\dot{\gamma}_{\tilde{r}}^{(1)}$ on their right or left sides, respectively. Finally, Eq. (10c) for $\dot{\gamma}_r^{(\ell+2)}$, with $\ell \geq 1$, yields

$$\begin{aligned} \dot{\mathcal{K}}_1^r(\ell+2) &= \Gamma_{2'}^r \circ \Pi_r \circ \dot{\gamma}_{\tilde{r}}^{(\ell)} \circ \Pi_r \circ \Gamma_2^r, \\ \dot{\mathcal{K}}_2^r(\ell+2) &= \dot{\gamma}_{\tilde{r}}^{(\ell+1)} \circ \Pi_r \circ \Gamma_2^r + \tilde{\Gamma}_{2'}^r \circ \Pi_r \circ \dot{\gamma}_{\tilde{r}}^{(\ell)} \circ \Pi_r \circ \Gamma_2^r, \\ \dot{\mathcal{K}}_{2'}^r(\ell+2) &= \Gamma_{2'}^r \circ \Pi_r \circ \dot{\gamma}_{\tilde{r}}^{(\ell)} \circ \Pi_r \circ \tilde{\Gamma}_2^r + \Gamma_{2'}^r \circ \Pi_r \circ \dot{\gamma}_{\tilde{r}}^{(\ell+1)}, \\ \dot{\mathcal{K}}_3^r(\ell+2) &= \dot{\gamma}_{\tilde{r}}^{(\ell+1)} \circ \Pi_r \circ \tilde{\Gamma}_2^r + \tilde{\Gamma}_{2'}^r \circ \Pi_r \circ \dot{\gamma}_{\tilde{r}}^{(\ell)} \circ \Pi_r \circ \tilde{\Gamma}_2^r \\ &\quad + \tilde{\Gamma}_{2'}^r \circ \Pi_r \circ \dot{\gamma}_{\tilde{r}}^{(\ell+1)}. \end{aligned} \tag{75c}$$

Here, $\dot{\mathcal{K}}_1^r(\ell+2) \neq 0$ since $\dot{\gamma}_{\tilde{r}}^{(1)}$ appears in the middle in the central term of Eq. (10c); hence, Eq. (69c) does not apply.

Note that these equations can also be used in the context of DMF²RG [32,33]. There, only the full vertex Γ is given as an input. While $\mathcal{K}_1^r, \mathcal{K}_2^r$ and $\mathcal{K}_{2'}^r$ can be deduced from Γ by sending certain frequencies to infinity (cf. Eqs. (70)) or using Eqs. (71), it is not possible to similarly extract \mathcal{K}_3^r in a given channel as some frequency limit of the full vertex Γ . However, the classes \mathcal{K}_3^r do not enter the right-hand sides of the flow equations (75) individually, but only the combination $R + \mathcal{K}_3 = R + \sum_r \mathcal{K}_3^r$. This is already clear from the general formulation of the mFRG flow equations (10). Consider, e.g., the 1ℓ contribution $\dot{\mathcal{K}}_2^r(1)$ of Eq. (75a). There, $\tilde{\Gamma}_{2'}^r$ contains $R + \mathcal{K}_3 + \gamma_{\tilde{r}} = R + \mathcal{K}_3 + \sum_{r' \neq r} (\mathcal{K}_1^{r'} + \mathcal{K}_2^{r'} + \mathcal{K}_{2'}^{r'})$, and hence only requires knowledge of the full $R + \mathcal{K}_3$. This holds equivalently for all insertions of the full vertex into flow equations at any loop order. Now, insertions of the *differentiated* vertex in loop order ℓ into the flow equations of order $\ell + 1$ and $\ell + 2$ do require a channel decomposition $\dot{\mathcal{K}}_3 = \sum_r \dot{\mathcal{K}}_3^r$. For example, the two-loop contribution $\dot{\mathcal{K}}_2^r(2)$ of Eq. (75b) contains $\dot{\gamma}_{\tilde{r}}^{(1)}$, which, by Eq. (73), involves differentiated vertices $\dot{\mathcal{K}}_3^{r' \neq r}(1)$. These are available via Eq. (75a). Therefore, in the DMF²RG context, one would start with $\mathcal{K}_1^r, \mathcal{K}_2^r, \mathcal{K}_{2'}^r$ and the full $R + \mathcal{K}_3$ from DMFT, compute the differentiated vertices $\dot{\mathcal{K}}_i^r$ independently (including $\dot{\mathcal{K}}_3^r$), successively insert them in higher loop orders, and eventually update \mathcal{K}_3 using $\dot{\mathcal{K}}_3 = \sum_{\ell,r} \dot{\mathcal{K}}_3^r(\ell)$ in each step of the flow (recall that R does not flow, $\dot{R} = 0$). The same reasoning also applies to the multi-boson terms M_r .

4.3 Relating SBE ingredients and asymptotic classes

The asymptotic classes and SBE ingredients are closely related [31]. This is not surprising as the properties of both follow from the assumption that the bare vertex contains no frequency dependence, except for frequency conservation. For convenience, we collect these relations below.

Comparison of Eqs. (43) and (71a) yields

$$w_r(\omega_r) = U + \mathcal{K}_1^r(\omega_r). \tag{76}$$

Similarly, using Eqs. (42), (43), (71b), and (71c), we can write the products of Hedin vertices and the screened interaction as

$$\bar{\lambda}_r \bullet w_r = U + \Gamma \circ \Pi_r \circ U = U + \mathcal{K}_1^r + \mathcal{K}_2^r, \tag{77a}$$

$$w_r \bullet \lambda_r = U + U \circ \Pi_r \circ \Gamma = U + \mathcal{K}_1^r + \mathcal{K}_{2'}^r. \tag{77b}$$

We now insert Eq. (76) for $U + \mathcal{K}_1^r$ and solve for $\lambda_r, \bar{\lambda}_r$, formally defining w_r^{-1} through $w_r \bullet w_r^{-1} = w_r^{-1} \bullet w_r = \mathbf{1}_r$. Thus, we obtain

$$\bar{\lambda}_r = \mathbf{1}_r + \mathcal{K}_2^r \bullet w_r^{-1}, \quad \lambda_r = \mathbf{1}_r + w_r^{-1} \bullet \mathcal{K}_{2'}^r, \tag{78}$$

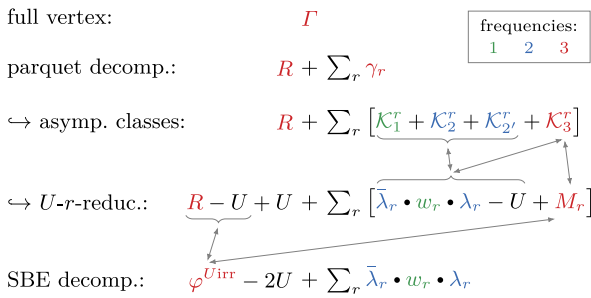


Fig. 11 Overview over vertex decompositions: The parquet decomposition (second line) can be grouped by asymptotic classes (third line) or U - r -reducibility (fourth line), highlighting the relation between these two notions. Arrows link terms that can be identified: $\mathcal{K}_3^r = M_r + \mathcal{K}_2^r \cdot w_r^{-1} \cdot \mathcal{K}_{2'}^r$ and $\mathcal{K}_1^r + \mathcal{K}_2^r + \mathcal{K}_{2'}^r + \mathcal{K}_2^r \cdot w_r^{-1} \cdot \mathcal{K}_{2'}^r = \bar{\lambda}_r \cdot w_r \cdot \lambda_r - U$ for the Π - r -reducible contributions, and $\varphi^{Uirr} = R - U + \sum_r M_r$ for the fully U - r -irreducible contributions. The colors indicate whether the objects depend on 1, 2, or 3 frequency arguments

which, when inserted into Eq. (33), yields

$$\begin{aligned} \nabla_r &= (\mathbf{1}_r + \mathcal{K}_2^r \cdot w_r^{-1}) \cdot w_r \cdot (\mathbf{1}_r + w_r^{-1} \cdot \mathcal{K}_{2'}^r) \\ &= U + \mathcal{K}_1^r + \mathcal{K}_2^r + \mathcal{K}_{2'}^r + \mathcal{K}_2^r \cdot w_r^{-1} \cdot \mathcal{K}_{2'}^r. \end{aligned} \quad (79)$$

Depending on model details, it may happen that not all components of w_r^{-1} are uniquely defined. However, the right-hand sides of Eqs. (78)–(79) are unambiguous as the SBE ingredients are well defined through Eqs. (41).

Recalling that $\gamma_r = \nabla_r - U + M_r$, we conclude that

$$M_r = \mathcal{K}_3^r - \mathcal{K}_2^r \cdot w_r^{-1} \cdot \mathcal{K}_{2'}^r. \quad (80)$$

Hence, ∇_r contains a part of \mathcal{K}_3^r , namely $\mathcal{K}_2^r \cdot w_r^{-1} \cdot \mathcal{K}_{2'}^r$, which can be fully expressed through functions that each depend on at most two frequencies. M_r contains the remaining part of \mathcal{K}_3^r , which must be explicitly parametrized through three frequencies and thus is numerically most expensive. A recent study of the Hubbard model showed that $\sum_r M_r$ is strongly localized in frequency space, particularly in the strong-coupling regime [31]. This allows for a cheaper numerical treatment of the vertex part truly depending on three frequencies and constitutes the main computational advantage of the SBE decomposition.

Equations (76)–(79) fully express the SBE ingredients through asymptotic classes. Analogous results were obtained by similar arguments in Appendix A of Ref. [31]. Figure 11 summarizes the relation between the two vertex decompositions and their ingredients.

Conversely, the asymptotic classes can also be expressed fully through the SBE ingredients. Using Eqs. (23), (68), (76), and (78), one finds

$$\mathcal{K}_1^r = w_r - U \quad (81a)$$

$$\mathcal{K}_2^r = (\bar{\lambda}_r - \mathbf{1}_r) \cdot w_r, \quad (81b)$$

$$\mathcal{K}_{2'}^r = w_r \cdot (\lambda_r - \mathbf{1}_r), \quad (81c)$$

$$\mathcal{K}_3^r = M_r + (\bar{\lambda}_r - \mathbf{1}_r) \cdot w_r \cdot (\lambda_r - \mathbf{1}_r). \quad (81d)$$

Moreover, Eqs. (25a), (70b), (70c), and (77) imply

$$\Gamma_2^r = \bar{\lambda}_r \cdot w_r, \quad (82a)$$

$$\Gamma_{2'}^r = w_r \cdot \lambda_r, \quad (82b)$$

$$\bar{\Gamma}_2^r = \bar{\lambda}_r \cdot w_r \cdot (\lambda_r - \mathbf{1}_r) + T_r \quad (82c)$$

$$\bar{\Gamma}_{2'}^r = (\bar{\lambda}_r - \mathbf{1}_r) \cdot w_r \cdot \lambda_r + T_r. \quad (82d)$$

For the latter two equations, we used Eq. (25a) in the form $\Gamma = \bar{\lambda}_r \cdot w_r \cdot \lambda_r + T_r$. Equivalently, using the definitions of the Hedin vertices in Eqs. (32), we can express \mathcal{K}_2^r , \mathcal{K}_3^r , and Eqs. (82) as

$$\mathcal{K}_2^r = T_r \circ \Pi_r \circ w_r, \quad (83a)$$

$$\mathcal{K}_{2'}^r = w_r \circ \Pi_r \circ T_r, \quad (83b)$$

$$\mathcal{K}_3^r = M_r + T_r \circ \Pi_r \circ w_r \circ \Pi_r \circ T_r, \quad (83c)$$

$$\Gamma_2^r = w_r + T_r \circ \Pi_r \circ w_r, \quad (83d)$$

$$\Gamma_{2'}^r = w_r + w_r \circ \Pi_r \circ T_r, \quad (83e)$$

$$\bar{\Gamma}_2^r = T_r + w_r \circ \Pi_r \circ T_r + T_r \circ \Pi_r \circ w_r \circ \Pi_r \circ T_r, \quad (83f)$$

$$\bar{\Gamma}_{2'}^r = T_r + T_r \circ \Pi_r \circ w_r + T_r \circ \Pi_r \circ w_r \circ \Pi_r \circ T_r. \quad (83g)$$

Since the asymptotic classes and SBE ingredients are closely related, the same is true for their mFRG flow. Indeed, it is straightforward to derive the mFRG SBE flow equations (48) from the flow equations (75) for $\dot{\mathcal{K}}_i^{r(\ell)}$. We briefly indicate the strategy, without presenting all details.

We differentiate the equations (81) expressing \mathcal{K}_i^r through SBE ingredients, and subsequently use Eqs. (32) to eliminate $\bar{\lambda}_r - \mathbf{1}_r$ and $\lambda_r - \mathbf{1}_r$. Thereby, we obtain

$$\dot{\mathcal{K}}_1^r = \dot{w}_r, \quad (84a)$$

$$\dot{\mathcal{K}}_2^r = \dot{\bar{\lambda}}_r \cdot w_r + T_r \circ \Pi_r \circ \dot{w}_r, \quad (84b)$$

$$\dot{\mathcal{K}}_{2'}^r = \dot{w}_r \circ \Pi_r \circ T_r + w_r \cdot \dot{\lambda}_r, \quad (84c)$$

$$\begin{aligned} \dot{\mathcal{K}}_3^r &= \dot{\bar{\lambda}}_r \cdot w_r \circ \Pi_r \circ T_r + T_r \circ \Pi_r \circ \dot{w}_r \circ \Pi_r \circ T_r \\ &\quad + T_r \circ \Pi_r \circ w_r \cdot \dot{\lambda}_r + \dot{M}_r. \end{aligned} \quad (84d)$$

Now, we use Eqs. (75) to express the $\dot{\mathcal{K}}_i^{r(\ell)}$ on the left through Γ_2^r , $\Gamma_{2'}^r$, $\bar{\Gamma}_2^r$, $\bar{\Gamma}_{2'}^r$, and Eqs. (82) to express the latter through SBE ingredients. By matching terms on the left and right in each loop order, we obtain flow equations for $\dot{w}^{(\ell)}$, $\dot{\bar{\lambda}}_r^{(\ell)}$, $\dot{\lambda}_r^{(\ell)}$ and $\dot{M}_r^{(\ell)}$. For example, at 1ℓ order, Eqs. (75a) and (84a) for $\dot{\mathcal{K}}_1^{r(1)}$ yield

$$\dot{w}_r^{(1)} = \Gamma_{2'}^{(1)} \circ \dot{\Pi}_r \circ \Gamma_2^{(1)} = w_r \cdot \lambda_r \circ \dot{\Pi}_r \circ \bar{\lambda}_r \cdot w_r, \quad (85)$$

consistent with Eq. (48a). Similarly, for $\dot{\mathcal{K}}_2^{r(1)}$, we obtain

$$\begin{aligned} \dot{\bar{\lambda}}_r^{(1)} \cdot w_r + T_r \circ \Pi_r \circ \dot{w}_r^{(1)} &= \bar{\Gamma}_2^{(1)} \circ \dot{\Pi}_r \circ \Gamma_2^{(1)} \\ &= T_r \circ \dot{\Pi}_r \circ \bar{\lambda}_r \cdot w_r + T_r \circ \Pi_r \circ w_r \cdot \lambda_r \circ \dot{\Pi}_r \circ \bar{\lambda}_r \cdot w_r. \end{aligned} \quad (86)$$

The second terms on the left and right cancel due to Eq. (85). The remaining terms, right-multiplied by w_r^{-1} , yield $\tilde{\lambda}_r^{(1)} = T_r \circ \tilde{H}_r \circ \bar{\lambda}_r$, consistent with Eq. (48a). All of the equations (48) can be derived in this manner.

5 Conclusions and outlook

The SBE decomposition of the four-point vertex was originally introduced in Hubbard-like models respecting SU(2) spin symmetry and was written in terms of physical (e.g., spin and charge) channels [26]. Inspired by Refs. [25–30], we here formulated the SBE decomposition without specifying the structure of non-frequency arguments (such as position or momentum, spin, etc.) starting from the parquet equations for general fermionic models. The only restriction on the structure of the bare vertex U is that, apart from being frequency-conserving, it is otherwise constant in frequency. Our formulation can thus be used as a starting point for a rather general class of models. It can also be easily extended to the Keldysh formalism or to other types of particles such as bosons or real fermions.

In this generalized framework, we re-derived self-consistent equations for the ingredients of the SBE decomposition $\nabla_r = \bar{\lambda}_r \cdot w_r \cdot \lambda_r$, the so-called SBE equations, by separating the BSEs for the two-particle reducible vertices regarding their U -reducibility. The U -reducible ∇_r have a transparent interpretation through bosonic exchange fluctuations and Hedin vertices, describing the coupling of these bosonic fluctuations to fermions. As our main result, we derived multiloop flow equations for the SBE ingredients in two different ways: first by inserting the SBE decomposition into parquet mFRG and second by differentiating the SBE equations. Thereby, we presented the multiloop generalization of the 1ℓ SBE flow of Ref. [31]. In addition, we gave a detailed discussion of the relation between the SBE ingredients, M_r and $\nabla_r = \bar{\lambda}_r \cdot w_r \cdot \lambda_r$, and the asymptotic classes \mathcal{K}_i^r of the two-particle reducible vertices. Finally, we also presented multiloop flow equations for the \mathcal{K}_i^r and thus provided a unified formulation for the mFRG treatment of the parquet and the SBE vertex decompositions.

A numerical study of the SBE mFRG flow for relevant model systems, such as the single-impurity Anderson model or the Hubbard model, is left for future work. Below, we outline some open questions to be addressed.

The numerically most expensive SBE ingredient is the fully U -irreducible vertex $\varphi^{U_{\text{irr}}}$, involving the multi-boson exchange terms M_r , because these all depend on three frequency arguments. One may hope that, for certain applications, it might suffice to neglect $\varphi^{U_{\text{irr}}}$ (as done in Ref. [35] for a DMFT treatment of the Hubbard model), or to treat it in a cheap fashion, e.g., by not keeping track of its full frequency dependence or by not letting it flow (cf. Ref. [31]). This spoils the parquet

two-particle self-consistency while retaining SBE self-consistency. It is an interesting open question which of the main qualitative features of the parquet solution, such as fulfillment of the Mermin–Wagner theorem [52], remain intact this way.

One formal feature, namely regulator independence, is maintained if multiloop flow equations in the SBE approximation are used. These equations are derived by setting $\varphi^{U_{\text{irr}}} = 0$ and $\dot{M}_r = 0$ from the beginning (Sect. 3.4) and are actually simpler than those obtained by setting $\dot{M}_r = 0$ in the full SBE mFRG flow. We left the derivation of a self-energy flow directly within the SBE approximation for future work. The combination of such a self-energy flow with the vertex flow of Sect. 3.4 would constitute the total derivative of the SBE approximation. Therefore, if loop convergence can be achieved when integrating these simplified flow equations, the results will be regulator independent, just as for the full SBE mFRG flow with $\varphi^{U_{\text{irr}}} = \sum_r M_r$ and $\dot{M}_r \neq 0$, reproducing the PA.

Even if it turns out that a full treatment of $\varphi^{U_{\text{irr}}}$ is required for capturing essential qualitative features of the vertex, this might still be numerically cheaper than a full treatment of \mathcal{K}_3 . The reason is that each \mathcal{K}_3^r contains a contribution, the $\mathcal{K}_2^r \cdot w_r^{-1} \cdot \mathcal{K}_2^r$ term in Eq. (79), which is included not in M_r but in ∇_r , and parametrized through the numerically cheaper Hedin vertices and screened interactions, see Fig. 11. If these terms decay comparatively slowly with frequency, their treatment via the \mathcal{K}_i^r decomposition would be numerically expensive, and the SBE decomposition could offer a numerically cheaper alternative. A systematic comparison of the numerical costs required to compute the multiloop flow of the two decompositions should thus be a main goal of future work.

Acknowledgements We thank F. Krien, J. Halbinger, and N. Ritz for critical reading of the manuscript. This research is part of the Munich Quantum Valley, which is supported by the Bavarian state government with funds from the Hightech Agenda Bayern Plus. We acknowledge funding for M.G. from the International Max Planck Research School for Quantum Science and Technology (IMPRS-QST), for A.G. and J.v.D. from the Deutsche Forschungsgemeinschaft under Germany’s Excellence Strategy EXC-2111 (Project No. 390814868), and for F.B.K. from the Alexander von Humboldt Foundation through the Feodor Lynen Fellowship.

Author contributions

M.G., E.W., A.G., and F.B.K. contributed to the derivation of the presented equations. All authors jointly prepared the manuscript.

Funding Open Access funding enabled and organized by Projekt DEAL.

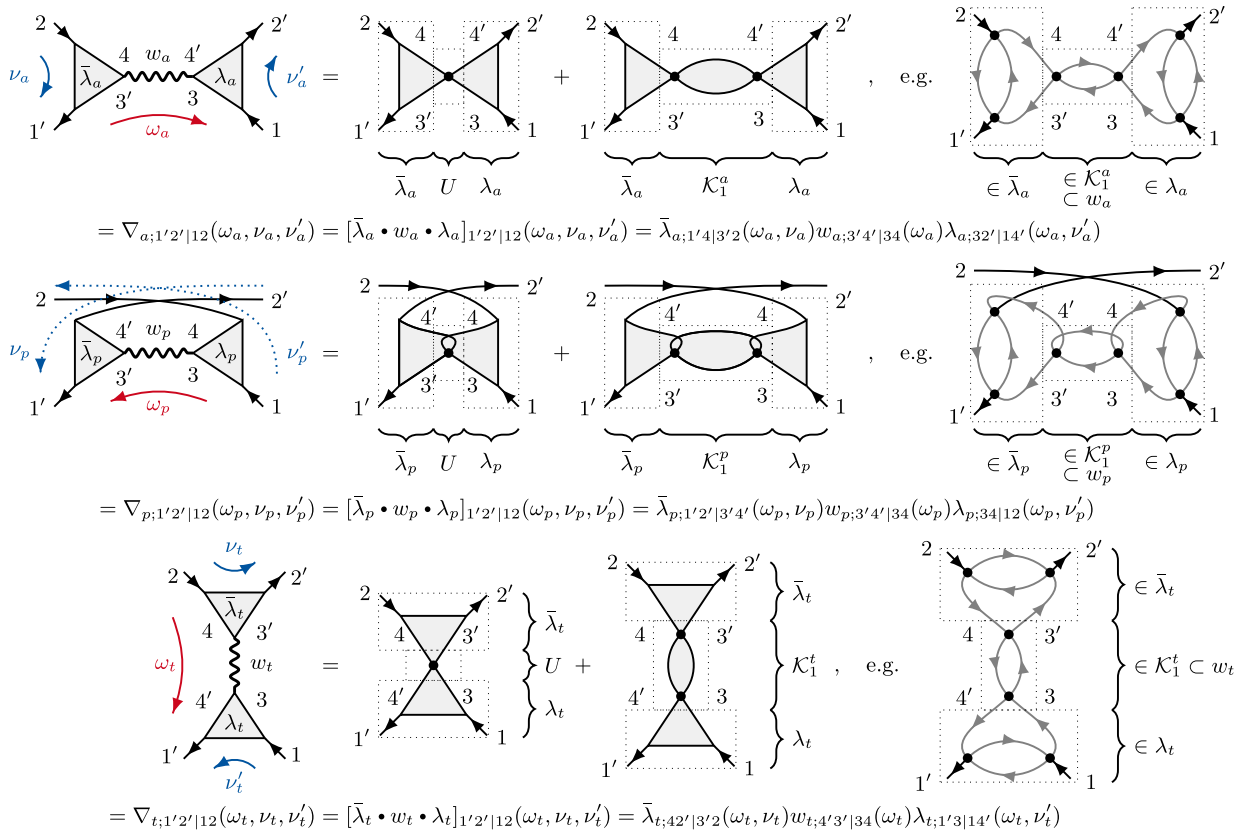


Fig. 12 Illustration of the structure of ∇_r using $w_r = U + K_1^r$ (Eq. (76)), including an exemplary sixth-order diagram. While $\bar{\lambda}_r, w_r, \lambda_r$ factorize w.r.t. their frequency dependence (since they are connected by bare vertices in ∇_r), they are viewed as four-point objects w.r.t. the other quantum numbers (the internal indices 3, 3', 4, 4' have to be summed over, cf. Eqs. (6))

Data Availability Statement This manuscript has no associated data or the data will not be deposited. [Authors' comment: Data sharing is not applicable to this article as no datasets were generated or analyzed during the current study.]

Open Access This article is licensed under a Creative Commons Attribution 4.0 International License, which permits use, sharing, adaptation, distribution and reproduction in any medium or format, as long as you give appropriate credit to the original author(s) and the source, provide a link to the Creative Commons licence, and indicate if changes were made. The images or other third party material in this article are included in the article's Creative Commons licence, unless indicated otherwise in a credit line to the material. If material is not included in the article's Creative Commons licence and your intended use is not permitted by statutory regulation or exceeds the permitted use, you will need to obtain permission directly from the copyright holder. To view a copy of this licence, visit <http://creativecommons.org/licenses/by/4.0/>.

A Diagrams of SBE ingredients

Figure 12 illustrates which parts of the U - r -reducible diagrams ∇_r belong to the Hedin vertices $\bar{\lambda}_r, \lambda_r$ and which parts belong to the screened interactions w_r (for exemplary low-order diagrams, see Fig. 5).

B Diagrams of asymptotic classes

We illustrate the channel-specific frequency parametrizations of the vertex (Fig. 3) in second-order perturbation theory in Fig. 13.

The bosonic frequency ω_r is transferred through the bubble in which each diagram is reducible, while the fermionic frequencies ν_r, ν'_r parametrize the frequency dependence on each side of the bubble. Evidently, the internal propagator lines only depend on the bosonic transfer frequency of the corresponding channel (and the internal integration frequency). The external fermionic frequency ν_r flows in and out at the same bare vertex, and so does ν'_r at another bare vertex, such that the value of each diagram is independent

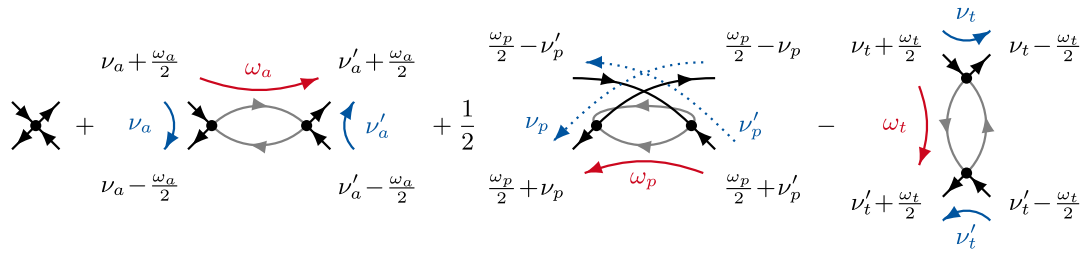


Fig. 13 Diagrams in second-order perturbation theory including the channel-specific frequency parametrization

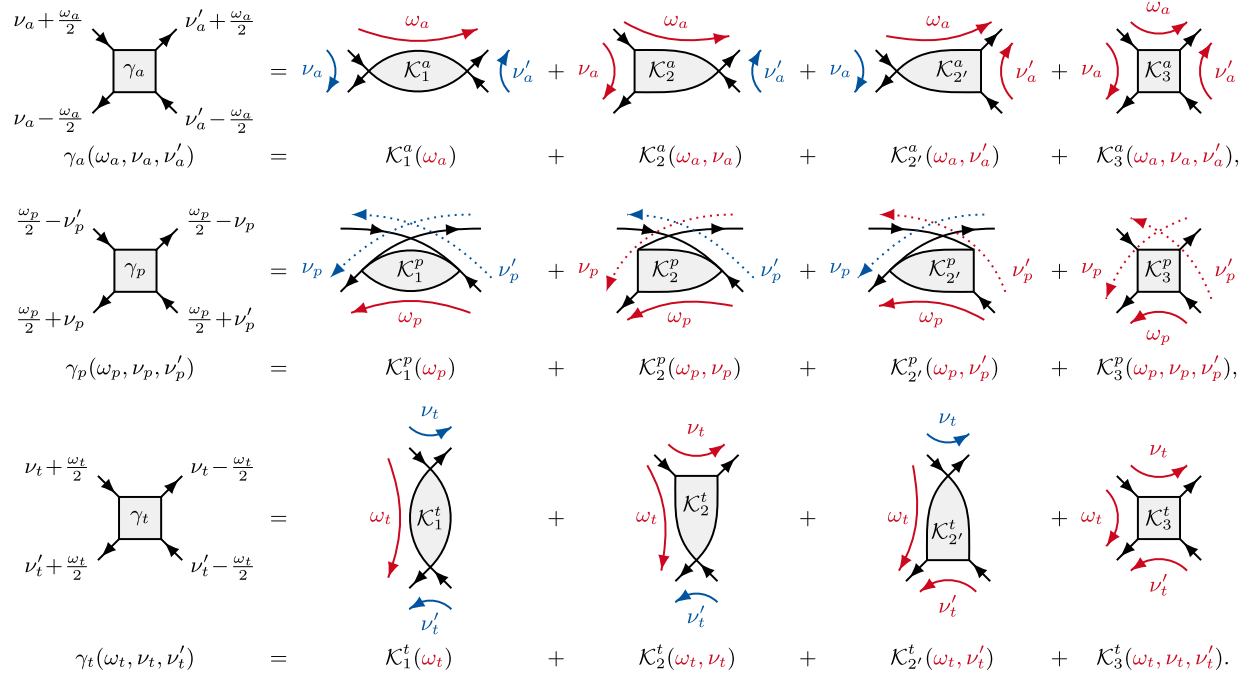


Fig. 14 Illustration of the decomposition of the two-particle reducible vertices γ_r into asymptotic classes, $\mathcal{K}_1^r + \mathcal{K}_2^r + \mathcal{K}_{2'}^r + \mathcal{K}_3^r$

of ν_r, ν'_r . This notion can be generalized [16], leading to the decomposition of each Π - r -reducible vertex γ_r into four different asymptotic classes, $\mathcal{K}_1^r + \mathcal{K}_2^r + \mathcal{K}_{2'}^r + \mathcal{K}_3^r$, depicted diagrammatically in Fig. 14. A formal definition is given by Eqs. (69) in the main text.

C Relation to SBE in physical channels

The SBE decomposition was originally defined in terms of the charge, spin, and singlet pairing channels [26]. These involve specific linear combinations of the spin components, chosen to diagonalize the spin structure in the BSEs for SU(2)-symmetric systems [9]. Assuming SU(2) spin symmetry, we show below how these “physical” SBE channels are related to the “diagrammatic” SBE channels used in the main text.

By spin conservation, each incoming spin $\sigma \in \{\uparrow, \downarrow\}$ must also come out of a vertex. The nonzero components thus are

$$\Gamma^{\sigma\bar{\sigma}} = \Gamma^{\sigma\bar{\sigma}|\sigma\bar{\sigma}}, \quad \hat{\Gamma}^{\sigma\bar{\sigma}} = \Gamma^{\sigma\bar{\sigma}|\bar{\sigma}\sigma}, \quad \Gamma^{\sigma\sigma} = \Gamma^{\sigma\sigma|\sigma\sigma}. \quad (87)$$

Furthermore, crossing symmetry relates $\Gamma^{\uparrow\downarrow}$ and $\hat{\Gamma}^{\uparrow\downarrow}$, and SU(2) spin symmetry yields $\Gamma^{\sigma\sigma} = \Gamma^{\sigma\bar{\sigma}} + \hat{\Gamma}^{\sigma\bar{\sigma}}$ [53].

On the level of the full vertex, one defines the charge, spin, and singlet or triplet pairing channels as [9, 38]

$$\Gamma^{\text{ch/sp}} = \Gamma^{\uparrow\uparrow} \pm \Gamma^{\uparrow\downarrow}, \quad \Gamma^{\text{tr/si}} = \Gamma^{\uparrow\downarrow} \pm \hat{\Gamma}^{\uparrow\downarrow}. \quad (88)$$

This notation carries over to all vertex objects like ∇^α , λ_r^α and w_r^α , with α denoting ch, sp, si, or tr.

The bare vertex has $U^{\uparrow\uparrow} = 0$ and $U^{\uparrow\downarrow} = -\hat{U}^{\uparrow\downarrow}$, so that

$$U^{\text{ch/sp}} = U^{\uparrow\uparrow} \pm U^{\uparrow\downarrow} = \pm U^{\uparrow\downarrow}, \quad (89a)$$

$$U^{\text{si}} = U^{\uparrow\downarrow} - \hat{U}^{\uparrow\downarrow} = 2U^{\uparrow\downarrow}. \quad (89b)$$

The bare interaction U^{tr} in the triplet pairing channel vanishes and does not give a U -reducible contribution [26].

We now show that, if the ingredients of the SBE decomposition Eq. (41a) are expressed through the physical charge and spin components (ch, sp) rather than the diagrammatic components ($\uparrow\uparrow, \uparrow\downarrow$) used here, one indeed obtains the original form of the SBE decomposition depicted in Fig. 1 of Ref. [26].

This is trivial to see for the fully U -irreducible part $\varphi^{U\text{irr}}$ (analogous to Eq. (88)) and the bare vertex U (Eqs. (89)). It remains to show that for the U - r -reducible terms $\nabla_r = \bar{\lambda}_r \bullet w_r \bullet \lambda_r$, the components ∇_r^α have the form given in Fig. 1 of Ref. [26], with $\alpha = \text{ch}$ or sp .

We start with the t channel. Defining sign factors for charge and spin channels, $s^{\text{ch}} = 1$ and $s^{\text{sp}} = -1$, we have

$$\begin{aligned} \nabla_t^\alpha &= \nabla_t^{\uparrow\uparrow} + s^\alpha \nabla_t^{\uparrow\downarrow} \\ &= \bar{\lambda}_t^{\sigma\uparrow|\sigma\uparrow} w_t^{\sigma'\sigma|\sigma'\sigma} \lambda_t^{\uparrow\sigma'|\uparrow\sigma'} + s^\alpha \bar{\lambda}_t^{\sigma\downarrow|\sigma\downarrow} w_t^{\sigma'\sigma|\sigma'\sigma} \lambda_t^{\uparrow\sigma'|\uparrow\sigma'} \end{aligned} \tag{90}$$

Here, we sum as usual over spin indices σ, σ' . Making use of $w_t^{\uparrow\uparrow} = w_t^{\downarrow\downarrow}$, $w_t^{\downarrow\uparrow} = w_t^{\uparrow\downarrow}$, and similarly for $\bar{\lambda}_t, \lambda_t$, we can collect the summands as

$$\begin{aligned} \nabla_t^\alpha &= (\bar{\lambda}_t^{\uparrow\uparrow} + s^\alpha \bar{\lambda}_t^{\downarrow\downarrow})(w_t^{\uparrow\uparrow} + s^\alpha w_t^{\downarrow\downarrow})(\lambda_t^{\uparrow\uparrow} + s^\alpha \lambda_t^{\downarrow\downarrow}) \\ &= \bar{\lambda}_t^\alpha w_t^\alpha \lambda_t^\alpha, \end{aligned} \tag{91}$$

which is equivalent to ∇^{ph} in Ref. [26]. (Note that in our convention of depicting diagrams, all diagrams are mirrored along the diagonal from the top left to bottom right (i.e., the bottom left and top right legs are exchanged) compared to the convention used in Ref. [26]: The ph (ph) channel corresponds to the t (a) channel.)

We continue with the a channel, which is related to the t channel by crossing symmetry,

$$\hat{\Gamma}^{\uparrow\downarrow}(\omega_a, \nu_a, \nu'_a) = -\Gamma^{\uparrow\downarrow}(\omega_t = \omega_a, \nu_t = \nu_a, \nu'_t = \nu'_a). \tag{92}$$

The frequency arguments on the right are defined according to the t -channel conventions $(\omega_t, \nu_t, \nu'_t)$, and then evaluated at the a -channel frequencies occurring on the left. In particular, we have (cf. Eq. (11) of Ref. [26])

$$\begin{aligned} \Gamma^\alpha(\omega_a, \nu_a, \nu'_a) &= -\frac{1}{2} \left[\Gamma^{\text{ch}} + (1 + 2s^\alpha) \Gamma^{\text{sp}} \right] (\omega_t = \omega_a, \nu_t = \nu_a, \nu'_t = \nu'_a). \end{aligned} \tag{93}$$

The U - a -reducible diagrams ∇_a can therefore be expressed through the U - t -reducible diagrams ∇_t :

$$\begin{aligned} \nabla_a^\alpha(\omega_a, \nu_a, \nu'_a) &= -\frac{1}{2} \left[\bar{\lambda}_t^{\text{ch}} w_t^{\text{ch}} \lambda_t^{\text{ch}} + (1 + 2s^\alpha) \bar{\lambda}_t^{\text{sp}} w_t^{\text{sp}} \lambda_t^{\text{sp}} \right] (\omega_a, \nu_a, \nu'_a), \end{aligned} \tag{94}$$

reproducing ∇^{ph} in Ref. [26]. The frequency arguments on the right have the same meaning as in Eq. (92).

Last, we consider the p channel. With $SU(2)$ symmetry, $\nabla_p^{\uparrow\uparrow} = \nabla_p^{\uparrow\downarrow} + \hat{\nabla}_p^{\uparrow\downarrow}$, we have

$$\begin{aligned} \nabla_p^\alpha &= \nabla_p^{\uparrow\uparrow} + s^\alpha \nabla_p^{\uparrow\downarrow} = \hat{\nabla}_p^{\uparrow\downarrow} + (1 + s^\alpha) \nabla_p^{\uparrow\downarrow} \\ &= \bar{\lambda}_p^{\uparrow\downarrow|\sigma\bar{\sigma}} w_p^{\sigma\bar{\sigma}|\sigma'\bar{\sigma}'} \lambda_p^{\sigma'\bar{\sigma}'|\uparrow\downarrow} \\ &\quad + (1 + s^\alpha) \bar{\lambda}_p^{\downarrow\uparrow|\sigma\bar{\sigma}} w_p^{\sigma\bar{\sigma}|\sigma'\bar{\sigma}'} \lambda_p^{\sigma'\bar{\sigma}'|\downarrow\uparrow}. \end{aligned} \tag{95}$$

Note that the spins in the first and second pair of spin indices of w_p have to be opposite, $\sigma\bar{\sigma}$ and $\sigma'\bar{\sigma}'$, since they connect to the same bare vertex (cf. Fig. 12), and $U^{\sigma\sigma} = 0$. Furthermore, the crossing relation $U^{\uparrow\downarrow} = -\hat{U}^{\uparrow\downarrow}$ implies

$w_p^{\uparrow\downarrow} = -\hat{w}_p^{\uparrow\downarrow}$. By use of this, we can combine the terms in the spin sums as

$$\begin{aligned} \nabla_p^\alpha &= \frac{s^\alpha}{2} (\bar{\lambda}_p^{\uparrow\downarrow} - \hat{\lambda}_p^{\uparrow\downarrow})(w_p^{\uparrow\downarrow} - \hat{w}_p^{\uparrow\downarrow})(\lambda_p^{\uparrow\downarrow} - \hat{\lambda}_p^{\uparrow\downarrow}) \\ &= \frac{s^\alpha}{2} \bar{\lambda}_p^{\text{si}} w_p^{\text{si}} \lambda_p^{\text{si}}, \end{aligned} \tag{96}$$

which gives ∇^{pp} in Ref. [26].

In summary, we thus reproduce the decomposition of Ref. [26]:

$$\Gamma^\alpha = \varphi^{U\text{irr},\alpha} + \nabla_a^\alpha + \nabla_p^\alpha + \nabla_t^\alpha - 2U^\alpha, \tag{97a}$$

where the U - r -reducible parts are defined as

$$\begin{aligned} \nabla_a^\alpha(\omega_a, \nu_a, \nu'_a) &= -\frac{1}{2} \nabla_t^{\text{ch}}(\omega_a, \nu_a, \nu'_a) \\ &\quad - \left(\frac{3}{2} - 2\delta_{\alpha,\text{sp}} \right) \nabla_t^{\text{sp}}(\omega_a, \nu_a, \nu'_a), \end{aligned} \tag{97b}$$

$$\nabla_p^\alpha(\omega_p, \nu_p, \nu'_p) = \left(\frac{1}{2} - \delta_{\alpha,\text{sp}} \right) [\bar{\lambda}_p^{\text{si}} w_p^{\text{si}} \lambda_p^{\text{si}}](\omega_p, \nu_p, \nu'_p), \tag{97c}$$

$$\nabla_t^\alpha(\omega_t, \nu_t, \nu'_t) = [\bar{\lambda}_t^\alpha w_t^\alpha \lambda_t^\alpha](\omega_t, \nu_t, \nu'_t). \tag{97d}$$

D Correlators and susceptibilities

Reference [26] established that the SBE ingredients $\bar{\lambda}_r, w_r, \lambda_r$ are related to three-point correlators and generalized susceptibilities. For completeness, we illustrate here how these relations arise within the present framework. The starting point is the general relation between the four-point correlator $G^{(4)}$ and the four-point vertex Γ ,

$$\begin{aligned} G_{12|1'2'}^{(4)} &= \langle c_1 c_2 \bar{c}_{2'} \bar{c}_{1'} \rangle = G_{1|1'} G_{2|2'} - G_{1|2'} G_{2|1'} \\ &\quad + G_{1|5'} G_{2|6'} \Gamma_{5'6'|56} G_{5|1'} G_{6|2'}. \end{aligned} \tag{98}$$

By combining two fermionic fields, one obtains the bosonic exchange field ψ , the pairing field ϕ , and its conjugate $\bar{\phi}$,

$$\psi_{12'}(\omega) = \sum_\nu c_1 \left(\nu - \frac{\omega}{2} \right) \bar{c}_{2'} \left(\nu + \frac{\omega}{2} \right) = \bar{\psi}_{2'1}(-\omega), \tag{99a}$$

$$\phi_{12}(\omega) = \sum_\nu c_1 \left(\frac{\omega}{2} + \nu \right) c_2 \left(\frac{\omega}{2} - \nu \right), \tag{99b}$$

$$\bar{\phi}_{1'2'}(\omega) = \sum_{\nu'} \bar{c}_{2'} \left(\frac{\omega}{2} - \nu' \right) \bar{c}_{1'} \left(\frac{\omega}{2} + \nu' \right). \tag{99c}$$

Three-point correlators and bosonic two-point correlators involving these fields can be obtained from $G^{(4)}$ by summing over the frequency $\nu_r^{(r)}$ in the channel-specific parametrization (cf. Equation (17) and Fig. 3):

$$\bar{G}_{r;12|1'2'}^{(3)}(\omega_r, \nu_r) = \sum_{\nu_r'} G_{12|1'2'}^{(4)}(\omega_r, \nu_r, \nu_r'), \tag{100a}$$

$$G_{r;12|1'2'}^{(3)}(\omega_r, \nu_r') = \sum_{\nu_r} G_{12|1'2'}^{(4)}(\omega_r, \nu_r, \nu_r'), \tag{100b}$$

$$D_{r;12|1'2'}(\omega_r) = \sum_{\nu_r, \nu_r'} G_{12|1'2'}^{(4)}(\omega_r, \nu_r, \nu_r'). \tag{100c}$$

For example, in the p channel, we have

$$\bar{G}_{p;12|1'2'}^{(3)} = \langle c_1 c_2 \bar{\phi}_{1'2'} \rangle, \quad D_{p;12|1'2'} = \langle \phi_{12} \bar{\phi}_{1'2'} \rangle. \tag{101}$$

The four-point correlator $G^{(4)}$ is closely related to the generalized susceptibilities $\chi_r^{(4)}$ [38]:

$$\begin{aligned} \chi_{a;12|1'2'}^{(4)}(\omega_a, \nu_a, \nu'_a) &= G_{12|1'2'}^{(4)}(\omega_a, \nu_a, \nu'_a) + \delta_{\omega_a,0} G_{1|2'}(\nu_a) G_{2|1'}(\nu'_a) \\ &= \delta_{\nu_a, \nu'_a} \Pi_{a;12|1'2'}(\omega_a, \nu_a) + [\Pi_a \circ \Gamma \circ \Pi_a]_{12|1'2'}(\omega_a, \nu_a, \nu'_a), \end{aligned} \tag{102a}$$

$$\begin{aligned} \chi_{p;12|1'2'}^{(4)}(\omega_p, \nu_p, \nu'_p) &= \frac{1}{4} G_{12|1'2'}^{(4)}(\omega_p, \nu_p, \nu'_p) \\ &= \delta_{\nu_p, \nu'_p} \frac{1}{2} \Pi_{p;12|1'2'}(\omega_p, \nu_p) - \delta_{\nu_p, -\nu'_p} \frac{1}{2} \Pi_{p;12|2'1'}(\omega_p, \nu_p) \\ &\quad + [\Pi_p \circ \Gamma \circ \Pi_p]_{12|1'2'}(\omega_p, \nu_p, \nu'_p), \end{aligned} \tag{102b}$$

$$\begin{aligned} \chi_{t;12|1'2'}^{(4)}(\omega_t, \nu_t, \nu'_t) &= G_{12|1'2'}^{(4)}(\omega_t, \nu_t, \nu'_t) - \delta_{\omega_t,0} G_{1|1'}(\nu'_t) G_{2|2'}(\nu_t) \\ &= \delta_{\nu_t, \nu'_t} \Pi_{t;12|1'2'}(\omega_t, \nu_t) + [\Pi_t \circ \Gamma \circ \Pi_t]_{12|1'2'}(\omega_t, \nu_t, \nu'_t). \end{aligned} \tag{102c}$$

In analogy to Eqs. (100), we then obtain three-point functions $\bar{\chi}_r^{(3)}, \chi_r^{(3)}$ and physical susceptibilities χ_r by summing over frequencies:

$$\bar{\chi}_{r;12|1'2'}^{(3)}(\omega_r, \nu_r) = \sum_{\nu'_r} \chi_{r;12|1'2'}^{(4)}(\omega_r, \nu_r, \nu'_r), \tag{103a}$$

$$\chi_{r;12|1'2'}^{(3)}(\omega_r, \nu'_r) = \sum_{\nu_r} \chi_{r;12|1'2'}^{(4)}(\omega_r, \nu_r, \nu'_r), \tag{103b}$$

$$\chi_{r;12|1'2'}(\omega_r) = \sum_{\nu_r, \nu'_r} \chi_{r;12|1'2'}^{(4)}(\omega_r, \nu_r, \nu'_r). \tag{103c}$$

The prefactor $\frac{1}{4}$ in Eq. (102b) ensures that the susceptibility χ_r in Eqs. (103c) is consistent with its counterpart in the main text (cf. Eq. (45c)).

To make a connection between $\bar{\chi}_r^{(3)}, \chi_r^{(3)}, \chi_r$ and SBE objects, we use Eqs. (102), multiply by the bare interaction U , and express the result in terms of the four-point vertex:

$$\bar{\chi}_r^{(3)} \bullet U = \Pi_r \circ (U + \Gamma \circ \Pi_r \circ U), \tag{104a}$$

$$U \bullet \chi_r^{(3)} = (U + U \circ \Pi_r \circ \Gamma) \circ \Pi_r, \tag{104b}$$

$$U \bullet \chi_r \bullet U = U \circ \Pi_r \circ U + U \circ \Pi_r \circ \Gamma \circ \Pi_r \circ U. \tag{104c}$$

Finally, comparing these expressions to Eqs. (42)–(44) shows their relation to the SBE ingredients:

$$\bar{\chi}_r^{(3)} = \Pi_r \circ \bar{\lambda}_r \bullet w_r \bullet U^{-1} = \Pi_r \circ \bar{\Gamma}_r^{(3)}, \tag{105a}$$

$$\chi_r^{(3)} = U^{-1} \bullet w_r \bullet \lambda_r \circ \Pi_r = \Gamma_r^{(3)} \circ \Pi_r, \tag{105b}$$

$$\chi_r = U^{-1} \bullet (w_r - U) \bullet U^{-1}. \tag{105c}$$

These relations are analogous to those given in Eqs. (6), (8) and (15) in Ref. [26]. Relations between the bosonic correlators $\bar{G}_r^{(3)}, G_r^{(3)}, D_r$ from Eqs. (100) and the SBE ingredients $\bar{\lambda}_r, w_r, \lambda_r$ are analogous up to disconnected terms and can be readily constructed from Eqs. (103), (102), and (105). For example, in the a channel, we have

$$\begin{aligned} \bar{G}_{a;12|1'2'}^{(3)}(\omega_a, \nu_a) &= [\Pi_a \circ \bar{\lambda}_a \bullet w_a \bullet U^{-1}]_{12|1'2'}(\omega_a, \nu_a) \\ &\quad - \delta_{\omega_a,0} G_{1|2'}(\nu_a) \sum_{\nu'_a} G_{2|1'}(\nu'_a), \\ D_{a;12|1'2'}(\omega_a) &= [U^{-1} \bullet (w_a - U) \bullet U^{-1}]_{12|1'2'}(\omega_a) \\ &\quad - \delta_{\omega_a,0} \sum_{\nu_a} G_{1|2'}(\nu_a) \sum_{\nu'_a} G_{2|1'}(\nu'_a). \end{aligned} \tag{106}$$

E Susceptibilities for Hubbard interaction

The susceptibilities defined in Eq. (45c) and in Appendix D exhibit general dependencies w.r.t. their non-frequency indices $12|1'2'$. In the following, we show how they are related to physical charge, spin, and pairing susceptibilities. To this end, we focus on models with a local (momentum-independent) bare interaction, which has only spin degrees of freedom subject to the Pauli principle. In the a and t channel, Eq. (44c) with $\mathcal{K}_1^r = w_r - U$ then reads

$$\mathcal{K}_1^{a;\sigma\sigma'|\sigma\sigma'} = U^{\sigma\bar{\sigma}|\bar{\sigma}'\sigma'} \chi_a^{\bar{\sigma}'\bar{\sigma}|\bar{\sigma}'\bar{\sigma}} U^{\bar{\sigma}'\sigma'|\sigma\bar{\sigma}}, \tag{107a}$$

$$\mathcal{K}_1^{t;\sigma\sigma'|\sigma\sigma'} = U^{\bar{\sigma}'\sigma'|\bar{\sigma}'\sigma'} \chi_t^{\bar{\sigma}\bar{\sigma}'|\bar{\sigma}\bar{\sigma}'} U^{\sigma\bar{\sigma}|\sigma\bar{\sigma}}. \tag{107b}$$

We further specify $U^{\sigma\bar{\sigma}|\bar{\sigma}'\sigma'} = u(\delta_{\sigma\sigma'} - \delta_{\sigma\bar{\sigma}'})$, with the (scalar) bare interaction strength u . With SU(2) symmetry, $\chi_r^{\sigma_1\sigma'_1|\sigma_2\sigma'_2} = \chi_r^{\bar{\sigma}_1\bar{\sigma}'_1|\bar{\sigma}_2\bar{\sigma}'_2}$, Eqs. (107) thus simplify to

$$\chi_{a/t}^{\sigma\sigma'|\sigma\sigma'} = \mathcal{K}_1^{a/t;\sigma\sigma'|\sigma\sigma'} / u^2. \tag{108}$$

In the p channel, we have

$$\mathcal{K}_1^{p;\sigma\sigma'|\sigma\sigma'} = \sum_{\sigma_1\sigma_2} U^{\sigma\sigma'|\sigma_1\bar{\sigma}_1} \chi_p^{\sigma_1\bar{\sigma}_1|\sigma_2\bar{\sigma}_2} U^{\sigma_2\bar{\sigma}_2|\sigma\sigma'} \tag{109a}$$

$$= U^{\sigma\sigma'|\sigma\sigma'} \tilde{\chi}_p^{\sigma\sigma'|\sigma\sigma'} U^{\sigma\sigma'|\sigma\sigma'}. \tag{109b}$$

Here, the second line (109b) follows from SU(2) and crossing symmetry. It employs

$$\begin{aligned} \tilde{\chi}_p(\omega_p) &= [\mathbf{1}_p \circ \tilde{\Pi}_p \circ \mathbf{1}_p](\omega_p) \\ &\quad + [\mathbf{1}_p \circ \tilde{\Pi}_p \circ \Gamma \circ \tilde{\Pi}_p \circ \mathbf{1}_p](\omega_p), \end{aligned} \tag{110}$$

where $\tilde{\Pi}_{p;34|3'4'} = G_{3|3'} G_{4|4'} = 2\Pi_{p;34|3'4'}$ does not include a prefactor $1/2$ (introduced in Eq. (5b) to avoid double counting within internal spin sums), since there are no spin sums in Eq. (109b). (This definition of the p susceptibility agrees with the related literature, e.g., Ref. [38].) With $U^{\sigma\sigma'|\sigma\sigma'} = -u\delta_{\sigma\bar{\sigma}'}$, we can write

$$\tilde{\chi}_p^{\sigma\sigma'|\sigma\sigma'} = \delta_{\sigma\bar{\sigma}'} \mathcal{K}_1^{p;\sigma\sigma'|\sigma\sigma'} / u^2, \tag{111}$$

in analogy to Eq. (108).

The relation between these “diagrammatic” susceptibilities χ_r and their “physical” counterparts can be made explicit by means of the bilinears

$$\rho_{\sigma\sigma'} = \bar{c}_\sigma c_{\sigma'}, \quad \delta\rho_{\sigma\sigma'} = \rho_{\sigma\sigma'} - (\rho_{\sigma\sigma})\delta_{\sigma\sigma'} \tag{112a}$$

$$\rho_{\sigma\bar{\sigma}'} = c_\sigma \bar{c}_{\sigma'}, \quad \rho_{\sigma\sigma'}^\pm = \bar{c}_{\sigma'} c_\sigma. \tag{112b}$$

Then, we have in the imaginary-time domain

$$\chi_a^{\sigma\sigma'|\sigma\sigma'}(\tau) = -\langle \delta\rho_{\sigma'\sigma}(\tau) \delta\rho_{\sigma\sigma'}(0) \rangle, \tag{113a}$$

$$\tilde{\chi}_p^{\sigma\sigma'|\sigma\sigma'}(\tau) = \langle \rho_{\sigma\sigma'}^-(\tau) \rho_{\sigma\sigma'}^+(0) \rangle, \tag{113b}$$

$$\chi_t^{\sigma\sigma'|\sigma\sigma'}(\tau) = \langle \delta n_\sigma(\tau) \delta n_{\sigma'}(0) \rangle. \tag{113c}$$

with $n_\sigma = \rho_{\sigma\sigma}$. Choosing the spin arguments as $\chi_r^{\uparrow\downarrow|\uparrow\downarrow} = \chi_r^{\uparrow\downarrow|\downarrow\uparrow}$, we furthermore get

$$\chi_a^{\uparrow\downarrow}(\tau) = -\langle S_-(\tau)S_+ \rangle, \quad (114a)$$

$$\tilde{\chi}_p^{\uparrow\downarrow}(\tau) = \langle \Delta_{\text{si}}(\tau)\Delta_{\text{si}}^\dagger(0) \rangle, \quad (114b)$$

$$\chi_t^{\uparrow\downarrow}(\tau) = \langle \delta n_\uparrow(\tau)\delta n_\downarrow(0) \rangle. \quad (114c)$$

Hence, $\chi_a^{\uparrow\downarrow}$ describes spin fluctuations ($S_- = \bar{c}_\downarrow c_\uparrow$, $S_+ = \bar{c}_\uparrow c_\downarrow$) and $\tilde{\chi}_p^{\uparrow\downarrow}$ singlet pairing fluctuations ($\Delta_{\text{si}} = c_\uparrow c_\downarrow$). By SU(2) spin symmetry, $\frac{1}{2}\chi_a^{\uparrow\downarrow}(\tau) = -\langle S_z(\tau)S_z \rangle$, with $S_z = \frac{1}{2}(n_\uparrow - n_\downarrow) = \frac{1}{2}(\delta n_\uparrow - \delta n_\downarrow)$. It then follows that

$$\begin{aligned} \chi_t^{\uparrow\downarrow}(\tau) - \frac{1}{2}\chi_a^{\uparrow\downarrow}(\tau) &= \frac{1}{2}(\langle \delta n_\uparrow(\tau)\delta n_\uparrow \rangle + \langle \delta n_\uparrow(\tau)\delta n_\downarrow \rangle) \\ &= \frac{1}{4}\langle \delta n(\tau)\delta n \rangle \end{aligned} \quad (115)$$

describes charge fluctuations with $n = n_\uparrow + n_\downarrow$.

References

1. T. Schäfer, N. Wentzell, F. Šimkovic, Y.Y. He, C. Hille, M. Klett, C.J. Eckhardt, B. Arzhang, V. Harkov, F.M. Le Régent et al., *Phys. Rev. X* **11**, 011058 (2021)
2. W. Metzner, M. Salmhofer, C. Honerkamp, V. Meden, K. Schönhammer, *Rev. Mod. Phys.* **84**, 299 (2012)
3. P. Kopietz, L. Bartosch, F. Schütz, *Introduction to the Functional Renormalization Group*, vol. 798 (Springer, Berlin, 2010)
4. J. Diekmann, S.G. Jakobs, *Phys. Rev. B* **103**, 155156 (2021)
5. F.B. Kugler, J. von Delft, *Phys. Rev. B* **97** (2018)
6. F.B. Kugler, J. von Delft, *Phys. Rev. Lett.* **120** (2018)
7. F.B. Kugler, J. von Delft, *New J. Phys.* **20**, 123029 (2018)
8. B. Roulet, J. Gavoret, P. Nozières, *Phys. Rev.* **178**, 1072 (1969)
9. N.E. Bickers, in *in: Sénéchal D., Tremblay A.-M., Bourbonnais C. (eds), Theoretical Methods for Strongly Correlated Electrons, CRM Series in Mathematical Physics* (Springer, New York, 2004)
10. A. Tagliavini, C. Hille, F.B. Kugler, S. Andergassen, A. Toschi, C. Honerkamp, *SciPost Phys.* **6**, 9 (2019)
11. C. Hille, F.B. Kugler, C.J. Eckhardt, Y.Y. He, A. Kauch, C. Honerkamp, A. Toschi, S. Andergassen, *Phys. Rev. Res.* **2**, 033372 (2020)
12. J. Thoenniss, M.K. Ritter, F.B. Kugler, J. von Delft, M. Punk, [arXiv:2011.01268](https://arxiv.org/abs/2011.01268) [cond-mat.str-el] (2020)
13. D. Kiese, T. Mueller, Y. Iqbal, R. Thomale, S. Trebst, *Phys. Rev. Res.* **4**, 023185 (2022)
14. P. Chalupa-Gantner, F.B. Kugler, C. Hille, J. von Delft, S. Andergassen, A. Toschi, *Phys. Rev. Res.* **4**, 023050 (2022)
15. G. Li, N. Wentzell, P. Pudleiner, P. Thunström, K. Held, *Phys. Rev. B* **93**, 165103 (2016)
16. N. Wentzell, G. Li, A. Tagliavini, C. Taranto, G. Rohringer, K. Held, A. Toschi, S. Andergassen, *Phys. Rev. B* **102**, 085106 (2020)
17. C. Husemann, M. Salmhofer, *Phys. Rev. B* **79**, 195125 (2009)
18. C. Husemann, K.U. Giering, M. Salmhofer, *Phys. Rev. B* **85**, 075121 (2012)
19. E.A. Stepanov, A. Huber, E.G.C.P. van Loon, A.I. Lichtenstein, M.I. Katsnelson, *Phys. Rev. B* **94**, 205110 (2016)
20. E.A. Stepanov, S. Brener, F. Krien, M. Harland, A.I. Lichtenstein, M.I. Katsnelson, *Phys. Rev. Lett.* **121**, 037204 (2018)
21. E.A. Stepanov, A. Huber, A.I. Lichtenstein, M.I. Katsnelson, *Phys. Rev. B* **99**, 115124 (2019)
22. E.A. Stepanov, V. Harkov, A.I. Lichtenstein, *Phys. Rev. B* **100**, 205115 (2019)
23. V. Harkov, M. Vandelli, S. Brener, A.I. Lichtenstein, E.A. Stepanov, *Phys. Rev. B* **103**, 245123 (2021)
24. E.A. Stepanov, Y. Nomura, A.I. Lichtenstein, S. Biermann, *Phys. Rev. Lett.* **127**, 207205 (2021)
25. F. Krien, *Phys. Rev. B* **99**, 235106 (2019)
26. F. Krien, A. Valli, M. Capone, *Phys. Rev. B* **100**, 155149 (2019)
27. F. Krien, A. Valli, *Phys. Rev. B* **100**, 245147 (2019)
28. F. Krien, A.I. Lichtenstein, G. Rohringer, *Phys. Rev. B* **102**, 235133 (2020)
29. F. Krien, A. Valli, P. Chalupa, M. Capone, A.I. Lichtenstein, A. Toschi, *Phys. Rev. B* **102**, 195131 (2020)
30. F. Krien, A. Kauch, K. Held, *Phys. Rev. Res.* **3**, 013149 (2021)
31. P.M. Bonetti, A. Toschi, C. Hille, S. Andergassen, D. Vilardi, *Phys. Rev. Res.* **4**, 013034 (2022)
32. C. Taranto, S. Andergassen, J. Bauer, K. Held, A. Katanin, W. Metzner, G. Rohringer, A. Toschi, *Phys. Rev. Lett.* **112**, 196402 (2014)
33. D. Vilardi, C. Taranto, W. Metzner, *Phys. Rev. B* **99**, 104501 (2019)
34. A.A. Katanin, *Phys. Rev. B* **99**, 115112 (2019)
35. V. Harkov, A.I. Lichtenstein, F. Krien, *Phys. Rev. B* **104**, 125141 (2021)
36. A. Altland, B.D. Simons, *Condensed Matter Field Theory* (Cambridge University Press, 2010)
37. A. Kamenev, *Field Theory of Non-equilibrium Systems* (Cambridge University Press, 2011)
38. G. Rohringer, A. Valli, A. Toschi, *Phys. Rev. B* **86**, 125114 (2012)
39. A. Toschi, A.A. Katanin, K. Held, *Phys. Rev. B* **75**, 045118 (2007)
40. K. Held, A.A. Katanin, A. Toschi, *Prog. Theor. Phys. Supp.* **176**, 117 (2008)
41. A.A. Katanin, *Phys. Rev. B* **70**, 115109 (2004)
42. T. Schäfer, G. Rohringer, O. Gunnarsson, S. Ciuchi, G. Sangiovanni, A. Toschi, *Phys. Rev. Lett.* **110**, 246405 (2013)
43. T. Schäfer, S. Ciuchi, M. Wallerberger, P. Thunström, O. Gunnarsson, G. Sangiovanni, G. Rohringer, A. Toschi, *Phys. Rev. B* **94**, 235108 (2016)
44. O. Gunnarsson, G. Rohringer, T. Schäfer, G. Sangiovanni, A. Toschi, *Phys. Rev. Lett.* **119**, 056402 (2017)
45. P. Chalupa, P. Gunacker, T. Schäfer, K. Held, A. Toschi, *Phys. Rev. B* **97**, 245136 (2018)
46. P. Thunström, O. Gunnarsson, S. Ciuchi, G. Rohringer, *Phys. Rev. B* **98**, 235107 (2018)
47. F.B. Kugler, S.S.B. Lee, J. von Delft, *Phys. Rev. X* **11**, 041006 (2021)
48. S.S.B. Lee, F.B. Kugler, J. von Delft, *Phys. Rev. X* **11**, 041007 (2021)
49. L. Hedin, *Phys. Rev.* **139**, A796 (1965)
50. E. Walter, Ph.D. thesis, Ludwig-Maximilians-Universität München (2021)
51. S. Aguirre Lamus, Master's thesis, Ludwig-Maximilians-Universität München (2020)
52. N.E. Bickers, D.J. Scalapino, *Phys. Rev. B* **46**, 8050 (1992)
53. G. Rohringer, Ph.D. thesis, TU Wien (2013)

3.3 Notes on implementations

The implementation of an mFRG solver in the SBE formulation has been left for future work. However, previous experience and intermediate results can presumably be transferred to such a project. These do not replace thorough profiling, but may guide the first steps to the development of a code.

To begin with, an implementation in the MF at finite temperature is numerically far less challenging than an implementation with continuous frequencies. The SBE parquet solver¹ that was published with [P2] may serve as reference (cf. Ref. [GSvDK24] for a further development of the code for systems without $SU(2)$ spin symmetry). By comparison of the parquet and flow equations (see Eqs. (41), (48) in Ref. [P1]) one finds that many operations are similar. Hence, optimizations may benefit both methods. As explained in [P2], the computation of the U - r -irreducible vertex, T_r , is a major bottleneck. It involves the combination of SBE contributions $\nabla_{\bar{r}} = \bar{\lambda}_{\bar{r}} \bullet w_{\bar{r}} \bullet \lambda_{\bar{r}}$ which are given in the \bar{r} -channel frequency convention and have to be rotated to the r -channel convention. Several optimizations were implemented to accelerate the computation: Firstly, since the \bullet -product implies a contraction over spin indices, physical spin channels were used in which the operation is diagonal. Secondly, even though the data in all contributions, w_r and λ_r , could be reduced by symmetry relations, all values were prepared to be directly accessible in memory. While this leads to higher memory consumption, it sped up the retrieval of data.² Lastly, T_r is precomputed and reused in the BSE for λ_r and M_r . This optimization, again, improved computation time at the cost of higher memory consumption. The \hat{T}_r in the mFRG equations consist of even more terms. As explained in Eq. (46) of Ref. [P1], the product structure of the SBE terms ∇_r leads to three terms in the differentiated SBE term $\hat{\nabla}_r$. Hence, it is expected that such optimizations are even more valuable for an implementation of the mFRG equations.

In the Keldysh formalism further complications arise due to the continuous frequencies and the additional index structure. For an implementation analogous to that in Ref. [P3], KF functions are sampled on a non-linear grid in each frequency direction. Function values are determined by multi-linear interpolation. While the SBE terms ∇_r and $\hat{\nabla}_r$ definitely can be precomputed in the r -channel frequency convention, sampling ∇_r on the grid of a different frequency convention might impair its resolution. Furthermore, the \bullet -product also implies a contraction over Keldysh indices. For a complete analogy to our implementation in [P3], w_r and λ_r would each carry four Keldysh indices. After suitable ordering of the Keldysh indices [see Eq. (2.69)], these contractions amount to matrix products. However, the Keldysh structure can be further simplified in the SBE formulation: Since w_r and λ_r effectively are two-point or three-point functions, the number of Keldysh indices can be reduced to two or three, respectively. The resulting SBE diagram $\nabla_r = \bar{\lambda}_r \bullet w_r \bullet \lambda_r$ is a four-point object again and can be inserted into the BSE for $\lambda_{r'}$ or $M_{r'}$. This is an advantage of the SBE decomposition over the asymptotic decomposition where the 2PR vertex is the *sum* of asymptotic contributions $\gamma_r = \sum_i K_{ir}$. Therefore, the asymptotic functions, K_{ir} , always carry four Keldysh indices while SBE components, w_r and λ_r , can be consistently treated with two or three indices, respectively.

¹ <https://github.com/dominikkiese/MBEsolver.jl>

² Symmetries were used to reduce the number of points which have to be computed via the BSE. The symmetry-reduced data also facilitated the task for some solvers for non-linear equations by reducing the number of parameters.

4 Quantum field-theoretic study of the Anderson impurity model

4.1 Overview

This chapter presents an imaginary- and real-frequency study with two diagrammatic methods: the parquet equations and the functional renormalization group. As a physical benchmark system we consider the single-impurity Anderson impurity model (AIM) as described in Sec. 2.2.5. This model is well studied and understood, e.g. with the numerical renormalization group [BCP08] which provides the benchmark results for our project. The AIM describes a single (magnetic) impurity in a metal. This model hosts interesting physical behavior such as the spontaneous formation of a local magnetic moment or the Kondo effect [Kon64] at low temperatures and strong interactions [And61, Hew97]. It has also been used to study transport through quantum point contacts [JPS10]. Furthermore, while the AIM is interesting on its own, it also serves as an auxiliary model for dynamic mean-field theory (DMFT) [GKKR96] where it is used to study lattice models such as the Hubbard model and the periodic Anderson model, for instance. DMFT has proven to accurately describe phases of matter with local correlations. To incorporate long-range correlations one could use diagrammatic methods. For instance, the dynamic vertex approximation (D Γ A) [TKH07] solves the parquet equations for a lattice model using a local approximation of the 2PI vertex $R = R_{\text{loc}}$ which is taken as an input from DMFT. Similarly, the DMF 2 RG uses the full vertex of an impurity model as a starting point for an fRG flow from an impurity to a lattice model [TAB $^+$ 14].

Our study uses the mentioned diagrammatic methods, i.e., the parquet equations and the functional renormalization group. Previous diagrammatic studies of the AIM were often performed in the Matsubara formalism, e.g., Refs. [KHP $^+$ 08, CGKH $^+$ 22]. Matsubara functions directly reveal static and thermodynamic properties which are evaluated at zero time or zero frequency. However, dynamical observables can only be obtained by an ill-conditioned analytic continuation of the numerical data, as detailed in Sec. 2.1.6. Diagrammatic calculations in the Keldysh formalism come at the cost of increased numerical complexity. Previous real-frequency studies either made strong approximations to the frequency dependence of the vertex [JS10] or solved a simplified set of equations, e.g. [KWC97]. In our studies we aim to pave the way for methods such as DMF 2 RG or D Γ A. Hence, we seek to demonstrate that diagrammatic calculations involving the full Keldysh- and frequency structure of the four-point vertex are feasible. While many recent applications of these methods make further approximations, e.g., to the inter-channel feedback in the Bethe–Salpeter equations or relinquish parquet self-consistency, we also show that full parquet self-consistency can be reached within the parquet approximation. As discussed in Sec. 2.2.4.2, parquet self-consistency (and regulator-independence) can also be reached in fRG by including multi-loop corrections. In App. B we show that – within the parquet approximation – both parquet equations and multi-loop fRG (mfRG) indeed lead to the same results. However, the multi-loop expansion of real-frequency vertices seems to develop structures which are more difficult to resolve than those in the actual full vertex obtained from summing up all multi-loop contributions.

In terms of quantitative results, the studied methods suffer from our diagrammatic approximations which already introduce truncations at fourth order in perturbation theory. Thus, we cannot hope to outperform specialized impurity solvers. To evaluate the accuracy of the methods we compare two-point functions with results from the numerical renormalization group (NRG) which yields numerically exact real-frequency results for low temperatures and arbitrary interaction strengths. Recently, an extension of the NRG even allows the computation of the vertex [LKvD21, LHS⁺24].

The following papers present the results of the project. While Ref. [P3] focuses on a comparison of the computed observables and checks the fulfillment of physical identities, the code publication in Ref. [P5] details the technical aspects of our work. In Ref. [P2] we further present a `Julia` library for diagrammatic calculations in the Matsubara formalism.

Real-frequency quantum field theory applied to the single-impurity Anderson model

by

A. Ge,¹ N. Ritz,¹ E. Walter,¹ S. Aguirre,¹ J. von Delft,¹ and F. B. Kugler^{2,3}

¹ Arnold Sommerfeld Center for Theoretical Physics, Center for NanoScience, and

Munich Center for Quantum Science and Technology,

Ludwig-Maximilians-Universität München, 80333 Munich, Germany

² Center for Computational Quantum Physics, Flatiron Institute, 162 5th Avenue, New York,

New York 10010, USA

³ Department of Physics and Astronomy and Center for Materials Theory, Rutgers

University, Piscataway, New Jersey 08854, USA

reprinted on pages 66–89

with permission from

***Phys. Rev. B* 109, 115128 (2024),**

DOI: 10.1103/PhysRevB.109.115128.

© 2024 American Physical Society.

Real-frequency quantum field theory applied to the single-impurity Anderson model

Anxiang Ge ^{1,*}, Nepomuk Ritz ^{1,*}, Elias Walter ¹, Santiago Aguirre¹, Jan von Delft ¹ and Fabian B. Kugler ^{2,3}

¹*Arnold Sommerfeld Center for Theoretical Physics, Center for NanoScience, and Munich Center for Quantum Science and Technology, Ludwig-Maximilians-Universität München, 80333 Munich, Germany*

²*Center for Computational Quantum Physics, Flatiron Institute, 162 5th Avenue, New York, New York 10010, USA*

³*Department of Physics and Astronomy and Center for Materials Theory, Rutgers University, Piscataway, New Jersey 08854, USA*



(Received 2 November 2023; revised 6 February 2024; accepted 6 February 2024; published 15 March 2024)

A major challenge in the field of correlated electrons is the computation of dynamical correlation functions. For comparisons with experiment, one is interested in their real-frequency dependence. This is difficult to compute because imaginary-frequency data from the Matsubara formalism require analytic continuation, a numerically ill-posed problem. Here, we apply quantum field theory to the single-impurity Anderson model using the Keldysh instead of the Matsubara formalism with direct access to the self-energy and dynamical susceptibilities on the real-frequency axis. We present results from the functional renormalization group (fRG) at the one-loop level and from solving the self-consistent parquet equations in the parquet approximation. In contrast with previous Keldysh fRG works, we employ a parametrization of the four-point vertex which captures its full dependence on three real-frequency arguments. We compare our results to benchmark data obtained with the numerical renormalization group and to second-order perturbation theory. We find that capturing the full frequency dependence of the four-point vertex significantly improves the fRG results compared with previous implementations, and that solving the parquet equations yields the best agreement with the numerical renormalization group benchmark data but is only feasible up to moderate interaction strengths. Our methodical advances pave the way for treating more complicated models in the future.

DOI: [10.1103/PhysRevB.109.115128](https://doi.org/10.1103/PhysRevB.109.115128)

I. INTRODUCTION

Strongly correlated electrons are of central interest in condensed-matter physics and a prime application for quantum field theory (QFT). Two current frontiers in this context are (i) dealing with two-particle correlations on top of the familiar one-particle correlations, and (ii) obtaining real-frequency information relevant to experiments, as opposed to imaginary-frequency information popular in theoretical analyses. Indeed, much attention has recently been devoted to the two-particle—or four-point (4p)—vertex of correlated systems, e.g., regarding efficient representations [1–7] or the divergences of two-particle irreducible vertices [8–22]. Moreover, new algorithms have emerged, such as diagrammatic Monte Carlo for real-frequency 2p functions (one frequency argument) working with analytic Matsubara summation [23–29] or real-time integration [30–33], as well as numerical renormalization group (NRG) computations of real-frequency 4p functions (three frequency arguments) [34,35].

Here, we combine aspects (i) and (ii) and study real-frequency two-particle correlations in a QFT framework within the Keldysh formalism (KF) [36–38]. We employ two related methods: functional renormalization group (fRG) flows at one-loop level [39] and solutions of the self-consistent parquet equations [40]. These approaches are promising candidates for real-frequency diagrammatic extensions [41] of

dynamical mean-field theory [42], where the self-consistently determined impurity model is solved with NRG [43]. In practice, this means using the NRG 4p vertex [34,35] as input for fRG [44,45] or the parquet equations [46,47]. Fully exploiting this nonperturbative input requires taking the full frequency dependence of the 4p vertex into account. The present work is a proof-of-principle study showing that it is indeed possible to track the three-dimensional *real-frequency* dependence of the 4p vertex with fRG and parquet methods.

To demonstrate our capability of handling 4p vertices in real frequencies, we choose the well-known [48] single-impurity Anderson model (AM) [49] as a test case. Its 4p vertex depends only on frequency and spin arguments, orbital or momentum degrees of freedom are not involved. Moreover, we can benchmark our results against numerically exact data obtained with NRG [43].

On a historical note, we mention some early pioneering works on the AM where multipoint functions depending on multiple real frequencies were computed using various diagrammatic methods [50–53]. Anders and Grewe [50,51] computed the finite-temperature impurity density of states and spin-fluctuation spectra up to order $O(1/N^2)$ in a large- N expansion using a resummation that included skeleton diagrams of the crossing variety up to infinite order. This approach involved the analytic continuation of 2p and 3p functions from imaginary to real frequencies. Kroha, Wölfle, and Costi [52,53] studied the AM in the strong-coupling limit using a slave-boson treatment of local fermions and a conserving T -matrix approximation. They computed the auxiliary (pseudofermion and slave boson) spectral functions in the

*These authors contributed equally to this work.

Kondo regime. Their approach involved the analytic continuation of T matrices (4p objects depending on three frequencies) from imaginary to real frequencies. This was possible due to two simplifications arising in their approach. First, the Bethe–Salpeter equations for the T matrices were simplified via ladder approximations that neglect interchannel feedback but are sufficient to capture the leading and subleading infrared singularities. Second, the auxiliary propagators involve projection factors that cause their contributions to vanish along the branch cuts encountered during the analytic continuation of the T matrices. As a result, only integrations along branch cuts of the conduction-electron propagators contribute to the auxiliary-particle self-energies. In particular, only one of the fifteen Keldysh components of the T matrices were involved in these computations.

In the present paper, we consider a more general setting. We compute the full 4p (impurity-electron) vertex, which requires a treatment of the complete Keldysh structure. Furthermore, the diagrammatic methods considered here—the fRG and the parquet equations—treat all three channels of two-particle fluctuations (density, magnetic, pairing) in an equitable manner, fully including interchannel feedback. The latter causes severe technical complications: each channel has its own frequency parametrization; hence, interchannel feedback involves interpolations between different frequency parametrizations, which in turn demand great care when working with discrete frequency grids. One of our goals is to develop numerical strategies for conquering these complications in a general, robust manner, as a first step toward studying more complicated models in future work.

Keldysh fRG flows with dynamic 2p and 4p functions were pioneered by Jakobs and collaborators [54–56] and subsequently used in Refs. [57–59]. In all of these works, the dependence of the 4p vertex on three frequencies was approximated by a sum of three functions, each depending on only one (bosonic) frequency. Here, we present Keldysh one-loop fRG flows with the full, three-dimensional frequency dependence of the vertex, finding remarkable improvement compared with previous implementations [54,55]. We also solve the parquet equations in the parquet approximation (PA) in this setting, yielding results closest to NRG in the regime where the parquet self-consistency iteration converges. This regime corresponds rather accurately to the condition $u < 1$, where $u = U/(\pi\Delta)$ is the dimensionless coupling constant that controls the (convergent bare) zero-temperature perturbation series [60]. For completeness, we also discuss second-order perturbation theory (PT2). Although the PT2 self-energy in the particle-hole symmetric AM (sAM) yields strikingly good results (for known reasons, see Sec. II E), the susceptibilities or the results in the asymmetric AM (aAM) clearly show the benefits of the infinite diagrammatic resummations provided by fRG and the PA.

A conceptual equivalence between truncated fRG flows and solutions of the parquet equations has been established via the multiloop fRG [61–63]. For the AM treated in imaginary frequencies, this equivalence was analyzed numerically in Ref. [64], and multiloop convergence was demonstrated up to moderate interaction strengths. We refrain from presenting a similar study in real frequencies here, leaving that for future work.

The rest of the paper is organized as follows: In Sec. II, we give a minimal introduction to the KF (Sec. II A) and summarize the methodical background for fRG and the PA (Secs. II B and II C). The AM is briefly introduced in Sec. II D, followed by a concise description of our benchmark methods for this model (Sec. II E). In Sec. III, we present our results, beginning with dynamical correlation functions computed directly on the real-frequency axis (Sec. III A). We then turn to various static properties in Sec. III B and check the fulfillment of zero-temperature identities between them (Sec. III C). The frequency-dependent two-particle vertex is shown in Sec. III D. We conclude in Sec. IV and give a brief outlook on possibilities for future work.

Nine Appendixes are devoted to technical matters. Appendix A summarizes our parametrization of the 4p vertex and its symmetry relations. Appendix B shows the frequency dependence of all vertex components, as obtained in the PA. The fully parametrized parquet and fRG flow equations are stated in Appendix C, and Appendix D discusses a channel-adapted evaluation of the Schwinger–Dyson equation for the self-energy in the PA. Appendix E deals with a known equal-time subtlety in the KF, relevant for computing, e.g., the Hartree self-energy in the aAM. In Appendix F, we give a concise definition of all diagrammatic contributions to PT2. We provide more details on the actual fRG and PA implementation in Appendix G and comment on the numerical costs in Appendix H. Finally, Appendix I scrutinizes the fRG static magnetic susceptibility at $u \gtrsim 1$ for different settings of the frequency resolution.

II. BACKGROUND

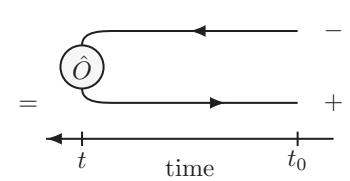
A. Keldysh formalism

The Keldysh formalism [36–38] is a suitable framework for studying systems out of equilibrium, as well as systems in thermal equilibrium if aiming for a finite-temperature real-frequency description. An extensive introduction can be found in Ref. [65]; more compact introductions in the context of fRG are also given in related Ph.D. theses [54,57,66,67]. Here, we only give a short summary of the concepts needed in this paper.

Consider a (potentially time-dependent) Hamiltonian $H(t)$ and a density matrix known at time t_0 , $\rho_0 = \rho(t_0)$. The expectation value of an operator \hat{O} at time t reads

$$\langle \hat{O}(t) \rangle = \text{Tr} \left[\tilde{\mathcal{T}} e^{-i \int_{t_0}^t dt' H(t')} \hat{O} \mathcal{T} e^{-i \int_{t_0}^t dt' H(t')} \rho_0 \right]. \quad (1)$$

Here, \mathcal{T} is the time-ordering operator, and $\tilde{\mathcal{T}}$ denotes antitime ordering. In the KF, one rewrites Eq. (1) as

$$\langle \hat{O}(t) \rangle = \text{Tr} \left[\mathcal{T}_c \left\{ e^{-i \int_t^{t_0} dt' H^+(t')} \hat{O} e^{-i \int_{t_0}^t dt' H^-(t')} \rho_0 \right\} \right]$$


$$= \quad (2)$$

The Hamiltonian, and all operators in it, acquire an additional contour index $c = \mp$, indicating whether they sit on the

forward (−) or backward (+) branch of the Keldysh double-time contour. The contour-ordering operator \mathcal{T}_C puts all operators on the backward branch left of those on the forward branch, and antitime orders (time orders) them on the backward (forward) branch.

In the above equation, \hat{O} , inserted at time t , can be placed on either branch. However, if \hat{O} is a product of multiple operators, they also come with contour indices to ensure the correct ordering. It follows that an n -point correlator generically has 2^n Keldysh components. For example, the two-point correlator in terms of the creation (ψ^\dagger) and the annihilation operator (ψ) reads

$$G^{c|c'}(t, t') = -i \langle \mathcal{T}_C \psi^c(t) \psi^{\dagger c'}(t') \rangle. \quad (3)$$

Resolving the contour indices c, c' yields the matrix

$$G^{c|c'} = \begin{pmatrix} G^{-| -} & G^{-| +} \\ G^{+| -} & G^{+| +} \end{pmatrix} = \begin{pmatrix} G^{\mathcal{T}} & G^{\mathcal{K}} \\ G^{\mathcal{A}} & G^{\mathcal{R}} \end{pmatrix}. \quad (4)$$

Using the redundancy $G^{\mathcal{K}} + G^{\mathcal{A}} - G^{\mathcal{T}} - G^{\mathcal{R}} = 0$, which holds as long as $t \neq t'$ (see Appendix E for the case $t = t'$), the Keldysh structure of G can be simplified. The Keldysh rotation invokes the Keldysh indices $k = 1$ and 2, where

$$\psi^1 = \frac{1}{\sqrt{2}}(\psi^- - \psi^+), \quad \psi^2 = \frac{1}{\sqrt{2}}(\psi^- + \psi^+), \quad (5)$$

and equivalently for ψ^\dagger . We can thus define a basis transformation matrix D via $\psi^k = D^{kc} \psi^c$:

$$D = \frac{1}{\sqrt{2}} \begin{pmatrix} 1 & -1 \\ 1 & 1 \end{pmatrix}, \quad D^{-1} = \frac{1}{\sqrt{2}} \begin{pmatrix} 1 & 1 \\ -1 & 1 \end{pmatrix}. \quad (6)$$

Rotating G as $G^{k|k'} = D^{kc} G^{c|c'} (D^{-1})^{c'k'}$ yields

$$G^{k|k'} = \begin{pmatrix} G^{1|1} & G^{1|2} \\ G^{2|1} & G^{2|2} \end{pmatrix} = \begin{pmatrix} 0 & G^{\mathcal{A}} \\ G^{\mathcal{R}} & G^{\mathcal{K}} \end{pmatrix}, \quad (7)$$

where $G^{1|1} = 0$ follows from the redundancy mentioned above. We find the retarded propagator

$$G^{\mathcal{R}}(t_1, t_2) = -i \Theta(t_1 - t_2) \{ \{ c(t_1), c^\dagger(t_2) \} \}, \quad (8)$$

where $\{ \cdot, \cdot \}$ denotes the anticommutator, and its advanced counterpart $G^{\mathcal{A}}(t_1, t_2) = [G^{\mathcal{R}}(t_2, t_1)]^*$, as well as the Keldysh propagator $G^{\mathcal{K}}(t_1, t_2) = -[G^{\mathcal{K}}(t_2, t_1)]^*$ [54].

For a time-independent problem, we have $G(t_1, t_2) = G(t_1 - t_2)$ and frequency conservation with

$$G(\nu) = \int dt e^{i\nu t} G(t), \quad G(t) = \int \frac{d\nu}{2\pi} e^{-i\nu t} G(\nu). \quad (9)$$

In the following, we consider thermal equilibrium at temperature T and chemical potential μ , set to zero. Then, the density matrix is $\rho_0 = e^{-H/T}/\mathcal{Z}$ (with $k_B = 1$ and $\mathcal{Z} = \text{Tr} e^{-H/T}$), and the Keldysh components of G fulfill the fluctuation-dissipation theorem (FDT) [54,65]

$$G^{\mathcal{K}}(\nu) = 2i \tanh\left(\frac{\nu}{2T}\right) \text{Im} G^{\mathcal{R}}(\nu). \quad (10)$$

B. Diagrammatic framework

The one-particle propagator can be expressed through the bare propagator G_0 and the self-energy Σ via the Dyson

equation. Using multi-indices 1, 1', etc., we have

$$G_{1|1'} = \overleftarrow{1} \overleftarrow{1'} = \overleftarrow{1} \overleftarrow{1'}_{G_0} + \overleftarrow{1} \overleftarrow{2'} \overleftarrow{\Sigma} \overleftarrow{2} \overleftarrow{1'}_G, \quad (11)$$

where the internal arguments 2, 2' are summed over. This equation is solved by $G = (G_0^{-1} - \Sigma)^{-1}$. The self-energy has a Keldysh structure similar to Eq. (7),

$$\Sigma^{k_1|k_2} = \begin{pmatrix} \Sigma^{1|1} & \Sigma^{1|2} \\ \Sigma^{2|1} & \Sigma^{2|2} \end{pmatrix} = \begin{pmatrix} \Sigma^K & \Sigma^R \\ \Sigma^A & 0 \end{pmatrix}, \quad (12)$$

and $\Sigma^K(\nu) = 2i \tanh(\frac{\nu}{2T}) \text{Im} \Sigma^R(\nu)$, cf. Eq. (10).

The two-particle (or four-point) correlation function $G^{(4)}$ can be expressed through the four-point vertex Γ ,

$$\begin{aligned} G_{12|1'2'}^{(4)} &= \overleftarrow{1} \overleftarrow{2} \overleftarrow{1'} \overleftarrow{2'} \overleftarrow{G^{(4)}} \\ &= \overleftarrow{1} \overleftarrow{2} \overleftarrow{1'} \overleftarrow{2'} - \overleftarrow{1} \overleftarrow{2} \overleftarrow{1'} \overleftarrow{2'} + \overleftarrow{1} \overleftarrow{2} \overleftarrow{1'} \overleftarrow{2'} \overleftarrow{\Gamma} \overleftarrow{2} \overleftarrow{1'} \overleftarrow{2'} \overleftarrow{1'}, \end{aligned} \quad (13)$$

where the internal arguments (3, 3', 4, 4') are again summed over. From $G^{(4)}$, one obtains susceptibilities by contracting pairs of external legs (see Appendix C for details).

The bare vertex, as the full vertex, is fully antisymmetric in its indices. Thus, a purely local and instantaneous interaction is of the type

$$\begin{aligned} (\Gamma_0)_{\sigma'_1 \sigma'_2 | \sigma_1 \sigma_2}(t'_1, t'_2 | t_1, t_2) \\ = -U \delta(t'_1 = t'_2 = t_1 = t_2) \delta_{\sigma_1, \bar{\sigma}'_2} (\delta_{\sigma'_1, \sigma_2} \delta_{\sigma'_2, \sigma_1} - \delta_{\sigma'_1, \sigma_1} \delta_{\sigma'_2, \sigma_2}), \end{aligned} \quad (14)$$

with $U > 0$ for a repulsive interaction. This corresponds to a Hugenholtz diagram (single dot) [68]

$$(\Gamma_0)_{1'2'|12} = \overleftarrow{1'} \overleftarrow{2'} \overleftarrow{1} \overleftarrow{2} \overleftarrow{\text{dot}} = \overleftarrow{\sigma} \overleftarrow{\sigma} \overleftarrow{\sigma} \overleftarrow{\sigma} \overleftarrow{\text{dot}} - \overleftarrow{\bar{\sigma}} \overleftarrow{\bar{\sigma}} \overleftarrow{\bar{\sigma}} \overleftarrow{\bar{\sigma}} \overleftarrow{\text{dot}}. \quad (15)$$

As the bare vertex is part of either H^+ or H^- in Eq. (2), all its contour indices must be equal [54],

$$(\Gamma_0)_{1'2'|12} = -c_1 \delta_{c'_1 = c'_2 = c_1 = c_2} (\Gamma_0)_{\sigma'_1 \sigma'_2 | \sigma_1 \sigma_2}(t'_1, t'_2 | t_1, t_2). \quad (16)$$

It acquires a minus sign when moved from the forward ($c_1 = -$) to the backward ($c_1 = +$) branch of the Keldysh contour. After Keldysh rotation, one obtains

$$(\Gamma_0)_{\sigma'_1 \sigma'_2 | \sigma_1 \sigma_2}^{k'_1 k'_2 | k_1 k_2} = \begin{cases} \frac{1}{2} (\Gamma_0)_{\sigma'_1 \sigma'_2 | \sigma_1 \sigma_2}, & \sum_i k_i \text{ odd} \\ 0, & \text{else,} \end{cases} \quad (17)$$

where $\sum_i k_i$ is short for $k'_1 + k'_2 + k_1 + k_2$.

C. Many-body approaches

So far, we defined the basic objects of interest, namely, one- and two-particle correlation functions in the KF, encapsulated in the self-energy Σ and the 4p vertex Γ ,

$$\Sigma_{1'1} = \text{diagram of } \Sigma \text{ with legs } 1' \text{ and } 1, \quad \Gamma_{1'2'|12} = \text{diagram of } \Gamma \text{ with legs } 1', 2', 1, 2. \quad (18)$$

One can derive a diagrammatic perturbation series for each of them. However, to extend our description from weak to intermediate coupling, we want to resum infinitely many diagrams. We use two strategies achieving this: fRG [39,69] and the PA [40]. We summarize both schemes in turn and then comment on their relation.

In fRG, one introduces a scale parameter Λ into the bare propagator G_0 , such that the theory is solvable at an initial value $\Lambda = \Lambda_i$, while the original problem is recovered at a final value $\Lambda = \Lambda_f$ (i.e., $G_0^{\Lambda_f} = G_0$). Here, we choose $G_0^{\Lambda_i}$ very small, so that Σ^{Λ_i} and Γ^{Λ_i} can be obtained by perturbation theory or by iterating the parquet equations (see below) until convergence. The final results $\Sigma^{\Lambda_f} = \Sigma$ and $\Gamma^{\Lambda_f} = \Gamma$ are obtained by solving a set of flow equations. In fact, the fRG provides an infinite hierarchy of flow equations, which is in principle exact but must be truncated in practice. The flow equations for $\dot{\Sigma} = \partial_\Lambda \Sigma$ and $\dot{\Gamma} = \partial_\Lambda \Gamma$ in diagrammatic notation are

$$\dot{\Sigma} = - \text{diagram of } \dot{\Sigma} \text{ with } \Gamma \text{ and a dashed line}, \quad (19a)$$

$$\dot{\Gamma} = \text{diagram of } \dot{\Gamma} \text{ with } \Gamma \text{ and a dashed line} + \frac{1}{2} \text{diagram of } \dot{\Gamma} \text{ with } \Gamma \text{ and a dashed line} \quad (19a)$$

$$- \text{diagram of } \dot{\Gamma} \text{ with } \Gamma \text{ and a dashed line} + \text{diagram of } \dot{\Gamma} \text{ with } \Gamma^{(6)} \text{ and a dashed line}. \quad (19b)$$

The propagator with a dash is the single-scale propagator $S = \partial_\Lambda G|_{\Sigma=\text{const}}$; propagator pairs with a dash indicate $\dot{\Gamma}^S = SG + GS$. We adopt the one-loop fRG scheme where the truncation consists of $\Gamma^{(6)} \approx 0$. As is commonly done, we then employ the so-called Katanin substitution [70] where $\dot{\Gamma}^S$ is replaced by $\dot{\Pi} = \dot{G}G + G\dot{G}$.

The parquet formalism consists of solving a self-consistent set of equations on the one- and two-particle level. It involves the Schwinger–Dyson equation (SDE)

$$\text{diagram of } \Sigma = - \text{diagram of } \Sigma \text{ with } \Gamma \text{ and a dashed line} - \frac{1}{2} \text{diagram of } \Sigma \text{ with } \Gamma \text{ and a dashed line}, \quad (20a)$$

where the first term is the Hartree self-energy Σ_H , as well as the Bethe–Salpeter equations (BSEs)

$$\text{diagram of } \gamma_a = \text{diagram of } \gamma_a \text{ with } I_a \text{ and } \Gamma, \quad (20b)$$

$$\text{diagram of } \gamma_p = \frac{1}{2} \text{diagram of } \gamma_p \text{ with } I_p \text{ and } \Gamma, \quad (20c)$$

$$\text{diagram of } \gamma_t = - \text{diagram of } \gamma_t \text{ with } I_t \text{ and } \Gamma. \quad (20d)$$

Here, γ_r is the two-particle reducible vertex in a given channel $r \in \{a, p, t\}$, while $I_r = \Gamma - \gamma_r$ is the corresponding two-particle irreducible vertex. The parquet equation

$$\Gamma = R + \gamma_a + \gamma_p + \gamma_t \quad (20e)$$

gives the full vertex in terms of the two-particle reducible vertices as well as the fully irreducible vertex R . The set of equations (20) is exact. However, R in Eq. (20e) is not determined by an integral equation itself and serves as an input, for which an approximation must be used in practice. The PA is the simplest such approximation:

$$R = \Gamma_0 + O[(\Gamma_0)^4] \approx \Gamma_0. \quad (21)$$

Thus, the set of equations (20) closes and can be solved by standard means.

The truncated (one-loop) fRG flow and the PA are closely related but differ in details. An equivalence between them is established by the multiloop fRG [61–63] (see also Refs. [64,71–76]): By incorporating additional terms into the flow equations, which simulate part of the intractable six-point vertex in the fRG hierarchy of flow equations, the scale derivative of the self-energy and vertex is completed to a total derivative of diagrams, which are precisely the diagrams contained in the PA. Hence, if multiloop convergence can be achieved, the regulator dependence of the truncated fRG flow is eliminated, and one obtains results equivalent to the PA. Here, we restrict ourselves to one-loop fRG flows. Our numerical explorations with multiloop fRG for the AM in the KF have so far shown that the additional terms are numerically less well behaved, requiring a prohibitively high numerical resolution. This task is therefore left for future work, where compression techniques such as the new quantum tensor cross interpolation scheme [7,33,77] could be used to keep the needed numerical resources manageable.

D. Single-impurity Anderson model

The formalism introduced above is completely general and can be applied, e.g., to lattice or impurity models alike. Comparing Keldysh to Matsubara approaches, the spatial or momentum degrees of freedom of lattice models are treated similarly in both cases. By contrast, the temporal or frequency dynamics are naturally very different. In impurity models, the frequency dynamics are isolated, saving the cost of including momentum variables. Hence, we consider in this paper the AM [49] in thermal equilibrium. Its physical behavior is well understood [48], and NRG [43] can be used to obtain highly accurate real-frequency benchmark data.

The model is defined by the Hamiltonian

$$H = \sum_{\epsilon\sigma} \epsilon c_{\epsilon\sigma}^\dagger c_{\epsilon\sigma} + (\epsilon_d + h)n_\uparrow + (\epsilon_d - h)n_\downarrow + Un_\uparrow n_\downarrow + \sum_{\epsilon\sigma} (V_\epsilon d_\sigma^\dagger c_{\epsilon\sigma} + \text{H.c.}), \quad (22)$$

with spinful bath electrons, created by $c_{\epsilon\sigma}^\dagger$, and a local level (d_σ^\dagger). The latter has an on-site energy ϵ_d and Coulomb repulsion U acting on $n_\sigma = d_\sigma^\dagger d_\sigma$. Although we consider $h = 0$, we include the magnetic field in Eq. (22) for a simple definition of the magnetic susceptibility. The bath electrons are integrated out, yielding the frequency-dependent retarded hybridization function $-\text{Im}\Delta^R(\nu) = \sum_\epsilon \pi |V_\epsilon|^2 \delta(\nu - \epsilon)$. We consider a flat hybridization in the wide-band limit, $\Delta_\nu^R = -i\Delta$, so that the bare impurity propagator reads

$$G_0^R(\nu) = \frac{1}{\nu - \epsilon_d + i\Delta}. \quad (23)$$

We use the dimensionless parameter $u = U/(\pi\Delta)$ for the interaction strength on the impurity in units of the hybridization strength to the bath. We focus on two choices of the on-site energy: one with particle-hole symmetry, $\epsilon_d = -U/2$, and one without, $\epsilon_d = 0$. We refer to these as the symmetric AM (sAM) and asymmetric AM (aAM), respectively.

For the sAM, $\Sigma_H = U/2$ is conveniently absorbed into the bare propagator,

$$G_0^R \rightarrow G_H^R = \frac{1}{\nu - \epsilon_d + i\Delta - \Sigma_H} = \frac{1}{\nu + i\Delta}. \quad (24)$$

For perturbative calculations in the aAM (as in PT2 or to initialize the parquet iterations), we also replace G_0 by G_H (see Appendix E for details).

For the fRG treatment, we use the hybridization flow [54], where Δ acts as the flow parameter and is decreased from a very large value to the actual value of interest. This is convenient because every point of the flow describes a physical system, at the given values of Δ , U , T . In other words, the fRG flow provides a complete parameter sweep in Δ , while the other parameters (U , T) remain fixed. Then, the fRG single-scale propagator is

$$S^R(\nu) = \partial_\Delta G^R(\nu)|_{\Sigma=\text{const}} = -i[G^R(\nu)]^2. \quad (25)$$

In the limit $\Delta \rightarrow \infty$, the values of Γ and Σ are [54]

$$\Gamma|_{\Delta=\infty} = \Gamma_0, \quad \Sigma^R|_{\Delta=\infty} = \Sigma_H = U\langle n_\sigma \rangle. \quad (26)$$

Note that while all vertex diagrams of second order or higher vanish as $\Delta \rightarrow \infty$, the first-order contribution of $\Sigma^{R/A}$ (the Hartree term Σ_H) is finite. As discussed in Appendix E, Σ_H is given by an integral over $G^<$, which gives a finite value $U\langle n_\sigma \rangle$ even in the limit $\Delta \rightarrow \infty$. In practice, we start the flow at a large but finite value of Δ , and use the self-consistent solution of the parquet equations as the initial conditions for Σ and Γ , as they can be easily obtained for sufficiently large Δ .

E. Benchmark methods

As a real-frequency benchmark method, we use NRG in a state-of-the-art implementation based on the QSpace tensor library [78–80]. We employ a discretization parameter of $\Lambda = 2$, average over $n_z = 6$ shifts of the logarithmic discretization grid [81], and keep up to 5000 SU(2) multiplets during the iterative diagonalization. Dynamical correlators are obtained via the full density-matrix NRG [82,83], using adaptive broadening [84,85] and a symmetric improved estimator for the self-energy [86]. We also extract zero-temperature quasiparticle parameters from the NRG low-energy spectrum [87–93]. Dividing the quasiparticle interaction \tilde{U} by the square of the quasiparticle weight Z^2 yields the 4p vertex at vanishing frequencies $\Gamma_{\uparrow\downarrow}(\mathbf{0})$. Thereby, we obtain $\Gamma_{\uparrow\downarrow}(\mathbf{0}) = -\tilde{U}/Z^2$ at $T = 0$ very efficiently and accurately. For a finite-temperature estimate, we divide \tilde{U} by the finite-temperature Z deduced from the dynamic self-energy as opposed to the zero-temperature Z following from the low-energy spectrum. We also compute the dynamical 4p vertex in the Keldysh formalism, exploiting the recent advances described in Refs. [34,35].

For completeness, we also compare our results to PT2. Perturbation theory of the AM is known to work well when expanding around the nonmagnetic Hartree–Fock solution [60,94–97]. PT2 famously and fortuitously (cf. the iterated perturbation theory in the DMFT context [42]) gives *very* good results for the self-energy of the sAM, where $\epsilon_d = -U/2$ and Σ_H cancel exactly. The reason is that Σ_{PT2} is correct in the limits $u \rightarrow 0$ and $u \rightarrow \infty$. In the latter case, the spectrum $-\frac{1}{\pi}\text{Im}G^R$ consists of two discrete peaks, and, in the sAM, the resulting expression for $\Sigma^R = 1/G_0^R - 1/G^R$ is $(U/2)^2/(\nu + i0^+)$, coinciding with PT2. One may further note that corrections to Σ_{PT2} start at order u^4 , as only even powers contribute to the expansion of Σ for the sAM, and that the expansion converges very quickly (see Figs. 3.6 and 3.7 in Ref. [95]). Additionally, the high-frequency asymptote $\lim_{\nu \rightarrow \infty} \nu(\Sigma^R - \Sigma_H)$ is fully captured by PT2, as the general expression $U^2\langle n_\sigma \rangle(1 - \langle n_\sigma \rangle)$ reduces to $(U/2)^2$ (with $\langle n_\sigma \rangle = 1/2$ in the sAM), i.e., the second-order result.

For the aAM, Σ_H must first be determined in a self-consistent way. This is crucial because $\langle n_\sigma \rangle$ is not well approximated by a few orders in u [recall the Friedel sum rule at $T = 0$ [98], $\langle n_\sigma \rangle = \frac{1}{2} - \frac{1}{\pi} \arctan\{[\epsilon_d + \Sigma(0)]/\Delta\}$]. The self-consistent Hartree propagator fulfills the Friedel sum rule at $T = 0$, but the resulting $\langle n_\sigma \rangle$ for given ϵ_d is of course not exact. When using PT2, we compute quantities of interest, such as Σ_{PT2} , using the Hartree propagator (see Appendix F for details). However, in contrast with the sAM, Σ_{PT2} is not exact at $u \rightarrow \infty$ (cf. Ref. [99]), odd powers in u contribute to Σ , and the high-frequency asymptote of Σ_{PT2} , involving $\langle n_\sigma \rangle$, is not reproduced exactly.

Finally, we also compare our fRG and PA results to “KISF calculations” mimicking the previous state of the art in Keldysh fRG. References [54,55,58] used a scheme where the full vertex is decomposed into the three channels [cf. Eq. (20e)] and, for each two-particle reducible vertex γ_r , only the dependence on the bosonic transfer frequency is retained [see Eq. (76) in Ref. [55]]:

$$\Gamma \approx \Gamma_0 + \sum_{r=a,p,t} \gamma_r(\omega_r). \quad (27)$$

Note that, within Matsubara fRG, Ref. [100] compared this simplification (called “Appr. 1” therein) to the full parametrization. When inserting the vertex parametrized according to Eq. (27) into the self-energy flow (19a), no further approximations are needed. However, when inserting the vertex on the right of the vertex flow equation (19b), the interchannel contributions are approximated by their static values [in thermal equilibrium with $\mu = 0$, see Eq. (83) in Ref. [55]]:

$$\Gamma_{\text{RHS}(\gamma_r)} \approx \Gamma_0 + \gamma_r(\omega_r) + \sum_{r' \neq r} \gamma_{r'}(\omega_{r'})|_{\omega_{r'}=0}. \quad (28)$$

With this approximation the only frequency dependence of the integrands lies in the propagator pair. By contrast, an exact decomposition of each γ_r has the form [2]

$$\gamma_r(\omega_r, \nu_r, \nu_r') = K_{1r}(\omega_r) + K_{2r}(\omega_r, \nu_r) + K_{2'r}(\omega_r, \nu_r') + K_{3r}(\omega_r, \nu_r, \nu_r'). \quad (29)$$

(The frequency arguments ω_r, ν_r, ν_r' are defined in Appendix A, Fig. 12.) Thus, the above approximation can be understood by retaining only the K_{1r} contributions while ensuring a static feedback (SF) between the different channels—hence the abbreviation KISF. Within KISF, there are different ways of treating the feedback from the self-energy. Previous works found better results at $T = 0$ by inserting only the static rather than full dynamic Σ into the propagator [56]. We confirm this finding at $T = 0$ but observed that the static Σ feedback has problems at $T \neq 0$, failing, e.g., the requirement $\text{Im}\Sigma < 0$. Instead, we obtained much better results (particularly fulfilling $\text{Im}\Sigma < 0$) by using the full dynamic Σ feedback together with the Katanin substitution [70].

F. Note on the numerical implementation

Compared with the more common Matsubara formalism (MF), the KF entails notable differences in the numerical implementation that we summarize here (see Appendix G for details). Most importantly, while finite-temperature Matsubara computations employ a discrete set of (imaginary) frequencies, Keldysh functions depend on continuous (real) frequencies. Furthermore, the Keldysh index structure increases the number of components of the correlators (to be computed and stored) by a factor of 4 and 16 for 2p and 4p objects, respectively. Hence, working in the KF requires considerably higher effort in terms of implementational complexity and numerical resources.

To minimize systematic numerical errors, a faithful representation of the vertex functions is essential. The de-

composition (29) of the reducible vertices [2] is beneficial for capturing the high-frequency asymptotics. Indeed, the lower-dimensional asymptotic functions, K_1 and $K_{2(\circ)}$, allow for a good resolution at comparably low numerical cost. A good resolution of the continuous Keldysh functions further necessitates a suitable choice of sampling points. We use a frequency grid with high resolution at small frequencies, where the vertices show sharp features, and fewer points at higher frequencies. In fRG with the hybridization flow, the frequency grids also have to be rescaled to account for changes scaling with Δ ; for fully adaptive grids (which were not required in this work, cf. Appendix G) see also Refs. [73,74,76].

Continuous-frequency computations also require efficient integration routines. We use an adaptive quadrature routine to capture the essential features of sharply peaked functions (cf. Appendix G). The additional numerical costs due to the Keldysh index structure can be mitigated by vectorization, i.e., by exploiting the matrix structure of the summation over Keldysh components. Storing all Keldysh components contiguously in memory allows for efficient access to matrix-valued vertex data, which can be combined to matrix-valued integrands via linear algebra operations. (Note that vectorization over Keldysh components requires a quadrature routine that accepts matrix-valued integrands.) Symmetries are used to reduce the data points that are computed directly, and most resulting symmetry relations are compatible with vectorization over Keldysh indices (see Appendix A).

Lastly, the fRG and the parquet solver generally have the advantage that computations can be parallelized efficiently over all combinations of external arguments. We use OMP and MPI libraries to parallelize execution across multiple CPUs and compute nodes.

III. RESULTS

In the results, we focus on retarded correlation functions like G^R , Σ^R , and χ^R . For brevity, we denote the real and imaginary parts of, say, G^R by G' and G'' , respectively, i.e., $G^R = G' + iG''$. Since the fRG flow varies Δ at fixed U and T , we consider a temperature of $T/U = 0.01$. Most plots show results both for the sAM ($\epsilon_d = -U/2$) and aAM ($\epsilon_d = 0$). Recall that $u = U/(\pi\Delta)$.

A. Dynamical correlation functions

As a first quantity that is directly measurable in experiment, we show in Fig. 1 the spectral function $\tilde{A}(\nu) \equiv \pi\Delta A(\nu) = -\Delta G''(\nu)$. The absorbed factor of $\pi\Delta$ ensures $\tilde{A}(0) = 1$ for the sAM and $T \rightarrow 0$. We consider three values of $u \in \{0.75, 1, 1.5\}$, referred to as “small,” “intermediate,” and “large” in the following (although truly large interactions in the AM rather are $u \gtrsim 2$ [60]). There are no PA results for large u , as we could not converge the real-frequency self-consistent parquet solver there.

At small u , the curves produced by all methods are almost indistinguishable. Small but noticeable deviations occur for the aAM at intermediate u , and pronounced deviations are found at large u . At $u = 1.5$ in the sAM, only the methods exact in the $u \rightarrow \infty$ limit (cf. Sec. II E), NRG and PT2, produce notable Hubbard bands centered at $\nu = \pm U/2$, while fRG also

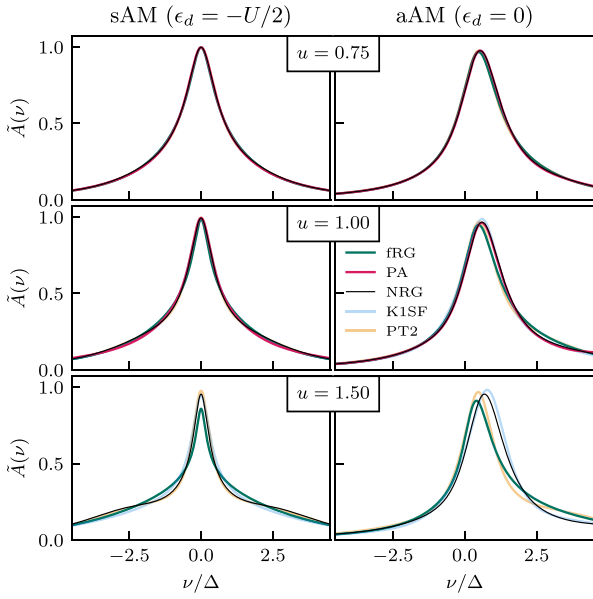


FIG. 1. Spectral functions $\tilde{A}(\nu) \equiv \pi \Delta A(\nu)$ for three interaction values u in the symmetric AM (sAM, left) and the asymmetric AM (aAM, right). Deviations between the methods appear with increasing u . Here and in all subsequent figures, we consider a temperature of fixed $T/U = 0.01$. At $u = 1.5$ in the sAM, the onset of Hubbard bands centered at $\nu = \pm U/2$ is only captured by NRG and (for reasons explained in Sec. II E) PT2. At this interaction strength, fRG underestimates the quasiparticle peak, and we were unable to converge the PA results.

underestimates the height of the quasiparticle peak. Nevertheless, one may come to the conclusion that all methods agree to a reasonable degree of accuracy. Note, although, that at small u , where Σ is small, $G^R = 1/([G_0^R]^{-1} - \Sigma^R)$ and thus also $A(\nu)$ are dominated by the bare propagator. As all nontrivial features of

$$A(\nu) = \frac{1}{\pi} \frac{\Delta - \Sigma''(\nu)}{[\nu - \epsilon_d - \Sigma'(\nu)]^2 + [\Delta - \Sigma''(\nu)]^2}$$

come from Σ , we can gain more insight by looking at Σ directly.

In Fig. 2, we plot the negative imaginary part of the retarded self-energy $-\Sigma''(\nu)$ in units of the hybridization strength Δ . This quantity is strictly non-negative [86], which is a useful and nontrivial consistency check for all our methods. Here, deviations between the methods are visible at each value of u . At small u , the results mostly agree, albeit better for the sAM than for the aAM. At small and intermediate u in the aAM, the PA matches NRG most closely and also captures the peak position correctly, in contrast with fRG, K1SF, and PT2. Strikingly, though, for intermediate u in the sAM (which is the more strongly correlated setting with lower quasiparticle weight Z , see Fig. 7), the PA shows considerable deviations from NRG: Σ'' has a “deformation” in that its maxima are misplaced outward. We performed a separate PA calculation in the MF to confirm that the corresponding MF result per-

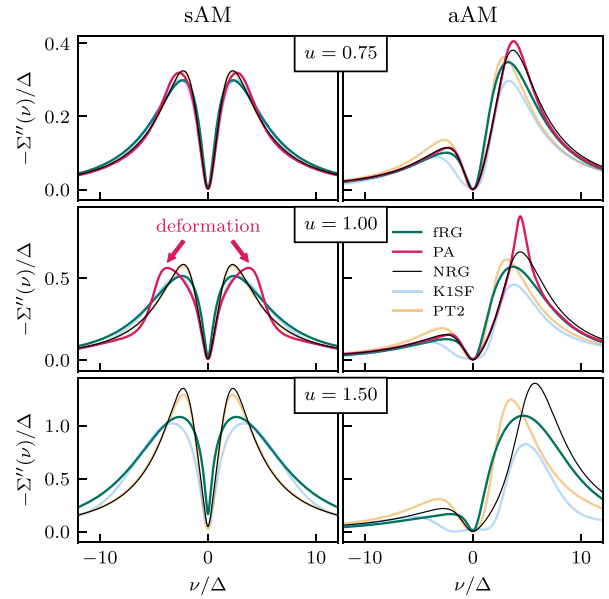


FIG. 2. Imaginary part of the retarded self-energy, organized as in Fig. 1. The limitations of PT2 in the aAM are clearly exposed. The PA results are closest to NRG at $u = 0.75$ for both sAM and aAM, and at $u = 1$ for the aAM (this corresponds to the regime of not too strong correlation, $Z \gtrsim 0.8$, see Fig. 7). Artifacts appear at $u = 1$ in the sAM (where $Z \approx 0.65$, see Fig. 7). Throughout, the fRG results with full frequency dependence match NRG better than those in the K1SF simplification.

fectly matches the “trivial” analytic continuation from KF to MF, $-\frac{1}{\pi} \int d\nu' \frac{\Sigma''(\nu')}{i\nu - \nu'}$, see Fig. 3. Hence, we conclude that the Keldysh self-energy did not acquire artifacts during the real-frequency self-consistent parquet iteration. Instead, the deformations are a deficiency of the PA solution at $u = 1$,

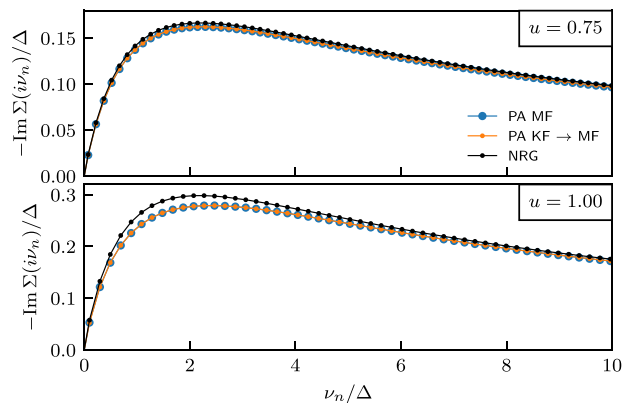


FIG. 3. Imaginary part of the Matsubara self-energy in NRG and the PA. The PA results stem from an independent solver implemented in the MF and from the “trivial” analytic continuation of Σ'' obtained in the KF. The *qualitative* difference between NRG and PA observed in the real-frequency results of Fig. 2 at $u = 1$ can hardly be guessed from these imaginary-frequency results.

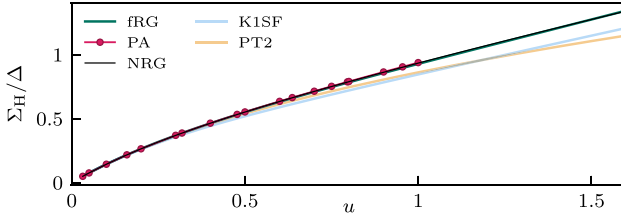


FIG. 4. Hartree self-energy $\Sigma_H = U\langle n_\sigma \rangle$ in the aAM. PT2 corresponds to self-consistent solutions of the Hartree term. Only fRG and PA agree well with NRG.

which are obvious in our Keldysh results, but could not have been guessed from the more benign Matsubara self-energy (Fig. 3).

We also observe from Fig. 2 that the PT2 results become much worse as soon as one leaves the special case of particle-hole symmetry (see Sec. II E). The results from fRG with full frequency dependence are better than those from K1SF, showing that the frequency dependence of Σ is only generated correctly if the dependence of the 4p vertex on its three frequencies is kept [39]. In fact, for large u in the aAM, the K1SF result becomes *negative* (with values on the order of 10^{-5}) at around $\nu/\Delta \simeq \pm 2$, thus failing the previously mentioned consistency check.

The inadequacies of a constant vertex manifest themselves even in the constant Hartree part of the self-energy, $\Sigma_H = U\langle n_\sigma \rangle$, shown in Fig. 4. The fRG and PA calculations produce the NRG value almost exactly, but the K1SF curve starts to deviate early. We attribute this to the fact that diagrammatic contributions beyond the K_1 level are neglected, introducing an error of $O(U^3)$ into the flow of Σ , including Σ_H , see Eq. (E5). The PT2 curve shows the converged values obtained from self-consistent evaluations of the Hartree diagram (see Appendix E), which enters the Hartree propagator used in all PT2 computations. The self-consistency is likely the reason why PT2 performs better than K1SF (which does not obey such a self-consistency) for small and intermediate u .

Apart from \tilde{A} and $\tilde{\Sigma}$, other dynamical quantities of interest are susceptibilities. In the diagrammatic methods, these are derived directly from the 4p vertex (see Appendix C). We consider the imaginary part of the retarded magnetic and density dynamical susceptibilities $\tilde{\chi}_{m/d}(\omega) \equiv \pi \Delta \chi_{m/d}(\omega)$, paying special attention to the peak position and height. The peak position of $\tilde{\chi}_m$ shown in Fig. 5 is proportional to the Kondo temperature and decreases with increasing u in the sAM. All methods apart from K1SF produce good results at small u with only minor deviations from NRG. The deviations are smallest in PA from small to intermediate u , until the PA results are no longer available at large u . fRG produces reasonable curves but, at large u , under- or overestimates the peak in the sAM and aAM, respectively. K1SF does not produce sensible results for any u considered, while PT2 performs well for the aAM but yields worse results than fRG in the sAM.

The density susceptibility shown in Fig. 6 is centered at larger frequencies and has smaller magnitude than its magnetic counterpart. Indeed, while $\tilde{\chi}_m$ and $\tilde{\chi}_d$ are equal at $u = 0$, increasing interaction values discriminate between spin fluctuations

(enhanced) and charge fluctuations (reduced). Here, fRG and the PA both produce acceptable results. However, the PA data at intermediate u and in the sAM show a deformation around $\omega/\Delta \simeq 5$, reminiscent of the deformation in Σ'' (cf. Fig. 2). The K1SF curve for $\tilde{\chi}_d$ (as for $\tilde{\chi}_m$) is not sensible, this time lying far above (rather than below) the NRG curve. PT2 for χ_d , differently from χ_m , is unreliable, yielding a qualitatively wrong double-peak structure.

In summary, we find that the PA results generically reproduce the NRG benchmark best, but are available only up to intermediate u . Our new fRG computations with the full frequency dependence of the vertex drastically improve upon the K1SF results in almost every case, but become quantitatively off with increasing u .

B. Static properties

We now turn to static quantities, obtained from Σ and Γ by setting all frequency arguments to zero. Although these can also be obtained using the imaginary-frequency MF (see Ref. [100] for an early MF fRG treatment of the AM), they serve as important consistency checks for our Keldysh computations. The zero-frequency fermion objects can be used for an effective low-energy description, and, by rescaling, converted to quasiparticle parameters as in Hewson's renormalized perturbation theory [101]. For the AM in the wide-band limit at $T = 0$, the static fermionic quantities can also be deduced from the static susceptibilities. We hence consider the static magnetic and charge susceptibilities as well, before analyzing the zero-temperature identities in the next section.

By virtue of the Δ flow, see Sec. II D, a single fRG computation suffices to obtain the *entire* dependence of, e.g., $Z(u)$ (at fixed T/U). By contrast, the PA requires separate computations for every value of u , resulting in a significantly bigger numerical effort. The top row of Fig. 7 shows the quasiparticle weight

$$Z = (1 - \partial_\nu \Sigma' |_{\nu=0})^{-1}, \quad (30)$$

as extracted from the slope at $\nu = 0$ of the real part of the retarded self-energy, Σ' . In all cases, the PA reproduces the NRG benchmark best, but is again only available up to $u \lesssim 1$. The fRG curve follows NRG for small u but starts to deviate already at intermediate u . K1SF performs very well in the sAM, but deviates from NRG in the aAM earlier than fRG. Since PT2 reproduces the NRG full self-energy very well for the sAM (cf. Fig. 2), the same applies to Z . In the aAM, PT2 also produces reasonable results for Z , in contrast with $\Sigma''(\nu)$ in Fig. 2.

The second row of Fig. 7 displays the scattering rate $-\Sigma''(0)$ on a logarithmic scale. In the sAM, all methods agree reasonably well up to intermediate u . Beyond that, fRG significantly overestimates $-\Sigma''(0)$ (cf. Fig. 2). In the aAM, the fRG results are slightly better. The PA yields the best agreement with NRG, except for $u \simeq 1$ in the aAM where numerical artifacts appear. K1SF shows large deviations early on, matching the observations in Fig. 2. PT2 reproduces NRG almost exactly, even though this is not the case for $\Sigma''(\nu)$ (Fig. 2) in the aAM.

The last row of Fig. 7 shows the effective interaction. The PA accurately reproduces the NRG results. In striking

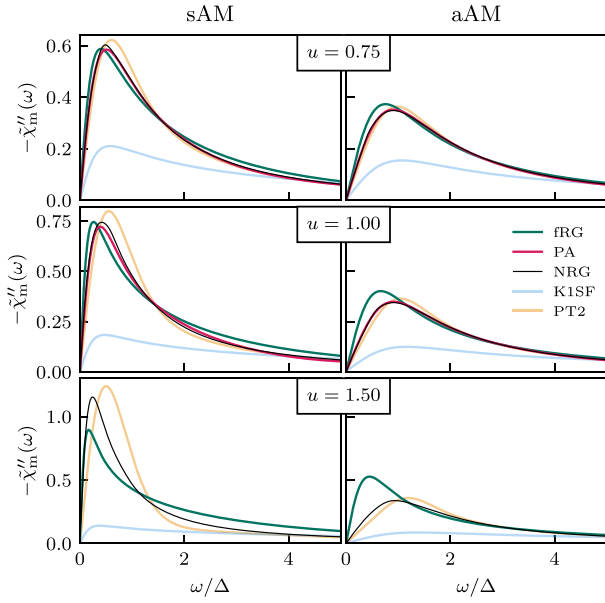


FIG. 5. Imaginary part of the dynamical magnetic susceptibility, $\tilde{\chi}_m(\omega) \equiv \pi \Delta \chi_m(\omega)$. At small to intermediate u , all methods (except K1SF) produce good results, while PA matches NRG best. Toward large u , fRG does not capture the peak correctly. PT2 performs well for the aAM but not the sAM; K1SF is off in all cases.

ing contrast, fRG overestimates the effective interaction very strongly. (This can also be seen in Fig. 11 below, third row, columns four to six, where the frequency-dependent vertex is plotted.) PT2 and K1SF yield only very weak renormalizations of the bare vertex (none at all in PT2 in the sAM).

Figure 8 shows the static magnetic and density susceptibilities,

$$\chi_m = \frac{1}{4} \partial_h \langle \tilde{n}_\uparrow - \tilde{n}_\downarrow \rangle |_{h=0}, \quad \chi_d = \frac{1}{4} \partial_{\epsilon_d} \langle \tilde{n}_\uparrow + \tilde{n}_\downarrow \rangle, \quad (31)$$

where $\tilde{n}_\sigma = n_\sigma - \langle n_\sigma \rangle$. Again, the PA results, where available, reproduce the NRG benchmark best. The fRG results are reasonable up to intermediate u for $\tilde{\chi}'_{m/d}(0) = \pi \Delta \chi_{m/d}$. A comparison with the results obtained by an independent MF computation (dashed lines in Fig. 8) reveals that the KF data at the largest u values is not fully converged in the size of the frequency grid (see Appendix I for details). As for the dynamical susceptibilities, K1SF does not produce sensible results at all. PT2 gives fairly good results, in particular for $\tilde{\chi}'_m$ in the aAM (see also Fig. 5), but $\tilde{\chi}'_d$ in the sAM quickly deviates from NRG rather strongly (as it did in Fig. 6).

In summary, for all the static properties shown in Figs. 7 and 8, the PA results agree very well with NRG for all u for which the parquet solver converged, i.e., up to $u \lesssim 1$. By contrast, fRG results begin to deviate from NRG somewhat earlier than PA, sometimes even much earlier. This difference is most striking for the effective interaction in the bottom panels of Figs. 7, where the performance of fRG is surprisingly (even shockingly) poor.

This comparatively poor performance of fRG may be due in part to the well-known fact that one-loop fRG results de-

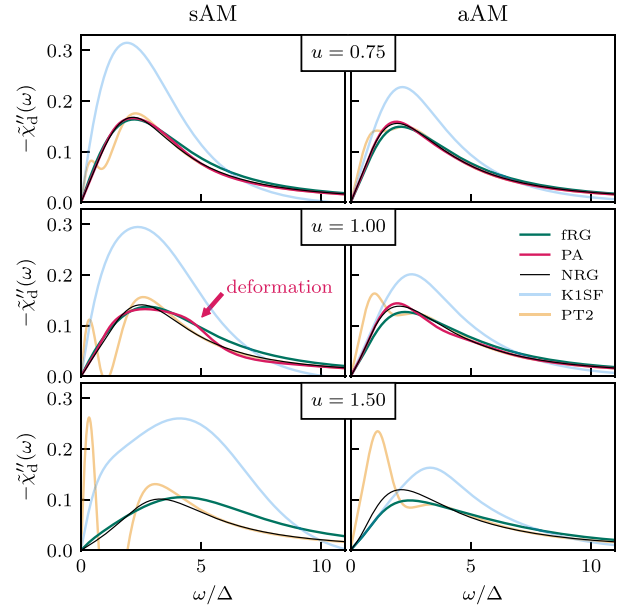


FIG. 6. Imaginary part of the dynamical density susceptibility, $\tilde{\chi}_d(\omega) \equiv \pi \Delta \chi_d(\omega)$. Both fRG and the PA produce good results. The artifact in the PA solution at $u = 1$ in the sAM observed in Fig. 2 is also seen here, while it was not apparent in Fig. 5. Neither PT2 nor K1SF produce sensible results for $\tilde{\chi}_d$.

pend on the choice of the fRG regulator. Figure 9 illustrates this in the present context by comparing our KF results with independent calculations in the MF. For the latter, we used

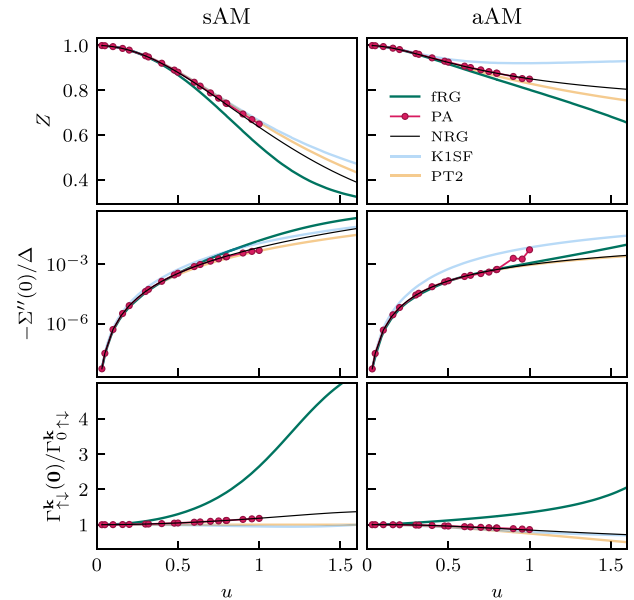


FIG. 7. Static fermionic properties as a function of u : quasiparticle weight Z , scattering rate $-\Sigma''(0)$ on a logarithmic scale, and effective interaction ($k = 12|22$) in units of the bare interaction. Overall, the PA (available for $u \lesssim 1$) matches NRG best, except for $\Sigma''(0)$ at $u \simeq 1$ in the aAM. All other methods agree reasonably well (except for Z and $\Sigma''(0)$ in the aAM in K1SF). Strikingly, fRG strongly overestimates the effective interaction.

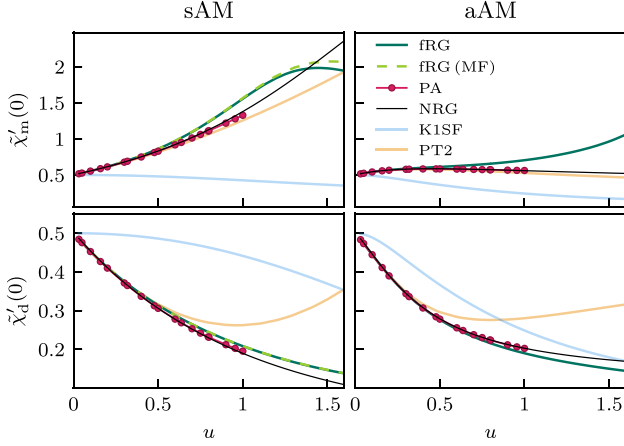


FIG. 8. Static susceptibilities as a function of u . fRG yields sensible results until $\tilde{\chi}'_m$ has a maximum at $u \approx 1.3$. PA data are available only for $u \lesssim 1$, but show excellent agreement with NRG there. Results from K1SF and PT2 (for $\tilde{\chi}'_d$) are rather bad.

three different regulators, called Δ flow (same as for our KF computations), U flow, and ω flow. [See Eqs. (3) and (4) in Ref. [64] for definitions of the U and ω flow. The ω and U flows require many more separate computations than the Δ flow, since the former two hold T/Δ fixed (the ω flow also T/U), while the latter holds T/U fixed.] From Fig. 9, we note three salient points. First, the MF and KF results for the Δ flow match. This is expected for numerically converged calculations and serves as a useful consistency check. Second, the U flow deviates from the NRG benchmark very early. Third, the best MF result is obtained from the ω flow (similarly as observed in Ref. [64]). Regrettably, though, this advantage of the MF ω flow is not relevant for the KF: there, the ω flow would violate causality [54] and hence cannot be used. This, and the poor performance of the U flow, is the reason why we chose the Δ flow for all our KF computations.

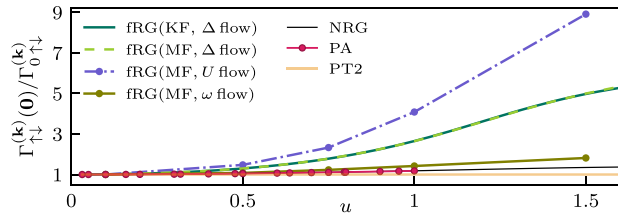


FIG. 9. Effective interaction ($\mathbf{k}=12|22$) of the sAM in units of the bare interaction, including fRG results in the MF obtained with three different regulators. The MF result in the Δ flow perfectly matches its KF counterpart. The U flow performs considerably worse, as it quickly deviates from NRG. By far the best result is obtained using the ω flow, which can however not be used in the KF (see the main text for details). In the MF, we approximate vanishing frequencies by averaging over the lowest Matsubara frequencies, $\gamma_r(\mathbf{0}) \approx \frac{1}{4} \sum_{\nu, \nu'=\pm\pi T} \gamma_r(0, \nu, \nu')$.

C. Zero-temperature identities

As an internal consistency check for each method, we consider four Fermi-liquid identities. These hold $T = 0$ and, more generally, at $T \ll T_K$, where T_K is the Kondo temperature. We deduce T_K as $T_K = 1/[4\chi'_m(0)]|_{T=0}$ [see, e.g., Eq. (20) in Ref. [102]] from zero-temperature NRG calculations. The resulting values for $u \in \{0.75, 1, 1.5\}$ are $T_K/U \in \{0.31, 0.18, 0.07\}$ for the sAM and $T_K/U \in \{0.58, 0.45, 0.32\}$ for the aAM. Note that the Kondo regime of the sAM corresponds to $u \gtrsim 2$ [101].

First, for a constant hybridization function in the wide-band limit, we have the following two ‘‘Yamada–Yosida (YY) identities’’ generalized to arbitrary ϵ_d [see Eq. (6.1) in Ref. [95] and Eq. (7) in Ref. [97], Eqs. (24)–(25) in Ref. [101], or Eqs. (4.30)–(4.33) in Ref. [103]]:

$$Z^{-1} = [\chi_m(0) + \chi_d(0)]/\rho(0), \quad (32a)$$

$$-\rho(0)\Gamma_{\uparrow\downarrow}(\mathbf{0}) = [\chi_m(0) - \chi_d(0)]/\rho(0). \quad (32b)$$

Here, $\rho(0) \equiv A(0)|_{T=0}$ is the spectral function evaluated at $\nu = 0$ and $T = 0$,

$$\begin{aligned} \rho(0) &= \frac{1}{\pi} \frac{\Delta}{[\epsilon_d + \Sigma'(0)]^2 + \Delta^2} \\ &= \frac{1}{\pi \Delta} \begin{cases} 1 & \text{for } \epsilon_d = -U/2 \\ \frac{1}{1 + [\Sigma'(0)/\Delta]^2} & \text{for } \epsilon_d = 0. \end{cases} \end{aligned} \quad (33)$$

Next, $\Gamma_{\uparrow\downarrow}(\mathbf{0})$ is the full Matsubara 4p vertex evaluated at vanishing frequencies (in the zero-temperature limit). The minus sign in Eq. (32b) stems from our convention of identifying, e.g., the bare Matsubara vertex $\Gamma_{0,\uparrow\downarrow}$ with $-U$. The analytic continuation of ℓ p functions between Matsubara and retarded Keldysh components involves a factor $2^{\ell/2-1}$ [see Eq. (69) in Ref. [34]]. Hence,

$$\Gamma_{\uparrow\downarrow}(\mathbf{0}) = 2\Gamma_{\uparrow\downarrow}^k(\mathbf{0}),$$

$$\mathbf{k} \in \{(12|22), (21|22), (22|12), (22|21)\}. \quad (34)$$

Another identity derived by YY [see Eqs. (13)–(15) and (18) in Ref. [97], Eqs. (31) and (34) in Ref. [101], or Eq. (4.37) in Ref. [103]] implies

$$-\Sigma''(\nu) = \frac{1}{2}\pi\rho(0)^3[\Gamma_{\uparrow\downarrow}(\mathbf{0})]^2(\nu^2 + \pi^2T^2) \quad (35)$$

for $|\nu|, T \ll T_K$. We check this relation by fitting $\Sigma'' \propto (\nu^2 + \pi^2T^2)$. Finally, the Korrington–Shiba (KS) identity [see Eq. (1.4) in Ref. [104]] reads

$$\lim_{\omega \rightarrow 0} \chi''_m(\omega)/\omega = 2\pi[\chi'_m(0)]^2. \quad (36)$$

To check the fulfillment of these identities, we analyze the relative difference $2(\text{LHS} - \text{RHS})/(\text{LHS} + \text{RHS})$ [LHS (RHS) = left- (right-) hand side] of Eqs. (32a), (32b), (35), (36), referred to as YY1, YY2, YY3, KS, respectively. These zero-temperature identities of the AM only hold if $T \ll T_K$. As we keep $T/U = 0.01$ constant, the temperatures increase with u , and $T \ll T_K$ is no longer fulfilled for $u \gtrsim 1$ in the sAM. Accordingly, there, the identities are violated even in NRG.

As can be seen in Fig. 10, the PA fulfills most identities very well (below 8% throughout), but is again available only up to $u \simeq 1$. The fRG results obey YY1 up to $u \lesssim 1$, but show clear deviations in all other identities, setting in already for

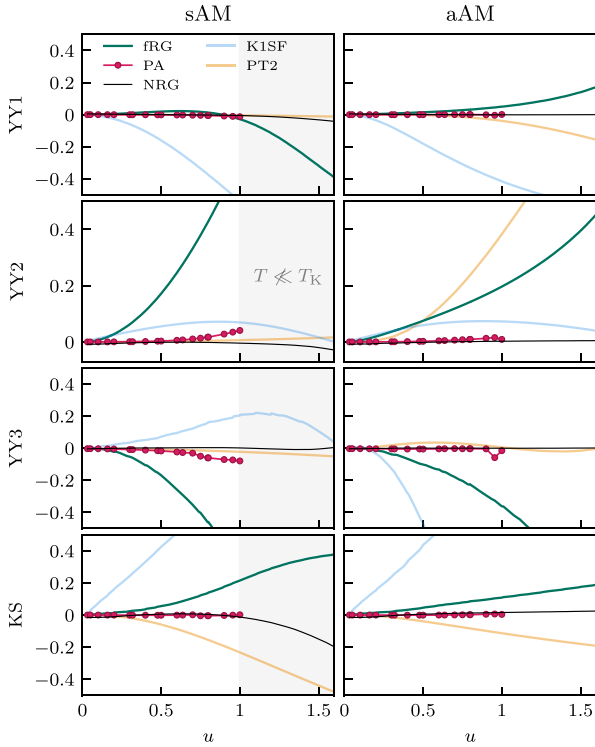


FIG. 10. Relative difference between the left- and right-hand sides of the four zero-temperature identities as a function of u . All calculations have finite $T/U = 0.01$; thus, even NRG violates the identities if $T \ll T_K$ is no longer fulfilled. Apart from NRG, the PA shows the smallest violations of these identities (below 8% throughout), but is only available for $u \lesssim 1$. The fRG data fulfill YY1 relatively well, but show clear deviations otherwise, setting in already for very small values of u . For YY2, e.g., the deviations become significant already at $u \gtrsim 0.25$. PT2 obeys the identities (except KS) in the sAM but not the aAM. K1SF shows major deviations throughout.

very small values of u . Except for the KS relation in the fourth row, PT2 mostly fulfills the identities for the sAM but less so for the aAM, while K1SF shows major deviations, even for small u .

D. Frequency dependence of the 4p vertex

Finally, we show fRG and PA results for the frequency dependence of the 4p vertex in the sAM and compare them to corresponding results from NRG. We restrict ourselves to a fully retarded Keldysh component [34] and show both the same-spin ($\uparrow\uparrow$) and the opposite-spin ($\uparrow\downarrow$) components. We plot the vertex in the two-dimensional frequency plane ($\omega_t = 0$, $\nu_t = \nu$, $\nu'_t = \nu'$) in the natural parametrization of the t channel for zero transfer frequency. Physically, this corresponds to the effective interaction of two electrons on the impurity with equal or opposite spins, respectively, and energies ν , ν' without energy transfer [69]. The NRG 4p results are computed with the scheme introduced in Refs. [34,35], utilizing the symmetric improved estimator of Ref. [105].

In Fig. 11, we compare results from fRG, the PA, and NRG for two values of the interaction $u \in \{0.5, 1\}$. We observe good

qualitative agreement throughout, as all methods capture all nontrivial features. At $u = 1$, however, we observe a qualitative discrepancy in the data: $\text{Re}\Gamma_{\uparrow\downarrow}^k$ is strictly positive in fRG and slightly negative in NRG (bottom part, top row, first panel from the right in Fig. 11). The PA result reaches even larger negative values and retains them for a large range of ν values. This strong negative signal appears to be an artifact of the PA; it would likely be canceled by additional contributions missed in the PA.

IV. CONCLUSIONS AND OUTLOOK

In this work, we have shown that real-frequency QFT calculations with full frequency resolution of the 4p vertex *are* feasible. We chose the AM for a proof-of-principle study and employed one-loop fRG flows and solutions of the parquet equations in the PA, benchmarked against NRG. We compared dynamical correlation functions as well as characteristic static quantities and performed a detailed numerical check of zero-temperature identities. We found that keeping the full frequency dependence of the 4p vertex in fRG strongly improves the accuracy compared with previous implementations using functions with at most one-dimensional frequency dependencies. Note that the present study is performed at finite temperature, $T/U = 0.01$, in contrast with previous work on spectral functions at $T = 0$ [55].

The numerical challenges imposed by the fully parametrized real-frequency 4p vertex were overcome via a suitably adapted frequency grid, vectorization over the Keldysh matrix structure, and a parallelized evaluation of the fRG or parquet equations (see Appendix G). We employed frequency grids with up to 125^3 data points, and our most expensive calculation consumed about 25 000 CPU hours for a single data point in the PA.

The PA results could be converged only for $u = U/(\pi\Delta)$ in the range $u \lesssim 1$, but there gave the best agreement with NRG (except at the boundary of the accessible u range). The PA also gave very good results for the effective interaction. However, by looking at $\Gamma_{\uparrow\downarrow}^k$ in a frequency range around the origin, it appears that the mechanism by which the PA achieves low values of $|\Gamma_{\uparrow\downarrow}^k(\mathbf{0})|$ (compared with, say, fRG) is different from that of NRG, as the PA data have a spuriously large regime of strongly negative values in $\text{Re}\Gamma_{\uparrow\downarrow}^k$.

The fRG calculations in the present context were comparatively economical, since a single run with the “ Δ flow” yields an entire parameter sweep in Δ . The flow could be followed to large values of u , well beyond 1, i.e., far beyond the regime where we could converge the PA. However, for $u \gtrsim 0.5$ these one-loop fRG results are significantly less accurate than the PA (as compared with NRG). Strikingly, fRG strongly overestimates the effective interaction $\Gamma_{\uparrow\downarrow}^k(\mathbf{0})$ by factors of three to four for u in the range 1 to 1.5. We compared the Keldysh to Matsubara fRG data obtained using three different regulators, and we found that, for $u > 0.5$, the latter strongly depend on the choice of regulator: For the Δ flow, the Matsubara results agree with the Keldysh results, while performing better than the U flow but worse than the ω flow. Regrettably, the ω flow is not available in the KF, where it violates causality. It would hence be worthwhile to find Keldysh fRG regulators akin to the ω flow but compatible with the KF requirements regarding causality and FDTs [54].

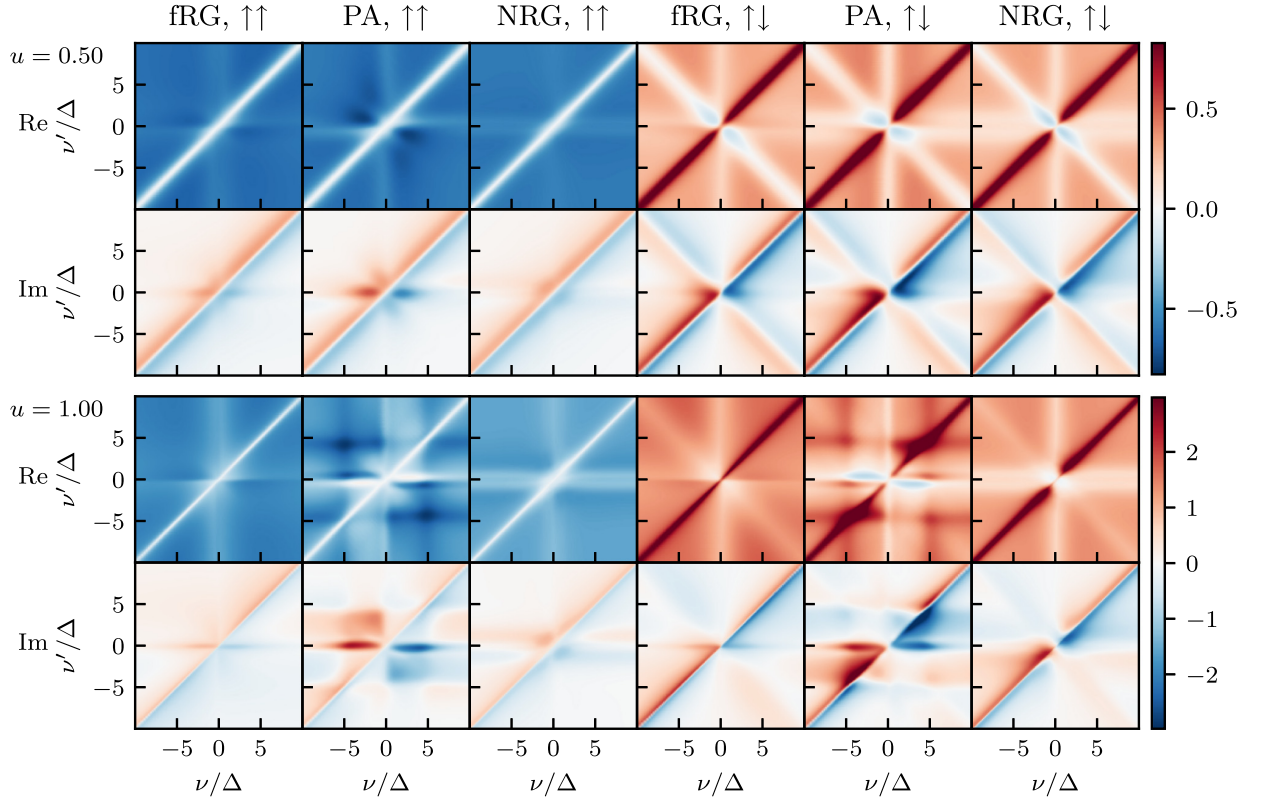


FIG. 11. Fully retarded ($k = 12|22$) Keldysh component of the full vertex, $[\Gamma_{\sigma\sigma'}^k(\omega_l = 0, \nu_l = \nu, \nu_l' = \nu') - \Gamma_{0,\sigma\sigma'}^k]/\Gamma_{0\uparrow\downarrow}^k$, for $u = 0.5$ (top panel) and $u = 1$ (bottom), computed using fRG, PA, and NRG (following Refs. [34,35]). We observe very good agreement for $u = 0.5$, which, qualitatively, mostly persists for higher interaction. However, $\text{Re}\Gamma_{\uparrow\downarrow}$ at $u = 1$ and low frequencies differs significantly between the methods: it is strictly positive in fRG, slightly negative in NRG, but much more strongly negative up to fairly large values of ν in the PA. Generally, the PA shows more complicated features than NRG for larger u , despite being numerically converged, indicating the breakdown of the PA.

The regulator dependence in fRG can be eliminated in the multiloop fRG framework, yielding results equivalent to the PA upon convergence in the number of loops [61–63]. This has been demonstrated numerically in imaginary frequencies for the AM [64] (and in Refs. [71,72] for the Hubbard model). Yet, using a multiloop extension of our Keldysh fRG code, we found the computation of multiloop contributions considerably harder for Keldysh vertices than for Matsubara vertices. The reason seems to be that, for real-frequency Keldysh vertices, the higher-loop contributions for increasing u show a considerably more complicated frequency structure than the original fRG vertex itself (similarly to how the PA vertex has more structure than its fRG counterpart in the bottom panel of Fig. 11). A more detailed analysis along these lines is, however, left for future work.

Our work paves the way for many follow-up studies. For instance, one can exploit the power of the KF to study nonequilibrium phenomena, and the AM with a finite bias voltage is tractable with only minor increase in the numerical costs [55,106]. Furthermore, we here considered moderate interaction strengths $u \lesssim 1.5$ because it is known that fRG and the PA are unable to access the nonperturbative regime of the AM [20,64] or, e.g., the Hubbard model [72,107]. An important future direction is, therefore, to use these methods

in a more indirect manner, as real-frequency diagrammatic extensions [41] of dynamical mean-field theory [42]. The first, established building block for this is the nonperturbative input, namely, 2p and 4p vertices, from NRG [34,35]. The present work presents another building block: real-frequency QFT with full frequency resolution of the 4p vertex. An important next step will be to use our diagrammatic framework to study the consistency of the NRG results for the 2p and 4p vertices, e.g., by checking whether they fulfill the SDE. The final building block will then be to include momentum degrees of freedom in real-frequency QFT approaches built on top of NRG.

Keeping track of the momentum dependence will lead to a major increase in numerical complexity. This can be addressed using economical implementations and compression algorithms such as truncated-unity approaches [108–111] or the new quantics tensor cross interpolation scheme [7,33,77]. The latter can be used to obtain highly compressed tensor network representations of multidimensional functions, potentially leading to exponential reductions in computational costs. First investigations have shown that the objects encountered in diagrammatic many-body approaches may indeed have strongly compressible quantics representations [7].

All raw data required to reproduce the plots as well as the full data analysis and the plotting scripts are available online

[112]. A separate publication of the fully documented source code used to generate the raw data is in preparation.

ACKNOWLEDGMENTS

We thank Jeongmin Shim and Seung-Sup B. Lee for providing data of the NRG 4p vertex as well as Severin Jakobs for a careful reading of the paper. The numerical simulations were performed on the Linux clusters and the SuperMUC cluster (project 23769) at the Leibniz Supercomputing Center in Munich. N.R. acknowledges funding from a graduate scholarship from the German Academic Scholarship Foundation (Studienstiftung des deutschen Volkes) and additional support from the ‘‘Marianne-Plehn-Programm’’ of the state of Bavaria. A.G. and J.v.D. were supported by the Deutsche Forschungsgemeinschaft under Germany’s Excellence Strategy EXC-2111 (Project No. 390814868), and the Munich Quantum Valley, supported by the Bavarian state government with funds from the Hightech Agenda Bayern Plus. F.B.K. acknowledges support by the Alexander von Humboldt Foundation through the Feodor Lynen Fellowship. The Flatiron Institute is a division of the Simons Foundation.

APPENDIX A: THE TWO-PARTICLE VERTEX

In compact notation, we denote the vertex by $\Gamma_{1'2'|12}$ where each leg carries a multi-index $i = (k_i, \sigma_i, \nu_i)$ with Keldysh index k_i , spin σ_i , and fermionic frequency ν_i . Generic symmetries of the full Keldysh vertex are derived in Ref. [56] and other symmetries (such as spin or particle-hole symmetry) are given in Ref. [113]. In the following, we recap these symmetries and detail the parametrization in our implementation. First, we work with Keldysh indices rather than contour indices. In this basis, the $11 \cdots 1$ ($22 \cdots 2$) component of a multipoint correlator (vertex) vanishes [56]. This simplifies, e.g., the Dyson equation, $G^R = [(G_0^R)^{-1} - \Sigma^R]^{-1}$ and implies $\Gamma^{22|22} = 0$. Furthermore, crossing symmetry gives

$$\Gamma_{1'2'|12} = -\Gamma_{2'1'|12} = -\Gamma_{1'2'|21} = \Gamma_{2'1'|21}, \quad (\text{A1})$$

and complex conjugation

$$\Gamma_{1'2'|12} = (-1)^{1+\sum_i k_i} \Gamma_{12|1'2'}^* \quad (\text{A2})$$

Thermal equilibrium entails (generalized) fluctuation-dissipation relations between different Keldysh components. However, we choose to vectorize the code over Keldysh components and thus do not use these relations (see Appendix G for details on the vectorization). For a comprehensive list of multipoint fluctuation-dissipation relations, we refer to Refs. [56,114,115]. They are very well fulfilled (percent level) by our numerical results.

In the absence of a magnetic field, spin conservation and the invariance under a global spin flip reduce the number of independent spin components. The remaining components are related by the SU(2) relation [113]

$$\Gamma_{\sigma\sigma|\sigma\sigma} = \Gamma_{\sigma\bar{\sigma}|\sigma\bar{\sigma}} + \Gamma_{\sigma\bar{\sigma}|\bar{\sigma}\sigma}, \quad (\text{A3})$$

where $\bar{\uparrow} = \downarrow$ and vice versa. Hence, the spin dependence of the vertex can be parametrized by

$$\Gamma_{\sigma'_1\sigma'_2|\sigma_1\sigma_2} = \Gamma_{\uparrow\downarrow}\delta_{\sigma'_1,\sigma_1}\delta_{\sigma'_2,\sigma_2} + \Gamma_{\uparrow\downarrow}\delta_{\sigma'_1,\sigma_2}\delta_{\sigma'_2,\sigma_1}. \quad (\text{A4})$$

The components on the right-hand side are related by crossing symmetry. It thus suffices to compute a single one of them. At particle-hole symmetry, we further have

$$\begin{aligned} \Gamma_{1'2'|12}(\nu'_1, \nu'_2| \nu_1, \nu_2) &= \Gamma_{12|1'2'}(-\nu_1, -\nu_2| -\nu'_1, -\nu'_2) \\ &\stackrel{(\text{A2})}{=} (-1)^{1+\sum_i k_i} \Gamma_{1'2'|12}(-\nu'_1, -\nu'_2| -\nu_1, -\nu_2)^*, \end{aligned} \quad (\text{A5})$$

with the multi-indices $i = (k_i, \sigma_i)$, reducing the number of independent frequency components even more.

By frequency conservation, $\nu'_1 + \nu'_2 = \nu_1 + \nu_2$, the vertex depends on only three independent frequencies. These are chosen differently for each two-particle reducible vertex γ_r (see Fig. 12), with the bosonic transfer frequency ω_r and the fermionic frequencies ν_r and ν'_r . The vertices γ_r have nontrivial asymptotics in the limits $\nu_r^{(\prime)} \rightarrow \infty$. One can decompose the reducible vertex γ_r in asymptotic classes, see Eq. (29) [2]. Since the bare interaction is frequency independent, the asymptotic classes K_{ir} can be identified with certain diagrams that are reducible in channel r [2,73]. Connecting two external legs to the same bare interaction vertex reduces the dependence by one external frequency argument. $K_{1r}(\omega_r)$ consists of all diagrams where the two external legs carrying frequency ν_r connect to the same bare vertex and the external legs carrying ν'_r connect to another one. Hence, K_{1r} only depends on ω_r . $K_{2r}(\omega_r, \nu_r)$ consists of all diagrams where the ν'_r legs connect to the same bare vertex while each of the other two legs connect to different bare vertices. $K_{2'r}(\omega_r, \nu'_r)$ is analogous to K_{2r} with the roles of ν_r and ν'_r interchanged. For $K_{3r}(\omega_r, \nu_r, \nu'_r)$ all external legs connect to different bare vertices. The bare vertices simplify not only the dependence of K_1, K_2 , and $K_{2'}$ on frequencies but also on Keldysh indices. If a bare vertex connects to two external legs, flipping their Keldysh indices, $\bar{1} = 2$ ($\bar{2} = 1$), leaves the function invariant, see Eq. (17). This gives, e.g.,

$$\begin{aligned} K_{1p}^{k_1 k_2 | k_1 k_2} &= K_{1p}^{\bar{k}_1 \bar{k}_2 | k_1 k_2} = K_{1p}^{k_1 k_2 | \bar{k}_1 \bar{k}_2} \\ &= K_{1p}^{\bar{k}_1 \bar{k}_2 | \bar{k}_1 \bar{k}_2}, \end{aligned} \quad (\text{A6a})$$

$$K_{2p, \sigma_1 \sigma_2 | \sigma_1 \sigma_2}^{k_1 k_2 | k_1 k_2} = K_{2p, \sigma_1 \sigma_2 | \sigma_1 \sigma_2}^{k_1 k_2 | \bar{k}_1 \bar{k}_2}. \quad (\text{A6b})$$

Note that the diagrammatic channels a and t flip under crossing symmetry, i.e., $\gamma_{a,1'2'|12} = -\gamma_{t,1'2'|21}$, while channel p is crossing symmetric itself. The symmetry relations in Eqs. (A1)–(A5) are formulated for full vertices. They can be adapted to the asymptotic classes K_{ir} by inserting the decomposition on both sides of each relation and taking the appropriate limits $\nu_r^{(\prime)} \rightarrow \infty$. For instance, $K_{\uparrow\downarrow,2p}$ is related to $K_{\uparrow\downarrow,2p}$ by

$$K_{\uparrow\downarrow,2p}^{k_1 k_2 | k_1 k_2}(\omega_p, \nu'_p) \stackrel{(\text{A2})}{=} (-1)^{1+\sum_i k_i} K_{\uparrow\downarrow,2p}^{k_1 k_2 | k_1 k_2}(\omega_p, \nu'_p). \quad (\text{A7})$$

For a formulation of the parquet and fRG equations in terms of asymptotic classes, we refer to Ref. [2] and to Eqs. (75) in Ref. [75].

As we vectorize over Keldysh indices, we explicitly keep track of all Keldysh components. The symmetry relations are then used to reduce the spin and frequency components [Eqs. (A1), (A2), and (A5) for $\Gamma_{\uparrow\downarrow}$]. To implement these symmetries for the K_{3r} class, it is convenient to express the

FIG. 12. We show the frequency conventions for the two-particle reducible vertices γ_r with $r = a, p, t$. Symmetric parametrizations with $\pm \frac{\omega}{2}$ ensure that vertex structures are centered around the frequency axis. The irreducible vertex R is shown in bosonic frequencies for completeness.

relations in terms of the three bosonic frequencies [100], giving

$$\begin{aligned} \Gamma_{\uparrow\downarrow; \omega_a, \omega_p, \omega_t}^{k_1 k_2' | k_1 k_2'} &\stackrel{(A2)}{=} [\Gamma_{\uparrow\downarrow; \omega_a, \omega_p, -\omega_t}^{k_1 k_2 | k_1' k_2'}]^* (-1)^{1+\sum_i k_i}, \\ &\stackrel{(A1)}{=} \Gamma_{\uparrow\downarrow; -\omega_a, \omega_p, -\omega_t}^{k_2 k_1' | k_2 k_1} \stackrel{(A5)}{=} [\Gamma_{\uparrow\downarrow; -\omega_a, -\omega_p, -\omega_t}^{k_1' k_2' | k_1 k_2}]^* (-1)^{1+\sum_i k_i}, \end{aligned} \quad (A8)$$

such that the sign of the bosonic frequencies define sectors that are related by symmetry.

APPENDIX B: FREQUENCY DEPENDENCE OF VERTEX COMPONENTS

Figures 13 and 14 show plots for the frequency dependence of the asymptotic classes K_2 and K_3 for each of the three two-particle channels $r \in \{a, p, t\}$, computed in the PA for $u = 0.5$ and $u = 1$, respectively. We use the natural frequency parametrization for each channel r and set the bosonic transfer frequency $\omega_r = 0$ in the plots for K_3 . The figures instructively show what types of nontrivial structures emerge during such calculations. In particular, one can clearly see that the frequency resolution needs to be very high throughout to resolve all sharp features (many occurring on scales much smaller than Δ). Moreover, the weak-coupling results may serve as benchmarks for future computations of Keldysh vertices using other methods, such as NRG or QMC.

APPENDIX C: FULLY PARAMETRIZED EQUATIONS

We can write the parquet equations (20) and one-loop fRG flow equations (19) entirely in terms of two functions, bubbles and loops. A bubble B_r in channel $r = a, p, t$ combines two vertices via a propagator pair

$$\Pi_{a, \omega_a, \nu_a}^{34|3'4'} = G_{\nu_a - \omega_a/2}^{3|3'} G_{\nu_a + \omega_a/2}^{4|4'}, \quad (C1a)$$

$$\Pi_{p, \omega_p, \nu_p}^{34|3'4'} = G_{\omega_p/2 + \nu_p}^{3|3'} G_{\omega_p/2 - \nu_p}^{4|4'}, \quad (C1b)$$

$$\Pi_{t, \omega_t, \nu_t}^{43|3'4'} = G_{\nu_t - \omega_t/2}^{3|3'} G_{\nu_t + \omega_t/2}^{4|4'}, \quad (C1c)$$

where we use the natural frequency parametrization for each channel (see Fig. 15) and superscripts indicate Keldysh indices $(34|3'4') = (k_3 k_4 | k_3' k_4')$. In the following, we give explicit formulas for the $\uparrow\downarrow$ -spin component of bubble diagrams that combine vertices V and W :

$$B_a[V, W]_{\uparrow\downarrow, \omega_a, \nu_a, \nu_a'}^{1'2'|12} = \int_{\bar{\nu}} V_{\uparrow\downarrow, \omega_a, \nu_a, \bar{\nu}}^{1'4'|32} \Pi_{a, \omega_a, \bar{\nu}}^{34|3'4'} W_{\uparrow\downarrow, \omega_a, \bar{\nu}, \nu_a'}^{3'2'|14}, \quad (C2a)$$

$$B_p[V, W]_{\uparrow\downarrow, \omega_p, \nu_p, \nu_p'}^{1'2'|12} = \int_{\bar{\nu}} V_{\uparrow\downarrow, \omega_p, \nu_p, \bar{\nu}}^{1'2'|34} \Pi_{p, \omega_p, \bar{\nu}}^{34|3'4'} W_{\uparrow\downarrow, \omega_p, \bar{\nu}, \nu_p'}^{3'4'|12}, \quad (C2b)$$

with $\int_{\bar{\nu}} = \int_{-\infty}^{\infty} d\bar{\nu}/2\pi i$ (the internal spin sum and crossing symmetry in B_p cancel the prefactor of $1/2$), and

$$\begin{aligned} B_r[V, W]_{\uparrow\downarrow, \omega_r, \nu_r, \nu_r'}^{1'2'|12} &= - \int_{\bar{\nu}} \Pi_{t, \omega_t, \bar{\nu}}^{43|3'4'} [V_{\uparrow\downarrow, \omega_r, \nu_r, \bar{\nu}}^{4'2'|32} W_{\uparrow\downarrow, \omega_t, \bar{\nu}, \nu_r'}^{1'3'|14} + V_{\uparrow\downarrow, \omega_r, \nu_r, \bar{\nu}}^{4'2'|32} W_{\uparrow\downarrow, \omega_t, \bar{\nu}, \nu_r'}^{1'3'|14}], \end{aligned} \quad (C2c)$$

where the $\uparrow\uparrow$ -spin component is obtained via Eq. (A4).

For the loop, we parametrize the vertex in the t -channel convention with $\omega_t = 0$ and write

$$L[\Gamma, G]_{\bar{\nu}}^{1'1} = - \int_{\bar{\nu}} G_{\bar{\nu}}^{2|2'} [\Gamma_{\uparrow\downarrow} + \Gamma_{\uparrow\uparrow}]_{0, \bar{\nu}, \bar{\nu}}^{1'2'|12}. \quad (C3)$$

Using the loop L and bubbles B_r , the parquet equations (20) read

$$\gamma_r = B_r[L_r, \Gamma], \quad (C4a)$$

$$\Sigma = L[\Gamma_0, G] + \frac{1}{2} L[B_a[\Gamma_0, \Gamma], G]. \quad (C4b)$$

In the SDE, the internal spin sum can be performed, canceling the factor of $1/2$ in Eq. (C4b) by crossing symmetry to give

$$\Sigma_{\text{SDE}, \bar{\nu}}^{1'1} = - \int_{\nu_r} G_{\nu_r}^{2|2'} [\Gamma_{0, \uparrow\downarrow} + B_a[\Gamma_0, \Gamma]_{\uparrow\downarrow, 0, \nu_r, \bar{\nu}}^{1'2'|12}]. \quad (C5)$$

The one-loop fRG flow equations [cf. Eq. (19)] are

$$\dot{\Sigma} = L(\Gamma, S), \quad \dot{\gamma}_r = \dot{B}_r(\Gamma, \Gamma), \quad (C6)$$

where the dot on \dot{B}_r denotes a differentiated propagator pair, $\partial_{\Lambda} \Pi_r = \dot{G}G + G\dot{G}$, including the Katanin substitution $S \rightarrow \dot{G} = S + G\dot{\Sigma}G$ [70].

Susceptibilities are obtained from $G^{(4)}$, Eq. (13), by contracting pairs of external legs and subtracting the disconnected parts [116, 117]. For the spin- $\uparrow\downarrow$ and spin- $\uparrow\uparrow$ components, we get

$$\chi_{a, \sigma\sigma', \omega_a}^{12|1'2'} = \int_{\nu} \Pi_{a, \omega_a, \nu}^{12|1'2'} + \int_{\nu} \int_{\nu'} \Pi_{a, \omega_a, \nu}^{14|1'4'} \Gamma_{\sigma\sigma', \omega_a, \nu\nu'}^{34|3'4'} \Pi_{a, \omega_a, \nu'}^{32|3'2'}, \quad (C7a)$$

$$\begin{aligned} \chi_{p, \sigma\sigma', \omega_p}^{12|1'2'} &= \int_{\nu} \Pi_{p, \omega_p, \nu}^{12|1'2'} (1 - \delta_{\sigma, \sigma'}) \\ &+ \int_{\nu} \int_{\nu'} \Pi_{p, \omega_p, \nu}^{12|3'4'} \Gamma_{\sigma\sigma', \omega_p, \nu\nu'}^{34|3'4'} \Pi_{p, \omega_p, \nu'}^{34|1'2'}, \end{aligned} \quad (C7b)$$

$$\begin{aligned} \chi_{t, \sigma\sigma', \omega_t}^{12|1'2'} &= - \int_{\nu} \Pi_{t, \omega_t, \nu}^{12|1'2'} \delta_{\sigma, \sigma'} \\ &+ \int_{\nu} \int_{\nu'} \Pi_{t, \omega_t, \nu}^{12|3'4'} \Gamma_{\sigma\sigma', \omega_t, \nu\nu'}^{34|3'4'} \Pi_{t, \omega_t, \nu'}^{34|1'2'}. \end{aligned} \quad (C7c)$$

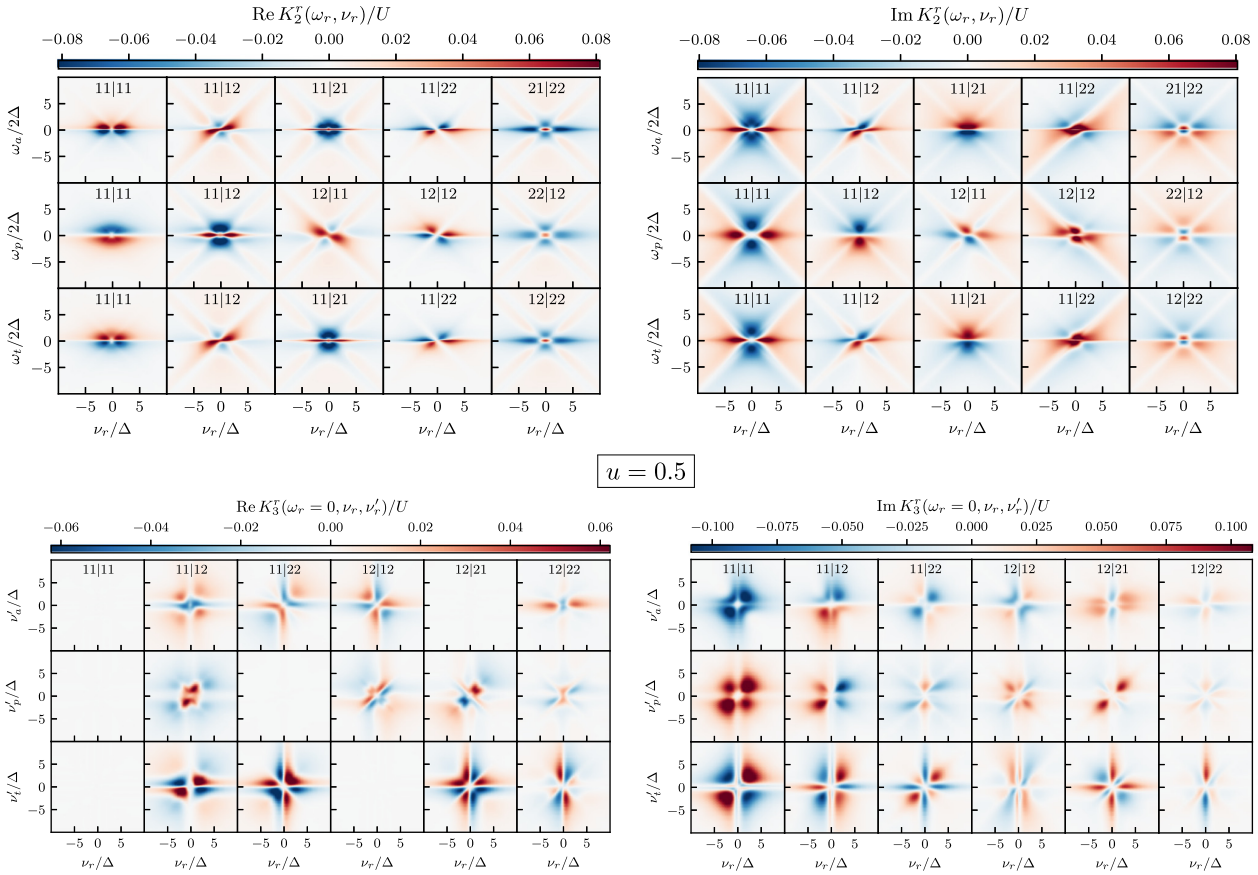


FIG. 13. Real (left) and imaginary (right) parts of K_2 (top) and K_3 (bottom) vertex components in the PA for $u = 0.5$. The three rows of each subfigure show results for the three two-particle channels $r \in \{a, p, t\}$. The columns show all independent Keldysh components. Natural frequency parametrizations were used and for K_3 the bosonic transfer frequency ω_r was set to zero. Consequently, some components of $\text{Re}K_3$ vanish.

From these functions, we obtain physical susceptibilities as $\chi_{d/m} = \chi_{t,\uparrow\uparrow} \pm \chi_{t,\uparrow\downarrow}$, or after exploiting spin and crossing symmetry, Eqs. (A1) and (A3),

$$\chi_d^{12|1'2'} = 2\chi_{t,\uparrow\downarrow}^{12|1'2'} - \chi_{a,\uparrow\downarrow}^{21|1'2'}, \quad (\text{C8a})$$

$$\chi_m^{12|1'2'} = -\chi_{a,\uparrow\downarrow}^{21|1'2'}. \quad (\text{C8b})$$

These functions have the Keldysh structure of 4p functions. To identify the retarded susceptibilities $\chi^R(\omega)$ in terms of 2p functions [analogous to the propagator, Eq. (7)], we use the bare three-leg Hedin vertex $\lambda_0^{(k_1 k_2) k_3}$ [118] where the Keldysh indices k_1, k_2 belong to $\chi^{12|1'2'}$ and k_3 to χ^R . In terms of contour indices, it reads $\lambda_0^{(c_1 c_2) c_3} = -c_1 \delta_{c_1=c_2=c_3}$; in Keldysh indices, the nonzero components are

$$\lambda_0^{(kk)2} = \frac{1}{\sqrt{2}} = \lambda_0^{(k\bar{k})1}. \quad (\text{C9})$$

Hence, two (un-)equal fermionic Keldysh indices translate to a “2” (“1”) for the bosonic line. We thus identify

$$\chi_r^R = \chi_r^{2|1} = 2\chi_r^{11|12}, \quad r = a, p, t. \quad (\text{C10})$$

In the parquet formalism, it was shown that the susceptibilities χ_r ($r \in \{a, p, t\}$) are related to asymptotic functions via [2]

$$(K_{1a})_{1'2'|12} = -(\Gamma_0)_{1'4|32}(\chi_a)_{34|3'4'}(\Gamma_0)_{3'2'|14}, \quad (\text{C11a})$$

$$(K_{1p})_{1'2'|12} = -(\Gamma_0)_{1'2'|34}(\chi_p)_{34|3'4'}(\Gamma_0)_{3'4'|12}, \quad (\text{C11b})$$

$$(K_{1t})_{1'2'|12} = -(\Gamma_0)_{4'2'|42}(\chi_t)_{34|3'4'}(\Gamma_0)_{1'3'|13}. \quad (\text{C11c})$$

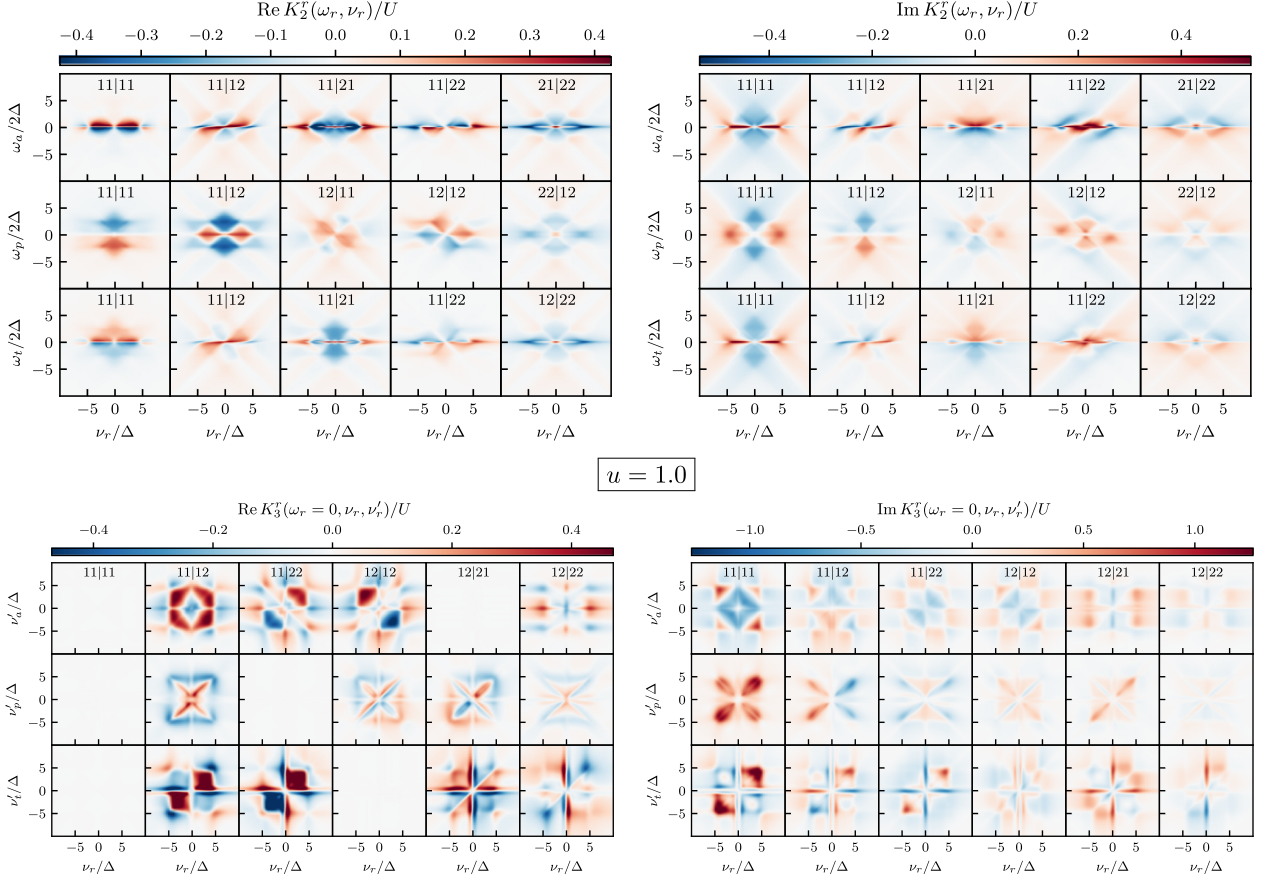
For the retarded spin- $\uparrow\downarrow$ -component, we have

$$K_{1r\uparrow\downarrow}^R = -U^2 \chi_{r\uparrow\downarrow}^R. \quad (\text{C12})$$

Although one-loop fRG does not fulfill the BSEs (20b)–(20d), Eq. (C12) can still be used as an estimate for susceptibilities. In the present context, these are often called “flowing” susceptibilities, while Eq. (C7) defines the “postprocessed” susceptibilities. The PA, fRG, and KISF results for χ_m and χ_d shown in the main text were computed using Eqs. (C11).

APPENDIX D: CHANNEL-ADAPTED SCHWINGER-DYSON EQUATION

In the parquet formalism, the frequency dependence of the self-energy $\Sigma(\nu)$ enters via the second term in the SDE (20a).


 FIG. 14. Same vertex components as in Fig. 13, computed in the PA for $u = 1$.

$$\begin{aligned}
 B_a[\Gamma_L, \Gamma_R] &= \begin{array}{c} \nu_a + \frac{\omega_a}{2} \quad \nu_a'' + \frac{\omega_a}{2} \quad \nu_a' + \frac{\omega_a}{2} \\ \Gamma^L \quad a \quad \Gamma^R \\ \nu_a - \frac{\omega_a}{2} \quad \nu_a'' - \frac{\omega_a}{2} \quad \nu_a' - \frac{\omega_a}{2} \end{array} \\
 B_p[\Gamma_L, \Gamma_R] &= \frac{1}{2} \begin{array}{c} \frac{\omega_p}{2} - \nu_p' \quad \frac{\omega_p}{2} - \nu_p'' \quad \frac{\omega_p}{2} - \nu_p \\ \Gamma^L \quad p \quad \Gamma^R \\ \frac{\omega_p}{2} + \nu_p \quad \frac{\omega_p}{2} + \nu_p' \quad \frac{\omega_p}{2} + \nu_p'' \end{array} \\
 B_t[\Gamma_L, \Gamma_R] &= - \begin{array}{c} \nu_t + \frac{\omega_t}{2} \quad \nu_t - \frac{\omega_t}{2} \\ \Gamma^L \quad t \quad \Gamma^R \\ \nu_t'' + \frac{\omega_t}{2} \quad \nu_t' - \frac{\omega_t}{2} \\ \nu_t' + \frac{\omega_t}{2} \quad \nu_t'' - \frac{\omega_t}{2} \end{array}
 \end{aligned}$$

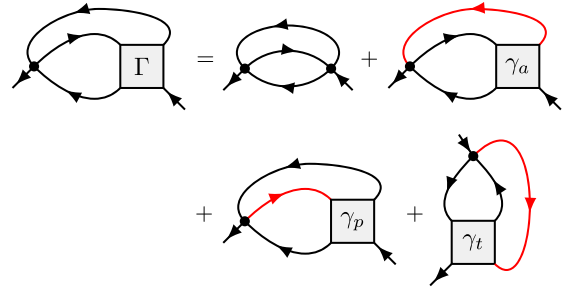
FIG. 15. Diagrammatic representation of the bubble functions in Eq. (C2).

In the following, we discuss three options for the numerical evaluation of this diagram.

First, using the parquet decomposition [Eq. (20e)], the second term of the SDE can be written in terms of bubbles B_r and loop L as (see Fig. 16) [72,107]

$$\Sigma^{\text{SDE1}} = L(B_a(\Gamma_0, \Gamma_0), G) + \sum_r L(B_r(\Gamma_0, \Gamma_r), G). \quad (\text{D1})$$

Here and below, a loop, L , acting on a t bubble, B_t , contracts the two right legs, as opposed to the two top legs for all other vertex types (cf. Fig. 16).


 FIG. 16. Rewriting of the SDE, where crossing symmetry was used for the γ_t part. The red line indicates which propagator enters the loop L in Eq. (D1).

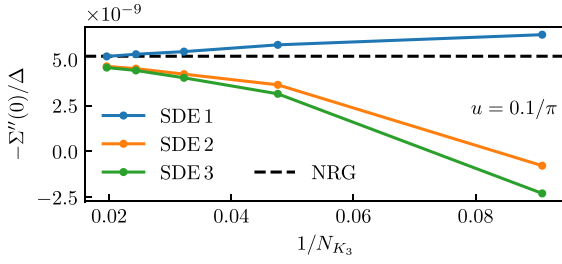


FIG. 17. Imaginary part of the retarded self-energy at $\nu = 0$, computed with the parquet solver and different versions of the SDE, shown as a function of N_{K_3} ($u = 0.1/\pi$, $T/U = 0.01$). The dashed line is the NRG result. For low N_{K_3} , SDE2 and SDE3 give the wrong sign. With increasing resolution, all results approach the correct value.

Second, the SDE in Eq. (20a), without further manipulation, reads

$$\Sigma^{\text{SDE2}} = L(B_r(\Gamma_0, \Gamma), G), \quad r \in \{a, p, t\}, \quad (\text{D2})$$

where the channel r can be freely chosen. Third, using $B_r(\Gamma_0, \gamma_r) = K_{1r} + K_{2r}$ [2], the SDE equivalently reads

$$\Sigma^{\text{SDE3}} = L(K_{1r} + K_{2r}, G). \quad (\text{D3})$$

Even though the above versions of the SDE are analytically equivalent, they vary in numerical accuracy and cost. Evaluating Σ^{SDE3} is cheaper than the others since it skips the computation of bubbles B_r . However, we found that Eq. (D1) is most accurate, since the γ_r are inserted into bubbles B_r of the same channel r . Using the natural frequency parametrization for the reducible vertices $\gamma_r(\omega_r, \nu_r, \nu'_r)$, Σ^{SDE1} also has the benefit that one only needs to interpolate along the ν_r direction.

To illustrate this point, we consider a third-order contribution to the self-energy:

$$L(B_t(\Gamma_0, K_{1t}), G) = L(B_a(\Gamma_0, K_{1t}), G), \quad (\text{D4})$$

$$(\text{D5})$$

Inserting K_{1t} into B_a as done on the right results in diagrams that belong to the asymptotic class K_{2a} . However, on the left, K_{1t} is inserted into B_t , resulting in diagrams belonging to K_{1t} . The latter can be treated with higher resolution and thus lead to better results for Σ , see Fig. 17. Note that the question how to best parametrize the SDE also arises in the context of the truncated-unity formalism for momentum-dependent models, where this choice was found to affect the quality of the results even more strongly due to the additional approximation from the truncation of the form-factor expansion [72,107].

APPENDIX E: EQUAL-TIME CORRELATORS AND HARTREE SELF-ENERGY

Parts of the following discussion can be found in previous works, see Refs. [54,59,66]. We reiterate some of the points made there and extend on them to the context of this work.

The definitions of G^{++} and G^{-} , Eqs. (3) and (4), are ambiguous at $t_1 = t_2$ because $\Theta(t_1 - t_2 = 0)$ is not uniquely defined. If two operators ψ, ψ^\dagger are placed at the same point on the Keldysh contour, it is *a priori* not clear how to order them. The ambiguity is resolved by demanding that ψ^\dagger be put left of ψ (“normal ordering”), which implies $G^{-}(t, t) = G^<(t, t) = G^{++}(t, t)$. Then, $G^< + G^> - G^T - G^{\bar{T}} = 0$ does actually *not* hold, and care is due with Keldysh-rotated quantities. Since the point $t_1 = t_2$ is of zero measure in time integrals, which occur when computing diagrams in frequency space, this subtlety is irrelevant for most practical purposes. However, there is one important exception of equal-time nature, namely, diagrams with loops that begin and end at the *same* bare vertex. With an instantaneous bare interaction, both incoming and outgoing legs have the same time argument, so that these diagrams involve the frequency-integrated (i.e., equal-time) propagator.

The equal-time propagator determines the Hartree self-energy of the AM (e.g., in PT2 calculations),

$$\Sigma_{\text{H}} = - \text{diagram} \quad (\text{E1})$$

Recall that, for the sAM ($\epsilon_d = -U/2$), the Hartree term is constant, $\Sigma_{\text{H}} = U/2$, and can be absorbed into the bare propagator $G_0^R \rightarrow G_{\text{H}}^R$, see Eq. (24). Subsequently, G_{H}^R is used for all computations involving bare propagators. In analogy, in the aAM, the bare propagator is replaced by the Hartree propagator, too. However, here, Σ_{H} is not constant and must be computed self-consistently (using, e.g., a simple bracketing algorithm), as it enters both sides of Eq. (E1). Now, a naive computation of the retarded component of this diagram after the Keldysh rotation (and in the frequency domain) would yield

$$\begin{aligned} \Sigma_{\text{H}}^R &= \Sigma_{\text{H}}^{1|2} = - \text{diagram} = - \underbrace{\text{diagram}}_{G^{11} \stackrel{?}{=} 0} - \text{diagram} \\ &\stackrel{?}{=} \frac{U}{2} \int \frac{d\nu'}{2\pi i} G^K(\nu'). \end{aligned} \quad (\text{E2})$$

This is, however, incorrect since $G^{11}(t|t) \neq 0$ after Keldysh rotation. The correct result can be found by staying in the contour basis, using that, at equal times, only $\Sigma_{\text{H}}^{-}(t, t) = -\Sigma_{\text{H}}^{++}(t, t)$ is nonzero. Keldysh rotation yields $\Sigma_{\text{H}}^R(t, t) = \Sigma_{\text{H}}^{-}(t, t)$, for which one has

$$\Sigma_{\text{H}}^R = \Sigma_{\text{H}}^{-} = - \text{diagram} = U \int \frac{d\nu'}{2\pi i} G^<(\nu'). \quad (\text{E3})$$

To compute Eq. (E3) in thermal equilibrium, one can relate $G^<$ to G^R using the inverse Keldysh rotation and the FDT

[Eq. (10)]:

$$\begin{aligned} G^<(v) &= \frac{1}{2}[-G^R(v) + G^A(v) + G^K(v)] \\ &= -2in_F(v)\text{Im}G^R(v), \end{aligned} \quad (\text{E4})$$

with the Fermi function $n_F(v) = 1/(1 + e^{v/T})$. This discussion of Σ_H also applies to the PA via the first term of the SDE (20a) (the second vanishes for $|v| \rightarrow \infty$).

In fRG, Σ_H is generally renormalized throughout the flow, according to Eq. (19a) for $\dot{\Sigma}$. In the limit $|v| \rightarrow \infty$, relevant for extracting the Hartree contribution, only those diagrams survive for which the in- and outgoing lines are attached to the same bare vertex:

$$\dot{\Sigma}_H = - \lim_{\nu \rightarrow \pm\infty} \text{Diagram} = - \text{Diagram} - K_{1t} - K_{2t}. \quad (\text{E5})$$

In practice, the Hartree contribution $\dot{\Sigma}_H$ is not computed separately but is part of the full self-energy flow. There, equal-time propagators are single-scale propagators, occurring in the following contributions:

$$\dot{\Sigma} = - \text{Diagram} - \text{Diagram} - K_{1t} - K_{2t}. \quad (\text{E6})$$

However, in the context of this work, it turns out that these specific equal-time loops *can* be computed from just the Keldysh-component of the single-scale propagator, as in the naive calculation Eq. (E2). The reason is that, in the hybridization flow, the retarded component of the single-scale propagator asymptotically scales as $\approx 1/v^2$ for $v \rightarrow \pm\infty$, see Eq. (25). Using the FDT in the forms of Eqs. (E4) and (10), we can write

$$\begin{aligned} S^K(v) &= 2i[1 - 2n_F(v)]\text{Im}S^R(v) \\ &= 2i\text{Im}S^R(v) + 2S^<(v). \end{aligned} \quad (\text{E7})$$

When computing $\int d\nu S^K(v)$, one can apply Cauchy's theorem to the first term, using its asymptotic behavior (see above). Closing the integration contour by an infinite semicircle in the upper half plane, avoiding the pole in the lower half plane, gives zero. Hence, in the hybridization flow, we have $\int d\nu S^K(v) = 2 \int d\nu S^<(v)$, and the subtlety discussed previously is irrelevant. Note that this argument may not apply to other regulators, where S has a different expression.

APPENDIX F: DIAGRAMMATIC DEFINITION OF SECOND-ORDER PERTURBATION THEORY

Following the previous discussion, the Hartree term in PT2 is determined self-consistently. The resulting Hartree propa-

gator G_H then fulfills the Dyson equation

$$\text{Diagram} = \text{Diagram} + \text{Diagram}. \quad (\text{F1})$$

In these and the following diagrams, the Hartree propagator G_H is represented by a black line, whereas the light gray line denotes the bare propagator G_0 . The dynamical part of the self-energy is computed from the first nontrivial term of the SDE, using G_H ,

$$\text{Diagram} \equiv \Sigma - \Sigma_H = -\frac{1}{2} \text{Diagram}. \quad (\text{F2})$$

The vertex in PT2 is given by the three diagrams

$$\Gamma - \Gamma_0 = \text{Diagram} + \frac{1}{2} \text{Diagram} - \text{Diagram}, \quad (\text{F3})$$

again evaluated with G_H in the internal lines. Susceptibilities are then computed from this vertex via the standard formula; for χ_a , e.g., (again using G_H throughout)

$$\begin{aligned} \chi_a &= \text{Diagram} + \text{Diagram} + \text{Diagram} \\ &+ \text{Diagram}. \end{aligned} \quad (\text{F4})$$

To obtain exactly the second-order contribution to the susceptibility, one insertion of the dynamical part of the self-energy into each line of the bubble term is required, which gives rise to the second and third diagrams shown.

We checked that, in the sAM at sufficiently low temperatures, our numerical PT2 solution matches the analytic $T = 0$ results of Ref. [95] [Eqs. (3.14) and (3.6)–(3.8) therein]

$$Z = 1 - (3 - \frac{1}{4}\pi^2)u^2, \quad (\text{F5a})$$

$$-\Sigma''(v)/\Delta = \frac{1}{2}u^2(v^2 + \pi^2 T^2)/\Delta^2, \quad |v|, T \ll \Delta, \quad (\text{F5b})$$

$$\tilde{\chi}_{m/d} = \frac{1}{2}[1 \pm u + (3 - \frac{1}{4}\pi^2)u^2]. \quad (\text{F5c})$$

APPENDIX G: IMPLEMENTATION DETAILS

Below, we describe our choices for the implementation of the parquet and fRG solver, the sampling of continuous functions, and the performance-critical quadrature routine. In the process, we also discuss the numerical accuracy of our results.

The evaluation of bubble diagrams, Eq. (C2), is a major bottleneck in our methods. However, computations for different external arguments can be distributed efficiently over multiple threads and compute nodes. It also proved beneficial to vectorize the sum over internal Keldysh indices by reordering and combining Keldysh indices k_i to Keldysh

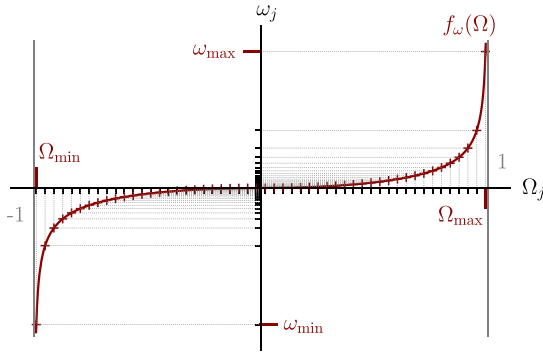


FIG. 18. Nonlinear frequency grid $\{\omega_j\}_{j=1}^N$ obtained via a transformation $f_A(\Omega)$, Eq. (G2), from an auxiliary linear grid $\{\Omega_j\}_{j=1}^N$ of size N .

multi-indices (k_m, k_n)

$$\Gamma^{k_1', k_2', k_1, k_2} \mapsto \begin{cases} \Gamma^{(k_1', k_2), (k_2', k_1)} & \text{for } a \text{ channel} \\ \Gamma^{(k_1', k_2'), (k_1, k_2)} & \text{for } p \text{ channel} \\ \Gamma^{(k_2', k_2), (k_1', k_1)} & \text{for } t \text{ channel,} \end{cases} \quad (\text{G1})$$

turning the Keldysh sum into an ordinary matrix product (which is optimized in common linear algebra libraries). This preprocessing step enables us to efficiently fetch matrix-valued integrands and to perform sums over Keldysh indices and spins in an optimized manner. It requires all Keldysh components to be present in the data, and, therefore, all of them are included in our computations. Consequently, FDTs could not be exploited to gain performance benefits as they merely relate different Keldysh components.

For the integrals over internal frequencies in Eqs. (C2) and (C3), we implemented an adaptive quadrature algorithm which picks sampling points based on a local error estimate and tolerance ($\epsilon_{\text{rel}} = 10^{-5}$). With various vertex components, the evaluation of a vertex at a certain frequency is rather expensive. Therefore, we choose a quadrature algorithm that reuses the previous function evaluations when it refines the quadrature value on a subinterval (4-point Gauss–Lobatto rule with 7-point Kronrod extension) [119]. Due to fine structures in the integrands, we found a higher-order quadrature rule to be beneficial for the convergence of the routine. To help the algorithm find the structure in the integrand, we subdivide the integration interval at the expected positions of structure in the vertices or the propagators. Quadrature of the integrand's tails at high frequency is performed numerically by means of a suitable substitution of the integration variable [120]. For matrix-valued integrands, we use the sup norm $\|\cdot\|_\infty$ to compute the error estimate for the quadrature.

Since Keldysh functions depend on continuous frequencies, a reliable and efficient representation is vital. We choose a nonuniform set of sampling points and obtain function values by (multi-)linear interpolation. The overall behavior of our functions is known: The self-energy and the asymptotic functions K_{ir} can have sharp structures at smaller frequencies while, at large frequencies, they decay to a constant value with an approximate ω^{-k} with $k \in \mathbb{N}$. To capture this behavior, we map an equidistant grid of an auxiliary variable $\Omega \in [-1, 1]$

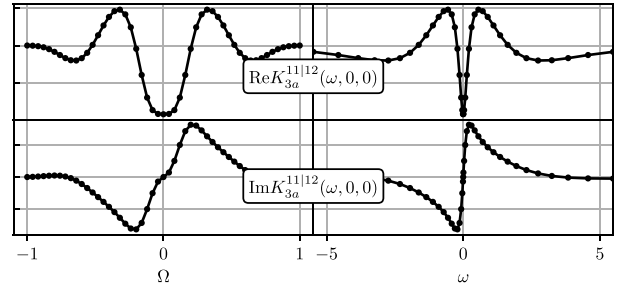


FIG. 19. Illustration of the resolution of vertex data for a slice through $\text{Re}K_{3a}^{11|12}$ and $\text{Im}K_{3a}^{11|12}$. The left panels show the data on the equidistant auxiliary grid, the right panels show the data on real frequencies. Many sampling points are placed around the center where structures are peaked, while the tails are treated with very few points. Here, we also see an artifact due to our choice of the grid function (G2): since the grid function has a discontinuity at second order, we see a saddle point in the bottom left panel even though the function is linear there. The good resolution of the central peak in the real part comes at the cost of a saddle point in the imaginary part.

to a nonuniform one via the function

$$\omega = f_A(\Omega) = \frac{A\Omega|\Omega|}{\sqrt{1-\Omega^2}}, \quad (\text{G2})$$

with constant $A > 0$, see Figs. 18 and 19. The resulting sampling points are dense around $\omega = 0$. At large frequencies, the function $f_A(\Omega)$ captures a $1/\omega^2$ decay effectively for $|\Omega| \lesssim 1$. Furthermore, the structures in the AM scale approximately with the hybridization Δ . Therefore, we choose the frequency-grid parameter A as multiples of Δ and $\omega_{\text{max}} = 100A$. With a fixed maximal frequency ω_{max} , the variable A determines the interval $[-\Omega_{\text{max}}, \Omega_{\text{max}}]$ used to construct the frequency grid via Eq. (G2). Our choices for A are given in Table I.

It is also possible to adapt the frequency-grid parameter A automatically. Interpolating the vertex linearly, we can approximate the error by the maximal curvature in the space of the linearly sampled auxiliary variable Ω . Hence, we can use the curvature as an error function to optimize the parameter A in Eq. (G2). The direction-dependent curvature of a multivariate function f is encoded in the Hessian, $H_{ij} = \partial_i \partial_j f(\mathbf{x})$. We can efficiently compute a scalar measure for the curvature via the Frobenius norm of the Hessian, giving

$$\|H\|_F^2 = \sum_{i,j} |H_{i,j}|^2 = \text{Tr}H^2 = \sum_i |\lambda_i|^2, \quad (\text{G3})$$

where λ_i are the eigenvalues of H . An approximation of the partial derivatives can be obtained with the finite differences method. However, for the studied parameter regime of the AM, we found (using Brent's method [121] as the minimizer) that optimizing the grid parameters A did not make a big difference compared with a simple rescaling according to Table I.

TABLE I. Frequency-grid parameter A for Eq. (G2).

	Σ	K_1	$K_{2,\omega}$	$K_{2,\nu}$	$K_{3,\omega}$	$K_{3,\nu}$
A/Δ	10	5	15	20	10	10

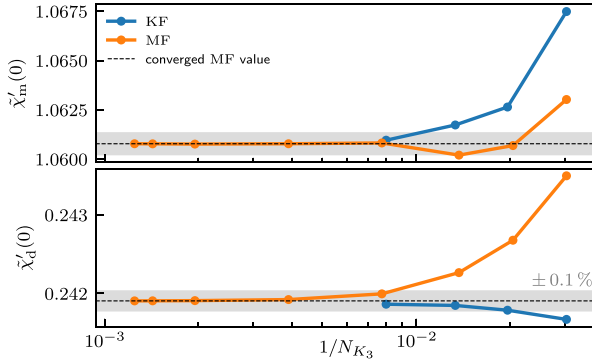


FIG. 20. Convergence with respect to frequency resolution for the static susceptibilities as in Fig. 8 from parquet solvers in the KF and the MF for $u = 0.75$ (a setting where K_2 and K_3 are relevant). The numbers of frequency points for K_1 and K_2 are chosen proportional to N_{K_3} . In the MF, we used $N_{K_3} = 33, 49, 73, 129, 257, 513, 701, 801$, in the KF $N_{K_3} = 33, 51, 75, 125$. The KF and MF results agree very well; the shaded region marks 0.1% deviation.

To verify convergence in the number of sampling points, we compared the static susceptibilities between implementations in the KF and the MF and found agreement up to 1%, see Fig. 20.

To solve the fRG equations (19) we employ a Runge–Kutta solver with adaptive step size control (Cash–Carp). The step size is chosen according to an error estimate and tolerance (here: relative error $\epsilon_{\text{rel}} = 10^{-6}$). Furthermore, we reparametrize the flow parameter $\Lambda(t) = f_{A=5}(t)$ to provide a good first guess for the step sizes, using the same function $f_A(t)$ as for frequencies ω , Eq. (G2), with $A = 5$. It provides large steps for high Λ and small steps for small Λ for equidistant t . As initial condition of Σ^{Λ_i} and Γ^{Λ_i} at large Λ_i , we use the converged parquet solution. As discussed in Sec. III, the PA gives good results in the perturbative regime.

To solve the self-consistent parquet equations f_{PA} in Eqs. (20), which constitute a fixed-point equation for the state $\Psi = (\Sigma, \Gamma)$, i.e., $\Psi = f_{\text{PA}}(\Psi)$, we perform fixed-point iterations until the result meets a tolerance criterion, here $\|\Psi - f_{\text{PA}}(\Psi)\|_{\infty} < 10^{-6} \|\Psi\|_{\infty}$. For intermediate to higher $u \gtrsim 1$, it proves beneficial to stabilize the algorithm with a partial update scheme, i.e.,

$$\Psi \leftarrow (1 - m)\Psi + m f_{\text{PA}}(\Psi), \quad (\text{G4})$$

with mixing factor $0 < m \leq 1$ (here typically $m = 0.5$). For faster convergence in the vicinity of the fixed point, we use Anderson acceleration [122, 123].

APPENDIX H: NUMERICAL COSTS

The numerically most complex objects in all calculations are the K_3 components of the two-particle reducible vertices, as they depend on three continuous frequency arguments independently. The numerical cost of a parquet or fRG computation is therefore $O(N_{K_3}^3)$, where N_{K_3} is the number of grid points per frequency used for K_3 . This applies to memory (as all this data has to be stored) and to computation time (as BSEs or fRG flow equations are evaluated for all external

TABLE II. Number of frequency points for different diagrammatic classes and methods. We use the same number of points for Σ as for K_1 . In most PA computations, $N_{K_3} = 51$, except for the largest values of u , which required $N_{K_3} = 101$ for converging the parquet solver.

	N_{K_1}	N_{K_2}	N_{K_3}
fRG	401	201	101
PA	401	201	51–101
PT2	801	0	0
K1SF	401	0	0

arguments). We give in Table II the number of frequency points used for each diagrammatic class. The self-energy was resolved on a grid with the same number of points as the K_1 class.

The numerical cost is further determined by the accuracy (or the convergence criteria) chosen for the iterative parquet solver or the Runge–Kutta solver in fRG flow (see Appendix G). Finally, the accuracy of the integrator also affects the numerical cost strongly (see again Appendix G). Our most costly computations were 150 iterations of the parquet solver with $N_{K_3} = 101$ (required for convergence in the region $u \lesssim 1$). On the KCS cluster at the Leibniz-Rechenzentrum der Bayerischen Akademie der Wissenschaften (LRZ), equipped with chips of the type *Intel® Xeon® Gold 6130 CPU @ 2.10 GHz* capable of hyperthreading, one such computation took about two days on 32 nodes, running 32 threads each.

APPENDIX I: CONVERGENCE OF $\tilde{\chi}_m(0)$

Figure 21 shows the static magnetic susceptibility of the sAM obtained with fRG, zooming into the regime $u \gtrsim 1$ (where deviations between MF and KF results become noticeable) and scrutinizing convergence with respect to frequency resolution. Compared with Fig. 8, there is an additional KF (MF) line with higher (lower) resolution, as determined by the number of frequency points used to resolve the K_3 class, N_{K_3} (cf. Fig. 20). The MF result appears converged in N_{K_3} , whereas the KF result is slightly improved by increasing N_{K_3} . The improvement is minor, however, and does not justify the additional numerical cost: The computation for $N_{K_3} = 125$ consumed roughly 30 000 CPU h, while the computation for $N_{K_3} = 101$ took only half that time. Nevertheless, one should keep in mind that these computations yield a full parameter sweep in u and are thus more economical than individual PA

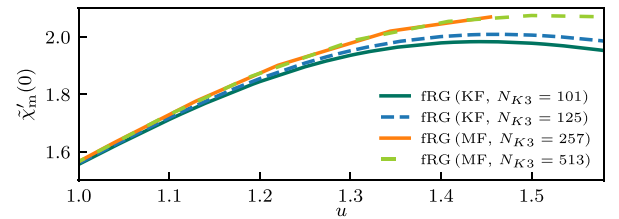


FIG. 21. Static magnetic susceptibility of the sAM obtained with fRG. Compared with Fig. 8, there is an additional KF (MF) line with higher (lower) resolution. The MF result appears converged in N_{K_3} ; the KF result is slightly improved by increasing N_{K_3} from 101 to 125.

computations. Further analysis, including line plots through all vertex components and asymptotic classes, is provided in the dataset attached to this paper. This analysis shows that the

resolution of fine structures in some Keldysh components of the K_3 class could still be improved using even higher values of N_{K_3} .

-
- [1] G. Li, N. Wentzell, P. Pudleiner, P. Thunström, and K. Held, Efficient implementation of the parquet equations: Role of the reducible vertex function and its kernel approximation, *Phys. Rev. B* **93**, 165103 (2016).
- [2] N. Wentzell, G. Li, A. Tagliavini, C. Taranto, G. Rohringer, K. Held, A. Toschi, and S. Andergassen, High-frequency asymptotics of the vertex function: diagrammatic parametrization and algorithmic implementation, *Phys. Rev. B* **102**, 085106 (2020).
- [3] H. Shinaoka, J. Otsuki, K. Haule, M. Wallerberger, E. Gull, K. Yoshimi, and M. Ohzeki, Overcomplete compact representation of two-particle Green's functions, *Phys. Rev. B* **97**, 205111 (2018).
- [4] F. Krien, A. Valli, and M. Capone, Single-boson exchange decomposition of the vertex function, *Phys. Rev. B* **100**, 155149 (2019).
- [5] H. Shinaoka, D. Geffroy, M. Wallerberger, J. Otsuki, K. Yoshimi, E. Gull, and J. Kuneš, Sparse sampling and tensor network representation of two-particle Green's functions, *SciPost Phys.* **8**, 012 (2020).
- [6] M. Wallerberger, H. Shinaoka, and A. Kauch, Solving the Bethe-Salpeter equation with exponential convergence, *Phys. Rev. Res.* **3**, 033168 (2021).
- [7] H. Shinaoka, M. Wallerberger, Y. Murakami, K. Nogaki, R. Sakurai, P. Werner, and A. Kauch, Multiscale space-time ansatz for correlation functions of quantum systems based on quantum tensor trains, *Phys. Rev. X* **13**, 021015 (2023).
- [8] T. Schäfer, G. Rohringer, O. Gunnarsson, S. Ciuchi, G. Sangiovanni, and A. Toschi, Divergent precursors of the Mott-Hubbard transition at the two-particle level, *Phys. Rev. Lett.* **110**, 246405 (2013).
- [9] V. Janiš and V. Pokorný, Critical metal-insulator transition and divergence in a two-particle irreducible vertex in disordered and interacting electron systems, *Phys. Rev. B* **90**, 045143 (2014).
- [10] E. Kozik, M. Ferrero, and A. Georges, Nonexistence of the Luttinger-Ward functional and misleading convergence of skeleton diagrammatic series for Hubbard-like models, *Phys. Rev. Lett.* **114**, 156402 (2015).
- [11] T. Ribic, G. Rohringer, and K. Held, Nonlocal correlations and spectral properties of the Falicov-Kimball model, *Phys. Rev. B* **93**, 195105 (2016).
- [12] T. Schäfer, S. Ciuchi, M. Wallerberger, P. Thunström, O. Gunnarsson, G. Sangiovanni, G. Rohringer, and A. Toschi, Non-perturbative landscape of the Mott-Hubbard transition: Multiple divergence lines around the critical endpoint, *Phys. Rev. B* **94**, 235108 (2016).
- [13] O. Gunnarsson, G. Rohringer, T. Schäfer, G. Sangiovanni, and A. Toschi, Breakdown of traditional many-body theories for correlated electrons, *Phys. Rev. Lett.* **119**, 056402 (2017).
- [14] J. Vučičević, N. Wentzell, M. Ferrero, and O. Parcollet, Practical consequences of the Luttinger-Ward functional multivaluedness for cluster DMFT methods, *Phys. Rev. B* **97**, 125141 (2018).
- [15] P. Thunström, O. Gunnarsson, S. Ciuchi, and G. Rohringer, Analytical investigation of singularities in two-particle irreducible vertex functions of the Hubbard atom, *Phys. Rev. B* **98**, 235107 (2018).
- [16] P. Chalupa, P. Gunacker, T. Schäfer, K. Held, and A. Toschi, Divergences of the irreducible vertex functions in correlated metallic systems: Insights from the Anderson impurity model, *Phys. Rev. B* **97**, 245136 (2018).
- [17] D. Springer, P. Chalupa, S. Ciuchi, G. Sangiovanni, and A. Toschi, Interplay between local response and vertex divergences in many-fermion systems with on-site attraction, *Phys. Rev. B* **101**, 155148 (2020).
- [18] C. Melnick and G. Kotliar, Fermi-liquid theory and divergences of the two-particle irreducible vertex in the periodic Anderson lattice, *Phys. Rev. B* **101**, 165105 (2020).
- [19] M. Reitner, P. Chalupa, L. Del Re, D. Springer, S. Ciuchi, G. Sangiovanni, and A. Toschi, Attractive effect of a strong electronic repulsion: The physics of vertex divergences, *Phys. Rev. Lett.* **125**, 196403 (2020).
- [20] P. Chalupa, T. Schäfer, M. Reitner, D. Springer, S. Andergassen, and A. Toschi, Fingerprints of the local moment formation and its Kondo screening in the generalized susceptibilities of many-electron problems, *Phys. Rev. Lett.* **126**, 056403 (2021).
- [21] S. Adler, F. Krien, P. Chalupa-Gantner, G. Sangiovanni, and A. Toschi, Non-perturbative intertwining between spin and charge correlations: A "smoking gun" single-boson-exchange result, *SciPost Phys.* **16**, 054 (2024).
- [22] M. Pelz, S. Adler, M. Reitner, and A. Toschi, Highly non-perturbative nature of the Mott metal-insulator transition: Two-particle vertex divergences in the coexistence region, *Phys. Rev. B* **108**, 155101 (2023).
- [23] A. Taheridehkordi, S. H. Curnoe, and J. P. F. LeBlanc, Algorithmic Matsubara integration for Hubbard-like models, *Phys. Rev. B* **99**, 035120 (2019).
- [24] A. Taheridehkordi, S. H. Curnoe, and J. P. F. LeBlanc, Algorithmic approach to diagrammatic expansions for real-frequency evaluation of susceptibility functions, *Phys. Rev. B* **102**, 045115 (2020).
- [25] B. D. E. McNiven, G. T. Andrews, and J. P. F. LeBlanc, Single particle properties of the two-dimensional Hubbard model for real frequencies at weak coupling: Breakdown of the Dyson series for partial self-energy expansions, *Phys. Rev. B* **104**, 125114 (2021).
- [26] B. D. E. McNiven, H. Terletska, G. T. Andrews, and J. P. F. LeBlanc, One- and two-particle properties of the weakly interacting two-dimensional Hubbard model in proximity to the van Hove singularity, *Phys. Rev. B* **106**, 035145 (2022).
- [27] J. P. F. LeBlanc, K. Chen, K. Haule, N. V. Prokof'ev, and I. S. Tupitsyn, Dynamic response of an electron gas: Towards the exact exchange-correlation kernel, *Phys. Rev. Lett.* **129**, 246401 (2022).
- [28] M. D. Burke, M. Grandadam, and J. P. F. LeBlanc, Renormalized perturbation theory for fast evaluation of Feynman

- diagrams on the real frequency axis, *Phys. Rev. B* **107**, 115151 (2023).
- [29] M. Grandadam and J. P. F. LeBlanc, Planckian behaviour in the optical conductivity of the weakly coupled Hubbard model, [arXiv:2303.04964](https://arxiv.org/abs/2303.04964).
- [30] C. Bertrand, S. Florens, O. Parcollet, and X. Waintal, Reconstructing nonequilibrium regimes of quantum many-body systems from the analytical structure of perturbative expansions, *Phys. Rev. X* **9**, 041008 (2019).
- [31] C. Bertrand, O. Parcollet, A. Maillard, and X. Waintal, Quantum Monte Carlo algorithm for out-of-equilibrium Green's functions at long times, *Phys. Rev. B* **100**, 125129 (2019).
- [32] C. Bertrand, D. Bauernfeind, P. T. Dumitrescu, M. Maćek, X. Waintal, and O. Parcollet, Quantum quasi Monte Carlo algorithm for out-of-equilibrium Green functions at long times, *Phys. Rev. B* **103**, 155104 (2021).
- [33] Y. Núñez Fernández, M. Jeannin, P. T. Dumitrescu, T. Kloss, J. Kaye, O. Parcollet, and X. Waintal, Learning Feynman diagrams with tensor trains, *Phys. Rev. X* **12**, 041018 (2022).
- [34] F. B. Kugler, S.-S. B. Lee, and J. von Delft, Multipoint correlation functions: Spectral representation and numerical evaluation, *Phys. Rev. X* **11**, 041006 (2021).
- [35] S.-S. B. Lee, F. B. Kugler, and J. von Delft, Computing local multipoint correlators using the numerical renormalization group, *Phys. Rev. X* **11**, 041007 (2021).
- [36] L. V. Keldysh, Diagram technique for nonequilibrium processes, *Sov. Phys. JETP* **20**, 1018 (1965).
- [37] J. Schwinger, Brownian motion of a quantum oscillator, *J. Math. Phys.* **2**, 407 (1961).
- [38] L. P. Kadanoff and G. A. Baym, *Quantum Statistical Mechanics* (Benjamin, New York, 1962).
- [39] W. Metzner, M. Salmhofer, C. Honerkamp, V. Meden, and K. Schönhammer, Functional renormalization group approach to correlated fermion systems, *Rev. Mod. Phys.* **84**, 299 (2012).
- [40] N. E. Bickers, Self-consistent many-body theory for condensed matter systems, in *Theoretical Methods for Strongly Correlated Electrons*, CRM Series in Mathematical Physics, edited by D. Sénéchal, A.-M. Tremblay, and C. Bourbonnais (Springer, New York, 2004).
- [41] G. Rohringer, H. Hafermann, A. Toschi, A. A. Katanin, A. E. Antipov, M. I. Katsnelson, A. I. Lichtenstein, A. N. Rubtsov, and K. Held, Diagrammatic routes to nonlocal correlations beyond dynamical mean field theory, *Rev. Mod. Phys.* **90**, 025003 (2018).
- [42] A. Georges, G. Kotliar, W. Krauth, and M. J. Rozenberg, Dynamical mean-field theory of strongly correlated fermion systems and the limit of infinite dimensions, *Rev. Mod. Phys.* **68**, 13 (1996).
- [43] R. Bulla, T. A. Costi, and T. Pruschke, Numerical renormalization group method for quantum impurity systems, *Rev. Mod. Phys.* **80**, 395 (2008).
- [44] C. Taranto, S. Andergassen, J. Bauer, K. Held, A. Katanin, W. Metzner, G. Rohringer, and A. Toschi, From infinite to two dimensions through the functional renormalization group, *Phys. Rev. Lett.* **112**, 196402 (2014).
- [45] D. Vilardi, C. Taranto, and W. Metzner, Antiferromagnetic and *d*-wave pairing correlations in the strongly interacting two-dimensional Hubbard model from the functional renormalization group, *Phys. Rev. B* **99**, 104501 (2019).
- [46] A. Toschi, A. A. Katanin, and K. Held, Dynamical vertex approximation: A step beyond dynamical mean-field theory, *Phys. Rev. B* **75**, 045118 (2007).
- [47] K. Held, A. A. Katanin, and A. Toschi, Dynamical vertex approximation: An introduction, *Prog. Theor. Phys. Suppl.* **176**, 117 (2008).
- [48] A. C. Hewson, *The Kondo Problem to Heavy Fermions* (Cambridge University Press, Cambridge, 1993).
- [49] P. W. Anderson, Localized magnetic states in metals, *Phys. Rev.* **124**, 41 (1961).
- [50] F. B. Anders and N. Grewe, Perturbational approach to the Anderson model: New results from a post-NCA treatment, *Europhys. Lett.* **26**, 551 (1994).
- [51] F. B. Anders, An enhanced perturbational study on spectral properties of the Anderson model, *J. Phys.: Condens. Matter* **7**, 2801 (1995).
- [52] J. Kroha, P. Wölfle, and T. A. Costi, Unified description of Fermi and non-Fermi liquid behavior in a conserving slave boson approximation for strongly correlated impurity models, *Phys. Rev. Lett.* **79**, 261 (1997).
- [53] J. Kroha and P. Wölfle, Fermi and non-Fermi liquid behavior of local moment systems within a conserving slave boson theory, *Acta Phys. Pol. B* **29**, 3781 (1998).
- [54] S. G. Jakobs, Functional renormalization group studies of quantum transport through mesoscopic systems, Ph.D. thesis, RWTH Aachen University, 2010.
- [55] S. G. Jakobs, M. Pletyukhov, and H. Schoeller, Nonequilibrium functional renormalization group with frequency-dependent vertex function: A study of the single-impurity Anderson model, *Phys. Rev. B* **81**, 195109 (2010).
- [56] S. G. Jakobs, M. Pletyukhov, and H. Schoeller, Properties of multi-particle Green's and vertex functions within Keldysh formalism, *J. Phys. A: Math. Theor.* **43**, 103001 (2010).
- [57] D. Schimmel, Transport through inhomogeneous interacting low-dimensional systems, Ph.D. thesis, Ludwig-Maximilians-Universität München, 2017.
- [58] D. H. Schimmel, B. Bruognolo, and J. von Delft, Spin fluctuations in the 0.7 anomaly in quantum point contacts, *Phys. Rev. Lett.* **119**, 196401 (2017).
- [59] L. Weidinger and J. von Delft, Keldysh functional renormalization group treatment of finite-ranged interactions in quantum point contacts, [arXiv:1912.02700](https://arxiv.org/abs/1912.02700).
- [60] V. Zlatić and B. Horvatić, Series expansion for the symmetric Anderson Hamiltonian, *Phys. Rev. B* **28**, 6904 (1983).
- [61] F. B. Kugler and J. von Delft, Multiloop functional renormalization group for general models, *Phys. Rev. B* **97**, 035162 (2018).
- [62] F. B. Kugler and J. von Delft, Multiloop functional renormalization group that sums up all parquet diagrams, *Phys. Rev. Lett.* **120**, 057403 (2018).
- [63] F. B. Kugler and J. von Delft, Derivation of exact flow equations from the self-consistent parquet relations, *New J. Phys.* **20**, 123029 (2018).
- [64] P. Chalupa-Gantner, F. B. Kugler, C. Hille, J. von Delft, S. Andergassen, and A. Toschi, Fulfillment of sum rules and Ward identities in the multiloop functional renormalization group solution of the Anderson impurity model, *Phys. Rev. Res.* **4**, 023050 (2022).
- [65] A. Kamenev, *Field Theory of Non-Equilibrium Systems* (Cambridge University Press, Cambridge, 2014).

- [66] C. F. Klöckner, Functional renormalization group approach to correlated quantum systems far from equilibrium, Ph.D. thesis, Freie Universität Berlin, 2019.
- [67] E. Walter, Real-frequency dynamics of quantum impurity models studied with fRG, NRG, CFT, Ph.D. thesis, Ludwig-Maximilians-Universität München, 2021.
- [68] J. W. Negele and H. Orland, *Quantum Many-Particle Systems* (CRC Press, Boca Raton, FL, 1998).
- [69] P. Kopietz, L. Bartosch, and F. Schütz, *Introduction to the Functional Renormalization Group* (Springer, Berlin, Heidelberg, 2010).
- [70] A. A. Katanin, Fulfillment of Ward identities in the functional renormalization group approach, *Phys. Rev. B* **70**, 115109 (2004).
- [71] A. Tagliavini, C. Hille, F. Kugler, S. Andergassen, A. Toschi, and C. Honerkamp, Multiloop functional renormalization group for the two-dimensional Hubbard model: Loop convergence of the response functions, *SciPost Phys.* **6**, 009 (2019).
- [72] C. Hille, F. B. Kugler, C. J. Eckhardt, Y.-Y. He, A. Kauch, C. Honerkamp, A. Toschi, and S. Andergassen, Quantitative functional renormalization group description of the two-dimensional Hubbard model, *Phys. Rev. Res.* **2**, 033372 (2020).
- [73] J. Thoenniss, M. K. Ritter, F. B. Kugler, J. von Delft, and M. Punk, Multiloop pseudofermion functional renormalization for quantum spin systems: Application to the spin-1/2 Kagome Heisenberg model, [arXiv:2011.01268](https://arxiv.org/abs/2011.01268).
- [74] D. Kiese, T. Müller, Y. Iqbal, R. Thomale, and S. Trebst, Multiloop functional renormalization group approach to quantum spin systems, *Phys. Rev. Res.* **4**, 023185 (2022).
- [75] M. Gievers, E. Walter, A. Ge, J. von Delft, and F. B. Kugler, Multiloop flow equations for single-boson exchange fRG, *Eur. Phys. J. B* **95**, 108 (2022).
- [76] M. K. Ritter, D. Kiese, T. Müller, F. B. Kugler, R. Thomale, S. Trebst, and J. von Delft, Benchmark calculations of multiloop pseudofermion fRG, *Eur. Phys. J. B* **95**, 102 (2022).
- [77] M. K. Ritter, Y. Núñez Fernández, M. Wallerberger, J. von Delft, H. Shinaoka, and X. Waintal, Quantics tensor cross interpolation for high-resolution parsimonious representations of multivariate functions, *Phys. Rev. Lett.* **132**, 056501 (2024).
- [78] A. Weichselbaum, Non-Abelian symmetries in tensor networks: A quantum symmetry space approach, *Ann. Phys. (NY)* **327**, 2972 (2012).
- [79] A. Weichselbaum, Tensor networks and the numerical renormalization group, *Phys. Rev. B* **86**, 245124 (2012).
- [80] A. Weichselbaum, X-symbols for non-Abelian symmetries in tensor networks, *Phys. Rev. Res.* **2**, 023385 (2020).
- [81] R. Žitko and T. Pruschke, Energy resolution and discretization artifacts in the numerical renormalization group, *Phys. Rev. B* **79**, 085106 (2009).
- [82] A. Weichselbaum and J. von Delft, Sum-rule conserving spectral functions from the numerical renormalization group, *Phys. Rev. Lett.* **99**, 076402 (2007).
- [83] R. Peters, T. Pruschke, and F. B. Anders, Numerical renormalization group approach to Green's functions for quantum impurity models, *Phys. Rev. B* **74**, 245114 (2006).
- [84] S.-S. B. Lee and A. Weichselbaum, Adaptive broadening to improve spectral resolution in the numerical renormalization group, *Phys. Rev. B* **94**, 235127 (2016).
- [85] S.-S. B. Lee, J. von Delft, and A. Weichselbaum, Double-holon origin of the subpeaks at the Hubbard band edges, *Phys. Rev. Lett.* **119**, 236402 (2017).
- [86] F. B. Kugler, Improved estimator for numerical renormalization group calculations of the self-energy, *Phys. Rev. B* **105**, 245132 (2022).
- [87] A. C. Hewson, A. Oguri, and D. Meyer, Renormalized parameters for impurity models, *Eur. Phys. J. B* **40**, 177 (2004).
- [88] J. Bauer and A. C. Hewson, Field-dependent quasiparticles in the infinite-dimensional Hubbard model, *Phys. Rev. B* **76**, 035118 (2007).
- [89] Y. Nishikawa, D. J. G. Crow, and A. C. Hewson, Renormalized parameters and perturbation theory for an n -channel Anderson model with Hund's rule coupling: Symmetric case, *Phys. Rev. B* **82**, 115123 (2010).
- [90] Y. Nishikawa, D. J. G. Crow, and A. C. Hewson, Renormalized parameters and perturbation theory for an n -channel Anderson model with Hund's rule coupling: Asymmetric case, *Phys. Rev. B* **82**, 245109 (2010).
- [91] A. Oguri, R. Sakano, and T. Fujii, $1/(N-1)$ expansion based on a perturbation theory in u for the Anderson model with N -fold degeneracy, *Phys. Rev. B* **84**, 113301 (2011).
- [92] F. B. Kugler, M. Zingl, H. U. R. Strand, S.-S. B. Lee, J. von Delft, and A. Georges, Strongly correlated materials from a numerical renormalization group perspective: How the Fermi-liquid state of Sr_2RuO_4 emerges, *Phys. Rev. Lett.* **124**, 016401 (2020).
- [93] K. Tsutsumi, Y. Teratani, K. Motoyama, R. Sakano, and A. Oguri, Role of bias and tunneling asymmetries in nonlinear Fermi-liquid transport through an $\text{SU}(n)$ quantum dot, *Phys. Rev. B* **108**, 045109 (2023).
- [94] K. Yosida and K. Yamada, Perturbation expansion for the Anderson Hamiltonian, *Prog. Theor. Phys. Suppl.* **46**, 244 (1970).
- [95] K. Yamada, Perturbation expansion for the Anderson Hamiltonian. II, *Prog. Theor. Phys.* **53**, 970 (1975).
- [96] K. Yosida and K. Yamada, Perturbation expansion for the Anderson Hamiltonian. III, *Prog. Theor. Phys.* **53**, 1286 (1975).
- [97] K. Yamada, Perturbation expansion for the Anderson Hamiltonian. IV, *Prog. Theor. Phys.* **54**, 316 (1975).
- [98] D. C. Langreth, Friedel sum rule for Anderson's model of localized impurity states, *Phys. Rev.* **150**, 516 (1966).
- [99] H. Kajueter and G. Kotliar, New iterative perturbation scheme for lattice models with arbitrary filling, *Phys. Rev. Lett.* **77**, 131 (1996).
- [100] C. Karrasch, R. Hedden, R. Peters, T. Pruschke, K. Schönhammer, and V. Meden, A finite-frequency functional renormalization group approach to the single impurity Anderson model, *J. Phys.: Condens. Matter* **20**, 345205 (2008).
- [101] A. C. Hewson, Renormalized perturbation calculations for the single-impurity Anderson model, *J. Phys.: Condens. Matter* **13**, 10011 (2001).
- [102] M. Filippone, C. P. Moca, A. Weichselbaum, J. von Delft, and C. Mora, At which magnetic field, exactly, does the Kondo resonance begin to split? A Fermi liquid description of the low-energy properties of the Anderson model, *Phys. Rev. B* **98**, 075404 (2018).
- [103] P. Kopietz, L. Bartosch, L. Costa, A. Isidori, and A. Ferraz, Ward identities for the Anderson impurity model: Derivation via functional methods and the exact renormalization group, *J. Phys. A: Math. Theor.* **43**, 385004 (2010).

- [104] H. Shiba, The Korringa relation for the impurity nuclear spin-lattice relaxation in dilute Kondo alloys, *Prog. Theor. Phys.* **54**, 967 (1975).
- [105] J.-M. Lihm, J. Halbinger, J. Shim, J. von Delft, F. B. Kugler, and S.-S. B. Lee, Symmetric improved estimators for multipoint vertex functions, [arXiv:2310.12098](https://arxiv.org/abs/2310.12098) [Phys. Rev. B (to be published)].
- [106] T. Fujii and K. Ueda, Perturbative approach to the nonequilibrium Kondo effect in a quantum dot, *Phys. Rev. B* **68**, 155310 (2003).
- [107] C. J. Eckhardt, C. Honerkamp, K. Held, and A. Kauch, Truncated unity parquet solver, *Phys. Rev. B* **101**, 155104 (2020).
- [108] C. Husemann and M. Salmhofer, Efficient parametrization of the vertex function, Ω scheme, and the (t, t') Hubbard model at van Hove filling, *Phys. Rev. B* **79**, 195125 (2009).
- [109] W.-S. Wang, Y.-Y. Xiang, Q.-H. Wang, F. Wang, F. Yang, and D.-H. Lee, Functional renormalization group and variational Monte Carlo studies of the electronic instabilities in graphene near 1/4 doping, *Phys. Rev. B* **85**, 035414 (2012).
- [110] J. Lichtenstein, D. S. d. I. Peña, D. Rohe, E. D. Napoli, C. Honerkamp, and S. A. Maier, High-performance functional renormalization group calculations for interacting fermions, *Comput. Phys. Commun.* **213**, 100 (2017).
- [111] C. J. Eckhardt, G. A. H. Schober, J. Ehrlich, and C. Honerkamp, Truncated-unity parquet equations: application to the repulsive Hubbard model, *Phys. Rev. B* **98**, 075143 (2018).
- [112] A. Ge, N. Ritz, E. Walter, S. Aguirre, J. von Delft, and F. Kugler, Data for: Real-frequency quantum field theory applied to the single-impurity Anderson model (2023), doi:[10.57970/xeqvs-w3p49](https://doi.org/10.57970/xeqvs-w3p49).
- [113] G. Rohringer, A. Valli, and A. Toschi, Local electronic correlation at the two-particle level, *Phys. Rev. B* **86**, 125114 (2012).
- [114] E. Wang and U. Heinz, Generalized fluctuation-dissipation theorem for nonlinear response functions, *Phys. Rev. D: Part. Fields* **66**, 025008 (2002).
- [115] A. Ge, J. Halbinger, S.-S. B. Lee, J. von Delft, and F. B. Kugler, Analytic continuation of multipoint correlation functions, [arXiv:2311.11389](https://arxiv.org/abs/2311.11389) [Ann. Phys. (to be published)].
- [116] G. Rohringer, New routes towards a theoretical treatment of nonlocal electronic correlations, Ph.D. thesis, Vienna University of Technology, 2013.
- [117] G. Eliashberg, Transport equation for a degenerate system of Fermi particles, *Sov. Phys. JETP* **14**, 886 (1962).
- [118] L. Hedin, New method for calculating the one-particle Green's function with application to the electron-gas problem, *Phys. Rev.* **139**, A796 (1965).
- [119] W. H. Press, S. A. Teukolsky, W. T. Vetterling, and B. P. Flannery, *Numerical Recipes: The Art of Scientific Computing*, 3rd ed. (Cambridge University Press, Cambridge, 2007).
- [120] M. Galassi (ed.), *GNU Scientific Library Reference Manual: for GSL version 1.12*, 3rd ed. (Network Theory, Bristol, 2009).
- [121] R. P. Brent, *Algorithms for Minimization without Derivatives* (Prentice-Hall, Inc., Englewood Cliffs, NJ, 1973).
- [122] D. G. Anderson, Iterative procedures for nonlinear integral equations, *J. Assoc. Comput. Mach.* **12**, 547 (1965).
- [123] H. F. Walker and P. Ni, Anderson acceleration for fixed-point iterations, *SIAM J. Numer. Anal.* **49**, 1715 (2011).

**KeldyshQFT: A C++ codebase for real-frequency multiloop
functional renormalization group and parquet computations
of the single-impurity Anderson model**

by

N. Ritz,¹ A. Ge,¹ E. Walter,¹ S. Aguirre,¹ J. von Delft,¹ and F. B. Kugler²

¹ Arnold Sommerfeld Center for Theoretical Physics, Center for NanoScience, and

Munich Center for Quantum Science and Technology,

Ludwig-Maximilians-Universität München, 80333 Munich, Germany

² Center for Computational Quantum Physics, Flatiron Institute, 162 5th Avenue, New York,

New York 10010, USA

reprinted on pages 91–112

with permission from

***J. Chem. Phys.* 161, 054118 (2024),**

DOI: 10.1063/5.0221340.

© 2024 AIP Publishing.

RESEARCH ARTICLE | AUGUST 07 2024

KeldyshQFT: A C++ codebase for real-frequency multiloop functional renormalization group and parquet computations of the single-impurity Anderson model

Special Collection: [Algorithms and Software for Open Quantum System Dynamics](#)

Nepomuk Ritz ; Anxiang Ge ; Elias Walter ; Santiago Aguirre; Jan von Delft ; Fabian B. Kugler 



J. Chem. Phys. 161, 054118 (2024)

<https://doi.org/10.1063/5.0221340>



Articles You May Be Interested In

Strong electron correlation in impurity models: singlet and triplet multiple scatterings

AIP Conference Proceedings (August 2009)

Superconductivity from repulsive interaction

AIP Conference Proceedings (August 2013)

The Resistive Net and Finite-Difference Equations

American Journal of Physics (September 1972)



The Journal of Chemical Physics

Special Topics Open for Submissions

[Learn More](#)



KeldyshQFT: A C++ codebase for real-frequency multiloop functional renormalization group and parquet computations of the single-impurity Anderson model

Cite as: J. Chem. Phys. **161**, 054118 (2024); doi: 10.1063/5.0221340

Submitted: 31 May 2024 • Accepted: 3 July 2024 •

Published Online: 7 August 2024



View Online



Export Citation



CrossMark

Nepomuk Ritz,^{1,a)} Anxiang Ge,¹ Elias Walter,¹ Santiago Aguirre,¹ Jan von Delft,¹
and Fabian B. Kugler²

AFFILIATIONS

¹Arnold Sommerfeld Center for Theoretical Physics, Center for NanoScience, and Munich Center for Quantum Science and Technology, Ludwig-Maximilians-Universität München, 80333 Munich, Germany

²Center for Computational Quantum Physics, Flatiron Institute, 162 5th Avenue, New York, New York 10010, USA

Note: This paper is part of the JCP Special Topic on Algorithms and Software for Open Quantum System Dynamics.

^{a)}Author to whom correspondence should be addressed: nepomuk.ritz@physik.uni-muenchen.de

ABSTRACT

We provide a detailed exposition of our computational framework designed for the accurate calculation of real-frequency dynamical correlation functions of the single-impurity Anderson model in the regime of weak to intermediate coupling. Using quantum field theory within the Keldysh formalism to directly access the self-energy and dynamical susceptibilities in real frequencies, as detailed in our recent publication [Ge *et al.*, Phys. Rev. B **109**, 115128 (2024)], the primary computational challenge is the full three-dimensional real-frequency dependence of the four-point vertex. Our codebase provides a fully MPI+OpenMP parallelized implementation of the functional renormalization group (fRG) and the self-consistent parquet equations within the parquet approximation. It leverages vectorization to handle the additional complexity imposed by the Keldysh formalism, using optimized data structures and highly performant integration routines. Going beyond the results shown in the previous publication, the code includes functionality to perform fRG calculations in the multiloop framework, up to arbitrary loop order, including self-consistent self-energy iterations. Moreover, implementations of various regulators, such as hybridization, interaction, frequency, and temperature, are supplied.

© 2024 Author(s). All article content, except where otherwise noted, is licensed under a Creative Commons Attribution (CC BY) license (<https://creativecommons.org/licenses/by/4.0/>). <https://doi.org/10.1063/5.0221340>

I. INTRODUCTION

In the study of strongly correlated electrons, dynamical correlation functions are quantities of major interest, as they provide insights into the collective behavior and emergent phenomena arising from electronic interactions. Capturing the effects of two-particle (or four-point) correlations is one of the current major frontiers in the field. Their dynamical properties are inherently difficult to compute, as they involve three independent frequency arguments.

While most previous works on this subject focused on four-point functions in imaginary frequencies in the Matsubara

formalism^{2,3} (MaF), obtaining real-frequency information is crucial for direct comparisons to experiments. The extraction of real-frequency data from the results of a calculation in the MaF is, in principle, possible via analytic continuation.⁴ However, it is hard to do so reliably in practice, as the conditions for the procedure outlined in Ref. 4 are not met by finite amounts of numerical data. This renders analytic continuation an ill-defined problem, despite numerous attempts.⁵⁻⁷ Furthermore, it had not been worked out in full detail until very recently⁸ how analytic continuation of four-point functions could be achieved even under the assumption of analytically available results.

Pioneering attempts to directly compute real-frequency dynamical four-point correlation functions using simplified approaches made use of diagrammatic ladder approximations^{9,10} or were restricted to a simplified frequency dependence.^{11–13} The first fully unbiased treatment of the fluctuations contributing to the four-point vertex was achieved only a few years ago using a multipoint extension of the numerical renormalization group (NRG).^{14,15}

Even more recently, we presented a similarly unbiased treatment of the four-point vertex of the single-impurity Anderson model using a QFT framework within the Keldysh formalism (KF), employing two related diagrammatic methods: the functional renormalization group (fRG) and the self-consistent parquet equations in the parquet approximation.¹ While we focused on the conceptual aspects and discussed the performance of the methods in great detail in the previous publication, here we wish to provide a detailed exposition of the computational framework for the numerical calculations of self-energies and vertex functions. In addition to what was shown in Ref. 1, the code discussed in this paper is capable of performing fRG calculations in the multiloop framework up to an arbitrary loop order, which connects the fRG to the parquet formalism.^{16–18}

This paper aims to serve as a reference for future extensions or revisions of the code. The codebase discussed here was developed by several people over the course of multiple years, during which some goals and priorities changed and the code had to be adapted accordingly. This paper will document how the code works and what was learned during its development.

Some general design choices made during development resulted in convenient features of the code and are recommended for future projects. In the following, we briefly discuss the most important features:

a. *Modularity.* Every main building block of the code and each functionality is implemented individually, using classes and functions that serve one purpose only. As a consequence, a developer can keep an overview of the functionality. It is also comparatively easy to reuse existing features and combine them into new functionality. For example, for both the computation of the Schwinger–Dyson equation during parquet computations and the evaluation of the flow equation for the self-energy during the solution of an mfRG flow, the same classes for vertices, propagators, self-energies, and the same function for contracting a loop are used, as described in Secs. II C and II D. In addition, modularity enables unit-testing of each functionality, something too often ignored during research software development. Modularity is probably the most important feature that should be prioritized in developing any research software.

b. *Flexibility.* A modular design makes the code flexible, too. Some additional choices were made to improve its flexibility even further. Most importantly, the code enables computations in three different formalisms: the finite-temperature Matsubara formalism (MaF), the zero-temperature Matsubara formalism, and the Keldysh formalism (KF), which works at any temperature and generalizes to systems out of thermal equilibrium. Consequently, some functionality had to be implemented multiple times, such as contractions, which require summations over discrete Matsubara frequencies in the finite-temperature MaF but integrations over continuous frequencies in the zero-temperature MaF and the KF. Additionally,

in the KF, all quantities are complex-valued, whereas they are real-valued in the MaF for particle–hole symmetry. Template parameters were introduced to enable the same functions to work with objects of different types. Despite the resulting additional complexity, this conveniently enables computations in each of these three formalisms in the same codebase, still using much of the same functionality.

c. *Performance.* Computing dynamical correlation functions is a computationally demanding task, especially for four-point functions that depend on three frequency arguments. Depending on the desired resolution, this requires both excessive memory to store these functions during computations and central processing unit (CPU) power to perform computations for each combination of arguments. Concerning the latter, using optimized data structures for efficient readouts of data as well as an efficient but still precise algorithm for integrating over frequencies (the numerical bottleneck) improved matters significantly. In addition, using a compiled programming language is basically a must, and keeping track of constant variables and member functions helps the compiler optimize the code.

d. *Scalability.* Apart from the simplest calculations, most diagrammatic calculations would not be feasible without parallelization. This is because practically all calculations in parquet formalism, or mfRG, require computations for all possible combinations of external arguments of the correlation functions. As those are independent from each other, it is possible and advisable to parallelize the demanding computations of bubbles and loops (see Sec. II D) in the external arguments. Using the OpenMP and MPI interfaces, this can easily be achieved for parallelization across different threads on the same node and across multiple nodes, respectively (for more details, see Sec. II G 1). As long as the memory requirements are met, the performance of the code scales almost perfectly with the computational resources.

At this point, we disclose that the present code also has a number of weaknesses that evolved over the course of development. If the reader intends to set up a new codebase for the purpose discussed here, we recommend considering the following points:

a. *Too many preprocessor macros (“flags”).* The code contains far too many preprocessor macros, used to specify different parameters and settings before compilation (see Sec. II I). This not only hampers readability but also increases the risk of errors, as it is never possible to test the full functionality of the code because one would have to compile and test all possible configurations independently. With simple combinatorics, this quickly becomes an overwhelming task. Using preprocessor macros is, however, useful for quick implementations of new functionality, which is why they accumulate over time.

b. *Too many overly complicated structures.* The code contains several classes that are way more complicated than they need to be, such as the different vertex classes or the data buffer (see Secs. II C 1 and II G 8). When they were set up, the goal was to keep them as general as possible, such that they could be used for all kinds of models in all kinds of formalisms. For this purpose, templates are used excessively as well. As a consequence, they are indeed flexible, but they are cumbersome to use in any specific context, and their implementations are difficult to grasp. In addition, the code takes a long time to compile and link, which is inconvenient for everyday

development. Ultimately, as a developer, one has to find the right trade-off between flexibility and simplicity.

c. *Too little use of existing implementations.* Several textbook algorithms, such as the Gauß-Lobatto routine for frequency integrations or the Cash–Karp routine for solving ODEs (see Secs. II G 5 and III C 1), were implemented by hand. The reason for this was the desire to comprehend and track the inner workings of the algorithms at every point during a calculation. In hindsight, much time and effort could have been saved if existing implementations of these algorithms had been used as “black boxes.”

d. *Language.* C++ is a very versatile language that runs on essentially any computer and can produce very fast code. However, a codebase written in C++ requires a lot of work to write and maintain. Initially, C++ was chosen for performance reasons. By now, however, there are established alternative programming languages that are easier to use, less error-prone, and (almost) as fast, such as Julia,¹⁹ Rust,²⁰ or Mojo.²¹

e. *Priorities.* Driven by the desire to obtain data with maximal resolution and precision, the top priority has always been performance. While this is very typical for codes written by physicists, it is not in line with the typical recommendation in software engineering, which would prioritize correctness and maintainability over performance.²² While we are confident that the code produces correct results after extensive benchmarks,¹ the code is not written in the simplest way and is not easily readable and maintainable. While we acknowledge that generating results quickly is deemed to be the most important aspect of research at present, we advocate for reconsidering the priorities during research software development for future projects.

The rest of the paper is structured as follows: In Sec. I A, we briefly introduce the single-impurity Anderson model (AM). In Sec. I B, we briefly recapitulate the main concepts of diagrammatic many-body theory. In Sec. I C, we comment on the complications that arise by performing computations in the very general Keldysh formalism, which is the main selling point of the present codebase.

In the second part of the paper, we give details on the code itself, introducing the main objects in Sec. II C and explaining the main functionality in Sec. II D. We list several options for postprocessing the raw data obtained after a completed calculation in Sec. II E and briefly explain how the data are organized in Sec. II F. Special emphasis is placed on performance-critical aspects of the code in Sec. II G. We comment on how the code is tested in Sec. II H. Finally, we provide an overview of the most important options for parameter choices that can be performed in Sec. II I, illustrating the versatility of the codebase.

In the third main part of the paper, we elaborate on how three different diagrammatic algorithms, perturbation theory, the parquet equations, and the mFRG, are implemented. In particular, we list the different flow schemes that are available in mFRG. Finally, Sec. IV presents a conclusion.

Before the end of this introduction, a disclaimer is in order: This paper does not mention every single class or function in the code but focuses on the most important aspects and functionalities. In addition, while the code enables computations in the KF and the MaF at both finite and zero temperatures, we focus our specific descriptions mainly on the KF functionality, as this is a unique feature of our codebase.

A. Model

We consider the single-impurity Anderson model (AM) in thermal equilibrium, one of the most studied models in all of condensed matter physics. Its physical behavior is well understood, and numerically exact benchmark data for single-particle correlation functions is available from NRG,²³ as are exact analytical results for static quantities at zero temperature from the Bethe ansatz.^{24,25} This makes it an ideal candidate for studies focused on reliable method development.

The AM is a minimal model for localized magnetic impurities in metals introduced by Anderson to explain the physics behind the Kondo effect.²⁶ It is defined by the Hamiltonian

$$H = \sum_{\epsilon\sigma} \epsilon c_{\epsilon\sigma}^\dagger c_{\epsilon\sigma} + \sum_{\sigma} \epsilon_d n_{d\sigma} + U n_{\uparrow} n_{\downarrow} + \sum_{\epsilon\sigma} (V_{\epsilon} d_{\sigma}^\dagger c_{\epsilon\sigma} + \text{H.c.}), \quad (1)$$

describing a local impurity d level with on-site energy ϵ_d , hybridized with spinful conduction electrons, created by $c_{\epsilon\sigma}^\dagger$, of the metal via a matrix element V_{ϵ} . Hence, it qualifies as an open quantum system. The electrons in the localized d state, where $n_{\sigma} = d_{\sigma}^\dagger d_{\sigma}$, interact according to the interaction strength U , whereas the c electrons of the bath are non-interacting. The bath electrons are hence formally integrated out, yielding the frequency-dependent retarded hybridization function $-\text{Im} \Delta^R(\nu) = \sum_{\epsilon} \pi |V_{\epsilon}|^2 \delta(\nu - \epsilon)$. We consider a flat hybridization in the wideband limit, $\Delta^R(\nu) = -i\Delta$, so that the bare impurity propagator reads $G_0^R(\nu) = (\nu - \epsilon_d + i\Delta)^{-1}$.

The code can treat all choices for the on-site energy ϵ_d . For the special choice $\epsilon_d = -U/2$, the model has particle–hole symmetry and is referred to as the symmetric Anderson model (sAM). This setting simplifies the calculations somewhat. For instance, in this case, the Hartree-term of the self-energy is constant $\Sigma_H = U/2$ (see also Sec. III A 1). In addition, in the MaF, all quantities become real-valued, whereas they are complex-valued otherwise. Hence, the code supplies a parameter flag to make use of these properties (see Sec. II 1). For general $\epsilon_d \neq -U/2$, we speak of the asymmetric Anderson model (aAM).

Some physical applications require an additional external magnetic field h , described by an additional term $h(n_{\uparrow} - n_{\downarrow})$ in the Hamiltonian. At present, the codebase is, however, not applicable in this setting, as this would break SU(2) symmetry, which is heavily used and hard-coded into the codebase (see Sec. II G 3). A generalization to $h \neq 0$ is possible but would require major effort.

While the present implementation is restricted to the AM, the code in principle can also treat other models: all data structures possess an additional internal index suitable for encoding additional dependencies and quantum numbers of more complicated models, such as a momentum dependence or multiple orbitals. Indeed, the first attempts to study the 2D Hubbard model had been started; however, the simplest KF perturbation theory calculations turned out to be too demanding at the time. The corresponding functionality is, therefore, not included in this release.

B. Diagrammatic many-body theory

The basic objects of interest in all our calculations are one- and two-particle correlation functions. Their non-trivial contributions due to interaction effects are contained in the self-energy Σ and the four-point vertex Γ ,

$$\Sigma = \text{---} \circlearrowleft \Sigma \text{---}, \quad \Gamma = \text{---} \square \Gamma \text{---} \quad (2)$$

The self-energy is used together with the bare propagator G_0 to express the one-particle propagator G via the Dyson equation

$$G = \text{---} \text{---} = \text{---} \text{---} + \text{---} \text{---} \circlearrowleft \Sigma \text{---} \text{---}, \quad (3)$$

which is formally solved by $G = 1/(G_0^{-1} - \Sigma)$. The vertex is the connected and amputated part of the two-particle correlation function $G^{(4)}$,

$$G^{(4)} = \text{---} \text{---} - \text{---} \text{---} + \text{---} \text{---} \square \Gamma \text{---} \text{---}, \quad (4)$$

from which physical susceptibilities can be obtained by contracting pairs of external legs (see Appendix C of Ref. 1 for details). The first-order contribution to the vertex is given by the fully antisymmetric, local, and instantaneous bare vertex, represented as a single dot,

$$\Gamma_0 = \text{---} \times \text{---} \sim U > 0, \quad (5)$$

in standard Hugenholtz notation. Using the bare vertex and the bare propagator G_0 , diagrammatic perturbation series for both the self-energy and the vertex can be derived, which will be the subject of Sec. III A. A perturbation series up to finite order in Γ_0 is, however, only appropriate for weak coupling strengths. In order to reach larger couplings, an infinite number of diagrams have to be summed. This is the purpose of two related formalisms, the parquet formalism and the multiloop functional renormalization group, to be discussed in Secs. III B and III C, respectively. Both formalisms employ the parquet decomposition to organize all diagrammatic contributions to Γ into one of four distinct categories: Two-particle reducible diagrams in one of the three two-particle channels a , p , and t , included in the three two-particle reducible vertices $\gamma_{r \in \{a,p,t\}}$ or two-particle irreducible diagrams, included in the fully irreducible vertex R ,

$$\Gamma = \text{---} \square R \text{---} + \text{---} \square \gamma_a \text{---} + \text{---} \square \gamma_p \text{---} + \text{---} \square \gamma_t \text{---} \quad (6a)$$

$$= \text{---} \times \text{---} + \text{---} \text{---} + \frac{1}{2} \text{---} \text{---} - \text{---} \text{---} + O[(\Gamma_0)^3]. \quad (6b)$$

Any specific diagram is said to be two-particle reducible if it can be disconnected by splitting a propagator pair. Otherwise, it is said to be two-particle irreducible. The parquet decomposition is exact, as it in essence just provides a classification of all diagrams that contribute to Γ . However, neither the parquet formalism nor the mfrG provide equations for R . In practice, some approximation is required. The simplest one is the parquet approximation (PA)

$$R = \Gamma_0 + O[(\Gamma_0)^4] \approx \Gamma_0, \quad (7)$$

which approximates the fully irreducible vertex R by the bare vertex Γ_0 . As it introduces an error in the fourth order in perturbation theory, it fails for large coupling strengths and is hence applicable only up to intermediate couplings. The PA was applied throughout in Ref. 1 and is the only one so far implemented in the codebase (see Sec. II C 1 for a comment on other possibilities).

C. Keldysh formalism

The following section assumes familiarity with the KF and describes challenges arising for computations with the KF rather than the more widespread MaF (for a more extensive discussion of the KF, see Refs. 27 and 28).

The KF^{29–31} works both out of equilibrium and in thermal equilibrium at arbitrary temperature, in a real-frequency description. This is an advantage over the more popular MaF, which works at imaginary (“Matsubara”) frequencies, requiring analytical continuation, a mathematically ill-defined problem if one works with a finite amount of imperfect numerical data. Still, the KF is seldomly used because practical calculations are more complicated for two main reasons.

In the KF, all operators acquire an additional contour index, which specifies whether they sit on the forward or backward branch of the Keldysh double-time contour. It follows that the four-point vertex, for example, has $2^4 = 16$ different components. While some of these components can be eliminated by causality or related to other components by fluctuation–dissipation relations in thermal equilibrium or symmetries, this additional index structure complicates the implementation and the numerics.

In thermal equilibrium, energy conservation can be leveraged by Fourier-transforming all correlation functions into frequency space. In contrast to the MaF at finite temperatures, this dependence is continuous. Hence, contractions over frequency arguments require numerically more expensive integrations instead of summations. The integrations become more costly at lower temperatures as the frequency dependence of the correlation functions becomes more sharply peaked. The four-point functions, which depend on three continuous frequency arguments, are the numerical bottleneck for which arbitrarily high resolutions are out of reach due to both computation and memory demands. Discretizing the frequency dependence in a clever way and using adaptive integration routines is, therefore, key, as discussed in Secs. II G 4 and II G 5.

Finally, the KF also allows for computations outside of thermal equilibrium. However, the present discussion is restricted to thermal equilibrium. Extending the code out of equilibrium is possible with moderate effort.

II. THE CODE

In part II of the paper, we describe the main building blocks of the code—the classes representing correlation functions and other functions for combining them in diagrammatic computations. Furthermore, we describe post-processing schemes and emphasize aspects important for performance. More information on the technical details of individual code pieces can be found in the documentation attached to the source code (see the code availability statement at the end of this paper).

A. Prerequisites

The code itself is written in C++17³² and is built using CMake,³³ demanding at least version 3.10. It requires the GSL,³⁴ boost,³⁵ and Eigen3³⁶ libraries, as well as the HDF5³⁷ library for input and output. For parallelization, the OpenMP³⁸ and MPI³⁹ interfaces are used. Notably, we do not supply precompiled executables that could be run directly, for several reasons: First, the code makes heavy use of preprocessor flags that must be set *before* compilation and that are in part used to specify the concrete problem at hand (see Sec. II I). Second, special compilers for the particular architecture at hand might be available, which could optimize the code during compilation and linking, improving the performance. The user should hence adapt the file CMakeLists.txt accordingly, such that the required libraries are included and linked properly and all compiler settings are as desired.

The technical documentation supplied with the code is generated automatically using the tools Doxygen,⁴⁰ Sphinx,⁴¹ Breathe,⁴² and CMake.

B. Basic structure

The structure of the main part of the codebase is depicted in Fig. 1. The main objects of interest are the SelfEnergy Σ and the four-point Vertex Γ . Separate classes have been implemented for both, discussed in detail below. Both classes use instances of the class that defines suitably chosen FrequencyGrids, to be discussed in Sec. II G 4, for discretizing the continuous frequency dependence. A self-energy and a vertex always come together in any practical calculation, representing data for a step of an mRG flow or an iteration of the parquet solver. The self-energy and vertex classes are hence combined in a State class $\Psi = (\Sigma, \Gamma)$. The algorithms discussed in Sec. III require computing bubble- and loop-type diagrams, the main functionality of the codebase. As detailed in Sec. II D 1 below, the bubble_function contracts two input vertices with a pair of propagators in one of the three two-particle channels to yield a new four-point vertex, which is stored as an instance of the Vertex class. For example, contracting two vertices Γ_1 and Γ_2 in the *a* channel is denoted as

$$B_a(\Gamma_1, \Gamma_2) = \Gamma_1 \circ \Pi_a \circ \Gamma_2 = \text{[Diagram]}, \quad (8)$$

see also Appendix C in Ref. 1 for a fully parametrized version. The required propagator pair Π belongs to a separate Bubble class

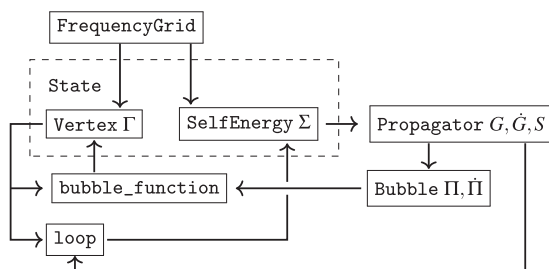


FIG. 1. Schematic depiction of the main parts of the codebase.

class, ensuring the correct combination of propagators and their parametrization. The propagators themselves are defined in the Propagator class, which essentially implements the Dyson equation, Eq. (3), combining G_0 and Σ . The former contains all the system parameters, including the regulator in mRG; the latter encodes the interaction effects. Both the Propagator and Bubble classes can handle differentiated objects arising in mRG (see Sec. III C). Finally, the loop function is used to contract two external legs of a four-point Vertex with a Propagator, yielding an instance of the SelfEnergy class, for example,

$$L(\Gamma, G) = \text{[Diagram]} \quad (9)$$

These types of diagrams are required, e.g., for the mRG flow equation of the self-energy or for the evaluation of the SDE after a previous bubble diagram computation.

C. Correlation function classes

In the following, we discuss the main building blocks of the code in more detail. We begin by outlining the self-energy and vertex classes. In addition, there are two helper classes: the first represents propagators, combining the bare propagator and the self-energy; the second combines a pair of propagators as needed for bubble-type diagrams.

1. The Vertex classes

In total, the code contains the four classes irreducible, rvert, fullvert, and GeneralVertex to store different types of four-point vertices.

The irreducible class contains the two-particle irreducible part of the vertex, R . In the PA, its 16 Keldysh components are just constants. It can easily be extended to hold nontrivial input data, for example, in the context of diagrammatic extensions⁴³ of dynamical mean-field theory⁴⁴ such as DfA⁴⁵ or DMF²RG.⁴⁶

The rvert class stores the two-particle reducible vertices $\gamma_{r \in \{a,p,t\}}$. Each of them is split up into their asymptotic classes,⁴⁷ K_1 , K_2 , and K_3 , where the $K_{2'}$ class is inferred from K_2 by crossing symmetry. Being one-, two-, and three-dimensional objects, respectively, each of those naturally has its own frequency grid. The rvert supplies several methods to store and read out data, either directly or interpolated. Conveniently, it can return all vertex parts where external legs either do or do not meet at the same bare vertex on the left or on the right-hand side by suitably combining the K_1 , $K_{2'}$, or $K_{2'}$ and K_3 classes, respectively. This turned out to be very handy for keeping track of contributions for the different asymptotic classes during calculations. In addition, the rvert class can track and, if desired, enforce symmetries in the Keldysh-, spin-, and frequency domains (see Sec. II G 3 for details). For debugging purposes, functionality not using symmetries is provided as well.

The fullvertex class combines one instance of the irreducible class and three instances of the rvert class, one for each two-particle channel a, p, t . It can then return the value of the full vertex, which is the sum of the four contributions for a given

Keldysh and spin component, interpolated at a given combination of frequencies. As each individual `rvert` instance, it can collect all those parts of the vertex where the external legs either do or do not meet at the same bare vertex on the left or on the right-hand side and includes functionality to exploit various symmetries. In addition, it can compute the p -norm of each asymptotic contribution, which is useful for debugging purposes and convergence criteria, e.g., in parquet computations.

While instances of the `fullvertex` class hold the data of the symmetry-reduced sector of a full vertex, certain diagrammatic equations involve subsets of vertex diagrams. One example is the r -channel-irreducible vertex used in the Bethe–Salpeter equations outlined in Sec. III B. Such diagrams do not necessarily obey all the symmetries of a full vertex, so they must be treated differently. These asymmetric cases are, therefore, encoded in the `GeneralVertex` class. It uses multiple instances of `fullvertex`, which together cover the symmetry-reduced sector of the asymmetric vertex data. Let us comment here that, while this approach is feasible, it turned out to be inconvenient in practice, as one always has to make sure that all sectors are covered, i.e., that all required `fullvertex` instances are provided. This is a source of logical errors that can sometimes be hard to find. In retrospect, it would have been better to pay the increased cost in memory to store all vertex contributions in the same object, making the code easier to read and to work with.

All vertex classes allow adding or subtracting two instances of the respective classes or multiplying a number with a vertex instance.

Splitting up the vertex functionality into so many different classes was made at the beginning of developing the code to provide enough flexibility, in particular regarding symmetries and a possible non-trivial input for the irreducible vertex. In hindsight, it turned out that for the computations performed in Ref. 1, this structure would not have been required in this generality.

2. The `SelfEnergy` class

The `SelfEnergy` class comes with a `dataBuffer` that stores the discrete values of the retarded and Keldysh components of the self-energy on a given frequency grid (see Secs. II G 4 and II G 8). When instantiating an object of the `SelfEnergy` type, a given frequency grid can either be supplied or a suitable one is generated automatically based on the value of the regulator Λ . In addition, the asymptotic value of the retarded component of the self-energy has to be set. Most of the time, this should be the Hartree value Σ_H , as the `SelfEnergy` inside the code is supposed to be used only for the dynamical, i.e., frequency-dependent, contributions of the self-energy, which excludes the constant Hartree value. For the sAM, the Hartree value is constant, $\Sigma_H = U/2$; in the asymmetric case, it has to be computed self-consistently beforehand. This can be performed inside the code using the `HartreeSolver` class (see Sec. III A 1).

The `SelfEnergy` class provides a host of methods used throughout the code. Most importantly, it can return the value of the self-energy either directly at a given input on the frequency grid (fast) or return an interpolated value at a given continuous frequency (not so fast). It can also set the value of Σ for a given input. In addition, one can compute the p -norm of Σ and the relative deviation to a different `SelfEnergy` instance using the maximum norm. This

is used to check convergence in parquet computations detailed in Sec. III B.

Finally, multiple operators are defined for the `SelfEnergy` class, which are used to add or subtract two `SelfEnergy` instances or to multiply some number with a `SelfEnergy` instance.

3. The `State` class

Instances of the `State` class are the high-level objects that are mainly used by the high-level algorithms discussed in Sec. III. The `State` class combines a `GeneralVertex` and a `SelfEnergy`, which together contain all non-trivial information that one might wish to compute. In that sense, it suffices to completely specify the “state” of the calculations. For the purpose of fRG calculations, the `State` class also holds the value of the flow parameter Λ .

As with the vertex classes and the `SelfEnergy` class, the `State` class also comes with operators that can be used to add and subtract states from one another and to multiply a number with a state. Under the hood, these operators just invoke the corresponding operators previously defined for the vertex and self-energy. Hence, all high-level algorithms can manipulate instances of the `State` class directly, e.g., by combining several iterations of the parquet solver in a mixing scheme.

4. The `Propagator` class

The `Propagator` class is special in the sense that it stores almost no data itself. Instead, it references instances of the `SelfEnergy` class and combines the analytical form of the bare propagator G_0 with the self-energy via the Dyson equation, $G = 1/[(G_0)^{-1} - \Sigma]$. To that end, it can return the value of a given propagator at some point, interpolated on the frequency grid of the referenced self-energy. This can be performed either directly for a given Keldysh component at some continuous frequency or vectorized over all Keldysh components. As G_0 depends on the formalism used and in mFRG on the choice of the regulator, separate methods for a variety of choices are provided. In addition, one can specify whether the full propagator G shall be computed, or the single-scale propagator S , the differentiated propagator including the Katanin extension,⁴⁸ or just the Katanin extension by itself (see Sec. III C). Note that the Katanin extension requires the self-energy differentiated with respect to the flow parameter Λ ; hence, the propagator class references *two* `SelfEnergy` instances, one non-differentiated and one differentiated.

5. The `Bubble` class

Finally, the `Bubble` class combines two propagators to yield a bubble in one of the three two-particle channels a , p , and t , according to Eqs. (C1a)–(C1c) in Ref. 1. For evaluating differentiated bubbles in mFRG, one of the propagators can be chosen to be the single-scale propagator S or the fully differentiated one \hat{G} . In that case, the bubble already takes care of the product rule, giving (symbolically) $\hat{\Pi}^S = GS + SG$ or $\hat{\Pi} = G\hat{G} + \hat{G}G$. Otherwise, it just yields $\Pi = GG$. The `Bubble` class provides functions for obtaining the value of a bubble in a given channel at specified bosonic and fermionic frequencies, either for one specific Keldysh component directly or vectorized over the Keldysh structure. This class simplifies bubble computations using the `bubble_function` (see Sec. II D 1).

D. Main functions for diagrammatic computations

Computing bubbles and loops involves contractions over quantum numbers and Keldysh indices, including integrations over frequencies for all possible combinations of external arguments, and is by far the most costly part for the numerics. A clean and efficient implementation of this functionality is, therefore, paramount and should be of the highest priority when setting up a new code. In the following, we provide technical details on this most important part of the code.

1. The `bubble_function`

The `bubble_function` implements Eqs. (C2a)–(C2c) from Ref. 1. It takes references to three vertices as arguments, one to store the result of the computation and two others to be connected by a `Bubble` object. This `Bubble` object can either be supplied as well or is initialized by an overload of the `bubble_function`, which in addition requires the two propagators that shall be used for the `Bubble`. The main work is then performed by an instance of the class `BubbleFunctionCalculator`, which performs the bubble contractions for each diagrammatic class separately. This is performed for every possible combination of external arguments, i.e., Keldysh indices and frequencies. At this point, the calculations are parallelized as outlined in Sec. II G 1. For each set of arguments, an `Integrand` object is instantiated, which puts together the two vertices and the bubble and performs the contraction over Keldysh indices if the flag `SWITCH_SUM_N_INTEGRAL` is set to 1. The `Integrand` class provides an operator that reads out the integrand at a given frequency. It is called by the integrator, invoked subsequently, and described in detail in Sec. II G 5. The results of all the frequency integrations are finally collected and *added* to the vertex object that was given as the first argument to the `bubble_function`. The choice not to output a completely new vertex but instead to add the result to an existing vertex has historical reasons to save memory. This increased the risk of logical errors during high-level algorithm implementations, though, and in hindsight, the `bubble_function` should better have been designed to output a completely new vertex object.

2. The `loop_function`

The `loop_function` implements Eq. (C3) from Ref. 1 and is structured similarly to the `bubble_function`. It takes a reference to self-energy for storing the result as well as references to a vertex and a propagator as arguments for the loop. For each external fermionic frequency, in which the computation is parallelized again, it invokes the integrator to perform a frequency integration using the `IntegrandSE` class. For the aAM, the asymptotic value of the just computed self-energy is extracted from the Hartree- and the $K_{1,t}$ and $K_{2,t}$ terms after the calculation. For the sAM, the asymptotic value of the self-energy is a known constant.

E. Postprocessing

The code provides a host of postprocessing functions. These are not required for the actual calculations themselves but are useful to extract additional information from their results, either as consistency checks or to infer derived quantities for later analysis.

1. Causality check for the self-energy

By causality, the imaginary part of the retarded component of the self-energy is strictly non-positive;⁴⁹ $\text{Im} \Sigma^R(\nu) \leq 0$ for all frequencies $\nu \in \mathbb{R}$. A violation of this condition not only constitutes an unphysical result but often leads to numerical instabilities. The code, therefore, provides the function `check_SE_causality` that checks this condition for a supplied instance of `SelfEnergy`. Typically, this function is invoked after each ODE step during an mFRG calculation or after each iteration of the parquet solver.

2. Fluctuation dissipation relations

In thermal equilibrium at temperature T , one has a fluctuation–dissipation relation (FDR)^{11,27} between the retarded and the Keldysh components of the propagator, $G^K(\nu) = 2i \tanh(\frac{\nu}{2T}) \text{Im} G^R(\nu)$, and the self-energy, $\Sigma^K(\nu) = 2i \tanh(\frac{\nu}{2T}) \text{Im} \Sigma^R(\nu)$. This relation can be used to infer the Keldysh components of the self-energy from the retarded component or vice versa; hence, it would in principle suffice to compute only one of the components. However, in the vectorized form of the code, both components of the self-energy are computed anyway. The FDR can hence be used as an internal consistency check, provided by the function `check_FDTs_selfenergy`. It computes Σ^K from Σ^R via the FDR and compares it to the independently computed Keldysh-component of the self-energy by computing the 2-norm of the difference.

As an additional consistency check, the fulfillment of fluctuation–dissipation relations for the K_1 classes, reading

$$\text{Im} K_1^R(\omega) = -\frac{i}{2} \tanh\left(\frac{\omega}{2T}\right) K_1^K(\omega), \quad (10)$$

can be examined. One may also want to check generalized FDRs for three-point and four-point contributions of the vertex.⁵⁰

3. Kramers–Kronig relation

For functions $f(\omega)$ that are analytic in the upper half plane, like retarded single-particle correlation functions, the Kramers–Kronig transform relates the real and imaginary parts via

$$\text{Re} f(\omega) = \frac{1}{\pi} \mathcal{P} \int_{-\infty}^{\infty} d\omega' \frac{\text{Im} f(\omega')}{\omega' - \omega}, \quad (11)$$

where \mathcal{P} denotes the Cauchy principal value. Inside the code, the function `check_Kramers_Kronig` can be used to test how well this generic analytic property is fulfilled.

4. Sum rule for the spectral function

The fermionic spectral function $A(\nu) = -\text{Im} G^R(\nu)/\pi$ must obey the sum rule

$$\int_{-\infty}^{\infty} d\nu A(\nu) = 1. \quad (12)$$

The function `sum_rule_spectrum` implements this integral as a consistency check.

5. Susceptibilities

Susceptibilities, which are of significant physical relevance, are derived from the vertex by contracting pairs of external legs. Diagrammatically, the formula for the a -channel susceptibility reads

$$\chi_a = \text{bubble} + \text{bubble} \Gamma \text{bubble}, \quad (13)$$

and similarly for the susceptibilities in the p and t channel. The fully parametrized equations are provided in Eq. (C7) of Ref. 1. Linear combinations of these diagrammatic susceptibilities yield the physical susceptibilities [see Eq. (C8) of Ref. 1]. The code computes susceptibilities using the function `compute_postprocessed_susceptibilities`, which can be invoked after a completed calculation using the name of the file that stores the results. It iterates through all layers that correspond to ODE steps or parquet iterations (see Sec. II F), evaluates Eq. (C7) using the vertex and self-energy for each, and stores the results as a new dataset in the same file.

It was found in Ref. 47 that for converged parquet computations, susceptibilities can more easily be extracted directly from the K_1 class. As discussed in Refs. 1 and 51, one can also choose to compute susceptibilities that way during fRG computations, even though the two schemes are inequivalent if multiloop convergence is not reached. The two different schemes of computing susceptibilities can then be used to gauge the quality of the truncation.

6. Vertex slices

Finally, the function `save_slices_through_fullvertex` can be used to read out two-dimensional “slices” of the full vertex. It takes the filename corresponding to the results of a finished calculation as an argument, iterates through all layers, and saves a two-dimensional cut of all Keldysh components of the full vertex in the t -channel parametrization for zero transfer frequency ($\omega_t = 0, v_t, v_t'$) for a given spin component. While this function does not perform any non-trivial calculations, it is useful for visualization purposes. If desired, the function can be straightforwardly adapted to store vertex slices at finite transfer frequencies, enabling full scans through the three-dimensional structure of the four-point vertex.

F. I/O

We use the HDF5 file format³⁷ for input and output purposes throughout. To organize the data for output, the contents of a state are split into different datasets that correspond, e.g., to all the asymptotic classes of the vertex in each channel, the self-energy, the frequency grids, and the most important parameters of the calculation. The output file is then organized on a high level in terms of “ Λ layers,” the idea being that each layer enables access to a different state stored in the same file. Thereby, a single file contains, e.g., the results of a full mFRG flow, where each “ Λ layer” corresponds to a different value of the regulator. Alternatively, this structure can be used to store the results of all iterations needed for solving the parquet equations. Of course, one can equally well use just a single layer to store the end result of a computation, such as a converged solution of the parquet equations or the result of a PT2 computation.

The function `write_state_to_hdf` creates a new file with a fixed number of layers and saves an initial state into the first layer. Additional states generated during subsequent computations can be added to the same file (but into a different layer to be specified) using the function `add_state_to_hdf`. In effect, these functions are wrappers of a host of additional functions that are able to store various data structures, such as scalars, vectors, or even Eigen-matrices, in an HDF file.

When using parallelization, as detailed in Sec. II G 1, one has to ensure that only one single process writes data into the output file. Collisions, where multiple processes simultaneously try to write to the same location in memory, will cause the program to crash.

It is possible to read data from an existing HDF file to generate a new state for subsequent computations. For this purpose, the function `read_state_from_hdf` reads a state from a specified layer of a provided HDF file. One can thus do checkpointing: If all steps of an mFRG flow or all iterations of the parquet solver are stored separately, a computation that was interrupted can be continued from the last step stored. This design feature is useful for large computations that have to be split over several separate jobs or in the case of a hardware error causing a job to crash. Setting up checkpointing functionality is, therefore, strongly recommended.

G. Performance

In the following, we discuss parts of the code of special importance for performance. Of course, there is always a trade-off between accuracy and performance, as, e.g., an arbitrary high frequency resolution quickly becomes prohibitive. Nevertheless, efficient implementations are necessary for challenging computations.⁵² For the precision-focused calculations for which this codebase was developed, these parts are, therefore, of utmost importance.

1. MPI+OpenMP parallelization

As mentioned in the beginning, mFRG and parquet computations can be heavily parallelized since the correlation functions are (repeatedly) evaluated independently for every possible combination of external arguments. Parallelization is especially advisable for computing bubbles of two four-point vertices, as outlined in Sec. II D 1. We use the OpenMP interface for parallelization across multiple threads on a single node and the MPI interface for parallelization across multiple nodes. While OpenMP parallelization works with shared memory, meaning that all threads have access to the same data on the node that they are running on, one has to be careful with MPI parallelization working on distributed memory. Processes that run on different nodes to compute, say, a four-point vertex for different sets of external arguments cannot write their results into the same instance of a four-point vertex. Hence, we introduce additional buffers distributed across the nodes. After the computation of, say, a four-point vertex is finished, these buffers are collected, and their contents are put together to yield the full result. While this scheme is initially somewhat cumbersome to set up, it pays off tremendously, as the code’s performance scales well with the computational resources, including multiple nodes. This is because, first, computations for different external arguments are independent from each other, so there is minimal communication between the nodes. Second, the number of external arguments required for

precision-focused calculations is large, so individual threads have little downtime waiting for other threads to finish. For example, the most expensive calculations in Ref. 1 involved 125 points along each of the three frequency axes, which were parallelized across 32 nodes running 32 threads each. Provided enough CPU power, the resolution could, in principle, be increased further but is ultimately limited by memory.

2. Vectorization

As outlined in Sec. I C, KF calculations require computing 2^n Keldysh components of n -point functions. These components can be arranged into a matrix, yielding, e.g., a 4×4 matrix for the four-point vertex. This structure can be exploited for summing over Keldysh indices by using vectorization and the data structures of the Eigen library,³⁶ significantly improving performance. This works because all Keldysh components are stored in contiguous sections of memory. Of course, the other parts of the code have to be able to use these data structures properly, which is why all functions that enable, e.g., access to the correlation functions (see Sec. II C) have two versions: one that can handle matrix-valued data when vectorization is used, and another used otherwise.

When using vectorization, all Keldysh components have to be stored explicitly. As a consequence, identities that relate different Keldysh components, such as certain symmetries or FDRs, cannot be used to reduce the numerical effort. Although maximal exploitation of symmetries initially was one of our main objectives, we later found that vectorization over Keldysh components is preferential despite the larger memory costs.

In the finite- T MaF, we use vectorization to represent the Matsubara frequency dependence of all correlation functions. This leads to massive speedups when performing Matsubara sums as matrix-multiplications.

3. Symmetries

Many symmetries for reducing the number of data points to be computed directly can still be used together with vectorization over Keldysh indices. These include crossing symmetry of the vertex, which relates a vertex to itself with one pair of external fermionic legs exchanged; complex conjugation of the vertex; SU(2) symmetry in the absence of a magnetic field (which, in combination with crossing symmetry, reduces the number of independent spin components to 1); and frequency symmetries in the presence of particle-hole symmetry. For explicit details on these symmetries, see Appendix A in Ref. 1.

Since frequency integrations are the most costly part of the computations, symmetry operations are not used for evaluating integrands on the fly. Instead, they are used to reduce the number of vertex components to be computed. Since the vectorized version of the code performs sums over Keldysh indices by matrix multiplication, the result of the integration contains all Keldysh components. Hence, we use the symmetry relations to reduce the other arguments, i.e., spin and frequency. Information about the symmetry-reduced components is encoded in symmetry tables. These contain entries for every channel, asymptotic class, spin component, and frequency sector and indicate whether a data point belongs to the symmetry-reduced sector or, otherwise, how to retrieve a value via symmetry relations.

4. Frequency grids

For numerical calculations, the continuous frequency dependence of correlation functions in the KF (and in the MaF at $T = 0$) must be discretized. Since these functions can become sharply peaked around certain frequencies, especially at lower temperatures, but simultaneously decay only slowly asymptotically (typically $\sim 1/\nu^2$ or even $\sim 1/\nu$ for some components), finding a suitable discretization that resolves all sharp structures but still captures the asymptotic decay is hard. Since the sharp features mostly occur at smaller frequencies (measured relative to the hybridization Δ), we use a frequency grid that provides high resolution at small frequencies and fewer points at high frequencies. To achieve this, an equidistant grid of an auxiliary variable $\Omega \in [-1, 1]$ is mapped to frequencies according to $\nu(\Omega) = A\Omega|\Omega|/\sqrt{1 - \Omega^2}$. The parameter $A > 0$ can be suitably chosen automatically or by hand for all quantities, as further explained in Appendix G of Ref. 1. However, we do not recommend optimizing A automatically, as this can become expensive and unreliable in the presence of numerical artifacts.

The frequency grid is implemented in the `FrequencyGrid` class. It specifies the grid parameters such as the number of grid points or the scale factor A , and can access both continuous frequencies ν and auxiliary variables Ω corresponding to a given discrete index. Crucially, this also works the other way around, yielding the discrete index that corresponds to the frequency closest to a given continuous frequency. This is needed for interpolations, discussed in Sec. II G 7.

An instance of the `FrequencyGrid` class is instantiated in every instance of one of the correlation function classes to parameterize their respective frequency dependencies. The vertex classes naturally require up to three instances of the `FrequencyGrid` each.

The frequency grids are rescaled during mFRG flow calculations, which use the hybridization flow scheme (see Sec. III C). The `FrequencyGrid` class provides all the functionality required for that purpose.

As a side note, two alternative frequency grids have been implemented. One is a hybrid grid, which consists of a quadratic part at small frequencies, a linear part at intermediate frequencies, and a rational part at large frequencies. The other uses polar coordinates to parameterize the two-dimensional frequency dependence of three-point functions, i.e., the K_2 and K_2' classes. Which grid is to be used is controlled by the `GRID` flag (see Sec. II I). In our experience, the non-linear grid explained at the beginning of this section is the most useful if the scale parameters A are chosen suitably.

5. Frequency integration

The following passage is taken almost verbatim from the Ph.D. thesis of E. Walter.²⁸

Computing numerical integrals with high accuracy is a crucial ingredient for obtaining correct results in the context of the diagrammatic calculations discussed here. At the same time, the integrator is also critical for the performance of the computation, since evaluating integrals constitutes the computationally most expensive part of the code. For these reasons, we use an adaptive integration routine that automatically determines where to evaluate the integrand within the integration domain. Regions with sharp features require many evaluation points in order to get high accuracy,

while in regions where the integrand is smooth, fewer evaluations suffice, which increases the performance of the computation. Such an adaptive integrator is really indispensable for the problem at hand. Non-adaptive routines like a simple trapezoidal or Simpson rule on an equidistant grid often lead to systematically wrong results.

We use n -point integration rules that approximate integrals of the kind $\int_a^b F(x) dx \approx \sum_{j=1}^n F(x_j) w_j$ with nodes x_j and corresponding weights w_j . The integrator we use and which is implemented in the `Adapt` class in the code is an adaptive 4-point Gauss–Lobatto routine with a 7-point Kronrod extension and a 13-point Kronrod extension as an error estimate, as detailed in Ref. 53. The benefit of Gauss–Lobatto rules, compared to, e.g., the widely used Gauss–Kronrod rules, is that the nodes include the endpoints of the integration domain. This allows us to subdivide the domain at the nodes of the integration rule and reuse points that have been computed previously, which is preferential in terms of performance. Similarly, the Kronrod extensions of a Gauss–Lobatto rule reuse all points from a corresponding lower-point rule and simply add additional points, which effectively allows us to get two different rules from one set of evaluation points.

The nodes x_j of the 4-point Gauss–Lobatto rule with 7-point and 13-point Kronrod extensions are distributed as shown in Fig. 2. There, the lower row indicates the values of the nodes for integration boundaries $a = -1$, $b = 1$ (for other values of a , b , the values have to be rescaled correspondingly). The four-point Gauss–Lobatto rule (GL4) and four-point Gauss–Lobatto with seven-point Kronrod extension (GLK7) use the following points:

$$\text{GL4}(x_0, x_6) = \sum_{j \in \{0,2,4,6\}} F(x_j) w_j, \quad (14a)$$

$$\text{GLK7}(x_0, x_6) = \sum_{j=0}^6 F(x_j) w_j. \quad (14b)$$

The smaller marks between the nodes x_0, \dots, x_6 in the graphical representation above indicate the additional 6 points that are added in the 13-point Kronrod extension (GLK13), which are only known numerically (these and the weights w_j are found in Ref. 53).

The recursive algorithm of the integrator then works as shown in Fig. 3. Note that the error estimate I_s is determined only once for the full integral and then reused for each subinterval in order to avoid infinite recursions in subintervals. A typical recommended value for the relative accuracy is $\varepsilon = 10^{-5}$, which is set by the global variable `integrator_tol` (see Table II).

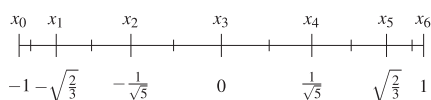


FIG. 2. Distribution of the nodes x_j of the 4-point Gauss–Lobatto rule with 7-point and 13-point Kronrod extensions. The lower row indicates the values of the nodes for integration boundaries $a = -1$, $b = 1$.

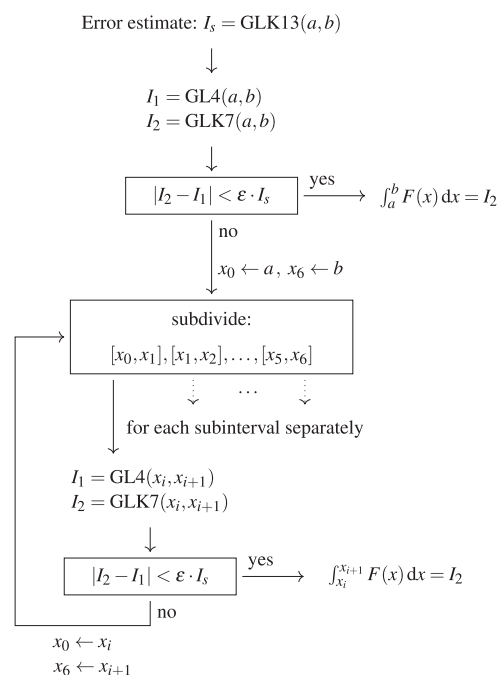


FIG. 3. Schematic illustration of the integration algorithm: an adaptive 4-point Gauss–Lobatto routine with a 7-point Kronrod extension and a 13-point Kronrod extension as an error estimate.

6. Asymptotic corrections to frequency integrals

In Sec. II G 5, it was explained how frequency integrations over a finite interval $[a, b]$ are performed. Since diagrammatic calculations require integrations over the full frequency axis (or summations over an infinite set of discrete Matsubara frequencies for the finite- T MaF), the contributions to the integral resulting from the high-frequency asymptotics of the integrands have to be treated as well. This is particularly relevant for slowly decaying integrands, which occur often, as the correlation functions arising in the present context typically only decay as $\sim 1/\nu$ or $\sim 1/\nu^2$.

In the KF and the zero- T MaF, involving continuous frequency integrations, a naïve treatment turned out to be sufficient: Since the frequency axes are discretized non-uniformly, as described in Sec. II G 4, the largest discrete frequency grid point is always so large that the high-frequency tails can be treated via quadrature, ignoring the minuscule contributions of even larger frequencies. For finite- T MaF computations, which involve infinite sums, the code provides two options for the treatment of high-frequency tails in the integrand: (i) The tails can be treated via quadrature by approximating the sum with an integral and then following the same logic as in the KF. (ii) For bubble computations, the lowest order contribution from the bare bubble, which is known analytically, can be used. This is justified by the fact that in the high-frequency asymptotic limit, the non-trivial contributions due to interactions encoded in the self-energy have decayed, and only the bare contribution is responsible for the asymptotic behavior. The first or second

option is chosen with the `ANALYTIC_TAILS` parameter flag (see also Sec. II I).

7. Interpolation routines

Whenever the value of a correlation function at some continuous frequency argument is required, in particular during frequency integrations, the data stored on discrete frequency grids has to be interpolated. In addition, the diagrammatic algorithms discussed here have feedback between the three two-particle channels, which all have their own channel-dependent parametrizations. This necessitates accurate interpolations between different frequency parametrizations; otherwise, errors accumulate over the course of a computation.

To handle the interpolation of multidimensional correlation functions, we implemented multilinear interpolation and cubic spline interpolation using cubic Hermite splines. While spline interpolation is robust against minor inaccuracies of the data points and offers faster convergence in the number of frequency points for smooth functions, multilinear interpolation is generally faster numerically. Having tried out both options, we prefer linear interpolation, as spline interpolation only really becomes useful for better precision if the function is already well resolved.

Regarding linear interpolation, the code offers options: One can either interpolate on the grid of frequencies ν or on the grid of auxiliary frequencies Ω , which are equidistantly spaced on the interval $[-1, 1]$ (see Sec. II G 4). We found the latter option to be more accurate. The global parameter `INTERPOLATION` specifies which type of interpolation shall be used (see also Sec. II I).

8. Data structures

The central low-level data structure used for storing and retrieving numerical data inside the code is the `dataBuffer` class. It was devised with the two main intentions of efficiency and flexibility in mind (see also our discussion of the main design choices for the codebase in the introduction, Sec. I). On the one hand, it should enable building integrands that return scalar- or vector-valued entries as efficiently as possible, particularly avoiding conditional (“if-else”) statements during runtime, as these prevent optimizations such as loop-vectorization or function inlining. On the other hand, it should be useable in all parts of the codebase, e.g., for both calculations with interpolations on continuous frequency grids and for finite- T MaF calculations, which only require indexing of discrete data points.

The `dataBuffer` class is structured as follows. It builds upon the `dataContainerBase` class, which is used to represent multi-dimensional tensors, allowing scalar and vector-valued access to contiguous elements. The `DataContainer` class then inherits `dataContainerBase`, adding frequency information. It contains a multi-dimensional frequency grid (see Sec. II G 4) to parameterize all its associated frequency arguments and provides functions to analyze the resolution of frequency grids. Inheriting the `DataContainer` class, the `Interpolator` classes then implement the different interpolation routines outlined in Sec. II G 7. Multilinear cubic spline interpolations require pre-computation and storage of interpolation coefficients, whereas linear interpolations happen on the fly. Finally, the `dataBuffer` class inherits both the

`Interpolator` and the `DataContainer` classes and can be used in actual computation. In addition, it can update and optimize grid parameters as required.

9. Template arguments

Another performance-critical aspect of the codebase is its heavy use of templates. In particular, the propagation of template arguments as specified by preprocessor flags enables the determination of the required diagrammatic combinations for any given computation at compile time. Selecting and combining the necessary vertex contributions this way, e.g., for contributions to specific asymptotic classes, enables further optimization by the compiler. However, the ubiquity of template arguments comes at the expense of readability in many places.

H. Tests

The code includes a large number (178 as of writing) of self-explanatory unit tests that run checks on the low-level parts of the codebase. They are implemented using the popular `Catch2` library⁵⁴ and are invoked from a separate C++ source file, `unit_tests.cpp`, which should be built separately from the main source file. From inside this file, more involved and expensive tests can be started if desired. These include detailed tests of the ODE solver or perturbation theory, which are too expensive to be part of the unit test suite. Finally, the code includes functionality to produce reference data that can be used later to compare the results of a calculation after changes to the code have been made. We have found it immensely useful to include many unit tests in the codebase, as they can tell almost immediately if a single technical part of the code has broken. Moreover, having a way to compare the results of very involved computations that involve large parts of the codebase at once is useful to catch logical errors. We wholeheartedly recommend both.

I. Parameters

Before any individual calculation can be started, a number of parameters have to be set. As the code provides a large degree of flexibility, the number of possible parameter choices is large. Most of these parameters are set inside the corresponding header files before compilation. The reason for this is that, depending on these choices, often different functionality of the code is invoked, depending, e.g., on the choice of formalism. This is achieved by defining preprocessor macros accordingly, which makes the corresponding functionality accessible. As discussed previously in too many preprocessor macros (“flags”), while this approach was useful for implementing new functionality quickly, in the long run, it turned out to be problematic with regard to the readability and maintainability of the code. Table I provides a list (albeit incomplete) of the most important preprocessor flags used in the code with a short description of each.

In addition, global parameters have to be set, which specify settings like the resolution of the frequency grid, convergence criteria, or start- and end-points of an mFRG flow. Table II provides a non-exhaustive list of those.

Finally, it should be mentioned that once the code has been compiled and the resulting executable is to be called, it requires three run-time arguments: The first one invokes an mFRG run if it

TABLE I. Incomplete list of the most important preprocessor macros to be set before compilation.

Macro name	Possible values	Description
ADAPTIVE_GRID	...	If defined, use the optimization routine to find the best scale factor A of the frequency grid; if undefined, just rescale the grid. Warning: Can be expensive and unreliable in the presence of numerical artifacts
ANALYTIC_TAILS	0, 1	0 for false; 1 for true. If true, the analytic expression for the bare bubble is used to treat the high-frequency asymptotics during bubble computations in the finite- T MaF
BARE_SE_FEEDBACK	...	If defined, only bare selfenergy is used. It only makes sense if STATIC_FEEDBACK is defined. Useful for benchmarks with previous Keldysh fRG schemes
CONTOUR_BASIS	0, 1	0 for false, 1 for true: If true, no Keldysh rotation is performed, and the contour basis is used instead to parameterize the Keldysh components of all correlation functions. It is useful for comparisons with results that use this convention. Not as well tested and, therefore, not recommended for production runs
DEBUG_SYMMETRIES	0, 1	0 for false; 1 for true. Performs computations without the use of symmetries, if true. Useful for debugging purposes
GRID	0, 1, 2	Controls which frequency grid is to be used. 0 for the non-linear grid, 1 for the hybrid grid, and 2 for the polar grid. Recommendation: 0. See also Sec. II G 4
KATANIN	...	If defined, the Katanin extension is used during fRG computations
KELDYSH_FORMALISM	...	Determines whether calculations shall be performed in the Keldysh or Matsubara formalism. 0 for Matsubara formalism (MaF); 1 for Keldysh formalism (KF)
MAX_DIAG_CLASS	1, 2, 3	Defines the diagrammatic classes that will be considered: 1 for only K_1 , 2 for K_1 and K_2 , and 3 for the full dependencies. Useful for debugging purposes and for computations in second-order perturbation theory, or if STATIC_FEEDBACK is defined, when only K_1 is required
NDEBUG	...	If defined, assert functions are switched off. Recommended setting for production runs
PARTICLE_HOLE_SYMM	0, 1	0 for false; 1 for true. If true, particle-hole symmetry is assumed
PT2_FLOW	...	If defined, only compute the flow equations up to $O(U^2)$. Only makes sense for pure K_1 calculations. It is useful as a consistency check together with independent PT2 calculations
REG	2, 3, 4, 5	Specifies the mFRG flow regulator to be used. 2: Δ -flow, 3: ω -flow, 4: U -flow, 5: T -flow. For details, see Sec. III C 2
REPARAMETRIZE_FLOWGRID	...	If defined, the flow parameter is reparametrized according to Sec. III C 1. Only recommended for the Δ -flow
SBE_DECOMPOSITION	0, 1	0 for false; 1 for true. If true, the SBE decomposition is used to parameterize the vertex and the flow equations. Only implemented in the MaF!
SELF_ENERGY_FLOW_CORRECTIONS	0, 1	0 for false; 1 for true. If true, corrections to the flow equations for the vertex from the self-energy, starting at $\ell = 3$, are included
STATIC_FEEDBACK	...	If defined, use static K_1 inter-channel feedback as performed in 11. Only makes sense for pure K_1 calculations
SWITCH_SUM_N_INTEGRAL	0, 1	0 for false; 1 for true. If true, the sum over internal Keldysh indices is performed before the frequency integration. Recommended setting: 1
USE_ANDERSON_ACCELERATION	0, 1	0 for false; 1 for true. If true, Anderson acceleration is used to converge parquet iterations and self-energy iterations in mFRG faster
USE_MPI	...	If defined, MPI is used for parallelization across multiple nodes
USE_SBEb_MFRG_EQS	0, 1	Determines which version of the SBE approximation shall be used. 0 for SBEa, 1 for SBEb. Only implemented in the MaF!
VECTORIZED_INTEGRATION	0, 1	0 for false; 1 for true. If true, integrals are performed with vector-valued integrands. For Keldysh, vectorization over Keldysh indices. For Matsubara at finite T , vectorization over the Matsubara sum
ZERO_TEMP	0, 1	0 for false; 1 for true. If true, temperature $T = 0$ is assumed

TABLE II. Incomplete list of global parameters to be set before compilation.

Parameter name	Type	Description
converged_tol	double	Tolerance for loop convergence in mFRG
COUNT	int	Used to set the number of frequency points in the MaF. For details, see the definitions in the file <code>frequency_parameters.hpp</code>
Delta_factor_K1	int	Scale factor for the frequency grid of the K1 vertex class
Delta_factor_SE	int	Scale factor for the frequency grid of the self-energy
Delta_factor_K2_w	int	Scale factor for the frequency grid of the bosonic frequency of the K2 and K2' vertex classes
Delta_factor_K2_v	int	Scale factor for the frequency grid of the fermionic frequency of the K2 and K2' vertex classes
Delta_factor_K3_w	int	Scale factor for the frequency grid of the bosonic frequency of the K3 vertex class
Delta_factor_K3_v	int	Scale factor for the frequency grid of the fermionic frequencies of the K3 vertex class
EQUILIBRIUM	bool	If true, use equilibrium FDRs for propagators
glb_mu	double	Chemical potential – w.l.o.g. ALWAYS set to 0.0 for the AM!
integrator_tol	double	Integrator tolerance
inter_tol	double	Tolerance for closeness to grid points when interpolating
INTERPOLATION	linear, linear_on_aux, cubic	Interpolation method to be used. <code>linear</code> : linear interpolation on the frequency grid. <code>linear_on_aux</code> : linear interpolation on the grid for the auxiliary frequency Ω . <code>cubic</code> : Interpolation with cubic splines (warning: expensive!)
Lambda_ini	double	Initial value of the regulator Λ for an mFRG flow
Lambda_fin	double	Final value of the regulator Λ for an mFRG flow
Lambda_scale	double	Scale of the log substitution, relevant in the hybridization flow
dLambda_initial	double	Initial step size for ODE solvers with adaptive step size control
nBOS	int	Number of bosonic frequency points for the K_1 vertex class
nFER	int	Number of fermionic frequency points for the self-energy
nBOS2	int	Number of bosonic frequency points for the K_2 and K_2' vertex classes
nFER2	int	Number of fermionic frequency points for the K_2 and K_2' vertex classes
nBOS3	int	Number of bosonic frequency points for the K_3 vertex class
nFER3	int	Number of fermionic frequency points for the K_3 vertex class
U_NRG	std::vector<double>	Vector with the values of U in units of Δ that an mFRG flow should cover. Serve as checkpoints for the flow. It is useful for benchmarking purposes if data from other methods at precise parameter points are available
VERBOSE	bool	If true, detailed information about all computational steps is written into the log file. Recommended setting for production runs: <code>false</code>
nmax_Selfenergy_iterations	int	Maximal number of self-energy iterations to be performed during an mFRG flow for $\ell \geq 3$. Default value: 10
tol_selfenergy_correction_abs	double	Absolute tolerance for self-energy iterations in mFRG. Default value: 10^{-9}
tol_selfenergy_correction_rel	double	Relative tolerance for self-energy iterations in mFRG. Default value: 10^{-5}

is a positive integer, specifying the maximal number of loop orders calculated during the mFRG flow. Alternatively, if it is set to 0 or -1 , a parquet or PT2 calculation is started, respectively. The second is a positive integer and specifies the number of nodes to be utilized. The third runtime argument defines the temperature for the

calculation and was introduced to easily enable parameter sweeps without having to recompile the code every time. Note that its value is irrelevant for calculations that have the flag `ZERO_TEMP` set to 1 or if an mFRG run is performed with the flag `REG` set to 5, which employs the temperature flow.

III. ALGORITHMS

In the third main part of the paper, we finally describe three diagrammatic algorithms that have been implemented. These are second-order perturbation theory (PT), a self-consistent solution of the parquet equations, and the flow equations provided by the multiloop functional renormalization group (mFRG). For all three methods, we first give some theoretical background before describing schematically how the algorithms are implemented and what functions are being used.

A. Perturbation theory

The simplest computations that can be performed with the code are perturbation theory calculations. While these are easy to implement in the second order, going to higher orders involves an increasing number of diagrams, which can in principle be evaluated separately. This is, however, not always straightforward, e.g., if symmetries are not to be exploited: individual diagrams of the perturbation series do not all have the same symmetries as a full vertex, such that symmetry-related diagrams have to be provided, which can become tedious. Alternatively, the flag `DEBUG_SYMMETRIES` can be set to 1, see Sec. II 1, in which case the code does not attempt to exploit symmetries. As higher-order perturbation theory has so far only been performed for testing purposes and consistency checks (see, e.g., Chap. 7 in Ref. 28), we refrain from going into further detail here. Instead, we focus just on the second-order case and on Hartree-Fock theory for the self-energy relevant to the aAM.

1. Hartree-Fock

As elaborated in Ref. 1, it is helpful to replace the bare propagator G_0 by the Hartree-propagator G_H , which is shifted by the Hartree-term of the self-energy,

$$G_0^R \rightarrow G_H^R = \frac{1}{v - \varepsilon_d + i\Delta - \Sigma_H^R}. \quad (15)$$

For the sAM, this is almost trivial, as the retarded component of the Hartree term reads $\Sigma_H^R = U/2$, which simply yields $G_H^R = (v + i\Delta)^{-1}$. For the aAM, on the other hand, the Hartree-term can be computed self-consistently.

For this purpose, the class `Hartree_Solver` provides the function `compute_Hartree_term_bracketing`. It computes Σ_H^R via

$$\Sigma_H^R = U \int \frac{dv'}{2\pi i} G_H^<(v'), \quad (16)$$

where in thermal equilibrium, the relation $G^<(v) = -2i n_F(v) \text{Im} G^R(v)$ is used with the Fermi function $n_F(v) = 1/(1 + e^{v/T})$. As Σ_H^R enters both sides of Eq. (16), this calculation is performed self-consistently using a simple bracketing algorithm.

In addition, the `Hartree_Solver` class provides the function `compute_Hartree_term_oneshot`, which evaluates Eq. (16) just once, given a provided self-energy for $G^R(v)$. This function is invoked in the context of parquet iterations and evaluations of mFRG flow equations to update the Hartree term of the aAM.

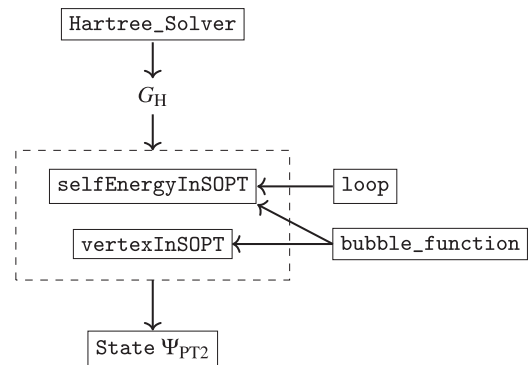


FIG. 4. Schematic depiction of the function `sopt_state`.

Finally, the `Hartree_solver` class provides functionality to check the fulfillment of the Friedel sum rule⁵⁵ $\langle n_\sigma \rangle = \frac{1}{2} - \frac{1}{\pi} \arctan [(\varepsilon_d + \Sigma(0))/\Delta]$, which the self-consistent Hartree term fulfills at $T = 0$.

2. Second order perturbation theory (PT2)

The self-energy and vertex in second-order perturbation theory are computed via the function `sopt_state`, which works as depicted in Fig. 4. It first initializes a bare state (see Sec. II C 3), given the system parameters and the current value of the regulator Λ . For the aAM, this already includes a self-consistent calculation of the Hartree term (see Sec. III A 1). Then, it invokes the function `selfEnergyInSOPT`, which computes the single diagram for the dynamical part of the self-energy in PT2 by first computing a bare bubble in the a -channel using the `bubble_function` (see Sec. II D 1), with two bare vertices, and then closing the loop over that bare bubble with the Hartree-propagator using the `loop` function (see Sec. II D 2).

Thereafter, the vertex is computed using the function `vertexInSOPT`, which simply invokes the `bubble_function` three times, once for each of the three two-particle channels a , p , and t , using two bare vertices, adding each result to the vertex.

In total, this procedure yields all diagrams for the dynamical part of the self-energy and the vertex in PT2, using the Hartree-propagator G_H . For the precise diagrammatic definition of PT2, see Appendix F in Ref. 1.

B. Parquet equations

The parquet formalism⁵⁶ provides a self-consistent set of equations for the self-energy Σ and the three two-particle reducible vertices γ_r with $r \in \{a, p, t\}$. The latter are given by the Bethe-Salpeter equations (BSEs)

$$\gamma_a = I_a \Gamma, \quad (17a)$$

$$\gamma_p = \frac{1}{2} I_p \Gamma, \quad (17b)$$

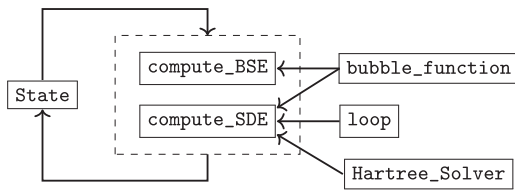


FIG. 5. Schematic depiction of the `parquet_solver` function.

$$\gamma_r = - \left(\text{diagram with } I_r \text{ and } \Gamma \right), \quad (17c)$$

where $I_r = \Gamma - \gamma_r$ is the two-particle irreducible vertex in channel r . The self-energy is given by the Schwinger–Dyson equation (SDE),

$$\Sigma = - \left(\text{diagram with } \Gamma \right), \quad (18)$$

which includes the Hartree term discussed in Sec. III A 1. Together, these equations close once the fully irreducible vertex R is provided, for example, by employing the PA, as discussed in Sec. I B.

In practice, these equations are solved iteratively. The code provides functions to evaluate the right-hand sides of the BSEs and the SDE, called `compute_BSE` and `compute_SDE`. Schematically, the parquet solver works as depicted in Fig. 5. Inside the code, a parquet computation is started by the function `run_parquet`. It first initializes a state using PT2, as detailed in Sec. III A 2, before the `parquet_solver` function is called. Internally, the `parquet_solver` calls `parquet_iteration`, which evaluates the BSEs and the SDE, given a provided input state, and combines them into an output state. The corresponding functions `compute_BSE` and `compute_SDE` use the machinery described in Secs. II C and II D to evaluate Eqs. (17) and (18). In practice, symmetrizing Eq. (17), i.e., computing the sum of the right-hand side as is and with I_r and Γ interchanged and dividing by two, has proven beneficial for stability.

In addition, we found it helpful to combine all three ways to evaluate the SDE, Eq. (18) (see Appendix D in Ref. 1).

The `parquet_solver` can either proceed directly from one iteration to the next, or it can combine multiple results from previous iterations using mixing schemes to improve convergence. For example, one can combine the two most recent iterations with a mixing factor as outlined in Eq. (G4) of Ref. 1. One may start with a mixing factor of around 0.5, which can be reduced automatically if the convergence properties of the calculation are poor. In addition, one can use Anderson acceleration^{57,58} to combine multiple previous iterations for a prediction of the next iteration. We have found that this leads to faster convergence in the vicinity of the solution but does not extend the parameter range where convergence can be reached.

The parquet solver can also be used for calculations in the random phase approximation (RPA). Switching off the BSEs in two of the three two-particle channels readily yields the RPA-ladder in the other channel.

C. mFRG

In fRG,⁵⁹ the self-energy and vertex are interpolated between the initial and final values of a single-particle parameter Λ introduced into the bare propagator G_0 . The initial value $\Lambda = \Lambda_i$ should be chosen such that the theory is solvable at that point; in practice, it typically suffices that very good approximations of Σ^{Λ_i} and Γ^{Λ_i} can be obtained by PT2 or by converging the parquet equations. The fRG then provides a set of differential “flow” equations in Λ for Σ^Λ and Γ^Λ , which yield the final results Σ^{Λ_f} and Γ^{Λ_f} at the actual point of interest $\Lambda = \Lambda_f$. In the multiloop fRG framework, these flow equations are derived from the parquet equations by differentiation with respect to the flow parameter Λ , as detailed in Ref. 18. This yields an infinite set of contributions of increasing “loop order” ℓ ,

$$\dot{\Gamma} = \sum_{r \in \{a,p,t\}} \dot{\gamma}_r, \quad (19a)$$

$$\dot{\gamma}_r = \sum_{\ell=1}^{\infty} \dot{\gamma}_r^{(\ell)}, \quad (19b)$$

where a dot represents a derivative with respect to Λ . Diagrammatically, the ℓ -loop contributions in the a channel read

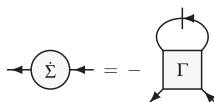
$$\dot{\gamma}_a^{(1)} = \left(\text{diagram with } \Gamma \right), \quad (20a)$$

$$\dot{\gamma}_a^{(2)} = \underbrace{\left(\text{diagram with } \dot{\gamma}_a^{(1)} \text{ and } \Gamma \right)}_{\dot{\gamma}_{a,L}^{(2)}} + \underbrace{\left(\text{diagram with } \Gamma \text{ and } \dot{\gamma}_a^{(1)} \right)}_{\dot{\gamma}_{a,R}^{(2)}}, \quad (20b)$$

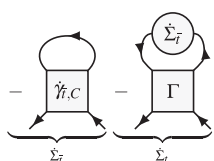
$$\dot{\gamma}_a^{(\ell+2)} = \underbrace{\left(\text{diagram with } \dot{\gamma}_a^{(\ell+1)} \text{ and } \Gamma \right)}_{\dot{\gamma}_{a,L}^{(\ell+2)}} + \underbrace{\left(\text{diagram with } \Gamma \text{ and } \dot{\gamma}_a^{(\ell)} \right)}_{\dot{\gamma}_{a,C}^{(\ell+2)}} + \underbrace{\left(\text{diagram with } \Gamma \text{ and } \dot{\gamma}_a^{(\ell+1)} \right)}_{\dot{\gamma}_{a,R}^{(\ell+2)}}, \quad (20c)$$

and analogously in the other two channels p and t . Here, $\gamma_r^{(\ell)} = \sum_{r' \neq r} \gamma_{r'}^{(\ell)}$, and Eq. (20c) applies for all higher loop orders $\ell + 2 \geq 3$. The double-dashed bubble in Eq. (20) corresponds to a sum of two terms, $\tilde{\Pi} = \dot{G}G + G\dot{G}$, where $\dot{G} = S + G\dot{\Sigma}G$ with the single-scale propagator $S = \partial_\Lambda G|_{\Sigma=\text{const}}$ and the Katanin substitution.⁴⁸

The multiloop flow equation for the self-energy reads



$$\text{Diagram (21a)} \quad (21a)$$



$$\text{Diagram (21b)} \quad (21b)$$

with $\dot{\gamma}_{i,C} = \sum_\ell (\dot{\gamma}_{a,C}^{(\ell)} + \dot{\gamma}_{p,C}^{(\ell)})$, where the single-dashed line denotes the single-scale propagator S from above.

Historically, fRG flow equations have been derived from a generating functional, yielding an exact hierarchy of flow equations which couple n -point vertices of increasing order.⁶⁰ As the six-point vertex, which contributes to the flow equation of Γ , see Eq. (19) in Ref. 1, is inaccessible numerically, its contribution is often neglected completely, resulting in the so-called “one-loop” flow equations. This, however, results in an unphysical dependence of the final result of the flow on the choice of regulator (as the flow equations no longer constitute total derivatives) and also introduces a bias toward ladder diagrams.^{16,61}

The multiloop framework builds upon the one-loop scheme by iteratively adding precisely those two-particle reducible diagrammatic contributions to the flow equations that are required to reinstate total derivatives with respect to Λ and thereby reproduce the solution of the parquet equations. In that sense, it provides an alternative scheme for solving the parquet iterations via differential equations. From a computational standpoint, the mfRG flow equations introduce a complication compared to the one-loop flow equations, in that the right-hand sides of the flow equations for both Γ and Σ involve the differentiated self-energy and vertex. In order to still be able to use standard algorithms for ordinary differential equations, a scheme was outlined in Ref. 16 to include those differentiated quantities iteratively. Starting from the one-loop term Eq. (21a) to evaluate the flow Eq. (20) for Γ , these are then iterated with the multiloop corrections (21b) at every step of the flow until convergence is reached. The number of iterations required for convergence at this point can again be reduced using Anderson acceleration, as described in Sec. III B.

From the code, an mfRG-flow computation can be started with the function `n_loop_flow`, which requires only the string for the name of the output file and a set of parameters. It is overloaded to enable checkpointing, i.e., it is possible to continue a previously started computation from a given iteration. This is particularly useful for demanding jobs that take a long time, and it is highly recommended to any user.

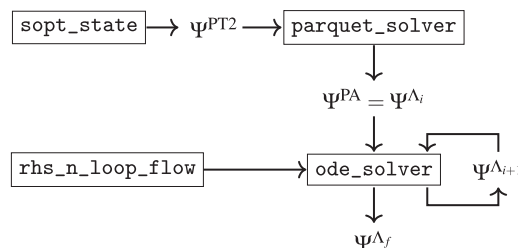


FIG. 6. Schematic depiction of the function `n_loop_flow`.

The function `n_loop_flow` works as shown in Fig. 6. It first initializes a state using PT2 with the function `sopt_state`, see Sec. III A 2, and then uses this result as a seed for a full parquet computation at the initial value of the regulator Λ_i with the `parquet_solver` function, see Sec. III B. This provides a suitable starting point for the following mfRG calculation.

The `ode_solver` function carries out the actual calculation of solving the mfRG flow. It uses an instance of the `rhs_n_loop_flow_t` class, which provides a wrapper to the function `rhs_n_loop_flow`, which in turn evaluates the right-hand side of the flow equations given an input state at a given value of Λ . This is performed iteratively by loop order according to flow Eq. (20), including self-consistent iterations for the self-energy starting at the three-loop level, as outlined earlier. The function `rhs_n_loop_flow` is structured as shown in Fig. 7. Starting from the self-energy and vertex from the previous step of the ODE-solver, it evaluates the right-hand sides of the flow equations by first computing the one-loop term of the flow equation for the self-energy, Eq. (21a), with the function `selfEnergyOneLoopFlow`. The result is then used to evaluate the one-loop term of the flow equation for the two-particle reducible vertices $\dot{\gamma}_r$ and Eq. (20), involving a fully differentiated bubble. Then, the one-loop result is used to evaluate the two-loop contribution, Eq. (20b), which consists of two terms: one where the differentiated one-loop contribution $\dot{\gamma}_r^{(1)}$ is used as the left part of a bubble contraction with the full vertex, and one where it is used on the right side. These two terms are computed using the functions `calculate_dGammaL` and `calculate_dGammaR`, respectively. Next, the three-loop contribution is computed, which involves both the one-loop and the two-loop results [see Eq. (20c)]. Again, the functions `calculate_dGammaL` and `calculate_dGammaR` are invoked, and in addition, the function `calculate_dGammaC` is invoked to compute the “center term” involving two bubble contractions of $\dot{\gamma}_r^{(1)}$ with the full vertex, once to the left and once to the right. As the structure of the flow equations does not change from this point on, this part is iterated until the maximally desired loop number n (which is given as a runtime parameter; see Sec. II 1) is reached. The resulting center terms of the a and p channels are then used to evaluate the multiloop corrections to the self-energy, according to Eq. (21b). This updates the differentiated bubble used in the computation of the one-loop terms $\dot{\gamma}_r^{(1)}$, such that the whole process is finally iterated from that point on until convergence is reached, as determined by the parameters `tol_selfenergy_correction_abs` and

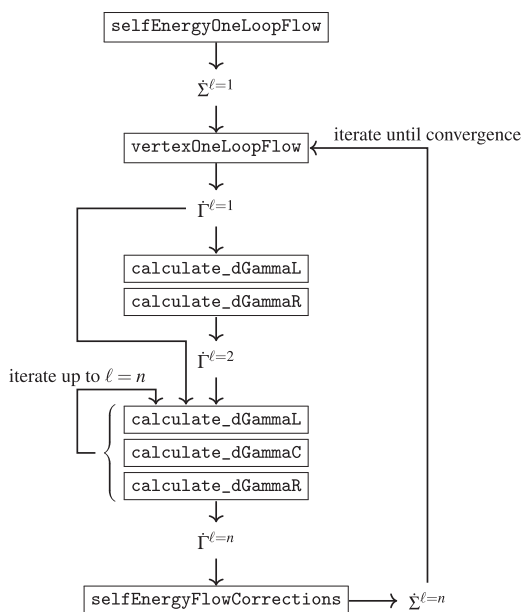


FIG. 7. Structure of the function `rhs_n_loop_flow`, including multiloop iterations up to loop order $\ell = n$ and self-consistent self-energy iterations due to the multiloop corrections.

`tol_selfenergy_correction_rel` (see Sec. II I). All functions invoked by `rhs_n_loop_flow`, of course, make heavy use of the main functionality outlined in Sec. II D.

As a side note, it is possible to parameterize the vertex using the single-boson exchange (SBE) decomposition^{62–67} and to rewrite the mfRG flow equations in this language, as outlined in Ref. 68. This is achieved by setting the flag `SBE_DECOMPOSITION` to 1. Two versions of the SBE approximation can be used, known as “SBEa” and “SBEb” in the literature.⁶⁹ Which version is to be used is controlled by the flag `USE_SBEb_MFRG_EQS` (see Sec. II I). This functionality is, so far, only implemented in the MaF. We, therefore, refrain from providing further details here.

In the final two parts of this section, we discuss the ODE-solver and the different flow schemes.

1. Details on the ODE-solver

To solve the mfRG flow equations accurately, a Cash–Karp routine⁷⁰ is implemented, which constitutes a fourth-order Runge–Kutta solver with adaptive step size control. An adaptive step-size control is crucial for obtaining accurate results and is hereby strongly recommended for solving fRG flow equations precisely. For a good first guess of the step size in the Δ -flow (see Sec. III C 2 a), the flow parameter is reparametrized as $\Lambda(t) = 5t|t|/\sqrt{1-t^2}$. For equidistant t , this parametrization provides large steps for large Λ and small steps for small Λ . This is sensible in the context of the Δ -flow, where Λ is gradually reduced to enter ever more challenging parameter regimes.

2. Flow schemes

In fRG, one chooses a regulator introduced into the bare propagator $G_0 \rightarrow G_0^\Lambda$, i.e., the flow scheme. While the solution of a truncated set of fRG flow equations will depend on this choice, a converged multiloop flow will not, as it reproduces the self-consistent solution of the parquet equations. It is generally advisable to choose the most convenient flow scheme for the problem at hand. In particular, the fRG flow can be used to compute a full parameter sweep in one go by choosing a physical parameter as the regulator. Compared to direct solutions of the parquet equations, which have to be computed individually at every point in parameter space, this makes mfRG computations more economical, provided they can be quickly converged in the loop order. In the following, we outline the flow schemes that have been implemented and can be used by setting the `REG` flag and the `Lambda_ini` and `Lambda_f` in parameters accordingly (see Tables I and II).

a. Δ -flow. The hybridization flow¹¹ uses Δ as the flow parameter, starting at a very large value and decreasing Δ to a smaller value, keeping the other parameters U and T fixed. The hybridization flow thus performs a parameter sweep in U/Δ for fixed T/U . The Keldysh fRG single-scale propagator reads

$$S^R(\nu) = \partial_\Delta G^R(\nu)|_{\Sigma=\text{const}} = -i[G^R(\nu)]^2.$$

In practice, we start the fRG flow from a solution of the parquet equations at large Δ (small U/Δ), where that solution can be easily obtained. For historical reasons, the hybridization flow is implemented as

$$G_\Lambda^R(\nu) = \frac{1}{\nu - \varepsilon_d + i(\Gamma + \Lambda)/2 - \Sigma_\Lambda^R(\nu)}, \quad (22)$$

inside the code, where Γ is fixed to some arbitrary value and Λ is used to fix the hybridization $\Delta = (\Gamma + \Lambda)/2$. Note that keeping T/U fixed during the Δ -flow is a somewhat unconventional choice, as in most works on the AM, the scale T/Δ is kept constant. As explained in Ref. 28, keeping T/Δ fixed during the Δ -flow would lead to additional sharply peaked terms in the single-scale propagator and has hence not been pursued yet.

b. U -flow. An alternative to the Δ -flow is the following flow scheme, first introduced in Ref. 71,

$$G_\Lambda^R(\nu) = \frac{\Lambda}{\nu - \varepsilon_d + i\Delta - \Lambda \Sigma_\Lambda^R(\nu)}, \quad (23)$$

starting at $\Lambda_i = 0$ (or very small, in practice) and flowing toward $\Lambda_f = 1$. The corresponding single-scale propagator then reads

$$S^R(\nu) = \partial_\Lambda G^R(\nu)|_{\Sigma=\text{const}} = \frac{\nu - \varepsilon_d + i\Delta}{[\nu - \varepsilon_d + i\Delta - \Lambda \Sigma_\Lambda^R(\nu)]^2}. \quad (24)$$

This flow scheme is called interaction- or U -flow because increasing Λ effectively amounts to increasing U . This can be shown by a simple rescaling argument: A bare diagram for Σ (or Γ) at order n has n factors of U and $2n - 1$ (or $2n - 2$) factors of $G_{0,\Lambda}$, each contributing one factor of Λ . The same scaling behavior in Λ can be achieved

without a Λ -dependent G_0 by multiplying U with Λ^2 and dividing out an extra Λ (or Λ^2). It hence holds that

$$\Sigma_\Lambda(U) = \Sigma(\Lambda^2 U)/\Lambda, \quad (25a)$$

$$\Gamma_\Lambda(U) = \Gamma(\Lambda^2 U)/\Lambda^2. \quad (25b)$$

Note that at zero temperature, the two flow schemes discussed so far should be equivalent: For $T = 0$, the only energy scales of the AM in the wideband limit are U and Δ , so there is only one external parameter U/Δ and it does not matter whether U is increased or Δ is decreased.

Historically, the U -flow has not been very popular, as it does not regulate IR divergences.⁵⁹ Nevertheless, it can be used for the AM. In Ref. 1, we found that, for a truncated 1-loop Keldysh fRG flow at *finite* T , this scheme produces inferior results compared to the Δ -flow when benchmarked against numerically exact NRG data. Still, the U -flow has the nice property that it keeps T/Δ fixed.

c. T-flow. Using temperature as the fRG flow parameter has been popular in the past when performing fRG computations in the MaF.^{72,73} It has been argued that temperature cannot be used for this purpose in Keldysh fRG computations,¹¹ the reason being that a truncated fRG flow does not preserve fluctuation–dissipation relations (FDRs). However, solutions to the parquet equations *do* fulfill the FDRs. If the FDRs are not used explicitly during mfRG calculations (as this would mix FDRs at different temperatures and hence introduce an inconsistency), it should also be possible to obtain these solutions by converging an mfRG flow. Instead of the standard FDR, which relates G^K and G^R , in this scheme, the general expression for the Keldysh component of the propagator should be used, which reads²⁸

$$G^K(\nu) = G^R(\nu) \left[\Sigma^K(\nu) - 2i\Delta \tanh\left(\frac{\nu}{2T}\right) \right] G^A(\nu). \quad (26)$$

The Keldysh component of the single-scale propagator is then

$$S^K(\nu) = \partial_T G^K(\nu) \Big|_{\Sigma=\text{const.}} = \frac{i\Delta\nu}{T^2 \cosh^2\left(\frac{\nu}{2T}\right)} |G^R(\nu)|^2. \quad (27)$$

Note that its retarded component is zero; $S^R(\nu) = 0$, as $G^R(\nu)$ does not depend explicitly on T . While preliminary numerical results suggest that this scheme indeed performs well, a systematic study of the temperature flow in Keldysh fRG is left for future work. So far, at the time of writing, the temperature flow described earlier can only be used in the KF; corresponding regulators in the MaF, as in Refs. 72 and 73, have not been implemented.

d. ν -flow. Using a frequency regulator of the form $G_{0,\Lambda}(i\nu) = G_0(i\nu)\Theta_\Lambda(i\nu)$ with $\Theta_\Lambda(i\nu) = \nu^2/(\nu^2 + \Lambda^2)$ has been a popular choice in the literature for (m)fRG calculations in the Matsubara formalism.^{74,75} However, in this form, the frequency regulator cannot be used in the Keldysh formalism, as the analytical continuation of $\Theta_\Lambda(i\nu)$ gives $\Theta_\Lambda^R(\nu) = \nu^2/(\nu^2 - \Lambda^2 + 2|\nu|j0^+)$ with a branch cut

for $\nu < 0$. One can, however, change the form of the regulator to $\Theta_\Lambda(i\nu) = |\nu|/(|\nu| + \Lambda)$, for which the retarded counterpart reads

$$\Theta_\Lambda^R(\nu) = \frac{\nu}{\nu + i\Lambda}, \quad (28)$$

which is a well-behaved function. This choice is implemented as

$$G_\Lambda^R(\nu) = \frac{\Theta_\Lambda^R(\nu)}{\nu - \varepsilon_d + i\Delta - \Theta_\Lambda^R(\nu)\Sigma_\Lambda^R(\nu)}. \quad (29)$$

The corresponding single-scale propagator then reads

$$S^R(\nu) = -\frac{i}{\nu} \frac{[\Theta_\Lambda^R(\nu)]^2 (\nu - \varepsilon_d + i\Delta)}{[\nu - \varepsilon_d + i\Delta - \Theta_\Lambda^R(\nu)\Sigma_\Lambda^R(\nu)]^2}. \quad (30)$$

With this choice, all causality relations and FDRs are satisfied. However, this regulator has two drawbacks compared to the other flow schemes: First, it does not produce a parameter sweep, as Λ does not directly correspond to a physical parameter. Second, computations become ever more challenging for smaller Λ : Even if all correlation functions are reasonably smooth in frequency space for $\Lambda = 0$, for small but finite Λ , they exhibit sharp features. While this is not an issue for finite-temperature Matsubara calculations, where only sums over discrete Matsubara frequencies are performed, it turns out to be a major inconvenience in the Keldysh context.

IV. CONCLUSION

In this paper, we outline the structure and design of our C++ codebase for diagrammatic calculations of the AM in the Keldysh formalism. We explained the building blocks for representing real-frequency correlation functions and the central routines used to compute them. We elaborated on all performance-critical aspects, allowing one to handle the three-dimensional frequency dependence of the four-point vertex, and summarized the implementation of the parquet and mfRG equations. By discussing the most convenient features of the codebase—modularity, flexibility, performance, and scalability—but also some of its design flaws in detail, we hope to provide guidance and inspiration to others who plan to write code for similar purposes.

Our codebase forms the basis for numerous future projects involving the dynamical correlation functions of electronic many-body systems. Since the AM is very well understood, we want to generalize our treatment to more complicated models with unexplored physics, like lattice models, possibly including multiple bands. The main problem in that regard is the numerical complexity. In addition to their real-frequency Keldysh structure, all functions would acquire momentum dependencies and orbital indices. Parametrizing those naively appears prohibitively costly. Fortunately, the new quantum tensor cross interpolation (QTCI) scheme^{76–78} is currently being developed, which can be used to obtain highly compressed tensor network representations of correlation functions and promises exponential reductions in computational costs. It remains to be seen how efficiently the Keldysh four-point vertex can be compressed using this method. If it turned out to be highly compressible, one could combine the diagrammatic approaches outlined here with non-perturbative results from dynamical mean-field theory to access

truly strongly correlated parameter regimes (see related works^{79–81} in the MaF). In particular, computing non-local real-frequency dynamical vertex corrections beyond DMFT for observables like optical conductivities with high precision is a formidable long-term goal.

Another possible future direction relates to nonequilibrium phenomena, for example, the influence of the full four-point vertex on observables like differential conductivities.^{12,82} Nonequilibrium physics has been the most popular application of the KF in the past, and the AM with a finite bias voltage is tractable with only a minor increase in both the numerical costs and the implementation effort.

In order to leverage ongoing efforts in the QTCI framework, an interface to the corresponding Julia package⁸³ would be required. Given that, in recent years, multiple Julia codes have been developed to perform calculations of two-particle correlation functions,^{84–87} it would be natural to switch to that language in the future, especially since it allows much simpler structures and, in general, performs almost as well as C++.

ACKNOWLEDGMENTS

We acknowledge Marc Ritter, Marcel Gievers, Benedikt Schneider, Björn Sbierski, Nils Niggemann, Dominik Kiese, Aiman Al-Eryani, Lennart Klebl, and Jacob Beyer for insightful conversations about fRG code structures over the years, Henri Menke for the suggestion to use a combination of Doxygen, Sphinx, and Breathe for the technical code documentation, and Markus Frankenbach for comments on the paper.

N.R. acknowledges funding from a graduate scholarship from the German Academic Scholarship Foundation (“Studienstiftung des deutschen Volkes”) and additional support from the “Marianne-Plehn-Programm” of the state of Bavaria. A.G. and J.v.D. were supported by the Deutsche Forschungsgemeinschaft under Germany’s Excellence Strategy EXC-2111 (Project No. 390814868) and the Munich Quantum Valley, supported by the Bavarian state government with funds from the Hightech Agenda Bayern Plus. This work was supported by Grant No. INST 86/1885-1 FUGG of the German Research Foundation (DFG). F.B.K. acknowledges support from the Alexander von Humboldt Foundation through the Feodor Lynen Fellowship. The Flatiron Institute is a division of the Simons Foundation.

AUTHOR DECLARATIONS

Conflict of Interest

The authors have no conflicts to disclose.

Author Contributions

N.R. and A.G. contributed equally to this work.

Nepomuk Ritz: Funding acquisition (equal); Software (supporting); Writing – original draft (lead); Writing – review & editing (lead). **Anxiang Ge:** Software (lead); Writing – review & editing (supporting). **Elias Walter:** Conceptualization (lead); Software (equal). **Santiago Aguirre:** Conceptualization (equal); Software (equal). **Jan von Delft:** Funding acquisition (lead); Supervision (equal);

Writing – review & editing (equal). **Fabian B. Kugler:** Supervision (equal); Writing – review & editing (supporting).

DATA AVAILABILITY

The code, which includes a link to the technical documentation, can be found online (see Ref. 88). It is published under the MIT license.

REFERENCES

- 1 A. Ge, N. Ritz, E. Walter, S. Aguirre, J. von Delft, and F. B. Kugler, “Real-frequency quantum field theory applied to the single-impurity Anderson model,” *Phys. Rev. B* **109**, 115128 (2024).
- 2 T. Matsubara, “A new approach to quantum-statistical mechanics,” *Prog. Theor. Phys.* **14**, 351–378 (1955).
- 3 A. A. Abrikosov, L. P. Gorkov, and I. E. Dzyaloshinski, *Methods of Quantum Field Theory in Statistical Physics* (Courier Corporation, 2012).
- 4 G. Baym and N. D. Mermin, “Determination of thermodynamic Green’s functions,” *J. Math. Phys.* **2**, 232–234 (1961).
- 5 M. Jarrell and J. Gubernatis, “Bayesian inference and the analytic continuation of imaginary-time quantum Monte Carlo data,” *Phys. Rep.* **269**, 133–195 (1996).
- 6 A. W. Sandvik, “Stochastic method for analytic continuation of quantum Monte Carlo data,” *Phys. Rev. B* **57**, 10287–10290 (1998).
- 7 J. Schött, I. L. M. Loch, E. Lundin, O. Grånäs, O. Eriksson, and I. Di Marco, “Analytic continuation by averaging Padé approximants,” *Phys. Rev. B* **93**, 075104 (2016).
- 8 A. Ge, J. Halbinger, S.-S. B. Lee, J. von Delft, and F. B. Kugler, “Analytic continuation of multipoint correlation functions,” *Ann. Phys.* **536**, 2300504 (2024).
- 9 J. Kroha, P. Wölfle, and T. A. Costi, “Unified description of Fermi and non-Fermi liquid behavior in a conserving slave boson approximation for strongly correlated impurity models,” *Phys. Rev. Lett.* **79**, 261–264 (1997).
- 10 J. Kroha and P. Wölfle, “Fermi and non-Fermi liquid behavior of local moment systems within a conserving slave boson theory,” *Acta Phys. Pol., B* **29**, 3781 (1998).
- 11 S. G. Jakobs, “Functional renormalization group studies of quantum transport through mesoscopic systems,” Ph.D. thesis, RWTH Aachen, 2010.
- 12 S. G. Jakobs, M. Pletyukhov, and H. Schoeller, “Nonequilibrium functional renormalization group with frequency-dependent vertex function: A study of the single-impurity Anderson model,” *Phys. Rev. B* **81**, 195109 (2010).
- 13 S. G. Jakobs, M. Pletyukhov, and H. Schoeller, “Properties of multi-particle Green’s and vertex functions within Keldysh formalism,” *J. Phys. A: Math. Theor.* **43**, 103001 (2010).
- 14 F. B. Kugler, S.-S. B. Lee, and J. von Delft, “Multipoint correlation functions: Spectral representation and numerical evaluation,” *Phys. Rev. X* **11**, 041006 (2021).
- 15 S.-S. B. Lee, F. B. Kugler, and J. von Delft, “Computing local multipoint correlators using the numerical renormalization group,” *Phys. Rev. X* **11**, 041007 (2021).
- 16 F. B. Kugler and J. von Delft, “Multiloop functional renormalization group for general models,” *Phys. Rev. B* **97**, 035162 (2018).
- 17 F. B. Kugler and J. von Delft, “Multiloop functional renormalization group that sums up all parquet diagrams,” *Phys. Rev. Lett.* **120**, 057403 (2018).
- 18 F. B. Kugler and J. von Delft, “Derivation of exact flow equations from the self-consistent parquet relations,” *New J. Phys.* **20**, 123029 (2018).
- 19 J. Bezanson, A. Edelman, S. Karpinski, and V. B. Shah, “Julia: A fresh approach to numerical computing,” *SIAM Rev.* **59**, 65–98 (2017).
- 20 N. D. Matsakis and F. S. Klock II, “The rust language,” in *ACM SIGAda Ada Letters* (ACM, 2014), Vol. 34, pp. 103–104.
- 21 See <https://www.modular.com/max/mojo> for Mojo—The programming language for all AI developers.
- 22 B. Stroustrup, in *Programming—Principles and Practice Using C++*, 3rd ed. (Addison Wesley, Boston, MA, 2023).

- ²³R. Bulla, T. A. Costi, and T. Pruschke, "Numerical renormalization group method for quantum impurity systems," *Rev. Mod. Phys.* **80**, 395–450 (2008).
- ²⁴V. Zlatić and B. Horvatić, "Series expansion for the symmetric Anderson Hamiltonian," *Phys. Rev. B* **28**, 6904–6906 (1983).
- ²⁵P. B. Wiegmann and A. M. Tsvelick, "Exact solution of the Anderson model: I," *J. Phys. C: Solid State Phys.* **16**, 2281 (1983).
- ²⁶P. W. Anderson, "Localized magnetic states in metals," *Phys. Rev.* **124**, 41–53 (1961).
- ²⁷A. Kamenev, in *Field Theory of Non-Equilibrium Systems*, 2nd ed. (Cambridge University Press, 2023).
- ²⁸E. Walter, "Real-frequency dynamics of quantum impurity models studied with fRG, NRG, CFT," Ph.D. thesis, LMU München, 2021.
- ²⁹L. V. Keldysh, "Diagram technique for nonequilibrium processes," *Sov. Phys. JETP* **20**, 1018–1026 (1965).
- ³⁰J. Schwinger, "Brownian motion of a quantum oscillator," *J. Math. Phys.* **2**, 407–432 (1961).
- ³¹L. P. Kadanoff and G. A. Baym, *Quantum Statistical Mechanics* (Benjamin, New York, 1962).
- ³²ISO/IEC 14882:2017 - Programming languages—C++, International Organization for Standardization, 2017.
- ³³Kitware, Inc., CMake documentation, <https://cmake.org/documentation/>.
- ³⁴GNU Scientific Library Reference Manual: For GSL version 1.12, 3rd ed., edited by M. Galassi (Network Theory, Bristol, 2009).
- ³⁵See <https://www.boost.org/> for Boost C++ Libraries.
- ³⁶G. Guennebaud, B. Jacob et al., Eigen: A C++ linear algebra library, <http://eigen.tuxfamily.org>.
- ³⁷The HDF Group, Hierarchical data format, version 5, <https://www.hdfgroup.org/HDF5/>.
- ³⁸See <https://www.openmp.org/> for the OpenMP API specification for parallel programming.
- ³⁹See <https://hpc.nmsu.edu/discovery/mpi/introduction/> for message passing interface: High performance computing.
- ⁴⁰D. van Heesch, Doxygen: A documentation system for C++, C, Java, Python and other languages, <https://www.doxygen.nl/>.
- ⁴¹See <https://www.sphinx-doc.org/> for Sphinx Documentation Generator.
- ⁴²See <https://breathe.readthedocs.io/en/latest/> for Breathe "latest" documentation.
- ⁴³G. Rohringer, H. Hafermann, A. Toschi, A. A. Katanin, A. E. Antipov, M. I. Katsnelson, A. I. Lichtenstein, A. N. Rubtsov, and K. Held, "Diagrammatic routes to nonlocal correlations beyond dynamical mean field theory," *Rev. Mod. Phys.* **90**, 025003 (2018).
- ⁴⁴A. Georges, G. Kotliar, W. Krauth, and M. J. Rozenberg, "Dynamical mean-field theory of strongly correlated fermion systems and the limit of infinite dimensions," *Rev. Mod. Phys.* **68**, 13–125 (1996).
- ⁴⁵A. Toschi, A. A. Katanin, and K. Held, "Dynamical vertex approximation: A step beyond dynamical mean-field theory," *Phys. Rev. B* **75**, 045118 (2007).
- ⁴⁶C. Taranto, S. Andergassen, J. Bauer, K. Held, A. Katanin, W. Metzner, G. Rohringer, and A. Toschi, "From infinite to two dimensions through the functional renormalization group," *Phys. Rev. Lett.* **112**, 196402 (2014).
- ⁴⁷N. Wentzell, G. Li, A. Tagliavini, C. Taranto, G. Rohringer, K. Held, A. Toschi, and S. Andergassen, "High-frequency asymptotics of the vertex function: Diagrammatic parametrization and algorithmic implementation," *Phys. Rev. B* **102**, 085106 (2020).
- ⁴⁸A. A. Katanin, "Fulfillment of Ward identities in the functional renormalization group approach," *Phys. Rev. B* **70**, 115109 (2004).
- ⁴⁹F. B. Kugler, "Improved estimator for numerical renormalization group calculations of the self-energy," *Phys. Rev. B* **105**, 245132 (2022).
- ⁵⁰E. Wang and U. Heinz, "Generalized fluctuation-dissipation theorem for nonlinear response functions," *Phys. Rev. D* **66**, 025008 (2002).
- ⁵¹C. Hille, F. B. Kugler, C. J. Eckhardt, Y.-Y. He, A. Kauch, C. Honerkamp, A. Toschi, and S. Andergassen, "Quantitative functional renormalization group description of the two-dimensional Hubbard model," *Phys. Rev. Res.* **2**, 033372 (2020).
- ⁵²D. Rohe, "Hierarchical parallelisation of functional renormalisation group calculations—hp-fRG," *Comput. Phys. Commun.* **207**, 160–169 (2016).
- ⁵³W. H. Press, S. A. Teukolsky, W. T. Vetterling, and B. P. Flannery, in *Numerical Recipes—The Art of Scientific Computing*, 3rd ed. (Cambridge University Press, 2007).
- ⁵⁴A modern, C++-native, test framework for unit-tests, TDD and BDD.
- ⁵⁵D. C. Langreth, "Friedel sum rule for Anderson's model of localized impurity states," *Phys. Rev.* **150**, 516–518 (1966).
- ⁵⁶N. E. Bickers, "Self-consistent many-body theory for condensed matter systems," in *Theoretical Methods for Strongly Correlated Electrons, CRM Series in Mathematical Physics*, edited by D. Sénéchal, A.-M. Tremblay, and C. Bourbonnais (Springer, New York, 2004).
- ⁵⁷D. G. Anderson, "Iterative procedures for nonlinear integral equations," *J. ACM* **12**, 547–560 (1965).
- ⁵⁸H. F. Walker and P. Ni, "Anderson acceleration for fixed-point iterations," *SIAM J. Numer. Anal.* **49**, 1715–1735 (2011).
- ⁵⁹W. Metzner, M. Salmhofer, C. Honerkamp, V. Meden, and K. Schönhammer, "Functional renormalization group approach to correlated fermion systems," *Rev. Mod. Phys.* **84**, 299–352 (2012).
- ⁶⁰C. Wetterich, "Exact evolution equation for the effective potential," *Phys. Lett. B* **301**, 90–94 (1993).
- ⁶¹F. B. Kugler and J. von Delft, "Fermi-edge singularity and the functional renormalization group," *J. Phys.: Condens. Matter* **30**, 195501 (2018).
- ⁶²F. Krien, "Efficient evaluation of the polarization function in dynamical mean-field theory," *Phys. Rev. B* **99**, 235106 (2019).
- ⁶³F. Krien, A. Valli, and M. Capone, "Single-boson exchange decomposition of the vertex function," *Phys. Rev. B* **100**, 155149 (2019).
- ⁶⁴F. Krien and A. Valli, "Parquetlike equations for the Hedin three-leg vertex," *Phys. Rev. B* **100**, 245147 (2019).
- ⁶⁵F. Krien, A. I. Lichtenstein, and G. Rohringer, "Fluctuation diagnostic of the nodal/antinodal dichotomy in the Hubbard model at weak coupling: A parquet dual fermion approach," *Phys. Rev. B* **102**, 235133 (2020).
- ⁶⁶F. Krien, A. Valli, P. Chalupa, M. Capone, A. I. Lichtenstein, and A. Toschi, "Boson-exchange parquet solver for dual fermions," *Phys. Rev. B* **102**, 195131 (2020).
- ⁶⁷F. Krien, A. Kauch, and K. Held, "Tiling with triangles: Parquet and GW methods unified," *Phys. Rev. Res.* **3**, 013149 (2021).
- ⁶⁸M. Gievers, E. Walter, A. Ge. J. von Delft, and F. B. Kugler, "Multiloop flow equations for single-boson exchange fRG," *Eur. Phys. J. B* **95**, 108 (2022).
- ⁶⁹K. Fraboulet, S. Heinzelmann, P. M. Bonetti, A. Al-Eryani, D. Vildardi, A. Toschi, and S. Andergassen, "Single-boson exchange functional renormalization group application to the two-dimensional Hubbard model at weak coupling," *Eur. Phys. J. B* **95**, 202 (2022).
- ⁷⁰J. R. Cash and A. H. Karp, "A variable order Runge-Kutta method for initial value problems with rapidly varying right-hand sides," *ACM Trans. Math. Software* **16**, 201–222 (1990).
- ⁷¹C. Honerkamp, D. Rohe, S. Andergassen, and T. Enss, "Interaction flow method for many-fermion systems," *Phys. Rev. B* **70**, 235115 (2004).
- ⁷²C. Honerkamp and M. Salmhofer, "Temperature-flow renormalization group and the competition between superconductivity and ferromagnetism," *Phys. Rev. B* **64**, 184516 (2001).
- ⁷³B. Schneider, J. Reuther, M. G. Gonzalez, B. Sbierski, and N. Niggemann, "Temperature flow in pseudo-Majorana functional renormalization for quantum spins," *Phys. Rev. B* **109**, 195109 (2024).
- ⁷⁴A. Tagliavini, C. Hille, F. B. Kugler, S. Andergassen, A. Toschi, and C. Honerkamp, "Multiloop functional renormalization group for the two-dimensional Hubbard model: Loop convergence of the response functions," *SciPost Phys.* **6**, 009 (2019).
- ⁷⁵P. Chalupa-Gantner, F. B. Kugler, C. Hille, J. von Delft, S. Andergassen, and A. Toschi, "Fulfillment of sum rules and Ward identities in the multiloop functional renormalization group solution of the Anderson impurity model," *Phys. Rev. Res.* **4**, 023050 (2022).
- ⁷⁶H. Shinaoka, M. Wallerberger, Y. Murakami, K. Nogaki, R. Sakurai, P. Werner, and A. Kauch, "Multiscale space-time ansatz for correlation functions of quantum systems based on quantum tensor trains," *Phys. Rev. X* **13**, 021015 (2023).

⁷⁷Y. Núñez Fernández, M. Jeannin, P. T. Dumitrescu, T. Kloss, J. Kaye, O. Parcollet, and X. Waintal, "Learning Feynman diagrams with tensor trains," *Phys. Rev. X* **12**, 041018 (2022).

⁷⁸M. K. Ritter, Y. Núñez Fernández, M. Wallerberger, J. von Delft, H. Shinaoka, and X. Waintal, "Quantics tensor cross interpolation for high-resolution parsimonious representations of multivariate functions," *Phys. Rev. Lett.* **132**, 056501 (2024).

⁷⁹M. Kitatani, T. Schäfer, H. Aoki, and K. Held, "Why the critical temperature of high- T_c cuprate superconductors is so low: The importance of the dynamical vertex structure," *Phys. Rev. B* **99**, 041115 (2019).

⁸⁰D. Vilardi, C. Taranto, and W. Metzner, "Antiferromagnetic and d -wave pairing correlations in the strongly interacting two-dimensional Hubbard model from the functional renormalization group," *Phys. Rev. B* **99**, 104501 (2019).

⁸¹P. M. Bonetti, A. Toschi, C. Hille, S. Andergassen, and D. Vilardi, "Single-boson exchange representation of the functional renormalization group for strongly interacting many-electron systems," *Phys. Rev. Res.* **4**, 013034 (2022).

⁸²T. Fujii and K. Ueda, "Perturbative approach to the nonequilibrium Kondo effect in a quantum dot," *Phys. Rev. B* **68**, 155310 (2003).

⁸³M. K. Ritter *et al.*, *Quanticstci.jl*, 2022.

⁸⁴D. Kiese, T. Müller, Y. Iqbal, R. Thomale, and S. Trebst, "Multiloop functional renormalization group approach to quantum spin systems," *Phys. Rev. Res.* **4**, 023185 (2022).

⁸⁵D. Kiese, A. Ge, N. Ritz, J. von Delft, and N. Wentzell, "MatsubaraFunctions.jl: An equilibrium Green's function library in the Julia programming language," *SciPost Phys. Codebases* **24** (2024).

⁸⁶D. Kiese, A. Ge, N. Ritz, J. von Delft, and N. Wentzell, "Codebase release 0.1 for MatsubaraFunctions.jl," *SciPost Phys. Codebases* **24-r0.1** (2024).

⁸⁷N. Niggemann, *Nilsniggemann/pmfrg.jl: v2.1.9*, 2023.

⁸⁸N. Ritz and A. Ge, *KeldyshQFT: A C++ Codebase for real-frequency multiloop functional renormalization group and parquet computations for the single-impurity Anderson model*.

**MatsubaraFunctions.jl: An equilibrium Green's function
library in the Julia programming language**

by

D. Kiese,¹ A. Ge,² N. Ritz,² J. von Delft,² and N. Wentzell¹

¹ Center for Computations Quantum Physics, Flatiron Institute,
162 5th Avenue, New York, NY 10010, USA

² Arnold Sommerfeld Center for Theoretical Physics, Center for NanoScience, and
Munich Center for Quantum Science and Technology,
Ludwig-Maximilians-Universität München, 80333 Munich, Germany

reprinted on pages 114–148

Reproduced under terms of the CC-BY license.

***SciPost Phys. Codebases* 24 (2024),**

DOI: 10.21468/SciPostPhysCodeb.24.

© 2024, The Authors, SciPost.

MatsubaraFunctions.jl: An equilibrium Green's function library in the Julia programming language

Dominik Kiese^{1*}, Anxiang Ge², Nepomuk Ritz², Jan von Delft² and Nils Wentzell¹

¹ Center for Computational Quantum Physics, Flatiron Institute,
162 5th Avenue, New York, NY 10010, USA

² Arnold Sommerfeld Center for Theoretical Physics, Center for NanoScience, and Munich
Center for Quantum Science and Technology, Ludwig-Maximilians-Universität München,
80333 Munich, Germany

* dkiese@flatironinstitute.org

Abstract

The Matsubara Green's function formalism stands as a powerful technique for computing the thermodynamic characteristics of interacting quantum many-particle systems at finite temperatures. In this manuscript, our focus centers on introducing `MatsubaraFunctions.jl`, a Julia library that implements data structures for generalized n -point Green's functions on Matsubara frequency grids. The package's architecture prioritizes user-friendliness without compromising the development of efficient solvers for quantum field theories in equilibrium. Following a comprehensive introduction of the fundamental types, we delve into a thorough examination of key facets of the interface. This encompasses avenues for accessing Green's functions, techniques for extrapolation and interpolation, as well as the incorporation of symmetries and a variety of parallelization strategies. Examples of increasing complexity serve to demonstrate the practical utility of the library, supplemented by discussions on strategies for sidestepping impediments to optimal performance.



Copyright D. Kiese *et al.*

This work is licensed under the Creative Commons
[Attribution 4.0 International License](https://creativecommons.org/licenses/by/4.0/).

Published by the SciPost Foundation.

Received 11-10-2023

Accepted 20-12-2023

Published 11-01-2024

doi:[10.21468/SciPostPhysCodeb.24](https://doi.org/10.21468/SciPostPhysCodeb.24)



Check for
updates

This publication is part of a bundle: Please cite both the article and the release you used.

DOI	Type
doi:10.21468/SciPostPhysCodeb.24	Article
doi:10.21468/SciPostPhysCodeb.24-r0.1	Codebase release

Contents

1 Motivation	2
2 Equilibrium Green's functions	3

3	Code structure	4
3.1	Basic types	4
3.2	Accessing and assigning Green's function data	6
3.3	Extrapolation of Matsubara sums	7
3.4	Padé approximants	8
3.5	Automated symmetry reduction	8
3.6	Running in parallel	9
3.7	Performance note	10
4	Examples	10
4.1	Hartree-Fock calculation in the atomic limit	10
4.2	<i>GW</i> calculation in the atomic limit	12
4.3	Multiboson exchange solver for the single impurity Anderson model	15
4.3.1	Single boson exchange decomposition of the parquet equations	16
4.3.2	Implementation in <code>MatsubaraFunctions.jl</code>	18
4.3.3	Benchmark results	22
5	Future directions	26
A	Extrapolation of Matsubara sums	27
B	Implementation details for the MBE solver	28
B.1	SU(2) symmetry	28
B.2	Time translation invariance	28
	References	29

1 Motivation

In condensed matter physics, strongly correlated electrons emerge as paradigmatic examples of quantum many-body systems that defy a description in terms of simple band theory, due to their strong interactions with each other and with the atomic lattice. Their study has led to a cascade of discoveries, ranging from high-temperature superconductivity in copper oxides (*cuprates*) [1, 2] to the Mott metal-insulator transition in various condensed matter systems such as, e.g., transition metal oxides or transition metal chalcogenides [3–5] and the emergence of quantum spin liquids in frustrated magnets [6, 7], to name but a few.

The study of correlated electron systems is equally exciting and challenging, not only because the construction of accurate theoretical models requires the consideration of many different degrees of freedom, such as spin, charge, and orbital degrees of freedom, as well as disorder and frustration, but also because of the scarcity of exactly solvable reference Hamiltonians. The single-band Hubbard model in more than one dimension, for example, has remained at the forefront of computational condensed matter physics for decades, although it in many respects can be regarded as the simplest incarnation of a realistic correlated electron system [8, 9]. It is therefore not surprising that a plethora of different numerical methods have been developed to deal with these models [10].

However, no single algorithm is capable of accurately describing all aspects of these complex systems: each algorithm has its strengths and weaknesses, and the choice of algorithm usually depends on the specific problem under investigation. For example, some algorithms, such as *exact diagonalization* (ED) [11–13] or the *density matrix renormalization*

group (DMRG) [14, 15] are better suited for studying ground-state properties, while others (*quantum Monte Carlo* (QMC) simulations [16–19], *functional renormalization group* (fRG) calculations [20–22], ...) perform better when one is interested in dynamic properties such as transport or response functions.

Another popular method, dynamical mean-field theory (DMFT) has been immensely successful; in particular it correctly predicts the Mott transition in the Hubbard model [23]. By approximating the electron self-energy to be local, it however disregards non-local correlation effects, leading to a violation of the Mermin-Wagner theorem [24, 25] as well as a failure to predict the pseudo-gap in the Hubbard model [10]. Non-local (e.g. cluster [26–29] or diagrammatic [30]) extensions of DMFT improve on that front, but are computationally much more expensive. Ultimately, the choice of algorithm is guided by the computational resources available and the trade-off between accuracy and efficiency, as well as by physical insights into which approximations may be justified more than others.

A common motif of many of these algorithms is that they rely on the computation of n -particle *Green's functions*, where usually $n = 1, 2$. Roughly speaking, these functions describe correlations within the physical system of interest, such as its response to an external perturbation. In thermal equilibrium, Green's functions are usually defined as imaginary-time-ordered correlation functions, which allows the use of techniques and concepts from statistical mechanics, such as the partition function and free energy. In Fourier space, the corresponding frequencies take on discrete and complex values. This *Matsubara* formalism is widely used to study strongly correlated electron systems, where it provides a powerful tool for calculating thermodynamic quantities, such as the specific heat and magnetic susceptibility, as well as dynamical properties, such as the electron self-energy and optical conductivity [31, 32].

In this manuscript, we present `MatsubaraFunctions.jl`, a software package written in Julia [33] that implements containers for Green's functions in thermal equilibrium. More specifically, it provides a convenient interface for quickly prototyping algorithms involving multivariable Green's functions of the form $G_{i_1 \dots i_n}(\omega_1, \dots, \omega_m)$, with lattice/orbital indices i_k ($k = 1, \dots, n$) and Matsubara frequencies ω_l ($l = 1, \dots, m$). In an attempt to mitigate monolithic code design and superfluous code reproduction, our goal is to promote a common interface between algorithms where these types of functions make up the basic building blocks. We implement this interface in Julia, since some more recently developed methods, such as the pseudofermion [34–41] and pseudo-Majorana fRG [42–45], seem to have been implemented in Julia as the preferred programming language. In the spirit of similar software efforts, such as the TRIQS library for C++ [46], this package therefore aims to provide a common foundation for these and related codes in Julia that is fast enough to facilitate large-scale computations on high-performance computing architectures [47], while remaining flexible and easy to use.

2 Equilibrium Green's functions

In this section, we give a brief introduction to equilibrium Green's functions and their properties. In its most general form, an imaginary time, n -particle Green's function $G^{(n)}$ is defined as the correlator [48]

$$G_{i_1 \dots i_{2n}}^{(n)}(\tau_1, \dots, \tau_{2n}) = \langle \hat{T} c_{i_1}^\dagger(\tau_1) c_{i_2}(\tau_2) \dots c_{i_{2n-1}}^\dagger(\tau_{2n-1}) c_{i_{2n}}(\tau_{2n}) \rangle, \quad (1)$$

where \hat{T} is the imaginary-time-ordering operator and $\langle \hat{O} \rangle = \frac{1}{Z} \text{Tr}(e^{-\beta \hat{H}} \hat{O})$ denotes the thermal expectation value of an operator \hat{O} with respect to the Hamiltonian \hat{H} at temperature $T = 1/\beta$. Note that natural units are used throughout, in particular we set $k_B \equiv 1$. Here, $c^{(\dagger)}$ are fermionic or bosonic creation and annihilation operators and $Z = \text{Tr}(e^{-\beta \hat{H}})$ is the partition function. The indices i_k represent additional degrees of freedom such as lattice site, spin and

orbital index. In order for the right-hand side in Eq. (1) to be well defined, it is necessary to restrict the τ arguments to an interval of length β , as can be seen, for example, from a spectral (*Lehmann*) representation of the expectation value [48]. Furthermore, the cyclicity of the trace implies that the field variables are anti-periodic in β for fermions, or periodic in β for bosons, respectively. This allows us to define their Fourier series expansion

$$c_i(\tau) = \frac{1}{\beta} \sum_{\nu_k} c_{i,k} e^{-i\nu_k \tau}, \quad \bar{c}_i(\tau) = \frac{1}{\beta} \sum_{\nu_k} \bar{c}_{i,k} e^{i\nu_k \tau}, \quad (2)$$

$$c_{i,k} = \int_0^\beta d\tau c_i(\tau) e^{i\nu_k \tau}, \quad \bar{c}_{i,k} = \int_0^\beta d\tau \bar{c}_i(\tau) e^{-i\nu_k \tau}, \quad (3)$$

where $\nu_k = \frac{\pi}{\beta} \begin{cases} 2k+1, \\ 2k, \end{cases}$ with $k \in \mathbb{Z}$ are the fermionic or bosonic Matsubara frequencies.¹

These definitions carry over to the n -particle Green's function $G^{(n)}$, giving

$$G_{i_1 \dots i_{2n}}^{(n)}(\tau_1, \dots, \tau_{2n}) = \frac{1}{\beta} \sum_{\nu_1} e^{i\nu_1 \tau_1} \dots \frac{1}{\beta} \sum_{\nu_{2n}} e^{-i\nu_{2n} \tau_{2n}} G_{i_1 \dots i_{2n}}^{(n)}(\nu_1, \dots, \nu_{2n}), \quad (4)$$

$$G_{i_1 \dots i_{2n}}^{(n)}(\nu_1, \dots, \nu_{2n}) = \int_0^\beta d\tau_1 e^{-i\nu_1 \tau_1} \dots \int_0^\beta d\tau_{2n} e^{i\nu_{2n} \tau_{2n}} G_{i_1 \dots i_{2n}}^{(n)}(\tau_1, \dots, \tau_{2n}). \quad (5)$$

3 Code structure

`MatsubaraFunctions.jl` is an open-source project distributed via Github [49] and licensed under the MIT license. Using Julia's built-in package manager, the code can be easily installed using

```
1 $ julia
2 julia> ]
3 pkg> add https://github.com/dominikkiese/MatsubaraFunctions.jl
```

from the terminal. Here, `]` activates the package manager from the Julia REPL, where `add` downloads the code and its dependencies. The following is an overview of the functionality of the package, starting with a discussion of its basic types and how to use them. A full documentation of the package is available from the github repository.

3.1 Basic types

The package evolves around three concrete Julia types: `MatsubaraFrequency`, `MatsubaraGrid` and `MatsubaraFunction`. A Matsubara frequency can be either fermionic or bosonic, that is, $\nu_k = \frac{\pi}{\beta}(2k+1)$ or $\nu_k = \frac{2\pi}{\beta}k$. For a given temperature $T = 1/\beta$ and Matsubara index k they can be constructed using

```
1 v = MatsubaraFrequency(T, k, Fermion)
2 w = MatsubaraFrequency(T, k, Boson)
```

Basic arithmetic operations on these objects include addition, subtraction and sign reversal, each of which creates a new `MatsubaraFrequency` instance.

¹This way, $e^{i\beta\nu_k} = -1$ for fermions and $e^{i\beta\nu_k} = +1$ for bosons such that anti-periodicity or periodicity, respectively, of $c_i(\tau)$ are ensured.

```

1 v1 = v + v # type(v1) = :Boson
2 v2 = w - v # type(v2) = :Fermion
3 v3 = -v    # type(v3) = :Fermion

```

MatsubaraGrids are implemented as sorted collections of uniformly (and symmetrically) spaced Matsubara frequencies. To construct them, users need only specify the temperature, number of positive frequencies, and the particle type.

```

1 T = 1.0
2 N = 128
3 g1 = MatsubaraGrid(T, N, Fermion) # total no. frequencies is 2N
4 g2 = MatsubaraGrid(T, N, Boson)   # total no. frequencies is 2N - 1

```

Note that the bosonic Matsubara frequency at zero is included in the positive frequency count. Grid instances are iterable

```

1 for v in g1
2   println(value(v))
3   println(index(v))
4 end

```

and can be evaluated using either a MatsubaraFrequency or Float64 as input.

```

1 idx = rand(eachindex(g1))
2 @assert g1(g1[idx]) == idx
3 @assert g1(value(g1[idx])) == idx

```

Here, we first select a random linear index idx and then evaluate $g1$ using either the corresponding Matsubara frequency $g1[idx]$ or its value. In the former case, $g1(g1[idx])$ returns the corresponding linear index of the frequency in the grid, whereas $g1(value(g1[idx]))$ finds the linear index of the closest mesh point.² The package supports storage of grid instances in H5 file format.

```

1 using HDF5
2 file = h5open("save_g1.h5", "w")
3 save_matsubara_grid!(file, "g1", g1)
4 g1p = load_matsubara_grid(file, "g1")
5 close(file)

```

Finally, a MatsubaraFunction is a collection of Matsubara grids with an associated tensor structure $G_{i_1 \dots i_n}$ for each point (ν_1, \dots, ν_m) in the Cartesian product of the grids. The indices i_k could, for example, represent lattice sites or orbitals. To construct a MatsubaraFunction users need to provide a tuple of MatsubaraGrid objects, as well as the dimension of each i_k .

```

1 T = 1.0
2 N = 128
3 g = MatsubaraGrid(T, N, Fermion)
4
5 # 1D grid, rank 1 tensor with index dimension 1 (scalar valued)
6 f1_complex = MatsubaraFunction(g, 1)
7 f1_real    = MatsubaraFunction(g, 1, Float64)
8
9 # 1D grid, rank 1 tensor with index dimension 5 (vector valued)

```

²In both cases the argument must be in bounds, otherwise an exception is thrown.

```

10 f2_complex = MatsubaraFunction(g, 5)
11 f2_real    = MatsubaraFunction(g, 5, Float64)
12
13 # 1D grid, rank 2 tensor with index dimension 5 (matrix valued)
14 f3_complex = MatsubaraFunction(g, (5, 5))
15 f3_real    = MatsubaraFunction(g, (5, 5), Float64)
16
17 # 2D grid, rank 2 tensor with index dimension 5 (matrix valued)
18 f4_complex = MatsubaraFunction((g, g), (5, 5))
19 f4_real    = MatsubaraFunction((g, g), (5, 5), Float64)

```

In addition, a floating point type can be passed to the constructor, which fixes the data type for the underlying multidimensional array.³ Similar to the grids, MatsubaraFunctions can be conveniently stored in H5 format.

```

1 using HDF5
2 file = h5open("save_f1_complex.h5", "w")
3 save_matsubara_function!(file, "f1_complex", f1_complex)
4 f1p = load_matsubara_function(file, "f1_complex")
5 close(file)

```

3.2 Accessing and assigning Green's function data

The library provides two possible ways to access the data of a MatsubaraFunction, using either the bracket (`[]`) or parenthesis (`()`) operator. While the notion of the former is that of a `Base.getindex`, the latter evaluates the MatsubaraFunction for the given arguments in such a way that its behavior is well-defined even for out-of-bounds access. The bracket can be used with a set of MatsubaraFrequency instances and tensor indices i_k , as well as with Cartesian indices for the underlying data array. It returns the value of the data exactly for the given input arguments, throwing an exception if they are not in bounds. In addition, the bracket can be used to assign values to a MatsubaraFunction as shown in the following example.

```

1 y = 0.5
2 T = 1.0
3 N = 128
4 g = MatsubaraGrid(T, N, Fermion)
5 f = MatsubaraFunction(g, 1)
6
7 for v in g
8     # if there is only one index of dimension 1, it does not need
9     # to be specified, i.e. f[v] can be used instead of f[v, 1]
10    # (also works for the '()' operator)
11    f[v] = 1.0 / (im * value(v) - y)
12 end
13
14 # access MatsubaraFunction data
15 v = g[rand(eachindex(g))]
16 println(f[v]) # fast data access, throws error if v is out of bounds

```

When `f` is evaluated using Matsubara frequencies within its grid, it returns the same result as if a bracket was used. However, if the frequencies are replaced by `Float64` values, a multilinear interpolation within the Cartesian product of the grids is performed. If the frequency / float arguments are out of bounds, MatsubaraFunctions falls back to extrapolation. The extrapolation algorithm distinguishes between one-dimensional and multidimensional frequency grids. In the 1D case, an algebraic decay is fitted to the high-frequency tail of

³By default, `ComplexF64` is used.

the `MatsubaraFunction`, which is then evaluated for the given arguments. The functional form of the asymptote is currently restricted to $f(\nu) = \alpha_0 + \frac{\alpha_1}{\nu} + \frac{\alpha_2}{\nu^2}$ (with $\alpha_0, \alpha_1, \alpha_2 \in \mathbb{C}$),⁴ which is motivated by the linear or quadratic decay that physical Green's functions typically exhibit. For multidimensional grids, a constant extrapolation is performed from the boundary. Different modes of evaluation are illustrated in an example below.

```

1 y = 0.5
2 T = 1.0
3 N = 128
4 g = MatsubaraGrid(T, N, Fermion)
5 f = MatsubaraFunction(g, 1)
6
7 for v in g
8     f[v] = 1.0 / (im * value(v) - y)
9 end
10
11 # access MatsubaraFunction data
12 v = g[rand(eachindex(g))]
13 println(f(v))           # fast data access, defined even if v is out of bounds
14 println(f(value(v)))   # slow data access, uses interpolation
15
16 # polynomial extrapolation in 1D, constant term set to 0 (the default)
17 vp = MatsubaraFrequency(T, 256, Fermion)
18 println(f(vp; extrp = ComplexF64(0.0)))

```

3.3 Extrapolation of Matsubara sums

A common task when working with equilibrium Green's functions is the calculation of Matsubara sums $\frac{1}{\beta} \sum_{\nu} f(\nu)$, where we have omitted additional indices of f for brevity. However, typical Green's functions decay rather slowly (algebraically) for large frequencies, which presents a technical difficulty for the accurate numerical calculation of their Matsubara sums: they may require some regulator function to control the convergence⁵ (difficult to implement) and a large number of frequencies to sum over (expensive). In contrast, there exist analytical results for simple functional forms of f even in cases where a straightforward numerical summation fails. `MatsubaraFunctions` provides the `sum_me` function, which can be used to calculate sums over complex-valued $f(\nu)$, if $f(z)$ (with $z \in \mathbb{C}$) decays to zero for large $|z|$ and is representable by a Laurent series in an elongated annulus about the imaginary axis (see App. A for details). An example for its use is shown below. Note that this feature is experimental and its API as well as the underlying algorithm might change in future versions.

```

1 y = 0.5
2 T = 1.0
3 N = 128
4 g = MatsubaraGrid(T, N, Fermion)
5 f = MatsubaraFunction(g, 1)
6
7 for v in g
8     f[v] = 1.0 / (im * value(v) - y)
9 end
10
11 # evaluate the series and compare to analytic result
12 rho(x, T) = 1.0 / (exp(x / T) + 1.0)
13 println(abs(sum_me(f) - (rho(+y, T) - 1.0)))

```

⁴Note that α_0 has to be provided by the user.

⁵For example, a factor $e^{i\nu\theta}$ might be necessary in cases where f decays linearly in ν .

3.4 Padé approximants

Although the Matsubara formalism provides a powerful tool for the calculation of thermodynamic quantities, it lacks the ability to directly determine, for example, dynamic response functions or transport properties associated with real-frequency Green's functions, which facilitate comparison with experiments. There have been recent advances in the use of real-frequency quantum field theory [50–53], yet the calculation of dynamic real-frequency Green's functions remains a technically challenging endeavor. In many applications, therefore, one resorts to calculations on the imaginary axis and then performs an analytic continuation in the complex upper half-plane to determine observables on the real-frequency axis. The analytic continuation problem is ill-conditioned, because there may be significantly different real-frequency functions describing the same set of complex-frequency data within finite precision. Nevertheless, there has been remarkable progress in the development of numerical techniques such as the maximum entropy method [54–56] or stochastic analytical continuation [57,58]. These methods are particularly useful when dealing with stochastic noise induced by Monte Carlo random sampling. A corresponding implementation in Julia is, for example, provided by the ACFLOW toolkit [59]. On the other hand, if the input data are known with a high degree of accuracy (as in the fRG and related approaches), analytic continuation using Padé approximants is a valid alternative. Here, one first fits a rational function to the complex frequency data which is then used as a proxy for the Green's function in the upper half-plane. If the function of interest has simple poles this procedure can already provide fairly accurate results, see e.g. Ref. [60]. In `MatsubaraFunctions` we implement the fast algorithm described in the appendix of Ref. [61], which computes an N -point Padé approximant for a given set of data points $\{(x_i, y_i) | i = 1, \dots, N\}$. A simple example of its use is shown below. Note that it might be necessary to use higher precision floating-point arithmetic to cope with rounding errors in the continued fraction representation used for calculating the Padé approximant.

```

1 # some dummy function
2 as = ntuple(x -> rand{BigFloat}, 4)
3 f(x) = as[1] / (1.0 + as[2] * x / (1.0 + as[3] * x / (1.0 + as[4] * x)))
4
5 # generate sample and compute Padé approximant
6 xdata = Vector{BigFloat}(0.01 : 0.01 : 1.0)
7 ydata = f.(xdata)
8 PA = PadéApprox(xdata, ydata)
9
10 @assert length(coeffs(PA)) == 5
11 @assert PA.(xdata) ≈ ydata

```

3.5 Automated symmetry reduction

In many cases, the numerical effort of computing functions in the Matsubara domain can be drastically reduced by the use of symmetries. For one-particle fermionic Green's functions $G_{i_1 i_2}(\nu)$, for example, complex conjugation implies that $G_{i_1 i_2}(\nu) = G_{i_2 i_1}^*(-\nu)$, relating positive and negative Matsubara frequencies. Our package provides an automated way to compute the set of irreducible `MatsubaraFunction` components,⁶ given a list of one or more symmetries as is illustrated in the following example

```

1 y = 0.5
2 T = 1.0
3 N = 128
4 g = MatsubaraGrid(T, N, Fermion)
5 f = MatsubaraFunction(g, 1)

```

⁶These are all elements of the underlying data array which cannot be mapped to each other by symmetries.

```

6
7 for v in g
8     f[v] = 1.0 / (im * value(v) - y)
9 end
10
11 # complex conjugation acting on Green's function
12 function conj(
13     w :: Tuple{MatsubaraFrequency},
14     x :: Tuple{Int64}
15 ) :: Tuple{Tuple{MatsubaraFrequency}, Tuple{Int64}, MatsubaraOperation}
16
17     return (-w[1],), (x[1],), MatsubaraOperation(sgn = false, con = true)
18 end
19
20 # compute the symmetry group
21 SG = MatsubaraSymmetryGroup([MatsubaraSymmetry{1, 1}(conj)], f)
22
23 # obtain another Green's function by symmetrization
24 function init(
25     w :: Tuple{MatsubaraFrequency},
26     x :: Tuple{Int64}
27 ) :: ComplexF64
28
29     return f[w, x...]
30 end
31
32 InitFunc = MatsubaraInitFunction{1, 1, ComplexF64}(init)
33 h = MatsubaraFunction(g, 1)
34 SG(h, InitFunc)
35 @assert h == f

```

Here, one first constructs an instance of type `MatsubaraSymmetry` by passing a function that maps the input arguments of `f` to new arguments extended by a `MatsubaraOperation`. The latter specifies whether the evaluation of `f` on the mapped arguments should be provided with an additional sign or complex conjugation. Next, the irreducible array elements are computed and an object of type `MatsubaraSymmetryGroup`⁷ is constructed from a vector of symmetries provided by the user. Here, the length of the vector is one (we only considered complex conjugation), but the generalization to multiple symmetries is straightforward (see Ref. [62] for more examples). A `MatsubaraSymmetryGroup` can be called with a `MatsubaraFunction` and an initialization function.⁸ This call will evaluate the `MatsubaraInitFunction` for all irreducible elements of the symmetry group of `f`, writing the result into the data array of `h`. Finally, all symmetry equivalent elements are determined without additional calls to the (costly) initialization function. Symmetry groups can be stored in H5 format as shown below.

```

1 using HDF5
2 file = h5open("save_SG.h5", "w")
3 save_matsubara_symmetry_group!(file, "SG", SG)
4 SGp = load_matsubara_symmetry_group(file, "SG")
5 close(file)

```

3.6 Running in parallel

To simplify code parallelization when using `MatsubaraFunctions.jl`, the package has some preliminary MPI support based on the `MPI.jl` wrapper and illustrated in an example below.

```

1 using MatsubaraFunctions
2 using MPI

```

⁷A `MatsubaraSymmetryGroup` contains all groups of symmetry equivalent elements and the operations needed to map them to each other.

⁸A `MatsubaraInitFunction` takes a tuple of Matsubara frequencies and tensor indices and returns a floating point type.

```

3
4 MPI.Init()
5 mpi_info()
6 mpi_println("I print on main.")
7 ismain = mpi_ismain() # ismain = true if rank is 0
8
9 y = 0.5
10 T = 1.0
11 N = 128
12 g = MatsubaraGrid(T, N, Fermion)
13 f = MatsubaraFunction(g, 1)
14
15 for v in g
16     f[v] = 1.0 / (im * value(v) - y)
17 end
18
19 # simple loop parallelization for UnitRange
20 for vidx in mpi_split(1 : length(g))
21     println("My rank is $(mpi_rank()): $(vidx)")
22 end
23
24 # simple (+) allreduce
25 mpi_allreduce!(f)

```

Calls of `MatsubaraSymmetryGroup` with an initialization function have an opt-in switch (`mode`) to enable parallel evaluation of the `MatsubaraInitFunction` (by default `mode = :serial`). If `mode = :polyester`, shared memory multithreading as provided by the Polyester Julia package [63] is used.⁹ This mode is recommended for initialization functions that are cheap to evaluate and are unlikely to benefit from `Threads.@threads` due to the overhead from invoking the Julia scheduler. For more expensive functions, users can choose between `mode = :threads`, which simply uses `Threads.@threads`, and `mode = :hybrid`. The latter combines both MPI and native Julia threads and can therefore be used to run calculations on multiple compute nodes.

3.7 Performance note

By default, types in `MatsubaraFunctions.jl` perform intrinsic consistency checks when they are invoked. For example, when computing the linear index of a `MatsubaraFrequency` in a `MatsubaraGrid`, we make sure that the particle types and temperatures match between the two. While this ensures a robust *modus operandi*, it unfortunately impacts performance, especially for larger projects. To deal with this issue, we have implemented a simple switch, `MatsubaraFunctions.sanity_checks()`, which, when turned off¹⁰ disables `@assert` expressions. It is not recommended to touch this switch until an application has been thoroughly tested, as it leads to wrong results on improper use. For the MBE solver discussed in Sec. 4.3.2, we found runtime improvements of up to 10% when the consistency checks were disabled.

4 Examples

4.1 Hartree-Fock calculation in the atomic limit

As a first example of the use of `MatsubaraFunctions.jl` we consider the calculation of the one-particle Green's function G using the Hartree-Fock (HF) approximation in the atomic limit of the Hubbard model, i.e., we consider the Hamiltonian

$$\hat{\mathcal{H}} = U\hat{n}_{\uparrow}\hat{n}_{\downarrow} - \mu(\hat{n}_{\uparrow} + \hat{n}_{\downarrow}), \quad (6)$$

⁹Here, the `batchsize` argument can be used to control the number of threads involved.

¹⁰`MatsubaraFunctions.sanity_checks() = false`.

where U denotes the Hubbard interaction and \hat{n}_σ are the density operators for spin up and down. In the following, we fix the chemical potential to $\mu = 0$, i.e., we consider the system in the strongly hole-doped regime.

The Hartree-Fock theory [64–66] is a widespread method in condensed matter physics used to describe, e.g., electronic structures and properties of materials [67, 68]. It is a mean-field approximation as it treats the electrons in a solid as independent particles being subject to an effective background field due to all the other particles.

In an interacting many-body system, the bare Green's function G_0 has to be dressed by self-energy insertions, here denoted by Σ , in order to obtain G , which is summarized in the Dyson equation

$$G = G_0[1 - \Sigma G_0]^{-1} = G_0 + G_0 \Sigma G_0 + G_0 \Sigma G_0 \Sigma G_0 + \dots, \quad (7)$$

where G_0 , G and Σ in general are matrix-valued. In HF theory one only considers the lowest order term contributing to the self-energy, which is linear in the interaction potential. For the spin-rotation invariant single-site system at hand, $\Sigma = \Sigma_\sigma = \Sigma$ and the HF approximation for the self-energy reads

$$\Sigma(\nu) \approx \frac{U}{\beta} \sum_{\nu'} G(\nu') e^{i\nu'0^+} = Un, \quad (8)$$

where n is the density per spin. The Dyson equation then takes the simple form

$$G(\nu) \approx [G_0^{-1}(\nu) - Un]^{-1}. \quad (9)$$

Below, we demonstrate how to set up and solve Eqs. (8) & (9) self-consistently for the density n using Anderson acceleration [69, 70] as provided by the NLSolve Julia package [71] in conjunction with MatsubaraFunctions.jl.

```

1 using MatsubaraFunctions
2 using NLSolve
3
4 const T = 0.3 # temperature
5 const U = 0.9 # interaction
6 const N = 1000 # no. frequencies
7
8 # initialize Green's function container
9 g = MatsubaraGrid(T, N, Fermion)
10 G = MatsubaraFunction(g, 1)
11
12 for v in g
13     G[v] = 1.0 / (im * value(v))
14 end
15
16 # set up fixed-point equation for NLSolve
17 function fixed_point!(F, n, G)
18
19     # calculate G
20     for v in grids(G, 1)
21         G[v] = 1.0 / (im * value(v) - U * n[1])
22     end
23
24     # calculate the residue
25     F[1] = density(G) - n[1]
26
27     return nothing
28 end
29
30 res = nlsolve((F, n) -> fixed_point!(F, n, G), [density(G)], method = :anderson)

```

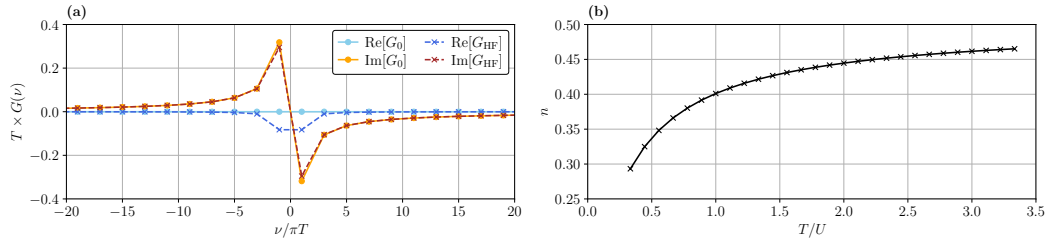


Figure 1: **Exemplary Hartree-Fock results.** (a) Comparison of the bare Green's function G_0 with the HF result G_{HF} for $T/U = \frac{1}{3}$. (b) Hartree-Fock density n as a function of temperature.

Here, we first build the `MatsubaraFunction` container for G and initialize it to $G_0(\nu) = \frac{1}{i\nu}$. This container is then passed to the fixed-point equation using an anonymous function, which mutates G on each call to incorporate the latest estimate of n .¹¹ Fig. 1 shows exemplary results for the full Green's function and HF density. As can be seen from Fig. 1(b) the latter deviates from its bare value $n_0 = \frac{1}{2}$ when the temperature is decreased and approaches $n = 0$ for $T \rightarrow 0$, as expected.

4.2 GW calculation in the atomic limit

In this section, we extend our Hartree-Fock code to include *bubble* corrections¹² in the calculation of the self-energy. The resulting equations, commonly known as the *GW* approximation, allow us to exemplify the use of more advanced library features, such as extrapolation of the single-particle Green's function and the implementation of symmetries. Therefore, they present a good starting point for the more involved application discussed in Sec. 4.3.1.

The *GW* approximation is a widely used method in condensed matter physics and quantum chemistry for calculating electronic properties of materials [72–74]. In addition to the Hartree term $\Sigma_{\text{H}} = Un$, which considers only the bare interaction, the mutual screening of the Coulomb interaction between electrons is partially taken into account. For spin-rotation invariant systems it is common practice to decouple these *screened interactions* η ¹³ into a density (or charge) component η^D and a magnetic (or spin) component η^M (see App. B), such that

$$\Sigma(\nu) \approx \frac{Un}{2} - \frac{1}{\beta} \sum_{\nu'} G(\nu') \left[\frac{1}{4} \eta^D(\nu - \nu') + \frac{3}{4} \eta^M(\nu - \nu') \right], \quad (10)$$

for the atomic limit Hamiltonian. The η are computed by summing a series of bubble diagrams in the particle-hole channel, i.e.,

$$\eta^{D/M}(\Omega) = \frac{\pm U}{1 \mp UP(\Omega)}, \quad (11)$$

where the *polarization bubble* P is given by

$$P(\Omega) = \frac{1}{\beta} \sum_{\nu} G(\Omega + \nu)G(\nu). \quad (12)$$

A diagrammatic representation of these relations is shown in Fig. 2. Finally, the set of equations is closed by computing G from the Dyson equation. Since the Green's function transforms as

¹¹Here, we make use of the `density` function, which calculates the Fourier transform $f(\tau \rightarrow 0^-)$ given a complex-valued input function $f(\nu)$.

¹²That is, Feynman diagrams formed by a closed loop of two single-particle Green's functions.

¹³Here, we denote the screened interactions by η instead of W to avoid conflicting notation with the code examples in Sec. 4.3.2.

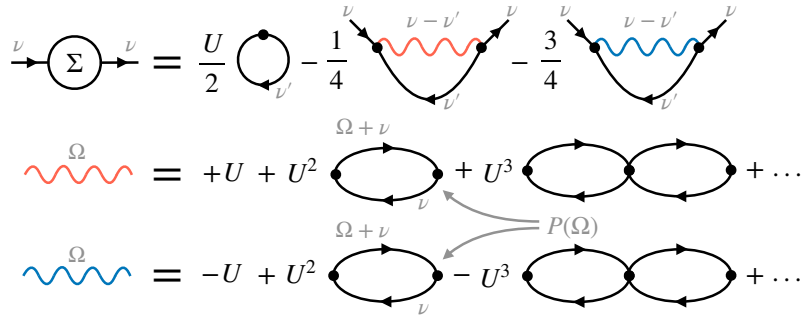


Figure 2: **Diagrammatic representation of spin-conserving GW equations in the atomic limit.** Wavy lines denote the screened interactions in the density (red) and magnetic (blue) channel. They are obtained by dressing the respective bare interactions with a series of bubble diagrams $P(\Omega)$, as illustrated in the second and third line from the top.

$G^*(\nu) = G(-\nu)$ under complex conjugation [48], we also have that

$$\begin{aligned} P(-\Omega) &= \frac{1}{\beta} \sum_{\nu} G(-\Omega + \nu)G(\nu) = \frac{1}{\beta} \sum_{\nu} G(-\Omega - \nu)G(-\nu) = \frac{1}{\beta} \sum_{\nu} G^*(\Omega + \nu)G^*(\nu) \\ &= P^*(\Omega), \end{aligned} \quad (13)$$

and likewise $\Sigma^*(\nu) = \Sigma(-\nu)$. Thus, the numerical effort for evaluating Eqs. (10) and (12) can be reduced by a factor of two using a `MatsubaraSymmetryGroup` object. To structure the GW code, we first write a solver class which takes care of the proper initialization of the necessary `MatsubaraFunction` instances.

```

1 using MatsubaraFunctions
2 using HDF5
3
4 conj(w, x) = (-w[1],), (x[1],), MatsubaraOperation(sgn = false, con = true)
5
6 struct Gwsolver
7     T    :: Float64
8     U    :: Float64
9     N    :: Int64
10    G    :: MatsubaraFunction{1, 1, 2, ComplexF64}
11    Sigma :: MatsubaraFunction{1, 1, 2, ComplexF64}
12    P     :: MatsubaraFunction{1, 1, 2, ComplexF64}
13    η_D  :: MatsubaraFunction{1, 1, 2, ComplexF64}
14    η_M  :: MatsubaraFunction{1, 1, 2, ComplexF64}
15    SGf  :: MatsubaraSymmetryGroup
16    SGb  :: MatsubaraSymmetryGroup
17
18 function Gwsolver(T, U, N)
19
20     # fermionic containers
21     gf = MatsubaraGrid(T, N, Fermion)
22     G  = MatsubaraFunction(gf, 1)
23     Sigma = MatsubaraFunction(gf, 1)
24
25     # bosonic containers
26     gb = MatsubaraGrid(T, N, Boson)
27     P  = MatsubaraFunction(gb, 1)
28     η_D = MatsubaraFunction(gb, 1)
29     η_M = MatsubaraFunction(gb, 1)
30
31     # symmetry groups
32     SGf = MatsubaraSymmetryGroup([MatsubaraSymmetry{1, 1}(conj)], G)
33     SGb = MatsubaraSymmetryGroup([MatsubaraSymmetry{1, 1}(conj)], P)

```

```

34
35     return new(T, U, N, G, Sigma, P, η_D, η_M, SGf, SGb)
36 end
37 end

```

As a second step, we implement the self-consistent equations, which we solve using Anderson acceleration. Note that we have rewritten the GW equation for the self-energy as

$$\Sigma(\nu) \approx U n - \frac{1}{\beta} \sum_{\nu'} G(\nu') \left[\frac{1}{4} \eta^D(\nu - \nu') + \frac{3}{4} \eta^M(\nu - \nu') + \frac{U}{2} \right], \quad (14)$$

which is beneficial since the product of G with the constant contributions to $\eta^{D/M}$ simply shifts the real part of the self-energy by $\frac{U n}{2}$ such that $\Sigma = \Sigma_H + \mathcal{O}(U^2)$.

```

1 function fixed_point!(F, x, S)
2
3     # update Sigma
4     unflatten!(S.Sigma, x)
5
6     # calculate G
7     for v in grids(S.G, 1)
8         S.G[v] = 1.0 / (im * value(v) - S.Sigma[v])
9     end
10
11    sum_grid = MatsubaraGrid(S.T, 4 * S.N, Fermion)
12
13    # calculate P using symmetries
14    function calc_P(wtpl, xtpl)
15
16        P = 0.0
17
18        for v in sum_grid
19            P += S.G(v + wtpl[1]) * S.G(v)
20        end
21
22        return S.T * P
23    end
24
25    S.SGb(S.P, MatsubaraInitFunction{1, 1, ComplexF64}(calc_P))
26
27    # calculate η_D and η_M
28    for w in S.P.grids[1]
29        S.η_D[w] = +S.U / (1.0 - S.U * S.P[w])
30        S.η_M[w] = -S.U / (1.0 + S.U * S.P[w])
31    end
32
33    # calculate Sigma using symmetries
34    function calc_Sigma(wtpl, xtpl)
35
36        Sigma = S.U * density(S.G)
37
38        for v in sum_grid
39            Sigma -= S.T * S.G(v) * (
40                0.25 * S.η_D(wtpl[1] - v; extrp = ComplexF64(+S.U)) +
41                0.75 * S.η_M(wtpl[1] - v; extrp = ComplexF64(-S.U)) +
42                0.50 * S.U)
43        end
44
45        return Sigma
46    end
47
48    S.SGf(S.Sigma, MatsubaraInitFunction{1, 1, ComplexF64}(calc_Sigma))
49
50    # calculate the residue
51    flatten!(S.Sigma, F)
52    F .-= x
53

```

```
54 return nothing
55 end
```

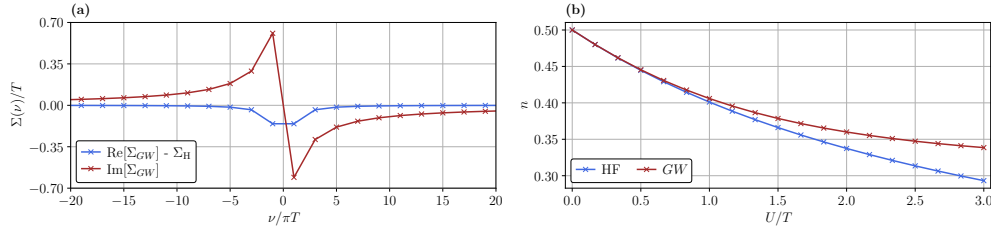


Figure 3: **Exemplary GW results.** (a) The complex-valued self-energy Σ_{GW} with its real part offset by the Hartree shift $\Sigma_H = Un_{GW}$ for $T/U = \frac{1}{3}$. (b) GW and Hartree-Fock densities as a function of U/T .

Here, we make use of the `flatten!` and `unflatten!` functions which allow us to parse `MatsubaraFunction` data into a one dimensional array.¹⁴ The fixed-point can now easily be computed with, for example,

```
1 const T = 0.3 # temperature
2 const U = 0.9 # interaction
3 const N = 1000 # no. frequencies
4
5 S = Gwsolver(T, U, N)
6 init = zeros(ComplexF64, length(S.Sigma))
7 res = nlsolve((F, x) -> fixed_point!(F, x, S), init, method = :anderson, m = 8, beta =
  ↪ 0.5, show_trace = true)
```

In Fig. 3 we show exemplary results for the self-energy and density obtained in GW . In contrast to the Hartree-Fock calculations in the previous section, Σ is now a frequency-dependent quantity, whose real part asymptotically approaches Un_{GW} . As can be seen from Fig. 3(b), these GW densities agree quantitatively with the HF result for weak interactions $U/T \lesssim \frac{1}{2}$, but yield larger densities for higher values of U as expected when the local interaction is partially screened.

4.3 Multiboson exchange solver for the single impurity Anderson model

Note: Readers who are not interested in the formal discussion presented below should feel free to skip this section and proceed directly to Section 5 on future directions.

In the following, we extend upon the previous computations for the Hubbard atom by coupling the single electronic level to a bath of non-interacting electrons. Specifically, we consider the *single-impurity Anderson model*, a minimal model for localized magnetic impurities in metals introduced by P.W. Anderson to explain the physics behind the Kondo effect [75]. It is defined by the Hamiltonian

$$H = \sum_{\sigma} \epsilon_d d_{\sigma}^{\dagger} d_{\sigma} + Un_{d,\uparrow} n_{d,\downarrow} + \sum_{k,\sigma} (V_k d_{\sigma}^{\dagger} c_{k,\sigma} + V_k^* c_{k,\sigma}^{\dagger} d_{\sigma}) + \sum_{k,\sigma} \epsilon_{k,\sigma} c_{k,\sigma}^{\dagger} c_{k,\sigma}, \quad (15)$$

describing an impurity d level ϵ_d , hybridized with conduction electrons of the metal via a matrix element V_k . The electrons in the localized d state, where $n_{d,\sigma} = d_{\sigma}^{\dagger} d_{\sigma}$, interact according to the interaction strength U , whereas the c electrons of the bath are

¹⁴We also export `flatten` which will allocate a new 1D array from the `MatsubaraFunction`.

non-interacting. Following [76], in a path-integral formulation for the partition function $Z = \int \prod_{\sigma} \mathcal{D}(\bar{d}_{\sigma}) \mathcal{D}(d_{\sigma}) \mathcal{D}(\bar{c}_{k,\sigma}) \mathcal{D}(c_{k,\sigma}) e^{-S}$ with the action $S = \int_0^{\beta} \mathcal{L}(\tau) d\tau$, the Lagrangian for the model is given by

$$\begin{aligned} \mathcal{L}(\tau) = & \sum_{\sigma} \bar{d}_{\sigma}(\tau) (\partial_{\tau} + \epsilon_d) d_{\sigma}(\tau) + \sum_{k,\sigma} \bar{c}_{k,\sigma}(\tau) (\partial_{\tau} + \epsilon_k) c_{k,\sigma}(\tau) \\ & + U n_{\uparrow}(\tau) n_{\downarrow}(\tau) + \sum_{k,\sigma} V_k [\bar{d}_{\sigma}(\tau) c_{k,\sigma}(\tau) + \bar{c}_{k,\sigma}(\tau) d_{\sigma}(\tau)], \end{aligned} \quad (16)$$

where $n_{\sigma}(\tau) = \bar{d}_{\sigma}(\tau) d_{\sigma}(\tau)$. Integrating over the only quadratically occurring Grassmann variables for the bath electrons, one formally obtains $Z = \int \prod_{\sigma} \mathcal{D}(\bar{d}_{\sigma}) \mathcal{D}(d_{\sigma}) e^{-S_{\text{red}}}$ with the reduced action given by

$$S_{\text{red}} = \int_0^{\beta} d\tau \int_0^{\beta} d\tau' \sum_{\sigma} \bar{d}_{\sigma}(\tau) [-G_{\sigma}^{(0)}(\tau - \tau')]^{-1} d_{\sigma}(\tau') + U \int_0^{\beta} d\tau n_{\uparrow}(\tau) n_{\downarrow}(\tau). \quad (17)$$

Switching to Matsubara frequencies as described in section 2, the non-interacting Green's function for the localized d electrons reads

$$G_{\sigma}^{(0)}(\nu_n) = \frac{1}{i\nu_n - \epsilon_d + \Delta(\nu_n)}. \quad (18)$$

Following [77] we choose an isotropic hybridization strength $V_k \equiv V$ and a flat density of states with bandwidth $2D$ for the bath electrons, leading to the hybridization function¹⁵ $\Delta(\nu_n) = i\frac{V^2}{D} \arctan \frac{D}{\nu_n}$. In the following, we set $V = 2$, measure energy in units of $V/2 = 1$ and set the half bandwidth to $D = 10$. In the context of this work, we focus on the particle-hole symmetric model, setting $\epsilon_d = -U/2$. Then, the Hartree term of the self-energy, $\Sigma_{\text{H}} = U/2$ is conveniently absorbed into the bare propagator,

$$G_{\sigma}^{(0)}(\nu_n) \rightarrow G_{\sigma}^{\text{H}}(\nu_n) = \frac{1}{i\nu_n - \epsilon_d + \Delta(\nu_n) - \Sigma_{\text{H}}} = \frac{1}{i\nu_n + \Delta(\nu_n)}. \quad (19)$$

Consequently, the Hartree propagator is used instead of the bare propagator throughout.

4.3.1 Single boson exchange decomposition of the parquet equations

Following [78], we now reiterate the single-boson exchange (SBE) decomposition of the four-point vertex and, subsequently, of the parquet equations. The starting point for the SBE decomposition, which was originally developed in [79–84], is the unambiguous classification of vertex diagrams according to their U -reducibility in each channel. In order to introduce this concept in the context of the parquet equations, we first have to discuss the similar concept of two-particle reducibility, which provides the basis for the parquet decomposition of the vertex,

$$\Gamma = \Lambda_{2\text{PI}} + \gamma_a + \gamma_p + \gamma_t. \quad (20)$$

This decomposition states that all diagrams which contribute to the two-particle vertex Γ can be classified as being part of one of four disjoint contributions: γ_r with $r \in \{a, p, t\}$ collects those diagrams which are two-particle reducible (2PR) in channel r , i.e., they can be disconnected by cutting a pair of propagator lines, which can either be aligned in an antiparallel (a), parallel (p) or transverse antiparallel (t) way. All remaining diagrams, which are not 2PR in either of the three channels, contribute to $\Lambda_{2\text{PI}}$, the fully two-particle irreducible (2PI) vertex. One can equally well decompose Γ w.r.t. its two-particle reducibility in one of the three channels,

¹⁵Note that we use a different sign convention for the hybridization function compared to [77].

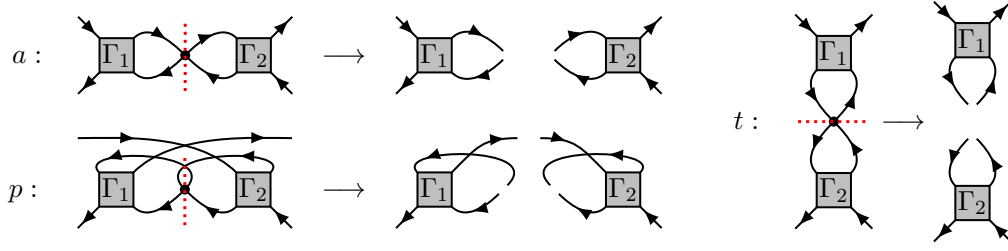


Figure 4: **Illustration of U -reducibility in the three two-particle channels a , p and t .** The Figure is analogous to Fig. 4 of [80] and adapted from [78]. Γ_1 and Γ_2 can be any vertex diagram or the unit vertex.

$\Gamma = I_r + \gamma_r$, which defines $I_r = \Lambda_{2\text{PI}} + \sum_{r' \neq r} \gamma_{r'}$, collecting all diagrams that are 2PI in channel r . The Bethe-Salpeter equations (BSEs) then relate the reducible diagrams to the irreducible ones,

$$\gamma_r = I_r \circ \Pi_r \circ \Gamma = \Gamma \circ \Pi_r \circ I_r. \quad (21)$$

This short-hand notation introduces the Π_r bubble, i.e., the propagator pair connecting the two vertices, see [78] for their precise channel-dependent definition, as well as for the connector symbol \circ , which channel-dependently denotes summation over internal frequencies and quantum numbers. The self-energy Σ , which enters the propagator via the Dyson equation $G = G_0 + G_0 \Sigma G$, is provided by the Schwinger-Dyson equation (SDE),

$$\Sigma = -(U + U \circ \Pi_p \circ \Gamma) \cdot G = -(U + \frac{1}{2} U \circ \Pi_a \circ \Gamma) \cdot G, \quad (22)$$

where U is the bare interaction and the symbol \cdot denotes the contraction of two vertex legs with a propagator. Together, equations (20), (21) and (22) are known as the *parquet equations* [85, 86] and can be solved self-consistently, if the 2PI vertex $\Lambda_{2\text{PI}}$ is provided [87–90]. Unfortunately, $\Lambda_{2\text{PI}}$ is the most complicated object, as its contributions contain nested contractions over internal arguments. Often, the parquet approximation (PA) is therefore employed, which truncates $\Lambda_{2\text{PI}}$ beyond the bare interaction U . In the context of the SBE decomposition relevant to this work, U -reducibility is an alternative criterion to the concept of two-particle reducibility for the classification of vertex diagrams. A diagram that is 2PR in channel r is also said to be U -reducible in channel r if it can be disconnected by removing one bare vertex that is attached to a Π_r bubble, as illustrated in Fig. 4. Furthermore, the bare vertex U is defined to be U -reducible in all three channels. The U -reducible diagrams in channel r are in the following denoted ∇_r and are said to describe *single-boson exchange* processes, as the linking bare interaction U , which would disconnect the diagram if cut, mediates just a single bosonic transfer frequency. The diagrams which are 2PR in channel r but not U -reducible in channel r are called multi-boson exchange diagrams and denoted M_r . With these classifications, the two-particle reducible vertices can be written as $\gamma_r = \nabla_r - U + M_r$, making sure to exclude U , which is contained in ∇_r but not in γ_r . The parquet decomposition (20) yields in this language,

$$\Gamma = \varphi^{U\text{irr}} + \sum_r \nabla_r - 2U, \quad \varphi^{U\text{irr}} = \Lambda_{2\text{PI}} - U + \sum_r M_r, \quad (23)$$

where $\varphi^{U\text{irr}}$ is the fully U -irreducible part of Γ . For a diagrammatic illustration of the first equation, see Fig. 8 in [78]. The channel-dependent decomposition of the vertex $\Gamma = I_r + \gamma_r = \nabla_r + T_r$ can also be split into U -reducible and U -irreducible parts in channel r , defining the U -irreducible remainder $T_r = I_r - U + M_r$ in channel r . Inserting all these definitions into the BSEs (21) and separating U -reducible and U -irreducible contributions gives the two sets of equations,

$$\nabla_r - U = I_r \circ \Pi_r \circ \nabla_r + U \circ \Pi_r \circ T_r = \nabla_r \circ \Pi_r \circ I_r + T_r \circ \Pi_r \circ U, \quad (24)$$

$$M_r = (I_r - U) \circ \Pi_r \circ T_r = T_r \circ \Pi_r \circ (I_r - U), \quad (25)$$

for each channel r . From equation (24) one can derive (see [78] for details) that the single-boson exchange terms can be written as $\nabla_r = \tilde{\lambda}_r \cdot \eta_r \cdot \lambda_r$, where $\tilde{\lambda}_r, \lambda_r$ denote the *Hedin vertices* [72] and η_r the screened interaction in channel r . The former are related to the U -irreducible vertex in channel r via $\tilde{\lambda}_r = \mathbf{1}_r + T_r \circ \Pi_r \circ \mathbf{1}_r = \mathbf{1}_r + \mathbf{1}_r \circ \Pi_r \circ T_r$ and can be understood as U -irreducible, amputated parts of three-point functions, as they depend on only two frequencies. In contrast to the GW approximation discussed in Sec. 4.2, the screened interaction η_r is now defined in terms of a Dyson equation, $\eta_r = U + U \cdot P_r \cdot \eta_r = U + \eta_r \cdot P_r \cdot U$, with the polarization $P_r = \lambda_r \circ \Pi_r \circ \mathbf{1}_r = \mathbf{1}_r \circ \Pi_r \circ \tilde{\lambda}_r$ dressed by vertex corrections. In the previous expressions, the connector \cdot denotes an internal summation similar to \circ , the only difference being that summation over frequencies is excluded. The corresponding unit vertex is denoted $\mathbf{1}_r$.

Lastly, one can rewrite the SDE in terms of the screened interaction and the Hedin vertex in channel r which yields, for example, $-\Sigma = (\eta_p \cdot \lambda_p) \cdot G = (\tilde{\lambda}_p \cdot \eta_p) \cdot G$ if one chooses $r = p$.

In summary, the SBE-equations to be solved read

$$\eta_r = U + U \cdot P_r \cdot \eta_r = U + \eta_r \cdot P_r \cdot U, \quad (26a)$$

$$P_r = \lambda_r \circ \Pi_r \circ \mathbf{1}_r = \mathbf{1}_r \circ \Pi_r \circ \tilde{\lambda}_r, \quad (26b)$$

$$\tilde{\lambda}_r = \mathbf{1}_r + T_r \circ \Pi_r \circ \mathbf{1}_r, \quad (26c)$$

$$\lambda_r = \mathbf{1}_r + \mathbf{1}_r \circ \Pi_r \circ T_r, \quad (26d)$$

$$T_r = \Gamma - \tilde{\lambda}_r \cdot \eta_r \cdot \lambda_r, \quad (26e)$$

$$\Gamma = \varphi^{U_{\text{irr}}} + \sum_r \tilde{\lambda}_r \cdot \eta_r \cdot \lambda_r - 2U, \quad (26f)$$

$$\varphi^{U_{\text{irr}}} = \Lambda_{2\text{PI}} - U + \sum_r M_r, \quad (26g)$$

$$M_r = (T_r - M_r) \circ \Pi_r \circ T_r = T_r \circ \Pi_r \circ (T_r - M_r), \quad (26h)$$

$$-\Sigma = (\eta_p \cdot \lambda_p) \cdot G = (\tilde{\lambda}_p \cdot \eta_p) \cdot G. \quad (26i)$$

As before, they require only the fully two-particle irreducible vertex $\Lambda_{2\text{PI}}$ as an input. Notably, if one employs the so-called SBE approximation [80], which amounts to setting $\Lambda_{2\text{PI}} = U$ as in the parquet approximation *and* neglecting multi-boson exchange contributions $M_r = 0$, all objects involved depend on at most two frequencies. This scheme is therefore numerically favorable compared to the PA if the SBE approximation can be justified [91]. In the context of this paper, we do not employ the SBE approximation, but include multi-boson exchange (MBE) contributions.

4.3.2 Implementation in MatsubaraFunctions.jl

In this section, we present the implementation of the PA in its MBE formulation using `MatsubaraFunctions.jl`. In doing so, we build upon the code structure developed in Sec. 4.2, i.e. we first define a solver class for which we later implement the self-consistent equations, as well as an interface to solve for the fixed point using Anderson acceleration, see Fig. 5. In order to keep the discussion concise, we refrain from showing all of the code and, instead, focus on computational bottlenecks and point out tricks to circumvent them. For completeness, however, we also make the entire code available via an open-source repository on Github, see Ref. [62] and provide additional implementation details in App. B.

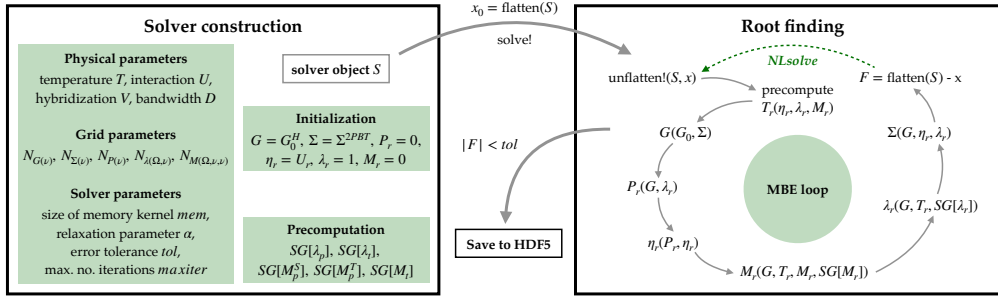


Figure 5: **Structure of the MBE code.** First, an instance S of type `MBE solver` is constructed by passing the SIAM parameters T , U , V and D and the sizes for the Matsubara grids. The self-energy Σ is initialized using second order perturbation theory (PT2), while all other MatsubaraFunctions are set to their bare values. In an optional step, MatsubaraSymmetryGroups for λ_r and M_r (here denoted by SG) can be precomputed. Next, the `solve!` function is used to find the fixed-point of the MBE equations using Anderson acceleration. To interface with `NLSolve`, the fields Σ , η_r , λ_r and M_r of S (which are sufficient to determine all other involved quantities) are flattened into a single one-dimensional array. After convergence, S is finally written to disk in H5 file format.

Extending the `GW solver` from Sec. 4.2 to the `MBE solver` needed here is a straightforward endeavor, since we just have to add containers and symmetry groups for the Hedin and multi-boson vertices. Furthermore, we extend the solver to include buffers which store the result of evaluating Eqs. (26c), (26d) and (26h), such that repetitive allocations of the multidimensional data arrays for λ_r and M_r are avoided. Note that, due to the symmetries of the SIAM studied here, it suffices to include either λ_r or $\tilde{\lambda}_r$, since $\lambda_r = \tilde{\lambda}_r$. In addition, all containers can be implemented as real-valued.¹⁶

```

1 function calc_T(
2     w  :: MatsubaraFrequency,
3     v  :: MatsubaraFrequency,
4     vp :: MatsubaraFrequency,
5     η_S :: MatsubaraFunction{1, 1, 2, Float64},
6     λ_S :: MatsubaraFunction{2, 1, 3, Float64},
7     η_D :: MatsubaraFunction{1, 1, 2, Float64},
8     λ_D :: MatsubaraFunction{2, 1, 3, Float64},
9     η_M :: MatsubaraFunction{1, 1, 2, Float64},
10    λ_M :: MatsubaraFunction{2, 1, 3, Float64},
11    M_S :: MatsubaraFunction{3, 1, 4, Float64},
12    M_T :: MatsubaraFunction{3, 1, 4, Float64},
13    M_D :: MatsubaraFunction{3, 1, 4, Float64},
14    M_M :: MatsubaraFunction{3, 1, 4, Float64},
15    U   :: Float64,
16    :: Type{ch_D}
17 )   :: Float64
18
19 # bare contribution
20 T = -2.0 * U
21
22 # SBE contributions
23 w1 = w + v + vp
24 η1_idx = MatsubaraFunctions.grid_index_extrp(w1, grids(η_D, 1))
25 λ1_idx1 = MatsubaraFunctions.grid_index_extrp(w1, grids(λ_D, 1))
26 λ1_idx2 = MatsubaraFunctions.grid_index_extrp(vp, grids(λ_D, 2))

```

¹⁶The Green's function G and the self-energy Σ are purely imaginary, such that $G = -i\tilde{G}$ and $\Sigma = -i\tilde{\Sigma}$. After plugging this factorization into Eqs. (26a)-(26i), all factors of i are cancelled out such that the resulting equations are entirely real.

```

27  λ1_idx3 = MatsubaraFunctions.grid_index_extrp( v, grids(λ_D, 2))
28
29  w2      = vp - v
30  v2      = w + v
31  η2_idx  = MatsubaraFunctions.grid_index_extrp(w2, grids(η_D, 1))
32  λ2_idx1 = MatsubaraFunctions.grid_index_extrp(w2, grids(λ_D, 1))
33  λ2_idx2 = MatsubaraFunctions.grid_index_extrp(v2, grids(λ_D, 2))
34
35  T += +0.5 * λ_S[λ1_idx1, λ1_idx2, 1] * η_S[η1_idx, 1] * λ_S[λ1_idx1, λ1_idx3, 1]
36  T += -0.5 * λ_D[λ2_idx1, λ1_idx3, 1] * η_D[η2_idx, 1] * λ_D[λ2_idx1, λ2_idx2, 1]
37  T += -1.5 * λ_M[λ2_idx1, λ1_idx3, 1] * η_M[η2_idx, 1] * λ_M[λ2_idx1, λ2_idx2, 1]
38
39  # MBE contributions
40  w_idx  = MatsubaraFunctions.grid_index_extrp( w, grids(M_S, 1))
41  v_idx  = MatsubaraFunctions.grid_index_extrp( v, grids(M_S, 2))
42  vp_idx = MatsubaraFunctions.grid_index_extrp(vp, grids(M_S, 2))
43
44  w1_idx = MatsubaraFunctions.grid_index_extrp(w1, grids(M_S, 1))
45  w2_idx = MatsubaraFunctions.grid_index_extrp(w2, grids(M_S, 1))
46  v2_idx = MatsubaraFunctions.grid_index_extrp(v2, grids(M_S, 2))
47
48  T += M_D[w_idx, v_idx, vp_idx, 1]
49  T += +0.5 * M_S[w1_idx, v_idx, vp_idx, 1]
50  T += +1.5 * M_T[w1_idx, v_idx, vp_idx, 1]
51  T += -0.5 * M_D[w2_idx, v_idx, v2_idx, 1]
52  T += -1.5 * M_M[w2_idx, v_idx, v2_idx, 1]
53
54  return T
55 end

```

Profiling the MBE code reveals that most of the time is spent calculating the irreducible vertices T_r , which are needed to compute both λ_r and M_r . In the former case, two legs of T_r are closed with a propagator bubble, while in the latter case, T_r enters both to the left and to the right of the respective (Bethe-Salpeter-like) equation. When optimizing the code, it is therefore crucial to find an efficient way to evaluate Eq. (26e). In the example above, an exemplary implementation of T_r in the density channel is shown. Here, we make use of the `grid_index_extrp` function, which given a Matsubara frequency and a grid g finds the linear index of the frequency in g or, if it is out of bounds, determines the bound of g that is closest. This function is normally used internally to perform constant extrapolation for `MatsubaraFunction` objects with grid dimension greater than one.¹⁷ Here, however, it can be used to precompute multiple linear indices at once, allowing us to exclusively use the `[]` operator and thus avoid unnecessary boundary checks. Note that we could have used tailfits for the screened interactions η_r but opt to utilize constant extrapolation instead.¹⁸

Furthermore, when T_r is inserted into the equations for the Hedin and multiboson vertices, it is summed up along one fermionic axis. Therefore, some frequencies, e.g. $w1 = w + v + vp$ in line 23 of the code snippet above, will assume the same value for many different external arguments. Hence, to circumvent repeated (but superfluous) `grid_index_extrp` calls, it is beneficial to precompute T_r on a finite grid, which needs to be large enough to maintain the desired accuracy. To this end, we add buffers for the irreducible vertices to our solver class, such that we can compute e.g. the density T^D and magnetic contributions T^M inplace and in parallel, as shown in the example below.

```

1 function calc_T_ph!(
2   T_D :: MatsubaraFunction{3, 1, 4, Float64},
3   T_M :: MatsubaraFunction{3, 1, 4, Float64},
4   η_S :: MatsubaraFunction{1, 1, 2, Float64},
5   λ_S :: MatsubaraFunction{2, 1, 3, Float64},

```

¹⁷Therefore it is not exported into the global namespace.

¹⁸Since η_r depends only on one frequency argument, it can be stored on a rather large grid, such that its asymptotic behavior is well-captured even without polynomial extrapolation.

```

6  η_D :: MatsubaraFunction{1, 1, 2, Float64},
7  λ_D :: MatsubaraFunction{2, 1, 3, Float64},
8  η_M :: MatsubaraFunction{1, 1, 2, Float64},
9  λ_M :: MatsubaraFunction{2, 1, 3, Float64},
10 M_S :: MatsubaraFunction{3, 1, 4, Float64},
11 M_T :: MatsubaraFunction{3, 1, 4, Float64},
12 M_D :: MatsubaraFunction{3, 1, 4, Float64},
13 M_M :: MatsubaraFunction{3, 1, 4, Float64},
14 U   :: Float64
15 )   :: Nothing
16
17 Threads.@threads for vp in grids(T_D, 3)
18   λ1_idx2 = MatsubaraFunctions.grid_index_extrp(vp, grids(λ_D, 2))
19   vp_idx  = MatsubaraFunctions.grid_index_extrp(vp, grids(M_S, 2))
20
21   for v in grids(T_D, 2)
22     w2 = vp - v
23     λ1_idx3 = MatsubaraFunctions.grid_index_extrp(v, grids(λ_D, 2))
24     η2_idx  = MatsubaraFunctions.grid_index_extrp(w2, grids(η_D, 1))
25     λ2_idx1 = MatsubaraFunctions.grid_index_extrp(w2, grids(λ_D, 1))
26     v_idx   = MatsubaraFunctions.grid_index_extrp(v, grids(M_S, 2))
27     w2_idx  = MatsubaraFunctions.grid_index_extrp(w2, grids(M_S, 1))
28
29     for w in grids(T_D, 1)
30       w1 = w + v + vp
31       v2 = w + v
32       η1_idx = MatsubaraFunctions.grid_index_extrp(w1, grids(η_D, 1))
33       λ1_idx1 = MatsubaraFunctions.grid_index_extrp(w1, grids(λ_D, 1))
34       λ2_idx2 = MatsubaraFunctions.grid_index_extrp(v2, grids(λ_D, 2))
35       w_idx  = MatsubaraFunctions.grid_index_extrp(w, grids(M_S, 1))
36       w1_idx = MatsubaraFunctions.grid_index_extrp(w1, grids(M_S, 1))
37       v2_idx = MatsubaraFunctions.grid_index_extrp(v2, grids(M_S, 2))
38
39       # compute SBE vertices
40       p1 = λ_S[λ1_idx1, λ1_idx2, 1] * η_S[η1_idx, 1] * λ_S[λ1_idx1, λ1_idx3, 1]
41       p2 = λ_D[λ2_idx1, λ1_idx3, 1] * η_D[η2_idx, 1] * λ_D[λ2_idx1, λ2_idx2, 1]
42       p3 = λ_M[λ2_idx1, λ1_idx3, 1] * η_M[η2_idx, 1] * λ_M[λ2_idx1, λ2_idx2, 1]
43
44       # compute MBE vertices
45       m1 = M_S[w1_idx, v_idx, vp_idx, 1]
46       m2 = M_T[w1_idx, v_idx, vp_idx, 1]
47       m3 = M_D[w2_idx, v_idx, v2_idx, 1]
48       m4 = M_M[w2_idx, v_idx, v2_idx, 1]
49
50       T_D[w, v, vp] = -2.0 * U + M_D[w_idx, v_idx, vp_idx, 1] + 0.5 * (p1 + m1 -
↪ p2 - m3) + 1.5 * (m2 - p3 - m4)
51       T_M[w, v, vp] = +2.0 * U + M_M[w_idx, v_idx, vp_idx, 1] - 0.5 * (p1 + m1 +
↪ p2 + m3) + 0.5 * (m2 + p3 + m4)
52     end
53   end
54 end
55
56 return nothing
57 end

```

Here, we also make use of the fact that many frequency arguments (and their respective linear indices) are shared between different channels, which speeds up the calculation of T even further. The implementation of, say, Eq. (26h) is now rather straightforward. M^D , for example, can be computed as shown below.

```

1 function calc_M!(
2   M   :: MatsubaraFunction{3, 1, 4, Float64},
3   Pi  :: MatsubaraFunction{2, 1, 3, Float64},
4   T   :: MatsubaraFunction{3, 1, 4, Float64},
5   M_D :: MatsubaraFunction{3, 1, 4, Float64},
6   SG  :: MatsubaraSymmetryGroup,
7       :: Type{ch_D}
8 )   :: Nothing
9

```

```

10 # model the diagram
11 function f(wtpl, xtpl)
12
13     w, v, vp = wtpl
14     val      = 0.0
15     v1, v2   = grids(Pi, 2)(grids(T, 3)[1]), grids(Pi, 2)(grids(T, 3)[end])
16     Pi_slice = view(Pi, w, v1 : v2)
17     M_D_slice = view(M_D, w, v, :)
18     T_L_slice = view(T, w, v, :)
19     T_R_slice = view(T, w, vp, :)
20
21     v1 = grids(T, 3)(grids(M_D, 3)[1])
22     vr = grids(T, 3)(grids(M_D, 3)[end])
23
24     for i in 1 : v1 - 1
25         val -= (T_L_slice[i] - M_D_slice[1]) * Pi_slice[i] * T_R_slice[i]
26     end
27
28     for i in v1 : vr
29         val -= (T_L_slice[i] - M_D_slice[i - v1 + 1]) * Pi_slice[i] * T_R_slice[i]
30     end
31
32     for i in vr + 1 : length(T_L_slice)
33         val -= (T_L_slice[i] - M_D_slice[vr - v1 + 1]) * Pi_slice[i] * T_R_slice[i]
34     end
35
36     return temperature(M) * val
37 end
38
39 # compute multiboson vertex
40 SG(M, MatsubaraInitFunction{3, 1, Float64}(f); mode = :hybrid)
41
42 return nothing
43 end

```

Here, we utilize the corresponding `MatsubaraSymmetryGroup` object with the hybrid MPI + Threads parallelization scheme. In addition, we make use of views for the bubble and vertices to avoid repeated memory lookups in the Matsubara summation.

4.3.3 Benchmark results

In this section, we benchmark the presented implementation of the MBE parquet solver against an independent implementation in C++. Our motivation for this comparison is twofold: Firstly, we want to verify the overall correctness of both implementations and, secondly, we want to test how robust the multiboson formalism is to implementation details. This regards, for example, the treatment of correlation functions at the boundaries of their respective frequency grids. While the Julia code relies on (polynomial or constant) extrapolation, the C++ code replaces correlators with their asymptotic value instead. Ideally, these details should be irrelevant, except in the most difficult parameter regimes. Both codes used the physical parameters as stated after Eq. (18) and the frequency parameters according to Tab. 1. We begin by examining the static properties of the model including the quasiparticle residue Z given by

$$Z^{-1} = 1 - \left. \frac{d\text{Im}[\Sigma(\omega)]}{d\omega} \right|_{\omega \rightarrow 0}, \quad (27)$$

as well as the susceptibilities in the density (D) and magnetic (M) channels. The latter can be obtained from the screened interactions analogous to Ref. [92], that is

$$\chi^{D/M} = \frac{\eta^{D/M} - U^{D/M}}{(U^{D/M})^2}. \quad (28)$$

The corresponding results are summarized in Fig. 6. Both codes are in quantitative agreement and predict a strong enhancement of magnetic fluctuations at low temperatures. However, as

Table 1: **Frequency parameters for the benchmark results in Figs. 6-9.** We show the total number of frequencies used for the various Matsubara functions. Since the boxes are symmetric around zero there is an even (odd) number of Matsubara frequencies along fermionic (bosonic) directions.

	total no. frequencies
G	4096
Σ	512
η	1023
λ	575×512
M	$383 \times 320 \times 320$

has been noted in Ref. [77], the characteristic signature for the formation of a local magnetic moment at the impurity, a decrease of χ^D for temperatures $T \lesssim 2$ (for the specific choice of numerical parameters used here), is not captured by the parquet approximation. Instead, χ^D increases monotonically over the entire range of temperatures considered and the system remains in a metallic state with well-defined quasiparticles (i.e. $0 < Z < 1$).

Figure 7 shows a direct comparison of the MBE vertices and their evolution with decreasing temperature within both codes. As can be seen from the middle column, showing the screened interaction, Hedin and multiboson vertex in the magnetic channel, most of the long-lived magnetic correlations are already captured by the screened interaction itself and thus by the corresponding single-boson exchange diagrams. In contrast, low-energy scattering processes mediated by multiple bosons seem to be less relevant, as indicated by a comparatively small M^M contribution. This picture is somewhat reversed in the other channels (left and right column in Fig. 7). In the density channel, for example, the largest contribution originates from short and also long-lived multiboson fluctuations, especially at low temperatures.

Figure 8 presents further results for M^X as a function of its two fermionic frequencies ν and ν' (with fixed $\Omega = 0$). Remarkably, the structure of these objects is dominated by cross-like structures similar to those discussed in Ref. [92], which become more pronounced when T is decreased. A comparison of the data obtained with both codes (shown in the second row of Fig. 8), reveals that it is precisely these structures that seem difficult to capture in numerical calculations, and where small differences in the implementation can have a significant effect. However, the relative difference between the results from both codes is still small ($\lesssim 0.01$).

As a final benchmark of the codes, we have considered their respective serial and parallel performance for a single evaluation of the parquet equations in SBE decomposition (see Fig. 9). Surprisingly, the Julia code based on `MatsubaraFunctions.jl` outperforms the C++ implementation by about a factor of four when run in production mode (i.e., with internal sanity checks disabled). We would like to note that this is most likely *not* due to a fundamental performance advantage of Julia over C++, but simply the result of several optimizations (such as those presented in Sec. 4.3.2) that were more easy to implement using `MatsubaraFunctions.jl`.

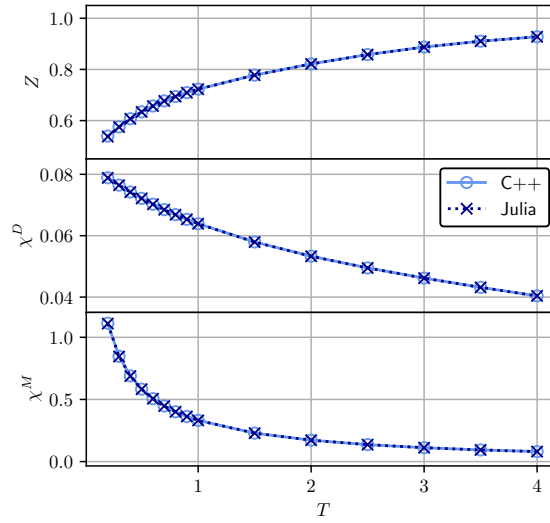


Figure 6: Results for the quasi-particle residue Z and the density/magnetic susceptibility $\chi^{D/M}$. The comparison shows good agreement between the two codes. Note that we approximated the derivative in Eq. (27) by a fourth order finite differences method.

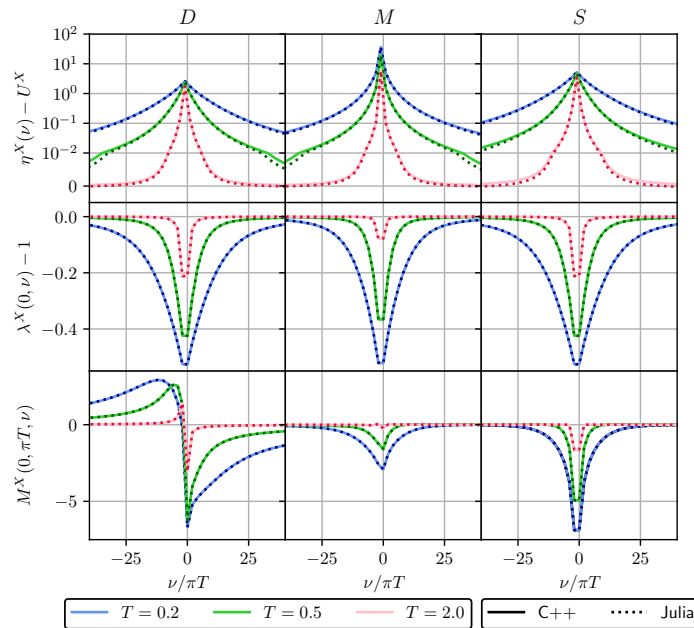


Figure 7: Benchmark of vertex quantities between the Julia and C++ code. We show frequency slices through various SBE ingredients (top to bottom: screened interactions, Hedin vertices, multiboson vertices) at different temperatures and channels. The comparison shows good agreement between both codes.

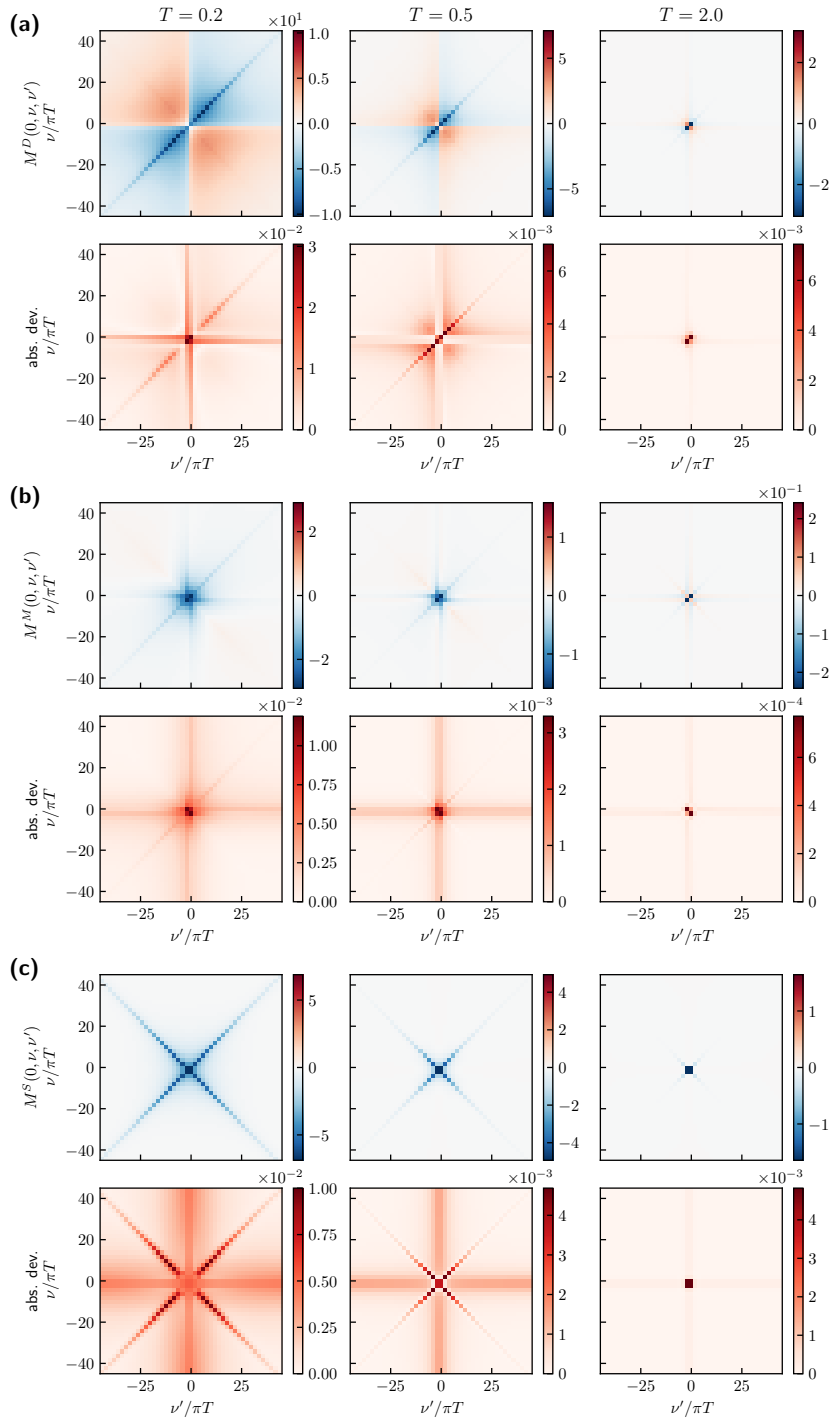


Figure 8: Slice through multi-boson contributions M^D , M^M and M^S . The upper panels show the data for different temperatures, the lower panels the absolute deviation between the Julia and the C++ implementation, respectively. For lower temperatures the features in the data require the computation and storage of a larger number of frequency points. The agreement of the data persists to the lowest temperature shown in this paper.

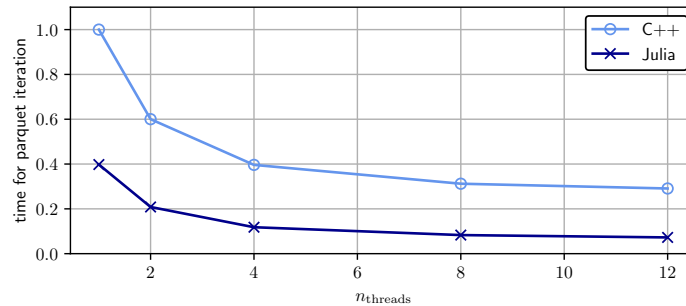


Figure 9: **Performance benchmark between the Julia and C++ code.** We show the time taken for a single evaluation of the parquet equations in SBE decomposition. Note that the runtimes have been normalized to the serial result of the C++ code.

5 Future directions

We have presented a first version of the `MatsubaraFunctions.jl` library and its basic functionality. Although the library already offers many features, most notably an automated interface for implementing and exploiting symmetries when working with Green’s functions (including several options for parallel evaluation), as well as high performance for larger projects (see Sec. 4.3.1 and the discussions therein), several generalizations of the interface and further optimizations are currently under development. In addition, we will add more support for generic grid types other than just Matsubara frequency grids. These could include, for example, momentum space grids and support for continuous variables (such as real frequencies). Note, however, that calculations in momentum or real space are already feasible with the current state of the package, if a suitable mapping from, say, wavevectors to indices is provided. Accuracy improvements for fitting high-frequency tails and more advanced extrapolation schemes for Matsubara sums are also in the works.

In the future, it will be very valuable to extend the ecosystem surrounding `MatsubaraFunctions.jl`. For example, many state-of-the-art diagrammatic solvers rely on the efficient evaluation of similar diagrams such as vertex-bubble-vertex contractions, which are a common feature of Bethe-Salpeter-type equations. These operations could be developed independently of the main library, providing even more quality-of-life options for the user. Moreover, such a toolkit would allow for the swift deployment of different types of solvers, including fRG solvers for quantum spin systems and self-consistent impurity solvers such as the MBE code presented in Sec. 4.3.2, to name but a few. With many new and exciting correlated materials becoming available, fast and flexible solvers are of utmost importance to facilitate scientific progress, and we strongly believe that a package like `MatsubaraFunctions.jl` could be a useful tool for their rapid development.

Acknowledgments

We would like to thank Fabian Kugler, Jae-Mo Lihm, Seung-Sup Lee, Friedrich Krien, Marc Ritter, Björn Sbierski and Benedikt Schneider for helpful discussions and collaboration on ongoing projects.

Funding information This work was funded in part by the Deutsche Forschungsgemeinschaft under Germany’s Excellence Strategy EXC-2111 (Project No. 390814868). It is part of

the Munich Quantum Valley, supported by the Bavarian state government with funds from the Hightech Agenda Bayern Plus. N.R. acknowledges funding from a graduate scholarship from the German Academic Scholarship Foundation (Studienstiftung des deutschen Volkes) and additional support from the ‘‘Marianne-Plehn-Programm’’ of the state of Bavaria. The numerical simulations were, in part, performed on the Linux clusters and the SuperMUC cluster (project 23769) at the Leibniz Supercomputing Center in Munich. The Flatiron Institute is a division of the Simons Foundation.

A Extrapolation of Matsubara sums

Suppose we want to compute the fermionic Matsubara sum $f(\tau \rightarrow 0^+) = \frac{1}{\beta} \sum_{\nu} f(\nu) e^{-i\nu 0^+}$. We assume that $f(z)$ with $z \in \mathbb{C}$ has a Laurent series representation in an elongated annulus about the imaginary axis which decays to zero for large $|z|$. If the poles and residues of f in the complex plane are known, this problem can in principle be solved by rewriting the Matsubara sum as a contour integral and applying Cauchy’s residue theorem after deforming the contour. Unfortunately, these poles are usually unknown and we have to resort to numerical calculations instead. There, however, we can only compute the sum over a finite (symmetric) grid of Matsubara frequencies, which converges very slowly if at all.

To tackle this problem, let us assume that f is known on a grid with sufficiently large maximum (minimum) frequency $\pm\Omega$, such that we can approximate

$$f(\nu) \approx \sum_{n=1}^N \frac{\alpha_n}{(i\nu)^n}, \quad (\text{A.1})$$

for $|\nu| > \Omega$. Neglecting the factor $e^{-i\nu 0^+}$ for brevity, this allows us to split up the expression for $f(\tau \rightarrow 0^+)$ as

$$\begin{aligned} \frac{1}{\beta} \sum_{\nu} f(\nu) &= \frac{1}{\beta} \sum_{\nu < -\Omega} f(\nu) + \frac{1}{\beta} \sum_{-\Omega \leq \nu \leq \Omega} f(\nu) + \frac{1}{\beta} \sum_{\nu > \Omega} f(\nu) \\ &\approx \frac{1}{\beta} \sum_{\nu < -\Omega} \sum_{n=1}^N \frac{\alpha_n}{(i\nu)^n} + \frac{1}{\beta} \sum_{-\Omega \leq \nu \leq \Omega} f(\nu) + \frac{1}{\beta} \sum_{\nu > \Omega} \sum_{n=1}^N \frac{\alpha_n}{(i\nu)^n}, \end{aligned} \quad (\text{A.2})$$

where (A.1) was used to approximate the semi-infinite sums. In many cases, the dominant asymptotic behavior of single-particle Green’s functions and one-dimensional slices through higher-order vertex functions is already well captured by an algebraic decay $(i\nu)^{-q}$ with $q = 1, 2$. Therefore, by truncating the asymptotic expansion at $N = 2$, we can rewrite the right-hand side as

$$\frac{1}{\beta} \sum_{\nu} f(\nu) \approx \frac{1}{\beta} \sum_{-\Omega \leq \nu \leq \Omega} f(\nu) + \sum_{n=1}^2 \left[\frac{1}{\beta} \sum_{\nu} \frac{\alpha_n}{(i\nu)^n} - \frac{1}{\beta} \sum_{-\Omega \leq \nu \leq \Omega} \frac{\alpha_n}{(i\nu)^n} \right]. \quad (\text{A.3})$$

The series in the bracket can be computed straightforwardly using Cauchy’s residue theorem and we find

$$\frac{1}{\beta} \sum_{\nu} f(\nu) e^{-i\nu 0^+} \approx \frac{1}{\beta} \sum_{-\Omega \leq \nu \leq \Omega} \left[f(\nu) - \frac{\alpha_2}{(i\nu)^2} \right] - \frac{\alpha_1}{2} - \beta \frac{\alpha_2}{4}. \quad (\text{A.4})$$

Thus, if the coefficients α_n are known (for example by fitting the high-frequency tails), this formula can provide a quick and dirty approximation to the infinite Matsubara sum.

B Implementation details for the MBE solver

In this section we provide additional information on the implementation of the MBE equations, which were introduced on a general basis in Sec. 4.3.1 of the main text. As for any application involving many-body Green's functions, it is crucial to choose an appropriate parametrization of the self-consistent equations that reflects the symmetries of the field theory under consideration. Here, we deal with the implementation of SU(2) symmetry (spin rotation invariance) as well as time translation invariance (energy conservation) for the MBE equations of the impurity model defined in Sec. 4.3.

B.1 SU(2) symmetry

Consider an SU(2) transformation $U = e^{i\epsilon\sigma}$, where $\epsilon \in \mathbb{R}^3$ and σ is the vector of Pauli matrices. Under U , the fermionic creation and annihilation operators transform into

$$c_s \rightarrow U_{ss'} c_{s'}, \quad c_s^\dagger \rightarrow c_{s'}^\dagger (U^\dagger)_{s's}, \quad (\text{B.1})$$

where we have omitted all indices except the spin $s = \{\uparrow, \downarrow\}$. For SU(2) symmetric actions it can be shown that single-particle Green's functions $G_{ss'}^{(1)}$ are diagonal and also invariant under spin flips, i.e. $G_{ss'}^{(1)} = G^{(1)} \delta_{ss'}$ [48]. Two-particle correlators $G_{s_1's_1s_2's_2}^{(2)}$, on the other hand, can be decomposed into two components $G^{(2)|=}$ and $G^{(2)|\times}$, which preserve the total spin between incoming and outgoing particles

$$G_{s_1's_1s_2's_2}^{(2)} = G^{(2)|=} \delta_{s_1's_1} \delta_{s_2's_2} + G^{(2)|\times} \delta_{s_1's_2} \delta_{s_2's_1}. \quad (\text{B.2})$$

Furthermore, the Bethe-Salpeter-like equations (24) can be diagonalized by introducing a singlet (S) and a triplet (T) component

$$\begin{aligned} G_p^{(2)|S} &= G_p^{(2)|=} - G_p^{(2)|\times}, \\ G_p^{(2)|T} &= G_p^{(2)|=} + G_p^{(2)|\times}, \end{aligned} \quad (\text{B.3})$$

in the p channel, and a density (D) and magnetic (M) contribution

$$\begin{aligned} G_t^{(2)|D} &= 2G_t^{(2)|=} + G_t^{(2)|\times}, \\ G_t^{(2)|M} &= G_t^{(2)|\times}, \end{aligned} \quad (\text{B.4})$$

in the t channel. Moreover, this change of basis has the advantage that physical response functions can be obtained directly from the screened interaction in the respective channel. The spin susceptibility χ^M , for example, is simply given by $-U^2 \chi^M = \eta^M + U$ for a local Hubbard U . For this reason, the $\{S, T, D, M\}$ basis is sometimes called the *physical* spin basis, whereas the decomposition into parallel ($=$) and crossed terms (\times) is known as the *diagrammatic* spin basis [48]. In the implementation of the MBE solver, the former is used.

B.2 Time translation invariance

The interacting part of the impurity action from Sec. 4.3 is static, i.e. the bare interaction U is τ -independent. Consequently, one and two-particle Green's functions are invariant under translations in imaginary time, which implies conservation of the total Matsubara frequency between incoming and outgoing legs [48] and, thus,

$$\begin{aligned} G^{(1)}(\nu, \nu') &= G^{(1)}(\nu) \times \beta \delta_{\nu|\nu'}, \\ G^{(2)}(\nu_1', \nu_1, \nu_2', \nu_2) &= G^{(2)}(\nu_1', \nu_1, \nu_2') \times \beta \delta_{\nu_1'+\nu_2'|\nu_1+\nu_2}. \end{aligned} \quad (\text{B.5})$$

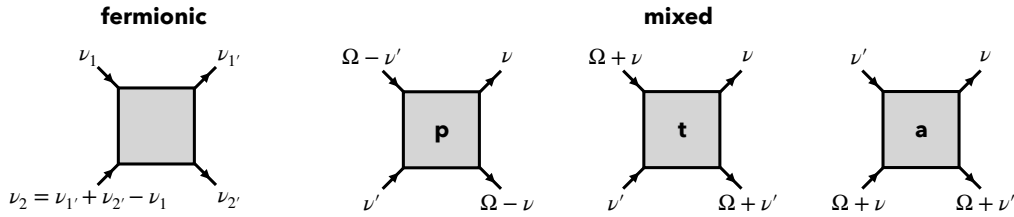


Figure 10: **Mixed frequency conventions.** In mixed notation, each 2PR channel is described in terms of one bosonic argument Ω and two fermionic frequencies ν, ν' as opposed to the purely fermionic notation shown on the left.

Note that we have suppressed additional indices, such as spin, for brevity. For two-particle quantities, it is convenient to adopt a *mixed* frequency convention for the 2PR channels, where, instead of three fermionic arguments, one bosonic transfer frequency Ω and two fermionic frequencies ν, ν' are used. The convention used for the MBE solver is shown in Fig. 10.

References

- [1] J. G. Bednorz and K. A. Müller, *Possible high T_c superconductivity in the Ba-La-Cu-O system*, Z. Phys. B - Condens. Matter **64**, 189 (1986), doi:[10.1007/BF01303701](https://doi.org/10.1007/BF01303701).
- [2] B. Keimer, S. A. Kivelson, M. R. Norman, S. Uchida and J. Zaanen, *From quantum matter to high-temperature superconductivity in copper oxides*, Nature **518**, 179 (2015), doi:[10.1038/nature14165](https://doi.org/10.1038/nature14165).
- [3] N. Mott, *Metal-insulator transitions*, CRC Press, Boca Raton, USA, ISBN 9780429094880 (2004), doi:[10.1201/b12795](https://doi.org/10.1201/b12795).
- [4] J. Hubbard, *Electron correlations in narrow energy bands*, Proc. R. Soc. Lond. A: Math. Phys. Sci. **276**, 238 (1963), doi:[10.1098/rspa.1963.0204](https://doi.org/10.1098/rspa.1963.0204).
- [5] M. Imada, A. Fujimori and Y. Tokura, *Metal-insulator transitions*, Rev. Mod. Phys. **70**, 1039 (1998), doi:[10.1103/RevModPhys.70.1039](https://doi.org/10.1103/RevModPhys.70.1039).
- [6] L. Savary and L. Balents, *Quantum spin liquids: A review*, Rep. Prog. Phys. **80**, 016502 (2016), doi:[10.1088/0034-4885/80/1/016502](https://doi.org/10.1088/0034-4885/80/1/016502).
- [7] J. Knolle and R. Moessner, *A field guide to spin liquids*, Annu. Rev. Condens. Matter Phys. **10**, 451 (2019), doi:[10.1146/annurev-conmatphys-031218-013401](https://doi.org/10.1146/annurev-conmatphys-031218-013401).
- [8] M. Qin, T. Schäfer, S. Andergassen, P. Corboz and E. Gull, *The Hubbard model: A computational perspective*, Annu. Rev. Condens. Matter Phys. **13**, 275 (2022), doi:[10.1146/annurev-conmatphys-090921-033948](https://doi.org/10.1146/annurev-conmatphys-090921-033948).
- [9] D. J. Scalapino, *A common thread: The pairing interaction for unconventional superconductors*, Rev. Mod. Phys. **84**, 1383 (2012), doi:[10.1103/RevModPhys.84.1383](https://doi.org/10.1103/RevModPhys.84.1383).
- [10] T. Schäfer et al., *Tracking the footprints of spin fluctuations: A multimethod, multimessenger study of the two-dimensional Hubbard model*, Phys. Rev. X **11**, 011058 (2021), doi:[10.1103/PhysRevX.11.011058](https://doi.org/10.1103/PhysRevX.11.011058).
- [11] H. Q. Lin, *Exact diagonalization of quantum-spin models*, Phys. Rev. B **42**, 6561 (1990), doi:[10.1103/PhysRevB.42.6561](https://doi.org/10.1103/PhysRevB.42.6561).

- [12] H. Q. Lin, J. E. Gubernatis, H. Gould and J. Tobochnik, *Exact diagonalization methods for quantum systems*, *Comput. Phys.* **7**, 400 (1993), doi:[10.1063/1.4823192](https://doi.org/10.1063/1.4823192).
- [13] A. Weiße and H. Fehske, *Computational many-particle physics*, Springer, Berlin, Heidelberg, Germany, ISBN 9783540746850 (2008), doi:[10.1007/978-3-540-74686-7](https://doi.org/10.1007/978-3-540-74686-7).
- [14] S. R. White, *Density matrix formulation for quantum renormalization groups*, *Phys. Rev. Lett.* **69**, 2863 (1992), doi:[10.1103/PhysRevLett.69.2863](https://doi.org/10.1103/PhysRevLett.69.2863).
- [15] U. Schollwöck, *The density-matrix renormalization group*, *Rev. Mod. Phys.* **77**, 259 (2005), doi:[10.1103/RevModPhys.77.259](https://doi.org/10.1103/RevModPhys.77.259).
- [16] N. Metropolis, A. W. Rosenbluth, M. N. Rosenbluth, A. H. Teller and E. Teller, *Equation of state calculations by fast computing machines*, *J. Chem. Phys.* **21**, 1087 (1953), doi:[10.1063/1.1699114](https://doi.org/10.1063/1.1699114).
- [17] D. Ceperley and B. Alder, *Quantum Monte Carlo*, *Science* **231**, 555 (1986), doi:[10.1126/science.231.4738.555](https://doi.org/10.1126/science.231.4738.555).
- [18] W. M. C. Foulkes, L. Mitas, R. J. Needs and G. Rajagopal, *Quantum Monte Carlo simulations of solids*, *Rev. Mod. Phys.* **73**, 33 (2001), doi:[10.1103/RevModPhys.73.33](https://doi.org/10.1103/RevModPhys.73.33).
- [19] F. Becca and S. Sorella, *Quantum Monte Carlo approaches for correlated systems*, Cambridge University Press, Cambridge, UK, ISBN 9781107129931 (2017), doi:[10.1017/9781316417041](https://doi.org/10.1017/9781316417041).
- [20] C. Wetterich, *Exact evolution equation for the effective potential*, *Phys. Lett. B* **301**, 90 (1993), doi:[10.1016/0370-2693\(93\)90726-X](https://doi.org/10.1016/0370-2693(93)90726-X).
- [21] P. Kopietz, L. Bartosch and F. Schütz, *Introduction to the functional renormalization group*, Springer, Berlin, Heidelberg, Germany, ISBN 9783642050930 (2010), doi:[10.1007/978-3-642-05094-7](https://doi.org/10.1007/978-3-642-05094-7).
- [22] W. Metzner, M. Salmhofer, C. Honerkamp, V. Meden and K. Schönhammer, *Functional renormalization group approach to correlated fermion systems*, *Rev. Mod. Phys.* **84**, 299 (2012), doi:[10.1103/RevModPhys.84.299](https://doi.org/10.1103/RevModPhys.84.299).
- [23] A. Georges, G. Kotliar, W. Krauth and M. J. Rozenberg, *Dynamical mean-field theory of strongly correlated fermion systems and the limit of infinite dimensions*, *Rev. Mod. Phys.* **68**, 13 (1996), doi:[10.1103/RevModPhys.68.13](https://doi.org/10.1103/RevModPhys.68.13).
- [24] N. D. Mermin and H. Wagner, *Absence of ferromagnetism or antiferromagnetism in one- or two-dimensional isotropic Heisenberg models*, *Phys. Rev. Lett.* **17**, 1307 (1966), doi:[10.1103/PhysRevLett.17.1307](https://doi.org/10.1103/PhysRevLett.17.1307).
- [25] P. C. Hohenberg, *Existence of long-range order in one and two dimensions*, *Phys. Rev.* **158**, 383 (1967), doi:[10.1103/PhysRev.158.383](https://doi.org/10.1103/PhysRev.158.383).
- [26] T. Maier, M. Jarrell, T. Pruschke and M. H. Hettler, *Quantum cluster theories*, *Rev. Mod. Phys.* **77**, 1027 (2005), doi:[10.1103/RevModPhys.77.1027](https://doi.org/10.1103/RevModPhys.77.1027).
- [27] G. Kotliar, S. Y. Savrasov, K. Haule, V. S. Oudovenko, O. Parcollet and C. A. Marianetti, *Electronic structure calculations with dynamical mean-field theory*, *Rev. Mod. Phys.* **78**, 865 (2006), doi:[10.1103/RevModPhys.78.865](https://doi.org/10.1103/RevModPhys.78.865).

- [28] A.-M. S. Tremblay, B. Kyung and D. Sénéchal, *Pseudogap and high-temperature superconductivity from weak to strong coupling. Towards a quantitative theory (review article)*, *Low Temp. Phys.* **32**, 424 (2006), doi:[10.1063/1.2199446](https://doi.org/10.1063/1.2199446).
- [29] A. I. Lichtenstein and M. I. Katsnelson, *Antiferromagnetism and d-wave superconductivity in cuprates: A cluster dynamical mean-field theory*, *Phys. Rev. B* **62**, R9283 (2000), doi:[10.1103/PhysRevB.62.R9283](https://doi.org/10.1103/PhysRevB.62.R9283).
- [30] G. Rohringer, H. Hafermann, A. Toschi, A. A. Katanin, A. E. Antipov, M. I. Katsnelson, A. I. Lichtenstein, A. N. Rubtsov and K. Held, *Diagrammatic routes to nonlocal correlations beyond dynamical mean field theory*, *Rev. Mod. Phys.* **90**, 025003 (2018), doi:[10.1103/RevModPhys.90.025003](https://doi.org/10.1103/RevModPhys.90.025003).
- [31] T. Matsubara, *A new approach to quantum-statistical mechanics*, *Prog. Theor. Phys.* **14**, 351 (1955), doi:[10.1143/PTP.14.351](https://doi.org/10.1143/PTP.14.351).
- [32] R. Kubo, *Statistical-mechanical theory of irreversible processes. I. General theory and simple applications to magnetic and conduction problems*, *J. Phys. Soc. Jpn.* **12**, 570 (1957), doi:[10.1143/JPSJ.12.570](https://doi.org/10.1143/JPSJ.12.570).
- [33] J. Bezanson, A. Edelman, S. Karpinski and V. B. Shah, *Julia: A fresh approach to numerical computing*, *SIAM Rev.* **59**, 65 (2017), doi:[10.1137/141000671](https://doi.org/10.1137/141000671).
- [34] J. Reuther and P. Wölfle, *$J_1 - J_2$ frustrated two-dimensional Heisenberg model: Random phase approximation and functional renormalization group*, *Phys. Rev. B* **81**, 144410 (2010), doi:[10.1103/PhysRevB.81.144410](https://doi.org/10.1103/PhysRevB.81.144410).
- [35] J. Reuther and R. Thomale, *Functional renormalization group for the anisotropic triangular antiferromagnet*, *Phys. Rev. B* **83**, 024402 (2011), doi:[10.1103/PhysRevB.83.024402](https://doi.org/10.1103/PhysRevB.83.024402).
- [36] J. Reuther, D. A. Abanin and R. Thomale, *Magnetic order and paramagnetic phases in the quantum $J_1 - J_2 - J_3$ honeycomb model*, *Phys. Rev. B* **84**, 014417 (2011), doi:[10.1103/PhysRevB.84.014417](https://doi.org/10.1103/PhysRevB.84.014417).
- [37] J. Reuther, R. Thomale and S. Trebst, *Finite-temperature phase diagram of the Heisenberg-Kitaev model*, *Phys. Rev. B* **84**, 100406 (2011), doi:[10.1103/PhysRevB.84.100406](https://doi.org/10.1103/PhysRevB.84.100406).
- [38] J. Thoenniss, M. K. Ritter, F. B. Kugler, J. von Delft and M. Punk, *Multiloop pseudofermion functional renormalization for quantum spin systems: Application to the spin- $\frac{1}{2}$ Kagomé Heisenberg model*, (arXiv preprint) doi:[10.48550/arXiv.2011.01268](https://doi.org/10.48550/arXiv.2011.01268).
- [39] D. Kiese, T. Müller, Y. Iqbal, R. Thomale and S. Trebst, *Multiloop functional renormalization group approach to quantum spin systems*, *Phys. Rev. Res.* **4**, 023185 (2022), doi:[10.1103/PhysRevResearch.4.023185](https://doi.org/10.1103/PhysRevResearch.4.023185).
- [40] M. K. Ritter, D. Kiese, T. Müller, F. B. Kugler, R. Thomale, S. Trebst and J. von Delft, *Benchmark calculations of multiloop pseudofermion fRG*, *Eur. Phys. J. B* **95**, 102 (2022), doi:[10.1140/epjb/s10051-022-00349-2](https://doi.org/10.1140/epjb/s10051-022-00349-2).
- [41] D. Kiese et al., *Pinch-points to half-moons and up in the stars: The Kagomé skymap*, *Phys. Rev. Res.* **5**, L012025 (2023), doi:[10.1103/PhysRevResearch.5.L012025](https://doi.org/10.1103/PhysRevResearch.5.L012025).
- [42] N. Niggemann, B. Sbierski and J. Reuther, *Frustrated quantum spins at finite temperature: Pseudo-Majorana functional renormalization group approach*, *Phys. Rev. B* **103**, 104431 (2021), doi:[10.1103/PhysRevB.103.104431](https://doi.org/10.1103/PhysRevB.103.104431).

- [43] N. Niggemann, J. Reuther and B. Sbierski, *Quantitative functional renormalization for three-dimensional quantum Heisenberg models*, SciPost Phys. **12**, 156 (2022), doi:[10.21468/SciPostPhys.12.5.156](https://doi.org/10.21468/SciPostPhys.12.5.156).
- [44] B. Sbierski, M. Bintz, S. Chatterjee, M. Schuler, N. Y. Yao and L. Pollet, *Magnetism in the two-dimensional dipolar XY model*, (arXiv preprint) doi:[10.48550/arXiv.2305.03673](https://doi.org/10.48550/arXiv.2305.03673).
- [45] N. Niggemann, Y. Iqbal and J. Reuther, *Quantum effects on unconventional pinch point singularities*, Phys. Rev. Lett. **130**, 196601 (2023), doi:[10.1103/PhysRevLett.130.196601](https://doi.org/10.1103/PhysRevLett.130.196601).
- [46] O. Parcollet, M. Ferrero, T. Ayrat, H. Hafermann, I. Krivenko, L. Messio and P. Seth, *TRIQS: A toolbox for research on interacting quantum systems*, Comput. Phys. Commun. **196**, 398 (2015), doi:[10.1016/j.cpc.2015.04.023](https://doi.org/10.1016/j.cpc.2015.04.023).
- [47] D. Rohe, *Hierarchical parallelisation of functional renormalisation group calculations – hp-fRG*, Comput. Phys. Commun. **207**, 160 (2016), doi:[10.1016/j.cpc.2016.05.024](https://doi.org/10.1016/j.cpc.2016.05.024).
- [48] G. Rohringer, *New routes towards a theoretical treatment of nonlocal electronic correlations*, PhD thesis, Technische Universität Wien, Wien, Germany (2013), doi:[10.34726/hss.2013.21498](https://doi.org/10.34726/hss.2013.21498).
- [49] *MatsubaraFunctions.jl*, GitHub (2023), <https://github.com/dominikkiese/MatsubaraFunctions.jl>.
- [50] S. G. Jakobs, M. Pletyukhov and H. Schoeller, *Nonequilibrium functional renormalization group with frequency-dependent vertex function: A study of the single-impurity Anderson model*, Phys. Rev. B **81**, 195109 (2010), doi:[10.1103/PhysRevB.81.195109](https://doi.org/10.1103/PhysRevB.81.195109).
- [51] D. H. Schimmel, B. Bruognolo and J. von Delft, *Spin fluctuations in the 0.7 anomaly in quantum point contacts*, Phys. Rev. Lett. **119**, 196401 (2017), doi:[10.1103/PhysRevLett.119.196401](https://doi.org/10.1103/PhysRevLett.119.196401).
- [52] L. Weidinger and J. von Delft, *Keldysh functional renormalization group treatment of finite-ranged interactions in quantum point contacts*, (arXiv preprint) doi:[10.48550/arXiv.1912.02700](https://doi.org/10.48550/arXiv.1912.02700).
- [53] A. Ge, N. Ritz, E. Walter, S. Aguirre, J. von Delft and F. B. Kugler, *Real-frequency quantum field theory applied to the single-impurity Anderson model*, (arXiv preprint) doi:[10.48550/arXiv.2307.10791](https://doi.org/10.48550/arXiv.2307.10791).
- [54] M. Jarrell and J. E. Gubernatis, *Bayesian inference and the analytic continuation of imaginary-time quantum Monte Carlo data*, Phys. Rep. **269**, 133 (1996), doi:[10.1016/0370-1573\(95\)00074-7](https://doi.org/10.1016/0370-1573(95)00074-7).
- [55] D. Bergeron and A.-M. S. Tremblay, *Algorithms for optimized maximum entropy and diagnostic tools for analytic continuation*, Phys. Rev. E **94**, 023303 (2016), doi:[10.1103/PhysRevE.94.023303](https://doi.org/10.1103/PhysRevE.94.023303).
- [56] O. Goulko, A. S. Mishchenko, L. Pollet, N. Prokof'ev and B. Svistunov, *Numerical analytic continuation: Answers to well-posed questions*, Phys. Rev. B **95**, 014102 (2017), doi:[10.1103/PhysRevB.95.014102](https://doi.org/10.1103/PhysRevB.95.014102).
- [57] K. S. D. Beach, *Identifying the maximum entropy method as a special limit of stochastic analytic continuation*, (arXiv preprint) doi:[10.48550/arXiv.cond-mat/0403055](https://doi.org/10.48550/arXiv.cond-mat/0403055).

- [58] A. W. Sandvik, *Constrained sampling method for analytic continuation*, Phys. Rev. E **94**, 063308 (2016), doi:[10.1103/PhysRevE.94.063308](https://doi.org/10.1103/PhysRevE.94.063308).
- [59] L. Huang, *Acflow: An open source toolkit for analytical continuation of quantum Monte Carlo data*, Comput. Phys. Commun. **292**, 108863 (2023), doi:[10.1016/j.cpc.2023.108863](https://doi.org/10.1016/j.cpc.2023.108863).
- [60] C. Karrasch, R. Hedden, R. Peters, T. Pruschke, K. Schönhammer and V. Meden, *A finite-frequency functional renormalization group approach to the single impurity Anderson model*, J. Phys.: Condens. Matter **20**, 345205 (2008), doi:[10.1088/0953-8984/20/34/345205](https://doi.org/10.1088/0953-8984/20/34/345205).
- [61] H. J. Vidberg and J. W. Serene, *Solving the Eliashberg equations by means of N-point Padé approximants*, J. Low Temp. Phys **29**, 179 (1977), doi:[10.1007/BF00655090](https://doi.org/10.1007/BF00655090).
- [62] *MBEsolver.jl*, GitHub (2023), <https://github.com/dominikkiese/MBEsolver.jl>.
- [63] *Polyester.jl*, GitHub (2023), <https://github.com/JuliaSIMD/Polyester.jl>.
- [64] D. R. Hartree, *The wave mechanics of an atom with a non-Coulomb central field. Part I. Theory and methods*, Math. Proc. Camb. Philos. Soc. **24**, 89 (1928), doi:[10.1017/S0305004100011919](https://doi.org/10.1017/S0305004100011919).
- [65] V. Fock, *Näherungsmethode zur Lösung des quantenmechanischen Mehrkörperproblems*, Z. Phys. **61**, 126 (1930), doi:[10.1007/BF01340294](https://doi.org/10.1007/BF01340294).
- [66] J. C. Slater, *A simplification of the Hartree-Fock method*, Phys. Rev. **81**, 385 (1951), doi:[10.1103/PhysRev.81.385](https://doi.org/10.1103/PhysRev.81.385).
- [67] E. J. Baerends, D. E. Ellis and P. Ros, *Self-consistent molecular Hartree-Fock-Slater calculations I. The computational procedure*, Chem. Phys. **2**, 41 (1973), doi:[10.1016/0301-0104\(73\)80059-X](https://doi.org/10.1016/0301-0104(73)80059-X).
- [68] F. Neese, F. Wennmohs, A. Hansen and U. Becker, *Efficient, approximate and parallel Hartree-Fock and hybrid DFT calculations. A 'chain-of-spheres' algorithm for the Hartree-Fock exchange*, Chem. Phys. **356**, 98 (2009), doi:[10.1016/j.chemphys.2008.10.036](https://doi.org/10.1016/j.chemphys.2008.10.036).
- [69] D. G. Anderson, *Iterative procedures for nonlinear integral equations*, J. ACM **12**, 547 (1965), doi:[10.1145/321296.321305](https://doi.org/10.1145/321296.321305).
- [70] H. F. Walker and P. Ni, *Anderson acceleration for fixed-point iterations*, SIAM J. Numer. Anal. **49**, 1715 (2011), doi:[10.1137/10078356X](https://doi.org/10.1137/10078356X).
- [71] *NLsolve.jl*, GitHub (2023), <https://github.com/JuliaNLSolvers/NLsolve.jl>.
- [72] L. Hedin, *New method for calculating the one-particle Green's function with application to the electron-gas problem*, Phys. Rev. **139**, A796 (1965), doi:[10.1103/PhysRev.139.A796](https://doi.org/10.1103/PhysRev.139.A796).
- [73] F. Aryasetiawan and O. Gunnarsson, *The GW method*, Rep. Prog. Phys. **61**, 237 (1998), doi:[10.1088/0034-4885/61/3/002](https://doi.org/10.1088/0034-4885/61/3/002).
- [74] G. Onida, L. Reining and A. Rubio, *Electronic excitations: Density-functional versus many-body Green's-function approaches*, Rev. Mod. Phys. **74**, 601 (2002), doi:[10.1103/RevModPhys.74.601](https://doi.org/10.1103/RevModPhys.74.601).
- [75] P. W. Anderson, *Localized magnetic states in metals*, Phys. Rev. **124**, 41 (1961), doi:[10.1103/physrev.124.41](https://doi.org/10.1103/physrev.124.41).

- [76] A. C. Hewson, *Renormalized perturbation calculations for the single-impurity Anderson model*, J. Phys.: Condens. Matter **13**, 10011 (2001), doi:[10.1088/0953-8984/13/44/314](https://doi.org/10.1088/0953-8984/13/44/314).
- [77] P. Chalupa, T. Schäfer, M. Reitner, D. Springer, S. Andergassen and A. Toschi, *Fingerprints of the local moment formation and its Kondo screening in the generalized susceptibilities of many-electron problems*, Phys. Rev. Lett. **126**, 056403 (2021), doi:[10.1103/PhysRevLett.126.056403](https://doi.org/10.1103/PhysRevLett.126.056403).
- [78] M. Gievers, E. Walter, A. Ge, J. von Delft and F. B. Kugler, *Multiloop flow equations for single-boson exchange fRG*, Eur. Phys. J. B **95**, 108 (2022), doi:[10.1140/epjb/s10051-022-00353-6](https://doi.org/10.1140/epjb/s10051-022-00353-6).
- [79] F. Krien, *Efficient evaluation of the polarization function in dynamical mean-field theory*, Phys. Rev. B **99**, 235106 (2019), doi:[10.1103/PhysRevB.99.235106](https://doi.org/10.1103/PhysRevB.99.235106).
- [80] F. Krien, A. Valli and M. Capone, *Single-boson exchange decomposition of the vertex function*, Phys. Rev. B **100**, 155149 (2019), doi:[10.1103/PhysRevB.100.155149](https://doi.org/10.1103/PhysRevB.100.155149).
- [81] F. Krien and A. Valli, *Parquetlike equations for the Hedin three-leg vertex*, Phys. Rev. B **100**, 245147 (2019), doi:[10.1103/PhysRevB.100.245147](https://doi.org/10.1103/PhysRevB.100.245147).
- [82] F. Krien, A. I. Lichtenstein and G. Rohringer, *Fluctuation diagnostic of the nodal/antinodal dichotomy in the Hubbard model at weak coupling: A parquet dual fermion approach*, Phys. Rev. B **102**, 235133 (2020), doi:[10.1103/PhysRevB.102.235133](https://doi.org/10.1103/PhysRevB.102.235133).
- [83] F. Krien, A. Valli, P. Chalupa, M. Capone, A. I. Lichtenstein and A. Toschi, *Boson-exchange parquet solver for dual fermions*, Phys. Rev. B **102**, 195131 (2020), doi:[10.1103/PhysRevB.102.195131](https://doi.org/10.1103/PhysRevB.102.195131).
- [84] F. Krien, A. Kauch and K. Held, *Tiling with triangles: Parquet and GW γ methods unified*, Phys. Rev. Res. **3**, 013149 (2021), doi:[10.1103/PhysRevResearch.3.013149](https://doi.org/10.1103/PhysRevResearch.3.013149).
- [85] C. De Dominicis and P. C. Martin, *Stationary entropy principle and renormalization in normal and superfluid systems. I. Algebraic formulation*, J. Math. Phys. **5**, 14 (1964), doi:[10.1063/1.1704062](https://doi.org/10.1063/1.1704062).
- [86] C. De Dominicis and P. C. Martin, *Stationary entropy principle and renormalization in normal and superfluid systems. II. Diagrammatic formulation*, J. Math. Phys. **5**, 31 (1964), doi:[10.1063/1.1704064](https://doi.org/10.1063/1.1704064).
- [87] N. E. Bickers, D. J. Scalapino and S. R. White, *Conserving approximations for strongly correlated electron systems: Bethe-Salpeter equation and dynamics for the two-dimensional Hubbard model*, Phys. Rev. Lett. **62**, 961 (1989), doi:[10.1103/PhysRevLett.62.961](https://doi.org/10.1103/PhysRevLett.62.961).
- [88] N. E. Bickers and S. R. White, *Conserving approximations for strongly fluctuating electron systems. II. Numerical results and parquet extension*, Phys. Rev. B **43**, 8044 (1991), doi:[10.1103/PhysRevB.43.8044](https://doi.org/10.1103/PhysRevB.43.8044).
- [89] N. E. Bickers, *Parquet equations for numerical self-consistent-field theory*, Int. J. Mod. Phys. B **05**, 253 (1991), doi:[10.1142/S021797929100016X](https://doi.org/10.1142/S021797929100016X).
- [90] N. E. Bickers, *Self-consistent many-body theory for condensed matter systems*, in *Theoretical methods for strongly correlated electrons*, Springer, New York, USA, ISBN 9780387217178 (2004), doi:[10.1007/0-387-21717-7_6](https://doi.org/10.1007/0-387-21717-7_6).

- [91] P. M. Bonetti, A. Toschi, C. Hille, S. Andergassen and D. Vilardi, *Single-boson exchange representation of the functional renormalization group for strongly interacting many-electron systems*, Phys. Rev. Res. **4**, 013034 (2022), doi:[10.1103/PhysRevResearch.4.013034](https://doi.org/10.1103/PhysRevResearch.4.013034).
- [92] N. Wentzell, G. Li, A. Tagliavini, C. Taranto, G. Rohringer, K. Held, A. Toschi and S. Andergassen, *High-frequency asymptotics of the vertex function: Diagrammatic parametrization and algorithmic implementation*, Phys. Rev. B **102**, 085106 (2020), doi:[10.1103/physrevb.102.085106](https://doi.org/10.1103/physrevb.102.085106).

5 Analytic Continuation – Relations between imaginary- and real-frequency functions

5.1 Overview

The Matsubara formalism is extremely convenient for calculations and derivations since the Keldysh counterpart of an ℓ -point Matsubara correlator has an additional index structure with 2^ℓ components. However, real-frequency correlators encode interesting observables such as the spectrum and dynamic susceptibilities.

Reference [BM61] has already shown that the analytic continuation of two-point correlators in the frequency representation is mathematically justified. The relevant relations are textbook knowledge and have been presented in Sec. 2.1.5. The equivalence between MF and KF relies on the analyticity of the regular MF correlator $\tilde{G}(z)$ in the upper and lower half of \mathbb{C} . The connection between MF and KF correlator becomes particularly apparent by comparison of the spectral representations in Eqs. (2.26) and Eq. (2.32c), revealing that the retarded and advanced correlators $G^{R/A}$ can be obtained from the regular Matsubara correlator $\tilde{G}(i\omega)$ by a simple substitution $G^{R/A}(\omega) = \tilde{G}(i\omega \rightarrow \omega \pm i0^+)$. Hence, the retarded and advanced correlators have their domain on the boundary of the regions of analyticity. The discontinuity at the boundary, $G^R - G^A$, (almost) fully encodes the spectral information in S^{std} (2.33b). The Keldysh component, G^K , in turn, is obtained from the fluctuation-dissipation theorem (2.33c).

Unfortunately, the situation is more complicated for higher-point functions: For four-point functions there are 16 Keldysh components and the generalized fluctuation-dissipation relations can only reduce the number of independent Keldysh components to 8 [WH02]. The number of analytic continuations grows to 32 [Eli62]. Out of these, four can be directly identified with fully-retarded Keldysh components. The other analytic continuations have no direct correspondence to a Keldysh component [Wel05]. Hence, a completely new strategy is needed. In the following, we provide one in [P4].

The starting point for our derivation in Ref. [P4] is the spectral representation derived in Refs. [KLvD21, HSS23]. There, it is shown that system-specific information is fully encoded in the PSFs \mathcal{S} . The kernels \mathcal{K} , on the other hand, are formalism-dependent but system-independent. Thus, our strategy is to express all PSFs in terms of suitable analytic continuations of the Matsubara correlator. The resulting formulas can then be inserted into the spectral representation for Keldysh correlators to express all Keldysh components with analytically continued Matsubara functions. While the presented calculations are rather long, the final formulas can be checked in a concise calculation by repeated use of the KMS condition (2.9b).

In [P4], it is assumed that the Matsubara correlators are known *analytically*. The analytic continuation of *numerical* Matsubara data is a related problem that is, however, outside the scope of this thesis. It additionally poses the difficulty that data may be incomplete or contain errors. Despite numerous improvements in the past years [FYG21, ZG24] this problem prevails due to the ill-conditioned Matsubara kernel.

Analytic Continuation of Multipoint Correlation Functions

by

A. Ge,¹ J. Halbinger,¹ S.B. Lee,^{2,3} J. von Delft,¹ and F. B. Kugler^{4,5}

¹ Arnold Sommerfeld Center for Theoretical Physics, Center for NanoScience, and
Munich Center for Quantum Science and Technology,
Ludwig-Maximilians-Universität München, 80333 Munich, Germany

² Department of Physics and Astronomy, Seoul National University, Seoul 08826, Republic of
Korea

³ Center for Theoretical Physics, Seoul National University, Seoul 08826, Republic of Korea

⁴ Center for Computational Quantum Physics, Flatiron Institute, 162 5th Avenue, New York,
New York 10010, USA

⁵ Department of Physics and Astronomy and Center for Materials Theory, Rutgers
University, Piscataway, New Jersey 08854, USA

reprinted on pages 151–196

Reproduced under terms of the CC-BY license.

***Ann. Phys.* 536, 2300504 (2024),**

DOI: 10.1002/andp.202300504.

© 2024, The Authors, Annalen der Physik published by Wiley-VCH GmbH.

Analytic Continuation of Multipoint Correlation Functions

Anxiang Ge,* Johannes Halbinger, Seung-Sup B. Lee, Jan von Delft, and Fabian B. Kugler

Conceptually, the Matsubara formalism (MF), using imaginary frequencies, and the Keldysh formalism (KF), formulated in real frequencies, give equivalent results for systems in thermal equilibrium. The MF has less complexity and is thus more convenient than the KF. However, computing dynamical observables in the MF requires the analytic continuation from imaginary to real frequencies. The analytic continuation is well-known for two-point correlation functions (having one frequency argument), but, for multipoint correlators, a straightforward recipe for deducing all Keldysh components from the MF correlator had not been formulated yet. Recently, a representation of MF and KF correlators in terms of formalism-independent partial spectral functions and formalism-specific kernels was introduced by Kugler, Lee, and von Delft [Phys. Rev. X 11, 041006 (2021)]. This representation is used to formally elucidate the connection between both formalisms. How a multipoint MF correlator can be analytically continued to recover all partial spectral functions and yield all Keldysh components of its KF counterpart is shown. The procedure is illustrated for various correlators of the Hubbard atom.

1. Introduction

Multipoint correlation functions, or correlators for short, are central objects of investigation in many-body physics. The fermionic one-particle or two-point (2p) correlator describes the propagation of a single particle, containing information on the spectrum of single-particle excitations. The two-particle or four-point (4p) correlator is associated with the effective interaction between two particles. Interesting observables, like optical and magnetic response functions, can be deduced from it. Additionally, the closely related 4p vertex, obtained by amputating all four external legs, is an essential ingredient in numerous many-body methods such as the functional renormalization group,^[1] the parquet formalism,^[2] and diagrammatic extensions of dynamical mean field theory.^[3]

The most common framework for studying systems in thermal equilibrium at temperature $T = 1/\beta$ is the imaginary-time Matsubara formalism (MF).^[4] It exploits the cyclicity of the trace and the fact that the statistical weight of a thermal state for a Hamiltonian H , $e^{-\beta H}$, corresponds to a time-evolution e^{-iHt} along the imaginary axis of the time argument. After a so-called Wick rotation, $t \rightarrow -i\tau$, the correlators are well-defined on the interval $\tau \in [-\beta, \beta]$ and there satisfy (anti)periodicity relations with period β . Correspondingly, they can be expressed through a Fourier series using a discrete set of imaginary frequencies, the so-called Matsubara frequencies, ensuring this (anti)periodicity. Due to this periodicity, the Fourier transform of a MF correlator is a function defined on a discrete set of imaginary frequencies, so-called Matsubara frequencies. To obtain a correlator of real times or real frequencies, one has to “unwind” the Wick rotation by performing a suitable analytic continuation. Numerically, however, the analytic continuation to real frequencies is a highly challenging problem.^[5,6]

The Keldysh formalism (KF) is another established framework.^[7] Unlike the MF, it is not restricted to thermal equilibrium. It directly works with real times and frequencies, obviating the need for an analytic continuation. However, this comes at the cost of an increased complexity: the KF is formulated on a doubled time contour, and an ℓ -point (ℓ p) function has 2^ℓ components.^[8,9] By contrast, every MF correlator is just a single function.

In thermal equilibrium, both MF and KF must in principle yield identical results for exact computations of any physical observable—the two formalisms only differ in the computational route to arrive at the result. In practice, though, it may be useful

A. Ge, J. Halbinger, J. von Delft
Arnold Sommerfeld Center for Theoretical Physics
Center for NanoScience, and Munich Center for Quantum Science and
Technology
Ludwig-Maximilians-Universität München
80333 Munich, Germany
E-mail: anxiang.ge@physik.uni-muenchen.de

S.-S. B. Lee
Department of Physics and Astronomy
Seoul National University
Seoul 08826, Republic of Korea
S.-S. B. Lee
Center for Theoretical Physics
Seoul National University
Seoul 08826, Republic of Korea

F. B. Kugler
Center for Computational Quantum Physics
Flatiron Institute
162 5th Avenue, New York, NY 10010, USA

F. B. Kugler
Department of Physics and Astronomy and Center for Materials Theory
Rutgers University
Piscataway, NJ 08854, USA

 The ORCID identification number(s) for the author(s) of this article can be found under <https://doi.org/10.1002/andp.202300504>

© 2024 The Authors. Annalen der Physik published by Wiley-VCH GmbH. This is an open access article under the terms of the [Creative Commons Attribution](#) License, which permits use, distribution and reproduction in any medium, provided the original work is properly cited.

DOI: 10.1002/andp.202300504

to transition from one formalism to the other, in order to exploit advantages from one or the other. The connection between the MF and KF by means of analytic continuation is well known for 2p functions, which effectively depend on a single time or frequency argument, see e.g., refs. [10–12]. For higher-point functions, progress has been made by various authors: Eliashberg discussed the analytic continuation of a specific 4p correlator from the MF to real frequencies,^[13] Evans^[14] and Kobes^[15,16] studied the correspondence between both formalisms for 3p correlators in refs. [14–16]. Evans then considered $\ell \geq 4$ multipoint correlators and showed that fully retarded and fully advanced Keldysh components can be obtained from analytic continuations of MF correlators.^[17] Weldon conducted a thorough analysis of real-frequency ℓ p functions and proved that these KF components are in fact the only ones that can be identified with an analytically continued MF function.^[18,19] Taylor extended Evans' results to arbitrary Keldysh components of the fermionic 4p correlator, assuming the absence of so-called anomalous terms in the MF correlator.^[20] (Anomalous terms can arise if the Lehmann representation of a correlator involves vanishing eigenenergy differences and zero bosonic Matsubara frequencies.) Guerin derived analogous results from diagrammatic arguments.^[21,22]

In this paper, we solve the problem of analytic continuation of multipoint functions from the MF to the KF in full generality: We develop a strategy for analytically continuing an arbitrary MF ℓ p correlator G (including anomalous terms) to all 2^ℓ components of the corresponding KF correlator G^k as functionals of G , i.e., $G^k = G^k[G]$. We exemplify the procedure for the most relevant cases $\ell \in \{2, 3, 4\}$.

Our strategy builds upon the spectral representation of general ℓ p correlators introduced in ref. [23]. There, the computation of MF and KF correlators is split into two parts: the calculation of formalism-independent but system-dependent partial spectral functions (PSFs), and their subsequent convolution with formalism-dependent but system-independent kernels. The main message of the present paper is that individual PSFs can be retrieved from the MF correlator, demonstrating the direct link between both formalisms.

In a nutshell, both MF and KF correlators have spectral representations involving sums over permutations of their constituent operators of the form

$$G(i\omega) = \sum_p G_p(i\omega_p), \quad G_p(i\omega_p) = (K * S_p)(i\omega_p) \quad (1a)$$

$$G^k(\omega) = \sum_p G_p^{k_p}(\omega_p), \quad G_p^{k_p}(\omega_p) = (K^{k_p} * S_p)(\omega_p) \quad (1b)$$

Here, the summands G_p and $G_p^{k_p}$ are real-frequency convolutions (denoted by $*$) of MF or KF kernels, K or K^{k_p} , with PSFs S_p . Importantly, the MF and KF correlators depend on the *same* PSFs, $G = G[S_p]$ and $G^k = G^k[S_p]$. The key insight of this work is that the so-called regular part of the *partial* MF correlator G_p , denoted \tilde{G}_p , can be expressed as an imaginary-frequency convolution (denoted by \star) of a kernel and the *full* MF correlator:

$$\tilde{G}_p(i\omega_p) = (\tilde{K} * S_p)(i\omega_p) = (K \star G)(i\omega_p) + \mathcal{O}(\frac{1}{\beta}) \quad (1c)$$

(The $\mathcal{O}(\frac{1}{\beta})$ terms can be identified analytically and discarded.) From this, we can extract S_p as a functional of G , thus inverting the relation $G[S_p] \rightarrow S_p[G]$. That enables us to express KF through MF correlators, $G^k = G^k[G]$.

Our analysis not only provides relations between functions in the MF and the KF, but also between different Keldysh components of the KF correlator. As an application of our general results, we derive a complete set of generalized fluctuation-dissipation relations (gFDRs) for 3p and 4p functions. These reproduce the results of Wang and Heinz^[24] for real fields and the generalization to fermionic ones.^[25] Moreover, we give a comprehensive discussion of the role of anomalous terms during analytic continuation and in gFDRs. Prior discussions of these topics have often neglected anomalous terms; indeed, their presence is acknowledged only in few works, such as refs. [26–28]. As an example of their physical importance, we mention that ref. [28] analyzed anomalous terms for the Mott–Hubbard metal–insulator transition in the Hubbard model using the dynamical mean-field theory and detected a degeneracy in the insulating regime by means of a finite anomalous term.

Conceptually, the Matsubara formalism (MF), using imaginary frequencies, and the Keldysh formalism (KF), formulated in real frequencies, give equivalent results for systems in thermal equilibrium. The MF has less complexity and is thus more convenient than the KF. However, computing dynamical observables in the MF requires the analytic continuation from imaginary to real frequencies. The analytic continuation is well-known for two-point correlation functions (having one frequency argument), but, for multipoint correlators, a straightforward recipe for deducing all Keldysh components from the MF correlator had not been formulated yet. Recently, a representation of MF and KF correlators in terms of formalism-independent partial spectral functions and formalism-specific kernels was introduced by Kugler, Lee, and von Delft. Regarding the number of independent components in the KF, one observes a general trend, obeyed by the known results for $\ell \in \{2, 3, 4\}$: Due to the doubled time contour, there are 2^ℓ Keldysh components. In the Keldysh basis, $2^\ell - 1$ of them are nonzero, and ℓ are fully retarded components. Now, there are $2^{\ell-1}$ gFDRs (2, 4, 8 for $\ell = 2, 3, 4$). Thus, the number of independent Keldysh components is $2^{\ell-1} - 1$ (1, 3, 7 for $\ell = 2, 3, 4$). It follows that, for $\ell \geq 4$, the fully retarded components do not suffice to encode the entire information of the Keldysh correlator.

The rest of the paper is organized as follows: In Section 2, we summarize the most important points of the spectral representation of ℓ p MF and KF correlators introduced in ref. [23] (Sections 2.1–2.3) and then introduce our general recipe for the analytic continuation of arbitrary ℓ p correlators (Sections 2.4 and 2.5). This recipe is applied to the 2p case in Section 3 and, after the investigation of analytic properties of regular ℓ p MF correlators in Section 4, also to the 3p and 4p cases in Sections 5 and 6. The results also lead to gFDRs between different Keldysh components of the KF correlator. In Section 7, we perform explicit analytic continuations from MF to KF correlators for the Hubbard atom. The Hubbard atom is a good example for a system with anomalous contributions and, here, serves as a simple, exactly solvable model with just the right degree of complexity for illustrating our approach. Section 8 presents another application

Table 1. Overview of notation for correlators and their contributions. In the top, we list symbols for the MF correlator and its contributions, then, notation for analytic continuations and discontinuities, and, lastly, notation for Keldysh correlators.

Symbol	Description
G	full MF correlator, Equations (9)
G_p	partial MF correlator, Equation (11b)
\tilde{G}, \hat{G}	regular and anomalous part of the MF correlator, Equations (14a) and (A5)
\tilde{G}_p	regular part of the partial MF correlator, Equation (14c)
$\hat{G}_i, \hat{G}_i^\Delta, \hat{G}_i^\Delta$	further decomposition of the anomalous MF correlator, Equations (A5b) and (73)
$\tilde{G}_{\bar{z}}, \hat{G}_{i\bar{z}}$	shorthand for analytic continuations of the regular/anomalous MF correlator, see Section 4.1
$\tilde{G}_{\bar{z}}^\omega, \hat{G}_{i\bar{z}}^\omega$	discontinuities of the regular/anomalous MF correlator, Equation (67)
$G^k, G^{[n_1 \dots n_d]}$	Keldysh correlator, Equations (19)
$G'^k, G'^{[n_1 \dots n_d]}$	primed Keldysh correlator, Equations (25)

of our continuation formulas, namely for the computation of vertex corrections to susceptibilities. We conclude in Section 9.

In Appendix A and B, we give details on the MF kernels and PSFs used in calculations throughout the paper. Appendix C is devoted to detailed calculations concerning the analytic continuation of 3p correlators. In Appendix D, we extend insights from 2p and 3p results to deduce the relation between 4p PSFs and analytically continued MF correlators. The spectral representations of various useful combinations of analytically continued MF correlators and anomalous parts are presented in Appendix E. Appendix F expresses the spectral representation of KF correlators in a form especially suited for deriving their connection to MF functions. In Appendix G, we check the consistency of our results for PSFs by using equilibrium properties. Finally, Appendix H gives details about simplifications used for the analytic continuation of Hubbard atom correlators and includes full lists of the especially important fermionic 4p KF correlators.

2. Spectral Representations of Matsubara and Keldysh Correlators

To make our presentation self-contained, we summarize the key elements of the conventions and results of ref. [23] for common notions (Section 2.1), the MF (Section 2.2), and the KF (Section 2.3). Table 1 provides an overview of our symbols for correlators and their contributions. Our general strategy for the analytic continuation from MF to KF correlators is described in Sections 2.4 and 2.5.

2.1. Formalism-Independent Expectations Values

Consider a tuple of ℓ operators $\mathbf{O} = (O^1, \dots, O^\ell)$ at real times $\mathbf{t} = (t_1, \dots, t_\ell)$, obeying the Heisenberg time evolution $O^i(t_i) = e^{iHt_i} O^i e^{-iHt_i}$ for a given Hamiltonian H . \mathbf{O} may include an even number of fermionic operators and any number of bosonic operators. Time-ordered products of such tuples, defined below,

involve permuted tuples $\mathbf{O}_p = (O^{\bar{1}}, \dots, O^{\bar{\ell}})$ and $\mathbf{t}_p = (t_{\bar{1}}, \dots, t_{\bar{\ell}})$, where $p = (\bar{1} \dots \bar{\ell})$ denotes the permutation of indices that replaces i by $p(i) = \bar{i}$. If $\ell = 3$ and $p = (\bar{1}\bar{2}\bar{3})$ is chosen as (312), e.g., then $\mathbf{t}_p = (t_{\bar{1}}, t_{\bar{2}}, t_{\bar{3}}) = (t_3, t_1, t_2)$. Thermal expectation values of permuted tuples are denoted by

$$S_p[\mathbf{O}_p](\mathbf{t}_p) = \zeta_p \left\langle \prod_{i=1}^{\ell} O^{\bar{i}}(t_{\bar{i}}) \right\rangle \quad (2)$$

For later convenience, the definition includes a sign factor ζ_p which equals -1 if the permutation from \mathbf{O} to \mathbf{O}_p involves an odd number of transpositions of fermionic operators; otherwise $\zeta_p = 1$. We will often suppress the operator arguments $[\mathbf{O}_p]$ for brevity, since the subscript on S_p specifies their order. The real-frequency Fourier transform of $S_p(\mathbf{t}_p)$ defines the so-called *partial spectral function* (PSF)

$$S_p(\boldsymbol{\varepsilon}_p) = \int_{-\infty}^{\infty} \frac{d^\ell \mathbf{t}_p}{(2\pi)^\ell} e^{i\boldsymbol{\varepsilon}_p \cdot \mathbf{t}_p} S_p(\mathbf{t}_p) \quad (3a)$$

Here, $\boldsymbol{\varepsilon}_p = (\varepsilon_{\bar{1}}, \dots, \varepsilon_{\bar{\ell}})$ is a permuted version of $\boldsymbol{\varepsilon} = (\varepsilon_1, \dots, \varepsilon_\ell)$, a tuple of continuous, real-frequency variables. We strictly associate each (integration) variable, such as t_i, ε_i , with the operator O^i carrying the same index. Time-translational invariance of $S_p(\mathbf{t}_p)$ implies energy conservation for $S_p(\boldsymbol{\varepsilon}_p)$, which is expressed as

$$S_p(\boldsymbol{\varepsilon}_p) = \delta(\varepsilon_{\bar{1} \dots \bar{\ell}}) S_p(\boldsymbol{\varepsilon}_p) \quad (3b)$$

Here, $\varepsilon_{\bar{1} \dots \bar{i}} = \varepsilon_{\bar{1}} + \dots + \varepsilon_{\bar{i}}$ is a shorthand for a frequency sum. We call it bosonic/fermionic if the frequencies $(\varepsilon_{\bar{1}}, \dots, \varepsilon_{\bar{i}})$ are associated with an even/odd number of fermionic operators, i.e., if the sign $\zeta^{\bar{1} \dots \bar{i}} = \zeta^{\bar{1}} \dots \zeta^{\bar{i}}$ equals ± 1 (with $\zeta^j = \pm 1$ for bosonic/fermionic operators O^j). The function S_p (calligraphic type) on the left of Equation (3b) is non-zero only if its arguments satisfy “energy conservation”, $\varepsilon_{\bar{1} \dots \bar{\ell}} = 0$; for S_p (italic type) on the right, this condition on $\boldsymbol{\varepsilon}_p$ is understood to hold by definition, e.g., by setting $\varepsilon_{\bar{\ell}} = -\varepsilon_{\bar{1} \dots \bar{\ell}-1}$. This convention for frequency arguments of functions typeset in calligraphics or italics also holds for the correlators, \mathcal{G} vs. G , and kernels, \mathcal{K} vs. K , defined below.

PSFs whose arguments are cyclically related are proportional to each other. For two cyclically related permutations, say $p = (\bar{1} \dots \bar{\lambda} - 1 \bar{\lambda} \dots \bar{\ell})$ and $p_\lambda = (\bar{\lambda} \dots \bar{\ell} \bar{1} \dots \bar{\lambda} - 1)$, the cyclicity of the trace of operator products ensures the equilibrium condition (called cyclicity relation in ref. [23])

$$S_p(\boldsymbol{\varepsilon}_p) = \zeta_p \zeta_{p_\lambda} e^{\beta \varepsilon_{\bar{1} \dots \bar{\lambda}-1}} S_{p_\lambda}(\boldsymbol{\varepsilon}_{p_\lambda}), \quad \zeta_p \zeta_{p_\lambda} = \zeta^{\bar{1} \dots \bar{\lambda}-1} \quad (4)$$

Explicit Lehmann-type representations for PSFs in terms of a complete set of eigenenergies and eigenstates of H are given in refs. [23, 29] and exploited for numerical computations; however, they are not needed in this work. Here, it suffices to assume that $S_p(\boldsymbol{\varepsilon}_p)$ may contain sums over Dirac delta functions and a part that is (piece-wise) continuous in its arguments. For future reference, we split it into *regular* and *anomalous* parts,

$$S_p(\boldsymbol{\varepsilon}_p) = \tilde{S}_p(\boldsymbol{\varepsilon}_p) + \hat{S}_p(\boldsymbol{\varepsilon}_p) \quad (5)$$

where the anomalous part, \hat{S}_p , comprises all terms containing bosonic Dirac $\delta(\varepsilon_{\bar{1} \dots \bar{i}})$ factors (i.e. ones having bosonic arguments)

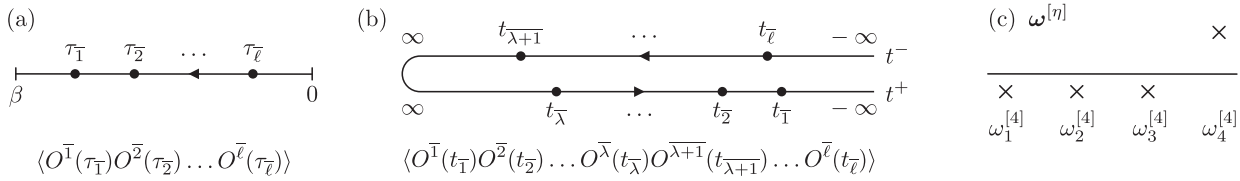


Figure 1. a) MF imaginary-time ordering: operators are arranged such that they are time-ordered (larger times to the left). b) KF real-time Keldysh ordering: operators are arranged such that all (forward-branch) times t^- appear to the right of all (backward-branch) times t^+ , with t^- times time-ordered (larger ones to the left) and t^+ times anti-time-ordered (smaller ones to the left). c) Depiction of imaginary shifts of frequencies $\omega_i^{[\eta]} = \omega_i + i\gamma_i^{[\eta]}$ with $i \in \{1, 2, 3, 4\}$ and $\eta = 4$ according to Equation (21).

setting $\varepsilon_{1\dots i} = 0$, while \tilde{S}_p contains everything else (including fermionic Dirac deltas). We will see later that \hat{S}_p gives rise to anomalous contributions to MF correlators, whereas \tilde{S}_p does not.

In the ensuing analysis, we make *no* assumptions on the behavior of the PSFs (apart from cyclicity). Thus, our analysis is equally applicable to finite systems or infinite systems in the thermodynamic limit, and whether or not an ordered phase is present. Any such information is fully encoded in the PSFs.

2.2. Matsubara Formalism

A ℓ p MF correlator \mathcal{G} is defined as a thermal expectation value of time-ordered operator products of the form

$$\mathcal{G}(\tau) = (-1)^{\ell-1} \left\langle \mathcal{T} \prod_{i=1}^{\ell} O^i(-i\tau_i) \right\rangle \quad (6)$$

where \mathcal{T} denotes time-ordering along the imaginary time axis (see Figure 1a). This time-ordering ensures that $\mathcal{G}(\tau)$ is periodic under $\tau_i \rightarrow \tau_i + \beta$ if O^i is bosonic, and anti-periodic if O^i is fermionic. Therefore, it suffices to confine all times to the interval $\tau_i \in [0, \beta)$, and the Fourier transform of a MF correlator is defined as

$$\mathcal{G}(i\omega) = \int_0^{\beta} d^{\ell} \tau e^{i\omega \cdot \tau} \mathcal{G}(\tau) = \beta \delta_{i\omega_{1\dots \ell}} G(i\omega) \quad (7)$$

where $\omega = (\omega_1, \dots, \omega_{\ell})$ is a tuple of discrete Matsubara frequencies (as indicated by the i in the argument of $\mathcal{G}(i\omega)$), with ω_i bosonic/fermionic if O^i is bosonic/fermionic. On the right, δ is the Kronecker delta for Matsubara frequencies, $\delta_{i\omega=0} = 1$ and $\delta_{i\omega \neq 0} = 0$. In Equation (7), it enforces “energy conservation”, $i\omega_{1\dots \ell} = 0$. This condition originates from time translation invariance of $\mathcal{G}(\tau)$; it is understood to hold for the argument of $G(i\omega)$ by definition.

As shown in ref. [23], it is possible to cleanly separate the analytical properties of correlators from the dynamical properties of the physical system of interest by expressing time-ordered products as sums over $\ell!$ parts, reflecting the $\ell!$ possible ways of ordering the time arguments:

$$\mathcal{G}(\tau) = \sum_p \mathcal{G}_p(\tau_p) \quad (8a)$$

$$\mathcal{G}_p(\tau_p) = \mathcal{K}(\tau_p) S_p(-i\tau_p) \quad (8b)$$

$$\mathcal{K}(\tau_p) = \prod_{i=1}^{\ell-1} [-\theta(\tau_i - \tau_{i+1})] \quad (8c)$$

Each *partial correlator* $\mathcal{G}_p(\tau_p)$ is a product of two factors: $S_p(-i\tau_p)$, a thermal expectation value of imaginary-time operators obtained by Wick rotation of Equation (2); and a kernel $\mathcal{K}(\tau_p)$, a product of Heaviside step functions enforcing time ordering: for given τ , only that partial correlator $\mathcal{G}_p(\tau_p)$ in Equation (8a) is nonzero for which the permuted tuple τ_p is time-ordered. \mathcal{K} is independent of the system and operators under consideration; all system-specific dynamical information is encoded in the PSFs S_p . Note that the (anti)periodic properties of $\mathcal{G}(\tau)$ under $\tau_i \rightarrow \tau_i + \beta$ do not hold for the individual partial correlators $\mathcal{G}_p(\tau_p)$; they emerge only once these are summed over all permutations, Equation (8a).

The product form of Equation (8b) for $\mathcal{G}_p(\tau_p)$ in the time domain implies that, in the Fourier domain, $\mathcal{G}(i\omega)$ can be expressed as a sum over convolutions:

$$\mathcal{G}(i\omega) = \sum_p \mathcal{G}_p(i\omega_p) \quad (9a)$$

$$\mathcal{G}_p(i\omega_p) = \int_0^{\beta} d^{\ell} \tau_p e^{i\omega_p \cdot \tau_p} \mathcal{G}_p(\tau_p) \quad (9b)$$

$$= [\mathcal{K} * S_p](i\omega_p) \quad (9c)$$

Here, the convolution $*$ is defined as

$$[\mathcal{K} * S_p](i\omega_p) = \int_{-\infty}^{\infty} d^{\ell} \varepsilon_p \delta(\varepsilon_{1\dots \ell}) \mathcal{K}(i\omega_p - \varepsilon_p) S_p(\varepsilon_p) \quad (9d)$$

where ε_p satisfies $\varepsilon_{1\dots \ell} = 0$ (due to Equation (3b)), and the transformed kernel is defined as follows, with $\Omega_p = i\omega_p - \varepsilon_p$:

$$\mathcal{K}(\Omega_p) = \int_0^{\beta} d^{\ell} \tau_p e^{i\Omega_p \cdot \tau_p} \mathcal{K}(\tau_p) \quad (10a)$$

$$= \beta \delta_{\Omega_{1\dots \ell}} K(\Omega_p) + \mathcal{R}(\Omega_p) \quad (10b)$$

In the second line, \mathcal{K} has been split into two contributions: $\beta \delta_{\Omega_{1\dots \ell}}$ times a *primary part* K , with $\Omega_{1\dots \ell} = 0$ understood for its argument, and a *residual part*, \mathcal{R} not containing $\beta \delta_{\Omega_{1\dots \ell}}$. Using $\delta_{\Omega_{1\dots \ell}} = \delta_{i\omega_{1\dots \ell}}$ (since $\varepsilon_{1\dots \ell} = 0$), each partial correlator $\mathcal{G}_p(i\omega_p)$ can correspondingly be split into primary and residual parts,

$$\mathcal{G}_p(i\omega_p) = \beta \delta_{\omega_{1\dots \ell}} G_p(i\omega_p) + \mathcal{G}_p^{\mathcal{R}}(i\omega_p) \quad (11a)$$

$$G_p(i\omega_p) = [K * S_p](i\omega_p) \quad (11b)$$

with $i\omega_{1\dots \ell} = 0$ understood for the argument of $G(i\omega_p)$, and $\mathcal{G}_p^{\mathcal{R}} = [\mathcal{R} * S_p]$. Since $\mathcal{K}(\tau_p)$ and $\mathcal{G}_p(\tau_p)$ lack the (anti)periodicity proper-

ties of $\mathcal{G}(\tau)$, the residual parts $\mathcal{R}(\Omega_p)$ and $\mathcal{G}_p^R(\mathbf{i}\omega_p)$ are nonzero *per se*. However, inserting Equation (11a) into Equation (9a) and noting from Equation (7) that $\mathcal{G}(\mathbf{i}\omega)$ is proportional to $\beta\delta_{\omega_{1\dots\ell}}$, one concludes that

$$G(\mathbf{i}\omega) = \sum_p G_p(\mathbf{i}\omega_p) \quad (12)$$

and $\sum_p \mathcal{G}_p^R(\mathbf{i}\omega_p) = 0$. Thus, the *full* (summed over p) MF correlator G involves only primary parts G_p ; the residual parts \mathcal{G}_p^R cancel out in the sum over all permutations. In the discussions below, we will therefore focus only on the primary parts K and G_p (as done in ref. [23]), ignoring the residual parts \mathcal{R} and \mathcal{G}_p^R for now. They will make a brief reappearance in Section 2.4, where we establish the connection between MF and KF correlators.

Explicit expressions for the primary kernel K were derived in refs. [23, 30] and are collected in Appendix A. Here, we just remark that K can be split into a *regular* kernel \tilde{K} and an *anomalous* kernel \hat{K} :

$$K(\Omega_p) = \begin{cases} \tilde{K}(\Omega_p) & \text{if } \prod_{i=1}^{\ell-1} \Omega_{\bar{1}\dots\bar{i}} \neq 0 \\ \hat{K}(\Omega_p) & \text{else} \end{cases} \quad (13a)$$

$$\tilde{K}(\Omega_p) = \prod_{i=1}^{\ell-1} \frac{1}{\Omega_{\bar{1}\dots\bar{i}}} \quad (13b)$$

The regular kernel \tilde{K} will play a crucial role for the analytic continuation of MF to KF correlators, since the latter can be expressed through kernels having the same structure as \tilde{K} (see Equation (19(d)) below). The anomalous kernel \hat{K} is nonzero only if we have $\Omega_{\bar{1}\dots\bar{i}} = 0$ for one or more values of $i < \ell$, requiring both $\omega_{\bar{1}\dots\bar{i}} = 0$ and $\varepsilon_{\bar{1}\dots\bar{i}} = 0$. The first condition requires $\omega_{\bar{1}\dots\bar{i}}$ to be bosonic (with $\zeta_{\bar{1}\dots\bar{i}} = +1$). The second condition requires the PSF $S_p(\varepsilon_p)$ to have an anomalous contribution $\hat{S}_p(\varepsilon_p)$ containing terms proportional to a bosonic Dirac $\delta(\varepsilon_{\bar{1}\dots\bar{i}})$; then (and only then), the ε_p integrals in the convolution $K * S_p$ receive a finite contribution from the point $\varepsilon_{\bar{1}\dots\bar{i}} = 0$. (See Appendix B.1 for a further discussion of this point.)

The regular/anomalous distinction made for the kernel implies, via Equations (11b) and (12), a corresponding decomposition of the full MF correlator G into regular (\tilde{G}) and anomalous (\hat{G}) parts:

$$G(\mathbf{i}\omega) = \tilde{G}(\mathbf{i}\omega) + \hat{G}(\mathbf{i}\omega) \quad (14a)$$

$$\tilde{G}(\mathbf{i}\omega) = \sum_p \tilde{G}_p(\mathbf{i}\omega_p) \quad (14b)$$

$$\tilde{G}_p(\mathbf{i}\omega_p) = [\tilde{K} * S_p](\mathbf{i}\omega_p) \quad (14c)$$

$$= \int_{-\infty}^{\infty} d^\ell \varepsilon_p \delta(\varepsilon_{\bar{1}\dots\bar{\ell}}) \prod_{i=1}^{\ell-1} \frac{S_p(\varepsilon_p)}{i\omega_{\bar{1}\dots\bar{i}} - \varepsilon_{\bar{1}\dots\bar{i}}} \quad (14d)$$

The *regular partial correlators* \tilde{G}_p , constructed via the regular kernel \tilde{K} , will be the central objects for the analytic continuation from MF to KF correlators, as discussed in Section 2.4 below. Their sum over all permutations defines the *regular full correlator* \tilde{G} . The *anomalous full correlator* \hat{G} collects all other contributions

to G ; these contain one (or multiple) factors $\beta\delta_{\omega_{\bar{1}\dots\bar{i}}}$ with $i < \ell$, i.e. they involve vanishing partial frequency sums (see Appendix A.2 for details). The contribution of \hat{G} to MF-to-KF analytical continuation has been rather poorly understood to date. In this work, we fully clarify how it enters: not directly, but indirectly, in that the central objects $\tilde{G}_p(\mathbf{i}\omega_p)$ can be expressed explicitly through the full $G = \tilde{G} + \hat{G}$ via imaginary-frequency convolutions of the form $[K \star G](\mathbf{i}\omega_p)$ (see Equation (31) below). There, \hat{G} must not be neglected.

2.3. Keldysh Formalism

A KF ℓ -p correlator in the *contour basis* is defined as

$$\mathcal{G}^c(\mathbf{t}) = (-i)^{\ell-1} \left\langle \mathcal{T}_c \prod_{i=1}^{\ell} O^i(t_i^{c_i}) \right\rangle \quad (15a)$$

$$= \sum_p \mathcal{K}^{c_p}(\mathbf{t}_p) S(\mathbf{t}_p) \quad (15b)$$

Here, \mathcal{T}_c denotes contour ordering on the Keldysh contour (see Figure 1b), and $t_i^{c_i}$ are real times. They carry a tuple of contour indices $\mathbf{c} = (c_1, \dots, c_\ell)$ with $c_i = -$ or $+$ if operator O^i resides on the forward (upper) or backward (lower) branch of the Keldysh contour, respectively. Equation (15b) is a permutation decomposition of the KF correlator $\mathcal{G}^c(\mathbf{t})$, analogous to Equation (8b) for $\mathcal{G}(\tau)$ in the MF. Importantly, it employs the *same* PSFs $S(\mathbf{t}_p)$ as there (which is why the KF and MF formalisms have the same physical information content). The Keldysh kernel $\mathcal{K}^{c_p}(\mathbf{t}_p)$ by definition (see ref. [23] for details) singles out that p for which the operators in $S_p(\mathbf{t})$ are contour ordered.

The Fourier transform of the KF correlator is

$$\mathcal{G}^c(\omega) = \int d^\ell t e^{i\omega t} \mathcal{G}^c(\mathbf{t}) = 2\pi \delta(\omega_{1\dots\ell}) \mathcal{G}^c(\omega) \quad (16)$$

Here, the Dirac $\delta(\omega_{1\dots\ell})$, following from time translation invariance, enforces $\omega_{1\dots\ell} = 0$; this condition is understood for the argument of $\mathcal{G}^c(\omega)$ by definition.

We now switch to the Keldysh basis. There, correlators $\mathcal{G}^k(\omega)$ carry a tuple of Keldysh indices, $\mathbf{k} = k_1 \dots k_\ell$, with $k_i \in \{1, 2\}$. They are obtained by applying a linear transformation D to each contour index,

$$\mathcal{G}^k(\omega) = \frac{1}{2} \sum_{c_1, \dots, c_\ell} \prod_{i=1}^{\ell} [D^{k_i c_i}] \mathcal{G}^c(\omega), \quad D^{k_i c_i} = (-1)^{k_i \delta_{c_i, +}} \quad (17)$$

(This convention differs by a prefactor from ref. [23], with $\mathcal{G}_{\text{here}}^k = 2^{\ell/2-1} \mathcal{G}_{\text{there}}^k$, to avoid a proliferation of factors of $2^{\ell/2-1}$ in later sections.) One thus obtains

$$G^k(\omega) = \sum_p G_p^{k_p}(\omega_p) \quad (18a)$$

$$G_p^{k_p}(\omega_p) = (K^{k_p} * S_p)(\omega_p) \quad (18b)$$

$$= \int d^\ell \varepsilon_p \delta(\varepsilon_{\bar{1}\dots\bar{\ell}}) K^{k_p}(\omega_p - \varepsilon_p) S_p(\varepsilon_p) \quad (18c)$$

Remarkably, the same convolution structure emerges as for the MF correlator $G(i\omega)$ (Equation (11b)), for the same reason (Fourier transforms of products yield convolutions). But now the frequency arguments are real, and the kernel $K^{k_p}(\omega_p)$ carries Keldysh indices, with $k_p = k_{\bar{1}} \dots k_{\bar{\ell}}$ a permuted version of the external Keldysh index k on G^k .

An explicit expression for this kernel, derived in ref. [23], is given in Equations (19) below. There, an alternative notation for Keldysh indices is employed. Each Keldysh index k , being a list with entries 1 or 2, is represented as a list $k = [\eta_1 \dots \eta_\alpha]$, where α is the total number of 2's in k and $\eta_i \in \{1, \dots, \ell\}$ denotes the position of the i th 2 in k in increasing order; e.g., $k = 1212 = [24]$. Similarly, permuted Keldysh indices are represented as $k_p = [\hat{\eta}_1 \dots \hat{\eta}_\alpha]$, where $\hat{\eta}_i$ denotes the position of the i th 2 in k_p . Its values can be deduced from the old η_j 's as follows: a 2 in slot η_j of k is moved by the permutation p to the new slot $\mu_j = p^{-1}(\eta_j)$; denoting the list of new 2-slots by $[\mu_1 \dots \mu_\alpha]$ and arranging it in increasing order yields the desired $[\hat{\eta}_1 \dots \hat{\eta}_\alpha]$. Note also that since $\hat{\eta}_j \in \{p^{-1}(\eta_1), \dots, p^{-1}(\eta_\alpha)\}$, we have $\bar{\hat{\eta}}_1 \in \{\eta_1, \dots, \eta_\alpha\}$; hence, $\bar{\hat{\eta}}_j$ is an element of the list specifying the external Keldysh index $k = [\eta_1 \dots \eta_\alpha]$. This will be crucial below. We illustrate these conventions for the permutation $p = (4123)$ and $k = 1212 = [24]$. Then, $k_p = 2121$, $[\mu_1 \mu_2] = [31]$ and $k_p = [\hat{\eta}_1 \hat{\eta}_2] = [13]$; moreover, $\bar{\hat{\eta}}_1 = \bar{1} = 4$ and $\bar{\hat{\eta}}_2 = \bar{3} = 2$ are both elements of $k = [24]$.

Expressed in this notation, Equations (18) read

$$G^{[\eta_1 \dots \eta_\alpha]}(\omega) = \sum_p G_p^{[\hat{\eta}_1 \dots \hat{\eta}_\alpha]}(\omega_p) \quad (19a)$$

$$G_p^{[\hat{\eta}_1 \dots \hat{\eta}_\alpha]}(\omega_p) = [K^{[\hat{\eta}_1 \dots \hat{\eta}_\alpha]} * S_p](\omega_p) \quad (19b)$$

with the permuted Keldysh kernel $K^{[\hat{\eta}_1 \dots \hat{\eta}_\alpha]}$ given by [23]

$$K^{[\hat{\eta}_1 \dots \hat{\eta}_\alpha]}(\omega_p) = \sum_{j=1}^{\alpha} (-1)^{j-1} K^{[\hat{\eta}_j]}(\omega_p) \quad (19c)$$

$$K^{[\eta]}(\omega_p) = \prod_{i=1}^{\ell-1} \frac{1}{\omega_{1 \dots i}^{[\eta]}} \quad (19d)$$

Equations (19) compactly express all partial correlators $G_p^{k_p} = G_p^{[\hat{\eta}_1 \dots \hat{\eta}_\alpha]}$, and hence also the full KF correlator $G^k = G^{[\eta_1 \dots \eta_\alpha]}$, through a set of ℓ so-called *fully retarded kernels* $K^{[\eta]}$. These are defined by Equation (19d) and depend on just a single index η , which takes the value $\hat{\eta}_j$ in Equation (19c). The superscript on the frequencies occurring therein denotes imaginary shifts $\omega_i \rightarrow \omega_i^{[\eta]} = \omega_i + i\gamma_i^{[\eta]}$, with $\gamma_i^{[\eta]} \in \mathbb{R}$ chosen such that $\gamma_{i \neq \eta}^{[\eta]} < 0$, $\gamma_\eta^{[\eta]} > 0$, and $\omega_{1 \dots \ell}^{[\eta]} = \omega_{1 \dots \ell}^{[\eta]} = 0$. Shifts of precisely this form are needed to regularize the Fourier integrals expressing $\mathcal{K}^{k_p}(\omega_p)$ through $\mathcal{K}^{k_p}(t_p)$. Indeed, for infinitesimal $\gamma_i^{[\eta]}$ each factor in Equation (19d) is the Fourier transform of a step function,

$$\pm i \int_{\mathbb{R}} dt \theta(\pm t) e^{i\omega t} = \frac{1}{\omega \pm i0^+} = P\left(\frac{1}{\omega}\right) \mp i\pi\delta(\omega) \quad (20)$$

giving the kernels both principal-value P and Dirac- δ contributions. We choose the same convention as in ref. [23],

$$\gamma_{i \neq \eta}^{[\eta]} = -\gamma_0, \quad \gamma_\eta^{[\eta]} = (\ell - 1)\gamma_0 \quad (21)$$

see Figure 1c, with γ_0 taken to be infinitesimal, $\gamma_0 = 0^+$, for analytical considerations. Below, we also use the shorthand $\omega_{i \dots j}^\pm = \omega_{i \dots j} \pm i0^+$ to indicate infinitesimal imaginary shifts for sums of frequencies.

Comparing the fully retarded kernel $K^{[\eta]}$ of Equation (19d) with the regular Matsubara kernel \tilde{K} of Equation (13b), we find that the former is the analytic continuation of the latter:

$$K^{[\eta]}(\omega_p) = \tilde{K}(i\omega_p \rightarrow \omega_p^{[\eta]}) \quad (22)$$

This remarkable relation between MF and KF kernels constitutes the nucleus from which we will develop our strategy for obtaining KF correlators via analytic continuation of MF correlators. Here, we just note that, by Equations (13b) and (20), the analytical continuation of the *regular* MF kernel on the right of Equation (22) generally yields both principal-value and Dirac- δ contributions. By contrast, we will find below that the analytic continuation of *anomalous* MF kernels yields solely Dirac- δ contributions in KF correlators [cf. Equations (84) and (101)].

Two well-known statements on general ℓ p correlators follow immediately from Equations (19). First, for $\alpha = 0$, they imply $G^\square = G^{1 \dots 1} = 0$. Second, for $\alpha = 1$, we have $\bar{\hat{\eta}}_1 = \eta_1$. Thus, $K^{[\hat{\eta}_1]}(\omega_p) = \tilde{K}(\omega_p^{[\eta_1]})$ by Equation (22), and Equation (19b) yields

$$G_p^{[\hat{\eta}_1]}(\omega) = [\tilde{K} * S_p](\omega_p^{[\eta_1]}) = \tilde{G}_p(i\omega_p \rightarrow \omega_p^{[\eta_1]}) \quad (23)$$

For the second step, we evoked Equation (14c). Importantly, the superscript on $\omega_p^{[\eta]}$ on the right, which specifies its imaginary frequency shifts, is fully determined by the external Keldysh index η and *not* dependent on p . It thus remains unchanged throughout the sum on p in Equation (18a) for the full correlator $G^{[\eta]}(\omega)$, which hence can be expressed as

$$G^{[\eta]}(\omega) = \tilde{G}(i\omega \rightarrow \omega^{[\eta]}) \quad (24)$$

The fully retarded ($\alpha = 1$) components of KF correlators are therefore fully determined, via analytic continuation, by the *regular* parts of MF correlators. Conversely, anomalous parts of MF correlators can only influence Keldysh components with $\alpha \geq 2$.

For later use, we also define primed partial correlators

$$G'^{\eta_1 \dots \eta_\alpha}(\omega) = \sum_p G_p'^{[\hat{\eta}_1 \dots \hat{\eta}_\alpha]}(\omega_p) \quad (25a)$$

$$G_p'^{[\hat{\eta}_1 \dots \hat{\eta}_\alpha]}(\omega_p) = [(K^{[\hat{\eta}_1 \dots \hat{\eta}_\alpha]})' * S_p](\omega_p) \quad (25b)$$

They differ from the unprimed correlators of Equation (19b) by the complex conjugation of the kernel, replacing $\omega_i + i\gamma_i^{[\eta]}$ by $\omega_i - i\gamma_i^{[\eta]}$, with $\gamma_i^{[\eta]}$ still determined by the rule Equation (21). For $\alpha = 1$, the corresponding $G'^{[\eta]}$ will be called *fully advanced* correlators. For fully retarded or advanced correlators, $G^{[\eta]}$ or $G'^{[\eta]}$, all frequencies $\omega_{i \neq \eta}$ acquire negative or positive imaginary shifts, respectively. Note that primed correlators G'^k may differ from

complex conjugated correlators G^{*k} as the complex conjugation generally affects the PSFs, too.

This concludes our summary of the results of ref. [23] needed for present purposes. In the next section, we introduce a general strategy for expressing KF correlators through analytically-continued MF correlators. It is well-known how to do this for all components of $2p$ correlators, and, as discussed above, for the fully retarded and advanced components of ℓp correlators. Our goal is a strategy applicable for all components of ℓp correlators.

2.4. The Bridge between the MF and KF Formalisms

Equation (23), expressing KF partial correlators through MF partial correlators for $\alpha = 1$, has a counterpart for arbitrary α , obtained via Equations (19), (22), and (14c):

$$G_p^{[\tilde{\eta}_1 \dots \tilde{\eta}_\alpha]}(\omega_p) = \sum_{j=1}^{\alpha} (-1)^{j-1} [\tilde{K} * S_p](\omega_p^{[\tilde{\eta}_j]}) \quad (26a)$$

$$= \sum_{j=1}^{\alpha} (-1)^{j-1} \tilde{G}_p(\mathbf{i}\omega_p \rightarrow \omega_p^{[\tilde{\eta}_j]}) \quad (26b)$$

with $\tilde{\eta}_j \in \{\eta_1, \dots, \eta_\alpha\}$. This is already one of our main results: The partial correlators serve as a bridge between the MF and KF. All components of the partial KF correlator $G_p^{k_p} = G_p^{[\tilde{\eta}_1 \dots \tilde{\eta}_\alpha]}$ can be obtained by taking linear combinations of analytic continuations of partial regular MF correlators, $\tilde{G}_p(\mathbf{i}\omega_p \rightarrow \omega_p^{[\tilde{\eta}_j]})$. The external Keldysh indices $\mathbf{k} = [\eta_1 \dots \eta_\alpha]$ and the permutation p together specify the imaginary frequency shifts, encoded in $\omega_p^{[\tilde{\eta}_j]}$, to be used.

Equation (23), expressing the full (p -summed) KF correlators through MF ones for $\alpha = 1$, does not have a counterpart for $\alpha > 1$. Then, the full correlators, given by

$$G^{[n_1 \dots n_\alpha]}(\omega) = \sum_p [K^{[\tilde{\eta}_1 \dots \tilde{\eta}_\alpha]} * S_p](\omega_p) \quad (27a)$$

$$= \sum_p \sum_{j=1}^{\alpha} (-1)^{j-1} \tilde{G}_p(\mathbf{i}\omega_p \rightarrow \omega_p^{[\tilde{\eta}_j]}) \quad (27b)$$

involve a sum \sum_j . The $\tilde{\eta}_j$ indices on the right now depend on p , so that the imaginary frequency shifts vary from one permutation to the next. As a result, the full $G^{[n_1 \dots n_\alpha]}$, unlike $G^{[n]}$, does not depend on a single set of frequency shifts and cannot be directly expressed through a mere analytic continuation of $\tilde{G}(\mathbf{i}\omega)$. Instead, Equation (27b) requires separate knowledge of each individual $\tilde{G}_p(\mathbf{i}\omega_p)$. Most computational methods capable of computing the full MF correlator $G(\mathbf{i}\omega)$ do not have access to the separate partial MF correlators $\tilde{G}_p(\mathbf{i}\omega_p)$. In the following, we therefore develop a strategy for extracting the partial MF correlators $\tilde{G}_p(\mathbf{i}\omega_p)$ from a full MF correlator $G(\mathbf{i}\omega)$ given as input, assuming the latter to be known analytically. By writing the resulting functions $\tilde{G}_p(\mathbf{i}\omega)$ in the form $[\tilde{K} * S_p][G]$, one can deduce explicit expressions for the PSFs $S_p[G]$ as functionals of the input G . By inserting these S_p into Equation (27a), one obtains $G^{[n_1 \dots n_\alpha]}[G]$ as a functional of G , thereby achieving the desired MF-to-KF analytic continuation.

We start in the MF time domain. There, a specific partial MF correlator $G_p(\tau_p)$ can be obtained from the full $G(\tau) = \sum_p G_p(\tau_p)$ (Equations (8)) using the projector property of MF kernels in the time domain, $\mathcal{K}(\tau_p)\mathcal{K}(\tau_{p'}) = (-1)^{\ell-1}\mathcal{K}(\tau_p)$ if $p = p'$ and 0 otherwise. Hence, we can express the partial correlator as

$$G_p(\tau_p) = (-1)^{\ell-1} \mathcal{K}(\tau_p) G(\tau) \quad (28)$$

Computing the discrete Fourier transform of Equation (28) according to Equation (9b), we obtain

$$G_p(\mathbf{i}\omega_p) = [\mathcal{K} \star G](\mathbf{i}\omega_p) \quad (29a)$$

with the imaginary-frequency convolution \star defined as

$$[\mathcal{K} \star G](\mathbf{i}\omega_p) = \frac{1}{(-\beta)^{\ell-1}} \sum_{\mathbf{i}\omega'_p} \delta_{\mathbf{i}\omega'_p, \mathbf{i}\omega_p} \mathcal{K}(\mathbf{i}\omega_p - \mathbf{i}\omega'_p) G(\mathbf{i}\omega'_p) \quad (29b)$$

We will typically sum over the $\ell - 1$ independent Matsubara frequency variables $\mathbf{i}\omega'_{1 \dots \ell}$, with $i \in \{1, \dots, \ell - 1\}$. Note that the arguments of $G(\mathbf{i}\omega')$ appear in *unpermuted* order, but are to be viewed as functions of the summation variables, i.e., $\mathbf{i}\omega' = \mathbf{i}\omega'(\omega'_p)$. We will often make this explicit using the notation $G_{\mathbf{i}\omega'_p} = G(\mathbf{i}\omega'(\omega'_p))$, where the subscript is a label indicating the $\ell - 1$ independent frequencies chosen to parametrize $\mathbf{i}\omega'$. Consider, e.g., $\ell = 3$ and choose $\mathbf{i}\omega_{\overline{1}}, \mathbf{i}\omega_{\overline{2}}$ as summation variables. For the permutation $p = (132)$, the correlator is then represented as $G_{\mathbf{i}\omega_{\overline{1}}, \mathbf{i}\omega_{\overline{2}}} = G_{\mathbf{i}\omega_1, \mathbf{i}\omega_{13}} = G(\mathbf{i}\omega(\mathbf{i}\omega_1, \mathbf{i}\omega_{13})) = G(\mathbf{i}\omega_1, -\mathbf{i}\omega_{13}, \mathbf{i}\omega_{13} - \mathbf{i}\omega_1)$.

Using Equation (11a) for $G_p(\mathbf{i}\omega_p)$ and Equation (10b) for $\mathcal{K}(\mathbf{i}\omega_p)$ in Equation (29a), we obtain

$$\begin{aligned} & \beta \delta_{\mathbf{i}\omega_{1 \dots \ell}} G_p(\mathbf{i}\omega_p) + G_p^{\mathcal{R}}(\mathbf{i}\omega_p) \\ &= \beta \delta_{\mathbf{i}\omega_{1 \dots \ell}} [K \star G](\mathbf{i}\omega_p) + [\mathcal{R} \star G](\mathbf{i}\omega_p) \end{aligned} \quad (30)$$

By construction, neither $G_p^{\mathcal{R}}$ nor \mathcal{R} contain an overall factor of β ; in this sense, they are $\mathcal{O}(\beta^0)$. Likewise, $\mathcal{R} \star G$ is $\mathcal{O}(\beta^0)$, for reasons explained below. Moreover, recall that MF-to-KF continuation via Equation (27b) requires only the regular part $\tilde{G}_p(\mathbf{i}\omega_p)$. We avoid anomalous contributions to $G_p(\mathbf{i}\omega_p)$ in Equation (30) by imposing the condition $\mathbf{i}\omega_{\overline{1 \dots i}} \neq 0$ on the external frequencies. Setting $\mathbf{i}\omega_{1 \dots \ell} = 0$, we conclude that

$$\begin{aligned} \tilde{G}_p(\mathbf{i}\omega_p) + \mathcal{O}\left(\frac{1}{\beta}\right) &= [K \star G](\mathbf{i}\omega_p), \quad (\mathbf{i}\omega_{\overline{1 \dots i}} \neq 0, \forall i < \ell) \\ &= \frac{1}{(-\beta)^{\ell-1}} \sum_{\mathbf{i}\omega'_p} \delta_{\mathbf{i}\omega'_p, \mathbf{i}\omega_p} \mathcal{K}(\mathbf{i}\omega_p - \mathbf{i}\omega'_p) G_{\mathbf{i}\omega'_p} \end{aligned} \quad (31)$$

To find $\tilde{G}_p(\mathbf{i}\omega_p)$, we should thus compute $K \star G$ with $\mathbf{i}\omega_{\overline{1 \dots i}} \neq 0$ and retain only the $\mathcal{O}(\beta^0)$ terms, ignoring all $\mathcal{O}(1/\beta^{i \geq 1})$ contributions. Note, however, that the full information on K and G , including both regular and anomalous terms, is needed on the right-hand side to obtain \tilde{G}_p on the left.

Equation (31) is an important intermediate result. It provides a recipe for extracting partial regular MF correlators from the full MF correlator by performing Matsubara sums $\sum_{\mathbf{i}\omega'_p}$. After performing the sums, the final results will be analytically continued to yield $\tilde{G}_p(\mathbf{i}\omega_p \rightarrow \omega_p^{[n]})$ through which all Keldysh correlators can

be expressed (Equation (27b)). However, we choose to fully evaluate the Matsubara sums *before* performing this analytic continuation. The reason is that we will evaluate the sums using contour integration and contour deformation. For the latter step, it is convenient if the arguments of $\tilde{G}_p(i\omega_p)$ all lie safely on the imaginary axis, where they do not impede contour deformation.

2.5. Converting Matsubara Sums to Contour Integrals

Next, we discuss three technical points relevant for performing Matsubara sums explicitly. To be concrete, we illustrate our general statements for the case $\ell = 2$. Other cases are discussed in subsequent sections.

2.5.1. Singularity-Free Kernels

The argument of the kernel $K(\Omega_p)$ in Equation (31) has the form $\Omega_p = i\omega_p - i\omega'_p$. This is always bosonic, being the difference of two same-type Matsubara frequencies. The Matsubara sums $\sum_{i\omega'_p}$ will thus contain terms with $\Omega_{1\dots i} = 0$. To facilitate dealing with these, we assume that the kernel has been expressed in “singularity-free” form, where case distinctions ensure that factors of $1/\Omega_{1\dots i}$ occur only if $\Omega_{1\dots i} \neq 0$. This is possible for the presented correlators, as shown in ref. [30] and discussed in Appendix A.1. These case distinctions are expressed via the symbol

$$\Delta_{\Omega_{1\dots i}} = \begin{cases} \frac{1}{\Omega_{1\dots i}} & \text{if } \Omega_{1\dots i} \neq 0 \\ 0 & \text{if } \Omega_{1\dots i} = 0 \end{cases} \quad (32)$$

Thus, $K(\Omega_p)$ is assumed to contain $1/\Omega_{1\dots i}$ only via $\Delta_{\Omega_{1\dots i}}$. A sum over a Δ symbol becomes a restricted sum, lacking the summand for which $\Delta = 0$. For $\ell = 2$, e.g., we have $K(\Omega_p) = \Delta_{\Omega_1} - \frac{1}{2}\beta\delta_{\Omega_1}$ (see Equation (A2a)), so that Equation (31) yields

$$\tilde{G}_p(i\omega_p) + \mathcal{O}\left(\frac{1}{\beta}\right) \stackrel{\ell=2}{=} \frac{1}{(-\beta)} \sum_{i\omega'_1}^{\neq i\omega_1} \frac{G_{i\omega'_1}}{i\omega_1 - i\omega'_1} + \frac{G_{i\omega_1}}{2} \quad (33)$$

This involves a restricted sum and an $\mathcal{O}(\beta^0)$ term resulting from $\beta\delta_{\Omega_1}$ collapsing the sum $\frac{1}{(-\beta)} \sum_{i\omega'_1}$ in Equation (31).

2.5.2. $\beta\delta$ Expansion of G

To facilitate the identification of the leading-in- β contributions to Equation (31), we assume that the anomalous \hat{G} contribution to $G_{i\omega'_p} = (\tilde{G} + \hat{G})_{i\omega'_p}$ has been expressed as an expansion in powers of $\beta\delta_{\Omega_{1\dots i}}$. Such a $\beta\delta$ expansion is always possible for the correlators under consideration in this work, as discussed in Appendix A.2. Whenever $\beta\delta_{\Omega_{1\dots i}}$ appears in a Matsubara sum $\frac{1}{(-\beta)} \sum_{i\omega'}$, the sum collapses and their β factors cancel. (This cancellation is why $R \star G$ in Equation (30) is $\mathcal{O}(\beta^0)$, as stated above, even if G contains anomalous terms.) For $\ell = 2$, e.g., we have $G_{i\omega'_1} = \tilde{G}_{i\omega'_1} + \beta\delta_{\Omega_1} \hat{G}_1$, with $\tilde{G}_{i\omega'_1}$ singularity-free at all Matsubara frequencies $i\omega'_1$ and \hat{G}_1 a constant (see Equation (40)). Thus,

Equation (33) becomes

$$\tilde{G}_p(i\omega_p) + \mathcal{O}\left(\frac{1}{\beta}\right) \stackrel{\ell=2}{=} \frac{1}{(-\beta)} \sum_{i\omega'_1}^{\neq i\omega_1} \frac{\tilde{G}_{i\omega'_1}}{i\omega_1 - i\omega'_1} + \frac{\tilde{G}_{i\omega_1}}{2} - \frac{\hat{G}_1}{i\omega_1} \quad (34)$$

Here, the condition $i\omega_1 \neq 0$ on the left was evoked to replace $\frac{1}{2}G_{i\omega_1}$ by $\frac{1}{2}\tilde{G}_{i\omega_1}$ on the right.

2.5.3. Converting Sums to Integrals

By restricting or collapsing Matsubara sums containing Δ or δ factors, one can ensure that the remaining sums are all of the form $\frac{1}{(-\beta)} \sum_{i\omega'} f(i\omega')$ or $\frac{1}{(-\beta)} \sum_{i\omega'}^{\neq i\omega} f(i\omega')$, where $f(z)$, viewed as a function of $z \in \mathbb{C}$, is *analytic* at each $i\omega'$ visited by the sum. (More precisely, for each $i\omega'$ in the sum, $f(z)$ is analytic in an open domain containing that $i\omega'$.) We express such sums in standard fashion as contour integrals:

$$\frac{1}{(-\beta)} \sum_{i\omega'} f(i\omega') = \oint_z n_z f(z) \quad (35a)$$

$$\frac{1}{(-\beta)} \sum_{i\omega'}^{\neq i\omega} f(i\omega') = \oint_z n_z f(z) - \text{Res}_{z=i\omega} (n_z f(z)) \quad (35b)$$

Here, $\oint_z = \oint_{2\pi i}^{dz}$ denotes counterclockwise integration around all points $i\omega'$ visited by the sum, and n_z is a Matsubara weighting function (MWF). We choose it as

$$n_z = \frac{\zeta}{e^{-\beta z} - \zeta} = \frac{1}{(-\beta)} \frac{1}{z - i\omega'} - \frac{1}{2} + \mathcal{O}(z - i\omega') \quad (36)$$

with $\zeta = \pm$ for bosonic/fermionic $i\omega'$. (n_z is related to standard Fermi and Bose distribution functions by $-\zeta(1 + n_z) = 1/(e^{\beta z} - \zeta)$.) The Laurent expansion on the right of Equation (36) shows that n_z has first-order poles with residues $1/(-\beta)$ at all Matsubara frequencies $i\omega'$. Therefore, the integral \oint_z along a contour including all $i\omega'$ frequencies recovers the unrestricted Matsubara sum of Equation (35a) (see left parts of Figure 2b,c). For the restricted sum of Equation (35b), the first term on the right represents an unrestricted sum, i.e. the restricted sum plus a contribution from $i\omega' = i\omega$, and the residue correction subtracts the latter. For example, consider the case, needed below, that $f(i\omega') = \tilde{f}(i\omega')/(i\omega - i\omega')$, with $\tilde{f}(z)$ analytic at $z = i\omega$. Then, $n_z f(z)$ has a pole of second order at $i\omega$, with

$$\begin{aligned} \text{Res}_{z=i\omega} \left(\frac{n_z \tilde{f}(z)}{i\omega - z} \right) &= \left(\partial_z [(i\omega - z)n_z \tilde{f}(z)] \right)_{z \rightarrow i\omega} \\ &= \frac{1}{2} \tilde{f}(i\omega) + \frac{1}{\beta} \left(\partial_z \tilde{f}(z) \right)_{z \rightarrow i\omega} \end{aligned} \quad (37)$$

Note that Equations (35) remain valid under shifts of the MWF by a constant, $n_z \rightarrow n_z + c$. We purposefully exploited this freedom to choose n_z to have $-\frac{1}{2}$ as the second term in the Laurent expansion. The reason is that this leads to a convenient cancellation between terms arising from a δ in K and residue corrections arising from Δ restrictions. For example, when evaluating

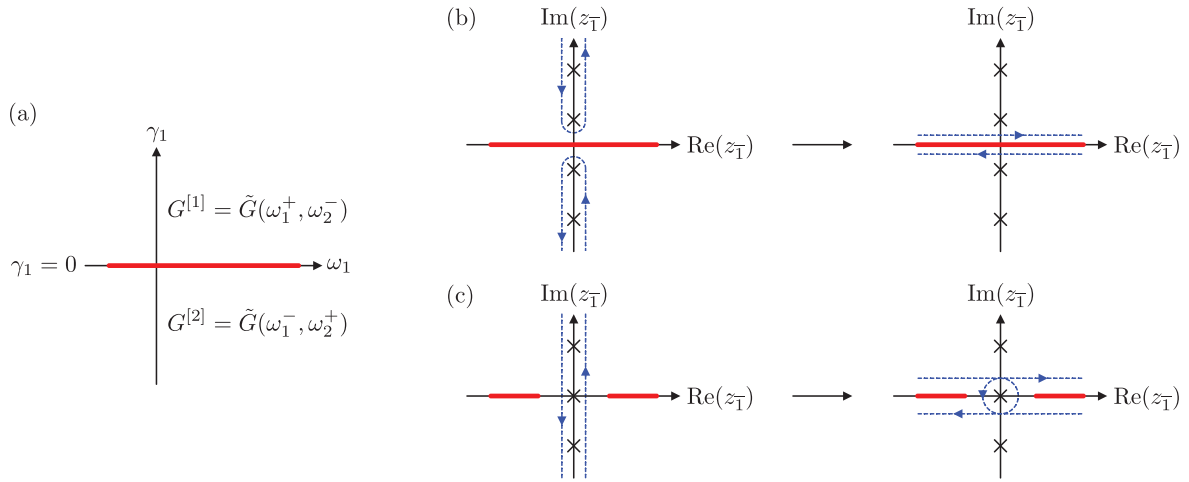


Figure 2. a) Analytic regions of a regular 2p MF correlator as a function of a complex frequency $\omega_1 + i\gamma_1$ with $\omega_1, \gamma_1 \in \mathbb{R}$. The thick, red line on the real axis depicts a possible branch cut of the correlator. b,c) Contours to evaluate the Matsubara summation in the (b) fermionic and (c) bosonic case, see Equations (43) and (44), respectively. Crosses indicate the poles of the MWF n_{z_T} at the Matsubara frequencies on the imaginary axis. The dashed blue contours, initially enclosing all Matsubara frequencies, are deformed away from the imaginary axis to run infinitesimally above and below the real axis. In the bosonic 2p case (c), the branch cut does not extend to $z_T = 0$ as the correlator, by definition, is free of any singularities at vanishing Matsubara frequencies.

the Matsubara sum in Equation (34) using Equations (35b) with $f(i\omega') = \tilde{G}_{i\omega'} / (i\omega - i\omega')$, we obtain:

$$\tilde{G}_p(i\omega_p) + \mathcal{O}\left(\frac{1}{\beta}\right) = \oint_{z_T} \frac{n_{z_T} \tilde{G}_{z_T}}{i\omega_1 - z_T} - \text{Res}_{z_T=i\omega_T} \left(\frac{n_{z_T} \tilde{G}_{z_T}}{i\omega_T - z_T} \right) + \frac{\tilde{G}_{i\omega_T}}{2} - \frac{\hat{G}_T}{i\omega_T} \quad (38a)$$

$$= \oint_{z_T} \frac{n_{z_T} \tilde{G}_{z_T}}{i\omega_1 - z_T} - \frac{1}{\beta} \left(\partial_{z_T} \tilde{G}_{z_T} \right)_{z_T=i\omega_T} - \frac{\hat{G}_T}{i\omega_T} \quad (38b)$$

The $\frac{1}{2} \tilde{G}_{i\omega_T}$ term in Equation (38a) conveniently cancels a contribution from the residue correction, evaluated using Equation (37). This cancellation results from our choice of n_z having $-\frac{1}{2}$ in its Laurent expansion. (Similar cancellations occur for $\ell > 2$; see, e.g., Appendix C.2.1.) The $-\frac{1}{\beta} (\partial_z \tilde{G}_z)_{z=i\omega_T}$ term in Equation (38b) is an example of an $\mathcal{O}\left(\frac{1}{\beta}\right)$ contribution that arises from $K \star G$ but is not part of \tilde{G}_p .

Having worked through the example of $\ell = 2$, we conclude this section with some general remarks about Equation (31) for \tilde{G}_p . Once the Matsubara sums from the imaginary-frequency convolution $K \star G$ have been expressed through contour integrals, one obtains the general form^[31]

$$\tilde{G}_p(i\omega_p) + \mathcal{O}\left(\frac{1}{\beta}\right) = \oint_{z_T} \dots \oint_{z_{T-1}} \tilde{K}(i\omega_p - z_p) n_{z_T} \dots n_{z_{T-1}} \tilde{G}_{z_T, \dots, z_{T-1}} + \text{contributions from } \hat{G} \quad (39)$$

Here, the $(\ell - 1)$ -fold contour integrals involve only the *regular* part, \tilde{G} , of the full MF correlator. Its anomalous part, \hat{G} , comes with factors $\beta\delta$ that collapse one or multiple sums in Equation (31). Therefore, contributions from \hat{G} to \tilde{G}_p contain at most $\ell - 2$ contour integrals.

The next step, discussed in detail in Section 3.2, is to deform the integration contour in such a way that it runs infinitesimally above and below the real axis. The anomalous contributions from \hat{G} can then be reincorporated into the real integrals using bosonic Dirac delta functions. As a result, one recovers precisely the form $\tilde{G}_p = \tilde{K} \star S_p$ of the spectral representation (14d): regular kernels \tilde{K} convolved with other functions, built from MWFs and analytic continuations of the various components of \tilde{G} and \hat{G} , the latter multiplied by bosonic Dirac δ functions. These other functions can thus be identified with the PSFs $S_p = \tilde{S}_p + \hat{S}_p$, now expressed through analytic continuations of G . This clarifies, on a conceptual level, how the information contained in the full MF correlator G needs to be repackaged to obtain PSFs, and the explicit formulas for $\ell = 2, 3, 4$ in Equations (47), (74), and (88) constitute the main results of this paper. These, in turn, can then be used to obtain KF correlators via Equation (27a).

To summarize, the MF-to-KF analytic continuation of arbitrary ℓ p correlation functions can be achieved via the following three-step strategy:

Step 1. Matsubara summation through contour integration: Insert the MF kernel K (expressed in singularity-free form) and the MF correlator G (expressed as a $\beta\delta$ expansion), including all regular and anomalous contributions, into Equation (31) for \tilde{G}_p . Restrict or collapse Matsubara sums containing Δ or $\beta\delta$ factors and express the remaining sums through contour integrals using Equations (35), to arrive at Equation (39).

Step 2. *Extraction of PSFs:* Deform the contours away from the imaginary axis to run along the real axis, while carefully tracking possible singularities of the MF correlators. Reincorporate anomalous contributions via bosonic Dirac delta functions. This results in a spectral representation of the form $\tilde{G}_p = \tilde{K} * S_p$. From this, read off the PSFs $S_p[G]$, expressed through products of MWFs and MF correlators, analytically continued to real frequencies (see, e.g., Equation (47)).

Step 3. *Construction of KF correlators:* Construct the full KF correlator $G^{[\hat{n}_1 \dots \hat{n}_\ell]}$, involving a sum \sum_p over terms of the form $[K^{[\hat{n}_1 \dots \hat{n}_\ell]} * S_p](i\omega_p)$ (Equation (27a)). Simplify the kernels $K^{[\hat{n}_1 \dots \hat{n}_\ell]}$ via a set of kernel identities (see, e.g., Equations (57)) and combine terms with similar structure from the sum \sum_p . Insert into the resulting expressions the PSFs from Step 2, and then compute the integrals involved in the $*$ convolution. This leads to equations expressing KF correlators through analytically continued MF correlators, $G^{[\hat{n}_1 \dots \hat{n}_\ell]}[G]$.

The result of Step 2 already constitutes an analytic continuation since the PSFs S_p suffice to construct the KF correlators via the spectral representation. Step 3 serves to give direct relations between both formalisms.

In Appendix G.2, we follow an independent approach and use the equilibrium condition to explicitly perform the following consistency check: given an arbitrary set of PSFs S_p as input, compute the MF correlator $G = \sum_p K * S_p$ and verify that the formulas $S_p[G]$ correctly recover the input PSFs from G , giving $S_p[G] = S_p$. This consistency check is presented for general 2p and 3p and for fermionic 4p correlators.

The next sections are devoted to explicitly working out the details of this strategy. To demonstrate its basic ideas, we first revisit the well-known 2p case in the following section. Though that is textbook material, we present it in a manner that readily generalizes to the higher-point correlators discussed in subsequent sections: 3p correlators in Section 5 and 4p correlators in Section 6.

3. Analytic Continuation of 2p Functions

In this section, we carry through the strategy outlined in Section 2.5 to obtain the MF-to-KF analytic continuation in the well-known 2p case. While our strategy may seem more cumbersome than traditional textbook discussions (see, e.g., ref. [32]), it has the merit of readily generalizing to $\ell > 2$. We first recapitulate the spectral representation and analytic properties of general 2p MF correlators (Section 3.1). Then, we express the PSFs in terms of analytically continued MF correlators (Section 3.2). Finally, we use these to recover familiar expressions for the retarded, advanced, and Keldysh components of the KF 2p correlator (Section 3.3).

3.1. Analytic Properties of the 2p MF Correlator

We begin by reviewing well-known analytical properties of the 2p MF correlator. This also serves to give concrete examples for our notational conventions.

$G(i\omega) = G(i\omega_1, i\omega_2)$ explicitly depends on one Matsubara frequency, $i\omega_1$ or $i\omega_2$, while the other frequency is fixed by energy conservation, $i\omega_{12} = 0$. Since we want to compute Equation (31) for arbitrary permutations $p = (\overline{12})$, it proves useful to develop an unbiased notation for the frequency dependence. The chosen explicit frequency dependence is indicated by a subscript in $G_{i\omega_\tau}$, such that $G_{i\omega_1} = G(i\omega(\omega_1)) = G(i\omega_1, -i\omega_1)$ and $G_{i\omega_2} = G(i\omega(\omega_2)) = G(-i\omega_2, i\omega_2)$. The most general form of $G_{i\omega_\tau}$, covering both fermionic and bosonic cases, reads

$$G(i\omega(\omega_\tau)) = G_{i\omega_\tau} = \tilde{G}_{i\omega_\tau} + \beta \delta_{i\omega_\tau} \hat{G}_\tau \quad (40)$$

in agreement with the general form Equation (A5). The regular part, $\tilde{G}_{i\omega_\tau}$, is singularity-free for all $i\omega_\tau$, including 0. \hat{G}_τ denotes the anomalous part, a constant, contributing only for $i\omega_\tau = 0$. The relation $G_{i\omega_1} = G_{i\omega_2}$ enforces $\hat{G}_1 = \hat{G}_2$.

One of the next steps involves the deformation of the integration contour \oint_{z_τ} from the imaginary axis toward the real axis. This requires knowledge of the analytic structure of the MF correlator. It can be made explicit via the spectral representation of G_{z_1} (Equations (14)), with the PSFs S_p viewed as input. For the regular part, we obtain

$$\tilde{G}_{z_1} = \int d^2\epsilon \delta(\epsilon_{12}) \left[\frac{S_{(12)}(\epsilon_1)}{z_1 - \epsilon_1} + \frac{S_{(21)}(\epsilon_2)}{-z_1 - \epsilon_2} \right] = \int d\epsilon_1 \frac{S_{\text{std}}(\epsilon_1)}{z_1 - \epsilon_1} \quad (41)$$

Here, we introduced the “standard” spectral function S_{std} , given by a commutator of PSFs resulting from the sum over the two permutations $p = (12)$ and (21) :

$$S_{\text{std}}(\epsilon_1) = S_{[1,2]_+}(\epsilon_1, -\epsilon_1) = S_{(12)}(\epsilon_1) - S_{(21)}(-\epsilon_1) \quad (42a)$$

$$S_{[1,2]_\pm}(\epsilon) = S_{(12)}(\epsilon_1) \pm S_{(21)}(\epsilon_2) \quad (42b)$$

Here, $\epsilon_{12} = 0$ is understood for the argument of $S_{[1,2]_\pm}(\epsilon)$. For PSF (anti)commutators, we always display the unpermuted ϵ and insert the permuted ϵ_p only for individual PSFs, as done on the right of Equation (42b). Evidently, \tilde{G}_{z_1} has poles (or branch cuts for continuous spectra) whenever the denominator $z_1 - \epsilon_1$ vanishes. This can happen only if $\text{Im}(z_1) = 0$ (or, more generally, $\text{Im}(z_\tau) = 0$), indicated in Figure 2 by thick, red lines on the real axis. Hence, the upper and the lower complex half plane are analytic regions of \tilde{G}_{z_1} , separated by a branch cut at $\text{Im}(z_1) = 0$.

3.2. Extraction of PSFs from Partial MF Correlators

In Section 2.5, we expressed the regular partial MF correlators $\tilde{G}_p(i\omega_p)$ for $\ell = 2$ in terms of a contour integral \oint_{z_τ} involving the regular MF correlator \tilde{G}_{z_τ} , see Equation (38b). That amounted to Step 1 of the three-step strategy. Turning to Step 2, we write $\tilde{G}_p(i\omega_p)$ in the form of a convolution $[\tilde{K} * S_p](i\omega_p)$, from which we then read out expressions for the PSFs $S_p[G]$.

To this end, we exploit the analyticity of \tilde{G}_{z_τ} in the upper and lower half-plane to deform the contours in \oint_{z_τ} from enclosing the imaginary axis to running infinitesimally above and below the branch cut. We denote the corresponding integration variables

along the branch cut by $\varepsilon_{\bar{1}}^{\pm} = \varepsilon_{\bar{1}} \pm i0^+$, with $\varepsilon_{\bar{1}} = \text{Re}(z_{\bar{1}})$ now being a real variable and $\pm i0^+$ infinitesimal shifts.

We discuss the cases of fermionic or bosonic frequencies separately. For fermions, the contour deformation of $\oint_{z_{\bar{1}}}$ in Equation (38b) is straightforward and yields (see Figure 2b)

$$\oint \frac{dz_{\bar{1}}}{2\pi i} \frac{n_{z_{\bar{1}}} \tilde{G}_{z_{\bar{1}}}}{i\omega_{\bar{1}} - z_{\bar{1}}} = \int_{-\infty}^{\infty} \frac{d\varepsilon_{\bar{1}}}{2\pi i} \frac{n_{\varepsilon_{\bar{1}}} \tilde{G}^{\varepsilon_{\bar{1}}}}{i\omega_{\bar{1}} - \varepsilon_{\bar{1}}} \quad (43)$$

Here, we defined $\tilde{G}^{\varepsilon_{\bar{1}}} = \tilde{G}_{\varepsilon_{\bar{1}}^+} - \tilde{G}_{\varepsilon_{\bar{1}}^-}$ as the discontinuity of $\tilde{G}_{z_{\bar{1}}}$ across the branch cut at $\text{Im}(z_{\bar{1}}) = 0$. Moreover, we extended the subscript notation introduced after Equation (29b) to real frequencies with infinitesimal imaginary shifts. (This notation is further discussed after Equation (47).)

In the bosonic case, the pole at $z_{\bar{1}} = 0$ has to be treated separately (see Figure 2c):

$$\begin{aligned} \oint \frac{dz_{\bar{1}}}{2\pi i} \frac{n_{z_{\bar{1}}} \tilde{G}_{z_{\bar{1}}}}{i\omega_{\bar{1}} - z_{\bar{1}}} &= \int_{-\infty}^{\infty} \frac{d\varepsilon_{\bar{1}}}{2\pi i} \frac{n_{\varepsilon_{\bar{1}}} \tilde{G}^{\varepsilon_{\bar{1}}}}{i\omega_{\bar{1}} - \varepsilon_{\bar{1}}} + \text{Res}_{z_{\bar{1}}=0} \left(\frac{n_{z_{\bar{1}}} \tilde{G}_{z_{\bar{1}}}}{i\omega_{\bar{1}} - z_{\bar{1}}} \right) \\ &= \int_{-\infty}^{\infty} \frac{d\varepsilon_{\bar{1}}}{2\pi i} \frac{n_{\varepsilon_{\bar{1}}} \tilde{G}^{\varepsilon_{\bar{1}}}}{i\omega_{\bar{1}} - \varepsilon_{\bar{1}}} + \mathcal{O}\left(\frac{1}{\beta}\right) \end{aligned} \quad (44)$$

Here, \int indicates a principal-value integral. The residue evaluates to a contribution of order $\mathcal{O}\left(\frac{1}{\beta}\right)$ as the bosonic MWF $n_{z_{\bar{1}}}$ is the only factor having a pole at $z_{\bar{1}} = 0$, with residue $1/(-\beta)$ there (remember that $i\omega_{\bar{1}} \neq 0$). Combining Equations (43), (44), and (38b), and omitting $\mathcal{O}\left(\frac{1}{\beta}\right)$ terms, we finally find

$$\tilde{G}_p(i\omega_p) = \int_{\varepsilon_{\bar{1}}} \frac{n_{\varepsilon_{\bar{1}}} \tilde{G}^{\varepsilon_{\bar{1}}}}{i\omega_{\bar{1}} - \varepsilon_{\bar{1}}} - \frac{\hat{G}_{\bar{1}}}{i\omega_{\bar{1}}} = \int_{\varepsilon_{\bar{1}}} \frac{n_{\varepsilon_{\bar{1}}} \tilde{G}^{\varepsilon_{\bar{1}}} + \hat{\delta}(\varepsilon_{\bar{1}}) \hat{G}_{\bar{1}}}{i\omega_{\bar{1}} - \varepsilon_{\bar{1}}} \quad (45)$$

On the right, we absorbed the anomalous \hat{G} contribution into the integral, defining $\hat{\delta}(\varepsilon_{\bar{1}}) = -2\pi i \delta(\varepsilon_{\bar{1}})$. Moreover, we introduced the symbol \int_{ε_i} as

$$\int_{\varepsilon_i} \dots = \begin{cases} \int_{-\infty}^{\infty} \frac{d\varepsilon_i}{2\pi i} \dots & \text{for fermionic } \varepsilon_i \text{ or anomalous frequency,} \\ \int_{-\infty}^{\infty} \frac{d\varepsilon_i}{2\pi i} \dots & \text{for bosonic } \varepsilon_i \text{ and regular frequency.} \end{cases} \quad (46)$$

We call a frequency ε_i *anomalous* if it is directly set to zero by a Dirac $\hat{\delta}(\varepsilon_i)$ in the integrand, and *regular* otherwise. Since the anomalous contribution arose from a Kronecker $\delta_{i\omega_{\bar{1}}}$, we arrive at a rule of thumb: when performing Matsubara sums via contour integration and contour deformation to the real axis, Kronecker deltas with Matsubara arguments lead to Dirac deltas with real arguments.

Importantly, Equation (45) has precisely the same form as Equation (14d) for $\ell = 2$, with the correspondence

$$(2\pi i) S_p(\varepsilon_{\bar{1}}) = n_{\varepsilon_{\bar{1}}} \tilde{G}^{\varepsilon_{\bar{1}}} + \hat{\delta}(\varepsilon_{\bar{1}}) \hat{G}_{\bar{1}} \quad (47)$$

This remarkable formula is the first central result of this section: it shows that a suitable analytic continuation of the MF correlator

$G(i\omega)$, combined with a MWF, fully determines the PSF and thus, via the spectral representation Equations (27a), the KF correlator G^k . It also clarifies the role of anomalous contributions. In subsequent sections, we will find analogous results for $\ell = 3, 4$.

To conclude this section, we elaborate on the meaning of the super- and subscript notation used above. The discontinuity in Equation (47), $\tilde{G}^{\varepsilon_{\bar{1}}} = \tilde{G}_{\varepsilon_{\bar{1}}^+} - \tilde{G}_{\varepsilon_{\bar{1}}^-}$, consists of analytically continued MF correlators, $\tilde{G}(i\omega) \rightarrow \tilde{G}(z)$. Here, the entries of $z = (\varepsilon_{\bar{1}}^{\pm}, \varepsilon_{\bar{2}}^{\mp})$ are infinitesimally shifted by $+i0^+$ or $-i0^+$, but constrained by energy conservation, $\varepsilon_{12} = 0$. The subscript on $\tilde{G}_{\varepsilon_{\bar{1}}^{\pm}}$ has the same meaning as for imaginary frequencies (see paragraph after Equation (29b)): it indicates the chosen explicit (real-)frequency dependence of $\tilde{G}(z)$, i.e., $\tilde{G}_{\varepsilon_{\bar{1}}^{\pm}} = \tilde{G}(z(\varepsilon_{\bar{1}}^{\pm}))$, uniquely determining the imaginary shifts in each entry of z . To be explicit, we have

$$\tilde{G}^{\varepsilon_1} = \tilde{G}(\varepsilon_1^+, -\varepsilon_1^+) - \tilde{G}(\varepsilon_1^-, -\varepsilon_1^-) \quad (48a)$$

$$\tilde{G}^{\varepsilon_2} = \tilde{G}(-\varepsilon_2^+, \varepsilon_2^+) - \tilde{G}(-\varepsilon_2^-, \varepsilon_2^-) \quad (48b)$$

Since $\varepsilon_2 = -\varepsilon_1$ (energy conservation) and hence $\varepsilon_2^+ = -\varepsilon_1^-$, we have $\tilde{G}^{\varepsilon_1} = -\tilde{G}^{\varepsilon_2} = \tilde{G}^{-\varepsilon_2}$. (Check for negative superscripts: $\tilde{G}^{-\varepsilon_2} = \tilde{G}_{(-\varepsilon_2)^+} - \tilde{G}_{(-\varepsilon_2)^-} = \tilde{G}_{-\varepsilon_2^-} - \tilde{G}_{-\varepsilon_2^+} = -\tilde{G}^{\varepsilon_2}$.)

For illustration, we give explicit formulas for S_p for the permutations $p = (12)$ and $p = (21)$,

$$\begin{aligned} (2\pi i) S_{(12)}(\varepsilon_1) &= n_{\varepsilon_1} [\tilde{G}(\varepsilon_1^+, -\varepsilon_1^+) - \tilde{G}(\varepsilon_1^-, -\varepsilon_1^-)] + \hat{\delta}(\varepsilon_1) \hat{G}_1 \\ (2\pi i) S_{(21)}(\varepsilon_2) &= n_{\varepsilon_2} [\tilde{G}(-\varepsilon_2^+, \varepsilon_2^+) - \tilde{G}(-\varepsilon_2^-, \varepsilon_2^-)] + \hat{\delta}(\varepsilon_2) \hat{G}_2 \end{aligned} \quad (49)$$

where we inserted Equation (48) for the discontinuities. The anomalous contributions satisfy $\hat{G}_1 = \hat{G}_2$ (as explained after Equation (40)) and exist only for bosonic correlators ($\zeta = 1$). Energy conservation $\varepsilon_2 = -\varepsilon_1$ then gives

$$\begin{aligned} (2\pi i) S_{(21)}(-\varepsilon_1) &= n_{-\varepsilon_1} [\tilde{G}(\varepsilon_1^-, -\varepsilon_1^-) - \tilde{G}(\varepsilon_1^+, -\varepsilon_1^+)] + \hat{\delta}(\varepsilon_1) \hat{G}_2 \\ &= \zeta e^{-\beta\varepsilon_1} (2\pi i) S_{(12)}(\varepsilon_1) \end{aligned} \quad (50)$$

For the last step, we used the identity $-n_{-\varepsilon_1} = \zeta e^{-\beta\varepsilon_1} n_{\varepsilon_1}$. As a useful consistency check, we note that Equation (50) corresponds to the equilibrium condition Equation (4) for PSFs (with $p = (21)$, $p_{\lambda} = (12)$ there, implying $\zeta_p = \zeta$, $\zeta_{p_{\lambda}} = +1$ and $\varepsilon_{\bar{1}} = \varepsilon_2 = -\varepsilon_1$, $\varepsilon_{p_{\lambda}(1)} = \varepsilon_1$).

Expressing the standard spectral function $S_{\text{std}}(\varepsilon_1)$ from Equation (42a) in terms of Equation (47), we find

$$\begin{aligned} (2\pi i) S_{\text{std}}(\varepsilon_1) &= n_{\varepsilon_1} \tilde{G}^{\varepsilon_1} + \hat{\delta}(\varepsilon_1) \hat{G}_1 - n_{-\varepsilon_1} \tilde{G}^{-\varepsilon_1} - \hat{\delta}(-\varepsilon_1) \hat{G}_2 \\ &= n_{\varepsilon_1} \tilde{G}^{\varepsilon_1} - n_{-\varepsilon_1} \tilde{G}^{-\varepsilon_1} = (n_{\varepsilon_1} + n_{-\varepsilon_1}) \tilde{G}^{\varepsilon_1} \\ &= -\tilde{G}^{\varepsilon_1} \end{aligned} \quad (51)$$

where we used $\tilde{G}^{-\varepsilon_1} = -\tilde{G}^{\varepsilon_1}$. Thus, the discontinuity $\tilde{G}^{\varepsilon_{\bar{1}}}$ in the PSFs (47) encodes $S_{\text{std}}(\varepsilon_1)$. Conversely, however, $S_{\text{std}}(\varepsilon_1)$ retains only the discontinuity $\tilde{G}^{\varepsilon_{\bar{1}}}$ in the PSFs (47), while the information on the MWF and the anomalous part, both contained in the S_p (49), is lost. In Appendix G.2, we use Equation (51) and the equilibrium condition to explicitly perform the following consis-

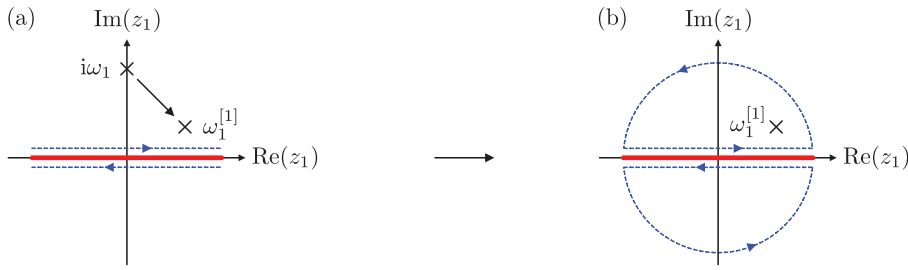


Figure 3. a) Analytic continuation of the Matsubara frequency $i\omega_1 \rightarrow \omega_1^{[1]} = \omega_1 + i\gamma_0$ in Equations (52) for fermionic frequencies. The imaginary part of the external frequency $\omega_1^{[1]}$ has to be larger than the imaginary parts of ϵ_1^\pm used to integrate infinitesimally above and below the real axis. The transition from (a) to (b) illustrates the closing of the contour in the upper/lower half-planes to evaluate the integral in Equation (53). As the integrand is independent of the fermionic MWF n_{ϵ_1} , the only contribution to the integral originates from the simple pole at $z_1 = \omega_1^{[1]}$.

tency check: given an arbitrary set of PSFs as input, compute the MF correlator $G = \sum_p K * S_p$ and verify that Equation (47) for S_p correctly recovers the input PSFs.

3.3. Keldysh Correlator

Next, we turn to Step 3 of our three-step strategy: we use the PSFs obtained above to explicitly construct the Keldysh components $G^{[1]}$, $G^{[2]}$, and $G^{[12]}$, expressed through analytically continued MF correlators. As the structure of KF correlators becomes more intricate with an increasing number of 2's in the Keldysh component, denoted by α in Equations (19), we discuss the different values of α separately in the following and throughout the rest of the paper.

3.3.1. Keldysh Components $G^{[n]}$

For $\alpha = 1$, the fully retarded or fully advanced Keldysh components $G^{[n]}$ can be deduced from the regular part of MF correlators alone (Equation (23)). Here, we follow the alternative and equivalent strategy of Step 3: we insert the PSFs from Equation (47) into the spectral representation (27a):

$$G^{[n]}(\omega) = \sum_p [K^{[n]} * S_p](\omega_p) = \sum_p [\tilde{K} * S_p](\omega_p^{[n]}) \quad (52a)$$

$$= \int d^2\epsilon \delta(\epsilon_{12}) \left(\frac{S_{(12)}(\epsilon_1)}{\omega_1^{[n]} - \epsilon_1} + \frac{S_{(21)}(\epsilon_2)}{\omega_2^{[n]} - \epsilon_2} \right) \quad (52b)$$

$$= \int d\epsilon_1 \frac{S_{[1,2]_-}(\epsilon_1, -\epsilon_1)}{\omega_1^{[n]} - \epsilon_1} \quad (52c)$$

Here, we used $\omega_2^{[n]} = -\omega_1^{[n]}$ (Equation (21)) and that the sum over both permutations, $p = (12)$ and (21) , leads to the appearance of the PSF commutator $S_{[1,2]_-}$ (equalling S_{std} , cf. Equation (42)).

Before proceeding, a general remark is in order: When the external variables $\omega_p^{[n]}$ appear in $*$ convolution integrals such as \int_{ϵ_1} in Equations (52), it is essential to maintain the hierarchy $\gamma_0 \gg 0^+$ for the infinitesimal imaginary shifts $\pm i\gamma_0$ and $\pm i0^\pm$ contained in the external frequencies $\omega_p^{[n]}$ and the integration variables ϵ_1^\pm , respectively. The reason is that the contour deformation

from \oint_{z_1} to \int_{ϵ_1} has been performed *before* the analytic continuation $i\omega_p \rightarrow \omega_p^{[n]}$ underlying Equations (27) and leading to Equation (52) (see Figure 3a). This hierarchy is particularly relevant for principle-value integrals \mathcal{P} (needed below); these exclude an interval $[-0^+, 0^+]$ around the origin, and γ_0 must lie outside this interval.

Inserting $S_{[1,2]_-}(\epsilon_1, -\epsilon_1) = S_{\text{std}}(\epsilon_1) = \tilde{G}^{\epsilon_1}/(-2\pi i)$ (from Equations (42a) and (51)), we find

$$G^{[n]}(\omega) = - \int_{\epsilon_1} \frac{\tilde{G}^{\epsilon_1}}{\omega_1^{[n]} - \epsilon_1} = - \int_{\epsilon_1} \frac{\tilde{G}_{\epsilon_1^+} - \tilde{G}_{\epsilon_1^-}}{\omega_1^{[n]} - \epsilon_1} = \tilde{G}_{\omega_1^{[n]}} \quad (53)$$

Importantly, no MWFs n_{ϵ_1} occur in Equation (53). For the last step, we were thus able to close the forward (backward) integration contour involving $\tilde{G}_{\epsilon_1^+}$ ($\tilde{G}_{\epsilon_1^-}$) in the upper (lower) half-plane. We then used Cauchy's integral formula for the simple pole at $\omega_1^{[n]}$ (see Figure 3b). Equation (53) expresses the fully retarded Keldysh correlators through analytic continuations of MF correlators, $G^{[n]}[G]$, as desired. To make contact with standard notation, we recall that the retarded and advanced 2p components are given by $G^R = G^{21} = G^{[1]}$ and $G^A = G^{12} = G^{[2]}$. Reinstating frequency dependencies, with $\omega_1^{[1]} = \omega_1 + i\gamma_0 \equiv \omega_1^+$ and $\omega_1^{[2]} = \omega_1 - i\gamma_0 \equiv \omega_1^-$, we get

$$G^R(\omega) = \tilde{G}(\omega_1^+, \omega_2^-), \quad G^A(\omega) = \tilde{G}(\omega_1^-, \omega_2^+) \quad (54)$$

This implies the well-known relation

$$G'^R(\omega) = G^A(\omega), \quad G'^A(\omega) = G^R(\omega) \quad (55)$$

3.3.2. Keldysh Component $G^{[12]}$

For $\alpha = 2$, both Keldysh indices equal 2, $G^{22} = G^{[12]}$. Then, the spectral representation in Equation (27a) requires the kernel (Equation (19c))

$$K^{[\hat{n}_1, \hat{n}_2]}(\omega_p) = (K^{[\hat{n}_1]} - K^{[\hat{n}_2]})(\omega_p) = \tilde{K}(\omega_p^{\hat{n}_1}) - \tilde{K}(\omega_p^{\hat{n}_2}) \quad (56)$$

for the case $[\eta_1 \eta_1] = [12] = [\hat{\eta}_1 \hat{\eta}_2]$. Evaluating this for $p = (12)$ and (21) , we find

$$\begin{aligned} K^{[12]}(\omega_{(12)}) &= \tilde{K}(\omega_{(12)}^{[1]}) - \tilde{K}(\omega_{(12)}^{[2]}) \\ &= \frac{1}{\omega_1^{[1]}} - \frac{1}{\omega_1^{[2]}} = \frac{-2i\gamma_0}{\omega_1^2 + \gamma_0^2} = \hat{\delta}_{\gamma_0}(\omega_1) \end{aligned} \quad (57a)$$

$$\begin{aligned} K^{[12]}(\omega_{(21)}) &= \tilde{K}(\omega_{(21)}^{[2]}) - \tilde{K}(\omega_{(21)}^{[1]}) \\ &= \frac{1}{\omega_2^{[2]}} - \frac{1}{\omega_2^{[1]}} = \frac{-2i\gamma_0}{\omega_2^2 + \gamma_0^2} = \hat{\delta}_{\gamma_0}(\omega_1) \end{aligned} \quad (57b)$$

On the right, we introduced a Lorentzian representation of a broadened Dirac delta function:

$$\hat{\delta}_{\gamma_0}(x) = \frac{-2i\gamma_0}{x^2 + \gamma_0^2}, \quad \lim_{\gamma_0 \rightarrow 0^+} \hat{\delta}_{\gamma_0}(x) = -2\pi i \delta(x) = \hat{\delta}(x) \quad (58)$$

Finally, we obtain $G^{[12]}$ by convolving the kernels (57) with the PSFs (47) according to Equation (27a):

$$\begin{aligned} G^{[12]} &= \sum_p [K^{[12]} * S_p](\omega_p) \\ &= \int_{\varepsilon_1} (2\pi i) S_{[1,2],\varepsilon}(\varepsilon_1, -\varepsilon_1) \hat{\delta}_{\gamma_0}(\omega_1 - \varepsilon_1) \\ &= \int_{\varepsilon_1} [(1 + 2n_{\varepsilon_1}) \tilde{G}^{\varepsilon_1} + 2\hat{\delta}(\varepsilon_1) \hat{G}_1] \hat{\delta}_{\gamma_0}(\omega_1 - \varepsilon_1) \\ &= N_{\omega_1} \tilde{G}^{\omega_1} + 4\pi i \delta(\omega_1) \hat{G}_1 \end{aligned} \quad (59)$$

For the last step we defined

$$N_{\omega_i} = -1 - 2n_{\omega_i} = \coth[\beta\omega_i/2]^{\zeta_i} \quad (60)$$

For bosonic correlators, N_{ω_i} is singular at $\omega_i = 0$, so that a principle-value integral is implied in Equation (59). Then, the product $N_{\omega_i} \tilde{G}^{\omega_i}$ should be evaluated via the limit $(N_{\omega_i} \tilde{G}^{\omega_i})_{\omega_i \rightarrow 0}$. More precisely, three limits are involved: 0^+ , γ_0 , and ω_i should all be sent to zero, while respecting $0^+ \ll \gamma_0 \ll |\omega_i|$ (see discussion after Equation (52)). In the following, we suppress the subscript γ_0 in Equation (58) and always take $\gamma_0 \rightarrow 0^+$ after evaluating a principal-value integral (if present).

Summarizing, all Keldysh components can be expressed through analytically continued MF functions. Comparing Equations (59) and (40), we find that the anomalous part, \hat{G}_1 , enters $G^{[12]}$ with a prefactor of $4\pi i \delta(\omega_1)$. Using our previous results from Equation (54), yielding $\tilde{G}^{\omega_i} = G^R(\omega_i) - G^A(\omega_i)$, and defining $G^{[12]} = G^K$, the above relation (59) can be identified as the FDR

$$G^K(\omega_1) = N_{\omega_1} [G^R(\omega_1) - G^A(\omega_1)] + 4\pi i \delta(\omega_1) \hat{G}_1 \quad (61)$$

Hence, the way in which anomalous MF terms appear in KF correlators is via Keldysh correlator G^K . The anomalous term contributes only if ω_1 is bosonic and vanishes.

We will refer to general relations between components of KF correlators in thermal equilibrium as *generalized fluctuation-*

dissipation relations (gFDRs). Equations (55) and (61) constitute the two gFDRs available for $\ell = 2$. In the absence of anomalous contributions, they reduce the three nonzero KF components to a single independent one (typically chosen as G^R).

4. Analytic Regions and Discontinuities of the MF Correlator

Step 2 of our three-step strategy, the extraction of PSFs, requires knowledge of possible singularities of the MF correlators. In the 2p case, for \tilde{G}_{z_i} , a branch cut divides the complex z_i plain into two analytic regions (see Figure 2a), and the discontinuity across the branch cut is given by the difference of the analytic continuations $\tilde{G}_{\omega_i^\pm}$. In this section, we generalize the concepts of and notations for branch cuts, analytic regions, and discontinuities to general ℓ , enabling a concise discussion of the analytic continuation of 3p and 4p MF correlators in Sections 5 and 6, respectively. We focus on the regular parts \tilde{G} of the MF correlators; the anomalous parts will be discussed separately in the sections for $\ell = 3$ and 4.

4.1. Analytic Regions of $\tilde{G}(z)$

Possible singularities of the regular part can be inferred from the spectral representation in Equation (14d)

$$\tilde{G}(z) = \int d^\ell \varepsilon_p \delta(\varepsilon_{\bar{1}\dots\bar{\ell}}) \sum_p \frac{S_p(\varepsilon_p)}{\prod_{i=1}^{\ell-1} (z_{\bar{1}\dots\bar{i}} - \varepsilon_{\bar{1}\dots\bar{i}})} \quad (62)$$

with $z_i = \omega_i + i\gamma_i$ and $z_{1\dots\ell} = 0$. Singularities can be located at the points where the imaginary part of the denominator vanishes, defining branch cuts by the condition

$$\text{Im}(z_I) = \gamma_I = 0 \quad (63)$$

where $z_I = \sum_{i \in I} z_i$ denotes a frequency sum over the elements of a non-empty subset $I \subseteq \{1, \dots, \ell\}$. In total, condition (63) defines $2^{\ell-1} - 1$ distinct branch cuts since frequency conservation implies $\text{Im}(z_I) = -\text{Im}(z_{I^c})$ where $I^c = \{1, \dots, \ell\} \setminus I$ is the complement of I , so that $\text{Im}(z_I) = 0$ and $\text{Im}(z_{I^c}) = 0$ describe the same branch cut. The branch cuts divide C^ℓ into regions of analyticity (regions without singularities), each corresponding to one particular analytic continuation of \tilde{G} .

We henceforth focus on the case, needed for Equation (27b), that all arguments of $\tilde{G}(z)$ are real, up to infinitesimal shifts. To be specific, we take the imaginary shifts of the frequency sums z_I to be infinitesimal, $|\gamma_I| = 0^+$ (with signs determined via conventions described below). Then, $\tilde{G}(z)$ is a function of $\ell - 1$ independent real frequencies ω_i , and the analytic region is indicated by including the $2^{\ell-1} - 1$ shift directions $\gamma_I = \pm 0^+$ in the argument of $\tilde{G}(z)$. Thus, for 2p, 3p, and 4p correlators, we need 1, 3, and 7 imaginary parts, respectively (see examples below for $\ell = 3, 4$ in Equations (65) and (66)).

For a compact presentation of our results, it is convenient to introduce notation that specifies all imaginary shifts via a $(\ell - 1)$ -tuple \check{z} whose components $\check{z}_i = \check{\omega}_i + i\check{\gamma}_i$ are frequency sums of the form $\check{z}_i = z_{I_i}$. Then, the argument of $\tilde{G}(z)$ is expressed as $z(\check{z})$, and the imaginary shifts of z are determined by those chosen for

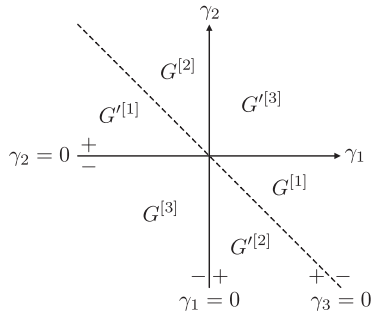


Figure 4. Regions of analyticity of regular 3p MF correlators. Lines with $\gamma_i = 0$ denote possible branch cuts of the correlators. (Figure adapted from ref. [17].) We label each region by that specific Keldysh correlator, $G^{[n]}$ or $G'^{[n]}$, whose imaginary shifts γ_i lie within that region: For $G^{[1]}$, only ω_1 has a positive imaginary shift, i.e., $\gamma_1 > 0$, $\gamma_2 < 0$, and $\gamma_3 < 0$, implying $G^{[1]}(\omega) = \tilde{G}(\omega_1^+, \omega_2^-, \omega_3^-)$. Primed correlators (Equations (25)) have inverted imaginary shifts, such that $G'^{[1]}(\omega) = \tilde{G}(\omega_1^-, \omega_2^+, \omega_3^+)$.

\check{z} . We will specify the $\ell - 1$ independent frequencies \check{z} chosen to parametrize $z(\check{z})$ using subscripts, $\tilde{G}_z = \tilde{G}(z(\check{z}))$, extending the subscript notation developed in Section 3.1 for $\ell = 2$ to the regular parts of ℓ p correlators. To uniquely determine the imaginary shifts in $z_i(\check{z})$, and hence the analytic region for \tilde{G}_z , we implicitly assign imaginary shifts to all \check{z}_i via the rule

$$2|\check{\gamma}_{i-1}| \leq |\check{\gamma}_i|, \quad \text{for } 1 < i < \ell \quad (64)$$

It ensures that the imaginary part of any $\text{Im}z_i$ is always nonzero, and that its sign is specified uniquely through the sign choices made for the shifts $\pm|\check{\gamma}_i|$. We specify these sign choices using superscripts on the corresponding real frequencies $\check{\omega}_i$, writing $\check{z}_i = \check{\omega}_i^\pm = \check{\omega}_i \pm i|\check{\gamma}_i|$.

Examples for $\ell = 3$: For $\ell = 3$, the branch cuts are given by $\gamma_1 = 0$, $\gamma_2 = 0$, and $\gamma_3 = 0$, see Figure 4. Therefore, three imaginary parts are required to uniquely identify one analytic region for a regular MF correlator $\tilde{G}(z)$, with $z = (z_1, z_2, z_3)$ and $z_i = \omega_i^\pm$. Consider, e.g., the set of independent frequencies $\check{z} = (\omega_1^+, \omega_2^-)$ with infinitesimal imaginary shifts fulfilling Equation (64). It yields the analytic continuation (see Figure 4 for the labels of analytic regions):

$$\tilde{G}_{\omega_1^+, \omega_2^-} = \tilde{G}(\omega_1^+, \omega_2^-, -\omega_{12}^-) = \tilde{G}(\omega_1^+, \omega_2^-, \omega_3^+) = G'^{[2]}(\omega) \quad (65a)$$

The third argument, $z_3 = -z_{12} = -\check{z}_1 - \check{z}_2 = -\omega_1^+ - \omega_2^-$, has a positive imaginary shift since $\text{Im}(z_3) = -\text{Im}(|\check{\gamma}_1| - |\check{\gamma}_2|) > 0$, by Equation (64). By contrast, for $\check{z} = (\omega_2^-, \omega_1^+)$, we obtain

$$\tilde{G}_{\omega_2^-, \omega_1^+} = \tilde{G}(\omega_1^+, \omega_2^-, -\omega_{12}^+) = \tilde{G}(\omega_1^+, \omega_2^-, \omega_3^-) = G^{[1]}(\omega) \quad (65b)$$

Evidently, $\tilde{G}_{\omega_2^-, \omega_1^+} \neq \tilde{G}_{\omega_1^+, \omega_2^-}$, because switching $\omega_1^+ \rightarrow \omega_2^-$ in the argument list of \check{z} also switches the relative magnitudes of their imaginary parts, due to Equation (64).

Note that the representation via subscripts is not unique. For instance, $G^{[1]}(\omega)$ can also be written as $\tilde{G}_{\omega_{12}^+, \omega_1^+}$, since the subscript $\check{z} = (\omega_{12}^+, \omega_1^+)$ yields $z(\check{z}) = (\omega_1^+, \omega_{12}^+ - \omega_1^+, -\omega_{12}^+) = (\omega_1^+, \omega_2^-, \omega_3^-)$, matching the arguments found in Equation (65b).

For the last step, the sign of the imaginary shift of the second argument follows from $\text{Im}(z_2) = \text{Im}(\omega_{12}^+ - \omega_1^+) = |\check{\gamma}_1| - |\check{\gamma}_2| < 0$.

Example for $\ell = 4$: For $\ell = 4$, the branch cuts are located at vanishing $\gamma_1, \gamma_2, \gamma_3, \gamma_4, \gamma_{12}, \gamma_{13}$, and γ_{14} , see Figure 5. Thus, seven imaginary parts are needed to uniquely identify one analytic region for a regular MF correlator $\tilde{G}(z)$. We therefore write its argument as $z = (z_1, z_2, z_3, z_4; z_{12}, z_{13}, z_{14})$, with $z_i = \omega_i^\pm$, also listing the arguments after the semicolon since the signs of their imaginary parts are needed to fully specify the analytic region. Consider, e.g., $\check{z} = (\omega_{13}^+, \omega_2^-, \omega_3^+)$. Then, $z_4 = -z_{123} = -\check{z}_1 - \check{z}_2 = -\omega_{13}^+ - \omega_2^- = -\omega_{123}^- = \omega_4^+$, $z_{12} = \check{z}_1 + \check{z}_2 - \check{z}_3 = \omega_{13}^+ + \omega_2^- - \omega_3^+ = \omega_{12}^-$, and $z_{14} = -z_{23} = -z_2 - z_3 = -\omega_2^- - \omega_3^+ = -\omega_{23}^+$; the signs of the imaginary shifts on the right sides follow via Equation (64). We thus obtain

$$\begin{aligned} \tilde{G}_{\omega_{13}^+, \omega_2^-, \omega_3^+} &= \tilde{G}(\omega_1^-, \omega_2^-, \omega_3^+, -\omega_{123}^-, \omega_{12}^-, \omega_{13}^+, -\omega_{23}^+) \\ &= \tilde{G}(\omega_1^-, \omega_2^-, \omega_3^+, \omega_4^+; \omega_{12}^-, \omega_{13}^+, \omega_{14}^-) = C_{1V}^{(34)} \end{aligned} \quad (66)$$

In the last line, the frequency arguments were expressed through those used to label the analytic regions in Figure 5.

4.2. Discontinuities of $\tilde{G}(z)$

The discontinuity of $\tilde{G}(z)$ across a given branch cut, defined by $\text{Im}z_i = \gamma_i = 0$, quantifies the difference between two neighboring analytic regions, R_+ and R_- , separated by $\gamma_i = 0$. We denote this discontinuity by $\tilde{G}(z^{R_+}) - \tilde{G}(z^{R_-})$. Explicitly, we have opposite imaginary shifts γ_i in the analytic regions, $\gamma_i^{R_+} = 0^+ = -\gamma_i^{R_-}$, and equivalent shifts for all other $\gamma_j^{R_+} = \gamma_j^{R_-}$ with $J \subsetneq \{1, \dots, \ell\}$ and $J \neq I$. To describe this discontinuity using \check{z} notation, we write $\check{z}^{R_\pm} = (\check{z}^{R_\pm}, \check{z}^r)$, where the first variable is chosen as the one whose imaginary part changes sign across the branch cut, $\check{z}_1^{R_\pm} = \omega_I^\pm$, and \check{z}^r denotes a tuple of $\ell - 2$ other, independent frequencies, with imaginary shifts given by the prescription (64). Then, extending the superscript notation from Section 3.1, we can express the discontinuity of $\tilde{G}(z)$ across $\text{Im}z_i = 0$ as

$$\tilde{G}_{\check{z}^r}^{\omega_I} = \tilde{G}_{\omega_I^+, \check{z}^r} - \tilde{G}_{\omega_I^-, \check{z}^r} = \tilde{G}_{\check{z}^{R_+}} - \tilde{G}_{\check{z}^{R_-}} \quad (67)$$

Similarly, we define consecutive discontinuities across two branch cuts, $\gamma_i = 0$ and $\gamma_j = 0$, to be evaluated as

$$\tilde{G}_{\check{z}_3, \dots, \check{z}_{\ell-1}}^{\omega_1, \omega_j} = \tilde{G}_{\omega_1^+, \check{z}_3, \dots, \check{z}_{\ell-1}}^{\omega_j} - \tilde{G}_{\omega_j^-, \check{z}_3, \dots, \check{z}_{\ell-1}}^{\omega_1} \quad (68)$$

where we have $\check{z}_1 = \omega_i^+$ and $\check{z}_2 = \omega_j^+$.

Examples for $\ell = 3$: For a discontinuity across $\gamma_2 = 0$ and $\check{z}^r = \omega_1^+$, we find

$$\begin{aligned} \tilde{G}_{\omega_1^+}^{\omega_2} &= \tilde{G}_{\omega_2^+, \omega_1^+} - \tilde{G}_{\omega_2^-, \omega_1^+} \\ &= \tilde{G}(\omega_1^+, \omega_2^+, -\omega_{12}^+) - \tilde{G}(\omega_1^+, \omega_2^-, -\omega_{12}^+) \\ &= \tilde{G}(\omega_1^+, \omega_2^+, \omega_3^-) - \tilde{G}(\omega_1^+, \omega_2^-, \omega_3^-) \\ &= G'^{[3]}(\omega) - G^{[1]}(\omega) \end{aligned} \quad (69)$$

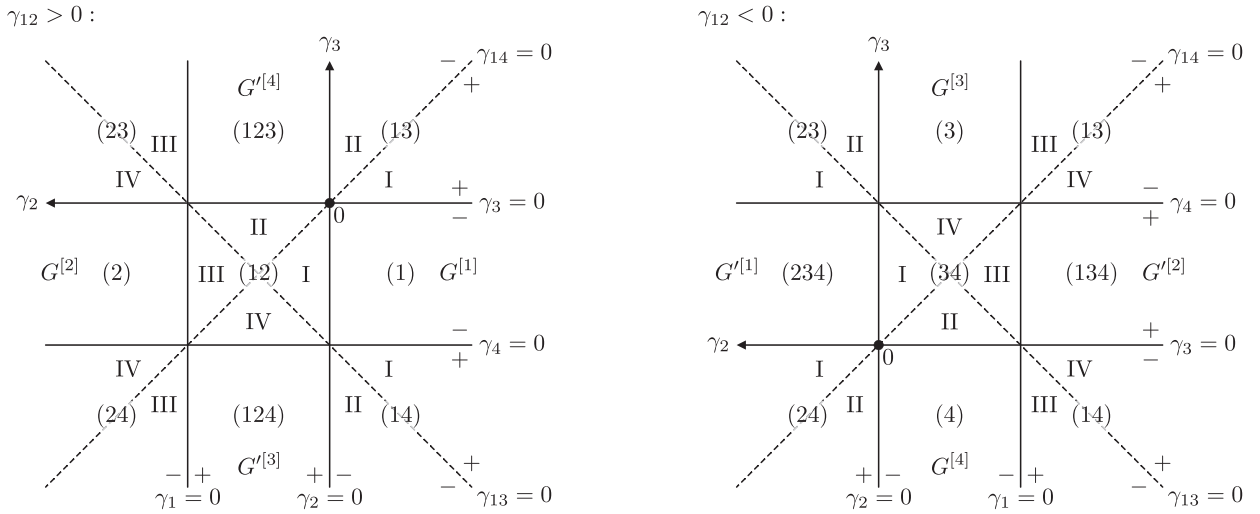


Figure 5. Regions of analyticity of regular 4p MF correlators (analogous to ref. [13]). Lines with $\text{Im } z_i = \gamma_i = 0$ and $\text{Im } z_{ij} = \gamma_{ij} = 0$ denote possible branch cuts. The rectangular regions are labeled by arabic numbers indicating which γ_i are positive; e.g., for region (124), we have $\gamma_1, \gamma_2, \gamma_4 > 0$ but $\gamma_3 < 0$. Consequently, regions composed of one or three arabic numbers correspond to fully retarded or advanced Keldysh components. Regions with two of the γ_i positive, like region (12), are further divided into four subregions by the branch cuts in γ_{ij} and are distinguished by roman numbers I–IV.

Two consecutive discontinuities across, e.g., $\gamma_1 = 0$ and $\gamma_2 = 0$ yield

$$\begin{aligned} \tilde{G}^{\omega_1, \omega_2} &= \tilde{G}_{\omega_2^+}^{\omega_1} - \tilde{G}_{\omega_2^-}^{\omega_1} = \tilde{G}_{\omega_1^+, \omega_2^+} - \tilde{G}_{\omega_1^+, \omega_2^-} - \tilde{G}_{\omega_1^-, \omega_2^+} + \tilde{G}_{\omega_1^-, \omega_2^-} \\ &= \tilde{G}(\omega_1^+, \omega_2^+, -\omega_{12}^+) - \tilde{G}(\omega_1^+, \omega_2^+, -\omega_{12}^-) \\ &\quad - \tilde{G}(\omega_1^+, \omega_2^-, -\omega_{12}^-) + \tilde{G}(\omega_1^-, \omega_2^-, -\omega_{12}^-) \\ &= G^{[3]} - G^{[2]} - G^{[2]} + G^{[3]} \end{aligned} \quad (70)$$

Example for $\ell = 4$: The discontinuity for, e.g., $\gamma_{123} = 0$ and $\tilde{z}^r = (\omega_3^+, \omega_1^-)$ evaluates to

$$\begin{aligned} \tilde{G}_{\omega_3^+, \omega_1^-}^{\omega_{123}} &= \tilde{G}_{\omega_{123}^+, \omega_3^+, \omega_1^-} - \tilde{G}_{\omega_{123}^-, \omega_3^+, \omega_1^-} \\ &= \tilde{G}(\omega_1^-, \omega_2^+, \omega_3^+, -\omega_{123}^+; \omega_{12}^-, \omega_{13}^-, -\omega_{23}^-) \\ &\quad - \tilde{G}(\omega_1^-, \omega_2^+, \omega_3^+, -\omega_{123}^-; \omega_{12}^-, \omega_{13}^-, -\omega_{23}^-) \\ &= C_1^{(23)} - C^{(234)} \end{aligned} \quad (71)$$

5. Analytic Continuation of 3p Correlators

The notation introduced in the previous section enables a concise discussion of the analytic continuation of 3p MF correlators in the following. Section 5.1 is devoted to the general structure of these correlators and the connection of their analytical continuations to 3p PSFs. In contrast to the 2p case, the derivation of these PSFs, constituting Steps 1 and 2 of our three-step strategy, is discussed in Appendix C.2; in the main text, we merely state the final result. In Section 5.2, we show that the PSFs yield all components of the KF correlator as linear combinations of analytically continued MF correlators.

5.1. Extraction of PSFs

A general 3p correlator can be decomposed into a regular and various anomalous parts (see Equation (A5) and Appendix C.1):

$$\begin{aligned} G(i\omega_1, \omega_2) &= G_{i\omega_1, i\omega_2} \\ &= \tilde{G}_{i\omega_1, i\omega_2} + \beta \delta_{i\omega_1} \hat{G}_{1, i\omega_2} + \beta \delta_{i\omega_2} \hat{G}_{2, i\omega_1} \\ &\quad + \beta \delta_{i\omega_2} \hat{G}_{12, i\omega_1} + \beta^2 \delta_{i\omega_1} \delta_{i\omega_2} \hat{G}_{1, 2} \end{aligned} \quad (72)$$

Here, \tilde{G} denotes the regular part, whereas \hat{G}_i represents the anomalous part w.r.t. frequency $i\omega_i$, i.e., \hat{G}_i comes with a factor of $\beta \delta_{i\omega_i}$ and is independent of $i\omega_i$. $\hat{G}_{1,2}$ is anomalous w.r.t. all frequencies and is a frequency-independent constant. (Note that, e.g., $\beta \delta_{i\omega_3} \hat{G}_3$ can be written as $\beta \delta_{i\omega_{12}} \hat{G}_{12}$ in the $\beta \delta$ expansion in Equation (72), implying relations like $\hat{G}_{12} = \hat{G}_3$. This unbiased notation allows us to write formulas that hold for any permutation p .)

The full correlator G as well as the components \tilde{G} and \hat{G}_i are, by definition, singularity-free for all Matsubara frequencies. For the anomalous contributions, we further have the decomposition

$$\hat{G}_{3; i\omega_1} = \hat{G}_{3; i\omega_1}^{\Delta} + \Delta_{i\omega_1} \hat{G}_{3; 1}^{\Delta} \quad (73)$$

where $\Delta_{i\omega_1}$ is defined in Equation (32) for a purely imaginary $\Omega_i = i\omega_i$. Here, $\hat{G}_{3; 1}^{\Delta}$ comprises all terms proportional to a $\Delta_{i\omega_1}$ symbol, and $\hat{G}_{3; i\omega_1}^{\Delta}$ contains the rest. Analogous definitions hold for all anomalous terms \hat{G}_i , see Appendix C.1 for a detailed discussion. The distinction between \hat{G}_i^{Δ} and \hat{G}_i^{Δ} is only needed if all three operators are bosonic, in which case all anomalous terms in Equation (72) can occur. For two fermionic and one bosonic

operator, all following results equally hold by replacing $\hat{G}_i^{\Delta} \rightarrow \hat{G}_i$ and $\hat{G}_i^{\Delta} \rightarrow 0$.

In Appendix C.2, we show that the PSFs can be expressed via analytic continuations of the general constituents of the 3p correlator [Equation (72)]:

$$(2\pi i)^2 S_p(\varepsilon_{\bar{1}}, \varepsilon_{\bar{2}}) = n_{\varepsilon_{\bar{1}}} n_{\varepsilon_{\bar{2}}} \tilde{G}^{\varepsilon_{\bar{1}}, \varepsilon_{\bar{2}}} + n_{\varepsilon_{\bar{1}}} n_{\varepsilon_{\bar{1}\bar{2}}} \tilde{G}^{\varepsilon_{\bar{1}\bar{2}}, \varepsilon_{\bar{1}}} + \hat{\delta}(\varepsilon_{\bar{1}}) n_{\varepsilon_{\bar{2}}} \hat{G}_{\bar{1}}^{\Delta, \varepsilon_{\bar{2}}} + \hat{\delta}(\varepsilon_{\bar{2}}) n_{\varepsilon_{\bar{1}}} \hat{G}_{\bar{2}}^{\Delta, \varepsilon_{\bar{1}}} + \hat{\delta}(\varepsilon_{\bar{3}}) n_{\varepsilon_{\bar{1}}} \hat{G}_{\bar{3}}^{\Delta, \varepsilon_{\bar{1}}} + \hat{\delta}(\varepsilon_{\bar{1}}) \hat{\delta}(\varepsilon_{\bar{2}}) \left(\hat{G}_{\bar{1}\bar{2}}^{\Delta} - \frac{1}{2} \hat{G}_{\bar{3}\bar{1}}^{\Delta} \right) \quad (74)$$

This is our main result for $\ell = 3$. Explicit expressions of the PSFs for individual permutations are obtained by inserting the permuted indices into the above equation. In Equations (C26), we provide an overview of all possibly occurring discontinuities expressed through the analytic regions in Figure 4. As for 2p PSFs, we provide a consistency check of Equation (74) in Appendix G.

5.2. 3p Keldysh Correlators

In the following two sections, we demonstrate how to construct KF correlators as linear combinations of analytically continued MF correlators using the PSFs in Equation (74), corresponding to Step 3 of our strategy. For $\alpha = 1$, Equation (23) gives the analytic continuation of G to fully retarded components $G^{[n]}$ for general ℓ . Therefore, we directly consider the more challenging cases of $\alpha = 2, 3$ in Sections 5.2.1 and 5.2.2, respectively. Lastly, in Section 5.2.3 we provide an overview of all Keldysh components and present gFDRs.

5.2.1. Keldysh Components $G^{[n_1 n_2]}$

To recapitulate, in Section 3.3.2 we performed manipulations on the level of the Keldysh kernels for $\ell = 2$ and $\alpha = 2$ by using the identity (58), which directly allowed us to evaluate the convolution with the PSFs. Even though the kernels for $\ell = 3$ are more complicated due to an additional factor in the denominator (see Equation (19d)), similar manipulations are presented in Appendix C.3.1 for the Keldysh component $G^{212} = G^{[13]}$. There, it is shown that simplifications of the 3p KF kernel $K^{[n_1 n_2]}$ (Equation (19c)) yield

$$G^{[13]}(\omega) = \int_{\varepsilon_1, \varepsilon_2} \hat{\delta}(\omega_1 - \varepsilon_1) \frac{(2\pi i)^2}{\omega_2^- - \varepsilon_2} S_{[1, [2, 3]_{-}]_+}(\varepsilon_1, \varepsilon_2, -\varepsilon_{12}) - \int_{\varepsilon_1, \varepsilon_2} \hat{\delta}(\omega_{12} - \varepsilon_{12}) \frac{(2\pi i)^2}{\omega_2^- - \varepsilon_2} S_{[[1, 2]_{-}, 3]_+}(\varepsilon_1, \varepsilon_2, -\varepsilon_{12}) \quad (75)$$

Similarly to the 2p case, we always display the unpermuted ε for PSF (anti)commutators and insert permuted ε_p only for individual PSFs, implying, e.g., $S_{[2, 3]_{-}]_+}(\varepsilon) = S_{(231)}(\varepsilon_2, \varepsilon_3) \pm S_{(213)}(\varepsilon_2, \varepsilon_1)$. For the integrations in Equation (75), we fixed the two independent frequencies ε_1 and ε_2 as integration variables. We thus ob-

tain, e.g.,

$$S_{[1, [2, 3]_{-}]_+}(\varepsilon) = S_{[1, 2, 3]_{-}}(\varepsilon) + S_{[2, 3]_{-} 1}(\varepsilon) = S_{(123)}(\varepsilon_1, \varepsilon_2) - S_{(132)}(\varepsilon_1, \varepsilon_3) + S_{(231)}(\varepsilon_2, \varepsilon_3) - S_{(321)}(\varepsilon_3, \varepsilon_2) \quad (76)$$

with $\varepsilon_3 = -\varepsilon_{12}$ being understood.

To relate the KF to the MF correlator, we insert Equation (74) into the PSF (anti)commutators of Equation (76) and simplify the results using relations for the discontinuities such as $\tilde{G}^{\varepsilon_2, \varepsilon_3} = -\tilde{G}^{\varepsilon_2, \varepsilon_1}$. Such identities follow by explicitly expressing the discontinuities in terms of $G^{[n]}$ and $G'^{[n]}$ correlators (see Equations (C26)). Then, the PSF (anti)commutator in Equation (76), e.g., reads

$$(2\pi i)^2 S_{[1, [2, 3]_{-}]_+}(\varepsilon_1, \varepsilon_2, -\varepsilon_{12}) = N_{\varepsilon_1} \tilde{G}^{\varepsilon_1, \varepsilon_2} - 2\hat{\delta}(\varepsilon_1) \hat{G}_1^{\Delta, \varepsilon_2} - 2\hat{\delta}(\varepsilon_1) \hat{\delta}(\varepsilon_2) \hat{G}_{1,2}^{\Delta} \quad (77)$$

Inserting Equation (77) (and a similar expression for $S_{[[1, 2]_{-}, 3]_+}$, see Equation (C31b)) into Equation (75) and evaluating one of the integrals via the δ -function, we find

$$G^{[13]}(\omega) = -N_{\omega_1} \int_{\varepsilon_2} \frac{\tilde{G}^{\omega_1, \varepsilon_2}}{\omega_2^- - \varepsilon_2} + 2\hat{\delta}(\omega_1) \left(\int_{\varepsilon_2} \frac{\hat{G}_1^{\Delta, \varepsilon_2}}{\omega_2^- - \varepsilon_2} - \frac{\hat{G}_{1,2}^{\Delta}}{\omega_2^-} \right) - N_{\omega_{12}} \int_{\varepsilon_2} \frac{\tilde{G}^{\omega_{12}, \varepsilon_2}}{\omega_2^- - \varepsilon_2} + 2\hat{\delta}(\omega_{12}) \left(\int_{\varepsilon_2} \frac{\hat{G}_3^{\Delta, \varepsilon_2}}{\omega_2^- - \varepsilon_2} - \frac{\hat{G}_{3,2}^{\Delta}}{\omega_2^-} \right) \quad (78)$$

Here, it becomes apparent why collecting PSFs in terms of (anti)commutators is beneficial. The integrands in Equation (78) do not contain any MWFs depending on the integration variable ε_2 , so that the only pole away from $\text{Im}(z_2) = 0$ comes from the denominators. Consequently, the integrals over ε_2 can be evaluated by closing the forward/backward integration contours in the upper/lower half-planes. Then, only the pole at $z_2 = \omega_2^-$ contributes (as illustrated in Figure 3 for the integral in Equation (53)), and the final result for the Keldysh correlator $G^{[13]}$ reads

$$G^{[13]} = N_{\omega_1} \tilde{G}_{\omega_2^-}^{\omega_1} + N_{\omega_{12}} \tilde{G}_{\omega_2^-}^{\omega_{12}} + 4\pi i \delta(\omega_1) \hat{G}_{1, \omega_2^-} + 4\pi i \delta(\omega_{12}) \hat{G}_{3, \omega_2^-} = N_{\omega_1} (G'^{[2]} - G^{[3]}) + N_{\omega_3} (G'^{[2]} - G^{[1]}) + 4\pi i \delta(\omega_1) \hat{G}_1^{[3]} + 4\pi i \delta(\omega_3) \hat{G}_3^{[1]} \quad (79)$$

Here, we used $N_{\omega_{12}} = -N_{\omega_3}$, expressed $\tilde{G}_{\omega_2^-}^{\omega_1}$ and $\tilde{G}_{\omega_2^-}^{\omega_{12}}$ in terms of the analytic regions in Figure 4, and defined the shorthand

$$\hat{G}_{i, \omega_j^\pm} = \hat{G}_{i, \omega_j^\pm}^{\Delta} + \frac{\hat{G}_{ij}^{\Delta}}{\omega_j^\pm} \quad (80)$$

We emphasize that Equation (80) should not be interpreted as a direct analytic continuation of Equation (73). Rather, it can

be obtained from Equation (73) by replacing $\Delta_{i\omega_j} \rightarrow 1/(i\omega_j)$ and only afterwards analytically continuing the resulting expression $i\omega_j \rightarrow \omega_j^\pm$. Additionally, we defined the shorthand $\hat{G}_i^{[n]} = \hat{G}_i(\omega^{[n]})$, such that, e.g., $\hat{G}_{1;\omega_2^-} = \hat{G}_{1;\omega_2^+} = \hat{G}_1^{[3]}$. The other two Keldysh components with $\alpha = 2$, $G^{[12]}$ and $G^{[23]}$, can be derived similarly, and their results are shown in Equations (84a) and (84c), respectively.

5.2.2. Keldysh Component $G^{[123]}$

In this section, we relate the Keldysh component $G^{[123]}$ to the analytic continued MF correlator. In the derivation of Equation (78), using the identity (58) for the $\alpha = 2$ kernel $K^{[\hat{n}_1, \hat{n}_2]}$ was essential. However, the Keldysh kernel for $G^{[123]}$, $K^{[\hat{n}_1, \hat{n}_2, \hat{n}_3]}$, involves three retarded kernels according to Equation (19c), impeding the direct application of Equation (58).

In Appendix C.3.2, we show that this problem can be circumvented by subtracting a fully retarded component, say, $G^{[3]}$. An analysis of the spectral representation of $G^{[123]} - G^{[3]}$ then leads to

$$\begin{aligned} & \frac{1}{(2\pi i)^2} (G^{[123]} - G^{[3]})(\omega) \\ &= \int_{\varepsilon_1, \varepsilon_2} \hat{\delta}(\omega_1 - \varepsilon_1) \hat{\delta}(\omega_2 - \varepsilon_2) S_{[[1,2],+,3],+}(\varepsilon_1, \varepsilon_2, -\varepsilon_{12}) \\ &+ \int_{\varepsilon_1, \varepsilon_2} \hat{\delta}(\omega_1 - \varepsilon_1) \frac{1}{\omega_2^- - \varepsilon_2} S_{[1,[2,3],-]}(\varepsilon_1, \varepsilon_2, -\varepsilon_{12}) \\ &+ \int_{\varepsilon_1, \varepsilon_2} \hat{\delta}(\omega_2 - \varepsilon_2) \frac{1}{\omega_1^- - \varepsilon_1} S_{[2,[1,3],-]}(\varepsilon_1, \varepsilon_2, -\varepsilon_{12}) \end{aligned} \quad (81)$$

Similar to Equations (76) and (78), we evaluate the PSF (anti)commutators by inserting Equation (74) (see Equation (C36)), and subsequently evaluate the integrals either via the δ -functions or via Cauchy's integral formula, yielding

$$\begin{aligned} & (G^{[123]} - G^{[3]})(\omega) \\ &= (1 + N_{\omega_1} N_{\omega_2}) \tilde{G}^{\omega_2, \omega_1} + N_{\omega_{12}} N_{\omega_1} \tilde{G}^{\omega_{12}, \omega_1} + \tilde{G}_{\omega_2}^{\omega_1} + \tilde{G}_{\omega_1}^{\omega_2} \\ &+ 4\pi i \delta(\omega_1) N_{\omega_2} \hat{G}_1^{\hat{\alpha}, \omega_2} + 4\pi i \delta(\omega_2) N_{\omega_1} \hat{G}_2^{\hat{\alpha}, \omega_1} \\ &+ 4\pi i \hat{\delta}(\omega_{12}) N_{\omega_1} \hat{G}_3^{\hat{\alpha}, \omega_1} + (4\pi i)^2 \delta(\omega_1) \delta(\omega_2) \hat{G}_{1,2} \end{aligned} \quad (82)$$

A more symmetric form of this result (see Equation (84d)) can be obtained by expressing all discontinuities in terms of the analytic regions in Figure 4 and applying the identity

$$1 + N_{\omega_1} N_{\omega_2} + N_{\omega_1} N_{\omega_3} + N_{\omega_2} N_{\omega_3} = 0 \quad (83)$$

which holds for $\ell = 3$ due to frequency conservation.

5.2.3. 3p Generalized Fluctuation-Dissipation Relations

Expressing all Keldysh components with $\alpha \geq 2$ through analytic continuations of MF correlators is equivalent to relating them to

fully retarded and advanced components. Indeed, as in the 2p case, knowledge of the fully retarded and advanced components *and* the anomalous terms suffices to obtain all Keldysh components, as brought to bear by the 3p gFDRs (where $N_i = N_{\omega_i}$)

$$\begin{aligned} G^{[12]} &= N_1 (\tilde{G}'^{[3]} - \tilde{G}^{[2]}) + N_2 (\tilde{G}'^{[3]} - \tilde{G}^{[1]}) \\ &+ 4\pi i \delta(\omega_1) \hat{G}_1^{[2]} + 4\pi i \delta(\omega_2) \hat{G}_2^{[1]} \end{aligned} \quad (84a)$$

$$\begin{aligned} G^{[13]} &= N_1 (\tilde{G}'^{[2]} - \tilde{G}^{[3]}) + N_3 (\tilde{G}'^{[2]} - \tilde{G}^{[1]}) \\ &+ 4\pi i \delta(\omega_1) \hat{G}_1^{[3]} + 4\pi i \delta(\omega_3) \hat{G}_3^{[1]} \end{aligned} \quad (84b)$$

$$\begin{aligned} G^{[23]} &= N_2 (\tilde{G}'^{[1]} - \tilde{G}^{[3]}) + N_3 (\tilde{G}'^{[1]} - \tilde{G}^{[2]}) \\ &+ 4\pi i \delta(\omega_2) \hat{G}_2^{[3]} + 4\pi i \delta(\omega_3) \hat{G}_3^{[2]} \end{aligned} \quad (84c)$$

$$\begin{aligned} G^{[123]} &= N_2 N_3 G^{[1]} + N_1 N_3 G^{[2]} + N_1 N_2 G^{[3]} \\ &+ (1 + N_2 N_3) G'^{[1]} + (1 + N_1 N_3) G'^{[2]} + (1 + N_1 N_2) G'^{[3]} \\ &+ 4\pi i \left[\delta(\omega_1) N_2 (\hat{G}_1^{\hat{\alpha}, [2]} - \hat{G}_1^{\hat{\alpha}, [3]}) + \delta(\omega_2) N_3 (\hat{G}_2^{\hat{\alpha}, [3]} - \hat{G}_2^{\hat{\alpha}, [1]}) \right. \\ &\left. + \delta(\omega_3) N_1 (\hat{G}_3^{\hat{\alpha}, [1]} - \hat{G}_3^{\hat{\alpha}, [2]}) \right] + (4\pi i)^2 \delta(\omega_1) \delta(\omega_2) \hat{G}_{1,2} \end{aligned} \quad (84d)$$

These gFDRs agree with the results in ref. [24], and generalize those by also including anomalous contributions. Applications of these formulas to the Hubbard atom are presented in Section 7.

6. Analytic Continuation of 4p Correlators

In this section, we demonstrate the MF-to-KF analytic continuation of fermionic 4p correlators. In Section 6.1, we first discuss our convention for labelling analytic regions and provide the expression of PSFs in terms of analytically continued MF correlators. In Section 6.2, we then generalize the key concept for the construction of 3p KF correlators, namely rewriting the KF spectral representation using kernel identities and PSF (anti)commutators, to arbitrary ℓ , and apply it to the relevant case $\ell = 4$.

6.1. Analytic Regions and Extraction of PSFs

As discussed in Section 4.1, the possible singularities of a regular 4p MF correlator are located at seven branch cuts, splitting the complex plane into a total of 32 regions (see Figure 5). Importantly, for $\ell \geq 4$, only few of these regions correspond to fully retarded or advanced Keldysh components, in contrast to $\ell = 2, 3$. We label analytic continuations of MF correlators by C , e.g.,

$$\tilde{G}(\omega_1^+, \omega_2^-, \omega_3^+, \omega_4^-, \omega_{12}^-, \omega_{13}^+, \omega_{14}^-) = C_{\text{III}}^{(13)} \quad (85)$$

The superscript of $C_{\text{III}}^{(13)}$ indicates which ω_i (with $1 \leq i \leq 4$) have a positive imaginary shift. Analytic regions with two ω_i 's having positive shifts are further divided into four subregions, denoted by roman numbers I – IV in the subscripts of C . This is necessary because for $C_{\text{III}}^{(13)}$, e.g., the superscripts do not uniquely determine

the imaginary parts of $\omega_1^+ + \omega_2^- = \omega_{12}^\pm$ and $\omega_1^+ + \omega_4^- = \omega_{14}^\pm$. Fully retarded or advanced Keldysh components, on the other hand, are directly related to analytic regions, $G^{(i)} = C^{(i)}$ with $i = \eta$ and $G^{(i)} = C^{(i)}$ with $i, j, k \neq \eta$, as depicted in Figure 5.

Priming correlators, i.e., complex conjugation of the imaginary parts of frequencies (Equation (25)), is directly applicable to the analytic regions. Consider, e.g., $C^{(1)}$, where only ω_1 has a positive imaginary part; then, priming $C^{(1)}$ yields $(C^{(1)})' = (G^{(1)})' = G^{(1)} = C^{(234)}$, where only ω_1 has a negative imaginary part. The roman subscripts are chosen such that they are unaffected by complex conjugation of imaginary parts, so that, e.g., $(C_{11}^{(14)})' = C_{11}^{(23)}$.

Finally, we note that double bosonic discontinuities, e.g., $\tilde{G}_{\omega_1^+}^{\omega_{13}, \omega_{14}}$, vanish since the fermionic 4p kernel contains only one bosonic frequency, see Appendix E.1.2. This implies that not all analytic regions displayed in Figure 5 are independent, since the following relations hold:

$$C_1^{(ij)} - C_{11}^{(ij)} + C_{111}^{(ij)} - C_{1111}^{(ij)} = 0, \quad \text{with } 1 \leq i < j \leq 4 \quad (86)$$

The identity for $(ij) = (12)$, e.g., follows from $\tilde{G}_{\omega_1^+}^{\omega_{13}, \omega_{14}} = 0$.

After establishing our convention for labeling analytic regions, we now apply our strategy for the analytic continuation to fermionic 4p MF correlators. Anomalous terms, requiring bosonic Matsubara frequencies, only occur for sums of two fermionic Matsubara frequencies, implying the general form (Equation (A5))

$$\begin{aligned} G(i\omega_1, \omega_2, \omega_3) &= G_{i\omega_1, \omega_2, \omega_3} \\ &= \tilde{G}_{i\omega_1, \omega_2, \omega_3} + \beta \delta_{i\omega_2} \hat{G}_{12, i\omega_1, \omega_3} \\ &\quad + \beta \delta_{i\omega_3} \hat{G}_{13, i\omega_1, \omega_2} + \beta \delta_{i\omega_4} \hat{G}_{14, i\omega_1, \omega_2} \end{aligned} \quad (87)$$

The anomalous terms need not be further distinguished by factors of $\Delta_{i\omega}$ as in Equation (73), since the remaining frequency arguments are fermionic ($i\omega_i \neq 0$).

Using Equation (87), Steps 1 and 2 of our three-step strategy are discussed in Appendix D; they yield the PSFs

$$\begin{aligned} (2\pi i)^3 S_p(\epsilon_1, \epsilon_2, \epsilon_3) &= n_{\epsilon_1} n_{\epsilon_2} n_{\epsilon_3} \tilde{G}^{\epsilon_1, \epsilon_2, \epsilon_3} + n_{\epsilon_1} n_{\epsilon_2} n_{\epsilon_{123}} \tilde{G}^{\epsilon_{123}, \epsilon_2, \epsilon_3} \\ &\quad + n_{\epsilon_1} n_{\epsilon_2} n_{\epsilon_{13}} \tilde{G}^{\epsilon_{13}, \epsilon_2, \epsilon_3} + n_{\epsilon_1} n_{\epsilon_2} n_{\epsilon_{23}} \tilde{G}^{\epsilon_{23}, \epsilon_2, \epsilon_3} \\ &\quad + n_{\epsilon_1} n_{\epsilon_{12}} n_{\epsilon_3} \tilde{G}^{\epsilon_1, \epsilon_{12}, \epsilon_3} + n_{\epsilon_1} n_{\epsilon_{12}} n_{\epsilon_{123}} \tilde{G}^{\epsilon_{123}, \epsilon_{12}, \epsilon_3} \\ &\quad + n_{\epsilon_1} n_{\epsilon_3} \hat{\delta}(\epsilon_{12}) \hat{G}_{12}^{\epsilon_1, \epsilon_3} + n_{\epsilon_1} n_{\epsilon_2} \hat{\delta}(\epsilon_{13}) \hat{G}_{13}^{\epsilon_1, \epsilon_3} \\ &\quad + n_{\epsilon_1} n_{\epsilon_2} \hat{\delta}(\epsilon_{14}) \hat{G}_{14}^{\epsilon_1, \epsilon_3} \end{aligned} \quad (88)$$

This is our main result for $\ell = 4$. Equations (D11) give an overview over all possibly occurring discontinuities expressed through the analytic regions in Figure 5. As for the 2p and 3p cases, we provide a consistency check of Equation (88) in Appendix G.

To conclude this section, we further comment on properties of the anomalous parts. As discussed in Appendix D.2, the anomalous contribution $\hat{G}_{12, \omega_1^+, \omega_3^-}$, e.g., can only depend on the frequencies $i\omega_1$ and $i\omega_2$ separately, but not on $i\omega_{12}$. For anomalous parts, the complex frequency plane is thus divided into only four analytic regions corresponding to the imaginary parts of ϵ_1^\pm and ϵ_3^\pm , in contrast to the six analytic regions for 3p correlators. This directly implies symmetries for discontinuities, such as $\hat{G}_{13}^{\epsilon_2, \epsilon_1} = \hat{G}_{13}^{\epsilon_1, \epsilon_2}$. Similarly as for the regular parts, we label analytic continuations of anomalous parts with \hat{C} , e.g.,

$$\hat{G}_{12, \omega_1^+, \omega_3^-} = \hat{C}_{12}^{(14)} \quad (89)$$

with the difference that subscripts indicate the anomalous contributions. Since $\hat{G}_{12, \omega_1^+, \omega_3^-}$ is always multiplied by $\delta(\omega_{12})$, the remaining frequencies must have imaginary parts ω_2^- and ω_4^+ . Accordingly, the superscript of $\hat{C}_{12}^{(14)}$ indicates the positive imaginary shifts of ω_1 and ω_4 .

6.2. 4p Keldysh Correlators

In this section, we discuss the construction of KF correlators as linear combinations of analytically continued MF correlators. In Equations (59), (75), and (81), we expressed various Keldysh components via a convolution of PSF (anti)commutators with modified KF kernels, which originated from kernel identities presented in Equations (57) and Appendix C.3. To generalize these insights to arbitrary ℓ p correlators and to present our results in a concise way, we now introduce further notation. The goal of this notation is to collect terms which are related to discontinuities, each expressible via a sum over restricted permutations, such as the $\sum_{\vec{I}|\vec{I}^2}$ terms in Equation (93).

The set of all indices $L = \{1, \dots, \ell\}$ can be partitioned into α subsets \vec{I} of length $|\vec{I}|$, such that $L = \bigcup_{j=1}^{\alpha} \vec{I}^j$ with $\vec{I} \cap \vec{I}^j = \emptyset$ for $j \neq 1$ and $\ell = \sum_{j=1}^{\alpha} |\vec{I}^j|$. For a general Keldysh component $[\eta_1 \dots \eta_\alpha]$, we define the subsets \vec{I} to contain at least the element $\eta_j \in \vec{I}$ for all $j \in \{1, \dots, \alpha\}$, implying $|\vec{I}| \geq 1$. For example, a possible choice of the subsets for $\ell = 4$ and $[\eta_1 \eta_2] = [12]$ is given by $\vec{I}^1 = \{1, 3\}$ and $\vec{I}^2 = \{2, 4\}$. With $\sum_{\vec{I}|\vec{I}^2}$, we denote sums over restricted permutations $p = \vec{I}^{-1} \vec{I}^2$ for which all indices in subset \vec{I}^1 appear to the left of those in subset \vec{I}^2 . Then, in the previous example, $\sum_{\vec{I}|\vec{I}^2}$ sums over $\vec{I}^{-1} \vec{I}^2 \in \{(1324), (3124), (1342), (3142)\}$.

Consequently, we always find $|\vec{I}^j| = |\vec{I}|$ and $\eta_j \in \vec{I}^j$ for all $j \in \{1, \dots, \alpha\}$. In the following, we denote the elements of \vec{I}^j by \vec{I}_i^j with $i \in \{1, \dots, |\vec{I}^j|\}$.

We further define the retarded product kernel

$$\tilde{K}_{\vec{I}^1 \dots \vec{I}^\alpha}(\omega_{\vec{I}^1}^{[\eta_1] \dots [\eta_\alpha]}) = \prod_{j=1}^{\alpha-1} [\hat{\delta}(\omega_{\vec{I}^j})] \prod_{j=1}^{\alpha} [\tilde{K}(\omega_{\vec{I}^j}^{[\eta_j]})] \quad (90a)$$

$$\tilde{K}(\omega_{\vec{I}^j}) = \prod_{i=1}^{|\vec{I}^j|-1} \frac{1}{\omega_{\vec{I}_i^j \dots \vec{I}_i^j}} \quad (90b)$$

The regular kernel in the last line is defined according to Equation (19d) but restricted to the subtuple of frequencies $\omega_{\vec{I}^j} = (\omega_{\vec{I}_1^j}, \dots, \omega_{\vec{I}_{|\vec{I}^j}^j})$. Additionally, we defined the shorthand

$\hat{\delta}(\omega_{\vec{j}}) = -2\pi i \delta(\omega_{\vec{j}})$ and $\omega_{\vec{j}} = \omega_{\vec{j}} = \sum_{i \in \vec{j}} \omega_i$. The superscript on $\omega_{\vec{j}}^{[n_1, \dots, n_\alpha]}$ indicates that the frequencies carry imaginary parts $\omega_i + i\gamma_i^{[n_j]}$ for $i \in \vec{j}$ and $j \in \{1, \dots, \alpha\}$, such that $\gamma_{\eta_j}^{[n_j]} > 0$ and $\gamma_{i \neq \eta_j}^{[n_j]} < 0$. The Dirac delta function also ensures conservation of imaginary parts, $\gamma_{\vec{j}} = 0$.

As an example, consider again $\ell = 4$ and $[\eta_1, \eta_2] = [12]$ with $\vec{I}^1 = \{3, 1\}$ and $\vec{I}^2 = \{2, 4\}$. Then, we find

$$\begin{aligned} \tilde{K}_{\vec{I}^1, \vec{I}^2}^{-1} \left(\omega_{\vec{I}^1, \vec{I}^2}^{[n_1, n_2]} \right) &= \hat{\delta}(\omega_{\vec{I}^1}) \tilde{K} \left(\omega_{\vec{I}^1}^{[n_1]} \right) \tilde{K} \left(\omega_{\vec{I}^2}^{[n_2]} \right) \\ &= \hat{\delta}(\omega_{13}) \frac{1}{\omega_3} \frac{1}{\omega_2} \end{aligned} \quad (91)$$

The retarded product kernels, together with PSF (anti)commutators, constitute the central objects for expressing Equations (19) in a form particularly suitable for relating KF components to analytically continued MF correlators.

6.2.1. Keldysh Components $G^{[\eta_1, \eta_2]}$

In Equations (42b) and (76), we introduced PSF (anti)commutators for $\ell = 2$ and $\ell = 3$, respectively. We generalize this notation to arbitrary subsets by defining

$$S_{\vec{I}^1, \vec{I}^2}^{\pm}(\epsilon) = S_{\vec{I}^1, \vec{I}^2}^{-1}(\epsilon_{\vec{I}^1, \vec{I}^2}) \pm S_{\vec{I}^1, \vec{I}^2}^{-1}(\epsilon_{\vec{I}^2, \vec{I}^1}) \quad (92)$$

where the PSF (anti)commutator takes unpermuted variables ϵ as its argument. In Appendix F.2, we then show that Keldysh components with $\alpha = 2$ can be rewritten as

$$G^{[\eta_1, \eta_2]}(\omega) = \sum_{(I^1, I^2) \in \mathcal{I}^{12}} \sum_{\vec{I}^1, \vec{I}^2} \left(\tilde{K}_{\vec{I}^1, \vec{I}^2}^{-1} \diamond S_{\vec{I}^1, \vec{I}^2}^{\pm} \right) \left(\omega_{\vec{I}^1, \vec{I}^2}^{[\eta_1, \eta_2]} \right) \quad (93)$$

Here, $\mathcal{I}^{12} = \{(I^1, I^2) | \eta_1 \in I^1, \eta_2 \in I^2, I^1 \cup I^2 = L, I^1 \cap I^2 = \emptyset\}$ is the set of all possibilities to partition $L = \{1, \dots, \ell\}$ into two non-empty subsets, I^1 and I^2 , such that $\eta_1 \in I^1$ and $\eta_2 \in I^2$. The convolution of a kernel with a PSF (anti)commutator is defined as

$$\begin{aligned} &\left(\tilde{K}_{\vec{I}^1, \vec{I}^2}^{-1} \diamond S_{\vec{I}^1, \vec{I}^2}^{\pm} \right) \left(\omega_{\vec{I}^1, \vec{I}^2}^{[\eta_1, \eta_2]} \right) \\ &= \int d^\ell \epsilon \delta(\epsilon_{1 \dots \ell}) \tilde{K}_{\vec{I}^1, \vec{I}^2}^{-1} \left(\omega_{\vec{I}^1, \vec{I}^2}^{[\eta_1, \eta_2]} - \epsilon_{\vec{I}^1, \vec{I}^2} \right) S_{\vec{I}^1, \vec{I}^2}^{\pm}(\epsilon) \end{aligned} \quad (94)$$

Further, as shown in Equation (F10), Equation (93) can be expressed in terms of analytically continued Matsubara correlators,

$$G^{[\eta_1, \eta_2]}(\omega) = \sum_{I^1 \in \mathcal{I}^1} \left[N_{\omega_{I^1}} \tilde{G}_{\omega^*}^{\omega_{I^1}} + 4\pi i \delta(\omega_{I^1}) \hat{G}_{I^1, \omega^*} \right] \quad (95)$$

with $\mathcal{I}^1 = \{I^1 \subsetneq L | \eta_1 \in I^1, \eta_2 \notin I^1\}$ the set of all subtuples of L containing η_1 but not η_2 . The $\ell - 2$ frequencies in $\omega^* = \{\omega_i^- | i \neq \eta_1, i \neq \eta_2\}$ all carry negative imaginary shifts, in accordance with the definition of $\omega^{[\eta_1, \eta_2]}$. The anomalous part $\hat{G}_{I^1, \omega^*} = \hat{G}_{I^1}(z(\omega^*))$ for complex z , which is independent of the anomalous frequency

ω_i and parametrized via ω^* , is defined as

$$\hat{G}_{I^1, \omega^*} = [\hat{G}_{I^1}(\mathbf{i}\omega)]_{\Delta_{i\omega} \rightarrow \frac{1}{i\omega}, i\omega \rightarrow z(\omega^*)} \quad (96)$$

We first replaced the symbol $\Delta_{i\omega}$ by $1/(i\omega)$ to obtain a functional form that we can analytically continue, and then continue it as $\mathbf{i}\omega \rightarrow z(\omega^*)$. Remarkably, Equation (95) holds for arbitrary ℓ , η_1 , and η_2 , and elucidates how anomalous terms enter the Keldysh components with $\alpha = 2$. Examples are found in Equation (59) for $\ell = 2$, where $[\eta_1, \eta_2] = [12]$, $\mathcal{I}^1 = \{1\}$, and ω^* is an empty set, or in Equation (79) for $\ell = 3$, where $[\eta_1, \eta_2] = [13]$, $\mathcal{I}^1 = \{1, 12\}$, and $\omega^* = \omega_2^-$.

For $\ell = 4$, consider $[\eta_1, \eta_2] = [12]$, implying the set $\mathcal{I}^1 = \{1, 13, 14, 134\}$ and $\omega^* = \omega_3^-, \omega_4^-$. Then, Equation (95) directly yields

$$\begin{aligned} G^{[12]}(\omega) &= N_1 \tilde{G}_{\omega_3^-, \omega_4^-}^{\omega_1} + N_{13} \tilde{G}_{\omega_3^-, \omega_4^-}^{\omega_{13}} + N_{14} \tilde{G}_{\omega_3^-, \omega_4^-}^{\omega_{14}} + N_{134} \tilde{G}_{\omega_3^-, \omega_4^-}^{\omega_{134}} \\ &\quad + 4\pi i \delta(\omega_{13}) \hat{G}_{13; \omega_3^-, \omega_4^-} + 4\pi i \delta(\omega_{14}) \hat{G}_{14; \omega_3^-, \omega_4^-} \end{aligned} \quad (97)$$

An expression for $G^{[12]}$ expressed in terms of analytic regions is given in Equation (102). Additionally, a full list of all $G^{[\eta_1, \eta_2]}$ is provided in Equations (101a)–(101f) (with relations such as $N_{134} \tilde{G}_{\omega_3^-, \omega_4^-}^{\omega_{134}} = -N_2 \tilde{G}_{\omega_3^-, \omega_4^-}^{\omega_2} = N_2 \tilde{G}_{\omega_3^-, \omega_4^-}^{\omega_2}$ used).

6.2.2. Other Keldysh Components

The derivation of $G^{[123]} - G^{[3]}$ in Section 5.2.2 can be extended to arbitrary ℓ and $[\eta_1, \eta_2, \eta_3]$ by keeping track of permutations that are cyclically related, generalizing Equation (81) to (see Appendix F.3 for details)

$$\begin{aligned} &(G^{[\eta_1, \eta_2, \eta_3]} - G^{[\eta_3]})(\omega) \\ &= \sum_{(I^1, I^{23}) \in \mathcal{I}^{123}} \sum_{\vec{I}^1, \vec{I}^{23}} \left[\tilde{K}_{\vec{I}^1, \vec{I}^{23}}^{-1} \diamond S_{\vec{I}^1, \vec{I}^{23}}^{\pm} \right] \left(\omega_{\vec{I}^1, \vec{I}^{23}}^{[\eta_1, \eta_3]} \right) \\ &\quad + \sum_{(I^2, I^{13}) \in \mathcal{I}^{213}} \sum_{\vec{I}^2, \vec{I}^{13}} \left[\tilde{K}_{\vec{I}^2, \vec{I}^{13}}^{-1} \diamond S_{\vec{I}^2, \vec{I}^{13}}^{\pm} \right] \left(\omega_{\vec{I}^2, \vec{I}^{13}}^{[\eta_2, \eta_3]} \right) \\ &\quad + \sum_{(I^1, I^2, I^3) \in \mathcal{I}^{123}} \sum_{\vec{I}^1, \vec{I}^2, \vec{I}^3} \left[\tilde{K}_{\vec{I}^1, \vec{I}^2, \vec{I}^3}^{-1} \diamond S_{\vec{I}^1, \vec{I}^2, \vec{I}^3}^{\pm} \right] \left(\omega_{\vec{I}^1, \vec{I}^2, \vec{I}^3}^{[\eta_1, \eta_2, \eta_3]} \right) \end{aligned} \quad (98)$$

Here, $\mathcal{I}^{123} = \{(I^1, I^2, I^3) | \eta_1 \in I^1, \eta_2 \in I^2, \eta_3 \in I^3, \vec{I} \cap \vec{I}' = \emptyset \text{ for } j \neq j'\}$ is the set of all possibilities to partition $L = \{1, \dots, \ell\}$ into three subsets, each of which contains one of the indices $\eta_j \in \vec{I}$. The remaining sets are defined as

$$\mathcal{I}^{123} = \{(I^1, I^{23}) | \eta_1 \in I^1, \eta_2, \eta_3 \in I^{23}, I^1 \cap I^{23} = \emptyset\} \quad (99a)$$

$$\mathcal{I}^{213} = \{(I^2, I^{13}) | \eta_2 \in I^2, \eta_1, \eta_3 \in I^{13}, I^2 \cap I^{13} = \emptyset\} \quad (99b)$$

Then, Equation (81) provides an example for $\ell = 3$ and $[\eta_1, \eta_2, \eta_3] = [123]$, where $\mathcal{I}^{123} = \{(1, 23)\}$, $\mathcal{I}^{213} = \{(2, 13)\}$ and $\mathcal{I}^{123} = \{(1, 2, 3)\}$.

For $\ell = 4$, consider $[\eta_1 \eta_2 \eta_3] = [123]$. Compared to the 3p case, the additional index allows for larger sets $I^{123} = \{(1, 234), (14, 23)\}$, $I^{213} = \{(2, 134), (24, 13)\}$, and $I^{132} = \{(1, 2, 34), (1, 24, 3), (14, 2, 3)\}$, resulting in (suppressing the frequency arguments of PSF (anti)commutators)

$$\begin{aligned} (G^{[123]} - G^{[3]})(\omega) &= \tilde{G}_{\omega_2^+ \omega_4^-}^{\omega_1} + \tilde{G}_{\omega_2^- \omega_4^+}^{\omega_2} + \tilde{G}_{\omega_1^+ \omega_3^-}^{\omega_2} + \tilde{G}_{\omega_1^- \omega_3^+}^{\omega_24} \\ &+ \int_{\varepsilon_1 \varepsilon_2 \varepsilon_3} \left[\hat{\delta}(\omega_1 - \varepsilon_1) \hat{\delta}(\omega_2 - \varepsilon_2) \frac{(2\pi i)^3}{\omega_3^+ - \varepsilon_3} S_{[[1,2]_+, [3,4]_-]} \right. \\ &+ \hat{\delta}(\omega_1 - \varepsilon_1) \hat{\delta}(\omega_3 - \varepsilon_3) \frac{(2\pi i)^3}{\omega_2^+ - \varepsilon_2} S_{[[1,2,4]_-,]_+, 3]_+} \\ &\left. + \hat{\delta}(\omega_2 - \varepsilon_2) \hat{\delta}(\omega_3 - \varepsilon_3) \frac{(2\pi i)^3}{\omega_1^+ - \varepsilon_1} S_{[[1,4]_-, 2]_+, 3]_+} \right] \quad (100) \end{aligned}$$

Here, we identified the terms in the first line of Equation (98) with discontinuities (see Appendix E.1). After inserting the PSFs (see Equations (F15)) and performing the remaining integrations using Cauchy's integral formula, we obtain Equation (101g).

For $\alpha \geq 4$, expressing the spectral representation of $G^{[n_1 \dots n_d]}$ in terms of retarded product kernels and PSF (anti)commutators becomes increasingly challenging. Nevertheless, we provide a formula for $G^{[1234]}$ and $\ell = 4$ in Equation (F16), with a list of all relevant PSF (anti)commutators given in Equation (F17). Equation (101k) then displays the result after evaluating all convolution integrals.

6.2.3. Overview of Keldysh Components

To summarize the results of the previous sections, we give an overview of all Keldysh components with $\alpha > 1$:

$$G^{[12]}(\omega) = N_1 \tilde{G}_{\omega_3^- \omega_4^-}^{\omega_1} + N_2 \tilde{G}_{\omega_3^- \omega_4^-}^{\omega_2} + N_{13} \tilde{G}_{\omega_3^- \omega_4^-}^{\omega_{13}} + N_{14} \tilde{G}_{\omega_3^- \omega_4^-}^{\omega_{14}} + 4\pi i \delta(\omega_{13}) \hat{G}_{13; \omega_3^-, \omega_4^-} + 4\pi i \delta(\omega_{14}) \hat{G}_{14; \omega_3^-, \omega_4^-} \quad (101a)$$

$$G^{[34]}(\omega) = N_3 \tilde{G}_{\omega_1^- \omega_2^-}^{\omega_3} + N_{13} \tilde{G}_{\omega_1^- \omega_2^-}^{\omega_{13}} + N_{14} \tilde{G}_{\omega_1^- \omega_2^-}^{\omega_{14}} + N_4 \tilde{G}_{\omega_1^- \omega_2^-}^{\omega_4} + 4\pi i \delta(\omega_{13}) \hat{G}_{13; \omega_1^-, \omega_2^-} + 4\pi i \delta(\omega_{14}) \hat{G}_{14; \omega_1^-, \omega_2^-} \quad (101b)$$

$$G^{[13]}(\omega) = N_1 \tilde{G}_{\omega_2^- \omega_4^-}^{\omega_1} + N_{12} \tilde{G}_{\omega_2^- \omega_4^-}^{\omega_{12}} + N_{14} \tilde{G}_{\omega_2^- \omega_4^-}^{\omega_{14}} + N_3 \tilde{G}_{\omega_2^- \omega_4^-}^{\omega_3} + 4\pi i \delta(\omega_{12}) \hat{G}_{12; \omega_2^-, \omega_4^-} + 4\pi i \delta(\omega_{14}) \hat{G}_{14; \omega_2^-, \omega_4^-} \quad (101c)$$

$$G^{[24]}(\omega) = N_2 \tilde{G}_{\omega_1^- \omega_3^-}^{\omega_2} + N_{12} \tilde{G}_{\omega_1^- \omega_3^-}^{\omega_{12}} + N_{14} \tilde{G}_{\omega_1^- \omega_3^-}^{\omega_{14}} + N_4 \tilde{G}_{\omega_1^- \omega_3^-}^{\omega_4} + 4\pi i \delta(\omega_{12}) \hat{G}_{12; \omega_1^-, \omega_3^-} + 4\pi i \delta(\omega_{14}) \hat{G}_{14; \omega_1^-, \omega_3^-} \quad (101d)$$

$$G^{[14]}(\omega) = N_1 \tilde{G}_{\omega_2^- \omega_3^-}^{\omega_1} + N_{12} \tilde{G}_{\omega_2^- \omega_3^-}^{\omega_{12}} + N_{13} \tilde{G}_{\omega_2^- \omega_3^-}^{\omega_{13}} + N_4 \tilde{G}_{\omega_2^- \omega_3^-}^{\omega_4} + 4\pi i \delta(\omega_{12}) \hat{G}_{12; \omega_2^-, \omega_3^-} + 4\pi i \delta(\omega_{13}) \hat{G}_{13; \omega_2^-, \omega_3^-} \quad (101e)$$

$$G^{[23]}(\omega) = N_2 \tilde{G}_{\omega_1^- \omega_4^-}^{\omega_2} + N_{12} \tilde{G}_{\omega_1^- \omega_4^-}^{\omega_{12}} + N_{13} \tilde{G}_{\omega_1^- \omega_4^-}^{\omega_{13}} + N_3 \tilde{G}_{\omega_1^- \omega_4^-}^{\omega_3} + 4\pi i \delta(\omega_{12}) \hat{G}_{12; \omega_1^-, \omega_4^-} + 4\pi i \delta(\omega_{13}) \hat{G}_{13; \omega_1^-, \omega_4^-} \quad (101f)$$

$$\begin{aligned} (G^{[123]} - G^{[3]})(\omega) &= (N_1 N_2 + 1) \tilde{G}_{\omega_3^+}^{\omega_2, \omega_1} + N_1 N_{12} \tilde{G}_{\omega_3^+}^{\omega_{12}, \omega_1} + N_1 N_3 \tilde{G}_{\omega_3^+}^{\omega_3, \omega_1} + (N_1 N_{13} - 1) \tilde{G}_{\omega_2^+}^{\omega_{13}, \omega_1} + N_2 N_3 \tilde{G}_{\omega_3^+}^{\omega_3, \omega_2} + (N_2 N_{23} - 1) \tilde{G}_{\omega_1^+}^{\omega_{23}, \omega_2} \\ &+ \tilde{G}_{\omega_2^- \omega_3^+}^{\omega_1} - \tilde{G}_{\omega_1^+ \omega_2^-}^{\omega_2} + \tilde{G}_{\omega_1^- \omega_3^+}^{\omega_2} - \tilde{G}_{\omega_2^+ \omega_1^-}^{\omega_{13}} + 4\pi i \delta(\omega_{12}) N_1 \hat{G}_{12; \omega_3^+}^{\omega_1} + 4\pi i \delta(\omega_{13}) N_1 \hat{G}_{13; \omega_2^+}^{\omega_1} + 4\pi i \delta(\omega_{14}) N_2 \hat{G}_{14; \omega_1^+}^{\omega_2} \quad (101g) \end{aligned}$$

$$\begin{aligned} (G^{[124]} - G^{[4]})(\omega) &= (N_1 N_2 + 1) \tilde{G}_{\omega_4^+}^{\omega_2, \omega_1} + N_1 N_{12} \tilde{G}_{\omega_4^+}^{\omega_{12}, \omega_1} + N_1 N_4 \tilde{G}_{\omega_4^+}^{\omega_4, \omega_1} + (N_1 N_{14} - 1) \tilde{G}_{\omega_2^+}^{\omega_{14}, \omega_1} + N_2 N_4 \tilde{G}_{\omega_4^+}^{\omega_4, \omega_2} + (N_2 N_{24} - 1) \tilde{G}_{\omega_1^+}^{\omega_{24}, \omega_2} \\ &+ \tilde{G}_{\omega_2^- \omega_4^+}^{\omega_1} - \tilde{G}_{\omega_1^+ \omega_2^-}^{\omega_24} + \tilde{G}_{\omega_1^- \omega_4^+}^{\omega_2} - \tilde{G}_{\omega_2^+ \omega_1^-}^{\omega_{14}} + 4\pi i \delta(\omega_{12}) N_1 \hat{G}_{12; \omega_4^+}^{\omega_1} + 4\pi i \delta(\omega_{13}) N_2 \hat{G}_{13; \omega_1^+}^{\omega_2} + 4\pi i \delta(\omega_{14}) N_1 \hat{G}_{14; \omega_2^+}^{\omega_1} \quad (101h) \end{aligned}$$

$$\begin{aligned} (G^{[134]} - G^{[4]})(\omega) &= (N_1 N_3 + 1) \tilde{G}_{\omega_4^+}^{\omega_3, \omega_1} + N_1 N_{13} \tilde{G}_{\omega_4^+}^{\omega_{13}, \omega_1} + N_1 N_4 \tilde{G}_{\omega_4^+}^{\omega_4, \omega_1} + (N_1 N_{14} - 1) \tilde{G}_{\omega_3^+}^{\omega_{14}, \omega_1} + N_3 N_4 \tilde{G}_{\omega_4^+}^{\omega_4, \omega_3} + (N_3 N_{34} - 1) \tilde{G}_{\omega_1^+}^{\omega_{34}, \omega_3} \\ &+ \tilde{G}_{\omega_3^- \omega_4^+}^{\omega_1} - \tilde{G}_{\omega_1^+ \omega_3^-}^{\omega_{34}} + \tilde{G}_{\omega_1^- \omega_4^+}^{\omega_3} - \tilde{G}_{\omega_3^+ \omega_1^-}^{\omega_{14}} + 4\pi i \delta(\omega_{12}) N_3 \hat{G}_{12; \omega_4^+}^{\omega_1} + 4\pi i \delta(\omega_{13}) N_1 \hat{G}_{13; \omega_4^+}^{\omega_1} + 4\pi i \delta(\omega_{14}) N_1 \hat{G}_{14; \omega_3^+}^{\omega_1} \quad (101i) \end{aligned}$$

$$\begin{aligned} (G^{[1234]} - G^{[4]})(\omega) &= (N_2 N_3 + 1) \tilde{G}_{\omega_4^+}^{\omega_3, \omega_2} + N_2 N_{23} \tilde{G}_{\omega_4^+}^{\omega_{23}, \omega_2} + N_2 N_4 \tilde{G}_{\omega_4^+}^{\omega_4, \omega_2} + (N_2 N_{24} - 1) \tilde{G}_{\omega_3^+}^{\omega_{24}, \omega_2} + N_3 N_4 \tilde{G}_{\omega_4^+}^{\omega_4, \omega_3} + (N_3 N_{34} - 1) \tilde{G}_{\omega_2^+}^{\omega_{34}, \omega_3} \\ &+ \tilde{G}_{\omega_3^- \omega_4^+}^{\omega_2} - \tilde{G}_{\omega_2^+ \omega_3^-}^{\omega_{34}} + \tilde{G}_{\omega_2^- \omega_4^+}^{\omega_3} - \tilde{G}_{\omega_3^+ \omega_2^-}^{\omega_{24}} + 4\pi i \delta(\omega_{12}) N_3 \hat{G}_{12; \omega_4^+}^{\omega_3} + 4\pi i \delta(\omega_{13}) N_2 \hat{G}_{13; \omega_3^+}^{\omega_2} + 4\pi i \delta(\omega_{14}) N_2 \hat{G}_{14; \omega_4^+}^{\omega_2} \quad (101j) \end{aligned}$$

$$\begin{aligned} G^{[1234]}(\omega) &= N_1 \tilde{G}_{\omega_2^- \omega_3^-}^{\omega_1} + N_2 \tilde{G}_{\omega_3^- \omega_4^-}^{\omega_2} + N_3 \tilde{G}_{\omega_1^- \omega_4^-}^{\omega_3} + N_4 \tilde{G}_{\omega_1^- \omega_2^-}^{\omega_4} + N_3 \tilde{G}_{\omega_2^+}^{\omega_3, \omega_4} + N_2 \tilde{G}_{\omega_1^+}^{\omega_2, \omega_3} + N_4 \tilde{G}_{\omega_3^+}^{\omega_4, \omega_1} + N_1 \tilde{G}_{\omega_4^+}^{\omega_1, \omega_2} + N_2 \tilde{G}_{\omega_3^+}^{\omega_2, \omega_4} \\ &+ N_4 \tilde{G}_{\omega_3^+}^{\omega_4, \omega_2} + N_1 \tilde{G}_{\omega_4^+}^{\omega_1, \omega_3} + N_3 \tilde{G}_{\omega_4^+}^{\omega_3, \omega_1} + (N_1 N_2 N_3 + N_1 + N_3) \tilde{G}^{\omega_3, \omega_2, \omega_1} + (N_1 N_2 N_4 + N_4 + N_2) \tilde{G}^{\omega_4, \omega_2, \omega_1} \\ &+ (N_1 N_2 N_{13} + N_1 - N_2) \tilde{G}^{\omega_{13}, \omega_2, \omega_1} + (N_1 N_2 N_{23}) \tilde{G}^{\omega_{23}, \omega_2, \omega_1} + N_1 (1 + N_{12} N_3) \tilde{G}^{\omega_3, \omega_{12}, \omega_1} + N_1 N_{12} N_4 \tilde{G}^{\omega_4, \omega_2, \omega_1} \\ &+ 4\pi i N_1 N_3 \delta(\omega_{12}) \hat{G}_{12}^{\omega_1, \omega_3} + 4\pi i N_1 N_2 \left[\delta(\omega_{13}) \hat{G}_{13}^{\omega_1, \omega_2} + \delta(\omega_{13}) \hat{G}_{14}^{\omega_1, \omega_2} \right] \quad (101k) \end{aligned}$$

These equations constitute the main results of the MF-to-KF analytic continuation: They relate all components of a fermionic KF 4p correlator to linear combinations of analytically continued regular and anomalous parts of the corresponding MF correlator, expressed in terms of discontinuities and statistical factors N_i .

6.2.4. 4p gFDRs

For 4p correlators, there are several regions of analyticity that cannot be identified with a KF correlator. Therefore, in contrast to $\ell \leq 3$, fully retarded and advanced Keldysh components do not suffice to determine all other Keldysh components. Nevertheless, different Keldysh components can be related to each other. We now present the strategy for deriving these gFDRs for the Keldysh component $G^{[12]}$.

Since every Keldysh component can be represented as a linear combination of analytically continued MF correlators, the analytic regions can serve as a basis to find relations among different Keldysh components. Expressing the discontinuities in Equation (101a) via analytic regions, the KF correlator $G^{[12]}$ reads

$$\begin{aligned} G^{[12]} = & N_1 \left(C_{\text{III}}^{(12)} - G^{[2]} \right) + N_{13} \left(C_{\text{II}}^{(12)} - C_{\text{III}}^{(12)} \right) \\ & + N_{14} \left(C_{\text{IV}}^{(12)} - C_{\text{III}}^{(12)} \right) + N_2 \left(C_1^{(12)} - G^{[1]} \right) \\ & + 4\pi i \delta(\omega_{13}) \hat{C}_{13}^{(12)} + 4\pi i \delta(\omega_{14}) \hat{C}_{14}^{(12)} \end{aligned} \quad (102)$$

where we inserted $G^{[1]} = C^{(1)}$ and $G^{[2]} = C^{(2)}$. Evidently, $G^{[12]}$ cannot be expressed in terms of fully retarded and advanced components only (modulo anomalous terms) due to the occurrence of $C_{\text{I/III/IV}}^{(12)}$. However, these analytic regions and the same anomalous contributions appear in the primed KF correlator $G'^{[34]}$ as well:

$$\begin{aligned} G'^{[34]} = & N_3 \left(C_{\text{II}}^{(12)} - G'^{[4]} \right) + N_{13} \left(C_{\text{III}}^{(12)} - C_{\text{II}}^{(12)} \right) \\ & + N_{14} \left(C_{\text{III}}^{(12)} - C_{\text{IV}}^{(12)} \right) + N_4 \left(C_{\text{IV}}^{(12)} - G'^{[3]} \right) \\ & - 4\pi i \delta(\omega_{13}) \hat{C}_{13}^{(12)} - 4\pi i \delta(\omega_{14}) \hat{C}_{14}^{(12)} \end{aligned} \quad (103)$$

Note that priming the $i\delta(\dots)$ factors amounts to complex conjugation, as these arise from the identity (58), i.e., $[i\delta(\dots)]' = -i\delta(\dots)$. Therefore, we make the ansatz of expressing $G^{[12]}$ as a linear combination of $G'^{[34]}$, $G^{[1]}$, $G^{[2]}$, $G'^{[3]}$, and $G'^{[4]}$, where the coefficients are determined by comparing terms proportional to the same analytic regions. Even though the resulting set of equations is overdetermined (including anomalous contributions, we have ten equations for five coefficients), we find the gFDR

$$\begin{aligned} G^{[12]} = & -N_1 G^{[2]} - N_2 G^{[1]} \\ & + \frac{N_1 + N_2}{N_3 + N_4} \left[G'^{[34]} + N_3 G'^{[4]} + N_4 G'^{[3]} \right] \end{aligned} \quad (104a)$$

The anomalous terms enter the right-hand side only implicitly via $G'^{[34]}$. However, using $\frac{N_1 + N_2}{N_3 + N_4} \delta(\omega_{13}) = -\delta(\omega_{13})$ and $\frac{N_1 + N_2}{N_3 + N_4} \delta(\omega_{14}) =$

$-\delta(\omega_{14})$, it is straightforward to show that the $\hat{C}_{13}^{(12)}$ and $\hat{C}_{14}^{(12)}$ contributions in the last line of Equation (102) are recovered by the corresponding terms in Equation (103) via Equation (104a). Conversely, the gFDR for $G'^{[34]}$ can be derived from Equation (104a) by solving for $G'^{[34]}$ and priming all correlators.

The gFDRs for all other Keldysh components with $\alpha \geq 2$ follow from the same strategy: Express Keldysh components in terms of linearly independent analytic regions and find relations between different components by solving a set of equations to determine coefficients. In addition to Equation (104a), we then obtain for $\alpha = 2$

$$\begin{aligned} G^{[13]} = & -N_1 G^{[3]} - N_3 G^{[1]} \\ & + \frac{N_1 + N_3}{N_2 + N_4} \left[G'^{[24]} + N_2 G'^{[4]} + N_4 G'^{[2]} \right] \end{aligned} \quad (104b)$$

$$\begin{aligned} G^{[14]} = & -N_1 G^{[4]} - N_4 G^{[1]} \\ & + \frac{N_1 + N_4}{N_2 + N_3} \left[G'^{[23]} + N_2 G'^{[3]} + N_3 G'^{[2]} \right] \end{aligned} \quad (104c)$$

for $\alpha = 3$

$$\begin{aligned} G^{[234]} = & (1 + N_2 N_4 + N_2 N_3 + N_3 N_4) G'^{[1]} - N_3 N_4 G^{[2]} - N_2 N_4 G^{[3]} \\ & - N_2 N_3 G^{[4]} - N_4 G^{[23]} - N_3 G^{[24]} - N_2 G^{[34]} \end{aligned} \quad (104d)$$

$$\begin{aligned} G^{[134]} = & (1 + N_1 N_4 + N_1 N_3 + N_3 N_4) G'^{[2]} - N_3 N_4 G^{[1]} - N_1 N_4 G^{[3]} \\ & - N_1 N_3 G^{[4]} - N_4 G^{[13]} - N_3 G^{[14]} - N_1 G^{[34]} \end{aligned} \quad (104e)$$

$$\begin{aligned} G^{[124]} = & (1 + N_1 N_2 + N_1 N_2 + N_2 N_4) G'^{[3]} - N_2 N_4 G^{[1]} - N_1 N_4 G^{[2]} \\ & - N_1 N_2 G^{[4]} - N_4 G^{[12]} - N_2 G^{[14]} - N_1 G^{[24]} \end{aligned} \quad (104f)$$

$$\begin{aligned} G^{[123]} = & (1 + N_1 N_2 + N_1 N_3 + N_2 N_3) G'^{[4]} - N_2 N_3 G^{[1]} - N_1 N_3 G^{[2]} \\ & - N_1 N_2 G^{[3]} - N_1 G^{[23]} - N_2 G^{[13]} - N_3 G^{[12]} \end{aligned} \quad (104g)$$

and for $\alpha = 4$

$$\begin{aligned} G^{[1234]} = & 2N_2 N_3 N_4 G^{[1]} + (N_2 N_3 N_4 + N_2 + N_3 + N_4) G'^{[1]} \\ & + 2N_1 N_3 N_4 G^{[2]} + (N_1 N_3 N_4 + N_1 + N_3 + N_4) G'^{[2]} \\ & + 2N_1 N_2 N_4 G^{[3]} + (N_1 N_2 N_4 + N_1 + N_2 + N_4) G'^{[3]} \\ & + 2N_2 N_3 N_4 G^{[4]} + (N_1 N_2 N_3 + N_1 + N_2 + N_3) G'^{[4]} \\ & + N_3 N_4 G^{[12]} + N_2 N_4 G^{[13]} + N_2 N_3 G^{[14]} \\ & + N_1 N_4 G^{[23]} + N_1 N_3 G^{[24]} + N_1 N_2 G^{[34]} \end{aligned} \quad (104h)$$

These results agree with the FDRs found in ref. [24], and therefore provide a consistency check for our approach. Moreover, we checked that the anomalous parts fulfill the same gFDRs. They enter Equations (104) only implicitly through $G^{[m_1 m_2]}$ and $G'^{[m_1 m_2]}$ on the right-hand sides, which contain anomalous parts via Equations (101a)–(101f). This is in contrast to the 2p and 3p cases in Equations (61) and (84), respectively. There, only fully retarded and advanced Keldysh correlators, which solely depend on the

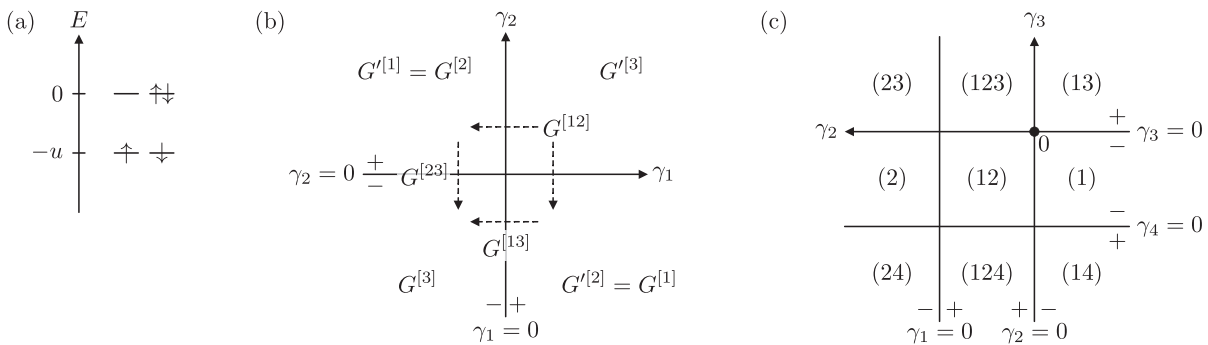


Figure 6. a) Degenerate energy levels of the half-filled Hubbard atom for $u > 0$. b) Relevant analytic regions of the regular part of the 3p electron-density correlator in Equation (113). As the correlator is independent of $i\omega_3 = -i\omega_{12}$, there are no poles on the line $\gamma_3 = 0$ in Figure 4, resulting in $G^{[1]} = G^{[2]}$ and $G^{[2]} = G^{[1]}$. The dashed arrows indicate the relevant discontinuities for the different Keldysh components with $\alpha = 2$, see Equation (84). c) Reduced analytic regions of the regular part of the fermionic 4p correlator in Equation (119). The regions labeled by (3), (4), (34), (134), and (234) in Figure 5 are missing.

regular part \tilde{G} of the corresponding MF correlator (see Equation (23)), occur on the right-hand side, and thus the anomalous parts have to enter the gFDRs explicitly.

7. Hubbard Atom

To illustrate the use of our analytic continuation formulas, we consider the Hubbard atom (HA) with the Hamiltonian

$$H = Un_1 n_1 - \mu(n_1 + n_1) \quad (105)$$

It describes an interacting system of spin- $\frac{1}{2}$ electrons on a single site, created by d_σ^\dagger , with $n_\sigma = d_\sigma^\dagger d_\sigma$ the number operator for spin $\sigma \in \{\uparrow, \downarrow\}$. The chemical potential μ is set to the half-filling value $\mu = u = U/2$ for compact results, where U is the interaction parameter. The Hilbert space of the HA is only four-dimensional, with the site being either unoccupied, $|0\rangle$, singly occupied, $|\uparrow\rangle$ or $|\downarrow\rangle$, or doubly occupied, $|\uparrow\downarrow\rangle$. The eigenenergies are (see Figure 6a)

$$E_0 = E_{\uparrow\downarrow} = 0, \quad E_\uparrow = E_\downarrow = -u \quad (106)$$

The partition sum evaluates to $Z = \text{tr}(e^{-\beta H}) = 2 + 2e^{\beta u}$.

This very simple model is interesting as it is accessible via analytically exact computations. It describes the Hubbard model and the single-impurity Anderson model in the atomic limit (where the interaction U dominates over all other energy scales) and can thus serve as a benchmark for numerical methods.^[23,33–35] Several correlators of the Hubbard atom were computed in the MF and studied extensively, like fermionic 2p (one-particle) and 4p (two-particle) correlators.^[36–40] Also its 3p MF functions have been computed and applied in previous works.^[41–43] The vertex of the Hubbard atom, obtained from the fermionic 4p correlator by dividing out external legs, was used as a starting point for an expansion around strong coupling.^[37,38,44,45] Additionally, it was found that (despite the simplicity of the model) the two-particle irreducible (2PI) vertices display a complicated frequency dependence, and their divergencies are subject to ongoing research.^[46–49] Such divergencies have been related

to the breakdown of the perturbative expansion due to the multivaluedness of the Luttinger–Ward functional^[46,50–52] and to the local moment formation in generalized susceptibilities.^[53,54]

2p and 3p bosonic correlators have gained interest in recent years as well. They describe not only the asymptotic behaviour of the 4p vertex for large frequencies^[40] or the interaction of electrons via the exchange of effective bosons,^[55,56] but they are also the central objects of linear and non-linear response theory.^[57,58]

KF correlators for the HA (beyond $\ell = 2$) were of smaller interest due to the lack of numerical real-frequency studies. However, substantial progress has been made in this direction.^[23,29,59–61] Hence, we exemplify the analytic continuation from MF to KF correlators on the example of the HA for various correlators of interest.

One further comment is in order: The following MF correlators are derived by first computing the PSFs, followed by a convolution with the MF kernels. From our experience, a direct insertion of these PSFs into the spectral representation of KF correlators yields cluttered expressions, cumbersome to simplify due to the infinitesimal imaginary shifts γ_0 . With the analytic continuation formulas, on the other hand, terms are conveniently preorganized, collecting those contributions with the same imaginary shifts. Additionally, the discontinuities conveniently yield Dirac delta contributions, as we will show below. In order to derive, e.g., our first results for the 4p correlator, Equations (H18), it is much more convenient to start from the analytic continuation formulas, Equations (101), than from the original KF Equation (19).

For a compact presentation of our results, we distinguish different correlators with operators in subscripts, e.g., $G[O^1, O^2](i\omega) = G_{O^1 O^2}(i\omega)$. Furthermore, we will make use of the identities (proven in Appendix H.1)

$$\frac{\omega^+}{(\omega^+)^2 - u^2} - \frac{\omega^-}{(\omega^-)^2 - u^2} = \frac{\pi}{i} [\delta(\omega + u) + \delta(\omega - u)] \quad (107a)$$

$$\frac{1}{(\omega^+)^2 - u^2} - \frac{1}{(\omega^-)^2 - u^2} = \frac{\pi i}{u} [\delta(\omega + u) - \delta(\omega - u)] \quad (107b)$$

All following correlators refer to the connected part.

7.1. Examples for $\ell = 2$

7.1.1. Fermionic 2p Correlator

To begin with, we consider the fermionic 2p correlator (propagator), with $\mathbf{O} = (d_{\uparrow}, d_{\uparrow}^{\dagger})$. By SU(2) spin symmetry, reversing all spins leaves the correlator invariant. As the nonzero matrix elements are $\langle \uparrow | d_{\uparrow}^{\dagger} | 0 \rangle = \langle \uparrow \downarrow | d_{\uparrow}^{\dagger} | \downarrow \rangle = 1$ and $\langle 0 | d_{\uparrow} | \uparrow \rangle = \langle \downarrow | d_{\uparrow} | \uparrow \downarrow \rangle = 1$, we can readily compute the PSFs, S_p , via Equation (22b) in ref. [23]. Evaluating the spectral representation yields

$$G_{d_{\uparrow}, d_{\uparrow}^{\dagger}}(i\omega) = \frac{i\omega}{(i\omega)^2 - u^2} = \tilde{G}(i\omega) \quad (108)$$

By construction, there is no anomalous part $\hat{G}_1 = 0$. The retarded and advanced component are directly obtained from Equation (54):

$$G_{d_{\uparrow}, d_{\uparrow}^{\dagger}}^{[1/2]}(\omega) = \frac{\omega^{\pm}}{(\omega^{\pm})^2 - u^2} \quad (109)$$

The Keldysh component involves the difference of the retarded and advanced component. Via Equation (107a), one gets

$$G_{d_{\uparrow}, d_{\uparrow}^{\dagger}}^{[12]}(\omega) = \pi i t [\delta(\omega + u) - \delta(\omega - u)] \quad (110)$$

where we used $N_{-\omega} = -N_{\omega}$ and defined $t = \tanh(\beta u/2)$.

7.1.2. Density–Density Correlator

Our second example is the density–density correlator $\mathbf{O} = (n_{\uparrow}, n_{\uparrow})$. The spectral representation in the MF yields a purely anomalous result

$$G_{n_{\uparrow}, n_{\uparrow}}(i\omega) = \beta \delta_{i\omega} \frac{1}{4} t = \beta \delta_{i\omega} \hat{G}_1 \quad (111)$$

The correlator $G_{n_{\uparrow}, n_{\uparrow}}$ discussed above describes the linear response of the spin-up occupation to a shift of the spin-down energy level, which lifts the degeneracy of the singly-occupied energy levels in Figure 6a. For decreasing temperatures, the system becomes increasingly susceptible to such perturbations. This is reflected by the $\beta = 1/T$ divergence for $T \rightarrow 0$ in the MF correlator of Equation (111), and the $\delta(\omega)$ behavior in Equation (112) for its Keldysh counterpart.

Using Equations (54) and (61), the Keldysh components read

$$\begin{aligned} G_{n_{\uparrow}, n_{\uparrow}}^{[1]}(\omega) &= G_{n_{\uparrow}, n_{\uparrow}}^{[2]}(\omega) = 0, \\ G_{n_{\uparrow}, n_{\uparrow}}^{[12]}(\omega) &= 4\pi i \delta(\omega) \frac{1}{4} t \end{aligned} \quad (112)$$

We again emphasize the importance of the anomalous term in the gFDR. If it were discarded, the Keldysh component $G_{n_{\uparrow}, n_{\uparrow}}^{[12]}$ would falsely vanish entirely.

7.2. Examples for $\ell = 3$

7.2.1. 3p Electron-Density Correlator

Our first example for $\ell = 3$ involves the operators $\mathbf{O} = (d_{\uparrow}, d_{\uparrow}^{\dagger}, n_{\uparrow})$. As only the third operator is bosonic, there is at most one anomalous term if $i\omega_3 = -i\omega_{12} = 0$. Indeed, the spectral representation evaluates to

$$\begin{aligned} G_{d_{\uparrow}, d_{\uparrow}^{\dagger}, n_{\uparrow}}(i\omega) &= \frac{u^2 - i\omega_1 i\omega_2}{[(i\omega_1)^2 - u^2][(i\omega_2)^2 - u^2]} + \beta \delta_{i\omega_{12}, 0} \frac{u t}{2} \frac{1}{(i\omega_1)^2 - u^2} \\ &= \tilde{G}(i\omega) + \beta \delta_{i\omega_{12}} \hat{G}_3(i\omega_1). \end{aligned} \quad (113)$$

Since the fully retarded and fully advanced components of the correlator trivially follow from the regular part, we focus on the $\alpha \geq 2$ components in the following. We begin with the Keldysh component $G^{[13]}$ in Equation (84b): The regular part is independent of $i\omega_3 = -i\omega_{12}$, such that the discontinuity across $\gamma_3 = -\gamma_{12} = 0$ vanishes, implying $G^{[2]} - G^{[1]} = 0$ (see Figure 6b). The discontinuity $G^{[2]} - G^{[3]}$, on the other hand, is nonzero and can be easily evaluated using Equations (107), leading to (see Appendix H.2)

$$\begin{aligned} G_{d_{\uparrow}, d_{\uparrow}^{\dagger}, n_{\uparrow}}^{[13]}(\omega) &= N_1 (\tilde{G}(\omega_1^+, \omega_2^-) - \tilde{G}(\omega_1^-, \omega_2^-)) + 4\pi i \delta(\omega_{12}) \hat{G}_3(\omega_1^+) \\ &= \pi i t \left[\frac{\delta(\omega_1 - u)}{\omega_2^+ + u} - \frac{\delta(\omega_1 + u)}{\omega_2^- - u} \right] \\ &\quad + 4\pi i \delta(\omega_{12}) \frac{u t}{2} \frac{1}{(\omega_1^+)^2 - u^2} \end{aligned} \quad (114)$$

Similarly, the remaining components with $\alpha = 2$, as well as the Keldysh component with $\alpha = 3$, read

$$\begin{aligned} G_{d_{\uparrow}, d_{\uparrow}^{\dagger}, n_{\uparrow}}^{[23]}(\omega) &= \pi i t \left[\frac{\delta(\omega_2 - u)}{\omega_1^- + u} - \frac{\delta(\omega_2 + u)}{\omega_1^- - u} \right] \\ &\quad + 4\pi i \delta(\omega_{12}) \frac{u t}{2} \frac{1}{(\omega_1^-)^2 - u^2}, \\ G_{d_{\uparrow}, d_{\uparrow}^{\dagger}, n_{\uparrow}}^{[12]}(\omega) &= \pi i t \left[\frac{\delta(\omega_1 - u)}{\omega_2^+ + u} - \frac{\delta(\omega_1 + u)}{\omega_2^+ - u} \right] \\ &\quad + \pi i t \left[\frac{\delta(\omega_2 - u)}{\omega_1^+ + u} - \frac{\delta(\omega_2 + u)}{\omega_1^+ - u} \right], \\ G_{d_{\uparrow}, d_{\uparrow}^{\dagger}, n_{\uparrow}}^{[123]}(\omega) &= \frac{u^2 - \omega_1^+ \omega_2^+}{[(\omega_1^+)^2 - u^2][(\omega_2^+)^2 - u^2]} \end{aligned} \quad (115)$$

Here, $G_{d_{\uparrow}, d_{\uparrow}^{\dagger}, n_{\uparrow}}^{[12]}$ includes two discontinuities across $\gamma_1 = 0$ and $\gamma_2 = 0$, but no contribution from \hat{G}_3 , leading to the different structure compared to the other two Keldysh components with $\alpha = 2$. Surprisingly, $G_{d_{\uparrow}, d_{\uparrow}^{\dagger}, n_{\uparrow}}^{[123]}$ is directly determined by $G^{[13]}$. All other contributions from regular and anomalous parts mutually cancel, see Appendix H.2.

7.2.2. Three-Spin Correlator

3p bosonic correlators are the central objects in non-linear response theory. Here, we consider the correlator for the spin operators $\mathbf{O} = (S_x, S_y, S_z)$, describing second-order changes in the magnetization by applying an external magnetic field. The spin

operators are given by

$$S_x = \frac{1}{2} \left(d_{\uparrow}^{\dagger} d_{\downarrow} + d_{\downarrow}^{\dagger} d_{\uparrow} \right), \quad S_y = -\frac{i}{2} \left(d_{\uparrow}^{\dagger} d_{\downarrow} - d_{\downarrow}^{\dagger} d_{\uparrow} \right),$$

$$S_z = \frac{1}{2} \left(n_{\uparrow} - n_{\downarrow} \right) \quad (116)$$

The spectral representation, using the MF kernel in Equation (A4b), then yields

$$G_{S_x, S_y, S_z}(\mathbf{i}\omega) = -\beta \delta_{i\omega_1} \tilde{Z} \Delta_{i\omega_2} + \beta \delta_{i\omega_2} \tilde{Z} \Delta_{i\omega_1} - \beta \delta_{i\omega_{12}} \tilde{Z} \Delta_{i\omega_1}$$

$$= \beta \delta_{i\omega_1} \hat{G}_1^{\Delta}(i\omega_2) + \beta \delta_{i\omega_2} \hat{G}_2^{\Delta}(i\omega_1) + \beta \delta_{i\omega_3} \hat{G}_3^{\Delta}(i\omega_1) \quad (117)$$

where $\tilde{Z} = ie^{\beta u} / (2Z)$.

From Equations (84a)–(84d), we deduce the only nonzero Keldysh components as

$$G_{S_x, S_y, S_z}^{[12]}(\omega) = -4\pi i \delta(\omega_1) \frac{\tilde{Z}}{\omega_2^+} + 4\pi i \delta(\omega_2) \frac{\tilde{Z}}{\omega_1^+},$$

$$G_{S_x, S_y, S_z}^{[13]}(\omega) = -4\pi i \delta(\omega_1) \frac{\tilde{Z}}{\omega_2^-} - 4\pi i \delta(\omega_{12}) \frac{\tilde{Z}}{\omega_1^+}, \quad (118)$$

$$G_{S_x, S_y, S_z}^{[23]}(\omega) = 4\pi i \delta(\omega_1) \frac{\tilde{Z}}{\omega_1^-} - 4\pi i \delta(\omega_{12}) \frac{\tilde{Z}}{\omega_1^-}$$

Even though anomalous parts contribute to $G^{[23]}$ as well, they solely originate from the \hat{G}_i^{Δ} terms, such that $G^{[23]}$ vanishes in this case.

7.3. Example for $\ell = 4$: Fermionic 4p Correlator

Finally, we consider the 4p correlator $G_{\sigma\sigma'}$ involving the operators $O = (d_{\sigma}^{\dagger}, d_{\sigma'}^{\dagger}, d_{\sigma}, d_{\sigma'})$. Let us showcase the analytic continuation for $G_{\uparrow\downarrow}$, which evaluates in the MF to

$$G_{\uparrow\downarrow}(\mathbf{i}\omega) = \frac{2u \prod_{i=1}^4 (i\omega_i) + u^3 \sum_{i=1}^4 (i\omega_i)^2 - 6u^5}{\prod_{i=1}^4 [(i\omega_i)^2 - u^2]}$$

$$+ \frac{u^2 [\beta \delta_{i\omega_{12}} t + \beta \delta_{i\omega_{13}} (t-1) + \beta \delta_{i\omega_{14}} (t+1)]}{\prod_{i=1}^4 (i\omega_i + u)}$$

$$= \tilde{G}(\mathbf{i}\omega) + \beta \delta_{i\omega_{12}} \hat{G}_{12}(\mathbf{i}\omega) + \beta \delta_{i\omega_{13}} \hat{G}_{13}(\mathbf{i}\omega)$$

$$+ \beta \delta_{i\omega_{14}} \hat{G}_{14}(\mathbf{i}\omega) \quad (119)$$

We study the analytic continuation to the Keldysh component $G^{[12]}$, expressed in terms of the analytic regions from Equation (102). Since the regular part only depends on the frequencies $i\omega_i$ individually, the discontinuities across $\gamma_{12} = 0$, $\gamma_{13} = 0$, and $\gamma_{14} = 0$ vanish (Figure 6c), resulting in

$$G_{\uparrow\downarrow}^{[12]}(\omega) = N_1 \left(C_{\text{III}}^{(12)} - C^{(2)} \right) + N_2 \left(C_1^{(12)} - C^{(1)} \right)$$

$$+ 4\pi i \delta(\omega_{13}) \hat{C}_{13}^{(12)} + 4\pi i \delta(\omega_{14}) \hat{C}_{14}^{(12)} \quad (120)$$

The remaining discontinuities can be computed without further complications. From Equation (119), we can already infer

some of their structures. Since the regular part has poles at $i\omega_1 \rightarrow z_1 = \pm u$ (or $i\omega_2 \rightarrow z_2 = \pm u$), we expect the discontinuity across $\gamma_1 = 0$ (or $\gamma_2 = 0$) to select these poles. Indeed, we find (see Appendix H.3)

$$G_{\uparrow\downarrow}^{[12]}(\omega) = 2\pi i u t \frac{\delta(\omega_1 - u) - \delta(\omega_1 + u)}{(\omega_2^+)^2 - u^2} \left(\frac{1}{\omega_{13}^-} + \frac{1}{\omega_{14}^-} \right)$$

$$+ (1 \leftrightarrow 2) + 4\pi i u^2 \frac{\delta(\omega_{13})(t-1) + \delta(\omega_{14})(t+1)}{[(\omega_1^+)^2 - u^2][(\omega_2^+)^2 - u^2]} \quad (121)$$

where $1 \rightarrow 2$ indicates that indices 1 and 2 are exchanged compared to the first term. This expression can be simplified even further by collecting terms proportional to t and rewriting the δ -functions in the resulting prefactor using Equations (58) and (107b). We eventually obtain

$$G_{\uparrow\downarrow}^{[12]}(\omega) = 4\pi i u^2 \frac{\delta(\omega_{14}) - \delta(\omega_{13})}{[(\omega_1^+)^2 - u^2][(\omega_2^+)^2 - u^2]}$$

$$+ 2u^2 t \left[\frac{1}{(\omega_1^+)^2 - u^2} \frac{1}{(\omega_2^-)^2 - u^2} \left(\frac{1}{\omega_{23}^-} + \frac{1}{\omega_{24}^-} \right) - \text{c.c.} \right] \quad (122)$$

where c.c. is the complex conjugate. The other Keldysh components follow by similar calculations, see Appendix H.4.

This concludes the section on HA examples for the analytic continuation of multipoint correlators. We again stress the simplicity of the analytic continuation procedure using our results for the Keldysh components expressed through analytic regions.

8. Vertex Corrections to Conductance

In this section, we consider a specific application of the analytic continuation of 4p functions regarding vertex corrections to the conductivity. One can deduce vertex corrections to real-frequency susceptibilities either by working directly in the KF or by using the MF and the analytic continuation method. The latter strategy was pursued by Eliashberg,^[13] converting Matsubara sums into contour integrals and thereby obtaining various vertex contributions which consist of linear combinations of the MF vertex analytically continued to specific regions. For the special case of the linear conductance through an interacting region coupled to two noninteracting leads, Oguri^[62] subsequently found that only one of these many vertex corrections contributes to the final result. A very similar formula for the linear conductance was later derived by Heyder et al.^[63] with a different line of argument, working entirely in the KF. With our insights on 4p analytic continuation and gFDRs, we can demonstrate the equivalence between the results by Oguri and Heyder et al. and connect the MF and KF derivations.

A general susceptibility χ can be expressed as in Figure 7. The first (“bubble”) term merely comprises two 2p correlators. We thus focus on the second term, the vertex correction, which in the MF reads

$$\chi_F(\mathbf{i}\omega) = \frac{1}{\beta^2} \sum_{iv, iv'} G(\mathbf{i}v) G(\mathbf{i}v + \mathbf{i}\omega) F(\mathbf{i}v, \mathbf{i}v', \mathbf{i}\omega) G(\mathbf{i}v') G(\mathbf{i}v' + \mathbf{i}\omega) \quad (123)$$



Figure 7. Diagrammatic representation of the susceptibility χ consisting of a bubble and a vertex contribution. Lines represent propagators G , and the square is a vertex F .

Definitions of the propagator G and vertex F can be found in Section III A of ref. [23]. The summand in Equation (123) is the connected 4p correlator. Due to their close relation, the vertex F inherits its analytic properties from the correlator. In fact, by a transformation of Keldysh correlators to the R/A basis,^[64,65] it can be easily shown that our formulas in Equation (101) identically hold for F , and we thus use the same symbols C to denote analytic continuations of F (see, e.g., Equation (124b)). Note that the Keldysh indices 1 and 2 exchange their meaning for F , such that, e.g., a fully retarded component reads $F^{[1]} = F^{1222}$ (while $G^{[1]} = G^{2111}$).

In ref. [13], Eliashberg converted the Matsubara sums in Equation (123) to contour integrals, thereby analytically continuing the MF functions and picking up contributions from all regions of analyticity (see Figure 5). In ref. [62], Oguri showed that the ω -linear part, needed for the linear conductance (lc), stems from only one function, $F^{(0)}$, see Equation (2.34) in ref. [62]. The corresponding vertex correction to the retarded susceptibility reads

$$\chi_{F,lc}^R(\omega) = - \int \int \frac{d\nu d\nu'}{(4\pi i)^2} G^R(\nu + \omega) G^A(\nu) G^A(\nu') G^R(\nu' + \omega) \times \left[\tanh\left(\frac{\nu + \omega}{2T}\right) - \tanh\left(\frac{\nu}{2T}\right) \right] F_O(\nu, \nu', \omega) \quad (124a)$$

$$F_O = -N_{\omega_3} C_{II}^{(12)} - N_{\omega_4} C_{IV}^{(12)} + N_{\omega_{13}} [C_{II}^{(12)} - C_{III}^{(12)}] + N_{\omega_{14}} [C_{IV}^{(12)} - C_{III}^{(12)}] \quad (124b)$$

where we used

$$(\omega_1, \omega_2, \omega_3, \omega_4) = (\nu + \omega, -\nu, \nu', -\nu' - \omega) \quad (125)$$

as frequency parametrization. Note that the results by Oguri and Eliashberg differ in their choice of the MWF; Equation (124b) corresponds to \mathcal{T}_{22} in Equation (12) of ref. [13].

An analogous result with an independent KF derivation was obtained in Equations (11) and (17) of ref. [63] by Heyder et al. There, the vertex correction to the linear conductance corresponds to

$$\chi_{F,lc}^R(\omega) = \int \int \frac{d\nu d\nu'}{(4\pi i)^2} G^R(\nu + \omega) G^A(\nu) G^A(\nu') G^R(\nu' + \omega) \times \left[\tanh\left(\frac{\nu + \omega}{2T}\right) - \tanh\left(\frac{\nu'}{2T}\right) \right] F_H(\nu, \nu', \omega) \quad (126a)$$

$$F_H = - (F^{[12]} + N_{\omega_1} F^{[2]} + N_{\omega_2} F^{[1]}) \quad (126b)$$

For an easier comparison with Equation (124a), we here used the tanh function instead of the Fermi distribution function. We also

absorbed a factor of 2 due to our choice of convention for the Keldysh rotation of multipoint functions (cf. Equation (17)).

To show that Equations (124a) and (126a) are equivalent, we translate the analytic continuations of the MF vertex in Equation (124b) to Keldysh components. First, we note that the linear combination of terms comprising F_O in Equation (124b) can also be expressed as follows, using (103):

$$F^{[34]} + N_{\omega_3} F^{[4]} + N_{\omega_4} F^{[3]} = N_{\omega_3} C_{II}^{(12)} + N_{\omega_4} C_{IV}^{(12)} + N_{\omega_{13}} [C_{III}^{(12)} - C_{II}^{(12)}] + N_{\omega_{14}} [C_{III}^{(12)} - C_{IV}^{(12)}] = -F_O \quad (127)$$

where we assumed vanishing anomalous parts. Next, we use the gFDR in Equation (104a) for vertices,

$$(N_{\omega_3} + N_{\omega_4}) (F^{[12]} + N_{\omega_1} F^{[2]} + N_{\omega_2} F^{[1]}) = (N_{\omega_1} + N_{\omega_2}) (F^{[34]} + N_{\omega_3} F^{[4]} + N_{\omega_4} F^{[3]}) \quad (128)$$

Together with Equation (125), this implies the equivalence of Equations (124a) and (126a) as

$$(N_{\omega_3} + N_{\omega_4}) F_H = (N_{\omega_1} + N_{\omega_2}) F_O \quad (129)$$

With the analytic continuation formulas and the gFDRs, we have thereby shown that both results agree and provided a direct transcription between two independent MF and KF derivations.

9. Conclusion

We showed how to perform the analytic continuation of multipoint correlators in thermal equilibrium from the imaginary-frequency MF to the real-frequency KF. To this end, we used the spectral representation derived in ref. [23], separating the correlator into formalism-independent partial spectral functions (PSFs) and formalism-specific kernels. From this analytical starting point, we showed that it is possible to fully recover all 2^ℓ components of the ℓ p KF correlator from the one ℓ p MF correlator. Our main result is that each of the $(\ell!)$ PSFs can be obtained by linear combinations of analytic continuations of the MF correlator multiplied with combinations of Matsubara weighting functions (MWFs). Explicit formulas are given in Equations (47) and (74) for arbitrary 2p and 3p correlators, respectively, and Equation (88) for fermionic 4p correlators. For these cases, we additionally derived direct MF-to-KF continuation formulas in Equation (61) ($\ell = 2$), Equations (84) ($\ell = 3$), and Equations (101) ($\ell = 4$), complementing the general Equation (23) for any ℓ .

We approached the problem of analytic continuation by comparing the spectral representations of general ℓ p MF (G) and KF ($G^{[n_1 \dots n_\ell]}$) correlators and by identifying the regular partial MF correlators, \tilde{G}_p , as the central link between them. A key insight was that the partial MF correlators can be obtained by an imaginary-frequency convolution of MF kernels with the full MF correlator, $\tilde{G}_p(i\omega_p) + \mathcal{O}(\frac{1}{\beta}) = (K \star G)(i\omega_p)$. Building on this formula, we developed a three-step strategy for the MF-to-KF analytic continuation, applicable to arbitrary ℓ p correlators and explicitly presented in the aforementioned cases $\ell \leq 4$. In the first step, we

used the kernel representation of ref. [30] to express the Matsubara sums, inherent in the imaginary-frequency convolution, through contour integrals enclosing the imaginary axis. In the second step, we deformed the contours toward the real axis, carefully tracking possible singularities of the MF correlator. This resulted in a spectral representation $\tilde{C}_p(i\omega_p) = (\tilde{K} * S_p)(i\omega_p)$, which allowed us to extract the PSFs, $S_p[G]$, as functionals of the regular and the various anomalous parts of G multiplied with MWFs. In the third and final step, we simplified the spectral representation for the KF components $G^{[n_1 \dots n_\alpha]}$, inserted the PSFs from the second step, and evaluated all real-frequency integrals to express the KF correlators as linear combinations of analytically continued MF correlators.

In our analysis, we explicitly considered so-called anomalous parts of the MF correlator which can occur, e.g., for conserved quantities or in finite systems with degenerate energy eigenstates. The analytical continuations of these terms do not contribute to fully retarded correlators, but they do contribute to other components of the KF correlator. In the KF, the notion of “anomalous terms” is not needed; instead, the corresponding contributions are included via δ -terms in the kernels, see Equation (20) and Equations (57)–(59) for $\ell = 2$.

Exploiting the relations between KF correlators and analytically continued MF functions, we derived generalized fluctuation-dissipation relations (gFDRs) for 3p and 4p correlators, Equations (84) and (104), establishing relations between the different KF components. We thereby reproduced the results of refs. [24, 25], while additionally including the anomalous terms.

We expect that similar results can be obtained for multipoint ($\ell > 2$) out-of-time-ordering correlators (OTOCs)^[66] which generalize the KF by additional copies of the Keldysh contour. Multipoint OTOCs, too, can be written as a sum over permutations of PSFs and kernels which encode the ordering on the desired number of branches. Importantly, the PSFs arising in this manner are precisely the same as those used in this work. Hence, the steps presented in Sections 3.3, 5.2 and 6.2 should be generalizable to multipoint OTOCs. Expressing the PSFs in terms of analytically continued MF correlators, analogous calculations would then reveal direct MF-to-OTOC continuation formulas. We leave this to future work.

As an application of our results, we considered various correlators of the Hubbard atom. Starting from their MF expressions, we calculated all components of the corresponding KF correlators using analytic continuation. For the fermionic 4p correlator, a full list of all Keldysh components for the two relevant spin configurations is given in Equations (H18) and (H20).

We further used our formulas to find KF expressions of the MF results derived in refs. [13, 62] for the linear conductance through an interacting system. There, the authors showed that only few analytic continuations of the vertex function are required for the vertex corrections to the linear conductance. Similar results were derived in ref. [63] working entirely in the KF. We reproduced their real-frequency results by analytic continuation and could thus provide a direct transcription between two independent derivations in the MF and the KF.

For future investigations, it would be interesting to apply our formulas in conjunction with the algorithmic Matsubara integration technique.^[60] There, the evaluation of Feynman diagrams yields an exact symbolic expression for $G(i\omega)$ that can

be readily continued to full Keldysh correlators or to PSFs. If, by contrast, the Matsubara results are only available as numerical data, the numerical analytic continuation is an ill-conditioned problem. Nevertheless, recent advances suggest that it can possibly be tamed to some extent by exploiting further information on mathematical properties of the function.^[67–69]

Numerically representing multipoint MF correlators is another fruitful direction to explore. References^[70,71] showed that 2p MF functions can be represented compactly by a suitable basis expansion. Yet, for multipoint functions, ref. [33] found that the overcompleteness of the basis hinders an extraction of the basis coefficients by projection. Here, a numerical counterpart of our method for recovering individual PSFs S_p (or partial correlators G_p) from a full correlator $G(i\omega)$ might be helpful. Finally, our formulas might also be useful for evaluating diagrammatic relations typically formulated for correlators while using the PSFs as the main information carriers. For recent developments regarding the numerical computation of MF or KF multipoint correlators using symmetric improved estimators, see ref. [61].

Appendix A: MF Kernels

This appendix is devoted to a discussion of the full primary MF kernel K , including both regular and anomalous terms. It is defined via Equation (10a) for the MF kernel $\mathcal{K}(\Omega_p)$. In ref. [23], it was shown that it can be computed via

$$\begin{aligned} \mathcal{K}(\Omega_p) &= \int_0^\beta d\tau'_\ell e^{\Omega_{\bar{1} \dots \bar{\ell}} \tau'_\ell} \prod_{i=\ell-1}^1 \left[- \int_0^{\beta-\tau'_{i+1} \dots \bar{\ell}} d\tau'_i e^{\Omega_{\bar{1} \dots \bar{i}} \tau'_i} \right] \\ &= \beta \delta_{\Omega_{\bar{1} \dots \bar{\ell}}} K(\Omega_p) + \mathcal{R}(\Omega_p) \end{aligned} \quad (\text{A1})$$

The residual part \mathcal{R} is not of interest, for reasons explained after Equation (12). The primary part $K(\Omega_p)$ is obtained^[72] by collecting all contributions multiplying $\beta \delta_{\Omega_{\bar{1} \dots \bar{\ell}}}$, and its argument satisfies $\Omega_{\bar{1} \dots \bar{\ell}} = 0$ by definition. Before presenting explicit expressions for K , let us briefly recall where it is needed in the main text.

The analytical continuation of MF to KF correlators, based on $\tilde{C}_p(i\omega_p \rightarrow \omega^{[p]})$ (Equation (26)), utilizes regular partial MF correlators, $\tilde{C}_p(i\omega_p) = [\tilde{K} * S_p](i\omega_p)$ (Equation (14c)). These are expressed through regular MF kernels $\tilde{K}(\Omega_p)$ having a simple product form, $\prod_{i=1}^{\ell-1} \Omega_{\bar{1} \dots \bar{i}}^{-1}$, with $\Omega_{\bar{1} \dots \bar{\ell}} = 0$ understood. The more complicated primary kernel $K(\Omega_p)$ is defined implicitly via Equation (10a). It includes both regular and anomalous parts, the latter involving vanishing partial frequency sums, $\Omega_{\bar{1} \dots \bar{i}} = 0$ with $i < \ell$. The primary kernel arises in two distinct contexts, involving either (i) imaginary-frequency convolutions \star or (ii) real-frequency convolutions $*$, with different requirements for the bookkeeping of anomalous contributions. We discuss them in turn.

- (i) For a specified permutation p , the regular partial $\tilde{C}_p(i\omega_p)$ can be extracted from the full MF correlator $G(i\omega')$ via a imaginary-frequency convolution, $[K \star G](i\omega_p)$ (Equation (31)). There, the argument of $K(\Omega_p)$ has the form $\Omega_p = i\omega_p - i\omega'_p$. This is always bosonic, being the difference of two same-type Matsubara frequencies. The convolution \star involves Matsubara sums $\sum_{i\omega'_p}$, generating many anomalous contributions with $\Omega_{\bar{1} \dots \bar{i}} = 0$. For these sums to be well-defined, the kernel $K(\Omega_p)$ must thus be represented in a form that (in contrast to $\tilde{K}(\Omega_p)$) is manifestly singularity-free for all values of $\Omega_{\bar{1} \dots \bar{i}}$, including 0.
- (ii) In Equation (31), \tilde{C}_p is given by that part of $[K \star G]$ that is $\mathcal{O}(\beta^0)$; sub-leading powers of β are not needed. Therefore, we seek the MF $G(i\omega')$ in the form of an $\beta\delta$ expansion, i.e. an expansion in powers of $\beta\delta_{\omega'_{\bar{1} \dots \bar{i}}}$.

Then each of them can collapse one Matsubara sum $1/(-\beta) \sum_{1\dots i} \omega'_{1\dots i}$ while their β factors cancel. To obtain a $\beta\delta$ expansion for $G(i\omega')$, it is convenient to express it via a permutation sum of real-frequency convolutions, $\sum_p [K * S_p](i\omega'_p)$ (Equation (11b)), and represent the kernel $K(\Omega_p)$, with argument $\Omega_p = i\omega'_p - \epsilon_p$, as a $\beta\delta$ expansion in powers of $\beta\delta_{\Omega'_{1\dots i}}$.

Fortunately, suitable representations of K satisfying the respective requirements of either (i) or (ii) are available in the literature.^[23,30,73,74] We discuss them for $\ell \leq 4$ in Appendices A.1 and A.2, respectively.

A.1. Singularity-Free Representation of K

Consider case (i), involving $K \star G$, where the argument of $K(\Omega_p)$ is a bosonic Matsubara frequency. We seek a singularity-free (sf) representation for K , to be denoted K^{sf} for the purpose of this appendix. That such a representation exists is obvious from the form of integrals in Equation (A1): inserting $\Omega_{1\dots i} = 0$ there reduces an exponential function to 1, so no contributions singular in $\Omega_{1\dots i}$ can arise. To find K^{sf} , one simply has to perform the integrals explicitly, treating the cases $\Omega_{1\dots i} \neq 0$ or $= 0$ separately and distinguish them using Kronecker symbols.

Such a direct computation of Equation (A1) has been performed in ref. [30] for arbitrary ℓ and an arbitrary number of vanishing partial frequency sums, $\Omega_{1\dots i} = 0$. The following equations summarize their results for $\ell \leq 4$:

$$K^{\text{sf}}(\Omega_p)^{\ell=2} = \Delta_{\Omega_1} - \frac{\beta}{2} \delta_{\Omega_1} \quad (\text{A2a})$$

$$K^{\text{sf}}(\Omega_p)^{\ell=3} = \Delta_{\Omega_{12}} \left(\Delta_{\Omega_1} - \frac{\beta}{2} \delta_{\Omega_1} \right) - \delta_{\Omega_{12}} \left(\Delta_{\Omega_1}^2 + \frac{\beta}{2} \Delta_{\Omega_1} - \frac{\beta^2}{6} \delta_{\Omega_1} \right) \quad (\text{A2b})$$

$$K^{\text{sf}}(\Omega_p)^{\ell=4} = \Delta_{\Omega_{123}} \left[\Delta_{\Omega_{12}} \left(\Delta_{\Omega_1} - \frac{\beta}{2} \delta_{\Omega_1} \right) - \delta_{\Omega_{12}} \left(\Delta_{\Omega_1}^2 + \frac{\beta}{2} \Delta_{\Omega_1} - \frac{\beta^2}{6} \delta_{\Omega_1} \right) \right] - \delta_{\Omega_{123}} \left[\Delta_{\Omega_{12}} \Delta_{\Omega_1} \left(\Delta_{\Omega_{12}} + \Delta_{\Omega_1} + \frac{\beta}{2} \right) - \frac{\beta}{2} \Delta_{\Omega_{12}} \delta_{\Omega_1} \left(\Delta_{\Omega_{12}} + \frac{\beta}{3} \right) - \delta_{\Omega_{12}} \Delta_{\Omega_1} \left(\Delta_{\Omega_1}^2 + \frac{\beta}{2} \Delta_{\Omega_1} + \frac{\beta^2}{6} \right) + \frac{\beta^3}{24} \delta_{\Omega_{12}} \delta_{\Omega_1} \right] \quad (\text{A2c})$$

Equations (A2) are manifestly singularity-free for all values of their frequency arguments—including those with $\Omega_{1\dots i} = 0$, for which $\Delta_{\Omega_{1\dots i}}$ terms vanish by definition (Equation (32)).

A.2. $\beta\delta$ Expansion for K

Next, consider case (ii), involving $G = \sum_p K * S_p$ (Equations (11b) and (12)), where the argument of $K(\Omega_p)$ has the form $\Omega_p = i\omega_p - \epsilon_p$, and we seek a $\beta\delta$ expansion for G . For this purpose, the kernels K^{sf} of Equations (A2) are inconvenient, because they contain some δ factors not accompanied by β . Instead, G can be expressed through an alternative kernel, to be denoted K^{alt} , which constitutes a $\beta\delta$ expansion itself and hence differs from K^{sf} , but yields the same result for G when summed over all permutations, so that

$$G(i\omega) = \sum_p [K^{\text{sf}} * S_p](i\omega) = \sum_p [K^{\text{alt}} * S_p](i\omega) \quad (\text{A3})$$

Explicit expressions for K^{alt} were given in ref. [23] for up to one potentially vanishing frequency (general 2p correlators, 3p correlators with one bosonic operator, and fermionic 4p correlators). By also allowing general 3p correlators, these results are extended to

$$K^{\text{alt}}(\Omega_p)^{\ell=2} = \frac{1}{\Omega_1} - \frac{\beta}{2} \delta_{\Omega_1} \quad (\text{A4a})$$

$$K^{\text{alt}}(\Omega_p)^{\ell=3} = \frac{1}{\Omega_1 \Omega_{12}} - \frac{\beta}{2} \left(\delta_{\Omega_{12}} \Delta_{\Omega_1} + \delta_{\Omega_1} \Delta_{\Omega_{12}} \right) + \frac{\beta^2}{6} \delta_{\Omega_1} \delta_{\Omega_{12}} \quad (\text{A4b})$$

$$K^{\text{alt}}(\Omega_p)^{\ell=4} = \frac{1}{\Omega_1 \Omega_{12} \Omega_{123}} - \frac{\beta}{2} \delta_{\Omega_{12}} \frac{1}{\Omega_1 \Omega_{123}} \quad (\text{A4c})$$

The kernels (A4) have the form $K^{\text{alt}} = \tilde{K} + \hat{K}^{\text{alt}}$, with regular part \tilde{K} as given in Equation (13b), while the anomalous part, \hat{K}^{alt} , comprises terms multiplied by one or multiple factors $\beta\delta_{\Omega_{1\dots i}}$. (We remark that the nomenclature *regular* and *anomalous* is used non-uniformly in the literature and our usage here may differ from refs. [23, 30, 73].) Whether or not $\Omega_{1\dots i} = i\omega_{1\dots i} - \epsilon_{1\dots i}$ can vanish at all depends on the fermionic or bosonic nature of the Matsubara frequencies. Take, e.g., $\ell = 4$ and all operators fermionic. Then, in Equation (A2c), all terms multiplied by $\delta_{\Omega_{123}}$ evaluate to $\delta_{\Omega_{123}} = 0$, since $i\omega_{123} \neq 0$ is a fermionic Matsubara frequency. For the computation of fermionic 4p correlators, all terms proportional to δ_{Ω_1} and $\delta_{\Omega_{123}}$ can thus be dropped. Even if $i\omega_{1\dots i}$ is bosonic and vanishes, $\Omega_{1\dots i} = 0$ additionally requires $\epsilon_{1\dots i} = 0$, enforced by a Dirac $\delta(\epsilon_{1\dots i})$ in the PSFs; see Appendix B.1 for further discussion of this point.

For a specified permutation p , the kernels K^{alt} are not singularity-free. In particular, the regular part \tilde{K} diverges if one (or multiple) $\Omega_{1\dots i} \rightarrow 0$. However, that singularity is canceled by $1/\Omega_{1\dots i} \rightarrow -1/\Omega_{1\dots i}$ from a cyclically related permutation in the sum over permutations in Equation (A3). This can be shown explicitly by treating nominally vanishing denominators as infinitesimal and tracking the cancellation of divergent terms while exploiting the equilibrium condition (4) (see Appendix B of ref. [23]).

The kernels K^{alt} , inserted into Equation (A4), result in the general form for MF correlators given in Equation (14):

$$G(i\omega) = \tilde{G}(i\omega) + \hat{G}(i\omega) \quad (\text{A5a})$$

$$\hat{G}(i\omega) = \sum_{j=1}^{\ell-1} \beta \delta_{i\omega_j} \hat{G}_j(i\omega) + \sum_{j=1}^{\ell-1} \sum_{k>j}^{\ell-1} \left(\beta \delta_{i\omega_j} \hat{G}_{jk}(i\omega) + \beta^2 \delta_{i\omega_j} \delta_{i\omega_k} \hat{G}_{j,k}(i\omega) \right) \quad (\text{A5b})$$

As for Equation (A4), this form of the anomalous part of the correlator applies to general 2p and 3p correlators as well as fermionic 4p correlators. The subscripts of \hat{G} indicate the frequency in which they are anomalous. Even though their arguments nominally include all frequencies $i\omega$, they are independent of their respective anomalous frequency; e.g., $\hat{G}_1(i\omega_1, i\omega_2) = \hat{G}_1(i\omega_2)$ for $\ell = 3$. Note that this decomposition of the correlator is convenient for the analytic continuation because the components, such as \tilde{G} and \hat{G}_j , have a functional form that allows their arguments to be analytically continued, $i\omega_j \rightarrow z_j$. In anomalous components this functional form is obtained by symbolically replacing all $\Delta_{i\omega}$ by $\frac{1}{i\omega}$ (see, e.g., Equation (80) and the discussion thereafter).

Appendix B: Discussion of PSFs

In Appendix B.1, we clarify the functional structure of PSFs and motivate their decomposition into regular and anomalous contributions, $S_p = \tilde{S}_p + \hat{S}_p$ (Equation (5)), analogous to that for MF correlators. This decomposition aids investigations in subsequent appendices. As an immediate application of the decomposition, we present an analysis of the effect of fully anomalous PSFs on 3p MF correlators in Appendix B.2.

B.1. Decomposition of PSFs

Interacting thermal systems typically have a continuum of energy levels. Ref. [27] argues that, in general, PSFs may contain contributions which diverge as $P(\frac{1}{\epsilon})$ for vanishing bosonic frequencies ϵ , with P the principal value. As our derivations do not make assumptions on the shape

of continuous PSF contributions, such terms require no further consideration. However, Dirac delta contributions in S_p can arise for finite systems or in the presence of conserved quantities. When these are present, MF partial correlators $G_p = K * S_p$ (Equation (11b)) can contain anomalous terms, \hat{G}_p , containing at least one factor $\delta_{i\omega_{\tau\dots i}}$, with $i < \ell$. These arise from anomalous $\delta_{\Omega_{\tau\dots i}}$ terms in the MF kernel $K(\Omega_p)$, with argument $\Omega_p = i\omega_p - \varepsilon_p$ (Equations (A3), (A4)). Such terms can contribute if $\Omega_{\tau\dots i} = 0$, requiring $i\omega_{\tau\dots i} = 0$ and $\varepsilon_{\tau\dots i} = 0$. The first condition requires that $i\omega_{\tau\dots i}$ is bosonic. This is the case if the sign $\zeta^{\tau\dots i} = \zeta^{\tau\dots i}$ equals +1 (with $\zeta^j = \pm 1$ for bosonic/fermionic operators \mathcal{O}). Then, the associated $\varepsilon_{\tau\dots i}$ is bosonic, too, according to the nomenclature introduced after Equation (3b). The second condition is met if the PSF $S_p(\varepsilon_p)$ contains a term proportional to a bosonic Dirac delta, i.e. one having a bosonic $\varepsilon_{\tau\dots i}$ as argument, e.g. $\delta(\varepsilon_{\tau\dots i})\tilde{S}_{\tau\dots i}$. Then, the ε_p integrals in the convolution $K * S_p$ receive a finite contribution from the point $\varepsilon_{\tau\dots i} = 0$. We summarize these conditions via the symbolic notation

$$\delta_{\Omega_{\tau\dots i}} = \delta_{i\omega_{\tau\dots i}} \delta_{\varepsilon_{\tau\dots i}} \quad (\text{B1})$$

needed only for bosonic $\Omega_{\tau\dots i}$. Here $\delta_{\varepsilon_{\tau\dots i}}$, carrying a continuous variable as subscript, is defined only for bosonic $\varepsilon_{\tau\dots i}$ and by definition “acts on” $S_p(\varepsilon_p)$ by extracting only those parts (if present) containing bosonic Dirac $\delta(\varepsilon_{\tau\dots i})$ factors. For the example above, $\delta_{\varepsilon_{\tau\dots i}}$ acts on $S_p(\varepsilon_p)$ as

$$\delta_{\varepsilon_{\tau\dots i}} S_p(\varepsilon_p) = \delta_{\varepsilon_{\tau\dots i}} \hat{S}_p(\varepsilon_p) \sim \delta(\varepsilon_{\tau\dots i}) \quad (\text{B2})$$

As we always assume an even number of fermionic operators, $\zeta^{1\dots\ell} = +1$ follows.

The motivation for splitting PSFs as $S_p = \tilde{S}_p + \hat{S}_p$ is now clear. The anomalous \hat{S}_p comprises all terms containing bosonic Dirac $\delta(\varepsilon_{\tau\dots i})$ factors, the regular \tilde{S} everything else. The regular part of the MF correlator, \hat{G} , receives contributions from both \tilde{S}_p and \hat{S}_p ; the anomalous part, \hat{G} , receives contributions only from \hat{S}_p , i.e. if $\hat{S}_p = 0$ for all p , then $\hat{G} = 0$.

For $\ell = 2$, the anomalous contribution consists of one term,

$$\hat{S}_p(\varepsilon_p) = \delta(\varepsilon_{\tau}) \tilde{S}_{p;\tau} \quad (\text{B3})$$

where $\tilde{S}_{p;\tau}$ is a constant. Due to the equilibrium condition (4), we can further conclude $\tilde{S}_{(12);1} = \tilde{S}_{(21);2}$.

For $\ell = 3$, the anomalous \hat{S}_p reads

$$\hat{S}_p(\varepsilon_p) = \delta(\varepsilon_{\tau}) \tilde{S}_{p;\tau}(\varepsilon_{\bar{\tau}}, \varepsilon_{\bar{\tau}}) + \delta(\varepsilon_{\bar{\tau}}) \tilde{S}_{p;\bar{\tau}}(\varepsilon_{\tau}, \varepsilon_{\tau}) + \delta(\varepsilon_{\tau}) \delta(\varepsilon_{\bar{\tau}}) \tilde{S}_{p;\tau\bar{\tau}} \quad (\text{B4})$$

Here, we inserted ε 's to emphasize that functions do not depend on these arguments, and $\tilde{S}_{p;\tau\bar{\tau}}$ is a constant. For bosonic 3p functions, $\tilde{S}_{p;\tau}$ and $\tilde{S}_{p;\bar{\tau}}$ do not contain further δ -factors that lead to anomalous parts, e.g., $\delta_{\varepsilon_{\bar{\tau}}} \tilde{S}_{p;\tau}(\varepsilon_{\tau}, \varepsilon_{\tau}) = 0$.

To further illustrate the symbolic $\delta_{\varepsilon_{\tau\dots i}}$ notation introduced in Equation (B1), it yields the following relations when applied to the above definitions, for bosonic ε_i :

$$\delta_{\varepsilon_{\tau}} S_p(\varepsilon_p) = \delta(\varepsilon_{\tau}) \tilde{S}_{p;\tau}(\varepsilon_p) + \delta(\varepsilon_{\bar{\tau}}) \delta(\varepsilon_{\bar{\tau}}) \tilde{S}_{p;\tau\bar{\tau}} \quad (\text{B5a})$$

$$\delta_{\varepsilon_{\bar{\tau}}} \delta_{\varepsilon_{\tau}} S_p(\varepsilon_p) = \delta(\varepsilon_{\bar{\tau}}) \delta(\varepsilon_{\tau}) \tilde{S}_{p;\tau\bar{\tau}} \quad (\text{B5b})$$

For fermionic $\ell = 4$, we only need

$$\hat{S}_p(\varepsilon_p) = \delta(\varepsilon_{\tau\bar{\tau}}) \tilde{S}_{p;\tau\bar{\tau}}(\varepsilon_p) \quad (\text{B6})$$

since, e.g., terms in the kernel proportional to $\delta_{i\omega_{\tau}-\varepsilon_{\tau}}$ do not lead to anomalous contributions by the fermionic nature of $i\omega_{\tau}$.

B.2. Effect of Fully Anomalous PSFs on 3p MF Correlators

In the Appendix C.1 below, we discuss the general structure of 3p MF correlators inferred by the decomposition of the PSFs. The regular PSFs, \tilde{S}_p , can only contribute to the regular part of the correlator. However, the effect of anomalous PSFs, \hat{S}_p , is more involved and is studied in detail in the following.

To this end, we consider PSFs with finite weight at vanishing frequency arguments. In particular, we assume the maximally anomalous form $S_p^{\text{ma}}(\varepsilon_{\bar{\tau}}, \varepsilon_{\bar{\tau}}) = \delta(\varepsilon_{\bar{\tau}}) \delta(\varepsilon_{\bar{\tau}}) \tilde{S}_{p;\bar{\tau}\bar{\tau}}$ (see Equation (B5b)). Then, the equilibrium condition Equation (4) implies $\tilde{S}_{(123);1;2} = \tilde{S}_{(231);2;3} = \tilde{S}_{(312);3;1}$ and $\tilde{S}_{(132);1;3} = \tilde{S}_{(321);3;2} = \tilde{S}_{(213);2;1}$, since $\zeta_p = \zeta_{p_i} = 1$ for purely bosonic correlators. For such PSFs, the 3p correlator evaluates to

$$\begin{aligned} G^{\text{ma}}(i\omega) &= \sum_p [K * S_p^{\text{ma}}](i\omega_p) \\ &= \left[\frac{\beta}{2} (\delta_{i\omega_1} \Delta_{i\omega_{12}} + \Delta_{i\omega_1} \delta_{i\omega_{12}}) + \frac{\beta^2}{6} \delta_{i\omega_1} \delta_{i\omega_{12}} \right] \tilde{S}_{(123);1,2} \\ &\quad + \left[\frac{\beta}{2} (\delta_{i\omega_2} \Delta_{i\omega_{23}} + \Delta_{i\omega_2} \delta_{i\omega_{23}}) + \frac{\beta^2}{6} \delta_{i\omega_2} \delta_{i\omega_{23}} \right] \tilde{S}_{(231);2,3} \\ &\quad + \left[\frac{\beta}{2} (\delta_{i\omega_3} \Delta_{i\omega_{31}} + \Delta_{i\omega_3} \delta_{i\omega_{31}}) + \frac{\beta^2}{6} \delta_{i\omega_3} \delta_{i\omega_{31}} \right] \tilde{S}_{(312);3,1} \\ &\quad + (2 \leftrightarrow 3) \\ &= \beta (\delta_{i\omega_1} \Delta_{i\omega_2} + \delta_{i\omega_2} \Delta_{i\omega_3} + \delta_{i\omega_3} \Delta_{i\omega_1}) (\tilde{S}_{(123);1,2} - \tilde{S}_{(132);1,3}) \\ &\quad + \frac{\beta^2}{2} \delta_{i\omega_1} \delta_{i\omega_2} (\tilde{S}_{(123);1,2} + \tilde{S}_{(132);1,3}) \end{aligned} \quad (\text{B7})$$

where $(2 \leftrightarrow 3)$ exchanges the indices of the frequencies and PSFs. The contribution of the regular kernel in Equation (A4b) vanishes due to $\frac{1}{i\omega_1 i\omega_{12}} + \frac{1}{i\omega_2 i\omega_{23}} + \frac{1}{i\omega_3 i\omega_{31}} = 0$ with $i\omega_3 = -i\omega_{12}$.

For later reference (see Appendices C.1 and E.2), we define the constants

$$\hat{G}_{1,2} = \frac{1}{2} (\tilde{S}_{(123);1,2} + \tilde{S}_{(132);1,3}) \quad (\text{B8a})$$

$$\hat{G}_{1,2}^{\Delta} = \hat{G}_{2,3}^{\Delta} = \hat{G}_{3,1}^{\Delta} = \tilde{S}_{(132);1,3} - \tilde{S}_{(123);1,2} \quad (\text{B8b})$$

such that G^{ma} reads

$$\begin{aligned} G^{\text{ma}}(i\omega) &= \beta (\delta_{i\omega_1} \Delta_{i\omega_2} \hat{G}_{1,2}^{\Delta} + \delta_{i\omega_2} \Delta_{i\omega_3} \hat{G}_{2,3}^{\Delta} + \delta_{i\omega_3} \Delta_{i\omega_1} \hat{G}_{3,1}^{\Delta}) \\ &\quad + \beta^2 \delta_{i\omega_1} \delta_{i\omega_2} \hat{G}_{1,2} \end{aligned} \quad (\text{B8c})$$

We emphasize that \hat{G}_{ij}^{Δ} and $\hat{G}_{1,2}$ are nonzero only if the full PSFs S_p contain fully anomalous contributions S_p^{ma} , which is only the case for all operators being bosonic. In the next section, the most general form of 3p correlators is discussed.

Appendix C: Calculations for 3p Correlators

This appendix is devoted to computations for the analytic continuation of 3p correlators, complementing the discussions in Section 5. First, in Appendix C.1, we discuss the general structure of MF correlators, needed in Appendix C.2 for the derivation of an explicit formula for partial MF correlators and the subsequent extraction of PSFs. In Appendix C.3, we then present manipulations needed to construct KF correlators from analytically continued MF correlators.

C.1. Structure of 3p Correlators

For 3p correlators, Equation (A5) implies the general form

$$\begin{aligned} G_{i\omega_1, i\omega_2} &= \tilde{G}_{i\omega_1, i\omega_2} + \hat{G}_{i\omega_1, i\omega_2} \\ \hat{G}_{i\omega_1, i\omega_2} &= \beta \delta_{i\omega_1} \hat{G}_{1; i\omega_2} + \beta \delta_{i\omega_2} \hat{G}_{2; i\omega_1} + \beta \delta_{i\omega_3} \hat{G}_{3; i\omega_1} + \beta^2 \delta_{i\omega_1} \delta_{i\omega_2} \hat{G}_{1,2} \end{aligned} \quad (C1)$$

Here, we used the subscript notation introduced in Section 4.

For the conversion of Matsubara sums to contour integrals we distinguish restricted from unrestricted sums (see e.g. Equation (35b)). Therefore we explicitly distinguish terms with $\Delta_{i\omega}$ factors, writing (cf. Equation (73))

$$\hat{G}_{i; i\omega_j} = \hat{G}_{i; i\omega_j}^{\Delta} + \Delta_{i\omega_j} \hat{G}_{i; i\omega_j}^{\Delta} \quad (C2)$$

In Equation (B8b), we have identified the constants \hat{G}^{Δ} with (maximally anomalous) PSFs. For alternative frequency parametrizations in Equations (B8), the constants in Equation (C2) read

$$\hat{G}_{1,2}^{\Delta} = -\hat{G}_{1,3}^{\Delta} = -\hat{G}_{2,1}^{\Delta} = \hat{G}_{2,3}^{\Delta} = \hat{G}_{3,1}^{\Delta} = -\hat{G}_{3,2}^{\Delta} \quad (C3)$$

such that, e.g., $\delta_{i\omega_1} \Delta_{i\omega_2} \hat{G}_{1,2}^{\Delta} = -\delta_{i\omega_1} \Delta_{i\omega_3} \hat{G}_{1,2}^{\Delta} = \delta_{i\omega_1} \Delta_{i\omega_3} \hat{G}_{1,3}^{\Delta}$, which follows from frequency conservation, $i\omega_{1\dots\ell} = 0$, and the $\delta_{i\omega_i}$ factor multiplying \hat{G}_i .

C.2. Partial MF 3p Correlators

In this appendix, we present explicit calculations concerning Steps 1 and 2 of our 3-step strategy. First, we introduce two identities used for simplifications in Step 1.

Consider the restricted Matsubara sum of Equation (35b) for $f(i\omega') = \tilde{f}(i\omega')/(i\omega - i\omega')$. Using Equation (37) for the residue term, one obtains

$$\frac{1}{(-\beta)} \sum_{i\omega'} \left(\Delta_{i\omega - i\omega'} - \frac{\beta}{2} \delta_{i\omega - i\omega'} \right) \tilde{f}(i\omega') = \oint_z \frac{n_z \tilde{f}(z)}{i\omega - z} + \mathcal{O}\left(\frac{1}{\beta}\right) \quad (C4)$$

Here, the restriction of the sum is implicit in the Δ symbol (Equation (32)), and the first term of Equation (37) was incorporated into the sum using the Kronecker δ . We can identify the summand on the left of Equation (C4) as the singularity-free 2p kernel of Equation (A2a), and therefore this identity constitutes the convenient cancellation in Equations (38) already on the level of kernels. Following the same line of arguments, one can show that

$$\frac{1}{(-\beta)^2} \sum_{i\omega'} \left(\Delta_{i\omega - i\omega'}^2 + \frac{\beta^2}{12} \delta_{i\omega - i\omega'} \right) \tilde{f}(i\omega') = \mathcal{O}\left(\frac{1}{\beta}\right) \quad (C5)$$

In the following, we focus on evaluating

$$\tilde{G}_{(123)}^r(i\omega_{(123)}) + \mathcal{O}\left(\frac{1}{\beta}\right) = [K \star G](i\omega_{(123)}) \quad (C6)$$

using the 3p kernel given in Equation (A2b) (with $\Omega_{(123)} = i\omega_{(123)} - i\omega'_{(123)}$), and the general form of the 3p correlator displayed in Equation (C1). For convenience, we focus on the identity permutation $p = (123)$; all other permutations can be obtained by replacing indices with their permuted ones, $i \rightarrow \bar{i}$. We split the calculation of Equation (C6) into regular (r) and anomalous (a) contributions from G :

$$\tilde{G}_{(123)}^r(i\omega_{(123)}) + \mathcal{O}\left(\frac{1}{\beta}\right) = [K \star \tilde{G}](i\omega_{(123)}) \quad (C7a)$$

$$\tilde{G}_{(123)}^a(i\omega_{(123)}) + \mathcal{O}\left(\frac{1}{\beta}\right) = [K \star \hat{G}](i\omega_{(123)}) \quad (C7b)$$

The computations are presented in Appendices C.2.1 and C.2.2, respectively, with the final result $\tilde{G}_{(123)} = \tilde{G}_{(123)}^r + \tilde{G}_{(123)}^a$ discussed in Appendix C.2.3. Additionally, we will use the super- and subscript notation introduced in Section 4 and suppress the frequency argument of $\tilde{G}_{(123)}^r$ and $\tilde{G}_{(123)}^a$.

C.2.1. Contributions from Regular Part

Step 1. *Matsubara summation through contour integration*: First, we concentrate on evaluating Equation (C7a):

$$\begin{aligned} \tilde{G}_{(123)}^r + \mathcal{O}\left(\frac{1}{\beta}\right) &= K \star \tilde{G} \\ &= \frac{1}{(-\beta)^2} \sum_{i\omega'_1, i\omega'_{12}} \left[\Delta_{\Omega_{12}} \left(\Delta_{\Omega_1} - \frac{\beta}{2} \delta_{\Omega_1} \right) \right. \\ &\quad \left. + \delta_{\Omega_{12}} \left(-\Delta_{\Omega_1}^2 - \frac{\beta}{2} \Delta_{\Omega_1} + \frac{\beta^2}{6} \delta_{\Omega_1} \right) \right] \tilde{G}_{i\omega'_1, i\omega'_{12}} \\ &= \frac{1}{(-\beta)^2} \sum_{i\omega'_1} \sum_{i\omega'_{12}}^{\neq i\omega'_{12}} \frac{1}{i\omega_{12} - i\omega'_{12}} \left(\Delta_{\Omega_1} - \frac{\beta}{2} \delta_{\Omega_1} \right) \tilde{G}_{i\omega'_1, i\omega'_{12}} \\ &\quad + \frac{1}{(-\beta)^2} \sum_{i\omega'_1} \sum_{i\omega'_{12}} \delta_{\Omega_{12}} \left(-\Delta_{\Omega_1}^2 - \frac{\beta}{2} \Delta_{\Omega_1} + \frac{\beta^2}{6} \delta_{\Omega_1} \right) \tilde{G}_{i\omega'_1, i\omega'_{12}} \end{aligned} \quad (C8)$$

The restricted sum over $i\omega'_{12}$ can be rewritten using Equation (C4), and collecting all resulting terms $\sim \delta_{\Omega_{12}}$ yields

$$\begin{aligned} \tilde{G}_{(123)}^r + \mathcal{O}\left(\frac{1}{\beta}\right) &= \frac{1}{(-\beta)} \sum_{i\omega'_1} \left(\Delta_{\Omega_1} - \frac{\beta}{2} \delta_{\Omega_1} \right) \oint_{z_{12}} \frac{n_{z_{12}} \tilde{G}_{i\omega'_1, z_{12}}}{i\omega_{12} - z_{12}} \\ &\quad + \frac{1}{(-\beta)^2} \sum_{i\omega'_1} \sum_{i\omega'_{12}} \delta_{\Omega_{12}} \left(-\Delta_{\Omega_1}^2 - \frac{\beta}{12} \delta_{\Omega_1} \right) \tilde{G}_{i\omega'_1, i\omega'_{12}} \end{aligned} \quad (C9)$$

The $i\omega'_1$ sums can be further simplified with the help of Equations (C4) and (C5) for the second and third line, respectively, reproducing Equation (39) for $\ell = 3$,

$$\tilde{G}_{(123)}^r + \mathcal{O}\left(\frac{1}{\beta}\right) = \oint_{z_1, z_{12}} \frac{n_{z_1} n_{z_{12}} \tilde{G}_{z_1, z_{12}}}{(i\omega_1 - z_1)(i\omega_{12} - z_{12})} + \mathcal{O}\left(\frac{1}{\beta}\right) \quad (C10)$$

with $\oint_{z_1, z_{12}} = \oint_{z_1} \oint_{z_{12}}$.

Step 2. *Extraction of PSFs*: Next, we deform the contours away from the imaginary axis, beginning with the contour integral over z_{12} . During the contour deformation, we have to carefully track possible singularities of $\tilde{G}_{z_1, z_{12}} = \tilde{G}(z_1, z_{12} - z_1, -z_{12})$. As explained in Section 4, possible branch cuts in the complex z_{12} plane lie on the lines defined by $\text{Im}(z_{12}) = 0$ or $\text{Im}(z_{12} - z_1) = 0$, see Figure C1a. The branch cut at $\text{Im}(z_{12}) = 0$ is taken into account by integrating infinitesimally above and below the real z_{12} axis, denoted by ε_{12}^{\pm} with $\text{Re}(z_{12}) = \varepsilon_{12}$.

The second branch cut $\text{Im}(z_{12} - z_1) = 0$ is included by substituting $z_{12} \rightarrow z_2 = z_{12} - z_1$, with z_2 being the new integration variable. Therefore, the contour is shifted onto the line $\text{Im}(z_{12} - z_1) = 0 \rightarrow \text{Im}(z_2) = 0$, i.e., onto the real axis of the complex z_2 plane, and integrating infinitesimally above and below the real axis of z_2 , denoted by ε_2^{\pm} with $\text{Re}(z_2) = \varepsilon_2$. The substitution also affects the argument of the MWF in Equation (C10). However, since the z_1 contour encloses only the poles of n_{z_1} , z_1 can be

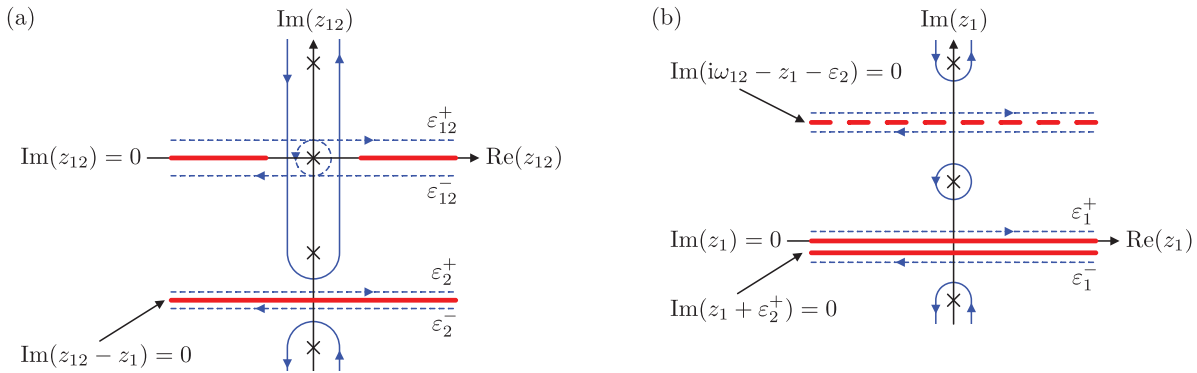


Figure C1. a) Contour deformation used in Equation (C12) for fermionic z_1 and z_2 , therefore bosonic z_{12} . Black crosses denote the poles of $n_{z_{12}}$ on the imaginary axis given by bosonic Matsubara frequencies. The blue, solid contour encloses all the poles on the imaginary axis. It is deformed into the blue, dashed contour to integrate along the possible branch cuts of $\tilde{G}_{z_1, z_{12}}$ denoted by the red, thick lines, located at $\text{Im}(z_{12}) = 0$ and $\text{Im}(z_{12} - z_1) = 0$. (b) Contour deformation used to obtain Equation (C15). The branch cut at $\text{Im}(z_1 + \epsilon_2^+) = 0$ lies infinitesimally close to the branch cut $\text{Im}(z_1) = 0$. Therefore, we integrate along the deformed blue, dashed contour, infinitesimally above and below the real axis, where the infinitesimal imaginary part of ϵ_2^+ , with $\text{Re}(z_1) = \epsilon_1$, has to be larger than that of ϵ_2^+ , i.e., $|\text{Im}(\epsilon_2^-)| > |\text{Im}(\epsilon_2^+)|$. The thick, red, dashed line denotes the pole at $\text{Im}(i\omega_{12} - z_1 - \epsilon_2)$ coming from the kernel. However, these poles only contribute at $\mathcal{O}(\frac{1}{\beta})$ and can be neglected, see the discussion after Equation (C17).

treated as a Matsubara frequency, implying $e^{-\beta z_1} = \zeta^1$ and therefore

$$\begin{aligned} n_{z_{12}} &= \frac{\zeta^{12}}{e^{-\beta z_{12}} - \zeta^{12}} \stackrel{z_{12} \rightarrow z_1 + z_2}{=} \frac{\zeta^1 \zeta^2}{e^{-\beta z_1} e^{-\beta z_2} - \zeta^1 \zeta^2} \\ &= \frac{\zeta^2}{e^{-\beta z_2} - \zeta^2} = n_{z_2} \end{aligned} \quad (\text{C11})$$

Adding the contributions from both branch cuts, the z_{12} dependent terms in Equation (C10) evaluate to

$$\oint_{z_{12}} \frac{n_{z_{12}} \tilde{G}_{z_1, z_{12}}}{i\omega_{12} - z_{12}} = \int_{\epsilon_{12}} \frac{n_{\epsilon_{12}} \tilde{G}_{z_1}^{\epsilon_{12}}}{i\omega_{12} - \epsilon_{12}} + \int_{\epsilon_2} \frac{n_{\epsilon_2} \tilde{G}_{z_1}^{\epsilon_2}}{i\omega_{12} - z_1 - \epsilon_2} + \mathcal{O}(\frac{1}{\beta}) \quad (\text{C12})$$

see also Figure C1a. The term $\mathcal{O}(\frac{1}{\beta})$ comes from the possible poles at $z_{12} = 0$ or $z_2 = 0$ (if z_{12} or z_2 are bosonic) which do not contribute at $\mathcal{O}(1)$, see Equation (44).

Inserting Equation (C12) into Equation (C10) yields

$$\begin{aligned} \tilde{G}_{(123)}^r + \mathcal{O}(\frac{1}{\beta}) &= \oint_{z_1} \frac{n_{z_1}}{i\omega_1 - z_1} \int_{\epsilon_2} \frac{n_{\epsilon_2} \tilde{G}_{z_1}^{\epsilon_2}}{i\omega_{12} - z_1 - \epsilon_2} \\ &+ \oint_{z_1} \frac{n_{z_1}}{i\omega_1 - z_1} \int_{\epsilon_{12}} \frac{n_{\epsilon_{12}} \tilde{G}_{z_1}^{\epsilon_{12}}}{i\omega_{12} - \epsilon_{12}} \end{aligned} \quad (\text{C13})$$

Next we focus on the contour deformation of z_1 . For the first term, we have illustrated possible branch cuts and the contours before and after the deformation in Figure C1b. As the z_1 contour is deformed away from the Matsubara frequencies, we merely have to consider the singularities in the integrand of the ϵ_2 integral. After Equation (C17), we will show that the singularities at $z_1 = i\omega_{12} - \epsilon_2$ contribute at order $\mathcal{O}(\frac{1}{\beta})$. We can thus focus on the branch cut in $\tilde{G}_{z_1}^{\epsilon_2}$. Previously we have taken the infinitesimal limit for the imaginary shifts of ϵ_2^\pm . Thus, during the z_1 contour deformation we have to ensure $|\text{Im}(\epsilon_2^-)| < |\text{Im}(\epsilon_2^+)|$, see Figure C1b. The z_1 contours infinitesimally above and below $\text{Re}(z_1)$ are summarized in a discontinuity

$$\tilde{G}_{\epsilon_2, \epsilon_1}^{\epsilon_2} = \tilde{G}_{\epsilon_1^+}^{\epsilon_2} - \tilde{G}_{\epsilon_1^-}^{\epsilon_2} \quad (\text{C14})$$

and we thus find for the first term in Equation (C13):

$$\oint_{z_1} \frac{n_{z_1}}{i\omega_1 - z_1} \int_{\epsilon_2} \frac{n_{\epsilon_2} \tilde{G}_{z_1}^{\epsilon_2}}{i\omega_{12} - z_1 - \epsilon_2} = \int_{\epsilon_1} \int_{\epsilon_2} \frac{n_{\epsilon_1} n_{\epsilon_2} \tilde{G}^{\epsilon_2, \epsilon_1}}{(i\omega_1 - \epsilon_1)(i\omega_{12} - \epsilon_{12})} + \mathcal{O}(\frac{1}{\beta}) \quad (\text{C15})$$

Repeating an analogous z_1 contour deformation for the second term in Equation (C13), we finally obtain

$$\tilde{G}_{(123)}^r = \int_{\epsilon_1, \epsilon_2} \frac{n_{\epsilon_1} n_{\epsilon_2} \tilde{G}^{\epsilon_2, \epsilon_1} + n_{\epsilon_1} n_{\epsilon_{12}} \tilde{G}^{\epsilon_{12}, \epsilon_1}}{(i\omega_1 - \epsilon_1)(i\omega_{12} - \epsilon_{12})} \quad (\text{C16})$$

which resembles the spectral representation in Equation (14d) for $\ell = 3$.

The term $\mathcal{O}(\frac{1}{\beta})$ on the right of Equation (C15) originates from the pole at $z_1 = i\omega_{12} - \epsilon_2$ in the denominator on the left, yielding

$$\mathcal{O}(\frac{1}{\beta}) = - \int_{\epsilon_2} \frac{n_{\epsilon_2} n_{-\epsilon_2} \tilde{G}_{i\omega_{12}}^{\epsilon_2}}{i\omega_2 - \epsilon_2} \quad (\text{C17})$$

with $\tilde{G}_{i\omega_{12}}^{\epsilon_2} = \tilde{G}(i\omega_{12} - \epsilon_2^+, \epsilon_2^+, -i\omega_{12}) - \tilde{G}(i\omega_{12} - \epsilon_2^-, \epsilon_2^-, -i\omega_{12})$. That the integral on the right indeed is $\mathcal{O}(\frac{1}{\beta})$, although it lacks an explicit prefactor $1/\beta$, can be seen by the following argument: The product of two MWFs $n_{\epsilon_2} n_{-\epsilon_2}$ has finite support on an interval $\epsilon_2 \in [-1/\beta, 1/\beta]$. Therefore, the integral scales as $1/\beta$.

To demonstrate this claim more explicitly, we proceed as follows. We note that we evaluated the imaginary-frequency convolution in Equation (C8) by evaluating first the ω'_{12} and then the ω'_1 sum. Due to frequency conservation, we could have also evaluated the convolution by first summing over, e.g., ω'_2 and then ω'_{12} , or ω'_1 and then ω'_2 , yielding

$$\begin{aligned} \omega'_2, \text{ then } \omega'_{12}: \quad K \star \tilde{G} &= \tilde{G}_{(123)}^r - \int_{\epsilon_2} \frac{n_{\epsilon_2} n_{-\epsilon_2} \tilde{G}_{i\omega_1}^{\epsilon_2}}{i\omega_2 - \epsilon_2} + \mathcal{O}(\frac{1}{\beta}) \\ \omega'_1, \text{ then } \omega'_2: \quad K \star \tilde{G} &= \tilde{G}_{(123)}^r - \int_{\epsilon_2} \frac{n_{\epsilon_2} n_{-\epsilon_2} \tilde{G}_{i\omega_1}^{\epsilon_2}}{i\omega_2 - \epsilon_2} \\ &+ \int_{\epsilon_{12}} \frac{n_{\epsilon_{12}} n_{-\epsilon_{12}} \tilde{G}_{i\omega_1}^{\epsilon_{12}}}{i\omega_{12} - \epsilon_{12}} + \mathcal{O}(\frac{1}{\beta}) \end{aligned} \quad (\text{C18})$$

Equating the two expressions yields a proof for Equation (C17):

$$\begin{aligned} & \int_{\varepsilon_2} \frac{n_{\varepsilon_2} n_{-\varepsilon_2} \tilde{G}_{i\omega_{12}}^{\varepsilon_2}}{i\omega_2 - \varepsilon_2} \\ &= \int_{\varepsilon_2} \frac{n_{\varepsilon_2} n_{-\varepsilon_2} \tilde{G}_{i\omega_1}^{\varepsilon_2}}{i\omega_2 - \varepsilon_2} + \int_{\varepsilon_{12}} \frac{n_{\varepsilon_{12}} n_{-\varepsilon_{12}} \tilde{G}_{i\omega_1}^{\varepsilon_{12}}}{i\omega_{12} - \varepsilon_{12}} + \mathcal{O}\left(\frac{1}{\beta}\right) \\ &= \oint_{z_2} \frac{n_{z_2} n_{-z_2} \tilde{G}_{i\omega_1, z_2}}{i\omega_2 - z_2} + \mathcal{O}\left(\frac{1}{\beta}\right) \\ &= -\frac{1}{(-\beta)^2} \sum_{i\omega'_2} \frac{\tilde{G}_{i\omega_1, i\omega'_2}}{(i\omega_2 - i\omega'_2)^2} - \frac{1}{12} \tilde{G}_{i\omega_1, i\omega_2} + \mathcal{O}\left(\frac{1}{\beta}\right) \\ &= \mathcal{O}\left(\frac{1}{\beta}\right) \end{aligned} \quad (\text{C19})$$

We obtained the third line by a contour deformation in analogy to the derivation of Equation (C12). Here, the second line can be expressed as a contour integral along the branch cuts at $\text{Im}(z_2) = 0$ and $\text{Im}(z_{12}) = 0$ (blue dashed lines in Figure C1a) and the contour in the third line encloses the Matsubara frequencies (blue solid lines in Figure C1a). For the last step, we used Equation (C5).

C.2.2. Contributions from Anomalous Parts

Step 1. Matsubara summation through contour integration: To evaluate Equation (C7b), we first focus on $\beta\delta_{i\omega'_3} \tilde{G}_{3;i\omega'_1}$, yielding $\tilde{G}_{3;(123)}^a$ in a decomposition $\tilde{G}_{3;(123)}^a = \sum_{i=1}^3 \tilde{G}_{i;(123)}^a$; the contributions from $\tilde{G}_{1;(123)}^a$ and $\tilde{G}_{2;(123)}^a$ follow from analogous calculations. Then, the imaginary-frequency convolution of the 3p kernel with $\beta\delta_{i\omega'_3} \tilde{G}_{3;i\omega'_1}$ can be rewritten as

$$\begin{aligned} & \tilde{G}_{3;(123)}^a + \mathcal{O}\left(\frac{1}{\beta}\right) = K \star \hat{G}_3 \\ &= \frac{1}{(-\beta)^2} \sum_{i\omega'_1, i\omega'_2} \left[\Delta_{\Omega_{12}} \left(\Delta_{\Omega_1} - \frac{\beta}{2} \delta_{\Omega_1} \right) \right. \\ & \quad \left. + \delta_{\Omega_{12}} \left(-\Delta_{\Omega_1}^2 - \frac{\beta}{2} \Delta_{\Omega_1} + \frac{\beta^2}{6} \delta_{\Omega_1} \right) \right] \beta\delta_{i\omega'_2} \hat{G}_{3;i\omega'_1} \\ &= -\frac{1}{i\omega_{12}} \frac{1}{(-\beta)} \sum_{i\omega'_1} \left(\Delta_{\Omega_1} - \frac{\beta}{2} \delta_{\Omega_1} \right) \hat{G}_{3;i\omega'_1} \\ &= -\frac{1}{i\omega_{12}} \frac{1}{(-\beta)} \sum_{i\omega'_1} \left(\Delta_{\Omega_1} - \frac{\beta}{2} \delta_{\Omega_1} \right) \hat{G}_{3;i\omega'_1}^{\Delta} \\ & \quad - \frac{1}{i\omega_{12}} \frac{1}{(-\beta)} \sum_{i\omega'_1}^{\neq 0} \left(\Delta_{\Omega_1} - \frac{\beta}{2} \delta_{\Omega_1} \right) \frac{\hat{G}_{3;1}^{\Delta}}{i\omega'_1} \end{aligned} \quad (\text{C20})$$

In the second step, we carried out the sum over $i\omega'_{12}$ and used $\delta_{\Omega_{12}} \delta_{i\omega'_{12}} = \delta_{i\omega_{12}} \delta_{i\omega'_{12}} = 0$, since we enforce the external Matsubara frequencies to be nonzero. In the third step, we further split the anomalous part according to Equation (C2).

The sums can be evaluated using Equation (C4) and yield

$$\begin{aligned} \tilde{G}_{3;(123)}^a + \mathcal{O}\left(\frac{1}{\beta}\right) &= -\frac{1}{i\omega_{12}} \oint_{z_1} \frac{n_{z_1} \hat{G}_{3;z_1}^{\Delta}}{i\omega_1 - z_1} - \frac{1}{i\omega_{12}} \oint_{z_1} \frac{n_{z_1}}{(i\omega_1 - z_1)} \frac{\hat{G}_{3;1}^{\Delta}}{z_1} \\ & \quad + \frac{1}{i\omega_{12}} \text{Res}_{z_1=0} \left(\frac{n_{z_1}}{(i\omega_1 - z_1)} \frac{\hat{G}_{3;1}^{\Delta}}{z_1} \right) + \mathcal{O}\left(\frac{1}{\beta}\right) \end{aligned} \quad (\text{C21})$$

where we excluded the contribution from $i\omega'_1 \rightarrow z_1 = 0$ by subtracting the residue.

Step 2. Extraction of PSFs: The first contour integral in Equation (C21) can be deformed analogously to the 2p case in Section 3.2. The integrand of the second contour integral only has poles on the imaginary axis since $\hat{G}_{3;1}^{\Delta}$ is a constant. Thus, the integral vanishes by closing the contour in the left and right half of the complex z_1 plane. Further evaluating the residue, we then obtain

$$\begin{aligned} \tilde{G}_{3;(123)}^a &= -\frac{1}{i\omega_{12}} \int_{\varepsilon_1} \frac{n_{\varepsilon_1} \hat{G}_3^{\Delta; \varepsilon_1}}{i\omega_1 - \varepsilon_1} - \frac{1}{2} \frac{\hat{G}_{3;1}^{\Delta}}{i\omega_1 i\omega_{12}} \\ &= \int_{\varepsilon_1, \varepsilon_2} \frac{\delta(\varepsilon_{12}) n_{\varepsilon_1} \hat{G}_3^{\Delta; \varepsilon_1} - \frac{1}{2} \delta(\varepsilon_1) \delta(\varepsilon_{12}) \hat{G}_{3;1}^{\Delta}}{(i\omega_1 - \varepsilon_1)(i\omega_{12} - \varepsilon_{12})} \end{aligned} \quad (\text{C22})$$

where we recovered the form of the spectral representation in Equation (14d) by introducing Dirac delta functions.

Similarly, the contributions from \hat{G}_1 , \hat{G}_2 , and also $\hat{G}_{1,2}$ to Equation (C7b) can be derived, leading to the general result

$$\begin{aligned} \tilde{G}_{(123)}^a &= \int_{\varepsilon_1, \varepsilon_2} \frac{1}{(i\omega_1 - \varepsilon_1)(i\omega_{12} - \varepsilon_{12})} \\ & \quad \times \left[\delta(\varepsilon_1) n_{\varepsilon_2} \hat{G}_1^{\Delta; \varepsilon_2} + \delta(\varepsilon_2) n_{\varepsilon_1} \hat{G}_2^{\Delta; \varepsilon_1} + \delta(\varepsilon_{12}) n_{\varepsilon_1} \hat{G}_3^{\Delta; \varepsilon_1} \right. \\ & \quad \left. + \delta(\varepsilon_1) \delta(\varepsilon_2) \left(\hat{G}_{1,2} - \frac{1}{2} \hat{G}_{3;1}^{\Delta} \right) \right] \end{aligned} \quad (\text{C23})$$

Here, only $\hat{G}_{3;1}^{\Delta}$ enters, since contributions from $\hat{G}_{1,2}^{\Delta}$ and $\hat{G}_{2,1}^{\Delta}$ cancel to due Equation (C3).

C.2.3. Final Result

The main results of the previous sections are Equations (C16) and (C23), yielding the spectral representation for $\tilde{G}_{(123)} = \tilde{G}_{(123)}^r + \tilde{G}_{(123)}^a$. The partial MF correlator $\tilde{G}_p = \tilde{G}_p^r + \tilde{G}_p^a$ for a general permutation p is then obtained by replacing any index by its permuted counterpart, $i \rightarrow p(i) = \bar{i}$. Thus, we obtain our final result

$$\tilde{G}_p(i\omega_p) = \int_{\varepsilon_1, \varepsilon_2} \frac{(2\pi i)^2 S_p(\varepsilon_1, \varepsilon_2)}{(i\omega_1 - \varepsilon_1)(i\omega_{12} - \varepsilon_{12})} \quad (\text{C24})$$

with the PSFs given by

$$\begin{aligned} & (2\pi i)^2 S_p(\varepsilon_1, \varepsilon_2) \\ &= n_{\varepsilon_1} n_{\varepsilon_2} \tilde{G}^{\varepsilon_2, \varepsilon_1} + n_{\varepsilon_1} n_{\varepsilon_2} \tilde{G}^{\varepsilon_1, \varepsilon_2} + \delta(\varepsilon_1) n_{\varepsilon_2} \hat{G}_1^{\Delta; \varepsilon_2} \\ & \quad + \delta(\varepsilon_2) n_{\varepsilon_1} \hat{G}_2^{\Delta; \varepsilon_1} + \delta(\varepsilon_3) n_{\varepsilon_1} \hat{G}_3^{\Delta; \varepsilon_1} + \delta(\varepsilon_1) \delta(\varepsilon_2) \left(\hat{G}_{1,2} - \frac{1}{2} \hat{G}_{3;1}^{\Delta} \right) \end{aligned} \quad (\text{C25})$$

PSFs for all six permutations are recovered by inserting the respective \bar{i} into above equation. They can be expressed in terms of analytic regions (cf. Figure 4) using

$$\tilde{G}^{\varepsilon_2, \varepsilon_1} = -\tilde{G}^{\varepsilon_{13}, \varepsilon_1} = -\tilde{G}^{\varepsilon_2, \varepsilon_3} = \tilde{G}^{\varepsilon_{13}, \varepsilon_3} = \tilde{G}^{[3]} - \tilde{G}^{[1]} - \tilde{G}^{[1]} + \tilde{G}^{[3]} \quad (\text{C26a})$$

$$\tilde{G}^{\varepsilon_1, \varepsilon_2} = -\tilde{G}^{\varepsilon_{23}, \varepsilon_2} = -\tilde{G}^{\varepsilon_1, \varepsilon_3} = \tilde{G}^{\varepsilon_{23}, \varepsilon_3} = \tilde{G}^{[3]} - \tilde{G}^{[2]} - \tilde{G}^{[2]} + \tilde{G}^{[3]} \quad (\text{C26b})$$

$$\tilde{G}^{\varepsilon_3, \varepsilon_1} = -\tilde{G}^{\varepsilon_{12}, \varepsilon_1} = -\tilde{G}^{\varepsilon_3, \varepsilon_2} = \tilde{G}^{\varepsilon_{12}, \varepsilon_2} = \tilde{G}^{[2]} - \tilde{G}^{[1]} - \tilde{G}^{[1]} + \tilde{G}^{[2]} \quad (\text{C26c})$$

$$\hat{G}_1^{\Delta;\varepsilon_2} = -\hat{G}_1^{\Delta;\varepsilon_3} = \hat{G}_1^{\Delta;[2]} - \hat{G}_1^{\Delta;[3]} \quad (\text{C26d})$$

$$\hat{G}_2^{\Delta;\varepsilon_1} = -\hat{G}_2^{\Delta;\varepsilon_2} = \hat{G}_2^{\Delta;[1]} - \hat{G}_2^{\Delta;[3]} \quad (\text{C26e})$$

$$\hat{G}_3^{\Delta;\varepsilon_1} = -\hat{G}_3^{\Delta;\varepsilon_2} = \hat{G}_3^{\Delta;[1]} - \hat{G}_3^{\Delta;[2]} \quad (\text{C26f})$$

$$\hat{G}_{1;2}^{\Delta} = -\hat{G}_{1;3}^{\Delta} = -\hat{G}_{2;1}^{\Delta} = \hat{G}_{2;3}^{\Delta} = \hat{G}_{3;1}^{\Delta} = -\hat{G}_{3;2}^{\Delta} \quad (\text{C26g})$$

$$\hat{G}_{\bar{1};\bar{2}} = \hat{G}_{1;2} \quad (\text{C26h})$$

with the definitions introduced in Section 5

$$G^{[1]} = \tilde{G}(\varepsilon_1^+, \varepsilon_2^-, \varepsilon_3^-), \quad G^{[1]} = \tilde{G}(\varepsilon_1^-, \varepsilon_2^+, \varepsilon_3^+) \quad (\text{C27a})$$

$$G^{[2]} = \tilde{G}(\varepsilon_1^-, \varepsilon_2^+, \varepsilon_3^-), \quad G^{[2]} = \tilde{G}(\varepsilon_1^+, \varepsilon_2^-, \varepsilon_3^+) \quad (\text{C27b})$$

$$G^{[3]} = \tilde{G}(\varepsilon_1^-, \varepsilon_2^-, \varepsilon_3^+), \quad G^{[3]} = \tilde{G}(\varepsilon_1^+, \varepsilon_2^+, \varepsilon_3^-) \quad (\text{C27c})$$

$$\hat{G}_1^{\Delta;[2]} = \hat{G}_1^{\Delta}(\circ, \varepsilon_2^+, \varepsilon_3^-), \quad \hat{G}_1^{\Delta;[3]} = \hat{G}_1^{\Delta}(\circ, \varepsilon_2^-, \varepsilon_3^+) \quad (\text{C27d})$$

$$\hat{G}_2^{\Delta;[1]} = \hat{G}_2^{\Delta}(\varepsilon_1^+, \circ, \varepsilon_3^-), \quad \hat{G}_2^{\Delta;[3]} = \hat{G}_2^{\Delta}(\varepsilon_1^-, \circ, \varepsilon_3^+) \quad (\text{C27e})$$

$$\hat{G}_3^{\Delta;[1]} = \hat{G}_3^{\Delta}(\varepsilon_1^+, \varepsilon_2^-, \circ), \quad \hat{G}_3^{\Delta;[2]} = \hat{G}_3^{\Delta}(\varepsilon_1^-, \varepsilon_2^+, \circ) \quad (\text{C27f})$$

Here, we have inserted a \circ at the position of the frequency arguments on which the function does not depend. Note that Equations (C26a)–(C26c) also imply, e.g., $\tilde{G}^{\varepsilon_2, \varepsilon_1} = \tilde{G}^{\varepsilon_1, \varepsilon_2} + \tilde{G}^{\varepsilon_3, \varepsilon_1}$. Relations of this form can be used to simplify PSF (anti)commutators, which appear in Section 5.2.

One additional comment is in order for the regular contributions in Equation (C25). Consider, e.g., permutation $p = (123)$ and n_{ε_1} a bosonic MWF. Then, if the regular contributions $\tilde{G}^{\varepsilon_2, \varepsilon_1}$ and $\tilde{G}^{\varepsilon_1, \varepsilon_2}$ contain terms proportional to Dirac $\delta(\varepsilon_1)$, the combination $n_{\varepsilon_1} \delta(\varepsilon_1)$ is ill-defined as the MWF diverges for vanishing frequencies. For their evaluation, however, we can use Equations (C26a)–(C26c) to rewrite

$$\begin{aligned} (2\pi i)^2 \tilde{S}_{(123)}(\varepsilon_1, \varepsilon_2) &= n_{\varepsilon_1} n_{\varepsilon_2} \tilde{G}^{\varepsilon_2, \varepsilon_1} + n_{\varepsilon_1} n_{\varepsilon_{12}} (\tilde{G}^{\varepsilon_1, \varepsilon_{12}} - \tilde{G}^{\varepsilon_2, \varepsilon_1}) \\ &= -n_{-\varepsilon_2} n_{\varepsilon_{12}} \tilde{G}^{\varepsilon_2, \varepsilon_1} + n_{\varepsilon_1} n_{\varepsilon_{12}} \tilde{G}^{\varepsilon_1, \varepsilon_{12}} \end{aligned} \quad (\text{C28})$$

Here, the first term does not include n_{ε_1} , and the discontinuity $\tilde{G}^{\varepsilon_1, \varepsilon_{12}}$ in the second term does not contain $\delta(\varepsilon_1)$ contributions (see, e.g., Equations (G10) and discussion thereafter), circumventing the occurrence of bosonic $n_{\varepsilon_1} \delta(\varepsilon_1)$ contributions.

C.3. Simplifications for KF Correlators for $\ell = 3$

In the following, we show that the spectral representation of Keldysh components can be recast into a form that is formally equivalent to Equations (19), but more convenient for the purpose of analytic continuation. The new representation enables us to insert the PSFs in Equation (C25) and obtain expressions for the Keldysh components in terms of analytic continuations of MF correlators. This constitutes Step 3 of our three-step strategy.

While the following calculations are demonstrated for explicit examples of 3p KF components, they can be generalized to arbitrary KF components and even to arbitrary ℓ p functions (see Appendix F).

Table C1. $\ell = 3$: Simplification of the Keldysh kernel (19c) for the KF correlator $G^{[13]}$ for all permutations by application of the identity (58). For permutations $p = (123)$ and $p = (321)$, manipulations presented in Equation (C30) were performed. Additionally, energy conservation and the constraints enforced by the δ -functions allow us to express all denominators through ω_2^- .

p	k_p	$[\hat{\eta}_1, \hat{\eta}_2]$	$[\bar{\eta}_1, \bar{\eta}_2]$	$K^{[\hat{\eta}_1, \hat{\eta}_2]}(\omega_p) = \tilde{K}(\omega_p^{\bar{\eta}_1}) - \tilde{K}(\omega_p^{\bar{\eta}_2})$
(123)	212	[13]	[13]	$\tilde{K}(\omega_{(123)}^{[1]}) - \tilde{K}(\omega_{(123)}^{[3]}) = \hat{\delta}(\omega_1) \frac{1}{\omega_2^-} - \hat{\delta}(\omega_{12}) \frac{1}{\omega_2^-}$
(132)	221	[12]	[13]	$\tilde{K}(\omega_{(132)}^{[1]}) - \tilde{K}(\omega_{(132)}^{[3]}) = -\hat{\delta}(\omega_1) \frac{1}{\omega_2^-}$
(213)	122	[23]	[13]	$\tilde{K}(\omega_{(213)}^{[1]}) - \tilde{K}(\omega_{(213)}^{[3]}) = \hat{\delta}(\omega_{12}) \frac{1}{\omega_2^-}$
(231)	122	[23]	[31]	$\tilde{K}(\omega_{(231)}^{[3]}) - \tilde{K}(\omega_{(231)}^{[1]}) = \hat{\delta}(\omega_1) \frac{1}{\omega_2^-}$
(312)	221	[12]	[31]	$\tilde{K}(\omega_{(312)}^{[3]}) - \tilde{K}(\omega_{(312)}^{[1]}) = -\hat{\delta}(\omega_{12}) \frac{1}{\omega_2^-}$
(321)	212	[13]	[31]	$\tilde{K}(\omega_{(321)}^{[3]}) - \tilde{K}(\omega_{(321)}^{[1]}) = -\hat{\delta}(\omega_1) \frac{1}{\omega_2^-} + \hat{\delta}(\omega_{12}) \frac{1}{\omega_2^-}$

C.3.1. Simplifications for KF Correlator $G^{[\eta_1, \eta_2]}$

We begin with outlining the necessary steps to express the KF component $G^{[\eta_1, \eta_2]}$ in terms of analytically continued MF correlators on the example $G^{[13]}$. The simplifications rely on repeated application of identity (58).

The spectral representation in Equations (19) serves as our starting point. As a first step, we bring the Keldysh kernel $K^{[\hat{\eta}_1, \hat{\eta}_2]}$ in a more convenient form, starting with permutation $p = (123)$, where $[\hat{\eta}_1, \hat{\eta}_2] = [13]$ and therefore

$$K^{[13]}(\omega_{(123)}) = \tilde{K}(\omega_{(123)}^{[1]}) - \tilde{K}(\omega_{(123)}^{[3]}) = \frac{1}{\omega_1^{[1]} \omega_{12}^{[1]}} - \frac{1}{\omega_1^{[3]} \omega_{12}^{[3]}} \quad (\text{C29})$$

In the first term, all frequency combinations in the denominator acquire a positive imaginary shift, whereas in the second term they obtain a negative imaginary shift. Adding and subtracting $1/(\omega_1^{[1]} \omega_{12}^{[3]})$, identity (58) leads to

$$\begin{aligned} K^{[13]}(\omega_{(123)}) &= \left(\frac{1}{\omega_1^{[1]}} - \frac{1}{\omega_1^{[3]}} \right) \frac{1}{\omega_{12}^{[3]}} + \left(\frac{1}{\omega_{12}^{[1]}} - \frac{1}{\omega_{12}^{[3]}} \right) \frac{1}{\omega_1^{[1]}} \\ &= \hat{\delta}(\omega_1) \frac{1}{\omega_2^-} + \hat{\delta}(\omega_{12}) \frac{1}{\omega_1^+} \end{aligned} \quad (\text{C30})$$

The kernels for all other permutations can be simplified in a similar manner, and the results are summarized in Table C1. Collecting all contributions proportional to either $\hat{\delta}(\omega_1)/\omega_2^-$ or $\hat{\delta}(\omega_{12})/\omega_2^-$ yields Equation (75). The PSF (anti)commutators therein are evaluated using the relations in Equations (C26) and result in

$$\begin{aligned} S_{[1, [2, 3]_-]_+} &= S_{(123)} - S_{(132)} + S_{(231)} - S_{(321)} \\ &= N_{\varepsilon_1} \tilde{G}^{\varepsilon_1, \varepsilon_2} - 2\hat{\delta}(\varepsilon_1) \hat{G}_1^{\Delta; \varepsilon_2} - 2\hat{\delta}(\varepsilon_1) \hat{\delta}(\varepsilon_2) \hat{G}_{1;2}^{\Delta} \end{aligned} \quad (\text{C31a})$$

$$\begin{aligned} S_{[[1, 2]_-, 3]_+} &= S_{(123)} - S_{(213)} + S_{(312)} - S_{(321)} \\ &= -N_{\varepsilon_{12}} \tilde{G}^{\varepsilon_{12}, \varepsilon_2} + 2\hat{\delta}(\varepsilon_{12}) \hat{G}_3^{\Delta; \varepsilon_2} + 2\hat{\delta}(\varepsilon_1) \hat{\delta}(\varepsilon_2) \hat{G}_{3;2}^{\Delta} \end{aligned} \quad (\text{C31b})$$

where we suppressed the frequency arguments of the PSFs.

C.3.2. Simplifications for KF Correlator $G^{[\eta_1, \eta_2, \eta_3]}$

In Section 5.2.2 it was pointed out that the Keldysh component $G^{[123]}$ can be computed by subtracting a fully retarded correlator, e.g. $G^{[3]}$, in order to reuse identity (58).

Table C2. $\ell = 3$: Keldysh kernel for $G^{[123]} - G^{[3]}$ in Equation (C32), evaluated for all permutations.

p	Kernel of $G^{[123]} - G^{[3]}$
(123)	$K^{[123]}(\omega_{(123)}) - \bar{K}(\omega_{(123)}^{[3]}) = \hat{\delta}(\omega_1)\hat{\delta}(\omega_2) + \hat{\delta}(\omega_1)\frac{1}{\omega_2^-}$
(132)	$K^{[123]}(\omega_{(132)}) - \bar{K}(\omega_{(132)}^{[3]}) = -\hat{\delta}(\omega_1)\frac{1}{\omega_2^-} - \hat{\delta}(\omega_2)\frac{1}{\omega_1^-}$
(213)	$K^{[123]}(\omega_{(213)}) - \bar{K}(\omega_{(213)}^{[3]}) = \hat{\delta}(\omega_1)\hat{\delta}(\omega_2) + \hat{\delta}(\omega_2)\frac{1}{\omega_1^-}$
(231)	$K^{[123]}(\omega_{(231)}) - \bar{K}(\omega_{(231)}^{[3]}) = -\hat{\delta}(\omega_2)\frac{1}{\omega_1^-} - \hat{\delta}(\omega_1)\frac{1}{\omega_2^-}$
(312)	$K^{[123]}(\omega_{(312)}) - \bar{K}(\omega_{(312)}^{[3]}) = \hat{\delta}(\omega_1)\hat{\delta}(\omega_2) + \hat{\delta}(\omega_2)\frac{1}{\omega_1^-}$
(321)	$K^{[123]}(\omega_{(321)}) - \bar{K}(\omega_{(321)}^{[3]}) = \hat{\delta}(\omega_1)\hat{\delta}(\omega_2) + \hat{\delta}(\omega_1)\frac{1}{\omega_2^-}$

The kernel of $G^{[3]}$ is simply given by $K^{[3]}(\omega_p) = \bar{K}(\omega_p^{[3]})$ and therefore permutation independent, as discussed before Equation (23). Since $G^{[123]} = G^{222}$ implies $k_p = 222$ and consequently $[\hat{\eta}_1\hat{\eta}_2\hat{\eta}_3] = [123]$ for any permutation, the kernel for $G^{[123]} - G^{[3]}$ reads

$$K^{[123]}(\omega_p) - K^{[3]}(\omega_p) = \bar{K}(\omega_p^{[1]}) - \bar{K}(\omega_p^{[2]}) + \bar{K}(\omega_p^{[3]}) - \bar{K}(\omega_p^{[3]}) \quad (\text{C32})$$

and therefore the effect of subtracting $G^{[3]}$ is permutation dependent.

We first consider permutation $p = (123)$, for which the difference of kernels simplifies to

$$\begin{aligned} K^{[123]}(\omega_{(123)}) - K^{[3]}(\omega_{(123)}) &= \bar{K}(\omega_{(123)}^{[1]}) - \bar{K}(\omega_{(123)}^{[2]}) \\ &= \frac{1}{\omega_1^{[1]}\omega_{12}^{[1]}} - \frac{1}{\omega_1^{[2]}\omega_{12}^{[2]}} = \hat{\delta}(\omega_1)\frac{1}{\omega_2^+} \end{aligned} \quad (\text{C33})$$

In the last step, we were able to use Equation (58) again, set $\omega_{12}^{[1]} = \omega_{12}^{[2]} = \omega_2^+$, and reduced $\omega_{12} = \omega_2$ due to the δ -function. For the comparison to kernels of other permutations, it is convenient to additionally add and subtract $\hat{\delta}(\omega_1)/\omega_2^-$ to obtain

$$K^{[123]}(\omega_{(123)}) - K^{[3]}(\omega_{(123)}) = \hat{\delta}(\omega_1)\hat{\delta}(\omega_2) + \hat{\delta}(\omega_1)\frac{1}{\omega_2^-} \quad (\text{C34})$$

For permutation $p = (132)$, Equation (C32) yields

$$\begin{aligned} \bar{K}(\omega_{(132)}^{[1]}) - \bar{K}(\omega_{(132)}^{[3]}) + \bar{K}(\omega_{(132)}^{[2]}) - \bar{K}(\omega_{(132)}^{[3]}) \\ = \hat{\delta}(\omega_1)\frac{1}{\omega_3^+} - \hat{\delta}(\omega_{13})\frac{1}{\omega_1^-} \end{aligned} \quad (\text{C35})$$

Using $\omega_3^+ = -\omega_1^-$ due to energy conservation and the δ -function, the first term matches the second term in Equation (C34). Therefore, PSFs of permutations $p = (123), (132)$ can be expressed through PSF (anti)commutators as in the previous section, motivating the manipulation from Equation (C33) to (C34).

A summary of the kernels for all permutations is given in Table C2. In these kernels, a total of three unique terms occur, given by $\hat{\delta}(\omega_1)\hat{\delta}(\omega_2)$, $\hat{\delta}(\omega_1)/\omega_2^-$, or $\hat{\delta}(\omega_2)/\omega_1^-$. Collecting all PSFs convoluted with the same expressions gives Equation (81), with the PSF (anti)commutators evaluating to

$$\begin{aligned} S_{[1,2]_+, [3]_+}(\epsilon_1, \epsilon_2) &= (1 + N_{\epsilon_1} N_{\epsilon_2}) \tilde{G}^{\epsilon_2, \epsilon_1} + N_{\epsilon_{12}} N_{\epsilon_1} \tilde{G}^{\epsilon_{12}, \epsilon_1} \\ &\quad - 2\hat{\delta}(\epsilon_1) N_{\epsilon_2} \hat{G}_1^{\hat{\Delta}; \epsilon_2} - 2\hat{\delta}(\epsilon_2) N_{\epsilon_1} \hat{G}_2^{\hat{\Delta}; \epsilon_1} \\ &\quad - 2\hat{\delta}(\epsilon_{12}) N_{\epsilon_1} \hat{G}_3^{\hat{\Delta}; \epsilon_1} + 4\hat{\delta}(\epsilon_1)\hat{\delta}(\epsilon_2)\hat{G}_{1,2}, \end{aligned}$$

$$S_{[1, [2, 3]_-]}(\epsilon_1, \epsilon_2) = \tilde{G}^{\epsilon_1, \epsilon_2},$$

$$S_{[2, [1, 3]_-]}(\epsilon_2, \epsilon_1) = \tilde{G}^{\epsilon_2, \epsilon_1} \quad (\text{C36})$$

This concludes our appendix on additional computations for the analytic continuation of 3p correlators.

Appendix D: Partial MF 4p Correlators

In this appendix, we discuss purely fermionic partial MF 4p correlators. However, we do not display explicit calculations here. Rather, we introduce an iterative procedure to derive the structure of 4p PSFs from 2p and 3p calculations. For a general fermionic MF 4p correlator, only the sums of two fermionic frequencies result in bosonic frequencies, which, in turn, might lead to anomalous terms. According to Equation (A5), the general form of the correlator thus reads

$$\begin{aligned} G_{i\omega_1, i\omega_2, i\omega_3} = &\tilde{G}_{i\omega_1, i\omega_2, i\omega_3} + \beta\hat{\delta}_{i\omega_{12}} \hat{G}_{12; i\omega_1, i\omega_3} \\ &+ \beta\hat{\delta}_{i\omega_{13}} \hat{G}_{13; i\omega_1, i\omega_2} + \beta\hat{\delta}_{i\omega_{23}} \hat{G}_{23; i\omega_1, i\omega_2} \end{aligned} \quad (\text{D1})$$

D.1. Regular Contributions

Step 1. Matsubara summation through contour integration: To derive partial MF 4p correlators, we insert Equation (D1) and the singularity-free 4p kernel (Equation (A2c)) into Equation (31):

$$\tilde{G}_{(1234)}(i\omega_{(1234)}) + \mathcal{O}\left(\frac{1}{\beta}\right) = [K \star G](i\omega_{(1234)}) \quad (\text{D2})$$

Here, we again consider the permutation $p = (1234)$ first, before obtaining the general result by replacing all indices $i \rightarrow \bar{i}$. By repeated use of the identities in Equations (C4) and (C5), together with the analogously proven new identity

$$\frac{1}{(-\beta)^3} \sum_{i\omega'} \Delta_{i\omega-i\omega'}^3 \tilde{f}(i\omega') = \mathcal{O}\left(\frac{1}{\beta}\right) \quad (\text{D3})$$

the imaginary-frequency convolution can again be expressed through contour integrals. Focusing on the regular contribution to the correlator, \tilde{G} , first, we indeed recover Equation (39) for $\ell = 4$:

$$\begin{aligned} \tilde{G}_{(1234)}^r(i\omega_{(1234)}) + \mathcal{O}\left(\frac{1}{\beta}\right) &= [K \star \tilde{G}](i\omega_{(1234)}) \\ &= \oint_{z_1} \oint_{z_{12}} \oint_{z_{123}} \frac{n_{z_1} n_{z_{12}} n_{z_{123}} \tilde{G}_{z_1, z_{12}, z_{123}}}{(i\omega_1 - z_1)(i\omega_{12} - z_{12})(i\omega_{123} - z_{123})} \end{aligned} \quad (\text{D4})$$

Step 2. Extraction of PSFs: For the deformation of the contour, it is instructive to recapitulate the 2p and 3p results for the regular contributions to the PSFs. As a function of complex frequencies, a general 2p MF correlator $\tilde{G}_{z_1} = \tilde{G}(z_1, -z_1)$ has one possible branch cut defined by $\text{Im}(z_1) = 0$, resulting in

$$(2\pi i) S_{(12)}^r(\epsilon_1) = n_{\epsilon_1} \tilde{G}^{\epsilon_1} \quad (\text{D5})$$

In the 3p case, the additional frequency dependence of $\tilde{G}_{z_1, z_{12}} = \tilde{G}(z_1, z_{12} - z_1, -z_{12})$ introduces two further branch cuts at $\text{Im}(z_{12}) = 0$ and $\text{Im}(z_{12} - z_1) = \text{Im}(z_2) = 0$, additionally to $\text{Im}(z_1) = 0$. According to Equation (C10), the contour of $\oint_{z_{12}}$ is deformed first, taking account of the latter two out of the three branch cuts. This yields a sum of the discontinuities $\tilde{G}_{z_1}^{\epsilon_{12}}$ and $\tilde{G}_{z_1}^{\epsilon_2}$, multiplied with the respective MWFs (Equation (C12)). The

subsequent contour deformation of $\hat{\phi}_{z_1}$ reduces to an effective 2p calculation, i.e., only the branch cut at $\text{Im}(z_1) = 0$ remains, resulting in

$$(2\pi i)^2 S_r^{(123)}(\epsilon_1, \epsilon_2) = n_{\epsilon_2} n_{\epsilon_1} \tilde{G}^{\epsilon_2, \epsilon_1} + n_{\epsilon_{12}} n_{\epsilon_1} \tilde{G}^{\epsilon_{12}, \epsilon_1} \quad (D6)$$

with the discontinuity in ϵ_1 to the right of ϵ_2 and ϵ_{12} .

In the 4p case, the new frequency z_{123} generates four additional branch cuts (see discussion in Section 4.1), defined by vanishing $\text{Im}(z_{123})$, $\text{Im}(z_{123} - z_1)$, $\text{Im}(z_{123} - z_2)$ or $\text{Im}(z_{123} - z_1 - z_2)$, yielding a total of seven possible branch cuts together with $\text{Im}(z_{12}) = 0$, $\text{Im}(z_{12} - z_1) = 0$, and $\text{Im}(z_1) = 0$ from the 3p case. Since $\hat{\phi}_{z_{123}}$ is deformed first according to Equation (D4), the four new branch cuts are taken into account via a sum of the discontinuities $\tilde{G}_{z_{12}, z_1}^{\epsilon_{12}, \epsilon_1}$, $\tilde{G}_{z_{12}, z_2}^{\epsilon_{12}, \epsilon_2}$, $\tilde{G}_{z_{12}, z_1}^{\epsilon_{12}, \epsilon_1}$, and $\tilde{G}_{z_{12}, z_1}^{\epsilon_{12}, \epsilon_1}$, multiplied with the respective MWFs. For each of these discontinuities, the subsequent contour deformations of $\hat{\phi}_{z_{12}}$ and $\hat{\phi}_{z_1}$ reduces to an effective 3p calculation. Consequently, we obtain

$$(2\pi i)^3 S_r^{(1234)}(\epsilon_1, \epsilon_2, \epsilon_3) = n_{\epsilon_3} n_{\epsilon_2} n_{\epsilon_1} \tilde{G}^{\epsilon_3, \epsilon_2, \epsilon_1} + n_{\epsilon_{123}} n_{\epsilon_2} n_{\epsilon_1} \tilde{G}^{\epsilon_{123}, \epsilon_2, \epsilon_1} + n_{\epsilon_{13}} n_{\epsilon_2} n_{\epsilon_1} \tilde{G}^{\epsilon_{13}, \epsilon_2, \epsilon_1} + n_{\epsilon_{23}} n_{\epsilon_2} n_{\epsilon_1} \tilde{G}^{\epsilon_{23}, \epsilon_2, \epsilon_1} + n_{\epsilon_3} n_{\epsilon_{12}} n_{\epsilon_1} \tilde{G}^{\epsilon_3, \epsilon_{12}, \epsilon_1} + n_{\epsilon_{123}} n_{\epsilon_{12}} n_{\epsilon_1} \tilde{G}^{\epsilon_{123}, \epsilon_{12}, \epsilon_1} + n_{\epsilon_{13}} n_{\epsilon_{12}} n_{\epsilon_1} \tilde{G}^{\epsilon_{13}, \epsilon_{12}, \epsilon_1} + n_{\epsilon_{23}} n_{\epsilon_{12}} n_{\epsilon_1} \tilde{G}^{\epsilon_{23}, \epsilon_{12}, \epsilon_1} \quad (D7)$$

We have also checked this result by explicit contour deformations in Equation (D4). There, the poles of the denominators can be ignored since they only contribute at order $\mathcal{O}(\frac{1}{\beta})$, similarly to Equation (C17) in the 3p case. To further simplify Equation (D7), we note that, for fermionic 4p correlators, two consecutive bosonic discontinuities have to vanish, i.e., $\tilde{G}^{\epsilon_{13}, \epsilon_{12}, \epsilon_1} = \tilde{G}^{\epsilon_{23}, \epsilon_{12}, \epsilon_1} = 0$, since their kernels carry one bosonic argument only (see Appendix E.1 for further details).

D.2. Anomalous Contributions

We do not present the derivations of the anomalous contributions of G to Equation (D2) explicitly here, as these correspond to 3p calculations. There is one crucial difference, however. The anomalous kernel in Equation (A4c) for the fermionic 4p case reduces to

$$\hat{K}^{\text{alt}}(\Omega_p) = -\frac{\beta}{2} \delta_{i\omega_{12} - \epsilon_1 - \epsilon_2} \frac{1}{(i\omega_{12} - \epsilon_1)(i\omega_{12} - \epsilon_2)} \quad (D8)$$

and thus only depends on fermionic Matsubara frequencies. Therefore, anomalous terms such as $\hat{G}_{13; i\omega_1, i\omega_2}$ only depend on the frequencies $i\omega_1$ and $i\omega_2$ separately, but not on their sum $i\omega_{12}$. In the complex frequency plane, this implies that $\hat{G}_{13; z_1, z_2}$ has branch cuts only for $\text{Im}(z_1) = 0$ and $\text{Im}(z_2) = 0$, but not for $\text{Im}(z_{12}) = 0$, in contrast to the regular 3p case. Additionally, since the denominators in Equation (D8) are non-singular due to the fermionic Matsubara frequencies, we need not distinguish the anomalous contributions by factors of $\Delta_{i\omega}$, e.g., splitting \hat{G}_{13} into $\hat{G}_{13}^{\hat{a}}$ and $\hat{G}_{13}^{\hat{b}}$ terms, as was the case for 3p functions (Equation (C2)).

D.3. Final Result

Finally, the fermionic partial 4p correlators for general permutations p is obtained from the full correlator via

$$\tilde{G}_p(i\omega_p) = \int_{\epsilon_1, \epsilon_2, \epsilon_3} \frac{(2\pi i)^3 S_p(\epsilon_1, \epsilon_2, \epsilon_3)}{(i\omega_{12} - \epsilon_1)(i\omega_{12} - \epsilon_2)(i\omega_{123} - \epsilon_3)} \quad (D9)$$

with the PSFs given by

$$(2\pi i)^3 S_p(\epsilon_1, \epsilon_2, \epsilon_3) = n_{\epsilon_3} n_{\epsilon_2} n_{\epsilon_1} \tilde{G}^{\epsilon_3, \epsilon_2, \epsilon_1} + n_{\epsilon_{123}} n_{\epsilon_2} n_{\epsilon_1} \tilde{G}^{\epsilon_{123}, \epsilon_2, \epsilon_1} + n_{\epsilon_{13}} n_{\epsilon_2} n_{\epsilon_1} \tilde{G}^{\epsilon_{13}, \epsilon_2, \epsilon_1} + n_{\epsilon_{23}} n_{\epsilon_2} n_{\epsilon_1} \tilde{G}^{\epsilon_{23}, \epsilon_2, \epsilon_1} + n_{\epsilon_3} n_{\epsilon_{12}} n_{\epsilon_1} \tilde{G}^{\epsilon_3, \epsilon_{12}, \epsilon_1} + n_{\epsilon_{123}} n_{\epsilon_{12}} n_{\epsilon_1} \tilde{G}^{\epsilon_{123}, \epsilon_{12}, \epsilon_1} + n_{\epsilon_{13}} n_{\epsilon_{12}} n_{\epsilon_1} \tilde{G}^{\epsilon_{13}, \epsilon_{12}, \epsilon_1} + n_{\epsilon_{23}} n_{\epsilon_{12}} n_{\epsilon_1} \tilde{G}^{\epsilon_{23}, \epsilon_{12}, \epsilon_1} \quad (D10)$$

For the anomalous parts, the order of discontinuities does not matter, as, e.g., $\tilde{G}_{12}^{\epsilon_3, \epsilon_1} = \tilde{G}_{12}^{\epsilon_1, \epsilon_3}$.

For completeness, we express the discontinuities in Equation (D10) in terms of analytic regions according to their definition in Section 6.1. This gives

$$\tilde{G}^{\epsilon_1, \epsilon_2, \epsilon_3} = -\tilde{G}^{\epsilon_{234}, \epsilon_2, \epsilon_3} = -\tilde{G}^{\epsilon_1, \epsilon_2, \epsilon_4} = \tilde{G}^{\epsilon_{234}, \epsilon_2, \epsilon_4} = -\tilde{G}^{\epsilon_1, \epsilon_{34}, \epsilon_3} = \tilde{G}^{\epsilon_{234}, \epsilon_{34}, \epsilon_3} = \tilde{G}^{\epsilon_1, \epsilon_{34}, \epsilon_4} = -\tilde{G}^{\epsilon_{234}, \epsilon_{34}, \epsilon_4} = C^{(3)} - C^{(4)} + C^{(123)} - C^{(124)} - C_{\text{III}}^{(13)} + C_{\text{III}}^{(14)} - C_{\text{III}}^{(23)} + C_{\text{III}}^{(24)} \quad (D11a)$$

$$\tilde{G}^{\epsilon_1, \epsilon_3, \epsilon_2} = -\tilde{G}^{\epsilon_{234}, \epsilon_3, \epsilon_2} = -\tilde{G}^{\epsilon_1, \epsilon_3, \epsilon_4} = \tilde{G}^{\epsilon_{234}, \epsilon_3, \epsilon_4} = -\tilde{G}^{\epsilon_1, \epsilon_{24}, \epsilon_2} = \tilde{G}^{\epsilon_{234}, \epsilon_{24}, \epsilon_2} = \tilde{G}^{\epsilon_1, \epsilon_{24}, \epsilon_4} = -\tilde{G}^{\epsilon_{234}, \epsilon_{24}, \epsilon_4} = C^{(2)} - C^{(4)} + C^{(123)} - C^{(134)} - C_{\text{III}}^{(12)} + C_{\text{III}}^{(14)} - C_{\text{III}}^{(23)} + C_{\text{III}}^{(34)} \quad (D11b)$$

$$\tilde{G}^{\epsilon_1, \epsilon_4, \epsilon_2} = -\tilde{G}^{\epsilon_{234}, \epsilon_4, \epsilon_2} = -\tilde{G}^{\epsilon_1, \epsilon_4, \epsilon_3} = \tilde{G}^{\epsilon_{234}, \epsilon_4, \epsilon_3} = -\tilde{G}^{\epsilon_1, \epsilon_{23}, \epsilon_2} = \tilde{G}^{\epsilon_{234}, \epsilon_{23}, \epsilon_2} = \tilde{G}^{\epsilon_1, \epsilon_{23}, \epsilon_3} = -\tilde{G}^{\epsilon_{234}, \epsilon_{23}, \epsilon_3} = C^{(2)} - C^{(3)} + C^{(124)} - C^{(134)} - C_{\text{III}}^{(12)} + C_{\text{III}}^{(13)} - C_{\text{III}}^{(24)} + C_{\text{III}}^{(34)} \quad (D11c)$$

$$\tilde{G}^{\epsilon_2, \epsilon_1, \epsilon_3} = -\tilde{G}^{\epsilon_{134}, \epsilon_1, \epsilon_3} = -\tilde{G}^{\epsilon_2, \epsilon_1, \epsilon_4} = \tilde{G}^{\epsilon_{134}, \epsilon_1, \epsilon_4} = -\tilde{G}^{\epsilon_2, \epsilon_{34}, \epsilon_3} = \tilde{G}^{\epsilon_{134}, \epsilon_{34}, \epsilon_3} = \tilde{G}^{\epsilon_2, \epsilon_{34}, \epsilon_4} = -\tilde{G}^{\epsilon_{134}, \epsilon_{34}, \epsilon_4} = C^{(3)} - C^{(4)} + C^{(123)} - C^{(124)} - C_{\text{II}}^{(13)} + C_{\text{II}}^{(14)} - C_{\text{II}}^{(23)} + C_{\text{II}}^{(24)} \quad (D11d)$$

$$\tilde{G}^{\epsilon_3, \epsilon_1, \epsilon_2} = -\tilde{G}^{\epsilon_{124}, \epsilon_1, \epsilon_2} = -\tilde{G}^{\epsilon_3, \epsilon_1, \epsilon_4} = \tilde{G}^{\epsilon_{124}, \epsilon_1, \epsilon_4} = -\tilde{G}^{\epsilon_3, \epsilon_{24}, \epsilon_2} = \tilde{G}^{\epsilon_{124}, \epsilon_{24}, \epsilon_2} = \tilde{G}^{\epsilon_3, \epsilon_{24}, \epsilon_4} = -\tilde{G}^{\epsilon_{124}, \epsilon_{24}, \epsilon_4} = C^{(2)} - C^{(4)} + C^{(123)} - C^{(134)} - C_{\text{II}}^{(12)} + C_{\text{II}}^{(34)} + C_{\text{IV}}^{(14)} - C_{\text{IV}}^{(23)} \quad (D11e)$$

$$\tilde{G}^{\epsilon_4, \epsilon_1, \epsilon_2} = -\tilde{G}^{\epsilon_{123}, \epsilon_1, \epsilon_2} = -\tilde{G}^{\epsilon_4, \epsilon_1, \epsilon_3} = \tilde{G}^{\epsilon_{123}, \epsilon_1, \epsilon_3} = -\tilde{G}^{\epsilon_4, \epsilon_{23}, \epsilon_2} = \tilde{G}^{\epsilon_{123}, \epsilon_{23}, \epsilon_2} = \tilde{G}^{\epsilon_4, \epsilon_{23}, \epsilon_3} = -\tilde{G}^{\epsilon_{123}, \epsilon_{23}, \epsilon_3} = C^{(2)} - C^{(3)} + C^{(124)} - C^{(134)} - C_{\text{IV}}^{(12)} + C_{\text{IV}}^{(13)} - C_{\text{IV}}^{(24)} + C_{\text{IV}}^{(34)} \quad (D11f)$$

$$\tilde{G}^{\epsilon_2, \epsilon_3, \epsilon_1} = -\tilde{G}^{\epsilon_{134}, \epsilon_3, \epsilon_1} = -\tilde{G}^{\epsilon_2, \epsilon_3, \epsilon_4} = \tilde{G}^{\epsilon_{134}, \epsilon_3, \epsilon_4} = -\tilde{G}^{\epsilon_2, \epsilon_{14}, \epsilon_1} = \tilde{G}^{\epsilon_{134}, \epsilon_{14}, \epsilon_1} = \tilde{G}^{\epsilon_2, \epsilon_{14}, \epsilon_4} = -\tilde{G}^{\epsilon_{134}, \epsilon_{14}, \epsilon_4} = C^{(1)} - C^{(4)} + C^{(123)} - C^{(234)} - C_{\text{I}}^{(12)} + C_{\text{I}}^{(34)} - C_{\text{II}}^{(13)} + C_{\text{II}}^{(24)} \quad (D11g)$$

The discontinuities in the anomalous parts Equation (D10) read

$$\hat{G}_{12}^{\varepsilon_1, \varepsilon_3} = -\hat{G}_{12}^{\varepsilon_2, \varepsilon_3} = -\hat{G}_{12}^{\varepsilon_1, \varepsilon_4} = \hat{G}_{12}^{\varepsilon_3, \varepsilon_4} = \hat{C}_{12}^{(13)} - \hat{C}_{12}^{(14)} - \hat{C}_{12}^{(23)} + \hat{C}_{12}^{(24)} \quad (\text{D13a})$$

$$\hat{G}_{13}^{\varepsilon_1, \varepsilon_2} = -\hat{G}_{13}^{\varepsilon_3, \varepsilon_2} = -\hat{G}_{13}^{\varepsilon_1, \varepsilon_4} = \hat{G}_{13}^{\varepsilon_3, \varepsilon_4} = \hat{C}_{13}^{(12)} - \hat{C}_{13}^{(14)} - \hat{C}_{13}^{(23)} + \hat{C}_{13}^{(24)} \quad (\text{D13b})$$

$$\hat{G}_{14}^{\varepsilon_1, \varepsilon_2} = -\hat{G}_{14}^{\varepsilon_4, \varepsilon_2} = -\hat{G}_{14}^{\varepsilon_1, \varepsilon_3} = \hat{G}_{14}^{\varepsilon_4, \varepsilon_3} = \hat{C}_{14}^{(12)} - \hat{C}_{14}^{(13)} - \hat{C}_{14}^{(24)} + \hat{C}_{14}^{(23)} \quad (\text{D13c})$$

with

$$\begin{aligned} \hat{C}_{12}^{(13)} &= \hat{G}_{12}(\varepsilon_1^+, \varepsilon_2^-, \varepsilon_3^+, \varepsilon_4^-), & \hat{C}_{12}^{(24)} &= \hat{G}_{12}(\varepsilon_1^-, \varepsilon_2^+, \varepsilon_3^-, \varepsilon_4^+), \\ \hat{C}_{12}^{(14)} &= \hat{G}_{12}(\varepsilon_1^+, \varepsilon_2^-, \varepsilon_3^-, \varepsilon_4^+), & \hat{C}_{12}^{(23)} &= \hat{G}_{12}(\varepsilon_1^-, \varepsilon_2^+, \varepsilon_3^+, \varepsilon_4^-), \\ \hat{C}_{13}^{(12)} &= \hat{G}_{13}(\varepsilon_1^+, \varepsilon_2^+, \varepsilon_3^-, \varepsilon_4^-), & \hat{C}_{13}^{(34)} &= \hat{G}_{13}(\varepsilon_1^-, \varepsilon_2^-, \varepsilon_3^+, \varepsilon_4^+), \\ \hat{C}_{13}^{(14)} &= \hat{G}_{13}(\varepsilon_1^+, \varepsilon_2^-, \varepsilon_3^-, \varepsilon_4^+), & \hat{C}_{13}^{(23)} &= \hat{G}_{13}(\varepsilon_1^-, \varepsilon_2^+, \varepsilon_3^+, \varepsilon_4^-), \\ \hat{C}_{14}^{(12)} &= \hat{G}_{14}(\varepsilon_1^+, \varepsilon_2^+, \varepsilon_3^-, \varepsilon_4^-), & \hat{C}_{14}^{(34)} &= \hat{G}_{14}(\varepsilon_1^-, \varepsilon_2^-, \varepsilon_3^+, \varepsilon_4^+), \\ \hat{C}_{14}^{(13)} &= \hat{G}_{14}(\varepsilon_1^+, \varepsilon_2^-, \varepsilon_3^+, \varepsilon_4^-), & \hat{C}_{14}^{(24)} &= \hat{G}_{14}(\varepsilon_1^-, \varepsilon_2^+, \varepsilon_3^-, \varepsilon_4^+) \end{aligned} \quad (\text{D14})$$

The remaining terms follow from $\hat{G}_{34} = \hat{G}_{12}$, $\hat{G}_{24} = \hat{G}_{13}$, and $\hat{G}_{23} = \hat{G}_{14}$.

Appendix E: Additional Spectral Representations

In this appendix, we derive spectral representations for discontinuities (Appendix E.1) and for anomalous parts (Appendix E.2) for general ℓ . These are used in Appendix F.2 to relate Keldysh components $G^{(1|n|2)}$ to discontinuities of regular parts and analytic continuations of anomalous parts, resulting in Equation (95) in Section 6.2.1. Additionally, they serve as a key ingredient in Appendix G for consistency checks performed on our results for the 2p, 3p, and 4p PSFs, where we express all occurring discontinuities through PSF (anti)commutators. We use the notation introduced in the beginning of Section 6.2 throughout this appendix.

E.1. Spectral Representation of Discontinuities

Here, we focus on the discontinuities of the regular MF correlator \tilde{C} , as introduced in Section 4. The results carry over to anomalous contributions \hat{G} , as presented in Appendix E.2. We first consider discontinuities of 3p correlators (Appendix E.1.1) and then their generalization to arbitrary ℓ (Appendix E.1.2).

E.1.1. Example for $\ell = 3$

Let us consider the discontinuity in Equation (69) as an example for $\ell = 3$. Inserting the spectral representation in Equations (14) yields

$$\begin{aligned} \frac{1}{(2\pi i)^2} \tilde{C}_{\omega_1^+}^{\omega_2} &= \frac{1}{(2\pi i)^2} (\tilde{C}_{\omega_2^+, \omega_1^+} - \tilde{C}_{\omega_2^-, \omega_1^+}) \\ &= \int_{\varepsilon_1} \int_{\varepsilon_2} \int_{\varepsilon_3} \delta(\varepsilon_{123}) \\ &\quad \times \frac{1}{\omega_1^+ - \varepsilon_1} \left[\frac{1}{\omega_{13}^- - \varepsilon_{13}} - \frac{1}{\omega_{13}^+ - \varepsilon_{13}} \right] S_{(132)}(\varepsilon_1, \varepsilon_3) \end{aligned}$$

$$\begin{aligned} &+ \frac{1}{\omega_{12}^+ - \varepsilon_{12}} \left[\frac{1}{\omega_2^+ - \varepsilon_2} - \frac{1}{\omega_2^- - \varepsilon_2} \right] S_{(213)}(\varepsilon_2, \varepsilon_1) \\ &+ \frac{1}{\omega_{23}^- - \varepsilon_{23}} \left[\frac{1}{\omega_2^+ - \varepsilon_2} - \frac{1}{\omega_2^- - \varepsilon_2} \right] S_{(231)}(\varepsilon_2, \varepsilon_3) \\ &+ \frac{1}{\omega_3^- - \varepsilon_3} \left[\frac{1}{\omega_{13}^- - \varepsilon_{13}} - \frac{1}{\omega_{13}^+ - \varepsilon_{13}} \right] S_{(312)}(\varepsilon_3, \varepsilon_1) \\ &= \int_{\varepsilon_1} \int_{\varepsilon_2} \int_{\varepsilon_3} \delta(\varepsilon_{123}) \left[\hat{\delta}(\omega_2 - \varepsilon_2) \frac{1}{\omega_1^+ - \varepsilon_1} S_{[2,13]_-}(\varepsilon_1, \varepsilon_2, \varepsilon_3) \right. \\ &\quad \left. + \hat{\delta}(\omega_2 - \varepsilon_2) \frac{1}{\omega_3^- - \varepsilon_3} S_{[2,31]_-}(\varepsilon_1, \varepsilon_2, \varepsilon_3) \right] \\ &= - \int_{\varepsilon_1} \frac{1}{\omega_1^+ - \varepsilon_1} S_{[2,1,3]_{-,-}}(\varepsilon_1, \omega_2, -\varepsilon_1 - \omega_2) \end{aligned} \quad (\text{E1})$$

where we used the identity (58) and energy conservation. The permutations $p = (123)$, (321) do not contribute to the discontinuity as their kernels only depend on the external frequencies ω_1^+ and ω_3^- with imaginary parts independent of ω_2^{\pm} .

For the discontinuity $\tilde{C}^{\omega_2, \omega_1} = \tilde{C}_{\omega_1^+}^{\omega_2} - \tilde{C}_{\omega_1^-}^{\omega_2}$, Equation (E1) yields

$$\begin{aligned} \tilde{C}^{\omega_2, \omega_1} &= (2\pi i)^2 S_{[2,1,3]_{-,-}}(\omega), \\ \tilde{C}^{\omega_{12}, \omega_1} &= (2\pi i)^2 S_{[1,2,3]_{-,-}}(\omega) \end{aligned} \quad (\text{E2})$$

The second identity for $\tilde{C}^{\omega_{12}, \omega_1}$ follows from a similar derivation as for $\tilde{C}^{\omega_2, \omega_1}$. Note that the above relations hold for permuted indices as well (see Equation (G11)). Thus, consecutive discontinuities eventually give a (nested) commutator of PSFs. For $\ell = 2$, this corresponds to the standard spectral function, $-\tilde{C}^{\omega_1} = (2\pi i) S_{[1,2]_-} = (2\pi i) S^{\text{std}}$.

E.1.2. Generalization to Arbitrary ℓ

For general ℓ p functions, the discontinuity in Equation (67) can be computed analogously by inserting the spectral representation. Then, only those permutations survive the difference for which the frequency combinations ω_l or $\omega_{l\ell}$ appear in the kernel $\tilde{K}(z_p)$, leading to

$$\tilde{C}_{z^l}^{\omega_l} = \tilde{C}_{\omega_1^+, z^l} - \tilde{C}_{\omega_1^-, z^l} = \sum_{\tilde{l}|l} [\tilde{K}_{\tilde{l}|l} \circ S_{[\tilde{l}, l]_{-,-}}] (z_{\tilde{l}|l}^{\omega_l}, z^l) \quad (\text{E3a})$$

$$\begin{aligned} \tilde{K}_{\tilde{l}|l}^{\omega_l}(z_{\tilde{l}|l}^{\omega_l}, z^l) &= \tilde{K}(z_{\tilde{l}|l}^{\omega_1^+}, z^l) - \tilde{K}(z_{\tilde{l}|l}^{\omega_1^-}, z^l) \\ &= \hat{\delta}(\omega_l) \tilde{K}(z_{\tilde{l}|l}^{\omega_1^+}) \tilde{K}(z_{\tilde{l}|l}^{\omega_1^-}) \end{aligned} \quad (\text{E3b})$$

$$\tilde{K}(z_{\tilde{l}|l}) = \prod_{i=1}^{|\tilde{l}|-1} \frac{1}{\omega_{1 \dots i}} \quad (\text{E3c})$$

The set $l^c = L \setminus l$ is complementary to l . Here, $z_p(\omega_l, z^l)$ expresses the permuted vector z_p in terms of ω_l and the remaining $\ell - 2$ independent frequencies z^l , and similarly $z_{\tilde{l}|l}^{\omega_l}$ for the subtuple $z_{\tilde{l}|l}$. Equation (E3c) defines a regular kernel for the subtuple $z_{\tilde{l}|l}$. In Equation (E3b), the difference of regular kernels leads to the Dirac delta factor due to $1/\omega_1^+ - 1/\omega_1^- = \hat{\delta}(\omega_l)$ and $1/\omega_{l^c}^+ - 1/\omega_{l^c}^- = -\hat{\delta}(\omega_l)$ (using Equation (58)). The definition of the regular product kernel in Equation (E3b) implies $\tilde{K}_{\tilde{l}|l}^{\omega_l} = \tilde{K}_{\tilde{l}|l}$; thus, the corresponding PSFs from permutations $\tilde{l}|l^c$ and $\tilde{l}|\tilde{l}$ have been combined in a PSF commutator in Equation (E3a).

Consider, e.g., the 3p discontinuity $\tilde{C}_{\omega_1^+}^{\omega_2}$ from Appendix E.1.1, where the sets in Equation (E3) are given by $l = \{2\}$, $l^c = \{1, 3\}$, and $z^l = \omega_1^+$. Then,

the sum over permutations $p = \bar{l}|l^c$ includes $\bar{l}|l^c \in \{2|13, 2|31\}$, and we obtain the PSF commutator contribution $S_{2,13}$ in Equation (E1) from Equation (E3).

For $\ell = 4$, let us consider $\hat{G}_{z_1, z_2}^{\omega_{13}}$ as an example. Then, the sets $l = \{1, 3\}$ and $l^c = \{2, 4\}$ yield the permutations $\{13|24, 13|42, 31|24, 31|42\}$, resulting in

$$\hat{G}_{z_1, z_2}^{\omega_{13}} = \int d^4 \varepsilon \frac{\delta(\varepsilon_{1234}) \delta(\varepsilon_{13})}{(z_1 - \varepsilon_1)(z_2 - \varepsilon_2)} S_{\bar{l}|l^c}(\varepsilon) \quad (\text{E4})$$

where we summarized all terms with the same kernels.

To compute consecutive discontinuities, such as $\hat{G}^{\omega_2, \omega_1}$ (see Equation (E2)), we can iterate the above procedure: By analyzing the spectral representation of the first discontinuity, we determine the branch cuts which lead to non-vanishing second discontinuities, and then compute these second discontinuities by use of identity (58). For fermionic 4p correlators, this iterative procedure implies that double bosonic discontinuities must vanish, e.g., $\hat{G}_{\omega_1^+}^{\omega_{13}, \omega_{14}} = 0$. This follows from the spectral representation of $\hat{G}_{z_1, z_2}^{\omega_{13}}$ in Equation (E4), where the kernels only depend on fermionic frequencies z_1, z_2 in the denominators. Hence, there is no $\text{Im}z_{14} = 0$ branch cut, and therefore $\hat{G}_{\omega_1^+}^{\omega_{13}, \omega_{14}}$ must vanish.

E.2. Spectral Representation of Anomalous Parts

In this appendix, we focus on the spectral representation for contributions to the MF correlator anomalous w.r.t. one frequency. We again start with an example for $\ell = 3$ (Appendix E.2.1), before generalizing to arbitrary ℓ (Appendix E.2.2).

E.2.1. Example for $\ell = 3$

Consider $\beta \delta_{i\omega_1} \hat{G}_1(i\omega)$ for $\ell = 3$. Only those terms in the 3p kernel Equation (A4b) proportional to $\delta_{\Omega_1} = \delta_{i\omega_1} \delta_{\varepsilon_1}$ and $\delta_{\Omega_{23}} = \delta_{i\omega_{23}} \delta_{\varepsilon_{23}} = \delta_{i\omega_1} \delta_{\varepsilon_1}$ can contribute to \hat{G}_1 . Hence, the anomalous PSFs S_p must contain factors $\delta(\varepsilon_1)$, i.e.,

$$\begin{aligned} & \beta \delta_{i\omega_1} \hat{G}_1(i\omega) \\ &= -\frac{1}{2} \beta \delta_{i\omega_1} \int d^3 \varepsilon \delta(\varepsilon_{123}) \left[\delta_{\varepsilon_1} S_{(123)}(\varepsilon_1, \varepsilon_2) \Delta_{i\omega_{12} - \varepsilon_{12}} \right. \\ & \quad + \delta_{\varepsilon_1} S_{(132)}(\varepsilon_1, \varepsilon_3) \Delta_{i\omega_{13} - \varepsilon_{13}} + \delta_{\varepsilon_{23}} S_{(231)}(\varepsilon_2, \varepsilon_3) \Delta_{i\omega_2 - \varepsilon_2} \\ & \quad \left. + \delta_{\varepsilon_{23}} S_{(321)}(\varepsilon_3, \varepsilon_2) \Delta_{i\omega_3 - \varepsilon_3} \right] \\ &= -\frac{1}{2} \beta \delta_{i\omega_1} \int d^3 \varepsilon \delta(\varepsilon_{123}) \left[\delta_{\varepsilon_1} S_{[1,23]_+}(\varepsilon_1, \varepsilon_2, \varepsilon_3) \Delta_{i\omega_2 - \varepsilon_2} \right. \\ & \quad \left. + \delta_{\varepsilon_1} S_{[1,32]_+}(\varepsilon_1, \varepsilon_2, \varepsilon_3) \Delta_{i\omega_3 - \varepsilon_3} \right] \\ &= -\frac{1}{2} \beta \delta_{i\omega_1} \int d^3 \varepsilon \delta(\varepsilon_{123}) \delta_{\varepsilon_1} S_{[1,2,3]_{-+}}(\varepsilon_1, \varepsilon_2, \varepsilon_3) \Delta_{i\omega_2 - \varepsilon_2} \quad (\text{E5}) \end{aligned}$$

where we used the symbolic Kronecker notation from Appendix B.1. The remaining contributions $p = (213), (312)$ can only contribute to the anomalous terms \hat{G}_2 and \hat{G}_3 , as they are not proportional to $\delta_{i\omega_1}$.

Note that, in the spectral representation (E5), the decomposition of $\hat{G}_{1;i\omega_2} = \hat{G}_{1;i\omega_2}^{\Delta} + \Delta_{i\omega_2} \hat{G}_{1,2}^{\Delta}$ follows from the PSF decomposition. Only PSF terms proportional to $\delta(\varepsilon_2)$, $\delta_{\varepsilon_1} \delta_{\varepsilon_2} S_{[1,2,3]_{-+}}$, contribute to $\hat{G}_{1,2}^{\Delta}$. In the absence of such $\delta(\varepsilon_2)$ contributions, we can evaluate $\Delta_{i\omega_2 - \varepsilon_2} \rightarrow 1/(i\omega_2 -$

$\varepsilon_2)$ and compute the discontinuity $\hat{G}_1^{\Delta; \omega_2} = \hat{G}_{1;\omega_2^+}^{\Delta} - \hat{G}_{1;\omega_2^-}^{\Delta}$:

$$\begin{aligned} \delta(\omega_1) \delta(\omega_2) \hat{G}_{1,2}^{\Delta} &= -\delta_{\omega_1} \delta_{\omega_2} S_{[1,2,3]_{-}}(\omega_1, \omega_2, -\omega_{12}), \\ \delta(\omega_1) \hat{G}_1^{\Delta; \omega_2} &= (2\pi i) \delta_{\omega_1} (1 - \delta_{\omega_2}) S_{[1,2,3]_{-}}(\omega_1, \omega_2, -\omega_{12}) \quad (\text{E6}) \end{aligned}$$

Here, we used $\delta_{\omega_1} S_{[1,2,3]_{-+}} = 2\delta_{\omega_1} S_{[1,2,3]_{-}}$ due to the equilibrium condition (4). These commutator representations will be used for the 3p consistency check in Appendix G.2.2.

E.2.2. Generalization to Arbitrary ℓ

Now, we generalize the insights from the $\ell = 3$ example to arbitrary ℓ . The result will be used in Appendix F to provide a general formula for the construction of KF components $C^{[l_1 l_2]}$ from MF functions.

In the $\beta\delta$ expansion of the MF kernel $K = \tilde{K} + \hat{K}^{\beta\delta} + \mathcal{O}(\delta^2)$, the $\beta\delta$ term reads (see Equation (45) in ref. [23])

$$\beta \hat{K}^{\beta}(\Omega_p) = -\frac{\beta}{2} \sum_{i=1}^{\ell-1} \delta_{\Omega_{\dots i}} \prod_{\substack{j=1 \\ j \neq i}}^{\ell-1} \Delta_{\Omega_{\dots j}} \quad (\text{E7})$$

which was originally derived for $\ell \leq 4$, but can be extended to arbitrary ℓ with the same line of arguments, starting from the results in ref. [30]. For general ℓ p functions and terms anomalous w.r.t. the frequency $i\omega_l = 0$, with $l \subset L = \{1, \dots, \ell\}$, only permutations of the form $p = \bar{l}|l^c$ and $p = \bar{l}^c|l$, with $l^c = L \setminus l$ again the complementary set to l , can lead to the $\beta\delta_{i\omega_l}$ factor coming from the anomalous kernel in Equation (E7), yielding

$$\begin{aligned} & \beta \delta_{i\omega_l} \hat{G}_l(i\omega) \\ &= -\frac{1}{2} \beta \delta_{i\omega_l} \sum_{\bar{l}|l^c} \int d^\ell \varepsilon_p \delta(\varepsilon_{1\dots\ell}) \prod_{i=1}^{|\bar{l}|-1} \Delta_{\Omega_{\dots i}} \prod_{i=1}^{|l^c|-1} \Delta_{\Omega_{\dots i}} \\ & \quad \times \delta_{\varepsilon_l} S_{\bar{l}|l^c}(\varepsilon_{\bar{l}|l^c}) \quad (\text{E8}) \end{aligned}$$

Equation (E5) is a direct application of this formula for $\ell = 3, l = \{1\}$, and $l^c = \{2, 3\}$, where the permutations $p = \bar{l}|l^c$ run over $\bar{l}|l^c \in \{1|23, 1|32\}$.

To make the connection to Keldysh correlators in the next appendix, we replace any $\Delta_{i\omega} \rightarrow 1/(i\omega)$ in the final expression for \hat{G}_l , which amounts to replacing $\Delta_{\Omega} \rightarrow 1/\Omega$ in the kernels, such that

$$\begin{aligned} \hat{G}_{l; \tilde{z}^l} &\equiv [\hat{G}_l(i\omega)]_{\Delta_{i\omega} \rightarrow \frac{1}{i\omega}, i\omega \rightarrow z(\tilde{z}^l)} \\ &= -\frac{1}{2} \sum_{\bar{l}|l^c} \int d^\ell \varepsilon_p \delta(\varepsilon_{1\dots\ell}) \tilde{K}(\tilde{z}^l - \varepsilon_l) \\ & \quad \times \tilde{K}(\tilde{z}^l - \varepsilon_{\bar{l}}) \delta_{\varepsilon_l} S_{\bar{l}|l^c}(\varepsilon_{\bar{l}|l^c}) \quad (\text{E9}) \end{aligned}$$

where we identified a product of regular kernels (see Equation (E3c)). The subscript \tilde{z}^l again denotes $\ell - 2$ independent frequencies parametrizing the $\ell - 1$ arguments z of $\hat{G}_l(z(\tilde{z}^l)) = \hat{G}_{l; \tilde{z}^l}$, with z independent of the anomalous frequency ω_l .

The anomalous parts \hat{G}_l typically enter the Keldysh components with prefactors depending on $4\pi i \delta(\omega_l)$. Including this factor, the spectral representation turns out to be particularly convenient, as we can make use of

Table F1. Keldysh kernel of $G^{[\eta_1 \eta_2 \eta_3]} - G^{[\mu_3]}$ (Equation (F11)) for different permutation classes depending on the order of the $\mu_i = p^{-1}(\eta_i)$. Manipulations similar to Equations (F12) and (F13) result in the alternative spectral representation in the third column, which can be further rewritten as Equation (98) using Equation (F14) (and equivalent identities).

p	$K^{[\eta_1 \eta_2 \eta_3]} - K^{[\mu_3]}$	$(G^{[\eta_1 \eta_2 \eta_3]} - G^{[\mu_3]})(\omega) = \sum_p [(K^{[\eta_1 \eta_2 \eta_3]} - K^{[\mu_3]}) * S_p](\omega_p)$
$\mu_1 < \mu_2 < \mu_3$	$K^{[\mu_1 \mu_2]}$	$= \sum_{(i^1, i^2, i^3) \in \mathcal{I}^{123}} \{ \sum_{i^1, i^2, i^3} [(\tilde{K}_{i^1, i^2, i^3} \diamond S_{i^1, i^2, i^3})(\omega_{i^1, i^2, i^3}^{[\eta_1][\eta_2][\eta_3]}) + (\tilde{K}_{i^1, i^2, i^3} \diamond S_{i^1, i^2, i^3})(\omega_{i^1, i^2, i^3}^{[\mu_1][\mu_2]})] \}$
$\mu_1 < \mu_3 < \mu_2$	$K^{[\mu_1 \mu_3]} - K^{[\mu_3 \mu_2]}$	$+ \sum_{i^1, i^3, i^2} [(\tilde{K}_{i^1, i^3, i^2} \diamond S_{i^1, i^3, i^2})(\omega_{i^1, i^3, i^2}^{[\eta_1][\eta_3]}) + (\tilde{K}_{i^1, i^3, i^2} \diamond S_{i^1, i^3, i^2})(\omega_{i^1, i^3, i^2}^{[\mu_1][\mu_3]})]$
$\mu_2 < \mu_1 < \mu_3$	$K^{[\mu_2 \mu_1]}$	$+ \sum_{i^2, i^1, i^3} [(\tilde{K}_{i^2, i^1, i^3} \diamond S_{i^2, i^1, i^3})(\omega_{i^2, i^1, i^3}^{[\eta_2][\eta_1][\eta_3]}) + (\tilde{K}_{i^2, i^1, i^3} \diamond S_{i^2, i^1, i^3})(\omega_{i^2, i^1, i^3}^{[\mu_2][\mu_1][\mu_3]})]$
$\mu_2 < \mu_3 < \mu_1$	$K^{[\mu_2 \mu_3]} - K^{[\mu_3 \mu_1]}$	$+ \sum_{i^2, i^3, i^1} [(\tilde{K}_{i^2, i^3, i^1} \diamond S_{i^2, i^3, i^1})(\omega_{i^2, i^3, i^1}^{[\eta_2][\eta_3][\eta_1]}) + (\tilde{K}_{i^2, i^3, i^1} \diamond S_{i^2, i^3, i^1})(\omega_{i^2, i^3, i^1}^{[\mu_2][\mu_3][\mu_1]})]$
$\mu_3 < \mu_1 < \mu_2$	$-K^{[\mu_1 \mu_2]}$	$+ \sum_{i^3, i^1, i^2} [(\tilde{K}_{i^3, i^1, i^2} \diamond S_{i^3, i^1, i^2})(\omega_{i^3, i^1, i^2}^{[\eta_3][\eta_1][\eta_2]}) - (\tilde{K}_{i^3, i^1, i^2} \diamond S_{i^3, i^1, i^2})(\omega_{i^3, i^1, i^2}^{[\mu_3][\mu_1][\mu_2]})]$
$\mu_3 < \mu_2 < \mu_1$	$-K^{[\mu_2 \mu_1]}$	$+ \sum_{i^3, i^2, i^1} [(\tilde{K}_{i^3, i^2, i^1} \diamond S_{i^3, i^2, i^1})(\omega_{i^3, i^2, i^1}^{[\eta_3][\eta_2][\eta_1]}) - (\tilde{K}_{i^3, i^2, i^1} \diamond S_{i^3, i^2, i^1})(\omega_{i^3, i^2, i^1}^{[\mu_3][\mu_2][\mu_1]})]$

Here, we collected all terms in Equation (F6) proportional to $\hat{\delta}(\omega_{i^1})$ and summed over all allowed partitions. Using the symmetry of the kernels (90a) and the (anti)commutator notation from Equation (92), we finally obtain

$$G^{[\eta_1 \eta_2]}(\omega) = \sum_{(i^1, i^2) \in \mathcal{I}^{12}} \sum_{i^1, i^2} \left(\tilde{K}_{i^1, i^2} \diamond S_{i^1, i^2} \right) (\omega_{i^1, i^2}^{[\eta_1][\eta_2]}) \quad (\text{F8})$$

Building on this expression, the KF component can be related to MF functions for arbitrary ℓ . For this purpose, we use the equilibrium condition to replace PSF commutators with anticommutators,

$$S_{i^1, i^2}^{\pm}(\epsilon_{i^1, i^2}) = N_{\epsilon_i} S_{i^1, i^2}^{\pm}(\epsilon_{i^1, i^2}) + \delta_{\epsilon_i} S_{i^1, i^2}^{\pm}(\epsilon_{i^1, i^2}) \quad (\text{F9})$$

$$N_{\epsilon_i} = \frac{\zeta^{\tilde{I}} e^{\beta \epsilon_i} + 1}{\zeta^{\tilde{I}} e^{\beta \epsilon_i} - 1} = \coth(\beta \epsilon_i / 2) \zeta^{\tilde{I}}$$

where N_{ϵ_i} is identical to the statistical factor in Equation (60), and we used the symbolic Kronecker notation from Appendix B.1. The sign factor is given by $\zeta^{\tilde{I}} = \pm 1$ for an even/odd number of fermionic operators in the set \tilde{I} . Inserting Equation (F9) into the representation (F8), we thus obtain

$$G^{[\eta_1 \eta_2]}(\omega) = \sum_{(i^1, i^2) \in \mathcal{I}^{12}} \sum_{i^1, i^2} \int d^\ell \epsilon \tilde{K}_{i^1, i^2}(\omega_{i^1, i^2}^{[\eta_1][\eta_2]} - \epsilon_{i^1, i^2}) \times \left(N_{\epsilon_i} S_{i^1, i^2}^{\pm}(\epsilon_{i^1, i^2}) + \delta_{\epsilon_i} S_{i^1, i^2}^{\pm}(\epsilon_{i^1, i^2}) \right) \hat{\delta}(\epsilon_{1 \dots \ell})$$

$$= \sum_{(i^1, i^2) \in \mathcal{I}^{12}} \left(N_{\omega_{i^1}} \tilde{G}_{\tilde{z}}^{\omega_{i^1}} + 4\pi i \delta(\omega_{i^1}) \hat{G}_{i^1, \tilde{z}} \right)$$

with $\tilde{z} = \{\omega_i^- | i \neq \eta_1, i \neq \eta_2\}$ (F10)

This remarkable formula generalizes Equation (23) for $G^{[\eta_1]}$, i.e. for $\alpha = 1$ and arbitrary ℓ , to $G^{[\eta_1 \eta_2]}$ ($\alpha = 2$). To obtain its final form, we used that the retarded product kernel (Equation (90a)) in the second line is proportional to $\hat{\delta}(\omega_{i^1} - \epsilon_{i^1})$ and thereby sets $N_{\epsilon_i} = N_{\omega_{i^1}} = N_{\omega_{i^1}}$ independent of the integration variables. In the second step, we then identified the spectral representations of discontinuities of the regular MF correlator $\tilde{G}_{\tilde{z}}^{\omega_{i^1}}$ (Equation (E3)) and of the anomalous contribution $\hat{G}_{i^1, \tilde{z}}$ (Equation (E10)). Note that the retarded product kernel coincides with the kernel (E3b) with a suitably continued \tilde{z} . In Equation (F10), the $\ell - 2$ frequencies in \tilde{z} carry negative imaginary shifts, in accordance with the definition of $\omega_{i^1, i^2}^{[\eta_1][\eta_2]}$.

F.3. Simplifications for $G^{[\eta_1 \eta_2 \eta_3]}$ for ℓ P Correlators

The calculation in Appendix C.3.2, too, can be generalized to arbitrary ℓ p correlators, in particular for the spectral representation of $G^{[\eta_1 \eta_2 \eta_3]} - G^{[\mu_3]}$. The Keldysh kernel for $G^{[\mu_3]}$ is given by $\tilde{K}(\omega_p^{[\mu_3]}) = K^{[\mu_3]}(\omega_p)$ for arbitrary permutations p , with $\mu_3 = p^{-1}(\eta_3)$. Then, the corresponding Keldysh kernel for $G^{[\eta_1 \eta_2 \eta_3]} - G^{[\mu_3]}$ reads

$$K^{[\eta_1 \eta_2 \eta_3]} - K^{[\mu_3]} = K^{[\eta_1]} - K^{[\eta_2]} + K^{[\eta_3]} - K^{[\mu_3]} \quad (\text{F11})$$

such that the effect of subtracting $K^{[\mu_3]}$ depends on the permutation. The permutations can be divided into six categories, depending on the order in which the $\mu_j = p^{-1}(\eta_j)$ occur, see Table F1. This is important since placing the μ_j in increasing order yields $[\eta_1 \eta_2 \eta_3]$, see discussion before Equations (19).

Here, we focus on the key steps in rewriting permutations with $\mu_1 < \mu_2 < \mu_3$, denoted by $\sum_{p | \mu_1 < \mu_2 < \mu_3}$. Defining $\mathcal{I}^{123} = \{(i^1, i^2, i^3) | \eta_1 \in i^1, \eta_2 \in i^2, \eta_3 \in i^3, i^b \cap i^{b'} = \emptyset \text{ for } b \neq b'\}$ as the set of all possibilities to partition $L = \{1, \dots, \ell\}$ into three blocks, each of which contains one of the indices $\eta_j \in \mathcal{I}$, we have

$$\sum_{p | \mu_1 < \mu_2 < \mu_3} [(K^{[\eta_1 \eta_2 \eta_3]} - K^{[\mu_3]}) * S_p](\omega_p)$$

$$= \sum_{p | \mu_1 < \mu_2 < \mu_3} (K^{[\mu_1 \mu_2]} * S_p)(\omega_p)$$

$$= \sum_{p | \mu_1 < \mu_2 < \mu_3} \sum_{\gamma = \mu_1}^{\mu_2 - 1} \left(\tilde{K}_{i^1 \dots \gamma | \gamma + 1 \dots \ell} * S_p \right) (\omega_{i^1 \dots \gamma | \gamma + 1 \dots \ell}^{[\eta_1][\eta_2]})$$

$$= \sum_{(i^1, i^2, i^3) \in \mathcal{I}^{123}} \sum_{i^1, i^2, i^3} \left(\tilde{K}_{i^1, i^2, i^3} \diamond S_{i^1, i^2, i^3} \right) (\omega_{i^1, i^2, i^3}^{[\eta_1][\eta_2]}) \quad (\text{F12})$$

In the first step, we used that $[\eta_1 \eta_2 \eta_3] = [\mu_1 \mu_2 \mu_3]$. In the second step, we inserted the kernel expansion Equation (F5) with $\bar{\mu}_j = \eta_j$. In the third step, we identified the sum over γ as a sum over all possibilities to subdivide the permutations into the form $p = i^1 \dots i^{\gamma-1} i^{\gamma} i^{\gamma+1} \dots i^{\ell}$ (which guarantees $\mu_1 < \mu_2 < \mu_3$), with the concatenation of $i^{\gamma-1}$ and i^{γ} denoted by $i^{\gamma-2, \gamma-1} = i^{\gamma-1} \dots i^{\gamma-1} i^{\gamma} \dots i^{\gamma-1}$.

Further, we use

$$\sum_{(i^1, i^2, i^3) \in \mathcal{I}^{123}} \sum_{i^1, i^2, i^3} \left(\tilde{K}_{i^1, i^2, i^3} \diamond S_{i^1, i^2, i^3} \right) (\omega_{i^1, i^2, i^3}^{[\eta_1][\eta_2]})$$

$$\begin{aligned}
 & - \sum_{(l^1, l^2, l^3) \in \mathcal{I}^{123}} \sum_{\bar{l}^1, \bar{l}^2, \bar{l}^3} \left(\tilde{K}_{\bar{l}^1 | \bar{l}^2 | \bar{l}^3} \diamond S_{\bar{l}^1 | \bar{l}^2 | \bar{l}^3} \right) (\omega_{\bar{l}^1 | \bar{l}^2 | \bar{l}^3}^{[l^1][l^2][l^3]}) \\
 & = \sum_{(l^1, l^2, l^3) \in \mathcal{I}^{123}} \sum_{\bar{l}^1, \bar{l}^2, \bar{l}^3} \left(\tilde{K}_{\bar{l}^1 | \bar{l}^2 | \bar{l}^3} \diamond S_{\bar{l}^1 | \bar{l}^2 | \bar{l}^3} \right) (\omega_{\bar{l}^1 | \bar{l}^2 | \bar{l}^3}^{[l^1][l^2][l^3]}) \quad (F13)
 \end{aligned}$$

which again follows by inserting Equation (F5), to arrive at the result in Table F1.

Contributions of different permutations can be further simplified, e.g., the second term of $p|\mu_1 < \mu_2 < \mu_3$ and the first term of $p|\mu_1 < \mu_3 < \mu_2$ can be collected, yielding

$$\begin{aligned}
 & \sum_{(l^1, l^2, l^3) \in \mathcal{I}^{123}} \sum_{\bar{l}^1, \bar{l}^2, \bar{l}^3} \left(\tilde{K}_{\bar{l}^1 | \bar{l}^2 | \bar{l}^3} \diamond S_{\bar{l}^1 | \bar{l}^2 | \bar{l}^3} \right) (\omega_{\bar{l}^1 | \bar{l}^2 | \bar{l}^3}^{[l^1][l^2][l^3]}) \\
 & + \sum_{(l^1, l^2, l^3) \in \mathcal{I}^{123}} \sum_{\bar{l}^1, \bar{l}^2, \bar{l}^3} \left(\tilde{K}_{\bar{l}^1 | \bar{l}^3 | \bar{l}^2} \diamond S_{\bar{l}^1 | \bar{l}^3 | \bar{l}^2} \right) (\omega_{\bar{l}^1 | \bar{l}^3 | \bar{l}^2}^{[l^1][l^2][l^3]}) \\
 & = \sum_{(l^1, l^2, l^3) \in \mathcal{I}^{123}} \sum_{\bar{l}^1, \bar{l}^2, \bar{l}^3} \left[\tilde{K}_{\bar{l}^1 | \bar{l}^2 | \bar{l}^3} \diamond S_{\bar{l}^1 | \bar{l}^2 | \bar{l}^3} \right] (\omega_{\bar{l}^1 | \bar{l}^2 | \bar{l}^3}^{[l^1][l^2][l^3]}) \quad (F14)
 \end{aligned}$$

with \mathcal{I}^{123} defined in Equation (99a). Using the symmetry of retarded product kernels, e.g., $\tilde{K}_{\bar{l}^1 | \bar{l}^2 | \bar{l}^3} = \tilde{K}_{\bar{l}^2 | \bar{l}^1 | \bar{l}^3}$, the spectral representation of $G^{[l^1 l^2 l^3]} - G^{[l^3]}$ finally results in Equation (98). Unlike for $\alpha = 2$ we don't have a general formula for the analytic continuation to $G^{[l^1 l^2 l^3]}$.

Equation (100) shows an example for $\ell = 4$. Inserting Equation (88) into the PSF (anti)commutators and abbreviating $S'_p = (2\pi i)^3 S_p$, we obtain the following relations:

$$\begin{aligned}
 S'_{[[\bar{1}, \bar{2}], \bar{3}], \bar{4}]_+} & = -N_4 \left(N_3 \tilde{G}^{\bar{\epsilon}_3, \bar{\epsilon}_2, \bar{\epsilon}_1} + N_{12} \tilde{G}^{\bar{\epsilon}_2, \bar{\epsilon}_3, \bar{\epsilon}_1} - 2\delta(\bar{\epsilon}_{12}) \tilde{G}^{\bar{\epsilon}_3, \bar{\epsilon}_1} \right), \\
 S'_{[[\bar{1}, \bar{2}], \bar{3}], \bar{4}]_+} & = N_{12} \left(N_4 \tilde{G}^{\bar{\epsilon}_4, \bar{\epsilon}_3, \bar{\epsilon}_2} + N_3 \tilde{G}^{\bar{\epsilon}_3, \bar{\epsilon}_4, \bar{\epsilon}_2} \right) - 2\delta(\bar{\epsilon}_{12}) N_3 \tilde{G}^{\bar{\epsilon}_1, \bar{\epsilon}_3} \quad (F15)
 \end{aligned}$$

Inserting these into the alternative spectral representation (98), we can evaluate the convolution integrals and obtain the relations in Equations (101g)-(101j), which express KF components in terms of MF functions and MWFs.

F.4. Simplifications for $G^{[1234]}$ for $\ell = 4$

For $\alpha = 4$, we can directly apply Equation (F5) on the Keldysh kernel, and a straightforward calculation gives

$$\begin{aligned}
 G^{[1234]}(\omega) & = \sum_{234} [\tilde{K}_{234|1} \diamond S_{[234, 1]_+}] (\omega_{234|1}^{[4][1]}) \\
 & + \sum_{134} [\tilde{K}_{134|2} \diamond S_{[134, 2]_+}] (\omega_{134|2}^{[4][2]}) \\
 & + \sum_{124} [\tilde{K}_{124|3} \diamond S_{[124, 3]_+}] (\omega_{124|3}^{[2][3]}) \\
 & + \sum_{123} [\tilde{K}_{123|4} \diamond S_{[123, 4]_+}] (\omega_{123|4}^{[3][4]}) \\
 & + [\tilde{K}_{4|123} \diamond S_{[[4, 1, 2], \dots, 3]_+}] (\omega_{4|123}^{[4][2][3]}) \\
 & + [\tilde{K}_{3|14|2} \diamond S_{[[3, [1, 4], \dots, 2]_+}] (\omega_{3|14|2}^{[3][1][2]})
 \end{aligned}$$

$$\begin{aligned}
 & + [\tilde{K}_{1|23|4} \diamond S_{[[1, [2, 3], \dots, 4]_+}] (\omega_{1|23|4}^{[1][3][4]}) \\
 & + [\tilde{K}_{2|34|1} \diamond S_{[[2, [3, 4], \dots, 1]_+}] (\omega_{2|34|1}^{[2][4][1]}) \\
 & + [\tilde{K}_{4|2|13} \diamond S_{[[4, 2], [1, 3], \dots]_+}] (\omega_{4|2|13}^{[4][2][3]}) \\
 & + [\tilde{K}_{1|3|24} \diamond S_{[[1, 3], [2, 4], \dots]_+}] (\omega_{1|3|24}^{[1][3][4]}) \\
 & + (-2\pi i)^3 \left(S_{[[2, 3], [1], \dots, 4]_-} + S_{[[3, 4], [2], \dots, 1]_-} \right. \\
 & \left. - S_{[[3, 4], [2], \dots, 1]_+} - S_{[[4, 1], [3], \dots, 2]_+} + S_{[[4, 2], [1, 3], \dots, 1]_+} \right) (\omega) \quad (F16)
 \end{aligned}$$

where \sum_I denotes a sum over permutations of the subset $I \subset \{1, \dots, \ell\}$. All occurring PSF (anti)commutators can be identified with one of the following four forms,

$$S'_{[[\bar{1}, \bar{2}], \bar{3}], \bar{4}]_+} = N_4 \tilde{G}^{\bar{\epsilon}_4, \bar{\epsilon}_3, \bar{\epsilon}_2} \quad (F17a)$$

$$S'_{[[\bar{1}, \bar{2}], \bar{3}], \bar{4}]_+} = N_4 \tilde{G}^{\bar{\epsilon}_4, \bar{\epsilon}_3, \bar{\epsilon}_2} + N_3 \tilde{G}^{\bar{\epsilon}_3, \bar{\epsilon}_4, \bar{\epsilon}_2} \quad (F17b)$$

$$\begin{aligned}
 S'_{[[\bar{1}, \bar{2}], \bar{3}], \bar{4}]_-} & = N_1 \tilde{G}^{\bar{\epsilon}_2, \bar{\epsilon}_4, \bar{\epsilon}_3} + N_2 \tilde{G}^{\bar{\epsilon}_1, \bar{\epsilon}_4, \bar{\epsilon}_3} + N_{13} \tilde{G}^{\bar{\epsilon}_1, \bar{\epsilon}_3, \bar{\epsilon}_2} \\
 & + N_{14} \tilde{G}^{\bar{\epsilon}_4, \bar{\epsilon}_3, \bar{\epsilon}_2} - 2\delta(\bar{\epsilon}_{13}) \tilde{G}^{\bar{\epsilon}_1, \bar{\epsilon}_2} - 2\delta(\bar{\epsilon}_{14}) \tilde{G}^{\bar{\epsilon}_1, \bar{\epsilon}_2} \quad (F17c)
 \end{aligned}$$

$$\begin{aligned}
 S'_{[[\bar{1}, \bar{2}], \bar{3}], \bar{4}]_+} & = N_1 N_3 \tilde{G}^{\bar{\epsilon}_1, \bar{\epsilon}_3} - (1 + N_1 N_2) \left(\tilde{G}^{\bar{\epsilon}_1, \bar{\epsilon}_2} + \tilde{G}^{\bar{\epsilon}_1, \bar{\epsilon}_2} \right) \\
 & - (1 + N_1 N_2) \left(N_3 \tilde{G}^{\bar{\epsilon}_3, \bar{\epsilon}_2, \bar{\epsilon}_1} + N_4 \tilde{G}^{\bar{\epsilon}_4, \bar{\epsilon}_2, \bar{\epsilon}_1} \right) \\
 & + N_{13} \tilde{G}^{\bar{\epsilon}_1, \bar{\epsilon}_3, \bar{\epsilon}_2} + N_{23} \tilde{G}^{\bar{\epsilon}_2, \bar{\epsilon}_3, \bar{\epsilon}_1} \\
 & - N_1 N_{12} \left(N_3 \tilde{G}^{\bar{\epsilon}_3, \bar{\epsilon}_2, \bar{\epsilon}_1} + N_4 \tilde{G}^{\bar{\epsilon}_4, \bar{\epsilon}_2, \bar{\epsilon}_1} \right) \quad (F17d)
 \end{aligned}$$

where we abbreviated $S'_p = (2\pi i)^3 S_p$ and $N_i = N_{\epsilon_i}$, and we used Equation (88) to evaluate above expressions. Inserting these into Equation (F16) and after application of Cauchy's integral formula, one obtains Equation (101k).

Appendix G: Consistency Checks

In Equations (47), (74), and (88), we expressed the 2p, 3p and 4p PSFs in terms of analytically continued MF functions. While the derivation of these important results extends over several pages, some consistency checks can be presented compactly. In Appendix G.1, we first show that our formulas fulfill the equilibrium condition (4). Since this was not explicitly imposed during the derivations, it serves as a strong test for our results. In Appendix G.2, we further show, for $\ell = 2, 3, 4$, that our formulas for $S_p[G]$, when expressing that G through PSFs, recover the input PSFs.

G.1. Fulfillment of the Equilibrium Condition

Here, we show that the results in (74) and (88) fulfill the equilibrium condition (4) (for the 2p case, this was already demonstrated in (50)). It suffices to show that they are fulfilled for p_λ with $\lambda = 2$, i.e., that for $p = (\bar{1} \dots \bar{\ell})$ we have

$$S_{(\bar{1} \dots \bar{\ell})}(\epsilon_{(\bar{1} \dots \bar{\ell})}) = \epsilon^{\bar{1}} e^{\beta \epsilon^{\bar{1}}} S_{(\bar{2} \dots \bar{\ell})}(\epsilon_{(\bar{2} \dots \bar{\ell})}) \quad (G1)$$

The result for general λ follows by induction.

We start with $\ell = 3$ and separate the contributions to the PSFs in Equation (74) from the regular \tilde{G} (denoted by S'_p) and the anomalous \hat{G} terms

(denoted by S_p^a), $S_p = S_p^r + S_p^a$. Inserting Equation (74) into Equation (G1) first yields

$$\begin{aligned} & \zeta^{\bar{1}} e^{\beta \varepsilon_{\bar{1}}} (2\pi i)^2 S_{(23\bar{1})}^r \\ &= \zeta^{\bar{1}} e^{\beta \varepsilon_{\bar{1}}} \left[n_{\varepsilon_2} n_{\varepsilon_3} \tilde{G}^{\varepsilon_2 \varepsilon_3} + n_{\varepsilon_2} n_{\varepsilon_{23}} \tilde{G}^{\varepsilon_2 \varepsilon_{23}} \right] \\ &= \zeta^{\bar{1}} e^{\beta \varepsilon_{\bar{1}}} \left[n_{\varepsilon_2} (n_{\varepsilon_3} - n_{\varepsilon_{23}}) \tilde{G}^{\varepsilon_2 \varepsilon_3} - n_{\varepsilon_2} n_{\varepsilon_{23}} \tilde{G}^{\varepsilon_2 \varepsilon_{23}} \right] \\ &= \zeta^{\bar{1}} e^{\beta \varepsilon_{\bar{1}}} \left[-n_{\varepsilon_{12}} n_{-\varepsilon_1} \tilde{G}^{\varepsilon_{12} \varepsilon_1} - n_{\varepsilon_2} n_{-\varepsilon_1} \tilde{G}^{\varepsilon_2 \varepsilon_1} \right] \\ &= (2\pi i)^2 S_{(12\bar{3})}^r \end{aligned} \quad (G2)$$

where we used in the second line $\tilde{G}^{\varepsilon_{23} \varepsilon_2} = -\tilde{G}^{\varepsilon_3 \varepsilon_2} - \tilde{G}^{\varepsilon_2 \varepsilon_1}$ (following from Equations (C26)), in the third line $n_{\varepsilon_2} (n_{\varepsilon_3} - n_{\varepsilon_{23}}) = -n_{\varepsilon_{12}} n_{-\varepsilon_1}$ and in the fourth line

$$\zeta^{\bar{1}} e^{\beta \varepsilon_{\bar{1}}} n_{-\varepsilon_1} = \frac{\zeta^{\bar{1}} e^{\beta \varepsilon_{\bar{1}}}}{\zeta^{\bar{1}} e^{\beta \varepsilon_{\bar{1}}} - 1} = -n_{\varepsilon_1} \quad (G3)$$

For the \hat{G} terms, we similarly obtain

$$\begin{aligned} & \zeta^{\bar{1}} e^{\beta \varepsilon_{\bar{1}}} (2\pi i)^2 S_{(23\bar{1})}^a \\ &= \zeta^{\bar{1}} e^{\beta \varepsilon_{\bar{1}}} \left[\delta(\varepsilon_2) n_{\varepsilon_3} \hat{G}_2^{\Delta \varepsilon_3} + \delta(\varepsilon_3) n_{\varepsilon_2} \hat{G}_3^{\Delta \varepsilon_2} \right. \\ & \quad \left. + \delta(\varepsilon_1) n_{\varepsilon_2} \hat{G}_1^{\Delta \varepsilon_2} + \delta(\varepsilon_2) \delta(\varepsilon_3) \left(\hat{G}_{2,3}^{\Delta} - \frac{1}{2} \hat{G}_{1,2}^{\Delta} \right) \right] \\ &= \zeta^{\bar{1}} e^{\beta \varepsilon_{\bar{1}}} \left[-\delta(\varepsilon_2) n_{-\varepsilon_1} \hat{G}_2^{\Delta \varepsilon_1} - \delta(\varepsilon_3) n_{-\varepsilon_1} \hat{G}_3^{\Delta \varepsilon_1} \right. \\ & \quad \left. + \delta(\varepsilon_1) n_{\varepsilon_2} \hat{G}_1^{\Delta \varepsilon_2} + \delta(\varepsilon_1) \delta(\varepsilon_2) \left(\hat{G}_{1,2}^{\Delta} - \frac{1}{2} \hat{G}_{3,1}^{\Delta} \right) \right] \\ &= (2\pi i)^2 S_{(12\bar{3})}^a \end{aligned} \quad (G4)$$

In the last step, we used that $\hat{G}_{\bar{1}} \neq 0$ and $\hat{G}_{\bar{1},2} \neq 0$ imply $\zeta^{\bar{1}} = +1$. Thus, we find that our 3p formula (74) indeed fulfills the equilibrium condition.

For 4p PSFs, we confirmed the fulfillment of the equilibrium condition by inserting the analytic regions (D11) for the discontinuities and by comparing the coefficients.

G.2. Full Recovery of Spectral Information

Equations (47), (74), and (88) contain formulas for PSFs, $S_p[G]$, as functionals of the MF correlator G for $\ell = 2, 3, 4$. In this section, we explicitly perform the following consistency check: given an arbitrary set of PSFs S_p as input, compute the MF correlator $G = \sum_p K * S_p$ and verify that $S_p[G]$ correctly recovers the input PSFs. To this end, we insert results from Appendix E to express the discontinuities in the formulas via PSF (anti)commutators. From the resulting expressions, we then show $S_p[G] = S_p$ by use of the equilibrium condition (4).

G.2.1. For $\ell = 2$

We first examine the relations between the MF correlator and the PSF contributions. Using the decomposition of PSFs from Appendix B.1, the standard spectral function reads

$$S_{\text{std}}(\varepsilon_1) = S_{[1,2]_{-}}(\varepsilon_1, -\varepsilon_1) = \tilde{S}_{[1,2]_{-}}(\varepsilon_1, -\varepsilon_1) \quad (G5)$$

For bosonic functions, $\zeta = +1$, there may be anomalous contributions $\delta(\varepsilon_{\bar{1}}) \tilde{S}_{p,\bar{1}}$. However, the equilibrium condition implies $\tilde{S}_{(12),1} = \tilde{S}_{(21),2}$, so that the anomalous contributions cancel in the PSF commutator. Instead, they solely enter the anomalous correlator, $\hat{G}(i\omega_1) = \beta \delta_{i\omega_1} \hat{G}_1$, via the spectral representation with kernel (A4a), yielding

$$\hat{G}_1 = -\tilde{S}_{(12),1} \quad (G6)$$

Now, we can show that Equation (47) recovers the input PSFs from the MF correlator. Inserting $\tilde{G}^{\varepsilon_1} = -\tilde{G}^{\varepsilon_2} = (-2\pi i) S_{\text{std}}(\varepsilon_1)$ (Equation (51)) and Equation (G6) into Equation (47) yields

$$S_p[G] = \frac{1}{2\pi i} \left[n_{\varepsilon_1} \tilde{G}^{\varepsilon_1} + \delta(\varepsilon_1) \hat{G}_1 \right] = -n_{\varepsilon_1} \tilde{S}_{[1,2]_{-}} + \delta_{\varepsilon_1} S_{(1\bar{2})} \quad (G7)$$

(Here and in the following, we suppress frequency arguments of PSFs.) To simplify the PSF commutator, we can use the equilibrium condition (4) to obtain

$$\begin{aligned} -n_{\varepsilon_1} \tilde{S}_{[1,2]_{-}} &= \frac{-1}{\zeta^{\bar{1}} e^{-\beta \varepsilon_1} - 1} [\tilde{S}_{(1\bar{2})} - \zeta^{\bar{1}} e^{-\beta \varepsilon_1} \tilde{S}_{(1\bar{2})}] \\ &= \tilde{S}_{(1\bar{2})} = (1 - \delta_{\varepsilon_1}) S_{(1\bar{2})} \end{aligned} \quad (G8)$$

For bosonic 2p functions, the MWF $n_{\varepsilon_{\bar{1}}}$ is undefined for $\varepsilon_{\bar{1}} = 0$. But since \tilde{S}_p then has no $\delta(\varepsilon_{\bar{1}})$ contribution, the left and right side of Equation (47) can only differ by zero spectral weight. We can nevertheless recover the correct value for $\tilde{S}_p(\varepsilon_{\bar{1}})$ at $\varepsilon_{\bar{1}} = 0$ if we demand that continuum contributions are (piece-wise) continuous. Then, the correct value at $\varepsilon_{\bar{1}} = 0$ is obtained from the formula in Equation (47) by taking the appropriate limit.

Inserting Equation (G8) into Equation (G7) results in

$$S_p[G] = (1 - \delta_{\varepsilon_1}) S_{(1\bar{2})} + \delta_{\varepsilon_1} S_{(1\bar{2})} = S_{(1\bar{2})} \quad (G9)$$

concluding our proof.

G.2.2. For $\ell = 3$

Following the line of argument for $\ell = 2$ from the previous section, we now check that the formula $S_p[G]$ recovers the input PSF S_p also for $\ell = 3$. Analogously to Equation (G8), the MWFs can be eliminated using the identity (suppressing frequency arguments)

$$S_{(12\bar{3})} = -n_{\varepsilon_1} S_{[1,2\bar{3}]_{-}} + \delta_{\varepsilon_1} S_{(1\bar{2}\bar{3})} \quad (G10a)$$

$$S_{(23\bar{1})} = n_{-\varepsilon_1} S_{[1,2\bar{3}]_{-}} + \delta_{\varepsilon_1} S_{(2\bar{3}\bar{1})} \quad (G10b)$$

Note that $\delta(\varepsilon_{\bar{1}})$ contributions cancel in $S_{[1,2\bar{3}]_{-}}$ for $\zeta^{\bar{1}} = +$ due to the equilibrium condition (as before), i.e., $S_{[1,2\bar{3}]_{-}} = (1 - \delta_{\varepsilon_1}) S_{[1,2\bar{3}]_{-}}$. Hence, such terms must be treated separately to obtain the PSF on the left.

In Appendix E.1, we have already shown that the discontinuities in the 3p PSF are proportional to nested PSF commutators. Analogously to the derivations for Equations (B8a), (E6), and (E2), we obtain the following relations:

$$\delta(\varepsilon_{\bar{1}}) \delta(\varepsilon_2) \hat{G}_{1,2}^{\Delta} = (2\pi i)^2 \frac{1}{2} \delta_{\varepsilon_1} \delta_{\varepsilon_2} S_{[1,2,3]_{+}}$$

$$\delta(\varepsilon_{\bar{1}}) \delta(\varepsilon_2) \hat{G}_{3,1}^{\Delta} = -(2\pi i)^2 \delta_{\varepsilon_1} \delta_{\varepsilon_2} S_{[1,2,3]_{-}}$$

$$\delta(\varepsilon_{\bar{1}}) \hat{G}_1^{\Delta \varepsilon_2} = -(2\pi i)^2 \delta_{\varepsilon_1} (1 - \delta_{\varepsilon_2}) S_{[1,2,3]_{-}}$$

$$\delta(\varepsilon_2) \hat{G}_2^{\Delta \varepsilon_1} = -(2\pi i)^2 \delta_{\varepsilon_2} (1 - \delta_{\varepsilon_1}) S_{[1,2,3]_{-}}$$

$$\delta(\varepsilon_3) \hat{G}_3^{\Delta \varepsilon_1} = -(2\pi i)^2 \delta_{\varepsilon_3} (1 - \delta_{\varepsilon_1}) S_{[1,2,3]_{-}}$$

$$\begin{aligned}\tilde{G}^{\varepsilon_2^-, \varepsilon_1^+} &= (2\pi i)^2 S_{[\bar{2}, [\bar{1}, \bar{3}]_-,]_-}, \\ \tilde{G}^{\varepsilon_1^-, \varepsilon_2^+} &= -(2\pi i)^2 S_{[\bar{3}, [\bar{1}, \bar{2}]_-,]_-}.\end{aligned}\quad (G11)$$

Inserting these into Equation (74) yields

$$\begin{aligned}S_p[G] &= \left[n_{\varepsilon_1^-} \left(n_{\varepsilon_2^-} \tilde{G}^{\varepsilon_2^-, \varepsilon_1^+} + \delta(\varepsilon_2^-) \hat{G}_{\bar{2}}^{\Delta; \varepsilon_1^+} + n_{\varepsilon_{12}^-} \tilde{G}^{\varepsilon_1^-, \varepsilon_2^+} + \delta(\varepsilon_3^-) \hat{G}_{\bar{3}}^{\Delta; \varepsilon_1^+} \right) \right. \\ &\quad \left. + \delta(\varepsilon_1^-) n_{\varepsilon_2^-} \hat{G}_{\bar{1}}^{\Delta; \varepsilon_2^+} - \frac{1}{2} \delta(\varepsilon_1^-) \delta(\varepsilon_2^-) \left(\hat{G}_{\bar{3}, \bar{1}}^{\Delta} - 2\hat{G}_{\bar{1}, \bar{2}} \right) \right] \frac{1}{(2\pi i)^2} \quad (G12a) \\ &= n_{\varepsilon_1^-} \left(n_{\varepsilon_2^-} S_{[\bar{2}, [\bar{1}, \bar{3}]_-,]_-} - \delta_{\varepsilon_2^-} (1 - \delta_{\varepsilon_1^-}) S_{[\bar{2}, \bar{1}, \bar{3}]_-} - n_{\varepsilon_{12}^-} S_{[\bar{3}, [\bar{1}, \bar{2}]_-,]_-} \right. \\ &\quad \left. - \delta_{\varepsilon_3^-} (1 - \delta_{\varepsilon_1^-}) S_{[\bar{1}, \bar{2}, \bar{3}]_-} \right) - n_{\varepsilon_2^-} \delta_{\varepsilon_1^-} (1 - \delta_{\varepsilon_2^-}) S_{[\bar{1}, \bar{2}, \bar{3}]_-} \\ &\quad + \delta_{\varepsilon_1^-} \delta_{\varepsilon_2^-} S_{[\bar{1}, \bar{2}, \bar{3}]_-} \quad (G12b)\end{aligned}$$

We can now check whether Equation (G12b) reproduces the full PSF, $S_{[\bar{1}, \bar{2}, \bar{3}]_-}$, by repeated application of Equations (G10). For this purpose, we use the PSF decomposition in Appendix B.1 to separately consider the contributions in the PSF proportional to $\delta(\varepsilon_1^-)$, and those which are not. Note that $S_{[\bar{2}, [\bar{1}, \bar{3}]_-,]_-}$ and $S_{[\bar{1}, \bar{2}, \bar{3}]_-}$ in the first line of Equation (G12b) contribute to both of these cases.

For PSF contributions not proportional to $\delta(\varepsilon_1^-)$, the last line of Equation (G12b) can be omitted (due to $\delta_{\varepsilon_1^-}$), so that

$$\begin{aligned}(1 - \delta_{\varepsilon_1^-}) S_p[G] &= -(1 - \delta_{\varepsilon_1^-}) n_{\varepsilon_1^-} \left(-n_{\varepsilon_2^-} S_{[\bar{2}, [\bar{1}, \bar{3}]_-,]_-} + \delta_{\varepsilon_2^-} S_{[\bar{2}, \bar{1}, \bar{3}]_-} \right. \\ &\quad \left. + n_{\varepsilon_{12}^-} S_{[\bar{3}, [\bar{1}, \bar{2}]_-,]_-} + \delta_{\varepsilon_3^-} S_{[\bar{1}, \bar{2}, \bar{3}]_-} \right) \\ &= -(1 - \delta_{\varepsilon_1^-}) n_{\varepsilon_1^-} \left(S_{[\bar{2}, \bar{1}, \bar{3}]_-} + S_{[\bar{1}, \bar{2}, \bar{3}]_-} \right) \\ &= -(1 - \delta_{\varepsilon_1^-}) n_{\varepsilon_1^-} S_{[\bar{1}, \bar{2}, \bar{3}]_-} = (1 - \delta_{\varepsilon_1^-}) S_{[\bar{1}, \bar{2}, \bar{3}]_-} \quad (G13)\end{aligned}$$

Here, we used Equations (G10) in the first and third step.

For PSF contributions proportional to $\delta(\varepsilon_1^-)$, the MWF $n_{\varepsilon_1^-}$ multiplying $S_{[\bar{2}, [\bar{1}, \bar{3}]_-,]_-}$ and $S_{[\bar{1}, \bar{2}, \bar{3}]_-}$ in Equation (G12b) seems to diverge in the bosonic case. This issue was already discussed in Equation (C28) (for unpermuted indices): There, $G^{\varepsilon_1^-, \varepsilon_2^+} = (2\pi i)^2 S_{[\bar{1}, [\bar{2}, \bar{3}]_-,]_-}$ does not contain factors $\delta(\varepsilon_1^-)$ due to the equilibrium condition, and therefore only the first term, expressed as $-n_{\varepsilon_{12}^-} n_{\varepsilon_2^-} S_{[\bar{2}, [\bar{1}, \bar{3}]_-,]_-}$, needs to be considered. As this PSF commutator does not contain factors $\delta(\varepsilon_2^-)$ due to the equilibrium condition, we obtain (using $n_{\varepsilon_2^-} = n_{\varepsilon_{12}^-} = n_{\varepsilon_3^-}$ and $\delta_{\varepsilon_2^-} = \delta_{\varepsilon_{12}^-} = \delta_{\varepsilon_3^-}$ due to $\delta_{\varepsilon_1^-}$)

$$\begin{aligned}\delta_{\varepsilon_1^-} S_p[G] &= \delta_{\varepsilon_1^-} \left(-n_{\varepsilon_2^-} n_{\varepsilon_2^-} S_{[\bar{2}, [\bar{1}, \bar{3}]_-,]_-} - n_{\varepsilon_{12}^-} (1 - \delta_{\varepsilon_2^-}) S_{[\bar{2}, \bar{1}, \bar{3}]_-} + \delta_{\varepsilon_2^-} S_{[\bar{1}, \bar{2}, \bar{3}]_-} \right) \\ &= \delta_{\varepsilon_1^-} \left(-n_{\varepsilon_2^-} (1 - \delta_{\varepsilon_2^-}) S_{[\bar{1}, \bar{3}, \bar{2}]_-} - n_{\varepsilon_{12}^-} (1 - \delta_{\varepsilon_2^-}) S_{[\bar{1}, \bar{2}, \bar{3}]_-} + \delta_{\varepsilon_2^-} S_{[\bar{1}, \bar{2}, \bar{3}]_-} \right) \\ &= \delta_{\varepsilon_1^-} \left(n_{\varepsilon_3^-} (1 - \delta_{\varepsilon_3^-}) S_{[\bar{3}, \bar{1}, \bar{2}]_-} + \delta_{\varepsilon_3^-} S_{[\bar{1}, \bar{2}, \bar{3}]_-} \right) \\ &= \delta_{\varepsilon_1^-} \left((1 - \delta_{\varepsilon_3^-}) S_{[\bar{1}, \bar{2}, \bar{3}]_-} + \delta_{\varepsilon_3^-} S_{[\bar{1}, \bar{2}, \bar{3}]_-} \right) \\ &= \delta_{\varepsilon_1^-} S_{[\bar{1}, \bar{2}, \bar{3}]_-} \quad (G14)\end{aligned}$$

Here, Equation (G10b) was applied in the first and the third step.

Therefore, we conclude that Equation (G12b) indeed recovers the input PSF $S_{[\bar{1}, \bar{2}, \bar{3}]_-}$, including terms proportional to $\delta(\varepsilon_1^-)$ in Equation (G14) and those which are not in Equation (G13).

G.2.3. For $\ell = 4$

Now, the same consistency check can be performed for fermionic 4p correlators. Similarly to Equation (G10), for 4p PSFs, we have

$$S_{[\bar{1}, \bar{2}, \bar{3}, \bar{4}]_-} = -n_{\varepsilon_1^-} S_{[\bar{1}, \bar{2}, \bar{3}, \bar{4}]_-} \quad (G15a)$$

$$S_{[\bar{1}, \bar{2}, \bar{3}, \bar{4}]_-} = -n_{\varepsilon_{12}^-} S_{[\bar{1}, \bar{2}, \bar{3}, \bar{4}]_-} + \delta_{\varepsilon_{12}^-} S_{[\bar{1}, \bar{2}, \bar{3}, \bar{4}]_-} \quad (G15b)$$

Here, the symbolic Kronecker δ only arises in the latter case, since ε_1^- is the energy difference for a fermionic operator. Starting from the formula in Equation (88), we obtain

$$\begin{aligned}S_p[G] &= \frac{n_{\varepsilon_1^-}}{(2\pi i)^3} \left[n_{\varepsilon_2^-} \left(n_{\varepsilon_3^-} \tilde{G}^{\varepsilon_3^-, \varepsilon_2^+} + n_{\varepsilon_{12}^-} \tilde{G}^{\varepsilon_2^-, \varepsilon_3^+} + n_{\varepsilon_{13}^-} \tilde{G}^{\varepsilon_1^-, \varepsilon_2^+} \right) \right. \\ &\quad \left. + n_{\varepsilon_{23}^-} \tilde{G}^{\varepsilon_2^-, \varepsilon_3^+} \right] + n_{\varepsilon_{12}^-} \left(n_{\varepsilon_3^-} \tilde{G}^{\varepsilon_3^-, \varepsilon_2^+} + n_{\varepsilon_{13}^-} \tilde{G}^{\varepsilon_1^-, \varepsilon_2^+} \right) \\ &\quad + n_{\varepsilon_3^-} \delta(\varepsilon_{12}^-) \hat{G}_{\bar{1}, \bar{2}}^{\varepsilon_1^-, \varepsilon_2^+} + n_{\varepsilon_2^-} \delta(\varepsilon_{13}^-) \hat{G}_{\bar{1}, \bar{3}}^{\varepsilon_1^-, \varepsilon_3^+} + n_{\varepsilon_2^-} \delta(\varepsilon_{23}^-) \hat{G}_{\bar{2}, \bar{3}}^{\varepsilon_2^-, \varepsilon_3^+} \\ &= -n_{\varepsilon_1^-} \left[n_{\varepsilon_2^-} \left(n_{\varepsilon_3^-} S_{[\bar{3}, [\bar{2}, \bar{1}, \bar{4}]_-,]_-} + n_{\varepsilon_{12}^-} S_{[\bar{2}, [\bar{1}, \bar{3}]_-,]_-} \right) \right. \\ &\quad \left. + n_{\varepsilon_{13}^-} S_{[\bar{1}, \bar{3}, \bar{2}, \bar{4}]_-} - \delta_{\varepsilon_{13}^-} S_{[\bar{1}, \bar{3}, \bar{2}, \bar{4}]_-} \right. \\ &\quad \left. + n_{\varepsilon_{23}^-} S_{[\bar{2}, \bar{3}, \bar{1}, \bar{4}]_-} - \delta_{\varepsilon_{23}^-} S_{[\bar{1}, \bar{4}, \bar{2}, \bar{3}]_-} \right) \\ &\quad \left. + n_{\varepsilon_{12}^-} \left(n_{\varepsilon_3^-} S_{[\bar{3}, [\bar{1}, \bar{2}, \bar{4}]_-,]_-} + n_{\varepsilon_{13}^-} S_{[\bar{1}, \bar{2}, \bar{3}, \bar{4}]_-} \right) - n_{\varepsilon_3^-} \delta_{\varepsilon_{12}^-} S_{[\bar{1}, \bar{2}, \bar{3}, \bar{4}]_-} \right] \\ &= n_{\varepsilon_1^-} \left[n_{\varepsilon_2^-} \left(S_{[\bar{3}, [\bar{2}, \bar{1}, \bar{4}]_-,]_-} + S_{[\bar{2}, [\bar{1}, \bar{3}]_-,]_-} \right) + S_{[\bar{1}, \bar{3}, \bar{2}, \bar{4}]_-} \right. \\ &\quad \left. + S_{[\bar{2}, \bar{3}, \bar{1}, \bar{4}]_-} \right) + n_{\varepsilon_{12}^-} (1 - \delta_{\varepsilon_{12}^-}) \left(S_{[\bar{3}, [\bar{1}, \bar{2}, \bar{4}]_-,]_-} + S_{[\bar{1}, \bar{2}, \bar{3}, \bar{4}]_-} \right) \\ &\quad \left. - n_{\varepsilon_3^-} \delta_{\varepsilon_{12}^-} \left(S_{[\bar{4}, [\bar{1}, \bar{2}, \bar{3}]_-,]_-} - S_{[\bar{1}, \bar{2}, \bar{3}, \bar{4}]_-} \right) \right] \\ &= n_{\varepsilon_1^-} \left[n_{\varepsilon_2^-} S_{[\bar{3}, \bar{4}, \bar{1}, \bar{2}]_-} + n_{\varepsilon_{12}^-} S_{[\bar{1}, \bar{2}, \bar{3}, \bar{4}]_-} - \delta_{\varepsilon_{12}^-} S_{[\bar{1}, \bar{2}, \bar{3}, \bar{4}]_-} \right] \\ &= -n_{\varepsilon_1^-} S_{[\bar{1}, \bar{2}, \bar{3}, \bar{4}]_-} \\ &= S_{[\bar{1}, \bar{2}, \bar{3}, \bar{4}]_-} \quad (G17)\end{aligned}$$

In the first step, we inserted expressions for the discontinuities, derived analogously to Equations (B8a), (E6), and (E2). We apply relations (G15) to eliminate the MWFs in the remaining steps. For the second step, we note that $S_{[\bar{3}, [\bar{1}, \bar{2}, \bar{4}]_-,]_-}$ and $S_{[\bar{1}, \bar{2}, \bar{3}, \bar{4}]_-}$ contain terms with and without $\delta(\varepsilon_{12}^-)$ factor. For the $\delta(\varepsilon_{12}^-)$ terms, the prefactor of $n_{\varepsilon_{12}^-}$ is undefined at ε_{12}^- . Analogously to the 3p calculation, we evaluate Equation (G16) using $\delta_{\varepsilon_{12}^-} (S_{[\bar{3}, [\bar{1}, \bar{2}, \bar{4}]_-,]_-} + S_{[\bar{1}, \bar{2}, \bar{3}, \bar{4}]_-}) = 0$ and $n_{\varepsilon_{34}^-} (-n_{\varepsilon_3^-} + n_{\varepsilon_4^-}) = n_{\varepsilon_3^-} n_{\varepsilon_4^-}$:

$$\begin{aligned}n_{\varepsilon_{12}^-} \left(n_{\varepsilon_3^-} S_{[\bar{3}, [\bar{1}, \bar{2}, \bar{4}]_-,]_-} + n_{\varepsilon_{12}^-} S_{[\bar{1}, \bar{2}, \bar{3}, \bar{4}]_-} \right) \\ = n_{\varepsilon_{12}^-} (1 - \delta_{\varepsilon_{12}^-}) \left(n_{\varepsilon_3^-} S_{[\bar{3}, [\bar{1}, \bar{2}, \bar{4}]_-,]_-} + n_{\varepsilon_{12}^-} S_{[\bar{1}, \bar{2}, \bar{3}, \bar{4}]_-} \right) \\ + \delta_{\varepsilon_{12}^-} n_{\varepsilon_3^-} n_{\varepsilon_4^-} S_{[\bar{1}, \bar{2}, \bar{3}, \bar{4}]_-} \quad (G18)\end{aligned}$$

To simplify the $\delta_{\varepsilon_{12}}$ terms in the third step, remember that the Kronecker symbol extracts those PSF contributions proportional to a $\delta(\varepsilon_{12})$, such that the equilibrium condition allows for manipulations like $\delta_{\varepsilon_{12}} S_{(1234)} = \delta_{\varepsilon_{12}} S_{(3412)}$. Finally, Equation (G17) shows that the formula in Equation (88) fully recovers the input PSFs from 4p MF correlators.

Appendix H: Additional Hubbard Atom Material

H.1. Useful Identities

In this section, we prove the identities given in Equations (107a) and (107b). The first identity follows from

$$\begin{aligned} & \lim_{\gamma_0 \rightarrow 0^+} \left(\frac{\omega + i\gamma_0}{(\omega + i\gamma_0)^2 - u^2} - \frac{\omega - i\gamma_0}{(\omega - i\gamma_0)^2 - u^2} \right) \\ &= -i \lim_{\gamma_0 \rightarrow 0^+} \left(\frac{\gamma_0}{(\omega + u)^2 + \gamma_0^2} + \frac{\gamma_0}{(\omega - u)^2 + \gamma_0^2} \right) \\ &= -i\pi[\delta(\omega + u) + \delta(\omega - u)] \end{aligned} \quad (\text{H1})$$

where we used Equation (58). Identity (107b) is derived via

$$\begin{aligned} & \lim_{\gamma_0 \rightarrow 0^+} \left(\frac{1}{(\omega + i\gamma_0)^2 - u^2} - \frac{1}{(\omega - i\gamma_0)^2 - u^2} \right) \\ &= \frac{i}{u} \lim_{\gamma_0 \rightarrow 0^+} \left(\frac{\gamma_0}{(\omega + u)^2 + \gamma_0^2} - \frac{\gamma_0}{(\omega - u)^2 + \gamma_0^2} \right) \\ &= \frac{i\pi}{u} [\delta(\omega + u) - \delta(\omega - u)]. \end{aligned} \quad (\text{H2})$$

H.2. Simplifications for 3p Electron-Density Correlator

In Section 7.2.1, we introduced the 3p electron-density correlator with regular and anomalous parts

$$\begin{aligned} \tilde{G}(i\omega_1, i\omega_2) &= \frac{u^2 - i\omega_1 i\omega_2}{[(i\omega_1)^2 - u^2][(i\omega_2)^2 - u^2]} \\ \hat{G}_3(i\omega_1) &= \frac{u}{2} \frac{1}{(i\omega_1)^2 - u^2} \end{aligned} \quad (\text{H3})$$

Here, we derive the explicit expression $G^{[2]} - G^{[3]}$ given in Equation (114),

$$\begin{aligned} G^{[2]} - G^{[3]} &= \tilde{G}(\omega_1^+, \omega_2^-) - \tilde{G}(\omega_1^-, \omega_2^-) \\ &= \frac{u^2}{(\omega_2^-)^2 - u^2} \left(\frac{1}{(\omega_1^+)^2 - u^2} - \frac{1}{(\omega_1^-)^2 - u^2} \right) \\ &\quad - \frac{\omega_2^-}{(\omega_2^-)^2 - u^2} \left(\frac{\omega_1^+}{(\omega_1^+)^2 - u^2} - \frac{\omega_1^-}{(\omega_1^-)^2 - u^2} \right) \end{aligned} \quad (\text{H4})$$

Using both identities (H1) and (H2), this expression can be further simplified to

$$G^{[2]} - G^{[3]} = \pi i \frac{u + \omega_2^-}{(\omega_2^-)^2 - u^2} \delta(\omega_1 + u) + \pi i \frac{\omega_2^- - u}{(\omega_2^-)^2 - u^2} \delta(\omega_1 - u) \quad (\text{H5})$$

Additionally multiplying both sides with $N_1 = N_{\omega_1}$ and using $N_{-\omega_1} = -N_{\omega_1}$, we recover the first term in the second line of Equation (114),

$$N_1(G^{[2]} - G^{[3]}) = \pi i t \left[\frac{\delta(\omega_1 - u)}{\omega_2^- + u} - \frac{\delta(\omega_1 + u)}{\omega_2^- - u} \right] \quad (\text{H6})$$

Next, we consider the Keldysh component $G_{d_1 d_1^\dagger n_1}^{[123]}$. Since the regular part in Equation (H3) is independent of $i\omega_3$, we can set $G^{[1]} = G^{[2]}$ and $G^{[2]} = G^{[1]}$ (see Figure 6b). Additionally using Equation (83) as well as $\hat{G}_1 = \hat{G}_2$ for the 3p electron-density correlator, the last FDR in Equation (84) reduces to

$$\begin{aligned} G_{d_1 d_1^\dagger n_1}^{[123]} &= G^{[3]} + N_1 N_2 (G^{[3]} - G^{[2]} - G^{[1]} + G^{[3]}) \\ &\quad + 4\pi i \delta(\omega_{12}) N_1 (\hat{G}_3^{[1]} - \hat{G}_3^{[2]}) \end{aligned} \quad (\text{H7})$$

Here, we show that all terms except $G^{[3]}$ cancel out. To this end, we can reuse Equation (H5) to obtain

$$\begin{aligned} & G^{[3]} - G^{[2]} - G^{[1]} + G^{[3]} \\ &= \tilde{G}(\omega_1^+, \omega_2^+, \omega_3^-) - \tilde{G}(\omega_1^-, \omega_2^+, \omega_3^-) - \tilde{G}(\omega_1^+, \omega_2^-, \omega_3^-) + \tilde{G}(\omega_1^-, \omega_2^-, \omega_3^-) \\ &= \pi i \delta(\omega_1 + u) \left(\frac{1}{\omega_2^+ - u} - \frac{1}{\omega_2^- - u} \right) \\ &\quad + \pi i \delta(\omega_1 - u) \left(\frac{1}{\omega_2^+ + u} - \frac{1}{\omega_2^- + u} \right) \\ &= 2\pi^2 [\delta(\omega_1 + u)\delta(\omega_2 - u) + \delta(\omega_1 - u)\delta(\omega_2 + u)] \\ &= 2\pi^2 \delta(\omega_{12}) [\delta(\omega_1 + u) + \delta(\omega_1 - u)] \end{aligned} \quad (\text{H8})$$

The discontinuity of \hat{G}_3 is easily evaluated with identity (H2)

$$\begin{aligned} \hat{G}_3^{[1]} - \hat{G}_3^{[2]} &= \frac{u}{2} t \left(\frac{1}{(\omega_1^+)^2 - u^2} - \frac{1}{(\omega_1^-)^2 - u^2} \right) \\ &= \pi i \frac{t}{2} [\delta(\omega_1 + u) - \delta(\omega_1 - u)] \end{aligned} \quad (\text{H9})$$

Inserting all terms (except $G^{[3]}$) in Equation (H7) and using again $N_i = N_{\omega_i} = -N_{-\omega_i}$, we find

$$\begin{aligned} & N_1 N_2 (G^{[3]} - G^{[2]} - G^{[1]} + G^{[3]}) + 4\pi i \delta(\omega_{12}) N_1 \sqrt{2} (\hat{G}_3^{[1]} - \hat{G}_3^{[2]}) \\ &= -2\pi^2 t^2 \delta(\omega_{12}) [\delta(\omega_1 + u) + \delta(\omega_1 - u)] \\ &\quad + 2\pi^2 t^2 \delta(\omega_{12}) [\delta(\omega_1 + u) + \delta(\omega_1 - u)] = 0 \end{aligned} \quad (\text{H10})$$

Thus, Equation (H7) reduces to

$$G_{d_1 d_1^\dagger n_1}^{[123]} = G^{[3]} \quad (\text{H11})$$

corresponding to the last equality in Equation (115).

H.3. Simplifications for Fermionic 4p Correlator

In this section, we present the steps needed to obtain the Keldysh component $G_{\uparrow\downarrow}^{[12]}$ in Section 7.3. The discontinuities can be easily evaluated after rewriting the regular part in terms of general complex frequencies as

$$\tilde{G}(z) = -\frac{u}{z_2^2 - u^2} \left[\frac{1}{z_1 + u} \left(\frac{1}{z_3 - u} + \frac{1}{z_4 - u} \right) + \frac{1}{z_3 + u} \left(\frac{1}{z_1 - u} + \frac{1}{z_4 - u} \right) + \frac{1}{z_4 + u} \left(\frac{1}{z_1 - u} + \frac{1}{z_3 - u} \right) \right] \quad (\text{H12})$$

The discontinuity $C_{\text{III}}^{(12)} - C^{(2)}$ in Equation (120) then reduces to

$$\begin{aligned} C_{\text{III}}^{(12)} - C^{(2)} &= \tilde{G}(\omega_1^+, \omega_2^+, \omega_3^-, \omega_4^-) - \tilde{G}(\omega_1^-, \omega_2^+, \omega_3^-, \omega_4^-) \\ &= \frac{2\pi i u}{(\omega_2^+)^2 - u^2} \left[\delta(\omega_1 + u) \left(\frac{1}{\omega_3^- - u} + \frac{1}{\omega_4^- - u} \right) + \delta(\omega_1 - u) \left(\frac{1}{\omega_3^- + u} + \frac{1}{\omega_4^- + u} \right) \right] \end{aligned} \quad (\text{H13})$$

The second discontinuity $C_{\text{I}}^{(12)} - C^{(1)}$ follows by exchanging $\omega_1 \rightarrow \omega_2$. Using the δ -functions to replace u by ω_1 and multiplying with N_1 , the Keldysh component $C_{\uparrow\downarrow}^{[12]}$ takes the form

$$\begin{aligned} G_{\uparrow\downarrow}^{[12]} &= \frac{2\pi i u t}{(\omega_2^+)^2 - u^2} [\delta(\omega_1 - u) - \delta(\omega_1 + u)] \left(\frac{1}{\omega_{13}^-} + \frac{1}{\omega_{14}^-} \right) \\ &+ \frac{2\pi i u t}{(\omega_1^+)^2 - u^2} [\delta(\omega_2 - u) - \delta(\omega_2 + u)] \left(\frac{1}{\omega_{23}^-} + \frac{1}{\omega_{24}^-} \right) \\ &+ 4\pi i u^2 \frac{\delta(\omega_{13}) (t-1) + \delta(\omega_{14}) (t+1)}{[(\omega_1^+)^2 - u^2][(\omega_2^+)^2 - u^2]} \end{aligned} \quad (\text{H14})$$

Collecting terms proportional to t and replacing the δ -functions of its coefficient using the identities in Equations (58) and (H2) yields

$$G_{\uparrow\downarrow}^{\text{I}}(\omega) = 0 \quad (\text{H18a})$$

$$G_{\uparrow\downarrow}^{\text{II}}(\omega) = \tilde{G}_{\uparrow\downarrow}(\omega_1^+, \omega_2^-, \omega_3^-, \omega_4^-) \quad (\text{H18b})$$

$$G_{\uparrow\downarrow}^{\text{III}}(\omega) = \tilde{G}_{\uparrow\downarrow}(\omega_1^-, \omega_2^+, \omega_3^-, \omega_4^-) \quad (\text{H18c})$$

$$G_{\uparrow\downarrow}^{\text{IV}}(\omega) = \tilde{G}_{\uparrow\downarrow}(\omega_1^-, \omega_2^-, \omega_3^+, \omega_4^-) \quad (\text{H18d})$$

$$G_{\uparrow\downarrow}^{\text{V}}(\omega) = \tilde{G}_{\uparrow\downarrow}(\omega_1^-, \omega_2^-, \omega_3^-, \omega_4^+) \quad (\text{H18e})$$

$$G_{\uparrow\downarrow}^{\text{VI}}(\omega) = \frac{2\pi i u^2 [\delta(\omega_{14}) - \delta(\omega_{13})]}{[(\omega_1^-)^2 - u^2][(\omega_2^-)^2 - u^2]} + u^2 t \left[\frac{1}{[(\omega_3^+)^2 - u^2][(\omega_4^+)^2 - u^2]} \left(\frac{1}{\omega_{24}^-} + \frac{1}{\omega_{14}^-} \right) - \text{c.c.} \right] \quad (\text{H18f})$$

$$G_{\uparrow\downarrow}^{\text{VII}}(\omega) = \frac{2\pi i u^2 \delta(\omega_{14})}{[(\omega_1^-)^2 - u^2][(\omega_3^+)^2 - u^2]} + u^2 t \left[\frac{1}{[(\omega_2^+)^2 - u^2][(\omega_4^+)^2 - u^2]} \left(\frac{1}{\omega_{34}^-} + \frac{1}{\omega_{14}^-} \right) - \text{c.c.} \right] \quad (\text{H18g})$$

$$\begin{aligned} G_{\uparrow\downarrow}^{[12]} &= \frac{4\pi i u^2 [\delta(\omega_{14}) - \delta(\omega_{13})]}{[(\omega_1^+)^2 - u^2][(\omega_2^+)^2 - u^2]} \\ &- 2u^2 t \left[\frac{1}{(\omega_2^+)^2 - u^2} \left(\frac{1}{(\omega_1^+)^2 - u^2} - \frac{1}{(\omega_1^-)^2 - u^2} \right) \left(\frac{1}{\omega_{13}^-} + \frac{1}{\omega_{14}^-} \right) \right. \\ &+ \frac{1}{(\omega_1^+)^2 - u^2} \left(\frac{1}{(\omega_2^+)^2 - u^2} - \frac{1}{(\omega_2^-)^2 - u^2} \right) \left(\frac{1}{\omega_{23}^-} + \frac{1}{\omega_{24}^-} \right) \\ &\left. + \frac{1}{[(\omega_1^+)^2 - u^2][(\omega_2^+)^2 - u^2]} \left(\frac{1}{\omega_{13}^-} - \frac{1}{\omega_{13}^-} + \frac{1}{\omega_{14}^-} - \frac{1}{\omega_{14}^-} \right) \right] \end{aligned} \quad (\text{H15})$$

By energy conservation, $\omega_{1234} = 0$, many terms in the bracket cancel, and we obtain the final result

$$\begin{aligned} G_{\uparrow\downarrow}^{[12]} &= \frac{4\pi i u^2 [\delta(\omega_{14}) - \delta(\omega_{13})]}{[(\omega_1^+)^2 - u^2][(\omega_2^+)^2 - u^2]} \\ &+ 2u^2 t \left[\frac{1}{[(\omega_1^+)^2 - u^2][(\omega_2^-)^2 - u^2]} \left(\frac{1}{\omega_{23}^-} + \frac{1}{\omega_{24}^-} \right) - \text{c.c.} \right] \end{aligned} \quad (\text{H16})$$

where c.c. denotes the complex conjugate.

H.4. Results for Fermionic 4p Correlator

In this section, we summarize results for all Keldysh components of the four-electron correlator for both the $G_{\uparrow\downarrow}$ and $G_{\uparrow\uparrow}$ component. They can be derived following similar calculations presented in the previous section. Defining

$$\tilde{C}_{\uparrow\downarrow}(z) = \frac{2u \prod_{i=1}^4 (z_i) + u^3 \sum_{i=1}^4 (z_i)^2 - 6u^5}{\prod_{i=1}^4 [(z_i)^2 - u^2]} \quad (\text{H17})$$

the results for $G_{\uparrow\downarrow}$ read

$$G_{\uparrow\downarrow}^{[23]}(\omega) = \frac{-2\pi i u^2 \delta(\omega_{13})}{[(\omega_1^-)^2 - u^2][(\omega_4^-)^2 - u^2]} + u^2 t \left[\frac{1}{[(\omega_2^+)^2 - u^2][(\omega_3^-)^2 - u^2]} \left(\frac{1}{\omega_{34}} + \frac{1}{\omega_{13}} \right) - \text{c.c.} \right] \quad (\text{H18h})$$

$$G_{\uparrow\downarrow}^{[14]}(\omega) = \frac{-2\pi i u^2 \delta(\omega_{13})}{[(\omega_2^-)^2 - u^2][(\omega_3^-)^2 - u^2]} + u^2 t \left[\frac{1}{[(\omega_1^+)^2 - u^2][(\omega_4^-)^2 - u^2]} \left(\frac{1}{\omega_{34}} + \frac{1}{\omega_{24}} \right) - \text{c.c.} \right] \quad (\text{H18i})$$

$$G_{\uparrow\downarrow}^{[13]}(\omega) = \frac{2\pi i u^2 \delta(\omega_{14})}{[(\omega_2^-)^2 - u^2][(\omega_4^-)^2 - u^2]} + u^2 t \left[\frac{1}{[(\omega_1^+)^2 - u^2][(\omega_3^-)^2 - u^2]} \left(\frac{1}{\omega_{34}} + \frac{1}{\omega_{23}} \right) - \text{c.c.} \right] \quad (\text{H18j})$$

$$G_{\uparrow\downarrow}^{[12]}(\omega) = \frac{2\pi i u^2 [\delta(\omega_{14}) - \delta(\omega_{13})]}{[(\omega_3^-)^2 - u^2][(\omega_4^-)^2 - u^2]} + u^2 t \left[\frac{1}{[(\omega_1^+)^2 - u^2][(\omega_2^-)^2 - u^2]} \left(\frac{1}{\omega_{24}} + \frac{1}{\omega_{23}} \right) - \text{c.c.} \right] \quad (\text{H18k})$$

$$G_{\uparrow\downarrow}^{[234]}(\omega) = \tilde{C}_{\uparrow\downarrow}(\omega_1^-, \omega_2^+, \omega_3^+, \omega_4^+) + 2\pi^2 u t [\delta(\omega_2 - u) + \delta(\omega_2 + u)] [\delta(\omega_{14}) - \delta(\omega_{13})] \frac{1}{(\omega_1^-)^2 - u^2} \quad (\text{H18l})$$

$$G_{\uparrow\downarrow}^{[134]}(\omega) = \tilde{C}_{\uparrow\downarrow}(\omega_1^+, \omega_2^-, \omega_3^+, \omega_4^+) + 2\pi^2 u t [\delta(\omega_1 - u) + \delta(\omega_1 + u)] [\delta(\omega_{14}) - \delta(\omega_{13})] \frac{1}{(\omega_2^-)^2 - u^2} \quad (\text{H18m})$$

$$G_{\uparrow\downarrow}^{[124]}(\omega) = \tilde{C}_{\uparrow\downarrow}(\omega_1^+, \omega_2^+, \omega_3^-, \omega_4^+) + 2\pi^2 u t [\delta(\omega_4 - u) + \delta(\omega_4 + u)] [\delta(\omega_{14}) - \delta(\omega_{13})] \frac{1}{(\omega_3^-)^2 - u^2} \quad (\text{H18n})$$

$$G_{\uparrow\downarrow}^{[123]}(\omega) = \tilde{C}_{\uparrow\downarrow}(\omega_1^+, \omega_2^+, \omega_3^+, \omega_4^-) + 2\pi^2 u t [\delta(\omega_3 - u) + \delta(\omega_3 + u)] [\delta(\omega_{14}) - \delta(\omega_{13})] \frac{1}{(\omega_4^-)^2 - u^2} \quad (\text{H18o})$$

$$G_{\uparrow\downarrow}^{[1234]}(\omega) = \frac{t}{u} [\omega_1^+ \tilde{C}_{\uparrow\downarrow}(\omega_1^+, \omega_2^-, \omega_3^-, \omega_4^-) + \omega_2^+ \tilde{C}_{\uparrow\downarrow}(\omega_1^-, \omega_2^+, \omega_3^-, \omega_4^-) + \omega_3^+ \tilde{C}_{\uparrow\downarrow}(\omega_1^-, \omega_2^-, \omega_3^+, \omega_4^-) + \omega_4^+ \tilde{C}_{\uparrow\downarrow}(\omega_1^-, \omega_2^-, \omega_3^-, \omega_4^+)] - 4\pi^3 i t^2 \delta(\omega_{12}) [\delta(u + \omega_1) - \delta(u - \omega_1)] [\delta(u + \omega_3) - \delta(u - \omega_3)] \quad (\text{H18p})$$

The same-spin correlator in the MF turns out to be purely anomalous

$$G_{\uparrow\uparrow}(i\omega) = \frac{u^2 (\beta \delta_{i\omega_{14}} - \beta \delta_{i\omega_{12}})}{\prod_{i=1}^4 (i\omega_i) - u} \quad (\text{H19})$$

Therefore, the derivation of the corresponding Keldysh correlators is straightforward and yields

$$G_{\uparrow\uparrow}^{\square}(\omega) = G_{\uparrow\uparrow}^{[1]}(\omega) = G_{\uparrow\uparrow}^{[2]}(\omega) = G_{\uparrow\uparrow}^{[3]}(\omega) = G_{\uparrow\uparrow}^{[4]}(\omega) = 0 \quad (\text{H20a})$$

$$G_{\uparrow\uparrow}^{[34]}(\omega) = 2\pi i u^2 \frac{\delta(\omega_{14})}{[(\omega_2^-)^2 - u^2][(\omega_4^+)^2 - u^2]} \quad (\text{H20b})$$

$$G_{\uparrow\uparrow}^{[24]}(\omega) = 2\pi i u^2 \frac{\delta(\omega_{14}) - \delta(\omega_{12})}{[(\omega_2^+)^2 - u^2][(\omega_4^+)^2 - u^2]} \quad (\text{H20c})$$

$$G_{\uparrow\uparrow}^{[23]}(\omega) = 2\pi i u^2 \frac{-\delta(\omega_{12})}{[(\omega_2^+)^2 - u^2][(\omega_4^-)^2 - u^2]} \quad (\text{H20d})$$

$$G_{\uparrow\uparrow}^{[14]}(\omega) = 2\pi i u^2 \frac{-\delta(\omega_{12})}{[(\omega_2^-)^2 - u^2][(\omega_4^+)^2 - u^2]} \quad (\text{H20e})$$

$$G_{\uparrow\uparrow}^{[13]}(\omega) = 2\pi i u^2 \frac{\delta(\omega_{14}) - \delta(\omega_{12})}{[(\omega_2^-)^2 - u^2][(\omega_4^-)^2 - u^2]} \quad (\text{H20f})$$

$$G_{\uparrow\uparrow}^{[12]}(\omega) = 2\pi i u^2 \frac{\delta(\omega_{14})}{[(\omega_2^+)^2 - u^2][(\omega_4^-)^2 - u^2]} \quad (\text{H20g})$$

$$G_{\uparrow\uparrow}^{[234]}(\omega) = 2\pi^2 u t \frac{1}{(\omega_1^-)^2 - u^2} [\delta(\omega_3 - u) + \delta(\omega_3 + u)] [\delta(\omega_{14}) - \delta(\omega_{12})] \quad (\text{H20h})$$

$$G_{\uparrow\uparrow}^{[134]}(\omega) = 2\pi^2 u t \frac{1}{(\omega_2^-)^2 - u^2} [\delta(\omega_4 - u) + \delta(\omega_4 + u)] [\delta(\omega_{14}) - \delta(\omega_{12})] \quad (\text{H20i})$$

$$G_{\uparrow\uparrow}^{[124]}(\omega) = 2\pi^2 u t \frac{1}{(\omega_3^-)^2 - u^2} [\delta(\omega_1 - u) + \delta(\omega_1 + u)] [\delta(\omega_{14}) - \delta(\omega_{12})] \quad (\text{H20j})$$

$$G_{\uparrow\uparrow}^{[123]}(\omega) = 2\pi^2 u t \frac{1}{(\omega_4^-)^2 - u^2} [\delta(\omega_2 - u) + \delta(\omega_2 + u)] [\delta(\omega_{14}) - \delta(\omega_{12})] \quad (\text{H20k})$$

$$G_{\uparrow\uparrow}^{[1234]}(\omega) = -4\pi^3 i t^2 [\delta(\omega_{12}) - \delta(\omega_{14})] [\delta(\omega_1 + u) - \delta(\omega_1 - u)] [\delta(\omega_3 + u) - \delta(\omega_3 - u)]. \quad (\text{H20l})$$

Acknowledgements

A.G. and J.H. contributed equally to this work. A.G., J.H., and J.v.D. were supported by the Deutsche Forschungsgemeinschaft under Germany's Excellence Strategy EXC-2111 (Project No. 390814868), and the Munich Quantum Valley, supported by the Bavarian state government with funds from the Hightech Agenda Bayern Plus. J.H. acknowledges support by the International Max Planck Research School for Quantum Science and Technology (IMPRS-QST). S.-S.B.L. is supported by the New Faculty Startup Fund from Seoul National University, and also by the National Research Foundation of Korea (NRF) grant funded by the Korean government (MSIT) (No. RS-2023-00214464). F.B.K. acknowledges support by the Alexander von Humboldt Foundation through the Feodor Lynen Fellowship. The Flatiron Institute is a division of the Simons Foundation. This research was supported in part by the National Science Foundation under PHY-1748958.

Open access funding enabled and organized by Projekt DEAL.

Conflict of Interest

The authors declare no conflict of interest.

Data Availability Statement

Data sharing is not applicable to this article as no new data were created or analyzed in this study.

Keywords

analytic continuation, Keldysh formalism, multipoint correlation functions, thermal field theory

Received: November 20, 2023

Revised: January 30, 2024

Published online: May 1, 2024

- [1] W. Metzner, M. Salmhofer, C. Honerkamp, V. Meden, K. Schönhammer, *Rev. Mod. Phys.* **2012**, *84*, 299.
- [2] N. E. Bickers, *Self-Consistent Many-Body Theory for Condensed Matter Systems*, Springer New York, New York, NY **2004**, pp. 237–296, ISBN 978-0-387-21717-8.
- [3] G. Rohringer, H. Hafermann, A. Toschi, A. Katanin, A. Antipov, M. Katsnelson, A. Lichtenstein, A. Rubtsov, K. Held, *Rev. Mod. Phys.* **2018**, *90*, 025003.
- [4] A. A. Abrikosov, I. Dzyaloshinskii, L. P. Gorkov, *Methods of Quantum Field Theory in Statistical Physics*, Dover, New York **1975**.
- [5] G. Cuniberti, E. De Micheli, G. A. Viano, *Commun. Math. Phys.* **2001**, *216*, 59.
- [6] J. E. Gubernatis, M. Jarrell, R. N. Silver, D. S. Sivia, *Phys. Rev. B* **1991**, *44*, 6011.
- [7] A. Kamenev, *Field Theory of Non-Equilibrium Systems*, Cambridge University Press, Cambridge **2013**.
- [8] L. V. Keldysh, *Zh. Eksp. Teor. Fiz.* **1964**, *47*, 1515; *Sov. Phys. JETP* **1965**, *20*, 1018.
- [9] J. Schwinger, *J. Math. Phys.* **1961**, *2*, 407.
- [10] A. Altland, B. Simons, *Condensed Matter Field Theory*, Cambridge University Press, Cambridge **2010**.
- [11] G. Baym, N. D. Mermin, *J. Math. Phys.* **1961**, *2*, 232.
- [12] J. W. Negele, H. Orland, *Quantum many-particle systems*, Perseus Books, New York, NY **1998**.
- [13] G. Eliashberg, *Sov. Phys. JETP* **1962**, *14*, 886.
- [14] T. Evans, *Phys. Lett. B* **1990**, *252*, 108.
- [15] R. Kobes, *Phys. Rev. D* **1990**, *42*, 562.
- [16] R. Kobes, *Phys. Rev. D* **1991**, *43*, 1269.
- [17] T. Evans, *Nucl. Phys. B* **1992**, *374*, 340.
- [18] H. A. Weldon, *Phys. Rev. D* **2005**, *71*, 036002.
- [19] H. A. Weldon, *Phys. Rev. D* **2005**, *72*, 096005.
- [20] J. C. Taylor, *Phys. Rev. D* **1993**, *47*, 725.
- [21] F. Guerin, *Nucl. Phys. B* **1994**, *432*, 281.
- [22] F. Guerin, *Phys. Rev. D* **1994**, *49*, 4182.
- [23] F. B. Kugler, S.-S. B. Lee, J. von Delft, *Phys. Rev. X* **2021**, *11*, 041006.
- [24] E. Wang, U. Heinz, *Phys. Rev. D* **2002**, *66*, 025008.
- [25] S. G. Jakobs, M. Pletyukhov, H. Schoeller, *J. Phys. A* **2010**, *43*, 103001.
- [26] K. W. H. Stevens, G. A. Toombs, *Proc. Phys. Soc.* **1965**, *85*, 1307.
- [27] P. C. Kwok, T. D. Schultz, *J. Phys. C* **1969**, *2*, 1196.
- [28] C. Watzenböck, M. Fellingner, K. Held, A. Toschi, *SciPost Phys.* **2022**, *12*, 184.
- [29] S.-S. B. Lee, F. B. Kugler, J. von Delft, *Phys. Rev. X* **2021**, *11*, 041007.
- [30] J. Halbinger, B. Schneider, B. Sbierski, *SciPost Phys.* **2023**, *15*, 183.
- [31] We verified this form explicitly for $\ell \leq 7$, using expressions for K derived in Ref. [30], but expect it to hold for arbitrary ℓ .
- [32] X.-G. Wen, *Quantum field theory of many-body systems: from the origin of sound to an origin of light and electrons*, OUP Oxford, Oxford **2004**.
- [33] M. Wallerberger, H. Shinaoka, A. Kauch, *Phys. Rev. Res.* **2021**, *3*, 033168.
- [34] F. Krien, A. Valli, *Phys. Rev. B* **2019**, *100*, 245147.
- [35] F. Krien, A. Kauch, K. Held, *Phys. Rev. Res.* **2021**, *3*, 013149.
- [36] H. Hafermann, C. Jung, S. Brener, M. I. Katsnelson, A. N. Rubtsov, A. I. Lichtenstein, *EPL* **2009**, *85*, 27007.
- [37] S. Pairault, D. Sénéchal, A.-M. Tremblay, *Eur. Phys. J. B* **2000**, *16*, 85.
- [38] G. Rohringer, A. Valli, A. Toschi, *Phys. Rev. B* **2012**, *86*, 125114.
- [39] G. Rohringer, Ph.D. thesis, Technische Universität Wien, **2013**, <https://repositum.tuwien.at/handle/20.500.12708/6957>.
- [40] N. Wentzell, G. Li, A. Tagliavini, C. Taranto, G. Rohringer, K. Held, A. Toschi, S. Andergassen, *Phys. Rev. B* **2020**, *102*, 085106.
- [41] T. Ayrál, O. Parcollet, *Phys. Rev. B* **2015**, *92*, 115109.
- [42] T. Ayrál, O. Parcollet, *Phys. Rev. B* **2016**, *93*, 235124.
- [43] E. G. C. P. van Loon, F. Krien, H. Hafermann, A. I. Lichtenstein, M. I. Katsnelson, *Phys. Rev. B* **2018**, *98*, 205148.
- [44] W. Metzner, *Phys. Rev. B* **1991**, *43*, 8549.
- [45] M. Kinza, J. Ortloff, J. Bauer, C. Honerkamp, *Phys. Rev. B* **2013**, *87*, 035111.
- [46] T. Schäfer, S. Ciuchi, M. Wallerberger, P. Thunström, O. Gunnarsson, G. Sangiovanni, G. Rohringer, A. Toschi, *Phys. Rev. B* **2016**, *94*, 235108.
- [47] P. Thunström, O. Gunnarsson, S. Ciuchi, G. Rohringer, *Phys. Rev. B* **2018**, *98*, 235107.
- [48] P. Chalupa, P. Gunacker, T. Schäfer, K. Held, A. Toschi, *Phys. Rev. B* **2018**, *97*, 245136.
- [49] M. Pelz, S. Adler, M. Reitner, A. Toschi, *Phys. Rev. B* **2023**, *108*, 155101.
- [50] O. Gunnarsson, G. Rohringer, T. Schäfer, G. Sangiovanni, A. Toschi, *Phys. Rev. Lett.* **2017**, *119*, 056402.
- [51] E. Kozik, M. Ferrero, A. Georges, *Phys. Rev. Lett.* **2015**, *114*, 156402.
- [52] J. Vučičević, N. Wentzell, M. Ferrero, O. Parcollet, *Phys. Rev. B* **2018**, *97*, 125141.
- [53] P. Chalupa, T. Schäfer, M. Reitner, D. Springer, S. Andergassen, A. Toschi, *Phys. Rev. Lett.* **2021**, *126*, 056403.
- [54] S. Adler, F. Krien, P. Chalupa-Gantner, G. Sangiovanni, A. Toschi, *SciPost Phys.* **2024**, *16*, 054.
- [55] F. Krien, A. Valli, M. Capone, *Phys. Rev. B* **2019**, *100*, 155149.
- [56] M. Gievers, E. Walter, A. Ge, J. von Delft, F. B. Kugler, *Eur. Phys. J. B* **2022**, *95*, 108.
- [57] R. Kubo, *J. Phys. Soc. Japan* **1957**, *12*, 570.
- [58] P. Kappl, F. Krien, C. Watzenböck, K. Held, *Phys. Rev. B* **2023**, *107*, 205108.
- [59] A. Ge, N. Ritz, E. Walter, S. Aguirre, J. von Delft, F. B. Kugler, *Phys. Rev. B* **2024**, *109*, 115128.
- [60] A. Taheridehkordi, S. H. Curnoe, J. P. F. LeBlanc, *Phys. Rev. B* **2019**, *99*, 035120.
- [61] J.-M. Lihm, J. Halbinger, J. Shim, J. von Delft, F. B. Kugler, S.-S. B. Lee, *Phys. Rev. B* **2024**, *109*, 125138.
- [62] A. Oguri, *J. Phys. Soc. Japan* **2001**, *70*, 2666.
- [63] J. Heyder, F. Bauer, D. Schimmel, J. von Delft, *Phys. Rev. B* **2017**, *96*, 125141.
- [64] P. Aurenche, T. Becherrawy, *Nucl. Phys. B* **1992**, *379*, 259.
- [65] M. van Eijck, C. G. Van Weert, *Phys. Lett. B* **1992**, *278*, 305.
- [66] A. I. Larkin, Y. N. Ovchinnikov, *Sov Phys JETP* **1969**, *28*, 1200.
- [67] J. Fei, C.-N. Yeh, E. Gull, *Phys. Rev. Lett.* **2021**, *126*, 056402.
- [68] J. Fei, C.-N. Yeh, D. Zgid, E. Gull, *Phys. Rev. B* **2021**, *104*, 165111.
- [69] Z. Huang, E. Gull, L. Lin, *Phys. Rev. B* **2023**, *107*, 075151.
- [70] H. Shinaoka, J. Otsuki, M. Ohzeki, K. Yoshimi, *Phys. Rev. B* **2017**, *96*, 035147.
- [71] J. Kaye, K. Chen, O. Parcollet, *Phys. Rev. B* **2022**, *105*, 235115.
- [72] In Ref. [23], after Equation (41), it was stated that the lower boundary terms yield K ; that is incorrect—they yield only \tilde{K} .
- [73] A. Shvaika, *Condens. Matter Phys.* **2006**, *9*, 447.
- [74] A. Shvaika, *Condens. Matter Phys.* **2016**, *19*, 33004.

6 Conclusion and outlook

In this thesis we studied the analytic structure of multipoint correlators in the Matsubara and Keldysh formalism and showed how they are related. We further applied quantum field-theoretic methods both in the MF and KF. The latter computes dynamical observables which can be directly compared to experiment. After a general introduction to correlators, one- and two-particle observables, their computation with the parquet equations and functional renormalization group in Chapter 2, we presented the projects published in Refs. [P1]-[P5].

In Chapter 3, we first recapitulated the single-boson exchange (SBE) decomposition [KVC19] of the four-point vertex which was originally introduced for Hubbard-like models with $SU(2)$ -spin symmetry. Using a multi-index notation we generalized the SBE notion to arbitrary instantaneous interactions and rederived the parquet equations. The main result of [P1] is the derivation of multiloop flow equations for the SBE components in different approximations. For completeness, we also showed the relation to the asymptotic decomposition [WLT⁺20] and the parquet and mFRG equations for the asymptotic functions.

The asymptotic decomposition was then used in our QFT study of the Anderson impurity model in Chapter 4, which we performed both in the MF and the KF. We solved the parquet equations (in the parquet approximation) and the flow equations of the functional renormalization group (in the one-loop approximation with Katanin substitution [Kat04]). Our study finds that real-frequency calculations with the full frequency dependence of the four-point vertex are indeed feasible even in the KF. The numerical challenges were addressed by suitably adapted non-linear frequency grids, vectorization over the matrix structure of the Keldysh indices, exploitation of symmetries, and massive parallelization. Real-frequency results were compared to analogous Matsubara results at zero frequency, finding good convergence in numerical parameters. We find that the full three-dimensional treatment of the vertex also improves accuracy compared to previous implementations, where strong approximations were made. Static and dynamic observables were also compared to reference data from the numerical renormalization group (NRG) [BCP08]: For the regime in which converged parquet results could be obtained ($u = U/(\pi\Delta) \lesssim 1$) we found that these give good agreement. While fRG data could be obtained for a wider range of parameters, they typically showed larger discrepancies already starting at $u \gtrsim 0.5$. The physical results of our study were presented in Ref. [P3] whereas the code release Ref. [P5] then explained the implementation details of our real-frequency solvers. A separate code release Ref. [P2] introduces a `Julia` package for calculations with Matsubara functions. It contains useful data structures, standard routines and code examples. The package aims to accelerate the prototyping of diagrammatic solvers in the MF.

For future projects, the presented real-frequency methods may be used for diagrammatic extensions of dynamical mean-field theory [GKKR96] to study lattice models with strong correlations such as the Hubbard model. For this purpose, the multipoint generalization of NRG [LKvD21, LHS⁺24] may be used as real-frequency impurity solver. In an upcoming publication [P6] we therefore study the fulfillment of physical relations by the NRG self-energy and vertex components. A direct generalization of our diagrammatic solvers to lattice models would lead to a major increase in the numerical effort, both in terms of memory consumption and computation time. For this purpose a more efficient representation will be needed. The quantics tensor train representation is a promising representation that can employ efficient

tensor network algorithms [NnFJD⁺22, SWM⁺23, RNnFW⁺24]. As a first step Ref. [P7] therefore studies the compressibility of vertices in the KF.

Another interesting direction for future explorations might be the incorporation of Ward identities into the parquet scheme. Ward identities are consequences of conservation laws and are not necessarily fulfilled when the parquet equations are approximated. Simultaneous fulfillment of parquet self-consistency and conservation laws is a very difficult task. After all, it is known that only the exact solution can fulfil both exactly. However, an approximate fulfillment of Ward identities might be achieved by a suitable ansatz for the fully two-particle irreducible vertex R , the fully U -irreducible vertex $\varphi^{U_{\text{irr}}}$ or the asymptotic rest function φ^{asy} .

The formal equivalence of Matsubara and Keldysh correlators is well-known for two-point functions. This is typically exploited in derivations to avoid the additional index structure in the KF. Retarded correlators are then recovered via analytic continuation. As a generalization, in Chapter 5 we present an approach for the analytic continuation of multipoint correlators. The starting point of our derivations are the spectral representations introduced in [KLvD21, HSS23] which separate correlators into formalism-independent partial spectral functions (PSFs) and formalism-specific kernels. We find that it is actually possible to recover all partial spectral functions from a Matsubara correlator. These fully encode the physical information and thereby allow to construct all Keldysh components in terms of linear combinations of analytically continued Matsubara functions. Furthermore, the formulas reveal that the Keldysh components are related by generalized fluctuation-dissipation relations. As another application of our formulas we derive expressions for three- and four-point correlators of the Hubbard atom in the KF, based on the corresponding formulas in the MF. Another promising direction for future explorations is the numerical representation of multipoint MF correlators. References [SOOY17, KCP22] demonstrated that two-point Matsubara correlators can be approximated compactly with a suitable set of basis functions. However, for multipoint functions, Ref. [WSK21] found that the overcompleteness of the basis prevents an extraction of the basis coefficients by projection. Instead, a fitting procedure with many basis functions is required, which limits the method's applicability. Therefore, a numerical counterpart of our method for recovering individual PSFs S_p (or partial correlators G_p) from a full correlator $G(i\omega)$ would be valuable. Finally, our formulas might also be useful for evaluating diagrammatic relations typically formulated for correlators while using the PSFs as the main information carriers.

Appendix A

Hubbard atom

The Hubbard atom is a popular toy model which can be obtained from the Hubbard model or Anderson model (2.78d) by taking the so-called atomic limit ($V \rightarrow 0$). It also has an analytic solution and has non-trivial multipoint contributions. Therefore, it serves as a good test bed for numerical implementations. The Hamiltonian of the half-filled Hubbard atom without magnetic field reads

$$\hat{H}^{\text{HA}} = U \hat{d}_{\uparrow}^{\dagger} \hat{d}_{\uparrow} \hat{d}_{\downarrow}^{\dagger} \hat{d}_{\downarrow} - \frac{U}{2} \sum_{\sigma=\uparrow,\downarrow} \hat{d}_{\sigma}^{\dagger} \hat{d}_{\sigma}. \quad (\text{A.1})$$

It describes a single site which can be occupied by an electron of spin $\sigma = \uparrow, \downarrow$. When two electrons occupy the site they experience an instantaneous repulsive interaction of strength U .

In this section we present, for ease of reference, formulas for the four-point vertex of the Hubbard atom which partly have been computed and published in the Matsubara formalism [Roh13, WLT⁺20]. For the Keldysh formalism we refer to Ref. [P4]. Alternatively, one may compute them by inserting the operators $\hat{d}^{(\dagger)}$ into the spectral representation [KvD18b]. For this purpose, we describe the Hilbert space as vectors in the basis $(|\emptyset\rangle, |\uparrow\rangle, |\downarrow\rangle, |\uparrow\downarrow\rangle)$ where $|\emptyset\rangle$ is an empty, $|\uparrow\downarrow\rangle$ a doubly occupied and $|\sigma\rangle$ singly occupied site. The corresponding eigenenergies are $(0, -\frac{U}{2}, -\frac{U}{2}, 0)$ and the creation and annihilation operators can be written as

$$\hat{d}_{\uparrow}^{\dagger} = \begin{pmatrix} 0 & 0 & 0 & 0 \\ 1 & 0 & 0 & 0 \\ 0 & 0 & 0 & 0 \\ 0 & 0 & 1 & 0 \end{pmatrix}, \quad \hat{d}_{\uparrow} = \begin{pmatrix} 0 & 1 & 0 & 0 \\ 0 & 0 & 0 & 0 \\ 0 & 0 & 0 & 1 \\ 0 & 0 & 0 & 0 \end{pmatrix}, \quad \hat{d}_{\downarrow}^{\dagger} = \begin{pmatrix} 0 & 0 & 0 & 0 \\ 0 & 0 & 0 & 0 \\ 1 & 0 & 0 & 0 \\ 0 & -1 & 0 & 0 \end{pmatrix}, \quad \hat{d}_{\downarrow} = \begin{pmatrix} 0 & 0 & 1 & 0 \\ 0 & 0 & 0 & -1 \\ 0 & 0 & 0 & 0 \\ 0 & 0 & 0 & 0 \end{pmatrix}, \quad (\text{A.2})$$

where the matrices are obtained from the Jordan–Wigner transformation [Col15].

In the following we use the parametrization and conventions in Sec. 2.2.5.1. The frequency convention is summarized in Fig. 2.7(a), or explicitly reads

$$(\nu_{1'}, \nu_{2'}, \nu_1, \nu_2) = (\nu_a, \nu'_a + \omega_a, \nu'_a, \nu_a + \omega_a) = (\nu_p + \omega_p, -\nu_p, \nu'_p + \omega_p, -\nu'_p) = (\nu'_t + \omega_t, \nu_t, \nu'_t, \nu_t + \omega_t). \quad (\text{A.3})$$

For notational convenience, we write the interaction parameter in terms of

$$u = \frac{U}{2}, \quad (\text{A.4})$$

to avoid proliferation of factors of $\frac{1}{2}$. Thus, 1-particle quantities read

$$G(i\omega) = \frac{1}{i\omega - \Sigma(i\omega)}, \quad (\text{A.5a})$$

$$\Sigma(i\omega) = \frac{u^2}{i\omega}. \quad (\text{A.5b})$$

For the spin components of the vertex we further abbreviate

$$\Gamma^{\uparrow\downarrow} = \Gamma_{\uparrow\downarrow\uparrow\downarrow}, \quad \Gamma^{\overline{\uparrow\downarrow}} = \Gamma_{\uparrow\downarrow\downarrow\uparrow}, \quad \Gamma^{\uparrow\uparrow} = \Gamma_{\uparrow\uparrow\uparrow\uparrow}. \quad (\text{A.6})$$

By SU(2)-spin symmetry (2.91) and crossing symmetry (2.86), these spin components are related, and it suffices to give the following formula for the $\Gamma^{\uparrow\downarrow}$ component [WLT⁺20, Roh13]

$$\Gamma^{\uparrow\downarrow} = \Gamma_{\text{reg}}^{\uparrow\downarrow} + \Gamma_{\text{ano},a}^{\uparrow\downarrow} + \Gamma_{\text{ano},p}^{\uparrow\downarrow} + \Gamma_{\text{ano},t}^{\uparrow\downarrow}, \quad (\text{A.7a})$$

where the regular part can be written in terms of the frequencies of the four fermionic legs

$$\Gamma_{\text{reg}}^{\uparrow\downarrow}(i\nu_{1'}, i\nu_{2'}, i\nu_1, i\nu_2) = -2u + u^3 \frac{\sum_i \nu_i^2}{\prod_i \nu_i} + 6u^5 \prod_i \frac{1}{\nu_i}, \quad (\text{A.7b})$$

with $i \in \{1, 2, 1', 2'\}$. The anomalous parts are most conveniently expressed in terms of the corresponding r -channel frequencies $(\omega_r, \nu_r, \nu'_r)$

$$\Gamma_{\text{ano},a}^{\uparrow\downarrow}(i\omega_a, i\nu_a, i\nu'_a) = -\beta\delta_{\omega_a,0} \mathcal{D}^{\nu_a, \nu'_a} u^2 2n(-u), \quad (\text{A.7c})$$

$$\Gamma_{\text{ano},p}^{\uparrow\downarrow}(i\omega_p, i\nu_p, i\nu'_p) = +\beta\delta_{\omega_p,0} \mathcal{D}^{\nu_p, \nu'_p} u^2 2n(u), \quad (\text{A.7d})$$

$$\Gamma_{\text{ano},t}^{\uparrow\downarrow}(i\omega_t, i\nu_t, i\nu'_t) = +\beta\delta_{\omega_t,0} \mathcal{D}^{\nu_t, \nu'_t} u^2 [n(u) - n(-u)], \quad (\text{A.7e})$$

where we abbreviated $n(\epsilon) = \frac{1}{1+e^{\beta\epsilon}}$ and $\mathcal{D}^{\nu, \nu'} = \frac{(\nu^2+u^2)(\nu'^2+u^2)}{\nu^2\nu'^2}$. For the distribution function we use the identity $n(\epsilon) = 1 - n(-\epsilon)$.

A.1 Asymptotic decomposition

For the asymptotic components we obtain

$$K_{1a}^{\uparrow\downarrow}(i\omega_a) = -u^2\beta\delta_{\omega,0}2n(-u), \quad (\text{A.8a})$$

$$K_{1p}^{\uparrow\downarrow}(i\omega_p) = +u^2\beta\delta_{\omega,0}2n(u), \quad (\text{A.8b})$$

$$K_{1t}^{\uparrow\downarrow}(i\omega_t) = +u^2\beta\delta_{\omega,0}[n(u) - n(-u)]. \quad (\text{A.8c})$$

It so happens that we can summarize all the $K_{2(\nu)}$ functions in terms of

$$K_{2(\nu)r}^{\sigma\sigma'}(i\omega_r, i\nu_r^{(\nu)}) = f_\lambda(\omega_r, \nu_r^{(\nu)}) \overline{w}_r^{\sigma\sigma'}(i\omega_r), \quad (\text{A.9a})$$

with

$$f_\lambda(\omega, \nu) = \frac{u^2}{\nu(\nu + \omega)}, \quad (\text{A.9b})$$

$$\overline{w}_r^{\sigma\sigma'}(i\omega_r) = -\Gamma_0^{\sigma\sigma'} + K_{1r}^{\sigma\sigma'}(i\omega_r). \quad (\text{A.9c})$$

Conveniently f_λ does not depend on the spin index or on the diagrammatic channel, which is partly due to the chosen frequency convention. This allows us to focus on the K_{1r} components. In the physical channels they give

$$K_{1t}^D(i\omega_t) = u^2 \beta \delta_{\omega_t, 0} 2n(u), \quad (\text{A.10a})$$

$$K_{1t}^M(i\omega_t) = u^2 \beta \delta_{\omega_t, 0} 2n(-u), \quad (\text{A.10b})$$

$$K_{1p}^S(i\omega_p) = 2K_1^D(i\omega_p), \quad (\text{A.10c})$$

$$K_{1p}^T(i\omega_p) = 0. \quad (\text{A.10d})$$

With these components we can express all other spin and diagrammatic components, thereby revealing all asymptotically non-trivial functions of the full vertex. The remaining part of the full vertex is collected in the asymptotic rest function

$$\varphi^{\text{asy}} = \Gamma - \Gamma_0 - \sum_r (K_{1r} + K_{2r} + K_{2'r}), \quad (\text{A.11})$$

which reads

$$\varphi^{\text{asy}; \sigma\sigma'} = \sum_{r=a,p,t} f_\lambda(\omega_r, \nu_r) \bar{w}_r^{\sigma\sigma'}(\omega_r) f_\lambda(\omega_r, \nu_r') \quad (\text{A.12})$$

where we expressed the right-hand side in the corresponding r -channel frequency convention $(\omega_r, \nu_r, \nu_r')$ for each summand.¹ In the same notation, we can even express the full vertex as

$$\Gamma^{\sigma\sigma'} = 4\Gamma_0^{\sigma\sigma'} + \sum_{r=a,p,t} [1 + f_\lambda(\omega_r, \nu_r)] \bar{w}_r^{\sigma\sigma'}(i\omega_r) [1 + f_\lambda(\omega_r, \nu_r')]. \quad (\text{A.13})$$

This expression is even more concise than previously published formulas (cf. Ref. [RVT12, WLT⁺20, KLvD21]). It encodes all spin channels in a clear manner and asymptotic functions can be read off easily. Interestingly, the three summands for $r = a, p, t$ factorize and can be written as products of one- and two-dimensional functions. While the second term in Eq. (A.13) is highly reminiscent of the SBE terms ∇_r which also factorize into lower-dimensional functions, it actually differs in details which we will see in the following.

A.2 SBE decomposition

To obtain the Hedin vertices we have to divide K_{2r} by the screened interaction w_r . This is done most conveniently in the physical spin channels which are diagonal in the t or p channel, respectively. Hence, the Hedin vertices read

$$\lambda_t^{\text{D/M}}(\omega_t, \nu_t) = f_\lambda(\omega_t, \nu_t) \frac{\bar{w}_t^{\text{D/M}}(i\omega_t)}{w_t^{\text{D/M}}(i\omega_t)}, \quad (\text{A.14a})$$

$$\lambda_p^S(\omega_p, \nu_p) = f_\lambda(\omega_p, \nu_p) \frac{\bar{w}_p^S(i\omega_p)}{w_p^S(i\omega_p)}. \quad (\text{A.14b})$$

Since for the triplet component we have $K_{2p}^T = 0$ the corresponding Hedin vertex vanishes.

¹ In Ref. [WLT⁺20] the expression for the asymptotic rest function has a typo and misses the Kronecker-delta contributions.

Knowing the exact formulas for the SBE terms ∇_r we also obtain the SBE rest-function

$$\varphi^{U_{\text{irr}}} = \Gamma - \sum_r \nabla_r + 2\Gamma_0, \quad (\text{A.15})$$

which reads

$$\varphi^{U_{\text{irr};X}} = \sum_r f_\lambda(\omega_r, \nu_r) \left[\bar{w}_r - \bar{w}_r \bullet (w_r)^{-1} \bullet \bar{w}_r \right]^X f_\lambda(\omega_r, \nu'_r), \quad (\text{A.16})$$

for any spin component X . Here, the \bullet -operator represents summation over spin indices in the respective channels which again is most conveniently performed in the physical channels $X = D, M, S$.

Appendix B

Multiloop convergence in Matsubara and Keldysh formalism

In Sec. 2.2.4 we summarized the parquet approach and the fRG with multiloop extension [KvD18a]. Both parquet and mfRG equations require the fully 2PI vertex R as external input. If the solution of the parquet equations is unique both methods should give the same result by construction. In this appendix we investigate the convergence of mfRG results in the parquet approximation ($R = \Gamma_0$) for the Anderson model. Using the hybridization flow $\Delta(\Lambda) = \Lambda/2$ every value of the flow parameter Λ corresponds to a different hybridization Δ . Hence, for any Λ along the flow we can solve the parquet equations with hybridization $\Delta(\Lambda)$ for comparison.

While the solution of parquet and (loop-order-converged) mfRG equations must coincide, they are obtained in very different ways. The parquet equations can be solved by finding the vector-valued fixed-point of a non-linear equation, i.e., summarizing self-energy and vertex into the vector $\psi = (\Sigma, \Gamma)$ the parquet equations have the form $\psi = \mathbf{f}_{\text{PA}}(\psi)$. For increasing coupling $u = U/(\pi\Delta)$ it becomes more and more difficult to obtain a converged self-consistent solution (see Chapter 4). The mfRG arrives at a result by integrating a flow equation. However, the mfRG equations (2.77) have the form $\dot{\psi} = \mathbf{f}_{\text{mfRG}}(\psi, \dot{\psi})$, i.e., they involve self-consistency in the self-energy flow $\dot{\Sigma}$ which is solved by self-energy iterations as described by Algorithm 1 in Ref. [KvD18b]. They further require a loop expansion of differentiated vertices $\dot{\gamma}_r = \sum_{\ell} \dot{\gamma}_r^{(\ell)}$ until contributions from higher ℓ are negligible. Since a large number of loops and self-energy iterations would be numerically expensive, the analysis of convergence with loop order indicates whether and where the mfRG method is applicable in practice.

An analysis of multiloop convergence for the Anderson model has already been performed in the Matsubara formalism [CGKH⁺22]. There, the final result ψ_f of an mfRG flow from initial Λ_i to final Λ_f was compared with the expected parquet solution. Loop convergence was analyzed by limiting the maximal loop order and the maximal self-energy iterations. Figures 4-6 in Ref. [CGKH⁺22] show that convergence to the parquet solution is indeed achieved. The required loop order depends on the choice of regulator and the physical parameters (about 15 - 61 loop orders and 3 - 9 self-energy iterations, see Tab. II in [CGKH⁺22]). Interestingly, the convergence slows down for increasing u which coincides with the difficulty of finding a parquet solution.

Here we follow a slightly different strategy to investigate the convergence of mfRG to parquet results. For a fixed flow parameter Λ^* we compare the Λ -derivative $\dot{\psi}$ obtained from the parquet method and the mfRG (starting from a converged parquet solution ψ^*). First, $\dot{\psi}_{\text{mfRG}}$ is determined by evaluation of the mfRG flow equations up to various loop-orders N_{loops} and various numbers of self-energy iterations. The reference values $\dot{\psi}_{\text{parquet}}$ are computed with a finite-differences method using parquet solutions for $\Delta \approx \Delta(\Lambda^*)$. As finite-differences method we use the one described in Ref. [For88]. We choose an equidistant

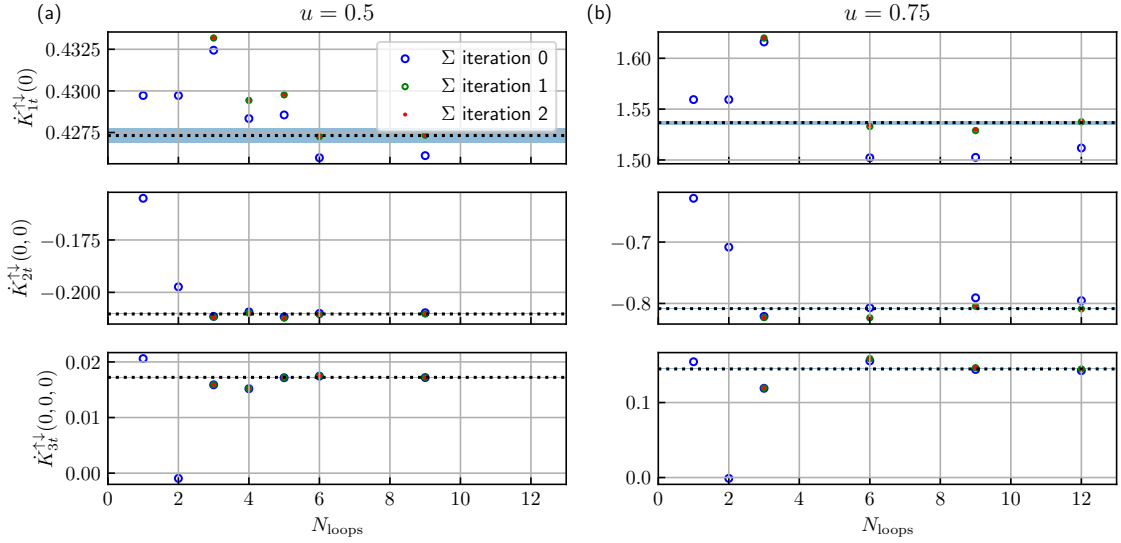


Figure B.1 We investigate multiloop convergence for the AIM in the MF at couplings (a) $u = 0.5$ and (b) $u = 0.75$. The three rows display the different asymptotic functions comprising $\hat{\gamma}_t$. (K_{2t} is identical to K_2 by symmetry.) The dotted line shows the numerical derivative of the parquet result and the blue shaded region indicates deviations within 0.1%. For $u = 0.5$ (perturbative regime) we find that five loops are sufficient to obtain a reasonably converged result. At $u = 0.75$ we see that loop convergence is achieved at 9 loops. The first self-energy iteration gives visibly better results. For fermionic Matsubara frequencies we approximate the value at zero frequency by averaging over the lowest points $\pm\pi T$.

set of Λ -values symmetrically around Λ^* . Here the step size $\delta_\Lambda = 0.01$ is chosen. With five points we approximate the derivative up to fourth order in δ_Λ .

This strategy effectively isolates systematic errors (due to truncation of the mFRG equations) from numerical errors which can accumulate and create feedback when integrating a flow. Furthermore, it greatly reduces the required numerical resources, since the analysis of multiloop convergence requires us to sweep through various values for the number of self-energy iterations N_Σ and maximal loop order N_{loops} . For a rough comparison of the numerical effort of the mFRG and parquet scheme, we may assume that each multiloop contribution $\hat{\gamma}_{r;L/C/R}^{(\ell)}$ in Eqs. (2.77) comes approximately at the same cost as a BSE (2.66). For N_Σ self-energy iterations and maximal loop order N_{loops} , a single evaluation of the mFRG equations corresponds to $N_\Sigma(N_{\text{loops}} - 1)$ BSE evaluations. In our scheme we need several parquet results. But this quickly pays off, since it reduces the number of evaluations of mFRG equations.

In Fig. B.1 we first analyze the convergence of the multiloop approximation $\sum_{\ell=1}^{N_{\text{loops}}} \hat{\gamma}_t^{(\ell)}$ in the Matsubara formalism. For comparison we show the parquet result (dotted line) and the region with 1% deviation (blue shaded area). The figure shows results for (a) $u = 0.5$ and (b) $u = 0.75$, respectively. For comparability, we focus on the point at zero frequency for which Matsubara functions have to coincide with the corresponding fully retarded Keldysh functions at zero frequency. Similar to [CGKH⁺22] we find that loop convergence is slower for stronger coupling. Convergence to the parquet result is reached within 6 or 9 loops, respectively. In both cases the first self-energy iteration gives visibly better results.

In Figs. B.2 and B.3, we then show real-frequency results. As expected from the calculations in the MF, we also confirm multiloop convergence in the right column of Fig. B.2. Most interestingly, however, we can analyze the frequency structure of individual multiloop

contributions (as shown in the left column of Figs. B.2 and B.3). The non-differentiated vertex Γ , one-loop contribution $\dot{\gamma}_r^{(1)}$ and multiloop contributions $\dot{\gamma}_{r;L/R/C}^{(\ell)}$ enter the integrand of higher-loop contributions $\dot{\gamma}_{r;L/R/C}^{(\ell+1)}$. Therefore, a good resolution of all vertex contributions is necessary to minimize propagation of numerical errors for an implementation of the mFRG flow equations with continuous frequencies.

As shown on the left side of Fig. B.2 the non-differentiated vertex (blue curve) tends to be the easiest to resolve. It is less sharply peaked and has less sign changes than the other curves. Among all components the ‘center’ contribution $\dot{\gamma}_{r;C}^{(\ell)}$ has the sharpest structures, demanding a particularly dense frequency grid. However, while the individual multiloop contributions develop sharp structures, their sum $\sum_{\ell=1}^{N_{\text{loops}}} \dot{\gamma}_r^{(\ell)}$ is rather well-behaved. Summed multiloop contributions for $N_{\text{loops}} = 1, 2, 3$ are shown in the right column of Fig. B.2. We observe that after combination of all contributions most structures cancel out and give a docile curve again.

We conclude that a calculation of the mFRG equations in the Keldysh formalism requires a higher resolution than a comparable parquet solver. This is partly due to the sharp features in the higher-loop contributions, partly to the iterative nature of the mFRG scheme which accumulates errors during the iterative loop expansion in the mFRG equations and during the iterative quadrature steps in Runge–Kutta methods. In addition, the mFRG equations do not fully circumvent the necessity of solving a self-consistent equation since the differentiated self-energy $\dot{\Sigma}$ and differentiated vertex $\dot{\gamma}_{r;C}$ also appear on the right-hand side of the mFRG equations. In comparison, the parquet equations directly compute the vertex Γ and self-energy Σ by self-consistency iterations. They thereby avoid the sharply peaked multi-loop contributions. Furthermore, fixed-point iterations suffer less from the propagation of errors. Therefore, for the chosen system and parameters the parquet approach tends to be more efficient than solving the mFRG equations.

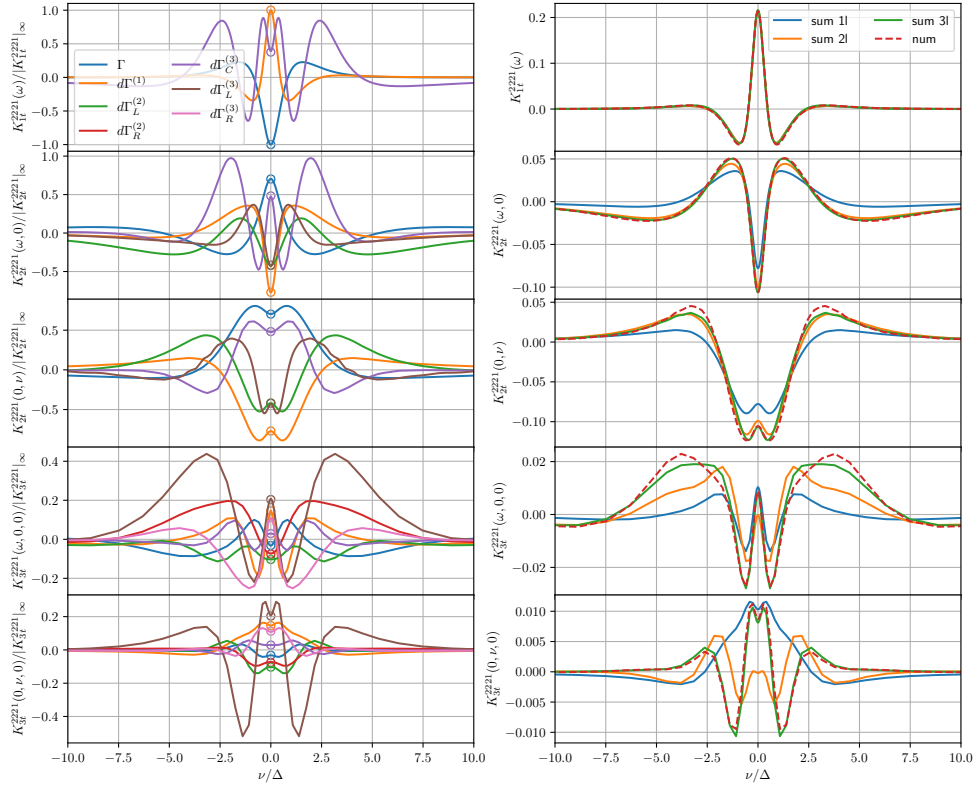
Multi-loop contributions for SIAM at $u = 0.5, T/U = 0.01$ (\uparrow)-component)

Figure B.2 We show multiloop contributions (2.77) to the fully retarded Keldysh vertex $\hat{\gamma}_t^{2221}$ at small coupling $u = 0.5$. Each row shows a slice through the asymptotic functions K_{it} ($i = 1, 2, 3$). The lines in the left column show the non-differentiated parquet result Γ (blue), the one-loop contribution $d\Gamma^{(1)}$ (2.77b), the ‘left’ $d\Gamma_L^{(\ell)}$ (2.77e), the ‘right’ $d\Gamma_R^{(\ell)}$ (2.77f) and the ‘center’ $d\Gamma_C^{(\ell)}$ (2.77g) contribution at different loop orders. We find good agreement with the Matsubara results (circles) at zero frequency. For better visibility all lines have been divided by the largest absolute value of the function. In the right column the red dashed line shows the numerical derivative (‘num’) computed from parquet results. We further show the summed multiloop contributions $\sum_{\ell=1}^{\ell_{\max}} \hat{\gamma}_t^{(\ell)}$ up to order $\ell_{\max} = 1, 2, 3$ (labeled by ‘sum $\ell_{\max}l$ ’). With increasing loop order ℓ_{\max} the curves approach the full derivative.

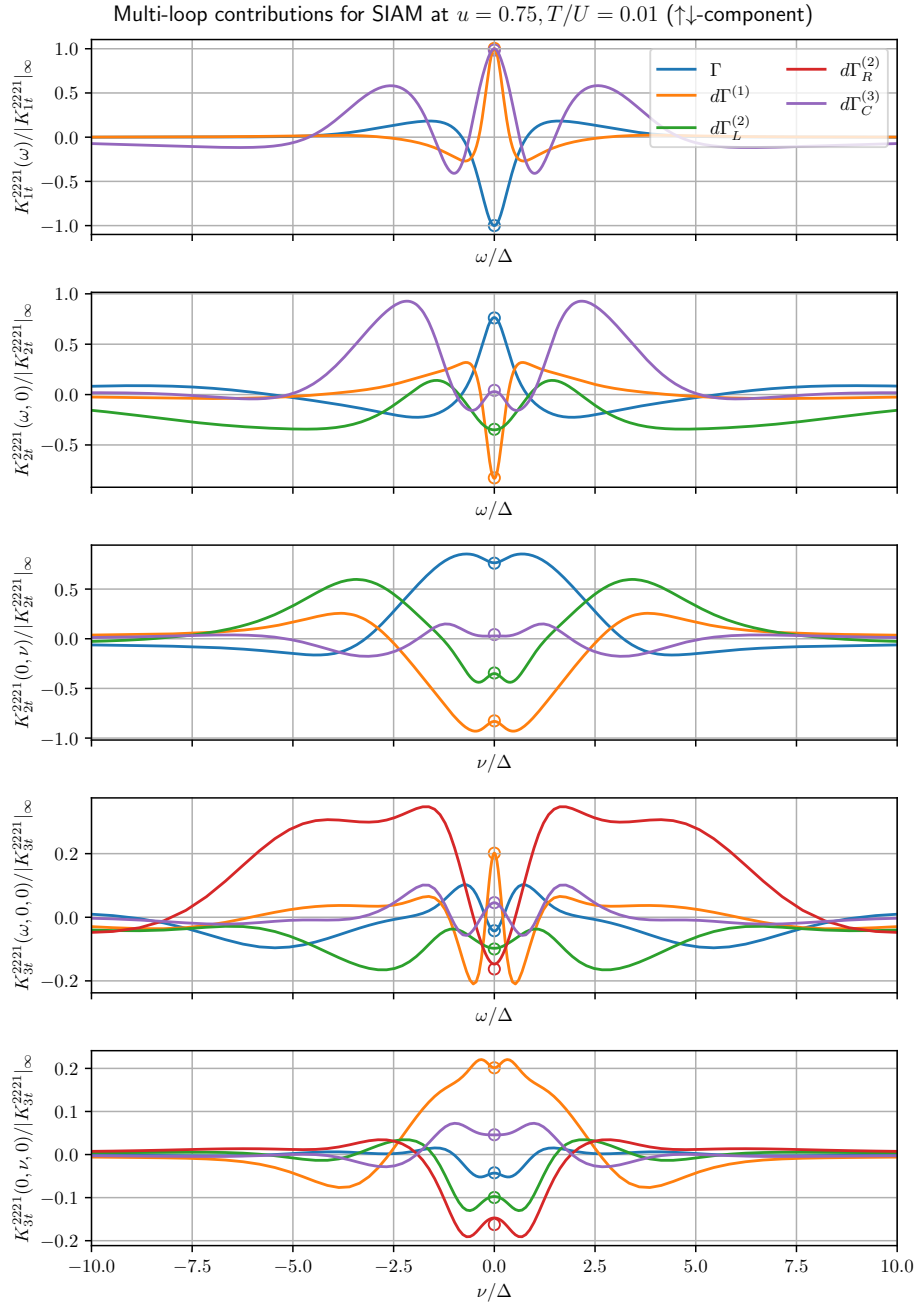


Figure B.3 Similar comparison as in the left column of Fig. B.2 for a different value of $u = 0.75$. Also here we find good agreement between Keldysh and Matsubara at zero frequency.

List of Figures

2.1	Keldysh contour	9
2.2	Parquet decomposition	21
2.3	Bethe–Salpeter equations	22
2.4	Schwinger–Dyson equations	23
2.5	1-loop flow equations	24
2.6	Multiloop flow equations	26
2.7	Frequency conventions	32
2.8	asymptotic functions	34
B.1	Convergence of mFRG (Anderson model $u = 0.5$ and $u = 0.75$)	204
B.2	Contributions to vertex flow in mFRG (Anderson model $u = 0.5$)	206
B.3	Contributions to vertex flow in mFRG (Anderson model $u = 0.75$)	207

Bibliography

- [Abr65] A. A. Abrikosov, *Electron scattering on magnetic impurities in metals and anomalous resistivity effects*, Physics Physique Fizika **2** (1965), 5–20. See page: 1
- [And61] P. W. Anderson, *Localized Magnetic States in Metals*, Phys. Rev. **124** (1961), 41–53. See page: 63
- [Ang08] M. Angst, *Correlated Electrons*, Neutron Scattering : Lectures of the JCNS Laboratory Course, Jülich & Garching, 1 Sep 2008, Sep 2008, Record converted from VDB: 12.11.2012. See page: 1
- [AS10] A. Altland and B. D. Simons, *Condensed Matter Field Theory*, 2 ed., Cambridge University Press, 2010. See pages: 12 and 16
- [AWH13] G. B. Arfken, H. J. Weber, and F. E. Harris, *Mathematical methods for Physics: A comprehensive guide*, 7 ed., Elsevier, 2013. See page: 14
- [BB15] P. Blanchard and E. Brüning, *Mathematical methods in Physics: Distributions, Hilbert space operators, variational methods, and applications in quantum physics*, vol. 69, Birkhäuser, 2015. See page: 13
- [BCP08] R. Bulla, T. A. Costi, and T. Pruschke, *Numerical renormalization group method for quantum impurity systems*, Rev. Mod. Phys. **80** (2008), 395–450. See pages: 2, 63, and 197
- [Bic04] N. E. Bickers, *Self-consistent many-body theory for condensed matter systems*, pp. 237–296, Springer New York, New York, NY, 2004. See pages: 2, 21, 28, and 31
- [BM61] G. Baym and N. D. Mermin, *Determination of thermodynamic Green’s functions*, J. Math. Phys. **2** (1961), 232–234. See pages: 6, 7, 12, and 149
- [BM86] J. G. Bednorz and K. A. Müller, *Possible high T_c superconductivity in the Ba-La-Cu-O system*, Z. Phys. B **64** (1986), 189–193. See page: 1
- [BTH⁺22] P. M. Bonetti, A. Toschi, C. Hille, S. Andergassen, and D. Vilaridi, *Single-boson exchange representation of the functional renormalization group for strongly interacting many-electron systems*, Phys. Rev. Res. **4** (2022), 013034. See page: 37
- [CGKH⁺22] P. Chalupa-Gantner, F. B. Kugler, C. Hille, J. von Delft, S. Andergassen, and A. Toschi, *Fulfillment of sum rules and Ward identities in the multiloop functional renormalization group solution of the Anderson impurity model*, Phys. Rev. Res. **4** (2022), 023050. See pages: 2, 27, 28, 63, 203, and 204
- [Col15] P. Coleman, *Introduction to Many-Body Physics*, Cambridge University Press, 2015. See pages: 16 and 199

- [COS18] N. Chikano, J. Otsuki, and H. Shinaoka, *Performance analysis of a physically constructed orthogonal representation of imaginary-time Green's function*, Phys. Rev. B **98** (2018), 035104. See page: 15
- [DJ21] J. Diekmann and S. G. Jakobs, *Parquet approximation and one-loop renormalization group: Equivalence on the leading-logarithmic level*, Phys. Rev. B **103** (2021), 155156. See page: 27
- [EFG⁺05] F. H. L. Essler, H. Frahm, F. Göhmann, A. Klümper, and V. E. Korepin, *The one-dimensional Hubbard model*, Cambridge University Press, 2005. See page: 1
- [EHHK20] C. J. Eckhardt, C. Honerkamp, K. Held, and A. Kauch, *Truncated unity parquet solver*, Phys. Rev. B **101** (2020), 155104. See page: 28
- [EKKH23] C. J. Eckhardt, P. Kappl, A. Kauch, and K. Held, *A functional-analysis derivation of the parquet equation*, SciPost Phys. **15** (2023), 203. See page: 21
- [Eli62] G.M. Eliashberg, *Transport equation for a degenerate system of Fermi particles*, Sov. Phys. JETP **14** (1962), 886–892. See page: 149
- [FB06] E. Freitag and R. Busam, *Funktionentheorie 1*, Springer-Lehrbuch, Springer Berlin Heidelberg, 2006. See page: 7
- [For88] B. Fornberg, *Generation of finite difference formulas on arbitrarily spaced grids*, Math. of Comput. **51** (1988), 699–706. See page: 203
- [FYG21] J. Fei, C. Yeh, and E. Gull, *Nevanlinna analytical continuation*, Phys. Rev. Lett. **126** (2021), 056402. See pages: 15 and 149
- [GKKR96] A. Georges, G. Kotliar, W. Krauth, and M. J. Rozenberg, *Dynamical mean-field theory of strongly correlated fermion systems and the limit of infinite dimensions*, Rev. Mod. Phys. **68** (1996), 13–125. See pages: 1, 28, 63, and 197
- [GML⁺11] E. Gull, A. J. Millis, A. I. Lichtenstein, A. N. Rubtsov, M. Troyer, and P. Werner, *Continuous-time Monte Carlo methods for quantum impurity models*, Rev. Mod. Phys. **83** (2011), 349–404. See page: 28
- [GSvDK24] M. Gievers, R. Schmidt, J. von Delft, and F. B Kugler, *Subleading logarithmic behavior in the parquet formalism*, arXiv preprint arXiv:2411.07226 (2024). See page: 61
- [Hew97] A. C. Hewson, *The Kondo problem to heavy fermions*, Cambridge Studies in Magnetism, no. 2, Cambridge university press, 1997. See page: 63
- [HLK21] V. Harkov, A. I. Lichtenstein, and F. Krien, *Parametrizations of local vertex corrections from weak to strong coupling: Importance of the Hedin three-leg vertex*, Phys. Rev. B **104** (2021), 125141. See pages: 2 and 37
- [HMPS04] R. Hedden, V. Meden, Th. Pruschke, and K. Schönhammer, *A functional renormalization group approach to zero-dimensional interacting systems*, Journal of Physics: Condensed Matter **16** (2004), 5279. See page: 23
- [HSS23] J. Halbinger, B. Schneider, and B. Sbierski, *Spectral representation of Matsubara n -point functions: Exact kernel functions and applications*, SciPost Phys. **15** (2023), 183. See pages: 8, 10, 11, 149, and 198

- [Hüf07] S. Hüfner, *Very high resolution photoelectron spectroscopy*, 1 ed., Lecture Notes in Physics, Springer Berlin Heidelberg, 2007. See page: 16
- [JPS10] S. G. Jakobs, M. Pletyukhov, and H. Schoeller, *Properties of multi-particle Green's and vertex functions within Keldysh formalism*, J. Phys. A **43** (2010), 103001. See pages: 6, 15, 30, 31, and 63
- [JS10] S. G. Jakobs and H. Schoeller, *Functional renormalization group studies of quantum transport through mesoscopic systems*, Ph.D. thesis, 2010. See pages: 5, 15, 21, 23, 24, 27, 29, and 63
- [Kad18] L. P. Kadanoff, *Quantum statistical mechanics*, CRC Press, 2018. See page: 15
- [Kam11] A. Kamenev, *Field theory of non-equilibrium systems*, Cambridge University Press, 2011. See pages: 1, 10, 18, and 19
- [Kat04] A. A. Katanin, *Fulfillment of Ward identities in the functional renormalization group approach*, Phys. Rev. B **70** (2004), 115109. See pages: 27 and 197
- [KBC⁺10] P. Kopietz, L. Bartosch, L. Costa, A. Isidori, and A. Ferraz, *Ward identities for the Anderson impurity model: derivation via functional methods and the exact renormalization group*, Journal of Physics A: Mathematical and Theoretical **43** (2010), 385004. See page: 28
- [KBS10] P. Kopietz, L. Bartosch, and F. Schütz, *Introduction to the functional renormalization group*, vol. 798, Springer Science & Business Media, 2010. See pages: 17, 21, 23, and 24
- [KCP22] J. Kaye, K. Chen, and O. Parcollet, *Discrete Lehmann representation of imaginary time Green's functions*, Phys. Rev. B **105** (2022), 235115. See page: 198
- [Kel] L. V. Keldysh, *Diagram technique for nonequilibrium processes*, pp. 47–55. See page: 1
- [KHP⁺08] C. Karrasch, R. Hedden, R. Peters, Th. Pruschke, K. Schönhammer, and V. Meden, *A finite-frequency functional renormalization group approach to the single impurity Anderson model*, Journal of Physics: Condensed Matter **20** (2008), 345205. See pages: 33 and 63
- [Klö19] Ch. Klöckner, *Functional renormalization group approach to correlated quantum systems far from equilibrium*, Ph.D. thesis, Freie Universität Berlin, 2019. See pages: 10, 15, and 19
- [KLvD21] F. B. Kugler, S. B. Lee, and J. von Delft, *Multipoint correlation functions: spectral representation and numerical evaluation*, Phys. Rev. X **11** (2021), 041006. See pages: 2, 5, 6, 8, 10, 11, 149, 198, and 201
- [Kon64] Jun Kondo, *Resistance Minimum in Dilute Magnetic Alloys*, Progress of Theoretical Physics **32** (1964), 37–49. See page: 63
- [KPBM10] C. Karrasch, M. Pletyukhov, L. Borda, and V. Meden, *Functional renormalization group study of the interacting resonant level model in and out of equilibrium*, Phys. Rev. B **81** (2010), 125122. See page: 27

- [Kub57] R. Kubo, *Statistical-mechanical theory of irreversible processes. I. General theory and simple applications to magnetic and conduction problems*, Journal of the Physical Society of Japan **12** (1957), 570–586. See page: 7
- [Kug19] F. B. Kugler, *Renormalization group approaches to strongly correlated electron systems*, Ph.D. thesis, LMU Munich, 2019. See pages: 21 and 28
- [KV19] F. Krien and A. Valli, *Parquetlike equations for the Hedin three-leg vertex*, Phys. Rev. B **100** (2019), 245147. See pages: 2 and 37
- [KVC19] F. Krien, A. Valli, and M. Capone, *Single-boson exchange decomposition of the vertex function*, Phys. Rev. B **100** (2019), 155149. See pages: 37 and 197
- [KvD18a] F. B. Kugler and J. von Delft, *Derivation of exact flow equations from the self-consistent parquet relations*, New Journal of Physics **20** (2018), 123029. See pages: 25, 27, 28, and 203
- [KvD18b] F. B. Kugler and J. von Delft, *Multiloop functional renormalization group for general models*, Physical Review B **97** (2018). See pages: 25, 27, 199, and 203
- [KvD18c] F. B. Kugler and J. von Delft, *Multiloop functional renormalization group that sums up all parquet diagrams*, Physical Review Letters **120** (2018). See page: 25
- [KWC97] J. Kroha, P. Wölfle, and T. A. Costi, *Unified description of Fermi and Non-Fermi Liquid Behavior in a Conserving Slave Boson Approximation for Strongly Correlated Impurity Models*, Phys. Rev. Lett. **79** (1997), 261–264. See page: 63
- [KWK⁺24] D. Kiese, N. Wentzell, I. Krivenko, O. Parcollet, K. Held, and F. Krien, *Embedded multi-boson exchange: A step beyond quantum cluster theories*, Phys. Rev. Res. **6** (2024), 043159. See page: 28
- [LHS⁺24] J. Lihm, J. Halbinger, J. Shim, J. von Delft, F. B. Kugler, and S. B. Lee, *Symmetric improved estimators for multipoint vertex functions*, Phys. Rev. B **109** (2024), 125138. See pages: 2, 28, 35, 64, and 197
- [LKvD21] S. B. Lee, F. B. Kugler, and J. von Delft, *Computing local multipoint correlators using the numerical renormalization group*, Phys. Rev. X **11** (2021), 041007. See pages: 2, 28, 64, and 197
- [Lut61] J. M. Luttinger, *Analytic properties of single-particle propagators for many-fermion systems*, Phys. Rev. **121** (1961), 942–949. See page: 14
- [MAE⁺08] V. Meden, S. Andergassen, T. Enss, H. Schoeller, and K. Schönhammer, *Fermionic renormalization group methods for transport through inhomogeneous Luttinger liquids*, New Journal of Physics **10** (2008), 045012. See page: 27
- [Mat55] T. Matsubara, *A new approach to quantum-statistical mechanics*, Progress of Theoretical Physics **14** (1955), 351–378. See page: 1
- [MS59] P. C. Martin and J. Schwinger, *Theory of many-particle systems. I*, Phys. Rev. **115** (1959), 1342–1373. See page: 7

- [MW66] N. D. Mermin and H. Wagner, *Absence of ferromagnetism or antiferromagnetism in one- or two-dimensional isotropic Heisenberg models*, Phys. Rev. Lett. **17** (1966), 1133–1136. See page: 28
- [Neg18] J. W. Negele, *Quantum many-particle systems*, CRC Press, 2018. See pages: 17 and 20
- [NnFJD⁺22] Y. Núñez Fernández, M. Jeannin, Ph. T. Dumitrescu, Th. Kloss, J. Kaye, O. Parcollet, and X. Waintal, *Learning Feynman diagrams with tensor trains*, Phys. Rev. X **12** (2022), 041018. See page: 198
- [P1] M. Gievers, E. Walter, A. Ge, J. von Delft, and F. B. Kugler, *Multiloop flow equations for single-boson exchange fRG*, The European Physical Journal B **95** (2022), 1–22. See pages: 2, 5, 35, 37, 61, and 197
- [P2] D. Kiese, A. Ge, N. Ritz, J. von Delft, and N. Wentzell, *MatsubaraFunctions.jl: An equilibrium Green's function library in the Julia programming language*, SciPost Phys. Codebases (2024), 24. See pages: 3, 5, 61, 64, and 197
- [P3] A. Ge, N. Ritz, E. Walter, S. Aguirre, J. von Delft, and F. B. Kugler, *Real-frequency quantum field theory applied to the single-impurity Anderson model*, Phys. Rev. B **109** (2024), 115128. See pages: 2, 5, 10, 16, 32, 33, 61, 64, and 197
- [P4] A. Ge, J. Halbinger, S. B. Lee, J. von Delft, and F. B. Kugler, *Analytic Continuation of Multipoint Correlation Functions*, Annalen der Physik **536** (2024), 2300504. See pages: 5, 12, 31, 149, and 199
- [P5] N. Ritz, A. Ge, E. Walter, S. Aguirre, J. von Delft, and F. B. Kugler, *KeldyshQFT: A C++ codebase for real-frequency multiloop functional renormalization group and parquet computations of the single-impurity Anderson model*, The Journal of Chemical Physics **161** (2024), 054118. See pages: 3, 5, 64, and 197
- [P6] N. Ritz, A. Ge, M. Pelz, J. von Delft, and F. B. Kugler, *Numerical fulfillment of the $U(1)$ Ward identity and the parquet equations for real-frequency correlation functions from the multipoint numerical renormalization group*, (in preparation), 2025. See pages: 2, 28, and 197
- [P7] M. Frankenbach, A. Ge, M. Ritter, N. Ritz, and J. von Delft, *Computing local vertex functions from NRG using tensor cross interpolation*, (in preparation), 2025. See page: 198
- [RHT⁺18] G. Rohringer, H. Hafermann, A. Toschi, A. A. Katanin, A. E. Antipov, M. I. Katsnelson, A. I. Lichtenstein, A. N. Rubtsov, and K. Held, *Diagrammatic routes to nonlocal correlations beyond dynamical mean field theory*, Rev. Mod. Phys. **90** (2018), 025003. See page: 1
- [RNnFW⁺24] M. K. Ritter, Y. Núñez Fernández, M. Wallerberger, J. von Delft, H. Shinaoka, and X. Waintal, *Quantics Tensor Cross Interpolation for high-resolution parsimonious representations of multivariate functions*, Phys. Rev. Lett. **132** (2024), 056501. See page: 198

- [Roh13] G. Rohringer, *New routes towards a theoretical treatment of nonlocal electronic correlations*, Ph.D. thesis, TU Wien, 2013. See pages: 21, 29, 30, 31, 32, 199, and 200
- [RVT12] G. Rohringer, A. Valli, and A. Toschi, *Local electronic correlation at the two-particle level*, Phys. Rev. B **86** (2012), 125114. See pages: 2, 23, 28, 31, and 201
- [Sch61] J. Schwinger, *Brownian motion of a quantum oscillator*, Journal of Mathematical Physics **2** (1961), 407–432. See page: 1
- [Smi92] R. A. Smith, *Planar version of Baym-Kadanoff theory*, Phys. Rev. A **46** (1992), 4586–4597. See page: 28
- [SOOY17] H. Shinaoka, J. Otsuki, M. Ohzeki, and K. Yoshimi, *Compressing Green’s function using intermediate representation between imaginary-time and real-frequency domains*, Phys. Rev. B **96** (2017), 035147. See pages: 2, 15, and 198
- [SWicv⁺21] Th. Schäfer, N. Wentzell, F. Šimkovic, Y. He, C. Hille, M. Klett, Ch. J. Eckhardt, B. Arzhang, V. Harkov, F. Le Régent, A. Kirsch, Y. Wang, A. J. Kim, E. Kozik, E. A. Stepanov, A. Kauch, S. Andergassen, Ph. Hansmann, D. Rohe, Y. M. Vilks, J. P. F. LeBlanc, Sh. Zhang, A.-M. S. Tremblay, M. Ferrero, O. Parcollet, and A. Georges, *Tracking the footprints of spin fluctuations: A multimethod, multimessenger study of the two-dimensional Hubbard model*, Phys. Rev. X **11** (2021), 011058. See page: 1
- [SWM⁺23] H. Shinaoka, M. Wallerberger, Y. Murakami, K. Nogaki, R. Sakurai, Ph. Werner, and A. Kauch, *Multiscale space-time ansatz for correlation functions of quantum systems based on quantum tensor trains*, Phys. Rev. X **13** (2023), 021015. See page: 198
- [TAB⁺14] C. Taranto, S. Andergassen, J. Bauer, K. Held, A. Katanin, W. Metzner, G. Rohringer, and A. Toschi, *From infinite to two dimensions through the functional renormalization group*, Phys. Rev. Lett. **112** (2014), 196402. See pages: 28 and 63
- [THK⁺19] A. Tagliavini, C. Hille, F. B. Kugler, S. Andergassen, A. Toschi, and C. Honerkamp, *Multiloop functional renormalization group for the two-dimensional Hubbard model: Loop convergence of the response functions*, SciPost Phys. **6** (2019), 009. See pages: 27 and 28
- [TKH07] A. Toschi, A. A. Katanin, and K. Held, *Dynamical vertex approximation: A step beyond dynamical mean-field theory*, Phys. Rev. B **75** (2007), 045118. See pages: 28, 37, and 63
- [VT97] Y.M. Vilks and A.-M.S. Tremblay, *Non-perturbative many-body approach to the Hubbard model and single-particle pseudogap*, J. Phys. I France **7** (1997), 1309–1368. See page: 28
- [Wal21] E. Walter, *Real-frequency dynamics of quantum impurity models studied with frg, nrg, cft*, Ph.D. thesis, Ludwig-Maximilians-Universität München, 2021. See pages: 5, 15, and 35
- [Wel05] H. A. Weldon, *Search for combinations of thermal n -point functions with analytic extensions*, Physical Review D **71** (2005), 036002. See page: 149

- [Wet93] Ch. Wetterich, *Exact evolution equation for the effective potential*, Physics Letters B **301** (1993), 90–94. See page: 24
- [WFHT22] C. Watzenböck, M. Feller, K. Held, and A. Toschi, *Long-term memory magnetic correlations in the Hubbard model: A dynamical mean-field theory analysis*, SciPost Phys. **12** (2022), 184. See page: 12
- [WH02] E. Wang and U. Heinz, *Generalized fluctuation-dissipation theorem for non-linear response functions*, Phys. Rev. D **66** (2002), 025008. See pages: 31 and 149
- [WLT⁺20] N. Wentzell, G. Li, Agnese T., C. Taranto, G. Rohringer, K. Held, A. Toschi, and S. Andergassen, *High-frequency asymptotics of the vertex function: Diagrammatic parametrization and algorithmic implementation*, Physical Review B **102** (2020), 085106. See pages: 28, 34, 197, 199, 200, and 201
- [WSK21] M. Wallerberger, H. Shinaoka, and A. Kauch, *Solving the Bethe-Salpeter equation with exponential convergence*, Phys. Rev. Res. **3** (2021), 033168. See page: 198
- [ZG24] L. Zhang and E. Gull, *Minimal pole representation and controlled analytic continuation of Matsubara response functions*, Phys. Rev. B **110** (2024), 035154. See pages: 15 and 149

